PhD Thesis

MORPHO-SEDIMENTARY DYNAMICS OF MOUNTAIN RIVERS AFFECTED BY HYDROPEAKS

Fanny Ville

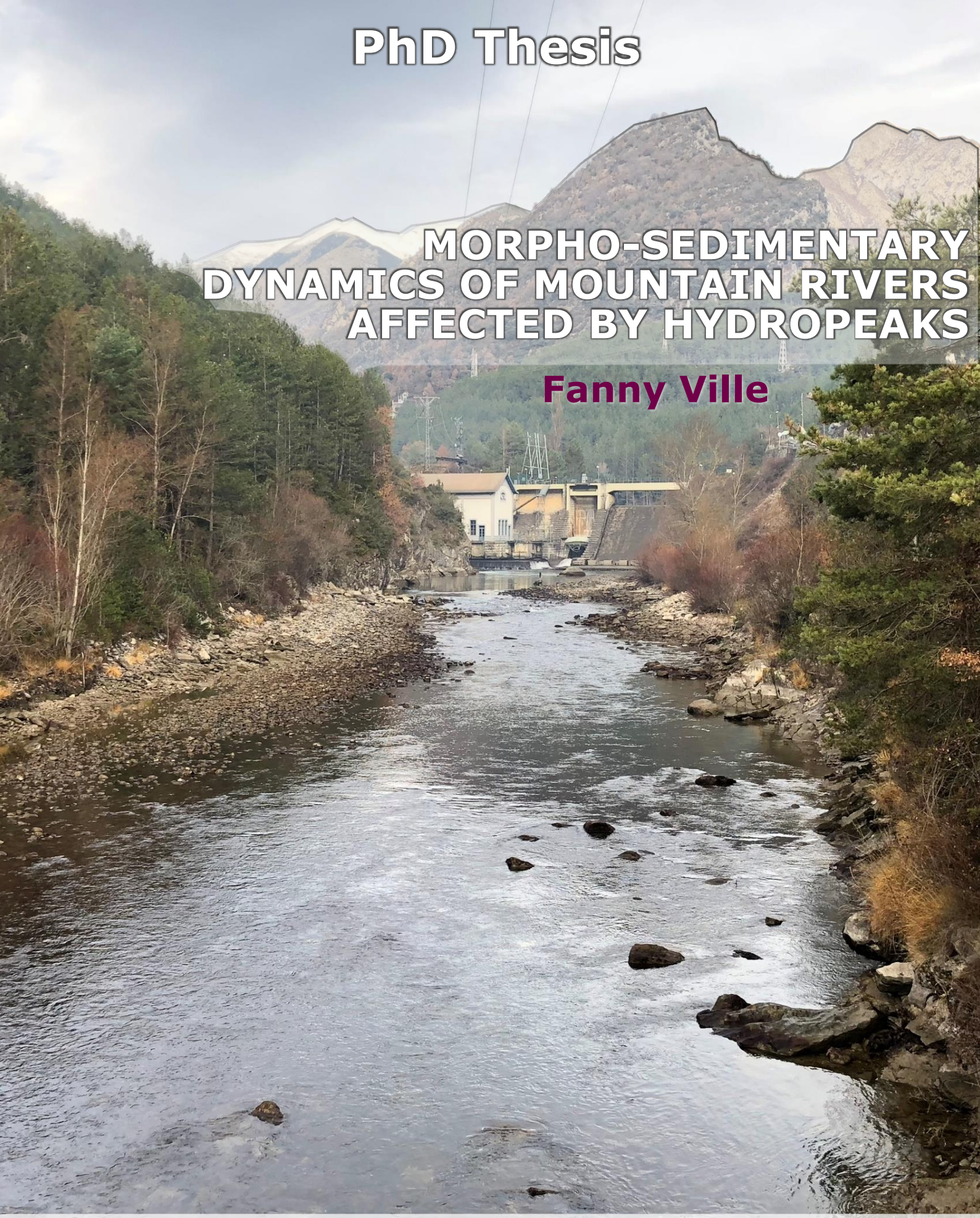

A thesis presented for the degree of doctor at the University of Lleida

2024

Universitat de Lleida

Fluvial Dynamics Research Group

RIUS

Cover photo: Ésera river downstream Campo Dam during base flow,

December 2018.

Author: Fanny Ville

Universitat de Lleida

TESI DOCTORAL

Morpho-sedimentary dynamics of mountain rivers affected by hydropeaks

Fanny VILLE

Memòria presentada per optar al grau de Doctor per la Universitat de Lleida
Programa de Doctorat en Gestió Forestal i del Medi Natural

Directors
Damià Vericat
Ramon J. Batalla
Colin Rennie

Tutor
Damià Vericat

2024

ACKNOWLEDGEMENTS

What an adventure this thesis, in Spain, in Catalonia, in Lleida. Some 6 or 7 years ago, I would never have imagined starting a doctoral thesis or even living in Catalonia. Now, after five years of effort and sacrifice, but also of adventure, joy and exploration of various aspects of professional and personal life, here I am, writing the last lines of this volume, which would not have been possible without the many people I have met along the way. I don't know what words to use to thank you, they will be weak compared to what you have given me.

I want first of all to thank and express my deep gratitude to my thesis supervisors, **Damià Vericat**, **Ramon J. Batalla** and **Colin Rennie**. Thank you for giving me the opportunity to carry out this thesis and for accompanying me. I am very lucky to have met you. Thank you for making such an interesting and diverse project possible. I would never have done a thesis other than this one. **Damià**, I don't have the words to thank you. Thank you for the sacrifices you made for all of us. Thank you for your generosity, from our first email exchange to this day. You have always found solutions to every problem, whether technical, administrative or 'social', and you have always found the right words to motivate me, to give me the strength to go far. Thank you for everything you taught me and for all those hours, often consecutive, of intense brainstorming in 5B that made our head hurt. It was all really enjoyable science. **Ramon**, my bad cop, from further away you pushed me with useful interventions at the right time every time. Thank you for giving me the time to explore so many paths, even when they didn't lead me along the shortest route. Thank you, Ramon, for the trust you placed in me and the resources you invested despite the relatively long time it took me to complete this thesis. **Colin**, thank you for your time and the interest you gave to my work, for your visits to Lleida to go through the data and your comments from a more external point of view, which helped to improve the famous PhotoMOB method, a little to the detriment of the ADCP data, it's true. These are waiting in the warmth of my disks among the 8 TB of accumulated data and files.

I would like to thank **Xavier Úbeda** and **Daniel Vázquez-Tarrío** for accepting to review this work, as well as **Carles Balasch**, and **Hervé Piégay** for agreeing to be a member of my thesis panel and to assess the quality of this work, which is a little long to read.

If I am where I am today, it's also thanks to the people I met along the way during my years of study, some of them probably unaware of it. From Tours, thank to **Stéphane Rodrigues** for his passionate and dynamic courses in fluvial geomorphology, to **Florence Curie** for having trained us very well in GIS and for having caught me on the fly when I was losing the motivation to continue, to **Nathalie Gassama** for having given me a 'boost', to **Sebastien Salvador** for his passionate courses and for having allowed me to do my degree thesis on the dynamics of suspended sediment in the small Louroux basin. Finally, thanks to **Juliane Ledys**, a friend from class and a wonderful girl! Thank you for your patience, thank you for teaching me determination and for showing me that when we don't know something, we look for it, and we end up finding it!

Further south from Tours, in Marseille, I met a trio who really got me into research: **Michal Tal**, Jonathan Coutaz and Daniel Vázquez-Tarrío. It was you, Michal, who started to get it into my head that a thesis was achievable, even if I thought it was something unattainable for someone like me. **Jonathan**, what can I say, I learnt a thousand things from you, you made me discover what gravel-bed rivers were, the technique of photogrammetry, and above all you made me (re)discover climbing. Thank you for this practical tool that frees the mind. Thank you for your precious advices. **Daniel Vázquez-Tarrío**, or **Danibib**, thank you for that time, which now seems so long ago, for your time and for sharing your knowledge with so much pedagogy. Not forgetting some great moments of laughter. I'm very grateful to you for always following me from afar, without you none of this would have happened, and for pushing me (enrolling me?) in this thesis. Now you are going to evaluate my work. I hope I am up to the level.

Still to the south, further west, near Toulouse, thank the whole ECOGEA team, and especially **Philippe Baran**, for taking me along various rivers and getting me started on characterising the risks associated with hydropeaking. I sincerely hope that we will be able to work together again and remake the world.

To carry out this thesis, even further south from my town, on the other side of the Pyrenees, nothing would have been possible without the welcome, help and availability of the members of the RIUS group and the environmental and soil science department (which has changed of name, but I am not good at remembering all these acronyms) and the friendship of some very precious people. **Maaneeel**, gràcies per la teua acollida, la teua ajuda, per guiar-me al principi, la teua amistat, el teu suport, els teus consells sobre arboricultura. **Antoni,** el meu veí d'oficina, gràcies per la teua amistat i suport. Gràcies per haver acceptat seguir-me (en diverses ocasions!), a l'Ésera i al Cinca per ficar GCPs. Quines aventures, pintura artística, escalada i una llarga espera enganxat de l'altre costat de l'Ésera durant una hydropunta. Gràcies durant els últims mesos per haver vingut amb mi al roco. **Meritxell**, la meua professora de Catala, he perdut molt desde que vas martxar. Ara em fa vergonya de expressar-me una mica. Com et puc donar les gràcies? No ho sé. Una gran part de les dades de qualitat recollides va ser gràcies a la teua ajuda, la teua meticulositat i la teua paciència. Totes aquelles sortides de camp, juntes, de tots els temps (calor extrema, pluja, tempesta, fred, vent), escalar per arribar a les estacions, a les ISCO, recollir dades, prendre notes, baixar, tornar a pujar, tornar enrere, tornar a donar la volta, recollir còdols, mesurar còdols. Gràcies per la iniciació a l'IBER, per la teua ajuda en el tractament dels DEM i per la qualitat del teu treball. **Estrella**, mi profesora de español, he progresado gracias a ti. Gracias por tu ayuda, tu disponibilidad, tu apoyo, tu amistad y tu atención. Gracias por cuidar de mí durante estos últimos meses difíciles. Ahora me toca a mí cuidar de ti. **Alvaro**, gracias por tu amistad, tu apoyo y tu pacífica presencia. **Théo**, mon compatriote, tu as rendu tout bien plus fun. A tots vosaltres, a més de Damià i Ramon, heu estat els meus pilars a Lleida, gràcies.

Moltes gràcies també al **David Estany** per ajudar-me a mantenir les estacions de mesura en bon funcionament, instal·lar-ne de noves i millorar-les, sense el teu preciós saber fer, això no hauria estat possible; à **Raúl López** pour sa grande pédagogie, sa confiance, le temps qu'il m'a accordé, toutes ses réponses très détaillées à mes interrogations, a la **Maria Bejar** para la transferencia de datos relativos al Cinca, datos clave para la tesis; a la **Montse** per deixar-me fer alguna filtració al laboratori de vegades, gràcies per la teua amabilitat i atenció; a l'**Antoni Palau (pare)** per aquelles discussions tan interessants sobre preses i bichos; i clars per a la **Clara**!!! per tots els papers, sobretot la teva paciència, perquè paper, signatures electròniques i jo, en fem tres!!! al **personal del Campus ESTEA** (que ha canviat de nom, amb unes noves sigles que ni tan sols vaig intentar recordar), a totes les persones que el fan funcionar, i als que em van atendre directament, a la consergeria i a seguretat al vespre i al matí (molt d'hora, molt tard).

I thank also all the people I might have forgotten in this long list.

Enfin, merci à ma famille et ma meilleure amie, **Mathilde**, malgré la distance et mon silence, tu es toujours là. J'ai hâte de pouvoir écrire de nouvelles histoires avec toi. **Papa**, **Léo** (mi hermano) Maman, merci pour votre soutien, par téléphone, pour avoir pris de mes nouvelles, car j'ai tendance à faire silence radio. Merci de vos quelques visites à Lleida. **Maman**, merci pour ton soutien inconditionnel, de la révision de photos de cailloux avec moi, jusqu'à la fin de cette thèse par les relectures attentives de ces chapitres à suivre. Tu connais tout de cette thèse.
Merci à toi **Alexandre Moron**, pour m'avoir suivi, pour avoir quitté la France, pour avoir fait ces sacrifices pour moi, pour m'avoir beaucoup donné, pour m'avoir écouté des heures durant parler de rivière, de débit, de cailloux, de PhotoMOB, pour m'avoir construit le cadre, la Pebble-Box et sûrement d'autres choses dont je ne me rappelle plus, pour avoir accepté de venir intensivement m'aider durant 2 mois pour suivre la mobilité et transporter tout le matériel. Tu connais aussi bien que moi comment bougent partiellement les cailloux de ces deux magnifiques rivières. Merci pour cette aventure et cet apprentissage de la vie en parallèle de la thèse, de ce mode de vie dans lequel tu nous as fait évoluer, et qui nous mènera loin, je le sais. Tu es mon roc, merci mon amour.

FOUNDING

This PhD was undertaken thanks to the financial support of the MorphHab (Grant No. PID2019-104979RBI00/AEI/10.13039/501100011033) and the MorphPeak (Grant No. CGL2016-78874-R/AEI/10.13039/501100011033) projects funded by the Research State Agency (AEI), Spanish Ministry of Economy and Competiveness, Science and Innovation, and the European Regional Development Fund Scheme.

The candidate had a grant funded by the Ministry of Economy, Industry and Competitiveness, Spain (BES-2017-081850) and is part of the Fluvial Dynamics Research Group –RIUS, a consolidated group recognized by the Generalitat de Catalunya (2021 SGR 01114).

INDEX

Summary

Many mountain rivers are subjected to hydropeaks, rapid water releases from hydroelectric power stations (HP) for electric production. This thesis focuses on the temporal and spatial (i.e. longitudinal) hydrological characterization of artificial fluctuations and their effects on bed mobility dynamics in two contrasting river systems. Two Pyrenean Mountain river segments were studied: a 12 km segment in the Upper Cinca and a 18.5 km segment in the Upper Ésera. Both are located at the end of the cascade of a modified Run-Of-River type HP network, i.e. turbining the natural water inflows but with the presence of dams allowing a storage capacity ranging from a few hours to a few days. The segment on the Cinca, downstream of a dam allowing water and sediment to pass through during flood periods, has a wide active width. The segment on the Ésera, downstream of a dam on the course of the river that does not allow sediment to pass through, has a single channel confined to a narrow, tortuous valley. The thesis encompasses the establishment, calibration, and maintenance of monitoring stations, field sampling, laboratory work, the creation of new analytical tools, hydraulic modelling, statistical treatment of the data, as well as remote sensing and Geographic Information System-based analyses.

The segment of the Ésera with the upstream largest relative cumulative storage capacity volume showed a more marked hydrological alteration. Around 70% of the volume flowing annually was in the form of hydropeaks (compared with 30-40% in the Cinca), while the base flows left in the river when the turbines were not producing were kept low by storing the water for future production. As a result, the median base flow to peak flow ratios during production were 1:12.6 compared with only 1:4 on the Cinca. The hydropeaks are generated mainly in the form of *Front Step,* implying rapid variations in hydraulic conditions downstream. Normalised ramping rates are 2 times higher in the Ésera than in the Cinca. The longitudinal propagation of the hydropeaks in the form of a wave affecting the channel and lateral margins (*ramping area*), differs according to the river morphology. A median reduction of 70% in the increase ramping rate was observed at 10 km from the HP on the Cinca, linked to a retention effect caused by the large wetted widths. In contrast, on the Ésera, despite a similar bed slope, but with a relatively smaller wetted width (width/depth ratio at median flow one-third lower), no significant attenuation was observed along the 18.5 km. The development of the PhotoMOB tool, which makes it possible to obtain the size and dynamics of particles from consecutive photos of the bed, has enabled detailed observations and analysis of the competence of hydropeaks and floods. The analysed hydropeaks did not lead to significant changes in the bed grain size distribution at the event scale. The mode of transport on these two segments is partially selective. However, in the Ésera, hydropeaks of median intensity could cause marginal mobility (<10%) in the ramping area up to entrain relatively coarse grain sizes without mobilizing relatively finer grains. For hydropeaks of higher intensity, often superimposed on rainfall events, partial destabilization (between 10 and 90%) of grain sizes similar to the 16th percentile of the distributions was observed on both segments, particularly downstream of tributaries. The upstream parts close to the HP show long-term alteration due to the presence and functioning of the latter, characterised by coarse and relatively stable surfaces associated with a partial sediment deficit on the Cinca and a more marked deficit on the Ésera.

Key words
hydropeaks, hydroelectricity, mountain rivers, Upper Cinca river, Upper Ésera river, longitudinal propagation of hydropeaks, PhotoMOB GIS tool, bed mobility, bed stability, incipient grain motion, selective mobility, partial mobility.

Resumen

Muchos ríos de montaña están sujetos a hidropuntas, rápidas liberaciones de agua de las centrales hidroeléctricas (CH) para la producción de electricidad. Esta tesis se centra en la caracterización hidrológica (temporal y espacial, es decir, longitudinal) de hidropuntas y sus efectos sobre la dinámica de movilidad del lecho de dos sistemas fluviales contrastantes. Se han estudiado dos tramos fluviales de montaña pirenaicos: un tramo de 12 km en el Alto Cinca y otro de 18,5 km en el Alto Ésera. Ambos se encuentran al final de la cascada de una red de centrales hidroeléctricas de tipo *Run-Of-River* modificado, es decir, turbinan los flujos naturales de agua, pero con la presencia de presas que permiten una capacidad de almacenamiento que va desde unas pocas horas hasta unos días. El tramo del Cinca, aguas abajo de una presa que permite la transferencia de agua y sedimentos durante crecidas, tiene una gran anchura activa.

El tramo del Ésera, aguas abajo de una presa en el curso del río que no permite la transferencia de sedimentos, tiene un único cauce confinado a un valle estrecho y tortuoso. La tesis abarca el establecimiento, calibración y mantenimiento de estaciones de monitoreo, muestreo de campo, trabajos de laboratorio, la creación de nuevas herramientas analíticas, modelización hidráulica, tratamiento estadístico de los datos, así como la aplicación de técnicas de teledetección y Sistemas de Información Geográfica. El segmento del Ésera con mayor volumen de capacidad acumulada de almacenamiento relativo aguas arriba muestra una alteración hidrológica más marcada. Alrededor del 70% del volumen que fluye anualmente proviene de hidropuntas (en comparación con el 30-40% en el Cinca), mientras que los caudales base que quedan en el río cuando las turbinas no estaban produciendo se mantenían bajos almacenando el agua para futuras producciones. Como resultado, las relaciones entre el flujo base medio y el flujo máximo durante la producción son de 1:12,6 en comparación con solo 1:4 en el Cinca. Las hidropuntas se generan principalmente en forma de *Front Step*, lo que implica rápidas variaciones en las condiciones hidráulicas aguas abajo. El incremento de caudal normalizado de la rampa de subida de las hidropuntas es 2 veces superior en el Ésera que en el Cinca. La propagación longitudinal de las hidropuntas en forma de onda afectando el cauce y los márgenes laterales (*zona de rampa*), difiere según la morfología del río. Se observa una reducción media del 70% en la tasa de cambio en la rampa de subida a 10 km de la HP en el Cinca, ligada a un efecto de retención causado por la mayor anchura del cauce mojado. Por el contrario, en el Ésera, a pesar de una pendiente del lecho similar, pero con un cauce mojado relativamente menor (la relación ancha/profundidad para un caudal medio es un tercio menor), no se observa atenuación significativa a lo largo de los 18,5 km. El desarrollo de la herramienta PhotoMOB, que permite obtener el tamaño y la dinámica de las partículas a partir de fotografías consecutivas del lecho, ha permitido realizar observaciones detalladas y analizar la competencia de las hidropuntas y las crecidas. Las hidropuntas analizadas no generan cambios significativos en la distribución del tamaño de partículas del lecho a escala de evento. El modo de transporte en estos dos segmentos es parcialmente selectivo. Sin embargo, en el Ésera, las hidropuntas de intensidad media pueden causar movilidad marginal (<10%) en el área mojada influenciada por las hidropuntas (zona de rampa), pudiendo también movilizar tamaños de grano relativamente gruesos sin movilizar los más finos. Para las hidropuntas de mayor intensidad, a menudo superpuestos a eventos de lluvia, se observó una desestabilización parcial (entre 10 y 90%) de tamaños similar al percentil 16 de las distribuciones granulométricas en ambos segmentos, particularmente aguas abajo de los afluentes. Las partes de aguas arriba cercanas a las CH presentan una alteración de larga duración debido a la presencia y funcionamiento de este último, caracterizándose por superficies rugosas y relativamente estables asociadas a un déficit parcial de sedimentos en el Cinca y un déficit más acusado en el Ésera.

Palabras clave
hidropuntas, hidroelectricidad, ríos de montaña, Río Alto Cinca, Río Alto Ésera, propagación longitudinal de hidropuntas, herramienta SIG PhotoMOB, inicio del movimiento de los granos, movilidad del lecho, estabilidad del lecho, movilidad selectiva, movilidad parcial.

Resum

Molts rius de muntanya estan sotmesos a hidropuntes, ràpides alliberacions d'aigua de les centrals hidroelèctriques (CH) per a la producció d'electricitat. Aquesta tesi es centra en la caracterització hidrològica (temporal i espacial, és a dir, longitudinal) de les hidropuntes i els seus efectes sobre la dinàmica de mobilitat de la llera de dos sistemes fluvials contrastants. S'han estudiat dos trams fluvials de muntanya pirenaiques: un tram de 12 km a l'Alt Cinca i un altre de 18,5 km a l'Alt Ésera. Tots dos es troben al final de la cascada d'una xarxa de centrals hidroelèctriques de tipus *Run-Of-River* modificat, és a dir, turbinant els fluxos naturals d'aigua, però amb la presència de preses que permeten una capacitat d'emmagatzematge que va des d'unes poques hores fins a uns dies. El tram del Cinca, agafant aigües avall d'una presa que permet la transferència d'aigua i sediments durant les crescudes, té una gran amplada activa. El tram de l'Ésera, agafant aigües avall d'una presa en el curs del riu que no permet la transferència de sediments, té un únic cabal confinat en un estret i tortuós congost. La tesi combina l'establiment, calibració i manteniment d'estacions de monitoratge, mostreig de camp, treballs de laboratori, la creació de noves eines analítiques, modelització hidràulica, tractament estadístic de les dades, així com l'aplicació de tècniques de teledetecció i Sistemes d'Informació Geogràfica.

El tram de l'Ésera amb major volum de capacitat acumulada d'emmagatzematge relatiu aigües amunt mostra una alteració hidrològica més marcada. Al voltant del 70% del volum que flueix anualment prové d' hidropuntes (en comparació amb el 30-40% al Cinca), mentre que els cabals base que resten al riu quan les turbines no estaven produint es mantenien baixos emmagatzemant l'aigua per a futures produccions. Com a resultat, les relacions entre el flux base mitjà i el flux màxim durant la producció són de 1:12,6 en comparació amb només 1:4 al Cinca. Les hidropuntes es generen principalment en forma de *Front Step*, el que implica ràpides variacions en les condicions hidràuliques aigües avall. L'increment de cabal normalitzat de la rampa de pujada de les hidropuntes és 2 vegades superior a l'Ésera que al Cinca. La propagació longitudinal de les hidropuntes en forma d'ona afectant el canal i els marges laterals (*zona de rampa*), difereix segons la morfologia del riu. Es va observar una reducció mitjana del 70% en la taxa de canvi en la rampa de pujada a 10 km de la HP al Cinca, lligada a un efecte de retenció causat per la major amplada del canal mullat. Pel contrari, a l'Ésera, malgrat una pendent del llit similar, però amb un canal mullat relativament menor (la relació amplada/profunditat per a un cabal mitjà és un terç menor), no es va observar atenuació significativa al llarg dels 18,5 km. El desenvolupament de l'eina PhotoMOB, que permet obtenir la mida i la dinàmica de les partícules a partir de fotografies consecutives del llit, ha permès realitzar observacions detallades i analitzar la competència de les hidropuntes i les crescudes. Les hidropuntes analitzades no generen canvis significatius en la distribució de la mida de partícules de la llera a escala d'esdeveniment. El mode de transport en aquests dos segments és parcialment selectiu. No obstant això, a l'Ésera, les hidropuntes d'intensitat mitjana poden causar mobilitat marginal (<10%) a l'àrea influïda per les hidropuntes (zona de rampa), podent també mobilitzar mides de gra relativament grollerses sense mobilitzar els materials més fins. Per a les hidropuntes de major intensitat, sovint superposats a esdeveniments de pluja, es va observar una desestabilització parcial (entre el 10 i el 90%) de mides semblants al percentil 16 de les distribucions granulomètriques en ambdós segments, particularment aigües avall dels afluents. Les parts d'aigües amunt properes a les CH presenten una alteració de llarga durada a causa de la presència i funcionament d'aquesta última, caracteritzant-se per superfícies rugoses i relativament estables associades a un dèficit parcial de sediments al Cinca i un dèficit més acusat a l'Ésera.

Paraules clau
hidropuntes, hidroelectricitat, rius de muntanya, Riu Cinca superior, Riu Ésera superior, propagació longitudinal d'hydropuntes, eina GIS PhotoMOB, inici del moviment dels grans, mobilitat del llit, estabilitat del llit, mobilitat selectiva, mobilitat parcial.

Résumé

De nombreuses rivières de montagne sont soumises à des éclusées, des lâchers d'eau rapides provenant de centrales hydroélectriques (CH) pour la production d'électricité. Cette thèse se concentre sur la caractérisation hydrologique temporelle et spatiale (c'est-à-dire longitudinale) des fluctuations artificielles et leurs effets sur la dynamique de la mobilité du lit dans deux systèmes fluviaux contrastés. Deux segments de rivière de montagnes pyrénéennes ont été étudiés : un segment de 12 km dans le Cinca supérieur et un segment de 18.5 km dans l'Ésera supérieur. Tous deux sont situés à la fin de la cascade d'un réseau CH de type *Run-Of-River* modifié, c'est-à-dire turbinant les apports d'eau naturels mais avec la présence de barrages permettant une capacité de stockage allant de quelques heures à quelques jours. Le tronçon sur le Cinca, en aval d'un barrage laissant passer l'eau et les sédiments en période de crue, présente une grande largeur active. Le tronçon de l'Ésera, en aval d'un barrage sur le cours de la rivière qui ne permet pas le passage des sédiments, présente un chenal unique confiné dans une vallée étroite et tortueuse. La thèse comprend l'établissement, l'étalonnage et l'entretien de stations de surveillance, l'échantillonnage sur le terrain, le travail en laboratoire, la création de nouveaux outils analytiques, la modélisation hydraulique, le traitement statistique des données, ainsi que des analyses basées sur la télédétection et les Systèmes d'Informations Géographiques.

Le segment de l'Ésera avec le volume de stockage cumulé relatif amont le plus important montrait une altération hydrologique plus marquée. Environ 70 % du volume s'écoulant annuellement se présentait sous la forme d'éclusées (contre 30 à 40 % dans la Cinca), tandis que les débits de base laissés à la rivière lorsque les turbines ne produisaient pas étaient maintenus à un faible débit dû au stockage de l'eau pour une production future. En conséquence, le rapport médian entre le débit de base et le débit de pointe pendant la production était de 1:12.6, contre seulement 1:4 pour la Cinca. Les éclusées sont générées principalement sous la forme de *Front Step*, impliquant des variations rapides des conditions hydrauliques en aval. Les gradients de vitesse de montée normalisés sont deux fois plus élevés dans l'Ésera que dans le Cinca. La propagation longitudinale des éclusées sous la forme d'une onde affectant le chenal et les marges latérales (*zone de marnage*), diffère selon la morphologie de rivière. Une réduction médiane de 70% des gradients de vitesse de montée a été observée à 10 km de la CH sur le Cinca, liée à un effet de rétention causé par les grandes largeurs mouillées. En revanche, sur l'Ésera, malgré une pente de lit similaire, mais avec une largeur mouillée relativement plus faible (rapport largeur/profondeur au débit médian inférieur d'un tiers), aucune atténuation significative n'a été observée sur les 18.5 km. Le développement de l'outil PhotoMOB, qui permet d'obtenir la taille et la dynamique des particules à partir de photos consécutives du lit, a permis d'observer et d'analyser en détail la compétence des éclusées et des crues. Les éclusées analysées n'ont pas conduit à des changements significatifs dans la distribution granulométrique du lit à l'échelle de l'événement. Le mode de transport sur ces deux segments est partiellement sélectif. Cependant, dans l'Ésera, les éclusées d'intensité médiane pouvaient provoquer une mobilité marginale (<10%) dans la zone de marnage jusqu'à entraîner des granulométries relativement grossières sans mobiliser de grains relativement plus fins. Pour les éclusées d'intensité plus élevée, souvent superposés à des événements pluvieux, une déstabilisation partielle (entre 10 et 90%) des granulométries similaires au 16ème percentile des distributions a été observée sur les deux segments, en particulier en aval des affluents. Les parties amont proches des CH montrent une altération à long terme due à la présence et au fonctionnement de ces dernières, caractérisée par des surfaces grossières et relativement stables associées à un déficit sédimentaire partiel sur le Cinca et plus marqué sur l'Ésera.

Mots clés
éclusées, hydroélectricité, rivières de montagne, la rivière Haute Cinca, la rivière Haute Ésera, propagation longitudinale des éclusées, outil SIG PhotoMOB, début de mise en mouvement des grains, mobilité du lit, stabilité du lit, mobilité sélective, mobilité partielle.

Chapter 1
Introduction

Ésera river flowing near the village of Santaliestra y San Quilez and upstream view of the catchment, 10/10/2019. Author: Damià Vericat

1.1 BACKGROUND AND RATIONALE OF THE THESIS

1.1.1 The fluvial system - or a giant conveyor belt

1.1.1.1 Watersheds and fluvial systems

Fluvial systems are defined by hydrographic watersheds, which are drainage areas delimited by water divide contour lines (Figure 1.1, **A**). Water droplets flowing through the basin act as an erosion agent that alters and erodes rocks and soils while transporting particles downhill. The convergence of liquid and solid flows forms rivers that continually transfer matter to seas and oceans (Knighton, 1998). Conceptually, Schumm (1977) classified river systems into three zones according to the dominant physical processes that induce characteristic forms and behaviours, and where slope processes have an impact on downstream dynamics. The fluvial systems can be imaged as a jerky a conveyor belt (Ferguson, 1981) as illustrated in Kondolf (1994, 1997), allowing the connection of these zones.

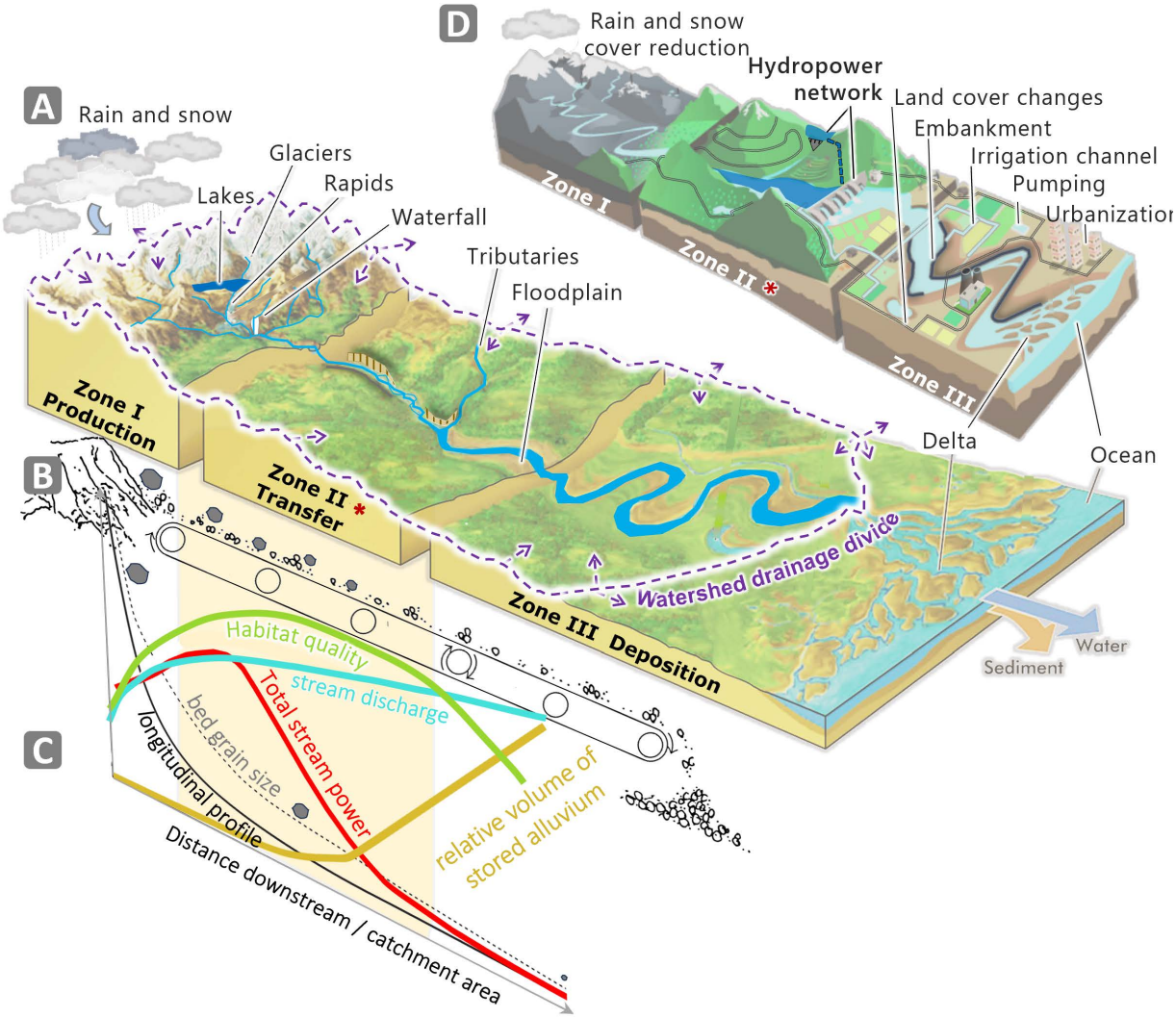

Figure 1.1: The fluvial system. (**A**) Schematic representation of a catchment showing Schumm's 3 conceptual zones (modified from Miller and Spoolman 2012) connected (**B**) like a conveyor belt described by Kondolf (1997) and (**C**) the change in slope, flow, bed grain size, total stream power, habitat quality and stored alluvium along the longitudinal profile (modified from Fryirs and Brierley, 2013 based on Church, 1992). (**D**) Schematic representation of an industrialized watershed (modified from Nepal et al. 2018). *zone concerned in this thesis.

The catchments' headwater, with their steep slopes and numerous narrow streams with rocky beds, are considered to form the **production** zone (**I**) of sediments of various sizes, up to the meter scale, resulting from processes of weathering and erosion by gravity and surface runoff. Channel bed materials are relatively stable but may be entrained during intense infrequent events. Then, in the **transfer zone** (**II**), liquid and solid flows converge downstream through a less dense river system, but still with a relatively steep gradient and high-energy flow (i.e. high stream power). Pockets of floodplain appear, channels are less confined and shaded, and riverbeds are predominantly alluvial and highly dynamic. Due to the higher temperature range in this lower land area, and the greater penetration of light into larger channels, a variety of aquatic plants can thrive and provide organic nutrients and oxygen to the river. This zone offers optimal water quality conditions for a wide range of animal species. The third zone is known as the **deposition zone** (**III**) characterized by a vast unconfined river corridor of fine and cohesive alluvial deposits due to a lack of energy caused by a gentle gradient. Water can often be turbid due to suspended transport of clay and silts which can reduce the development of aquatic plants and macro-invertebrate

However, this zonation through which water, sediments and biological communities cascade is not always linear. The dominant processes vary in space and time, allowing instead defining uniform river segments and distinctive physical habitats that may change abruptly and reappear in different parts of the river system (Fryirs and Brierley, 2013; Rice et al., 2001).

1.1.1.2 The Fluvial balance

These variations in river processes are influenced by local constraints (control variables) such as topography, climate and geology. These affect the driving variables of liquid flow ($\mathbf{Q_L}$) and solid flow ($\mathbf{Q_s}$), which vary in frequency and magnitude over different time scales. When certain thresholds are exceeded, the shape of the river adapts (width, depth, slope, planform, grain size). Lane (1955) conceptualized this dynamic relationship as an equilibrium between control and adjustment variables in the form $\mathbf{Q_sD} \sim \mathbf{Q_LS}$. The point at which the two parts of this relationship are equal constitutes a threshold. Changes in forces can trigger channel degradation or aggregation, as illustrated in the Figure 1.2, p.8). For example, if flow and slope ($\mathbf{Q_L}$ and **S**), i.e. transport capacity, are greater than sediment supply (quantity $\mathbf{Q_s}$ and sediment size **D**), the excess energy in the system will tilt the balance and cross the threshold (Figure 1.2 **C**, p.8), leading to processes of material erosion (i.e. channel degradation) and their downstream transport (i.e. evacuation) . The river segment can be qualified as supply-limited. Conversely, if the supply of sediment is greater than the transport capacity, or if there is an increase in the size of the sediment available, deposition occurs, making this a transport-limited segment. These complex dynamic interactions can be described as a process-response (Petts and Amoros, 1996) in which actions and feedback mechanisms maintain the river reach in a state of dynamic equilibrium. Permanent adjustments take place around a particular state with no net change in morphology on short time scales, but on longer time scales the system may show a gradual evolution towards another state (Schumm, 1977).

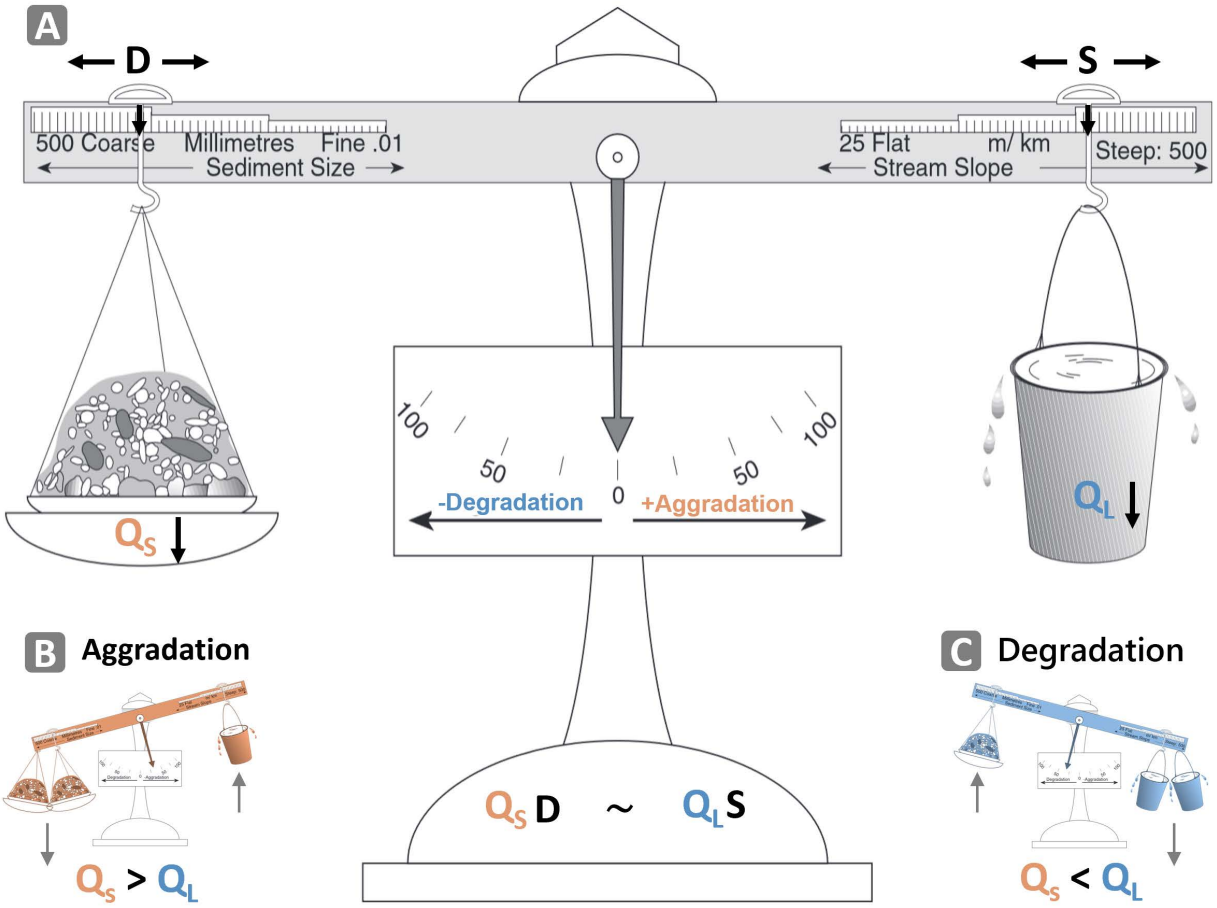

Figure 1.2: (**A**) Illustration of the Lane's balance between stream power (stream slope x discharge) and sediment supply (sediment size x sediment supply). Modified from Charlton (2008) adapted after Brierley and Fryirs (2005). (**B**) Example of an aggradation situation where the system lacks the energy to transport the sediment and (**C**) situation where the excess energy tilts the balance and crosses the threshold, leading to processes of channel degradation.

The diversity of channel morphologies resulting from this interaction has been conceptually classified by many authors (Figure 1.3) in relation, for instance, to the degrees of valley confinement, energy (i.e. gradient), sediment supply, available sediment size, alluvial bed stability, or number of channels (Brierley and Fryirs, 2005; Buffington and Montgomery, 2013; Kondolf et al., 2016; Schumm, 1977; Schumm, 1985). Changes in the system can occur gradually or abruptly due to internal or external disturbances (Brunsden, 2001; Brunsden and Thornes, 1979; Schumm, 1969). The magnitude of adjustments depends on the specific river system (Fryirs and Brierley, 2013).

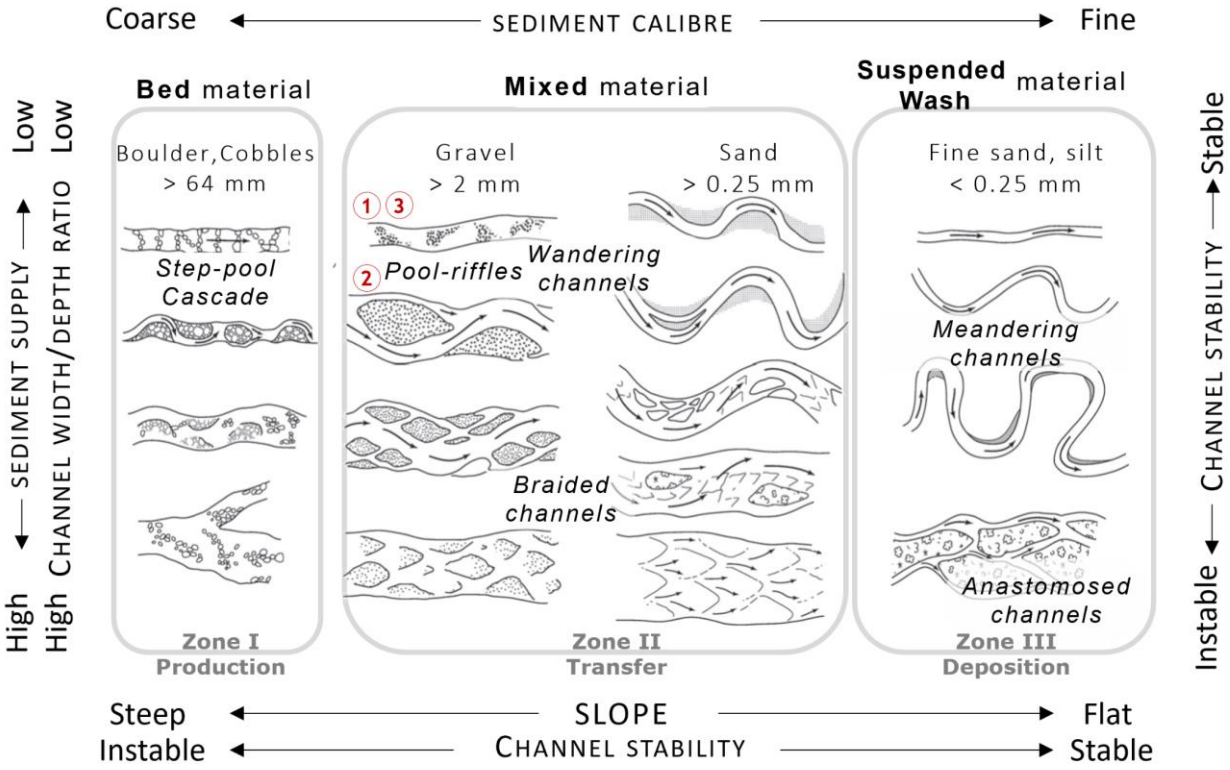

Figure 1.3: Conceptual classification of channel forms associated with the predominant factors influencing them (Modified from Church, 2006). The numbers indicate the dominant morphology of the rivers studied in this thesis: (**1**) Ésera river, (**2**) Cinca river and (**3**) Noguera Pallaresa river.

1.1.1.3 Grain dynamics

1.1.1.3.1 Grain transport

Grains can be characterized by measuring the size or the length of the 3 axes, *a* (the longest), *b* (intermediate, perpendicular to *a*) and *c* (the shortest, perpendicular to *b*) (Figure 1.4, **A**). Based on these measurements, Zingg (1935) classified pebbles into four basic shapes: disc, spherical, bladed, and rod-like. But, for the sake of simplicity and rapidity, the *b*-axis is the preferred measurement used to characterize grain size, as it has the advantage of reflecting grain weight (Fryirs and Brierley, 2013). The Wentworth scale is the main used to divide and name sediments into various grain fractions such as boulder, cobble, gravel, sand, silt and clay (Figure 1.4, **C**) based on size intervals of the b-axis. Bed grains form the substrate for aquatic habitats. The greatest number of species is usually associated with complex heterogeneous substrates composed of cobbles, gravels and sands (Gordon et al., 2004).

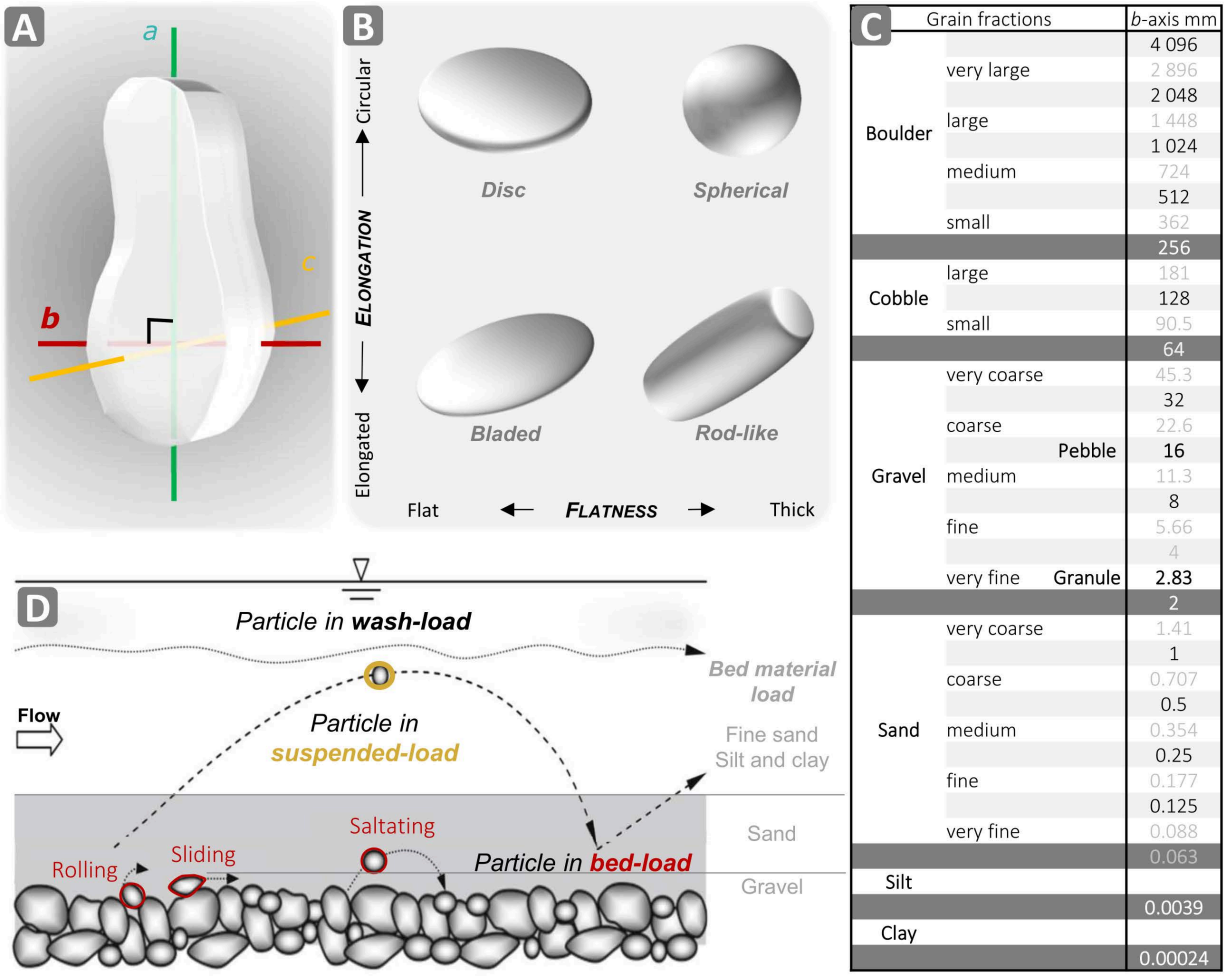

Figure 1.4: (**A**) Grain measurement axis, (**B**) Main grain shape according to Zingg (1935), (**C**) Wentworth grain size scale, (**D**) Main grain transport modes in relation to their size and degree of interaction with the bed. Modified from Dey (2014).

The size of the particles is one of the main factors controlling their initiation of motion, mode of transport (Einstein et al., 1940), and distance travelled (Church, 2006). This is in turn influenced by the hydraulic properties of the exposed flow. There are two main types of transport (Figure 1.4, **D**). The wash-load corresponding of fine materials remaining in water column without settling on the bed. High concentrations can be harmful for aquatic organisms. This mode of transport dominates in lowland areas (sedimentation zone 3), often forming anastomosing or meandering channels (Figure 1.3, p.9). Whereas the bed material load corresponds to sediment in contact with the bed, either intermittently or almost permanently (Dey, 2014). **Suspended load** is fine materials, including sands, carried out in suspension and deposited when flow velocity decreases. **Bedload** is referred to coarser materials (starting from coarse sands and fine gravels) transported by sliding, rolling or saltation (a succession of small jumps), remaining within a narrow layer close to the bed and moving only intermittently after long rest periods. Bedload-dominated transport occurs in high gradient regions, while mixed loads – i.e. both bedload and suspended load - occur in channels with lower gradients and can be wandering or braided morphology. Stability of morphology of alluvial bed and their evolution as well as integrity of aquatic habitat is influenced by the mobility of sediments at the grain scale.

1.1.1.3.2 Grain incipient motion

Sediment movement initiation is a threshold phenomenon (Shields, 1936). The grains arranged on the bed are forming the roughness whose importance varies according of the height with which the grains **protrude**. It affects fluid velocity, generating an increasing gradient towards the top. Velocities near the bed are slower than those near the surface. This slower region, called the **boundary layer**, is where important processes responsible for the entrainment of sediments take place. Initiation of motion occurs when the destabilizing force of the fluid exerted on the grain, blocked against a pivot point, exceeds a critical resistance threshold, below which the grain remains immobile (Komar, 1987; Wiberg and Smith, 1987). Figure 1.5, (p.12), illustrates this balance. The destabilizing force has two components: the drag force ($\mathbf{F_D}$) tangential to the bed in the same direction as the flow and which is a function of velocity, and the lift force ($\mathbf{F_l}$) which acts vertically as a function of pressure. Conversely, in addition to the internal friction of fluid movement (viscosity), the weight of the immersed grains **Fg**, and the frictional resistance **Fr** at their surface, act as flow-resistant stabilizing forces (Dey, 2014; Dey and Ali, 2019). These latter are influenced by the intergranular friction (Hodge et al., 2013; Turowski et al., 2011; Yager et al., 2018). This mean that resistances of a grain may increase or decrease according of its **protrusion , exposure,** degree of the **pivot angle**, grain **imbrication** (as illustrated in Figure 1.5 on the right, where a group of inclined grains partially overlap due to deposition in a directed flow – Church, 2006), their **packing** level (whether tightly or low packed), orientation, and even shape (Cassel et al., 2021; Deal et al., 2023).

The destabilizing moment when the critical hydraulic conditions are reached is called the **critical shear stress**. In addition to this simple balance of forces, other complex and random mechanisms can trigger movement. When the flow encounters an obstacle, perturbations in the velocity and pressure fields (i.e. acceleration above with increase in lift forces, velocity drops downstream creating eddies) can influence the drag and lift forces exerted on other (smaller) grains hidden behind. These grains may be agitated or set in motion when they are relatively finer (e.g. small yellow vs blue grain in the Figure 1.5, (**c**), (p.12), thus cancelling out the hiding effect (Grass, 1970; Nelson et al., 1995). Diplas et al. (2008) additionally demonstrated that this phenomenon could also be dependent on the duration during which these fluctuations occur. Initiation of movement is therefore a complex phenomenon controlled by very local factors

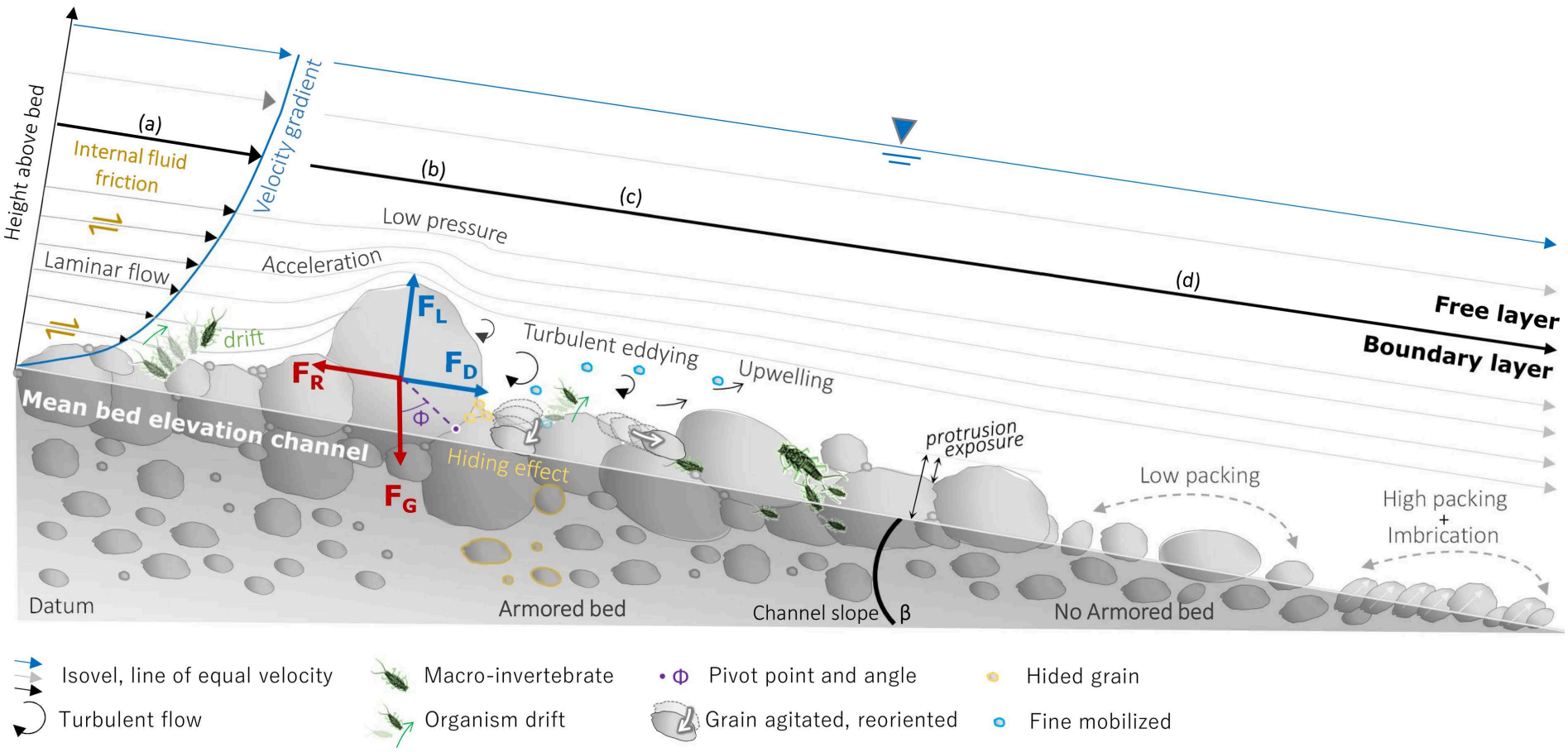

Figure 1.5: Schematic illustration from upstream to downstream on an inclined bed, (**a**) where an average velocity profile is first shown, (b) encountering an obstacle that protrudes strongly into the flow and hides finer grains behind it. The stabilizing (red) and destabilizing (blue) forces are shown schematically. This very coarse grain contributes to the armour layer over the finer materials in the subsurface. The isovels show a perturbed velocity flows above the obstacle and (c) turbulence downstream, agitating, or entraining grains out of the bed and drifting organisms. (d) Arrangement of materials on the bed surface: protrusion, exposure, compaction, imbrication.

1.1.1.3.3 Bed mobility

Bed mobility can be characterized by two methods: flow competence and reference transport (Yager and Schott, 2013). The first method examines the largest particle mobilised for a given flow rate and considers this value as its critical stress (Andrews and Parker, 1987; Carling, 1983; Komar, 1987). The second, records the shear stress (or other relevant flow parameter) at which sediment movement occurs in order to define thresholds in terms of the proportion of the area disturbed, the total number of mobile grains, or total per grain size fraction (Haschenburger and Wilcock, 2003; Wilcock and Southard, 1988). For each, the critical threshold corresponds to the observed shear stress that generated the movement of a minimum quantity (Diplas, 1987; Parker et al., 1983; Parker and Klingeman, 1982; Wilcock and McArdell, 1997; Wilcock and Southard, 1988).

Both methods have limitations and (e.g. outlier sampling Wilcock (1992); sensitivity of the number of samples (Paintal, 1971)) may not be comparable (Batalla and Martín-Vide, 2001; Buffington and Montgomery, 1997). Both can present a margin of error due to spatial and temporal variability in critical destabilizing forces. Section averaged critical stress values are often used, but real local critical values can be greatly different. Also, it may depend on the history of the flow (Reid et al., 1985). A grain of a specific size, observed to be mobile beyond a critical threshold at a given time, may be rearranged with neighbouring grains, leading to a new intergranular fraction and a different critical threshold for future destabilizing events. This is called the stress history effect. (Ockelford et al., 2019; Ockelford and Haynes, 2013; Pender et al., 2007). Nevertheless, these can be used to characterize riverbed destabilization trends. Two types of view coexist and overlap.

The first, from the flow competence method, defines the degree of influence that hydraulic forces have on grain mobilization as a function of weight/size for a given river system or segment. Mobility can be **selective** (i.e. pure weight-driven). The larger the grains, the greater their weight, the greater the hydraulic forces required to initiate movement (Miller et al., 1977). By contrast, mobility can be described as **equal**. Initiation of movement does not depend on particle size. Different fractions have the same critical threshold (Parker et al., 1983; Wilcock and Southard, 1988). In a bed with a mixed load, the arrangement of the grains allows masking effects of the coarse particles on the fine particles, reducing the mobility of the latter (Komar, 1987), as shown by the yellow grains in the Figure 1.5, (p.12). Finally, **partially selective** mobility, represents all the degrees of combination between these two extremes. Relatively fine sediments are more mobile than coarse ones, but still less than if they came from a uniform bed of small size. This first classification does not provide information on the level of bed destabilization, only on the degree of relationship with destabilizing forces. The mobilization of a coarse grain for a given flow does not imply that all the grains of that size have been mobilized. Methods based on a minimum transport rate can be used to define the intensity. Depending on the proportion of the study area mobilized or the total number of grains mobilized per fraction, there may be (i) **no mobility** (< 10%), (ii) **partial mobility** or (iii) **full mobility** (>90%) (Haschenburger and Wilcock, 2003; Parker, 2008; Wilcock and McArdell, 1993). An event could move only 30% of the grains (i.e. partial mobility), while entraining all the available sizes due to an identical critical threshold (i.e. equal mobility). According to both visions, mobility is equal but also partial. The first view allows to characterize the functioning of a river segment, while the second describes a given event mobility magnitude.

1.1.2 Human activity - a grain of sand in the gears of the river conveyor belt

1.1.2.1 Energy

Past and present human activities have strongly impacted transfer flow processes within catchment areas. Cendrero et al. (2020) describe humanity as a geomorphological agent influencing natural systems, with a great acceleration since the mid-twentieth century. The acceleration of human disturbance is reflected in the rapid loss of biodiversity (e.g. a 84% decrease in the average abundance of terrestrial freshwater species between 1970 and 2016 according to Almond et al. (2020)) and associated ecosystem services. Economic, industrial and technological development, powered by fossil fuels (coal at the end of the 19th century, petrol and gas after the second world war) has increased our capacity to mechanically move large masses of material and reshape the landscape (Schmutz, 2018). The industrialised river landscapes have undergone major changes compared with their original characteristics (Figure 1.1, p.6). Changes in land use, drainage of flood plains, groundwater pumping, gravel mining extraction in river thalwegs, canalization or bank stabilization, or even the construction of dams for flood control, farmland irrigation and hydroelectricity, are many examples of the modification and regulation of water and sediment flux (Schmutz, 2018; Tockner and Mehner, 2022)

In a near future, due to pressing issues (e.g. accumulation of greenhouse gases, depletion of fossil resources), increased pressure and new developments in the basins could occur due to the call for a rapid low-carbon electricity transition through renewable energy deployment (IPCC, 2023). According to Ritchie et al. (2023), in 2022, global primary energy consumption (electricity, transport, heating, plus inefficiencies and energy lost in the transformation of raw resources into a secondary form) was still 80% based on fossil sources (Figure 1.6, **A**, p.15). However, from the early 2000s to 2022, global renewable electricity generation has tripled to 8500 terawatt-hours, driven by a more than five-fold increase in wind and solar power respectively over the last decade (2012-2022) (Figure 1.6, **B**, p.15).

In this challenge to reduce the use of fossil fuels, **hydropower** could help to ensure the stability of electricity production by counterbalancing any drop in energy injection into the grid due to the intermittence of certain renewable production. Hydropower currently accounts for 15% of the world's energy mix and 50% of renewable generation. In 2022, 4400 terawatt-hours were produced by hydroelectricity. It is expected that this production will reach more than 7000 terawatt-hours in 2050 (development mainly in Asia and Africa)

1.1.2.2 Hydropower

Hydropower already plays a significant role in some countries, such as Spain where it accounts for 7% of the energy mix and 15% of renewable generation. Figure 1.6, part **C** and **D**, p.15, illustrates an example of electricity production on a weekday (Thursday) in the Iberian Peninsula (on the left a windy day and on the right a day with no wind, days with no solar production have not been identified) where hydropower supports peak demand (morning and evening). Because of its working mechanism, this form of production allows great flexibility of use to meet fluctuating market demand.

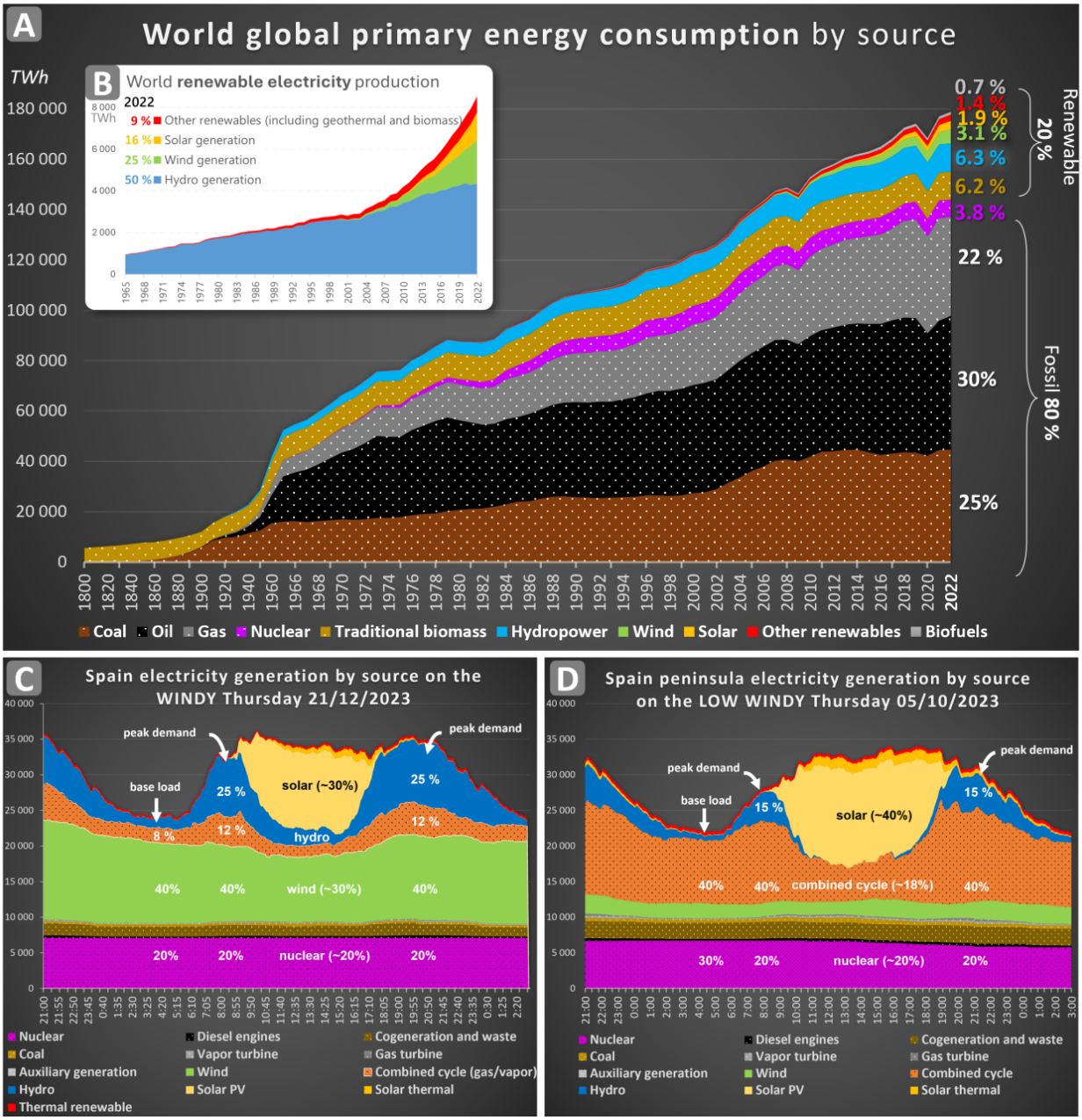

Figure 1.6: (**A**) Estimated global primary energy consumption by source in terawatt-hours, with their respective shares in 2022 on the right. Dotted area represents carbon emitting energy sources. (**B**) Evolution of global renewable electricity production between 1965 and 2022. On the left are the shares for 2022. (**C**) Electricity production by production source in the Iberian Peninsula on a windy day and (**D**) with less wind day. Source: (**A**) and (**B**) from Ritchie et al. (2023), and (**C**) and (**D**) from Red Eléctrica de España (2023).

1.1.2.2.1 Hydropower schemes

Hydropower capacity is depending on the amount of water flow available and the head (i.e. energy potential due to the height of fall), which determines the pressure acting on the turbine. Hydroelectricity is therefore mainly developed in mountainous regions receiving large amounts of precipitation with steep gradients (i.e. high-biodiversity transfer zones (Figure 1.1, p.6)). The water is diverted through pipes to turbines, transforming the kinetic energy as it falls into mechanical energy by activating the turbines and then into electrical energy thanks to the generator and finally released to the river, generating artificial fluctuations downstream. To meet a sudden demand for electricity on a sub-daily scale, a power plant can operate in **hydropeaking** mode by rapidly feeding the turbines with the available water before stopping just as quickly once the peak has passed. The rapid flow fluctuations downstream are termed **hydropeaks**; their patterns depend on the type of hydroelectric facilities. There are a variety of hydroelectric systems depending on the landscape configuration, but generally in mountain areas four main operating regimes can be distinguished (Figure 1.7, p.18): (i) pump and storage, (ii) storage dam, (iii) run-of-river (ROR), (iv) modified run-of-river (Kaunda et al., 2012; Kumar et al., 2011; McManamay et al., 2016; Smokorowski, 2022)

Pumped storage uses an upper reservoir from which the water is diverted to be turbined in a lower power station and then returned to a near river or generally stored in an existing lake or reservoir (Figure 1.7 **A1**, p.18). The water is then pumped back up during off-peak hours. This upper reservoir can be considered as a battery. This system is cost-effective in mountainous areas with steep slopes providing great head over short distance, allowing to move water with minimal friction losses.

In a **storage system**, water is stored in reservoirs created by dams or lakes at high altitude, which can be considered as a battery for the future electricity production. To meet demand, the water is diverted to the turbines either at the foot of the dam or channelled via penstocks and diversion bays to the power station further down the valley. The facilities can operate in base-load mode (i.e. with a constant supply) or in hydropeaking mode to meet sudden demands for electricity. Several run-of-river power stations may cascade downstream, using the same water to produce additional hydroelectricity.

Run-Of-River (ROR) system has no storage. Water availability depends on river flow and of upstream releases if other facilities are present. Water is diverted to a power station via a headrace (i.e. a canal whose elevation is maintained at the same level as the water intake to maintain a significant head), resulting in a reduction of flow in the bypassed river section downstream the diversion weir.

Modified ROR (MROR) has a small reservoir to store water at very short term. Unlike simple ROR, when they are in cascade the same volume of water flows downstream into the river, but its release can be modulated slightly during the day (Figure 1.7 **A4** an **A5**, p.18)

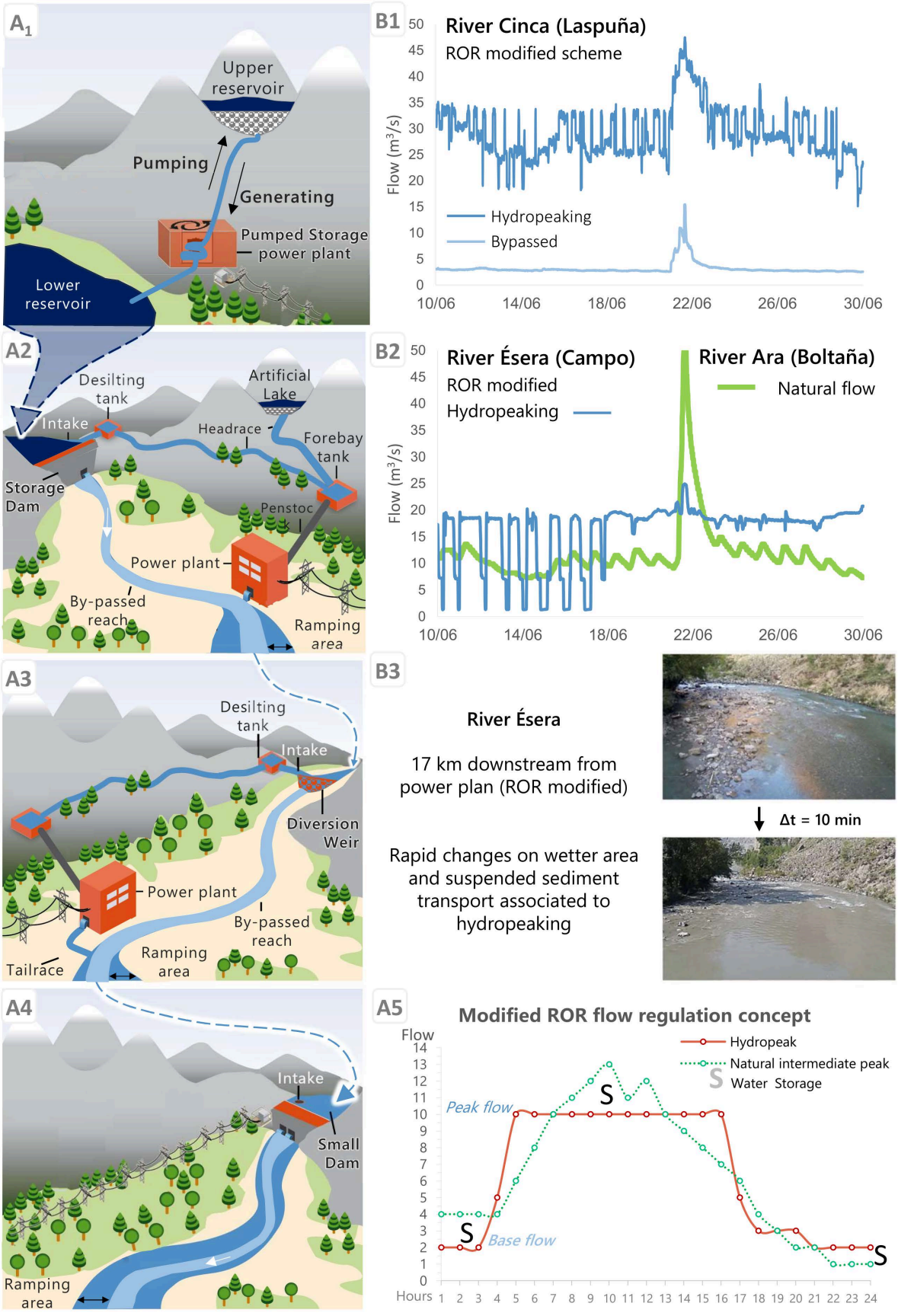
A1
Upper reservoir
Pumping
Generating
Pumped Storage power plant
Lower reservoir
B1
River Cinca (Laspuña)
ROR modified scheme
Flow (m³/s)
Hydropeaking
Bypassed
10/06
14/06
18/06
22/06
26/06
30/06
A2
Desilting tank
Artificial Lake
Intake
Headrace
Forebay tank
Storage Dam
Penstoc
Power plant
By-passed reach
Ramping area
B2
River Ésera (Campo)
ROR modified
Hydropeaking
River Ara (Boltaña)
Natural flow
Flow (m³/s)
10/06
14/06
18/06
22/06
26/06
30/06
A3
Desilting tank
Intake
Diversion Weir
Power plant
By-passed reach
Ramping area
Tailrace
B3
River Ésera
17 km downstream from power plan (ROR modified)
Δt = 10 min
Rapid changes on wetter area and suspended sediment transport associated to hydropeaking
A4
Intake
Small Dam
Ramping area
A5
Modified ROR flow regulation concept
Flow
Hydropeak
Natural intermediate peak
Water Storage
Peak flow
Base flow
Hours

Figure 1.7 (from previous page): (**A**) Hydroelectric installations: (A_1) Pumping and storage system. (A_2) Storage system. (**A3**) Run-of-river system. (A_4) Modified ROR and (A_5) presumed flow modulation. Modified from Kumar et al., (2011). (**B**) Example of hydropower flow regimes for two Pyrenean rivers (Cinca and Ésera) and for the unregulated river Ara. (B_1) For the Cinca, the bypassed and hydropeaked flow regimes are illustrated by comparing locations upstream and downstream of the hydropower water release. (B_2) The Ésera can see its flow increase from 1.5 to 19 m3/s in a few minutes, while the variations in the Ara, with similar mean annual flows, are smoother. (B_3) Photographs illustrating changes in turbidity and water level over a 10-minute period in the river Ésera, 17 km downstream of the ROR dam. Adapted from Batalla et al., (2021).

Despite its status as a renewable, low-carbon energy source, hydropower modifies the abiotic and biotic flows in rivers.

1.1.2.2.2 Hydro-sediment alteration

Numerous studies since the 1990s, mainly focused on ecology (Bipa et al., 2024; Vanzo et al., 2023), have shown negative effects linked to the hydropeak regime (for instance on hydrology, hydraulic temperature, water oxygenation, water quality, food web, organic matter cycle). This effects influence habitat quality for numerous species of fish, invertebrates, algae, insects, amphibians and plants (Bipa et al., 2024; Greimel et al., 2018; Hauer et al., 2016; Smokorowski, 2022; Vanzo et al., 2023). However, several authors (Batalla et al., 2021; Greimel et al., 2018; Hauer et al., 2018a; Hayes et al., 2022; Hayes et al., 2023; Ligon et al., 1995) highlighted the paucity of studies concerning the impact of hydropeaking on bedload dynamics in rivers, which could be crucial for preserving the integrity of fluvial biological habitats. This fact is evident in Vanzo et al. (2023) word cloud diagram, which summarizes the most commonly used words in the state of the art they drew up, as well as the earlier one by Hauer et al. (2017b), here in (Figure 1.8)

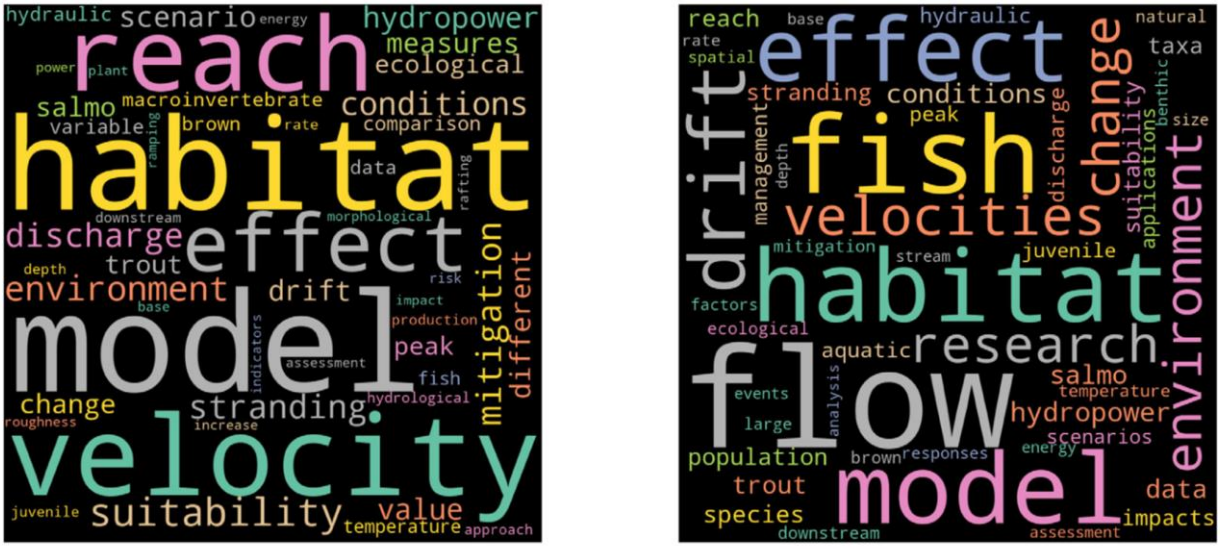

(a) Articles from Hauer et al. (2017) (b) Articles from Vanzo et al. (2023)

Figure 1.8: Word cloud diagram showing the most recurrent words in current hydropeaking research. From Vanzo et al. (2023).

As covered in Section 1.1.1.2, alterations of the hydro-sedimentary regime resulting from a hydroelectric project can significantly disrupt the fluvial system downstream.

Intermittent water releases in impacted river segments take the form of sudden waves of flow that rapidly flood the lateral zones (Figure 1.7 **B3**, p.18), and also rapidly dry them out when the turbines stop operating (i.e. called ramping or dewatering zones). These flow waves modify hydraulic conditions such as depth, velocity and shear stress (Gore et al., 1994), with patterns that differ greatly from natural fluctuations (Figure 1.7 **B2**, p.18). For example, the rate of flow change due to up-ramping or down-ramping of turbines is much faster than for natural conditions (Courret et al., 2021), particularly for ROR installations (Ashraf et al., 2018). The presence of a dam or diversion weir can disrupt sediment continuity and reduce or even cancel downstream supply (Vericat and Batalla, 2006). Turbined water depleted in sediment, termed *hungry water* by Kondolf (1997), can have a high undissipated erosive energy capacity. The bed may then undergo a degradation process (*supply-limited* channel) as well as aggradation further downstream. Vericat et al. (2008c) showed in an unimpacted gravel river where frequent flows (exceeded around 15% of the time) near or even below the mean critical discharge could lead to the mobilization of fine sediment (mainly sand up to a few fine and medium gravels). In an impacted river, Hauer et al. (2019) showed that these fine granulometric fractions were deposited mainly in the dewatered zone. When these areas are flooded - probably creating turbulence around the very coarse particles - the hydropeaks could therefore act on their dynamics by frequently selectively remobilizing these fine fractions. Negative responses from the biological community (drift of organisms) have been observed when the bed is destabilized and the transport of sediment in suspension is increased (Béjar et al., 2017). Other research indicates that inter-event flows also very near or below the critical threshold for movement initiation can significantly increase bed stability through reorientation, vertical settlement and grain compaction generating higher granular friction (Mao, 2018; Masteller et al., 2019a; Ockelford and Haynes, 2013; Pender et al., 2007; Perret et al., 2020). Frequent winnowing of fine material and stabilization of coarser material can create a homogeneous layer of coarse sediment that requires higher flows to be entrained (i.e. armour layer, Figure 1.5, p.12).

At the same time, water impoundments tend to reduce the intensity and occurrence of natural high flood peaks (Batalla et al., 2004; Górski et al., 2012) which could just possibly remobilize this armour layer. Smokorowski et al. (2011) observed fewer competent events in affected segments that could mobilize medium-sized bed grains compared with unimpacted systems. In a modified cascade ROR system, most of the water volume returns to the river. However, despite the low volumes of water stored, it is possible that daily regulation for small and medium-sized mountain rivers could have a negative effect on the magnitude of the intermediate natural peak flows that could occur, for example during heavy rainfall but very localized in the basin (Figure 1.7, p.18). Although a less significant regulation of high natural peak flows is observed compared to the storage system, these impacted sections could be affected to a certain extent by the armouring and by the stabilization of the grains due to the hydropeaks, which correspond to frequent flows of low magnitude lower than natural floods.

Generally, bed textures evolve in a downstream direction with the inflow of water and sediment from tributaries (Rice et al., 2001 ; Schmidt and Wilcock, 2008; Svendsen et al., 2009). Depending on the morphology of river segments and grain size (i.e. microhabitat at patch scale), (Gore et al., 1994; Hauer et al., 2014b; Schmutz et al., 2015; Vanzo et al., 2016b) the intensity of organism responses (e.g. voluntary or involuntary displacement) to disturbance differs indicating that bed material can play a key role.

In this context, where hydroelectricity is present in a wide range of mountainous river styles and will continue to play an increasingly important role, it is necessary to examine its impact to produce sustainable hydroelectric power. The reactions of the systems affected differ according to the spatial and temporal influx of water and sediment controlled by the characteristics of the catchment, morphology of valley and channel, hydropower schemes, and patterns of hydropeaks. referred as geomorphological context (Wohl, 2018)

Within this framework, the thesis examines the effect of the hydropeaks on the morpho-sedimentary dynamics of two mixed-load river segments in basins with contrasting characteristics, the upper Cinca (12 km) and the Ésera (17 km), located in the Southern Pyrenees. Until September 2018, when the thesis began, no article had yet dealt specifically with this issue in this specific region.

1.2 HYPOTHESIS, OBJECTIVES AND STRUCTURE OF THE THESIS

The overall aim of this thesis is to assess the spatio-temporal hydropeaking influence on the morpho-sedimentary dynamics of two contrasted mountain rivers.

HYPOTHESIS

The following hypotheses are tested in the thesis:

H1. The consequence of water releases on the hydrological regime of rivers, and their propagation downstream, varies according to the hydro-geomorphological context and the hydroelectric power facilities.

H2. Hydraulic competence of hydropeaking on the onset of bed-material movement differs depending on the geomorphological context.

H3. The mobility dynamics of bed grains due to hydropeaks, corresponding to the frequent entrainment of relatively fine grains, is difficult to measure accurately using existing methods whose detection limit is too low and thus require a new approach.

H4. Hydraulic capacity of hydropeaking on the intensity of destabilization of bed grains differs depending on the geomorphological context.

H5. Despite presenting destabilization forces below the critical threshold of grain motion, hydropeaks influence the texture of the bed by modifying the arrangement of the grains (compaction, imbrication, orientation), as well as the dynamics of the fine sediments (transported in suspension) stored in the river bed, and therefore the mobility of the sediments for the next event.

OBJECTIVES

Based on the main aim and the hypotheses, this thesis addresses the following specific objectives:

O1. Study of the hydrological and hydraulic characteristics of hydropeaking.

O2. Analysis of the spatiotemporal variability of flow competence (based on theoretical bed mobility equations).

O3. Develop an GIS open-source tool to study bed grain mobility in gravel bed rivers subjected to flood and hydropeaks.

O4. Apply the tool to characterize grain destabilization intensity in time and space.

The thesis also provides a discussion and a review on the next works already initiated to integrate the spatiotemporal impacts of hydropeaking and floods on hydraulics, bedload and suspended sediment transport as well as bed texture for a better understanding of channel morpho-dynamics.

STRUCTURE

Firstly, this thesis analyses the **hydrological characteristics of the hydropeaks** detected at the two rivers at different time scales with the objectives to classify hydropeaks and determine their frequency during contrasted (hydrologically) years. Additionally, hydrological characteristics of floods and hydropeaks are also analysed at multiple points along each river aiming at studying the spatial variability of these characteristics (Chapter 3, p.71).

Secondly, the **onset of bed-material movement** in the Ésera river is examined spatially (upstream-downstream) to characterize the type of mobility (Chapter 4, p.137). These results are then compared with those from the Upper Noguera Pallaresa river (South Pyrenees), published during the thesis period (Vericat et al., 2020). This paper is simply an appendix at the end of this report and does not count for thesis examination and eventual approval. The results were also compared with those of Cinca, obtained outside the framework of this thesis and published by the research group in the same interval (López et al., 2020).

Thirdly, a central part of the thesis work involved the conceptualization and development of the PhotoMOB method, particularly well-suited to partial transport, for measuring the intensity of grain mobility at high resolution, and the quantification of the associated errors, as well as verifying the compatibility of the results obtained with other methods (Chapters 5, p.165).

Fourthly, the **PhotoMOB** method was applied in various sections of the two rivers over a period of two months, to measure the **intensity of mobility** differentiating between hydropeaks and flood in a longitudinal point of view (Chapter 6, p.261).

Lastly, it is worth to remarks that various other tasks have been initiated (Chapter 8, p.313). The calibration of an unsteady 2D hydraulic model is underway to study the spatial hydraulic variations of hydropeaks propagation and to calculate the missing local constraints for initiating movement, in order to transform chapter 6 into a paper. In the Ésera river, high-resolution topographic data have been acquired in the upstream and downstream reaches of the study segment to study the temporal evolution of bed texture on a near-daily scale. More over the calibration of a method for the apparent measurement of bed velocity and the estimation of bedload transport rates during the hydropeaks, influencing the remodelling of the morphology of the channel and the physical habitats, was carried out using indirect measurements (ADCP) and *in situ* sampling (sampling of the bedload with a Helly-Smith sampler). And, to study the dynamics of the suspended load on the scale of each hydropeaks and flood event detected in the previous chapters, field data were acquired and continuous estimates of the concentration of suspended loads were made.

1.3 FRAMEWORK OF THE THESIS

Figure 1.9 (p.23) shows the structure of the thesis with the different chapters (a total of 8), associated objectives, and journals where papers have been published (n=2), are in the process of publication (n=2) or in preparation (n=2). Following the regulation of the University of Lleida (Article 28 of the Normativa acadèmica de doctorat de la Universitat de Lleida), each of these papers can be considered as a self - contained unit, with an introduction section outlining the specific research context and objectives, the full details of the methods used, the results and discussion.

The present chapter, Chapter 1, represents a general introduction of the thesis. Chapter 2 provide details of the study area and an overview of the approaches and methods used for respective chapters. As the thesis is presented as a compilation of papers, each paper will provide the specific details of the materials and methods. Even so, Chapter 2 introduces the general design of the PhD to provide the whole spectrum of data sources, methods and techniques. Chapter 3 consists of two parts, *time* and *space*, being related to Objective 1. The *space* aspect is only developed to a limited extent since it is still a paper in preparation. Chapter 4 is related to Objective 2. The two papers corresponding to Chapter 5 have been submitted to an international journal and are pending revision. This chapter is related to Objective 3. The material and preliminary results related to Objective 4 of the thesis are presented in Chapter 6. Finally, Chapter 7 contains a discussion, integrating the results of all the chapters, allowing general conclusions to be drawn in relation to each of the objectives of the work and the associated limitations identified. Lastly, Chapter 8 provides an overview of the work initiated as a result of the points highlighted in the discussion and limitations in Chapter 7. Finally, several annexes are included containing publication and presentation carried out during the thesis.

Chapters 2, 3 and 5 are divided into two parts, which makes the numbering of each part and its subdivisions more complex. In these chapters, the first digit corresponds to the number of the chapter, the second indicates the number of the part (1 or 2) and the following digits refer to the subdivisions.

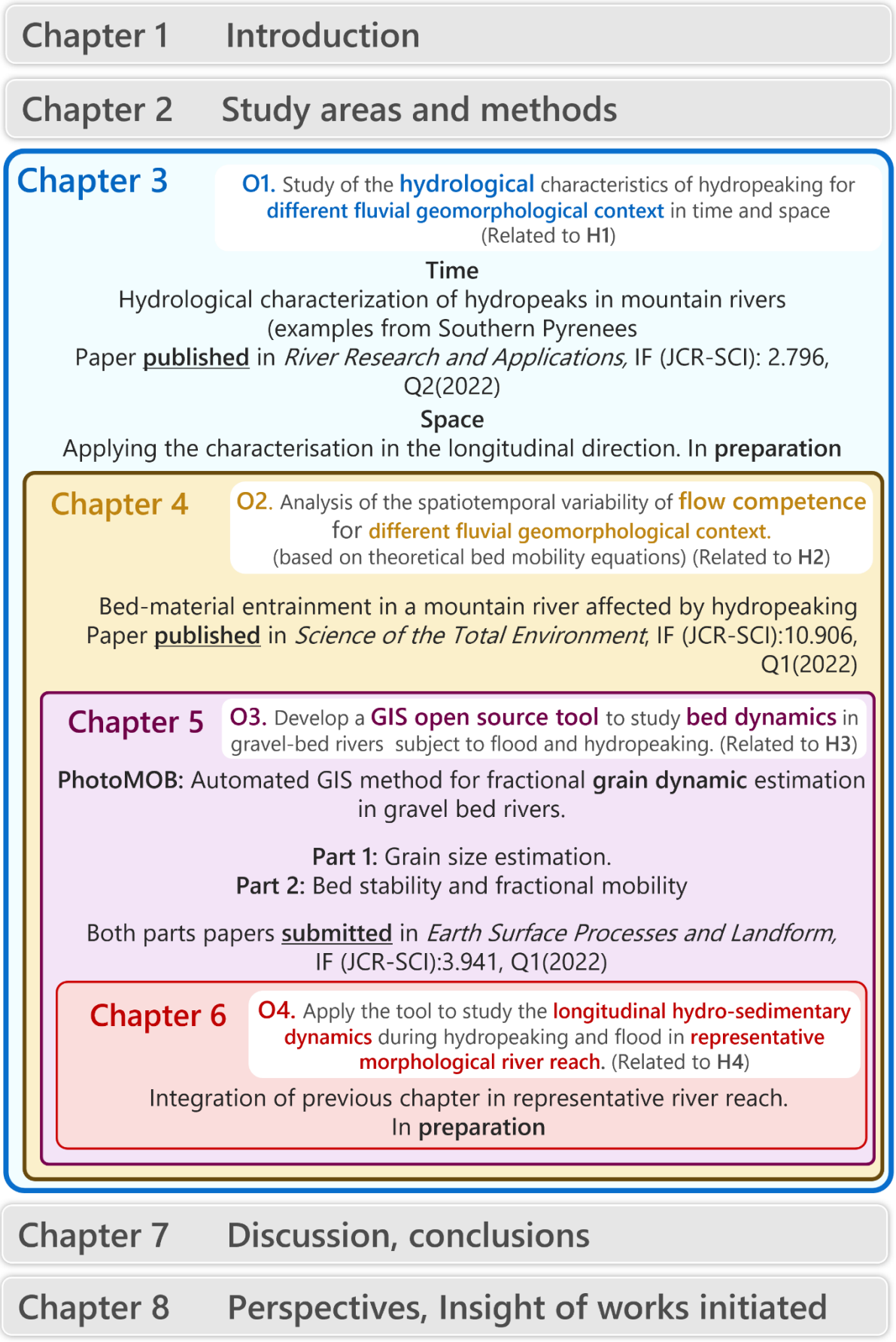

Figure 1.9: Structure of the thesis with the different chapters, associated objectives, and where papers have been published, will be submitted, or are being developed.

REFERENCES

Almond, R.E.A., **Grooten, M.** and **Petersen, T.** (2020) Living Planet Report 2020. Bending the curve of biodiversity loss. *WWF*, Gland, Switzerland. https://wwfin.awsassets.panda.org/downloads/lpr_2020_full_report.pdf

Andrews, E.D. and **Parker, G.** (1987) Formation of a coarse surface layer as the response to gravel mobility. In: John Wiley & Sons (Ed. C.R. Thorne, J.C. Bathurst, and R.D. Hey), 269–325. ,https://cir.nii.ac.jp/crid/1574231874050281856

Ashraf, F.B., **Haghighi, A.T.**, **Riml, J.**, **Alfredsen, K.**, **Koskela, J.J.**, **Kløve, B.** and **Marttila, H.** (2018) Changes in short term river flow regulation and hydropeaking in Nordic rivers. *Scientific Reports*, **8**, 17232. DOI:10.1038/s41598-018-35406-3

Batalla, R.J., **Gibbins, C.N.**, **Alcázar, J.**, **Brasington, J.**, **Buendia, C.**, **Garcia, C.**, **Llena, M.**, **López, R.**, **Palau, A.**, **Rennie, C.**, **Wheaton, J.M.** and **Vericat, D.** (2021) Hydropeaked rivers need attention. *Environmental Research Letters*, **16**, 021001. DOI:10.1088/1748-9326/abce26

Batalla, R.J., **Gómez, C.M.** and **Kondolf, G.M.** (2004) Reservoir-induced hydrological changes in the Ebro River basin (NE Spain). *Journal of Hydrology*, **290**, 117–136. DOI:10.1016/j.jhydrol.2003.12.002

Batalla, R.J. and **Martín-Vide, J.P.** (2001) Thresholds of particle entrainment in a poorly sorted sandy gravel-bed river. *CATENA*, **44**, 223–243. DOI:10.1016/S0341-8162(00)00157-0

Béjar, M., **Gibbins, C.N.**, **Vericat, D.** and **Batalla, R.J.** (2017) Effects of Suspended Sediment Transport on Invertebrate Drift. *River Res. Appl.*, **33**, 1655–1666. DOI:10.1002/rra.3146

Bipa, N.J., **Stradiotti, G.**, **Righetti, M.** and **Pisaturo, G.R.** (2024) Impacts of hydropeaking: A systematic review. *Science of The Total Environment*, **912**, 169251. DOI:10.1016/j.scitotenv.2023.169251

Brierley, G.J. and **Fryirs, K.A.** (2005) Geomorphology and river management: applications of the river styles framework. *Blackwell publ*, Malden.

Brunsden, D. (2001) A critical assessment of the sensitivity concept in geomorphology. *CATENA*, **42**, 99–123. DOI:10.1016/S0341-8162(00)00134-X

Brunsden, D. and **Thornes, J.B.** (1979) Landscape Sensitivity and Change. *Transactions of the Institute of British Geographers*, **4**, 463. DOI:10.2307/622210

Buffington, J.M. and **Montgomery, D.R.** (2013) 9.36 Geomorphic Classification of Rivers. *Elsevier*, 730–767. DOI:10.1016/B978-0-12-374739-6.00263-3

Buffington, J.M. and **Montgomery, D.R.** (1997) A systematic analysis of eight decades of incipient motion studies, with special reference to gravel-bedded rivers. *Water Resources Research*, **33**, 1993–2029. DOI:10.1029/96WR03190

Carling, P.A. (1983) Threshold of coarse sediment transport in broad and narrow natural streams. *Earth Surface Processes and Landforms*, **8**, 1–18. DOI:10.1002/esp.3290080102

Cassel, M., **Lavé, J.**, **Recking, A.**, **Malavoi, J.-R.** and **Piégay, H.** (2021) Bedload transport in rivers, size matters but so does shape. *Sci Rep*, **11**, 508. DOI:10.1038/s41598-020-79930-7

Cendrero, A., **Forte, L.M.**, **Remondo, J.** and **Cuesta-Albertos, J.A.** (2020) Anthropocene Geomorphic Change. Climate or Human Activities? *Earth's Future*, **8**, e2019EF001305. DOI:10.1029/2019EF001305

Charlton, R. (2008) Fundamentals of fluvial geomorphology, 1. publ. *Routledge*, London.

Church (2006) BED MATERIAL TRANSPORT AND THE MORPHOLOGY OF ALLUVIAL RIVER CHANNELS. *Annual Review of Earth and Planetary Sciences*, **34**, 325–354. DOI:10.1146/annurev.earth.33.092203.122721

Church, M. (1992) Channel morphology and typology. In: (Ed. P. Calow and G.E. Petts), *Blackwell Scientific*, vol 1, pages 126–143.

Courret, D., **Baran, P.** and **Larinier, M.** (2021) An indicator to characterize hydrological alteration due to hydropeaking. *Journal of Ecohydraulics*, **6**, 139–156. DOI:10.1080/24705357.2020.1871307

Deal, E., **Venditti, J.G.**, **Benavides, S.J.**, **Bradley, R.**, **Zhang, Q.**, **Kamrin, K.** and **Perron, J.T.** (2023) Grain shape effects in bed load sediment transport. *Nature*, **613**, 298–302. DOI:10.1038/s41586-022-05564-6

Dey, S. (2014) Fluvial Hydrodynamics: Hydrodynamic and Sediment Transport Phenomena. *Springer Berlin Heidelberg*, Berlin, Heidelberg. DOI:10.1007/978-3-642-19062-9

Dey, S. and **Ali, S.Z.** (2019) Bed sediment entrainment by streamflow: State of the science. *Sedimentology*, **66**, 1449–1485. DOI:10.1111/sed.12566

Diplas, P. (1987) Bedload Transport in Gravel-Bed Streams. *Journal of Hydraulic Engineering*, **113**, 277–292. DOI:10.1061/(ASCE)0733-9429(1987)113:3(277)

Diplas, P., **Dancey, C.L.**, **Celik, A.O.**, **Valyrakis, M.**, **Greer, K.** and **Akar, T.** (2008) The Role of Impulse on the Initiation of Particle Movement Under Turbulent Flow Conditions. *Science*, **322**, 717–720. DOI:10.1126/science.1158954

Einstein, H.A., **Anderson, A.G.** and **Johnson, J.W.** (1940) A distinction between bed-load and suspended load in natural streams. *Eos, Transactions American Geophysical Union*, **21**, 628–633. DOI:https://doi.org/10.1029/TR021i002p00628

Ferguson, R.I. (1981) Channel form and channel changes. In: (Ed. J. Lewin), *George Allen & Unwin*, London, 90–125.

Fryirs, K.A. and **Brierley, G.J.** (2013) Geomorphic analysis of river systems: an approach to reading the landscape, 1. publ. *Wiley-Blackwell*, Chichester.

Gordon, N., **McMahon, T.**, **Finlayson, B.**, **Gippel, C.** and **Nathan, R.** (2004) Stream Hydrology An Introduction for Ecologists. 446 pp.

Gore, J.A., **Niemela, S.**, **Resh, V.H.** and **Statzner, B.** (1994) Near-substrate hydraulic conditions under artificial floods from peaking hydropower operation: A preliminary analysis of disturbance intensity and duration. *Regulated Rivers: Research & Management*, **9**, 15–34. DOI:10.1002/rrr.3450090103

Górski, K., **Van Den Bosch, L.V.**, **Van De Wolfshaar, K.E.**, **Middelkoop, H.**, **Nagelkerke, L.A.J.**, **Filippov, O.V.**, **Zolotarev, D.V.**, **Yakovlev, S.V.**, **Minin, A.E.**, **Winter, H.V.**, **De Leeuw, J.J.**, **Buijse, A.D.** and **Verreth, J.A.J.** (2012) POST-DAMMING FLOW REGIME DEVELOPMENT IN A LARGE LOWLAND RIVER (VOLGA, RUSSIAN FEDERATION): IMPLICATIONS FOR FLOODPLAIN INUNDATION AND FISHERIES. *River Research and Applications*, **28**, 1121–1134. DOI:10.1002/rra.1499

Grass, A.J. (1970) Initial Instability of Fine Bed Sand. *Journal of the Hydraulics Division*, **96**, 619–632. DOI:10.1061/JYCEAJ.0002369

Greimel, F., **Schülting, L.**, **Graf, W.**, **Bondar-Kunze, E.**, **Auer, S.**, **Zeiringer, B.** and **Hauer, C.** (2018) Hydropeaking Impacts and Mitigation. In: (Ed. S. Schmutz and J. Sendzimir), *Springer International Publishing*, Cham, 91–110. DOI:10.1007/978-3-319-73250-3_5

Haschenburger, J.K. and **Wilcock, P.R.** (2003) Partial transport in a natural gravel bed channel. *Water Resources Research*, **39**, 2002WR001532. DOI:10.1029/2002WR001532

Hauer, C., **Holzapfel, P.**, **Tonolla, D.**, **Habersack, H.** and **Zolezzi, G.** (2019) In situ measurements of fine sediment infiltration (FSI) in gravel-bed rivers with a hydropeaking flow regime. *Earth Surf. Process. Landf.*, **44**, 433–448. DOI:10.1002/esp.4505

Hauer, C., **Siviglia, A.** and **Zolezzi, G.** (2017) Hydropeaking in regulated rivers. From process understanding to design of mitigation measures. *Science of The Total Environment*, **579**, 22–26. DOI:10.1016/j.scitotenv.2016.11.028

Hauer, C., **Unfer, G.**, **Holzapfel, P.**, **Haimann, M.** and **Habersack, H.** (2014) Impact of channel bar form and grain size variability on estimated stranding risk of juvenile brown trout during hydropeaking. Earth Surface Processes and Landforms. doi: 10.1002/esp.3552 DOI:10.1002/esp.3552

Hauer, C., **Wagner, B.**, **Aigner, J.**, **Holzapfel, P.**, **Flödl, P.**, **Liedermann, M.**, **Tritthart, M.**, **Sindelar, C.**, **Pulg, U.**, **Klösch, M.**, **Haimann, M.**, **Donnum, B.O.**, **Stickler, M.** and **Habersack, H.** (2018) State of the art, shortcomings and future challenges for a sustainable sediment management in hydropower: A review. *Renewable and Sustainable Energy Reviews*, **98**, 40–55. DOI:10.1016/j.rser.2018.08.031

Hauer, F.R., **Locke, H.**, **Dreitz, V.J.**, **Hebblewhite, M.**, **Lowe, W.H.**, **Muhlfeld, C.C.**, **Nelson, C.R.**, **Proctor, M.F.** and **Rood, S.B.** (2016) Gravel-bed river floodplains are the ecological nexus of glaciated mountain landscapes. *Science Advances*, **2**, e1600026. DOI:10.1126/sciadv.1600026

Hayes, D.S., **Bruno, M.C.**, **Alp, M.**, **Boavida, I.**, **Batalla, R.J.**, **Bejarano, M.D.**, **Noack, M.**, **Vanzo, D.**, **Casas-Mulet, R.**, **Vericat, D.**, **Carolli, M.**, **Tonolla, D.**, **Halleraker, J.H.**, **Gosselin, M.-P.**, **Chiogna, G.**, **Zolezzi, G.** and **Venus, T.E.** (2023) 100 key questions to guide hydropeaking research and policy. *Renewable and Sustainable Energy Reviews*, **187**, 113729. DOI:10.1016/j.rser.2023.113729

Hayes, D.S., **Schülting, L.**, **Carolli, M.**, **Greimel, F.**, **Batalla, R.J.** and **Casas-Mulet, R.** (2022) Hydropeaking: Processes, Effects, and Mitigation. *Elsevier*, 134–149. DOI:10.1016/B978-0-12-819166-8.00171-7

Hodge, R.A., **Sear, D.A.** and **Leyland, J.** (2013) Spatial variations in surface sediment structure in rifflepool sequences: a preliminary test of the Differential Sediment Entrainment Hypothesis (DSEH). *Earth Surface Processes and Landforms*, **38**, 449–465. DOI:10.1002/esp.3290

IPCC (2023) Summary for Policymakers. *Intergovernmental Panel on Climate Change (IPCC)*, Geneva, Switzerland, 42p. DOI:10.59327/IPCC/AR6-9789291691647.001

Kaunda, C.S., **Kimambo, C.Z.** and **Nielsen, T.K.** (2012) Hydropower in the Context of Sustainable Energy Supply: A Review of Technologies and Challenges. *ISRN Renewable Energy*, **2012**, 1–15. DOI:10.5402/2012/730631

Knighton, D. (1998) Fluvial forms and processes: a new perspective, Rev. and update ed. *Arnold*, London ; New York.

Komar, P.D. (1987) Selective gravel entrainment and the empirical evaluation of flow competence. *Sedimentology*, **34**, 1165–1176. DOI:10.1111/j.1365-3091.1987.tb00599.x

Kondolf, G.M. (1997) Hungry Water: Effects of Dams and Gravel Mining on River Channels. *Environmental Management*, **21**, 533–551. DOI:10.1007/s002679900048

Kondolf, G.M., **Piégay, H.**, **Schmitt, L.** and **Montgomery, D.R.** (2016) Geomorphic classification of rivers and streams. In: 1st edn. (Ed. G.M. Kondolf and H. Piégay), *Wiley*, 133–158. DOI:10.1002/9781118648551.ch7

Kumar, A., **Schei, T.**, **Ahenkorah, A.**, **Rodriguez, R.C.**, **Devernay, J.-M.**, **Freitas, M.**, **Hall, D.**, **Killingtveit, Å.** and **Liu, Z.** (2011) Chapitre 5 : Hydropower. In: Cambridge University Press (Ed. C.D. Morejon and T. Krug), Cambridge, United Kingdom; New York, NY, USA, 5, 60. ,https://www.ipcc.ch/site/assets/uploads/2018/03/Chapter-5-Hydropower-1.pdf

Lane, E.W. (1955) The importance of fluvial morphology in hydraulic engineering. *Proc. Am. Soc. Civ. Eng.*, **745**, 21.

Ligon, F.K., **Dietrich, W.E.** and **Trush, W.J.** (1995) Downstream Ecological Effects of Dams. *BioScience*, **45**, 183–192. DOI:10.2307/1312557

López, R., **Garcia, C.**, **Vericat, D.** and **Batalla, R.J.** (2020) Downstream changes of particle entrainment in a hydropeaked river. *Science of The Total Environment*, **745**, 140952. DOI:10.1016/j.scitotenv.2020.140952

Mao, L. (2018) The effects of flood history on sediment transport in gravel-bed rivers. *Geomorphology*, **322**, 196–205. DOI:10.1016/j.geomorph.2018.08.046

Masteller, C.C., **Finnegan, N.J.**, **Turowski, J.M.**, **Yager, E.M.** and **Rickenmann, D.** (2019) History-dependent threshold for motion revealed by continuous bedload transport measurements in a steep mountain stream. *Geophysical Research Letters*, **46**, 2583–2591. DOI:10.1029/2018GL081325

Mathias Kondolf, G. (1994) Geomorphic and environmental effects of instream gravel mining. *Landscape and Urban Planning*, **28**, 225–243. DOI:10.1016/0169-2046(94)90010-8

McManamay, R.A., **Oigbokie, C.O.**, **Kao, S.-C.** and **Bevelhimer, M.S.** (2016) Classification of US Hydropower Dams by their Modes of Operation: Hydropower Modes of Operation. *River Research and Applications*, **32**, 1450–1468. DOI:10.1002/rra.3004

Miller, G.T. and **Spoolman, S.E.** (2012) Living in the environment, 17. ed., international ed. *Brooks/Cole Cengage Learning*, Pacific Grove, Calif.

Miller, M.C., **McCAVE, I.N.** and **Komar, P.D.** (1977) Threshold of sediment motion under unidirectional currents. *Sedimentology*, **24**, 507–527. DOI:10.1111/j.1365-3091.1977.tb00136.x

Nelson, J.M., **Shreve, R.L.**, **McLean, S.R.** and **Drake, T.G.** (1995) Role of Near-Bed Turbulence Structure in Bed Load Transport and Bed Form Mechanics. *Water Resources Research*, **31**, 2071–2086. DOI:10.1029/95WR00976

Nepal, S., **Avash P** and **Shrestha, A.B.** (2018) Revisiting Key Questions Regarding Upstream-Downstream Linkages of Land and Water Management in the Hindu Kush Himalaya (HKH) Region. doi: 10.13140/RG.2.2.34784.53769 DOI:10.13140/RG.2.2.34784.53769

Ockelford, A.M. and **Haynes, H.** (2013) The impact of stress history on bed structure. *Earth Surf. Process. Landf.*, **38**, 717–727. DOI:10.1002/esp.3348

Ockelford, A., **Woodcock, S.** and **Haynes, H.** (2019) The impact of inter-flood duration on non-cohesive sediment bed stability. *Earth Surf. Process. Landf.*, **44**, 2861–2871. DOI:10.1002/esp.4713

Paintal, A.S. (1971) Concept Of Critical Shear Stress In Loose Boundary Open Channels. *Journal of Hydraulic Research*, **9**, 91–113. DOI:10.1080/00221687109500339

Parker, G. (2008) Transport of Gravel and Sediment Mixtures. In: *Sedimentation Engineering*, *American Society of Civil Engineers*, Reston, VA, 165–251. DOI:10.1061/9780784408148.ch03

Parker, G. and **Klingeman, P.C.** (1982) On why gravel bed streams are paved. *Water Resources Research*, **18**, 1409–1423. DOI:10.1029/WR018i005p01409

Parker, G., **Klingeman, P.C.** and **McLean, D.G.** (1983) Bedload and size distribution in paved gravel-bed streams. *Journal of Hydraulic Engineering*, **108**, 544–571. ,https://api.semanticscholar.org/CorpusID:129650052

Pender, G., **Haynes, H.** and **Pender, G.** (2007) Stress History Effects on Graded Bed Stability. DOI:10.1061/(ASCE)0733-9429(2007)133:4(343)

Perret, E., **Berni, C.** and **Camenen, B.** (2020) How does the bed surface impact low-magnitude bedload transport rates over gravel-bed rivers? *Earth Surface Processes and Landforms*, **45**, 1181–1197. DOI:10.1002/esp.4792

Petts, G.E. and **Amoros, C.** (1996) The Fluvial Hydrosystems. *Springer Netherlands*, Dordrecht.

Red Eléctrica de España (2023) Electricity demand tracking in real time. Spanish peninsula. Generation mix (MW). ,https://demanda.ree.es/visiona/home

Reid, I., **Frostick, L.E.** and **Layman, J.T.** (1985) The incidence and nature of bedload transport during flood flows in coarse-grained alluvial channels. *Earth Surface Processes and Landforms*, **10**, 33–44. DOI:10.1002/esp.3290100107

Rice, S.P., **Greenwood, M.T.** and **Joyce, C.B.** (2001) Tributaries, sediment sources, and the longitudinal organisation of macroinvertebrate fauna along river systems. *Canadian Journal of Fisheries and Aquatic Sciences*, **58**, 824–840. DOI:10.1139/f01-022

Ritchie, H., **Rosado, P.** and **Roser, M.** (2023) Energy - based on dataset : Ember - yearly electricity data (2023); ember - european electricity review (2022) with major processing by our world in data. "Electricity generation from other renewables, excluding bioenergy" [dataset]. Ember, "yearly electricity data"; ember, "european electricity review" [original data]. ,https://ourworldindata.org/energy

Schmidt, J.C. and **Wilcock, P.R.** (2008) Metrics for assessing the downstream effects of dams. *Water Resources Research*, **44**, 2006WR005092. DOI:10.1029/2006WR005092

Schmutz, S. (2018) Riverine ecosystem management: Science for governing towards a sustainable future, 1st edition. *Springer Berlin Heidelberg*, New York, NY.

Schmutz, S., **Bakken, T.H.**, **Friedrich, T.**, **Greimel, F.**, **Harby, A.**, **Jungwirth, M.**, **Melcher, A.**, **Unfer, G.** and **Zeiringer, B.** (2015) Response of fish communities to hydrological and morphological alterations in hydropeaking rivers of austria. River Research and Applications. DOI:10.1002/rra.2795

Schumm, S.A. (1985) Patterns of alluvial rivers. *Annual Review of Earth and Planetary Sciences*, **13**, 5–27. DOI:10.1146/annurev.ea.13.050185.000253

Schumm, S.A. (1969) River Metamorphosis. *Journal of the Hydraulics Division*, **95**, 255–274. DOI:10.1061/JYCEAJ.0001938

Schumm, S.A. (1977) The fluvial system. *Wiley*, New York.

Shields, J.C. (1936) Application of similarity principles and turbulence research to bed-load movement. *Soil Conservation Service*. ,http://resolver.tudelft.nl/uuid:a66ea380-ffa3-449b-b59f-38a35b2c6658

Smokorowski, K.E. (2022) The ups and downs of hydropeaking: a Canadian perspective on the need for, and ecological costs of, peaking hydropower production. *Hydrobiologia*, **849**, 421–441. DOI:10.1007/s10750-020-04480-y

Smokorowski, K.E., **Metcalfe, R.A.**, **Finucan, S.D.**, **Jones, N.**, **Marty, J.**, **Power, M.**, **Pyrce, R.S.** and **Steele, R.** (2011) Ecosystem level assessment of environmentally based flow restrictions for maintaining ecosystem integrity: a comparison of a modified peaking versus unaltered river. *Ecohydrology*, **4**, 791–806. DOI:10.1002/eco.167

Svendsen, K.M., **Renshaw, C.E.**, **Magilligan, F.J.**, **Nislow, K.H.** and **Kaste, J.M.** (2009) Flow and sediment regimes at tributary junctions on a regulated river: impact on sediment residence time and benthic macroinvertebrate communities. *Hydrological Processes*, **23**, 284–296. DOI:10.1002/hyp.7144

Tockner, K. and **Mehner, T.** (eds) (2022) Encyclopedia of inland waters, 2nd ed. *Elsevier*, Amsterdam.

Turowski, J.M., **Badoux, A.** and **Rickenmann, D.** (2011) Start and end of bedload transport in gravel-bed streams: START AND END OF BEDLOAD TRANSPORT. *Geophysical Research Letters*, **38**, DOI:10.1029/2010GL046558

Vanzo, D., **Bejarano, M.D.**, **Boavida, I.**, **Carolli, M.**, **Venus, T.E.** and **Casas-Mulet, R.** (2023) Innovations in hydropeaking research. *River Research and Applications*, **39**, 277–282. DOI:10.1002/rra.4118

Vanzo, D., **Zolezzi, G.** and **Siviglia, A.** (2016) Eco-hydraulic modelling of the interactions between hydropeaking and river morphology. *Ecohydrology*, **9**, 421–437. DOI:10.1002/eco.1647

Vericat, D. and **Batalla, R.J.** (2006) Sediment transport in a large impounded river: The lower Ebro, NE Iberian Peninsula. *Geomorphology*, **79**, 72–92. DOI:10.1016/j.geomorph.2005.09.017

Vericat, D., **Batalla, R.J.** and **Gibbins, C.N.** (2008) Sediment entrainment and depletion from patches of fine material in a gravel-bed river. *Water Resour. Res.*, **44**, 1–15. DOI:10.1029/2008WR007028

Vericat, D., **Ville, F.**, **Palau-Ibars, A.** and **Batalla, R.J.** (2020) Effects of hydropeaking on bed mobility: Evidence from a pyrenean river. *Water*, **12**, 178. DOI:10.3390/w12010178

Wiberg, P.L. and **Smith, J.D.** (1987) Calculations of the critical shear stress for motion of uniform and heterogeneous sediments. *Water Resources Research*, **23**, 1471–1480. DOI:10.1029/WR023i008p01471

Wilcock, P.R. (1992) Flow competence: A criticism of a classic concept. *Earth Surf. Process. Landforms*, **17**, 289–298. DOI:10.1002/esp.3290170307

Wilcock, P.R. and **McArdell, B.W.** (1993) Surface-based fractional transport rates: Mobilization thresholds and partial transport of a sand-gravel sediment. *Water Resour. Res.*, **29**, 1297–1312. DOI:10.1029/92WR02748

Wilcock, P.R. and **McArdell, B.W.** (1997) Partial transport of a sand/gravel sediment. *Water Resour. Res.*, **33**, 235–245. DOI:10.1029/96WR02672

Wilcock, P.R. and **Southard, J.B.** (1988) Experimental study of incipient motion in mixed-size sediment. *Water Resources Research*, **24**, 1137–1151. DOI:10.1029/WR024i007p01137

Wohl, E. (2018) Geomorphic context in rivers. *Progress in Physical Geography: Earth and Environment*, **42**, 841–857. DOI:10.1177/0309133318776488

Yager, E.M., **Schmeeckle, M.W.** and **Badoux, A.** (2018) Resistance Is Not Futile: Grain Resistance Controls on Observed Critical Shields Stress Variations. *J. Geophys. Res. Earth Surf.*, **123**, 3308–3322. DOI:10.1029/2018JF004817

Yager, E.M. and **Schott, H.E.** (2013) 9.7 The Initiation of Sediment Motion and Formation of Armor Layers. In: *Treatise on Geomorphology*, *Elsevier*, 87–102. DOI:10.1016/B978-0-12-374739-6.00232-3

Zingg, T. (1935) Beitrag zur Schotteranalyse. Doctoral thesis, ETH Zurich DOI:10.3929/ETHZ-A-000103455

Chapter 2

Study area and methods

Upper Cinca River showing its bedrock at low flow during a preparatory photogrammetry campaign, 09/10/2019. Author: Fanny Ville

Overview

This chapter has two sections: Study Area and Methods. Both sections provide additional information obtained during the PhD that does not conform a scientific manuscript but that helped characterizing the study basins and the discussion of the results. Additionally, the methods provide more details of the wide techniques and methodologies developed and applied during the PhD, beyond the specific and general described in the papers.

In this chapter the two parts makes the section numbering more complex. The first digit corresponds to the number of the chapter, the second indicates the number of the part (1 or 2) and the following digits refer to the subdivisions.

Part 1 : Study area

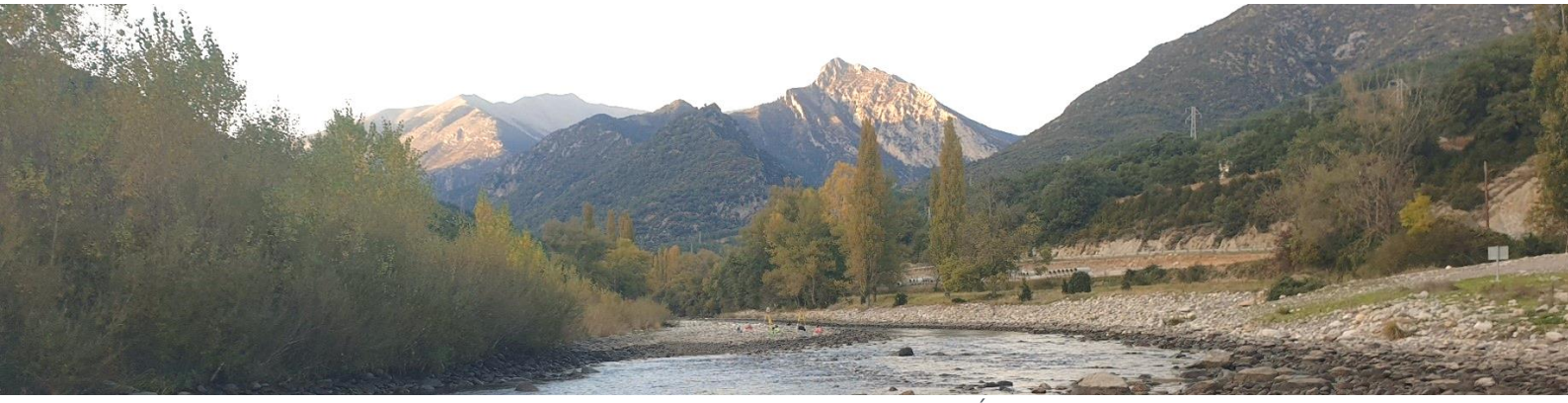

Campo Downstream study reach at low flow, 07/11/2018 (Upper Ésera River). Author: Fanny Ville

The purpose of this first part of Chapter 2 is to present and describe the study areas where data were collected in order to achieve the objectives of the thesis. First, the physical characteristics or properties of the basins (i.e., relief, topography, valley morphology, bed materials) and their hydroelectric facilities are described. Next, some details about the intrinsic structural properties and external forcing and drivers of both catchments are described and discussed in order to provide an overall view of sediment sources and flow regimes in both.

2.1.1 BASINS CHARACTERISTICS

2.1.1.1 The Upper Cinca and Ésera catchments

The upper Cinca and Ésera rivers, shown in the figure (Figure 2.1), are located on the southern slopes of the Spanish Pyrenees. The Ésera runs to the west of the Cinca (sharing drainage divide), joining the latter on its left bank after travelling some 130 km from its source and draining 1 535 km² of land. The Cinca is one of the Ebro's main tributaries in terms of water and sediment supply. The upper part of these two rivers supply water to the Mediano, Grado and Barassona reservoirs (Figure 2.1, **A**), which have a total storage capacity of 920 hm^3 to meet water needs, mainly irrigation of agricultural land and hydroelectric generation (total capacity: 134 Mw) supporting economic development further down the valley.

The outlet of the Upper Cinca basin is located a few hundred meters upstream (US) of the town of Ainsa, and drains an area of 835.3 km² (Figure 2.1, B). Its source is at an altitude of 3 355 m a.s.l. on the Monte Perdido peak, 57.80 km upstream. In the basin, the altitude varies between 529 m a.s.l. at the outlet and 3 375 m a.s.l. at the Posets peak (head of the Cinqueta tributary catchment); i.e. the catchment's relief is 2 846 m.

The Upper Ésera basin covers 733 km², with its outlet located near the village of Santaliestra y San Quílez. Its basin is 1.5 times longer than that of the Cinca, but its altitude gradient is similar, with a minimum at the outlet (539 m) and a maximum at 3,404 m, located 79.80 km upstream at the summit of Aneto (highest peak of the Pyrenees).

Both basins have 75% medium to steep slopes (values between 16° and 45°), and 10% very steep slopes (values higher than 45°), making them poorly populated areas. Artificial surface cover is less than 1% and agricultural surface cover is only 3% for the Cinca and 6% for the Ésera, and this is very localized. The remainder is covered by forests (48% and 41%) and areas with little or no cover (41% and 53%, herbaceous substratum, base soil, river, glacier).

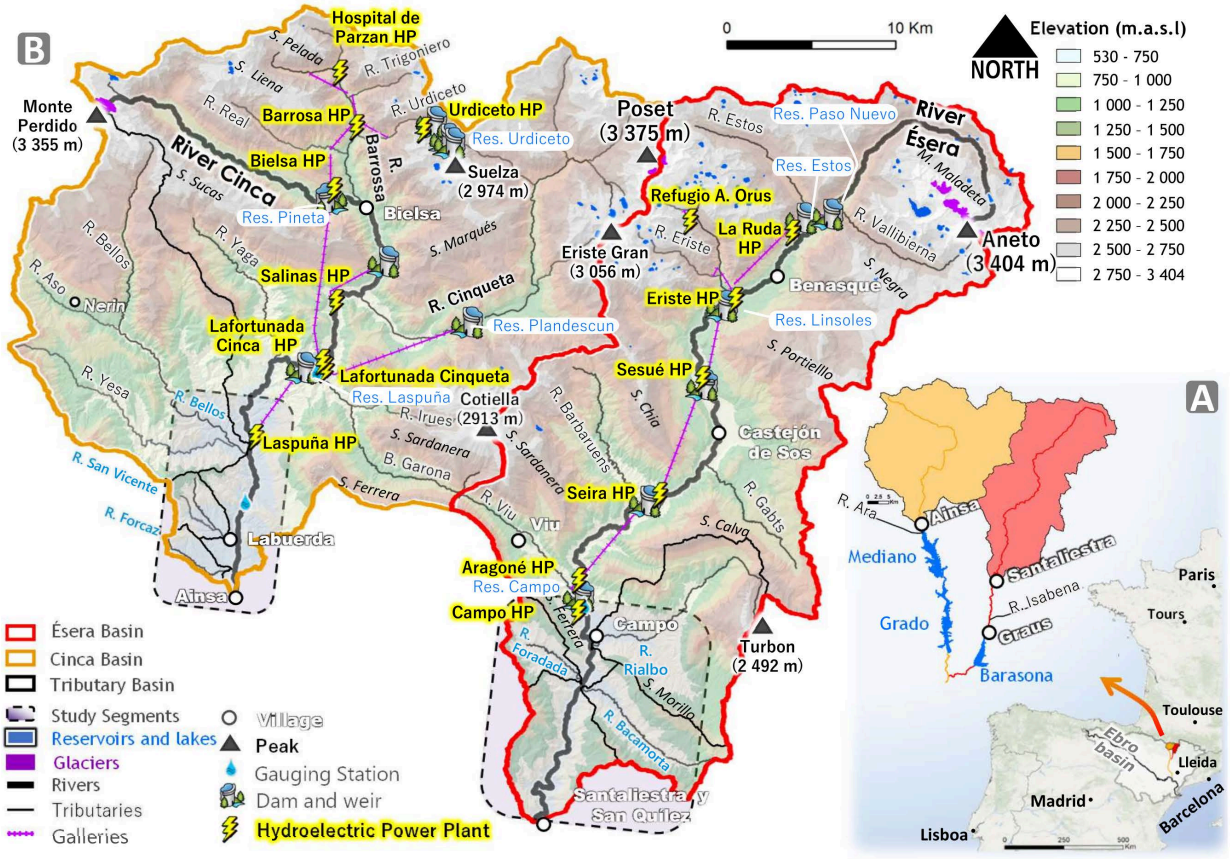

Figure 2.1: Locations of the Upper Cinca and Ésera Basins. Hydroelectric schemes in both catchments are also represented. Hydrographic network and catchment delineation calculated by means of GIS from Digital Elevation Model (DEM) of 5 m of spatial resolution (data source: Spanish National Centre of Geographic Information (2015)). Hydroelectric facilities (data sources: Transición Ecológica y el Reto Demográfico, 2021; Ebro. Oficina de Planificación Hidrológica, 2007). Glacier exent from Vidaller et al. (2021) and lake from Dirección General de Medio Natural (2018)

2.1.1.2 The Upper Cinca and Ésera hydroelectric power schemes and their relation with the longitudinal profile

The Cinca basin is occupied by a network of 8 hydroelectric plants with a total capacity of 113 Mw, built between 1923 and 1993. The relief allowed the construction of a network of plants with heads ranging from 51 to 430 m. The cumulative head is 1 720 m. The Urdecito plant is a pumped storage plant with the highest head (430 m). The other plants (Hospital de Parzan, Barrossa, Bielsa, Salinas, Lafortunada Cinca, Lafortunada Cinqueta and Laspuña) form a modified run of river (mROR) system. Water is diverted from various lakes and reservoirs with a total storage capacity of 6.3 hm^3 (equivalent to about 2.5 days of potentially storable runoff) and then conveyed to the turbines via a network of tunnels, canals and penstocks about 60 km long. The 23 km section between the Bielsa and Laspuña stations can be described as a bypassed. This means that only a minimum flow runs through the river, while a larger flow is diverted to the turbines. The Pineta, Plandescun and Laspuña reservoirs are equipped with gates and flaps to allow water and sediment to pass during floods. Therefore, although sediment transport regime may be affected by the dam, their spatial continuity is not disturbed, as flows during flood events.

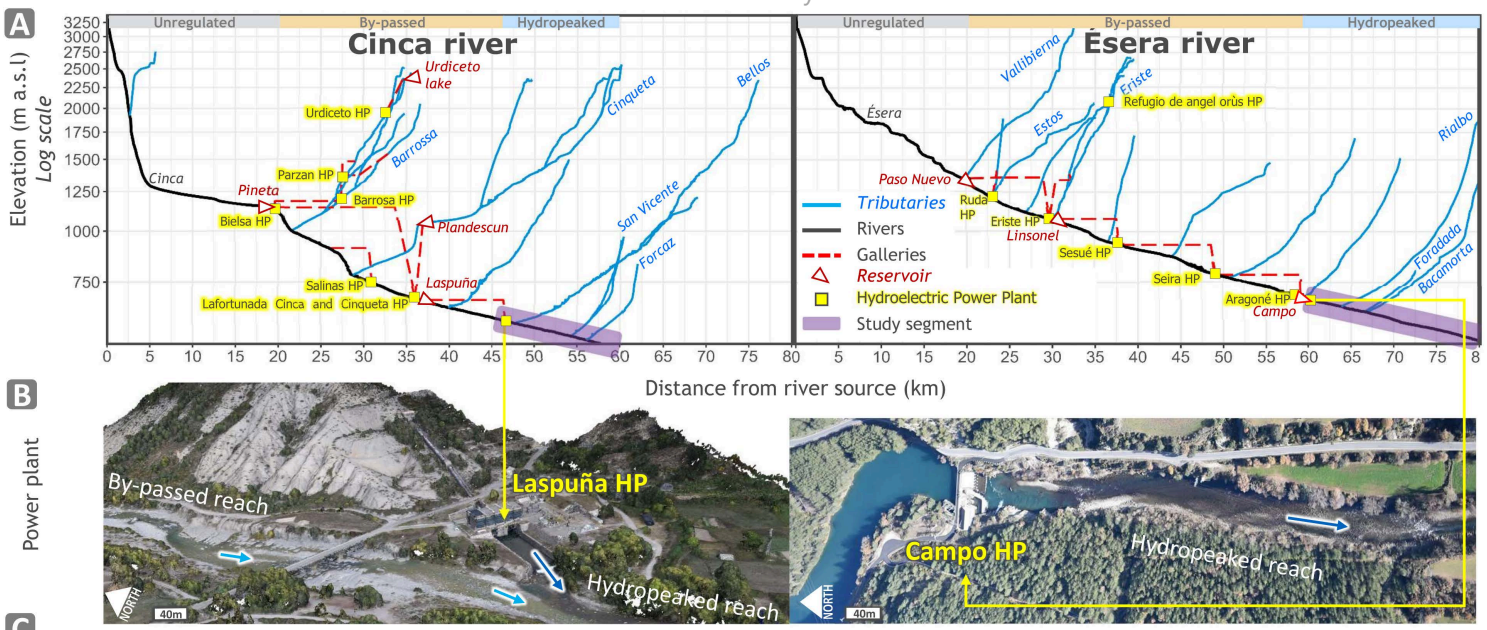

C

River	Power plant name	Year a	Operating	Qmax b (m3/s)	Turbine	Water supply c	Volume reservoir d (Hm3)	Fall (m)	Power (Mw)	Production (Gwh / year)
Cinca	URDICETO	1930	Pumped storage	2.0	2 pump unit and turbine Pelton	Intake: lake urdiceto, reservoir Baranetas	5 , 0.02	430	7.2	0.6
Cinca	HOSPITAL DE PARZAN	1993	RoR, Diversion	0.9	-	-	-	125	1.1	-
Cinca	BARROSA	1930	RoR, Diversion	3.4	1 horizontal Francis turbine unit.	Intake: weirs of Hospital Parzan, Trigoniero, Avellanera	-	340	3.6	16.7
Cinca	BIELSA	1949	RoR, Diversion	5.0	1 horizontal Francis turbine unit	Intake : reservoir Barossa, Chisagues rio real	-	51	1.6	4.9
Cinca	SALINAS (SAN MARCIAL)	1958	RoR, Diversion	2.2	1 horizontal Francis turbine unit	Intake: reservoir Salina	-	161	2.4	11.7
Cinca	LAFORTUNADA CINCA	1923	RoR, Modified	12.0	3 vertical Pelton groups	Intake: reservoir Pineta	0.26	362	42.0	160.5
Cinca	LAFORTUNADA CINQUETA	1932	RoR, Modified	16.0	2 vertical Pelton groups	Intake: reservoir Plandescun	0.80	173	41.4	90.7
Cinca	**LASPUÑA**	**1965**	**RoR, Modified**	**26.0**	**2 horizontal Francis turbine unit**	**Intake: reservoir Laspuña**	**0.35**	**77**	**13.6**	**55.9**
						Total Cinca:	**6.43**	**1720**	**112.9**	**341.0**
Ésera	REFUGIO DE ANGEL ORÚS	-	RoR, Diversion	0.1	-	Intake: Torrente Llardana	-	135	-	-
Ésera	RUDA		RoR, Diversion	0.1	-	Intake: Rigau	-	202	0.2	-
Ésera	ERISTE	1969	RoR, Modified	36.9	2 Francis vertical axis turbine group	Intake: reservoir PasoNuevo, reservoir Estos, Eriste, Aigreta de la vall	3.15, 0.08, -,-	283	80.0	150.0
Ésera	SESUE	1964	RoR, Modified	32.2	2 Francis horizontal axis turbine group	Intake: reservoir Linsonel	2.17	147	36.0	100.0
Ésera	SEIRA	1918	RoR, Modified	24.0	4 Francis horizontal axis turbine group	Intake: reservoir Villanova	0.03	146	25.0	87.8
Ésera	ARGONE	1947	RoR, Modified	20.0	2 Francis vertical axis turbine group	InIntake: reservoir Seira	0.01	93	14.5	52.5
Ésera	**CAMPO**	**1929**	**RoR, Modified**	**20.0**	**1 Francis horizontal axis turbine unit**	**InIntake: reservoir Campo**	**0.09**	**12**	**1.8**	**5.4**
						Total Ésera:	**5.53**	**1017**	**155.1**	**395.7**

Figure 2.2: (**A**) Hydroelectric schemes across the longitudinal profile of the Upper River Cinca and Ésera. (**B**) Left, view of the river Cinca at the Laspuña Hydropower station or HP (point cloud view from a photogrametric flight performed during the PhD). Right, view of the river Ésera at the Campo reservoir and dam (aerial photo performed during the PhD). (**C**) Hydroelectric facilities characteristics (data sources: Transición Ecológica y el Reto Demográfico, 2021; Ebro. Oficina de Planificación Hidrológica, 2007; Galan, 2012). **a**: year of commissioning, **b**: maximum turbine flow capacity, **c**: source of water inflow, **d**: volumes of the various reservoirs.

The Ésera river presents over a 40 km section between the Paso Nuevo and Campo dams a network of 7 hydroelectric power stations built between 1920 and 1972 with a total capacity of 155 Mw. Together they form a MROR-type scheme. The water from the main river and its tributaries is diverted from reservoirs or water intakes and conveyed to the turbines via a network of 35 km of tunnels and penstocks, with falls ranging from 93 to 283 m. The total height of fall is 1 017 m. The last power station is located at the foot of the small Campo dam on the course of the river, where the head corresponds only to the height of the dam (12 m). The total storage capacity for the whole basin is 5.53 hm^3 (i.e. around 4 days of potentially storable runoff). The Paso Nuevo, Linsonel and Campo dams are equipped with spillways and bottom gates, but sediment does not seem to be able to pass through them. The segment studied can therefore be described as supply

2.1.1.3 The Upper Cinca and Ésera study segments

Figure 2.3, shows the local context of the study segments with the valley confinement configuration, continuous estimation of median grain size, valley width and wetted extension for several flows (maximum and median geometries of the segments are shown in Table 2.1), as well as the talweg profile and water surface elevation profile for a 1-year flood (return period). The data used and their processing methods are explained in Section 2.2.2.4.2.1 (this chapter).

The Cinca segment is 12 km long, with an average gradient of 0.70%. It begins 2 km upstream of Laspuña HP and ends 10 km downstream, near the town of Ainsa. The Laspuña dam is located around 20 km upstream of the study segment. It diverts water from the river to the power station, which has a maximum turbine flow capacity of 26 m^3s^{-1}. In the case of a significant influx of water, when the dam is full and the power station's maximum flow is reached, the dam is opened to let the surplus water and sediments through. Peak flows from the hydropeaks can therefore reach values greater than 26 m^3s^{-1}. The main tributary, the River Bellos (182 km^2, or 22% of the study catchment) joins the Cinca one kilometre downstream of Laspuña HP. Between 6.8 and 8.6 km downstream, the two smaller rivers San Vicente and Forcaz (10 and 5 km^2) join the main course, each accounting for around 1% of the Cinca catchment area at its outlet. The segment consists of a wide valley in which the river flows fairly freely (Figure 2.3, A and C). Only 5% of the active channel is confined by the valley margins on both sides, while 59% is constrained on one side and has a divagation space on the other side, and 36% is completely free. The median width of the valley bottom is around 200 meters, reaching a maximum of 600 meters at kilometre 7.5, where there is a gravel mining site. The wandering morphology of this very dynamic segment (cf. Figure 1.3, form point 2, (p.9)) is made up of a main channel and secondary channels around wide sediment banks (Figure 2.4) whose lateral and longitudinal positions vary frequently over time. Some bedrock outcrops are visible, notably between km 8 and the confluence with the Forcaz. The bed slope is flatter. The estimated of the median particle size (D_{50}) shown in Figure 2.3 **B** corresponds to the median obtained at several cross-sectional points covering the entire wetted extent during an annual flood (1-year recurrence interval). The segment presents a homogeneous grain size with, however, a slight increase in size in its second half. This can be explained by the fact that the valley is wider downstream, so the annual flood inundate larger area and competence changes accordingly. The D_{50} estimate includes wider cross-sections covering lateral areas with potentially coarser deposits. The areas of Laspuña US and DS as well as Escalona and Ainsa correspond to sections studied in the next chapter of the thesis while those of, Farm and Camping were analysed as part of work carried out by the RIUS research group but outside the scope of the thesis. Nevertheless, these results are compared with those obtained on the river Ésera and discussed in Chapter 4.

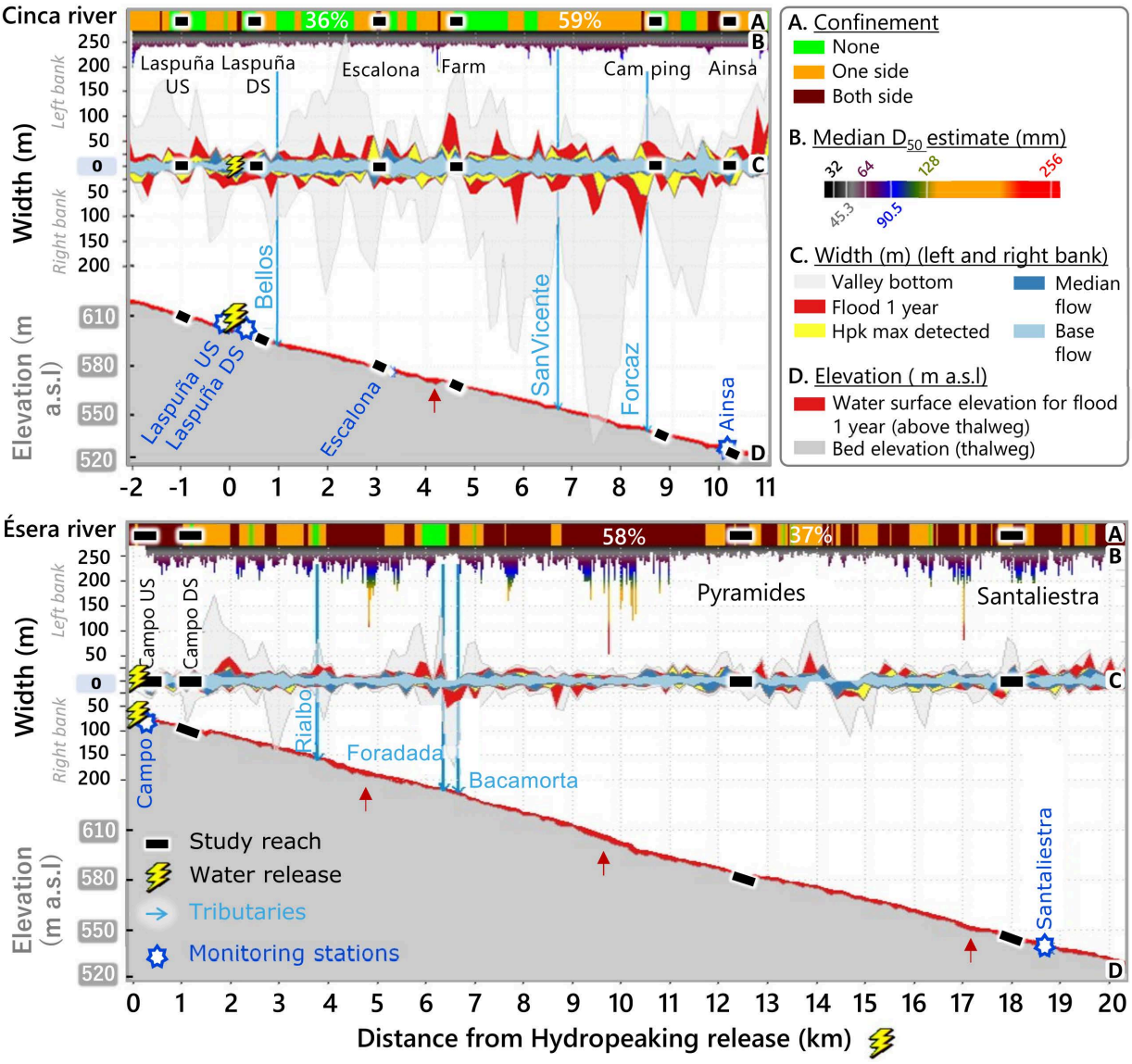

Figure 2.3: Longitudinal profile of the Cinca (top) and Ésera (bottom). **A**: degree of valley confinement, **B**: estimated median D_{50} per cross-section, **C**: valley bottom width and wetted width either side of the centre line at low flow (i.e. 2 m^3s^{-1}) for different flows simulated using the IBER hydrodynamic model (Bladé et al., 2014). The median discharge values are 25 and 15 m^3s^{-1} respectively for the Cinca and Ésera rivers. The maximum hydropeak flows detected are 50 and 30 m^3s^{-1} respectively, while 1-year floods are 210 and 100 m^3s^{-1}, respectively. **D**: Bed and water surface elevation for an annual flood at the talweg.

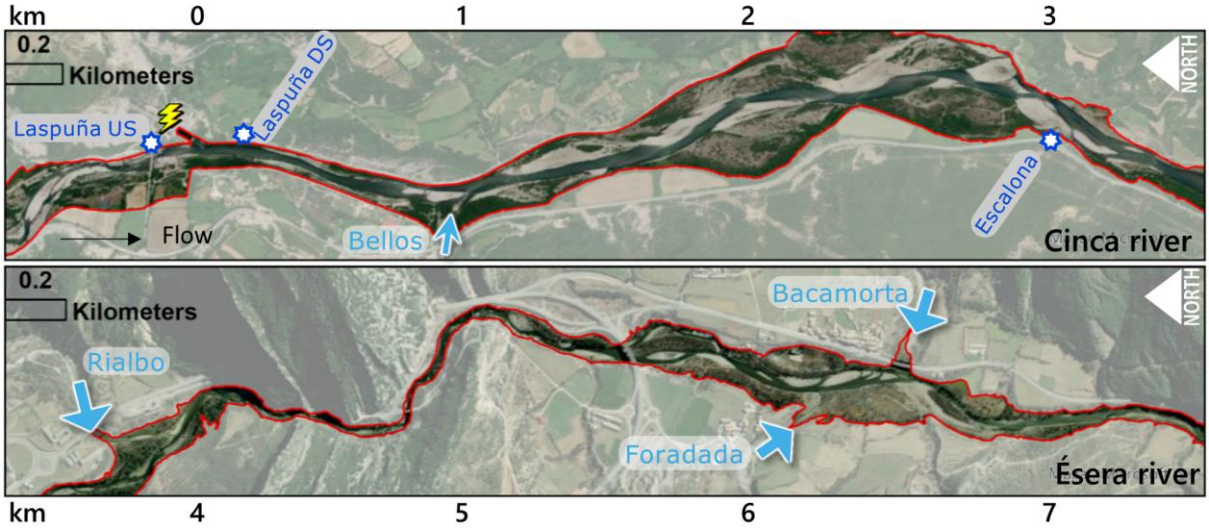

Figure 2.4: Aerial view of a portion of the study segment of approximately 4 km from the Cinca (top) and Ésera (bottom). The red line denotes the valley bottoms. The Cinca shows wandering channel morphology. The section of the Ésera shows a succession of gorges and alluvial pockets. . Arrows indicate main tributaries. The Laspuña HP is indicated together with the location of three of the study sections in the Cinca.

The study segment of the Ésera has an average gradient of 0.73%, similar to that of the Cinca. It begins at the foot of the Campo dam and ends 18 km downstream (distance from the talweg) in the village of Santaliestra y San Quílez. The power station has a maximum turbine flow capacity of 20 m^3s^{-1}. However, the power stations upstream of this cascade have higher capacities (Figure 2.3 **C**). When the small Campo dam is full, these peaks are not completely modulated. Flow peaks with the characteristic shape of hydropeaks have been observed up to 30 m^3s^{-1}. The main tributary, the Rialbo river (30.5 km^2, or 10% of the catchment studied) converges 3.9 kilometres downstream of the Campo dam. It is followed by the Bacamorta and Foradada rivers (30 and 13 km^2) between kilometres 6 and 7, representing 4% and 2% of the catchment area respectively at the outlet. The river is confined within a very steep and narrow valley, with 58% of its length confined on both sides by margins forming numerous gorge sections (narrow, deep, and with steep rock walls), 37% constrained on one bank and only 5% free in alluvial pockets (Figure 2.4). The median width of the valley bottom is around 57 m, reaching a maximum of 245 m at kilometre 1.5. Bedrock outcrops are observed in several places. The constraining shapes of the valley impose a morphology of pool-riffles and planned bed succession to the channel, whose position is stable over time (cf. Figure 1.3, form point 1, (p.9)). The water surface elevation for an annual flood in Figure 2.3 **D** shows a particular behaviour in the gorges sections (red arrows). These sections have a higher water level forming like long pool. Similar observations on the Fraser River (British Columbia, Canada) led (Rennie et al., 2018) to conceptualize this phenomenon. It can be explained by a slowing of velocities due to high wall friction and secondary circulation generating high roughness, so resistance to flow increases while the slope of the water surface and the depth-averaged velocity decrease. This example shows that flow propagation and therefore hydropeaks can be very different depending on geomorphological constraints. Four sections, Campo US, Campo DS, Pyramides and Santaliestra distributed from the foot of the dam to 18 km downstream were sampled and monitored to meet the objectives of the thesis. Campo US is not upstream of the dam but at its foot. The two reaches near the village of Campo have been named US (upstream) and DS (downstream) to differentiate them. This is in contrast to the Cinca, where Laspuña US is actually located upstream of the HP.

In comparison with the Cinca, although the estimated average D_{50} value over the two sections is similar (i.e. 64.1 mm for the Cinca and 62.8 mm for the Ésera), grain sizes are more heterogeneous on the Ésera, i.e. greater sorting. The confined areas of gorges (from km 4 to 5; 9 to 11 and km17) can show a D_{50} greater than 90.5 mm, while the long and more open section (km 12 to 16), downstream of the tributaries and the main section of gorge (9 to 11 km), has much smaller grain sizes (i.e. 45.5 mm or less).

Despite a similar median value for mean depths presented in Table 2.1, the wetted widths of the Cinca are greater (Table 2.1 and Figure 2.3 **C**). The median wetted width to depth ratio (w/d) of the Cinca is almost twice that of the Ésera (Table 2.1 column 7).

Table 2.1: Maximum and median water depth and width for cross-sections extracted every 20 metres along the two study segments.

RIVER	Flow	Max width (m)	Max mean depth (m)	Median width (m)	Median mean depth (m)	Median w/d (-)
Cinca	Base flow	73.1	1.5	22.1	0.2	**100.0**
Cinca	Median flow	96.7	1.9	29.0	0.6	**51.3**
Cinca	1-year flood	208.6	3.9	63.2	1.7	**37.0**
Cinca	Valley	599.3		197.4		
Ésera	Base flow	41.5	3.0	13.3	0.3	**44.8**
Ésera	Median flow	52.0	3.5	21.3	0.7	**32.6**
Ésera	1-year flood	78.1	4.6	34.1	1.7	**20.2**
Ésera	Valley	245.4		56.7		

The two segments therefore have similar average slopes and grain sizes, while the morphology of their valley, channels and channel stability differ substantially (see Figure 1.3). Each of the two segments studied has a confluence with 3 tributaries, one principal and two smaller.

2.1.1.4 Grain shapes in the study segments

The grains measured in the two river segments to characterize the shape of the fluvial sediments (more details in Chapter 5) show a median spherical shape according to Zinng's classification (Figure 2.5). The sediments of the Ésera are often flatter and more elongated. Despite the differences in size and shape between the rivers, both show a similar evolution of median shape with increasing size (*b*-axis). For clarity, grains from both rivers have been grouped by grain size fraction and the median shape for each fraction is highlighted in Figure 2.5. The lower limit of each fraction is indicated (i.e. 8 mm fraction include grains measuring >=8 mm and <11.3 mm). The trend can be divided into 3 phases: (i) Firstly, between the 8 and 11 mm fractions, there is a significant progressive decrease in elongation and an increase in sphericity, while flattening remains stable. (ii) Secondly, between 11 and 45 mm, the median shape of the particles becomes progressively more elongated and flatter towards a bladed shape. (iii) Finally, there is a change in trend for the particles above 64 mm, they become more compact with a discoidal tendency.

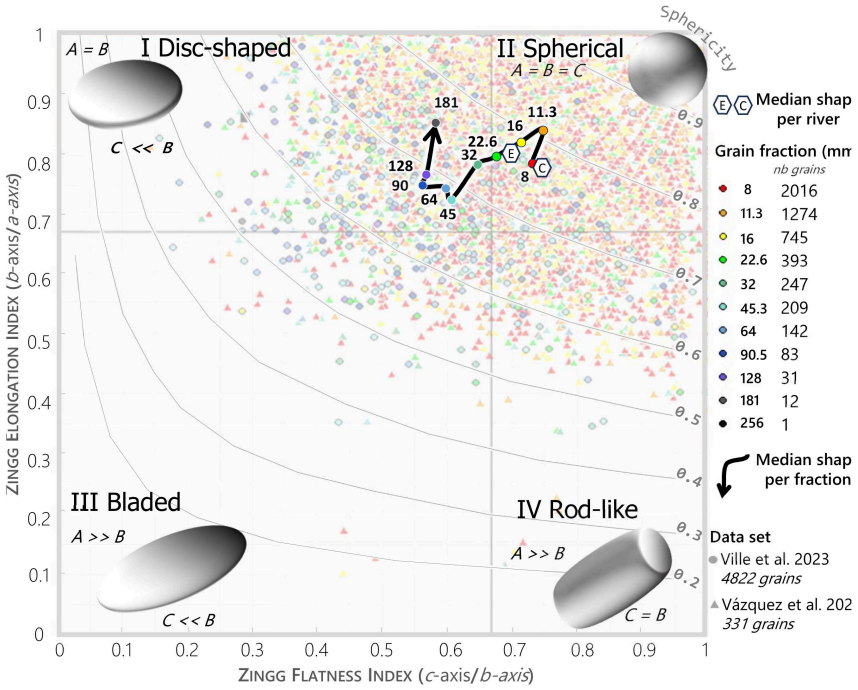

Figure 2.5: Grain shape according to the Zingg (1935) classification of the 5 153 grains measured in the two river segments using (i) a Pebble-Box for the dataset acquired during the thesis, and (ii) using a calliper for the Vazquez et al. 2024 dataset. Median Zingg flatness and elongation indexes for rivers (hexagonal symbol) and by particle size fraction with grain coming from both rivers (coloured round dot with arrow).

2.1.2 INTRINSIC PROPERTIES AND EXTERNAL FORCING CONTROLLING SEDIMENT SOURCES AND FLOWS

2.1.2.1 Intrinsic structural properties

The Pyrenees, oriented WE, arose from phases of sedimentary deposition intercalated between two orogenic phases (Choukroune, 1992; Ríos et al., 1979). The first created the single continent (i.e. Pangea) as well as the Hercynian mountain range around -360 to -290 million years, followed by a period of erosion and then continental plate spreading. The second phase, the Alpine orogeny, took place between the Iberian and European plates around -40 to -20 million years (Figure 2.6). The Pyrenees are still undergoing a period of erosion.

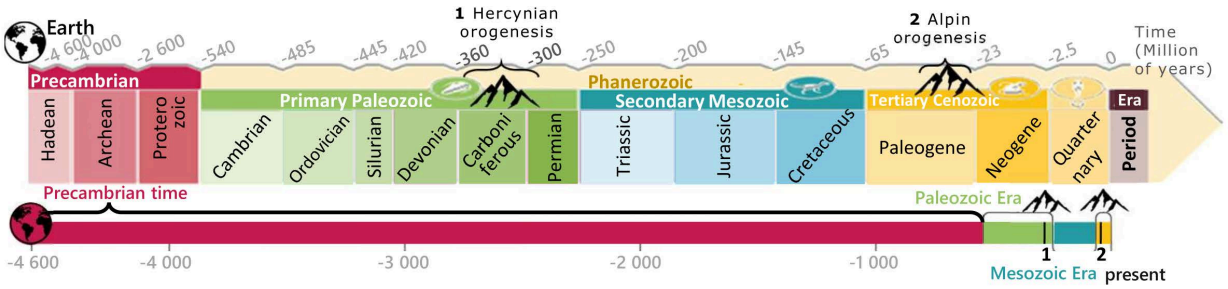

Figure 2.6: Geological time scale from the formation of the earth to the present day, showing the phases in the formation of the Pyrenees. At the top, the period is detailed, at the bottom, the time scale is respected.

Within the catchments, as shown in Figure 2.7 **A**, there are various NE-SW orientated formations that can be classified into 4 main units (Rios Aragues et al., 1982; Ríos Aragues et al., 2002; Robador Moreno and Zamorano Cáceres, 2012; Teixell et al., 2016).

(*i*) The Axial Pyrenees correspond to the most northeastern areas. They are mainly composed of metamorphic rocks (schist and marble) and igneous rocks (granite and granodiorite) resulting from the Hercynian orogeny in the Palaeozoic era (Figure 2.6). They represent 20% of the upstream catchment area of the Cinca and 47% of that of the Ésera (Figure 2.7 **A**). Across the 3 highest summits (i.e. from west to east: Monte Perdido, Poset and Aneto), 2.5 km^2 of glaciers still remained in 2020 despite a significant reduction (-24%) observed between 2011 and 2020 (Vidaller et al., 2021) and an overall loss of -88.3% since 1850 (Rico et al., 2017). According to estimates made by López-Moreno et al. (2020a), although these Pyrenean glaciers are melting every year, their net contribution to rivers is very modest at only around 0.54 hm^3/year. In addition, some of the water from the Aneto glacier makes little or no contribution to the water supply of the Ésera, as part of it flows underground through the limestone karst towards the Garonne, on the northern French side of the Pyrenees (López Moreno et al., 2002). However, the gradual retreat of the Pyrenean glaciers could have an impact on the rate of erosion by releasing more sediments as this axial area of the Pyrenees often has steep slopes with little or no vegetation (Figure 2.7 **B** and **C**). However, Alatorre et al., (2010) estimated that the axial zone of the Pyrenees in the Ésera basin could present a temporary storage of material in the form of small depressions, lakes or perched plains, which could slightly limit its capacity to supply material (green coloured zone on the slope map Figure 2.7 **B**). In addition, the presence of dams on the Ésera since the 1920s has created a barrier to the transport of coarse sediments.

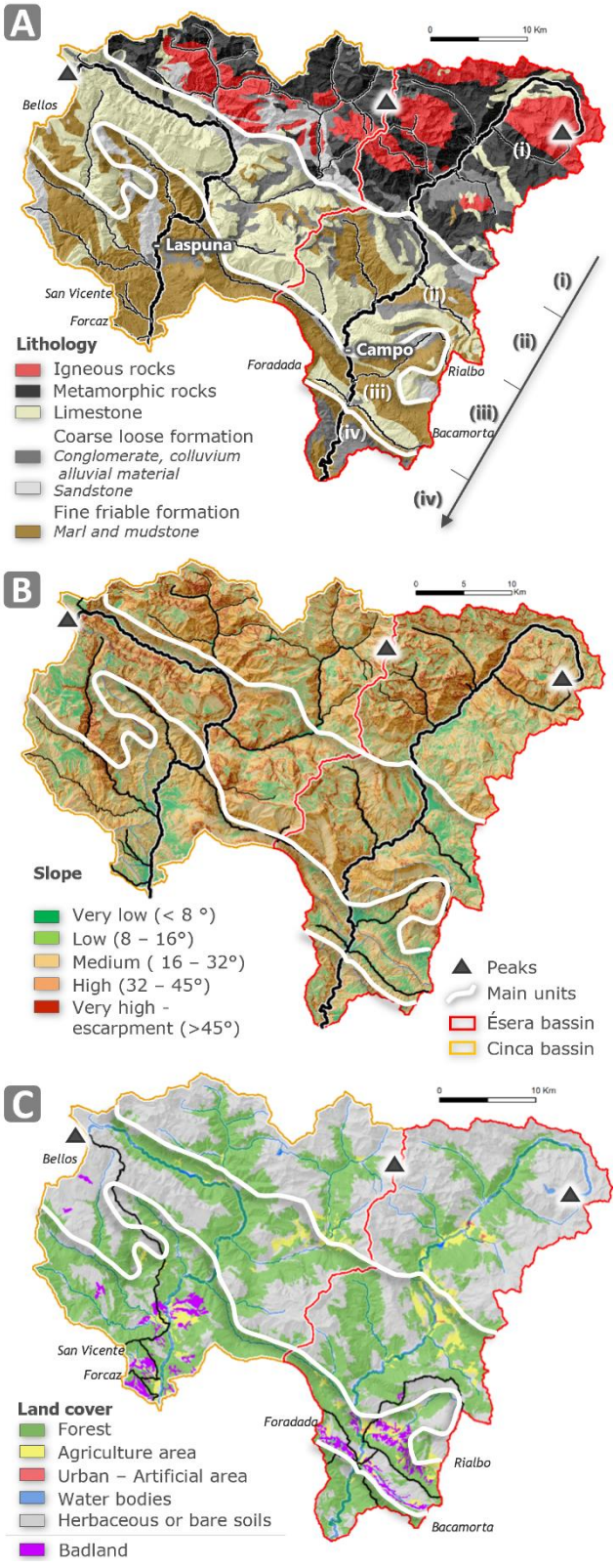

Figure 2.7: Physical context of the upper Cinca and Ésera catchment areas. **A**. Main lithology (data source: Instituto Geográfico de Aragón, 1993). **B.** Slope (in degrees) calculated from a (DEM) of 5 m spatial resolution (data source: Spanish National Centre of Geographic Information, 2015). **C**. Land use map (data source: European Environment Agency, 2018).

(*ii*) In the central part, the internal mountain ranges corresponding to sedimentary formations dating from the Cretaceous and Palaeocene appear superimposed as a result of the second phase of compression and folding during the Alpine orogeny at the end of the Paleogene. These are mainly limestones and sandstones forming relief with very steep cliffs.

(*iii*) The internal depressions in the southernmost and lowest parts of the basin (< 1 000 m altitude), where the study segments and small tributaries (San Vicente, Forcaz, Bacamorta, Foradada) are also located, are composed mainly of highly erodible materials (e.g. marls and sandstone) forming relatively flat reliefs encircled by the limestone walls of the sierras. In certain non-vegetated areas with significant slopes, these friable marl and clay materials are known as badlands and form a very irregular relief with gullies carved out by runoff water and erosion. These formations are mainly found on the tributaries of the segments studied close to the hydrographic network and cover up to 6% of the Rialbo sub-basin (Figure 2.7 **C**). López-Tarazón et al. (2012) demonstrated on the Isabena River (a downstream tributary of the Ésera (Figure 2.1, **A**, p.34)) that even when a tiny part (1%) of a basin contains badlands, these can be the main source of fine sediments, especially when the badlands are connected to the hydrographic network. In the Upper Cinca, Llena et al. (2021) showed as at the annual scale these landscapes can supply up to 40% of the total yield. They also demonstrated as their contribution is controlled by pulses, and the role of the channel network acting as sediment source or sink. In the same Cinca, Béjar et al. (2018) reported how tributaries may significantly change the spatial distribution of suspended sediment concentrations, causing in some occasions an additive supply may affect significantly sediment loads. According to estimates by Alatorre et al. (2010), the Rialbo and Bacamorta tributaries would be the two main suppliers of fine materials in the entire Upper Ésera, contributing 28 000 and 45 000 t/year respectively. In addition, Lobera et al. (2016) demonstrated on the Ésera, 30 km downstream of our study segment, that even low flows could be responsible for 30% of the suspended transport of these materials.

(*iv*) Finally, in the most downstream part of the Ésera, are the pre-Pyrenean molasses, composed mainly of coarse, non-cohesive materials such as conglomerates. The morphology of today's landscape was shaped during the Quaternary period. Successive phases of glaciation and deglaciation controlled river flow and the availability of sediments. The valleys, cirques and moraines are linked to the glaciations, while the conglomerate alluvial terraces were formed during the deglaciations. Coarse loose formations and sandstones can provide the bed load, while easily erodible materials (marl, mudstone) provide fine materials transported in suspension.

2.1.2.2 External forcing and drivers

The climate of this region shows significant North/South variations in terms of temperature and precipitation linked to the altitudinal gradient. The highest parts can receive up to 2000 mm of annual precipitation, while the valley bottoms only receive between 800 and 600 mm (Figure 2.8 **A1**). Based on the data available from the Atlas Climático de Aragón website (ARAGON, 2020), with a spatial resolution of one kilometre, the Cinca catchment receives an average water volume of 1 034 hm^3 per year, while the Ésera only receives 776 hm^3 (Figure 2.8 **A2**). The catchments of the two smaller tributaries of the Ésera, despite having lower rainfall than the Cinca, receive a greater total volume of water due to their surface area being 3 times greater (Figure 2.8 **A1** and **A2**). These tributaries are therefore more likely to influence the hydro-sedimentary dynamics of the Ésera than those of the Cinca.

Figure 2.8 **A3** shows that rainfall occurs mainly in autumn (October and November) and in spring, between April and June, generating high flows (Figure 2.8 **D**). In November, the Escalona station shows greater variability discharge than Campo due to the recurrent occurrence of intense, highly localized thunderstorms in the Cinca's largest catchment area. This situation results in significant flood peaks compared with those observed on the Ésera. Summer is relatively dry (with occasional rainfall), as in winter, resulting in low flows (Figure 2.8 **D**), equivalent to around 50% of the average annual flow.

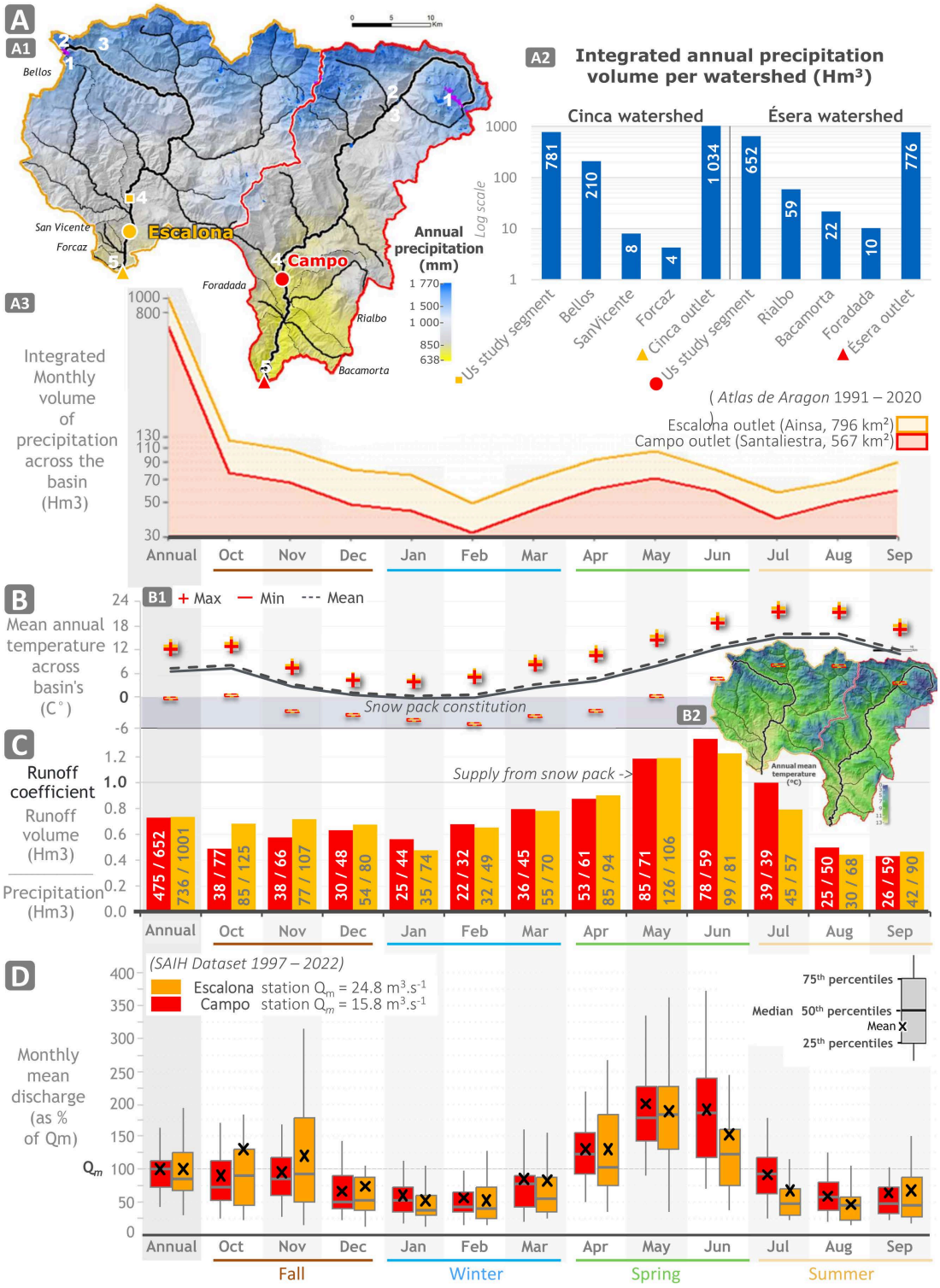

Figure 2.8: Climactic context. **A**. Rainfall. **A1** Spatial mean annual rainfall (1991-2020). **A2** Integration of mean annual precipitation volumes for upstream sub-basins, tributary basins and the study basin at the outlet. **A3** integration of the mean annual and monthly precipitation volumes across the surface area drained to the Escalona and Campo stations. **B** Temperature. **B1** Average, maximum and minimum temperatures over the two study basins on an annual and monthly basis (1991-2020). **B2** Spatial mean annual temperature. **C** Annual and monthly runoff coefficients at the Escalona and Campo stations (Runoff volume at the station / integration of precipitated volume over the surface area drained to the station). **D** Annual and monthly mean discharge normalized by mean annual flow (Q_m) et Escalona and Campo station (1997-2022). Data sources: Saz et al. (2020)

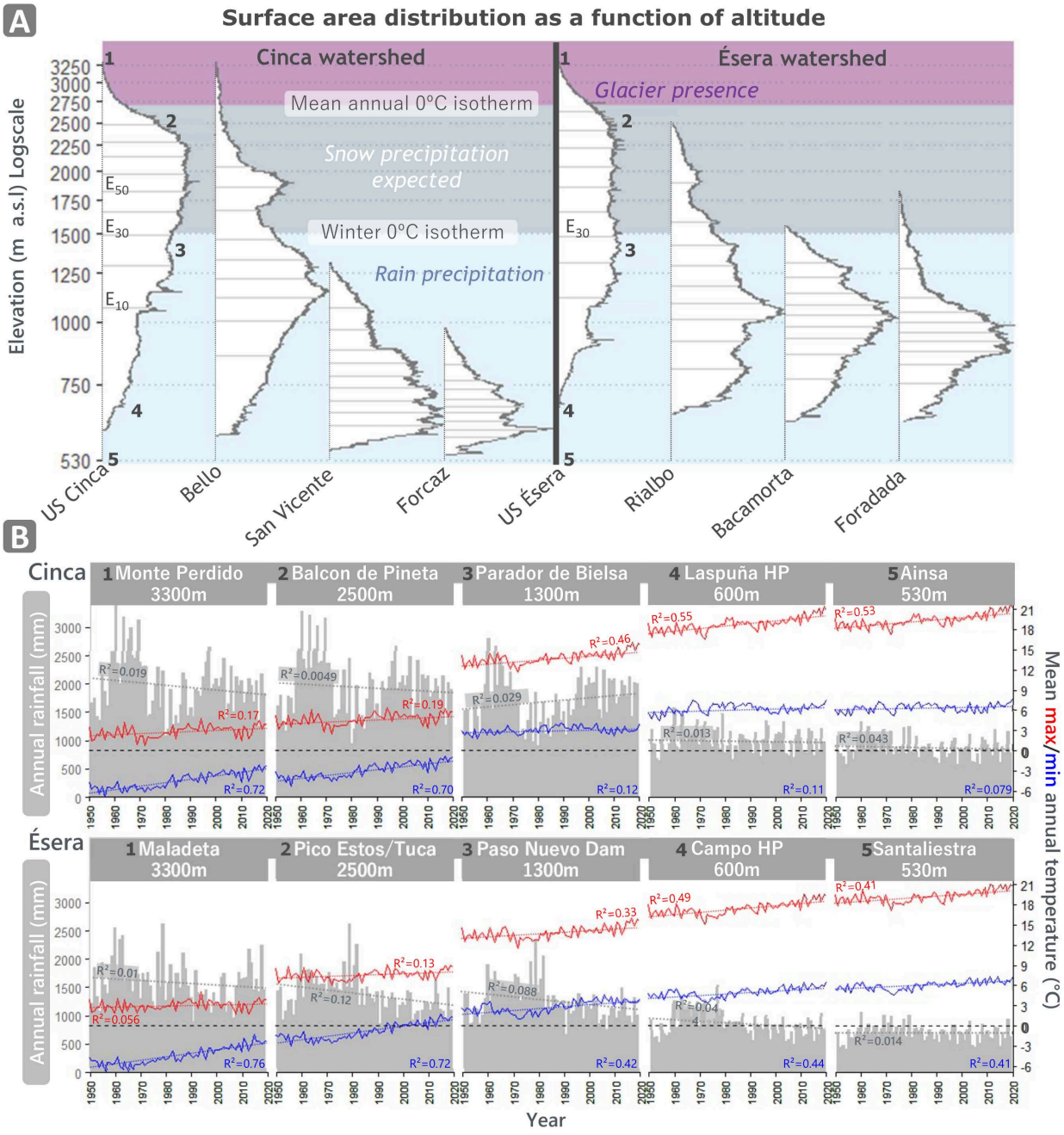

Figure 2.9: A. Distribution of basin surfaces according to altitude. The decile distributions are represented by the grey transverse lines. For example, 30% of the upstream basins of the Cinca and Ésera rivers are below 1500 m a.s.l., while the remaining 70% are above this elevation. **B** Evolution of annual precipitation accumulation and mean annual maximum and minimum temperatures at different points at the same altitude in each basin. The positions of these points (1 to 5) are marked in part of (above) and located in Figure 2.8 A1. The R^2 correlation coefficients indicate the degree of correlation of changes in climatic variables (rainfall and temperatures) over the years.

The winter reduction in flow is explained by average temperatures in the two basins being close to zero between December and February, favouring precipitation in the form of solid snow, and its storage (Figure 2.8). Temperatures are mainly determined by the altitudinal gradient (Figure 2.8 **B2** and Figure 2.9). The altitude of the winter 0°C isotherm lies between 1 500 m and 1 700 m (García-Ruiz et al., 1986), which corresponds to the approximate limit at which a snowpack can form during the coldest months of the year. Above 2 000 m altitude, snow cover can last up to 6 months (López-Moreno et al., 2017) thanks to the negative temperatures from November to April.

The highest flows are observed in spring, with maximum values in May representing ~200% of the mean annual flow (i.e. 2 times the mean annual flow). The quantities of water flowing at the outlets are much greater than those falling on the basins for the rest of the year. Figure 2.8 C shows runoff coefficients (volume flowing to the outlet over volume precipitated over the whole basin) greater than 1 between May and June. Melt water linked to the rise in temperatures in April therefore becomes the main source of the flow measured at the outlets. The snow cover acts as a natural reservoir of water (López-Moreno et al., 2020b). According to estimates by the Confederación Hidrográfica del Ebro (CHE) based on the years 2015-2019, each basin has an average snow reserve equivalent in water volume to 150 hm^3 (Information extracted from the www.cheebro.es, at section: Gestión de la cuenca - Información hidrológica - Datos Históricos - Evolución anual reserva nieve: https://www.chebro.es/web/guest/evoluci%C3%B3n-anual-reserva-nieve1)

The upstream basins of the Cinca and Ésera rivers both have around 70% of their surface area above 1 500 m a.s.l. (i.e. hivernal 0° C isotherm, Figure 2.9 **A**). The main tributary of each segment also has elevated areas suitable for snow accumulation (~40% for the Bellos and 25% for the Rialbo). The smaller tributaries, on the other hand, do not appear to have such areas. Spring water inflows to the study segments will come mainly from the drained upstream basins and, to some extent, from the main tributaries located 3 km downstream of the HP for the Bellos and 1 km for the Rialbo (Figure 2.3)

The Cinca basin receives 25% more rainfall and 30% more runoff than the Ésera basin, for a basin 13% larger. The mean and median annual flows measured at the Escalona gauging station for the period 1997-2022 are 24.8 and 17.8 m^3s^{-1} respectively, while they are only 15.8 and 11.7 m^3s^{-1} for Campo. The average annual runoff at Escalona is 736 hm^3, while at Campo it is around a third less, at 475 hm^3. Annual floods on the Cinca and Ésera rivers are estimated at around 211 and 100 m^3/s respectively, and large-scale floods (i.e. those with a 10-year recurrence interval) reach 859 and 369 m^3s^{-1} (Figure 2.10). The data and calculation methods are fully described in Section 2.2.2.4.2.5 of this chapter. In order to allow comparisons between the two basins, these values have been normalized by the median flow (Q_{50}). An annual flood on the Cinca at Escalona is equivalent to 12 times the median flow, while on the Ésera at Campo it is equivalent to 9 times the median flow.

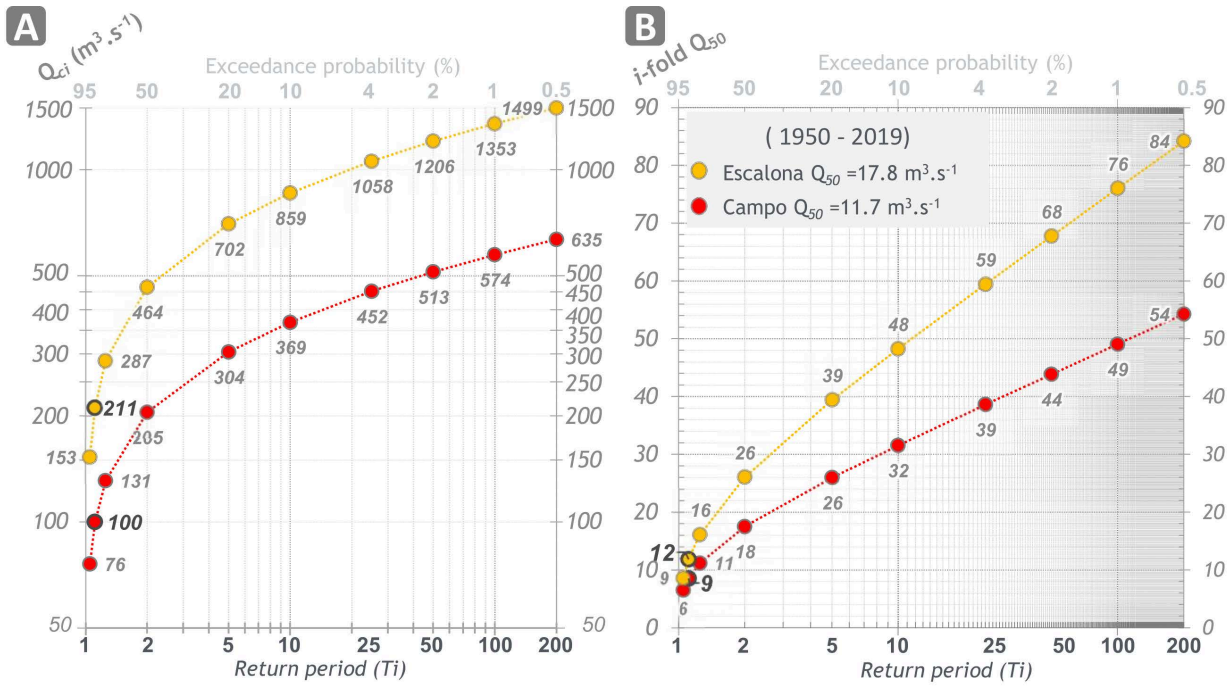

Figure 2.10: **A** Flow values for different return periods or probability of occurrence. For example, an instantaneous flow (Q_{ci}) of 205m^3s^{-1} at Campo occurs statistically once every two years. Such a flood has a 50% chance of occurring in any one year. **B** Normalized instantaneous flow (i-fold Q_{50}) for different return periods or probability of occurrence. For example, a flow of 18-fold the Q_{50} at Campo occurs statistically once every two years. Such a flood has a 50% chance of occurring in any one year.

Finally, it should be noted that while the amount of precipitation does not show a clear pattern over time (1950 - 2020, low R^2) in the whole analysed stations, the same cannot be said for temperatures. Figure 2.9 **B** shows more significant changes over time with an increase in estimates mean annual maximum and minimum temperatures. These marked increases from the 1970s onwards are more significant in higher altitude areas (here from 2 500 m). This warming mainly concerns minimum temperatures (blue curve, R^2>0.7). For example, at the summit of the Estos peak (point n°2 in Ésera basin Figure 2.9 B, located on the map in Figure 2.8 **A1**), average annual minimum temperatures have risen by 3.5°C and have become positive, rising from around -2°C to +1.5°C over the last fifty years. In the same region of the Pyrenees, López-Moreno et al. (2020b) reported similar significant changes in accumulated stocks and their duration from 2 100 m. These changes may already have influenced the winter dynamics of snow cover and therefore have repercussions on the distribution of water inputs throughout the year, since around 30% of the upstream basins are located above this altitude.

Despite their differences in size and flow rate that may have a direct impact on competence and capacity, the two rivers have a similar hydrological regime, dominated by spring melt due to large areas of snow accumulation, and major rainfall events in autumn responsible for two-thirds of the maximum annual flood peak (the final third in spring).

Part 2 : Methods

Bed mobility tracing and ADCP flow measurement at Pyramides reach (Upper Ésera River), 17/10/2020. Author: Fanny Ville

The objective of this second part of Chapter 2 is to present the materials, techniques and methods used for data collection (Section 2.2.1), and data processing (Section 2.2.2) beyond what is presented in the papers; i.e. the general methodological design is presented here. Figure 2.11 illustrates the different types of raw data collected and then the processing steps required to obtain the processed data providing the basis for the analyses of the different chapters and, consequently papers, of the thesis.

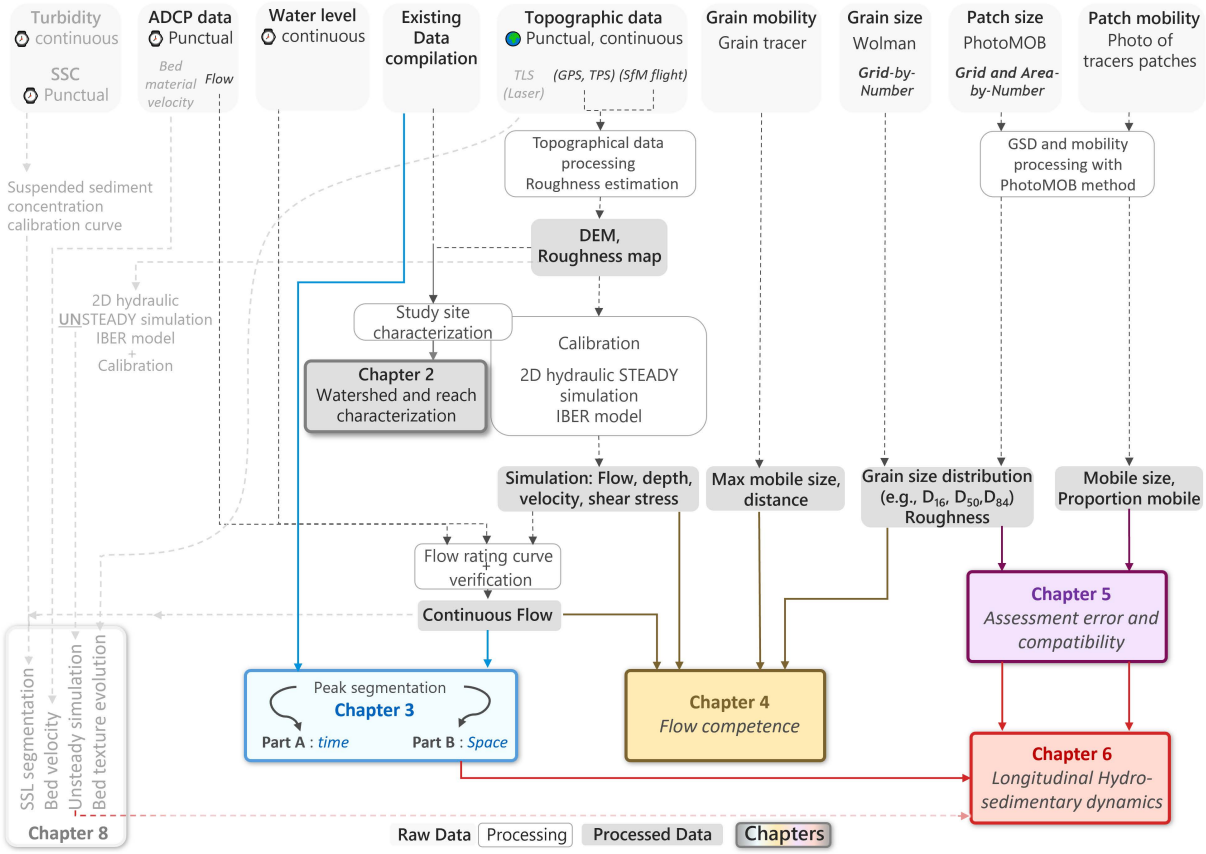

Figure 2.11: Methodological design. Illustration of the types of data acquired, their processing and their interconnection with the different chapters of the thesis. Note that some of the methods are presented in some degree of transparency since, although those data have been acquired and some preliminary results are available, do not conform a chapter providing results. These data have been

used to present future work that will be developed thanks to the application of the methodological design obtained in this PhD and the preliminary analyses develop in such data.

The spatial and temporal distribution of data acquisition specific to each chapter of the thesis are presented in Figure 2.12. A network of 6 permanent monitoring stations was set up, 4 on the Cinca segment: Laspuña US monitoring station (LUSMS), Laspuña DS monitoring station (LDSMS), Escalona monitoring station (EMS), Ainsa monitoring station (AMS); and 2 on the Ésera segment: Campo monitoring station (CMS) and Santaliestra monitoring station (SMS). A temporary station on the Ésera, i.e. Pyramides monitoring station (PMS), was installed for two months in October and November 2020.

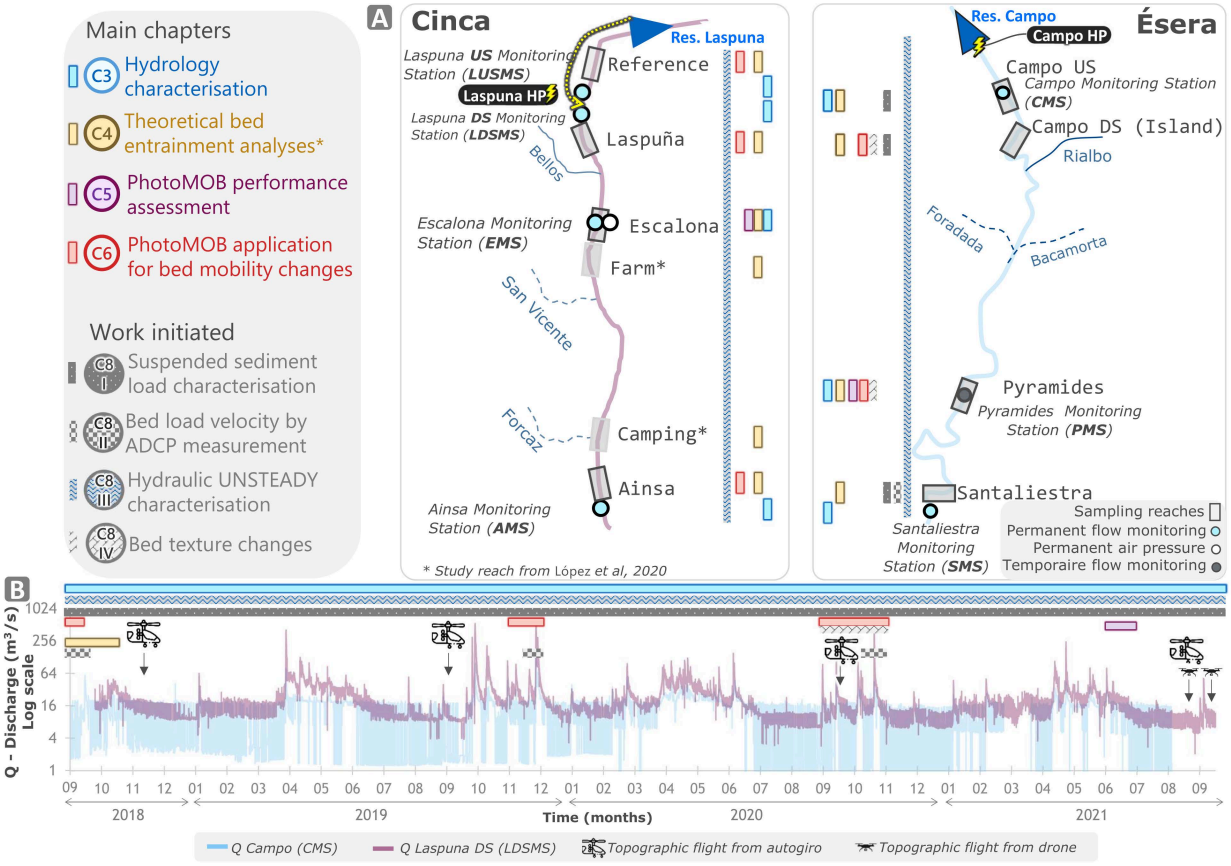

Figure 2.12: Spatial (**A**) and temporal (**B**) scales of analysis in relation to each of the thesis chapters (see Chapter 1 for a full description of this)

2.2.1 DATA ACQUISITION

2.2.1.1 Data mining

2.2.1.1.1 Physical catchment properties

The data used to characterize the basins, such as surface area, slope, longitudinal profile and Valley Bottom, comes from LIDAR points and Digital Elevation Models (DEM) with a resolution of 5 meters downloaded from the Spanish National Centre of Geographic Information (2015) website. The geological features were derived from the Geological Map of Instituto Geográfico de Aragón at a scale of 1:300 000 (Instituto Geográfico de Aragón, 1993), while land cover was determined using the Corine Land Cover dataset with a raster cell resolution of 100 meters (European Environment Agency, 2018).

2.2.1.1.2 Climatic data

Spatial characterization of the mean climate (temperature and precipitation) for the period 1991-2020 at catchment scale (Figure 2.8), was carried out using data from the Aragon Climatic Atlas, with continuous rasters of 1000 x 1000 m. Daily estimates for the period 1950-2020 are also available, again using rasters with a resolution of 1000 x 1000. These were used in Chapter 2 to analyse the mean annual climate change at different altimetric points in the basins (Figure 2.9 **B**) and also to estimate the rainfall supply due to precipitation upstream in basins for Chapter 6. Finally, data the Water Authority (CHE) network of monitoring stations, at a temporal resolution of 15 minutes, were also examined.

Physical and climatic characteristics of each drainage area were analyzed using ESRI® ArcMap™ 10.8.

2.2.1.1.3 Flow

The discharge (Q) and flood regimes were characterized on the basis of the daily flow series available (1959-2019) from the CHE at the Escalona (EA051) and Campo (EA258) gauging stations, located in the study segment. Data for this station can be also obtained from the Sistema Automático de Información Hidrológica (SAIH) or from the Centro de Estudios y Experimentación de Obras Públicas (CEDEX). Three variables were analysed on an annual scale: (a) runoff in hm^3; (b) maximum annual daily flow (Qc) in m^3s^{-1}; and (c) maximum instantaneous flow (Qci) in m^3s^{-1}. Runoff was used to study total water variability and to classify hydrological years (i.e. from 1st October to 31st September) into three categories: dry, average and wet. Qc and Qci data were used to analyse flood frequency and magnitude. Discharge data at a temporal resolution of 15min at these same gauging stations, available for a shorter period (1997-2021), were used to corroborate or not the rating curve established to convert water levels into discharge and characterize the hydropeaks (Chapter 3). It should be noted that these official measuring stations seem to underestimate the flow during low flow compared with our discharge measurements. The data from the Escalona station seems to be significantly biased for low flows. In order to characterize the impact of hydropeaks and their propagation downstream with as little error as possible, flow data collected, processed, analysed and published during previous theses within the RIUS research group on the same study area were used (Béjar et al., 2018 and Lobera et al., 2016).

2.2.1.2 Field and laboratory work

2.2.1.2.1 Flow and hydraulic measurements

Continuous temporal water level data at several stations along the two river segments (6 permanent stations and 1 temporary station, blue bar in Figure 2.12 A) at an interval of 15 minutes were required to study the propagation of hydropeaks (Chapter 3 part 2) and the dynamics of grain mobility (Chapter 4 and 6). Three types of sensors measuring the height of the water column were used: (i) a TruTrack® WT-HR capacitive water level sensor at LUSMS; (ii) a Campbell® CS451 pressure transducer controlled at AMS by a Campbell® CR200X data logger and at CMS and SMS by a Campbell® CR300X; and (iii) Solinst® Levelogger Junior Edge pressure sensors at LUSMS, LDSMS and EMS. The output of the capacitive sensors and pressure transducers corresponded directly to the height of the water column. However, the use of Solinst® water pressure sensors also required the atmospheric pressure to be taken into account, which led to the installation of a Solinst® Barologger sensor at the EMS. Maintenance campaigns were carried out every fortnight, as far as possible, to check that the stations were working properly, clean the probes, detect any problems or discrepancies in the measurements and repair them if necessary.

Water surface elevation (WSE) in m a.s.l was measured using the Real-Time-Kinematic Global Navigation Satellite System (RTK-GNSS) to establish a relationship between the relative variation in water level measured by the sensors and the WSE. In this PhD we used a Leica® GS15 system. The aim was then to be able to transform the water level relative to the probes into WSE.

Flow passing though the monitored sections was measured using a SonTek® RiverSurveyor M9 Acoustic Doppler Current Profiler (ADCP). The ADCP integrates the spatial velocity measurements in the water column over the entire section and calculates the flow rate instantaneously. To ensure the consistency of the flow rate obtained, a minimum of three repetitions (replicates) were carried out. Measurements were taken at low to medium flow. Each flow value measured, at a given time and at a given station, can be linked to the WSE value measured by the probes. A total of 36 gauges distributed over all stations were carried out at different water levels. Due to the constraints of the terrain (slope, channel width, inaccessible banks), the measurements were mainly carried out on the Ésera river where bridges close to the measurement stations were present.

2.2.1.2.2 Topography

Different survey techniques were combined, taking into account the difficulty of the terrain, canopy coverage and satellite coverage, to obtain topographic data at different spatial scales (river segment - tens of km; river reach- tens of meters) and at different resolutions.

DEMs are the main input data for flow propagation in hydraulic models. To generate high-resolution DEMs (cm precision) at the scale of the river segment, topographic surveys were carried out by means of Digital Photogrammetry in 2018, 2019 and 2020. This involved: (i) establishing non-permanent ground control points (GCPs) along the river segment using RTK-GNNS. These points will be useful for post-processing, (ii) the acquisition of control points (CP) using the RTK-GNSS for quality assessment, (iii) the acquisition of high-resolution aerial photographs using an Autogiro, and (iv) ADCP measurements at the same time as the flight to obtain flow and bathymetry measurements.

At the scale of the study reach, where numerous observations and measurements were made (Chapters 3, 4 and 6), more precise topography was required. A Leica® BLK360 Terrestrial Laser Scanner (TLS) was used (mm to cm precision) to obtain this precision on the emerged parts, while in the wet areas, photogrammetry at a shorter distance from a drone platform coupled with ADCP measurements made possible more precise bathymetry (wet channel topography).

Finally, at the monitoring stations scale, which are often located close to obstacles preventing good GNSS signal reception, such as a bridge or vertical wall, and creating disturbances (e.g. shadows) for photogrammetric processing, the precise position (X, Y and Z coordinates) of the 0 level of the sensors and the cross-section in line with them were measured using a TPS Leica® TS02 total station. In wet channels these measurements were carried out with the ADCP.

2.2.1.2.3 Bed grain size characterization

Punctual measurements of grain size were carried out to characterize the riverbed and calculate its roughness coefficient for the application of bedload transport formulae (Chapters 4 and 6). Different methods were used depending on the size of the sediment and whether it was surface or subsurface material.

Subsurface sediments were sampled once for each segment in the most downstream reaches (ASM and SMS). The Grain Size Distribution (GSD) by fraction according to the Wentworth scale (presented in the introduction) was obtained using the volume-by-weight method (Bunte and Abt, 2001). Over a sample area of 1 m^2, surface sediments were removed to a depth equal to the largest particle found in the surface. In order to obtain an accurate estimate of the particle size distribution, a minimum sampling volume is required (Church et al., 1987).

Of the total volume of sediment sampled, in both samples (AMS, SMS), the average weight of the 3 largest particles did not exceed 5% of the total weight and the largest did not exceed 1.5%. Sediment particles larger than fine gravel (5.66 mm) were sieved directly on site. Smaller sediments were brought back to the laboratory, dried and sieved using a Filtra® FLT0200 shaker. In total around 580 kg of sediment was sieved.

GSD of surface sediments in all reaches was characterized using two different techniques that can provide data comparable to the volume-by-weight method (Graham et al., 2012):

(i) The first method, called Grid-by-Number (GbN), the pebble count procedure was used (Wolman, 1954). A predefined number of grains (a minimum of 100) were collected along a grid with a spacing at least one times larger than the coarsest particle in order to avoid measuring the same particle twice. Their *b*-axis was measured by passing the grain through a template consisting of several square holes of different sizes, based on the Wentworth interval. Materials smaller than 8 mm, which are more difficult to sample manually, were not taken into account.

(ii) The second method, called Area-by-Number (AbN), was applied by taking one or more 1m² photographs of the bed surface. These images were analysed using the *PhotoMOB* GIS toolbox (described in the next section and analysed in detail in Chapter 5). This toolbox was entirely developed, validated and applied in this PhD. During validation, the grain sizes obtained from the photos were compared with those of the grains actually present on the bed surface and measured using a Pebble-Box device. This one allows to measure the 3 grain axes quickly and with little bias (details in Chapter 5). The detection limit depends on the resolution of the photographs. However, to remain consistent with the pebble-count method, grains smaller than 8 mm were also excluded.

2.2.1.2.4 Bed mobility

Bed mobility was estimated in all the study reaches using indirect tracing methods (Hassan and Ergenzinger, 2003) for grain sizes > 8 mm. These measurements were used to analyse spatial variability, and to construct specific prediction models (theoretical) for each river reach (Chapters 4 and 6).

Painted tracers were used in two different ways:

(i) Sediments of various sizes, representative of the entire site, were collected, dried and painted. Their size was measured and they were then placed in a transverse line in the channel. Their position was recorded using an RTK-GNNS system. An initial peak was waited for the grains to settle into a naturally stable position. After a targeted hydropeak or flood, the position of the displaced grains and their size were measured again. This enabled the range of grain sizes mobilized to be observed (Chapter 4) and transport distances to be estimated.

(ii) Painted areas of 1m² were distributed at different locations on the sedimentary bars in order to trace all the grain sizes present on the bed. After an event, the position of the particles that have moved can be recorded using a RTK GNNS system and the distance traveled can be calculated. In addition, a new photo of the initial zone can be taken (POST) and compared with the first (PRE) in order to identify the grains that have remained in place and those that are newly visible, and to calculate mobility statistics (Chapter 6). This image processing was carried out using the *PhotoMOB* method developed as part of the thesis (Chapter 5), as already indicated.

With the first approach, the sedimentary structure is altered, whereas with the second approach it is not. However, the latter allows to measure the mobility of the bed in the wet channels which cannot be painted.

2.2.2 DATA PROCESSING

2.2.2.1 DEM generation

The bed topography was characterized in order to obtain a continuous and detailed topographic model of the study segments, in order to estimate the bed roughness and carry out hydraulic simulations, whose results are used for all the Chapters 2 to 8.

Punctual data obtained from RTK-GNSS and TPS were processed with the Leica® Infinity software to obtain the coordinates of topographic points and record them with the correct coordinate system (UTM-ETRS89 zone 31N). Digital Photogrammetry based on the Structure from Motion (SfM) algorithms using Agisoft's Metashape® software was applied to obtain topographic point clouds from photographs acquired using autogiro or drone. A total of 10 clouds were produced. Details of each campaign are presented in Table 2.2.

Table 2.2: Details of campaigns and photogrammetric clouds

Flight	Platform	Area covered (km^2)	Nb photos	Nb GCPs	Point density ($points/m^2$)	Total computation time (days)	Size point cloud file (GB)
2018 Ésera	Autogiro	15.30	837	45	24	4.70	5.58
2018 Cinca	Autogiro	22.50	1329	42	34	9.80	6.20
2019 Ésera	Autogiro	14.20	1241	148	46	9.20	9.05
2019 Cinca	Autogiro	12.80	2007	69	63	16.90	9.84
2020 Ésera	Autogiro	14.80	1553	180	45	11.30	11.68
2020 Cinca	Autogiro	15.40	2921	110	16	8.90	3.19
2021 Campo	Drone	0.08	264	8	825	0.60	0.70
2021 Laspuña	Drone	0.14	483	21	409	0.80	1.70
2021 Escalona	Drone	0.03	456	22	1390	0.13	0.62
2021 Escalona	Autogiro	0.39	56	22	451	1.00	2.77

The campaigns between 2018 and 2020 were used to generate topographic point clouds over the entire two study segments. The 2021 campaigns at Campo US and Laspuña (US and DS), coupled with ADCP bathymetry, were used to obtain a more accurate topography of these reaches in order to generate better rating curves later on. As the bed of these two zones is considered to be stable over time, these new data were incorporated into the point clouds from previous years, forming a 'hybrid' cloud. The 2021 campaign at Escalona using an autogyro and drone was carried out over a large emergent sedimentary bar in order to calibrate a roughness prediction model.

The generation of the final product, i.e. the DEMs, required a total of 7 steps. These steps are described in more detail for the 2019 Ésera campaign in Chapter 4, but a summary is given here. (i) The photographs (total number in column 4 of Table 2.2) were aligned and a sparse point cloud was formed from the common visible features in several photographs showing different views of the same area. (ii)These were then scaled and georeferenced using the GCPs (from 42 to 180 for the 2018 to 2020 campaigns). (iii) The software then applies a multi-view stereo algorithm to increase the density of the points and perform orthorectification. The result is a dense topographic point cloud (point density/m^2 in Table 2.2 column 6) and an orthomosaic image with a resolution of 0.1m. These processes required between 1 and 2 full weeks of uninterrupted computing and generated point clouds of between 5 and 17 GB in size. (iv) They were then filtered to remove noise and vegetation using CloudCompaire® software via the CSF Filter tool (Zhang et al., 2016). The CPs over the dry areas were used to determine the altimetric quality (z) obtained over these zones (Table 2.3 columns 4 to 6).

Table 2.3: Altimetric quality of point clouds on dry areas

Flight	Platform	Nb dry check points	Point cloud Z error (mm) Dry area		
			Bias	MAE	RMSE
2018 Ésera	Autogiro	210	-0.125	0.340	0.757
2018 Cinca	Autogiro	71	0.154	0.235	0.337
2019 Ésera	Autogiro	286	-0.077	0.098	0.127
2019 Cinca	Autogiro	391	-0.003	0.086	0.127
2020 Ésera	Autogiro	237	-0.051	0.076	0.100
2020 Cinca	Autogiro	318			
2021 Campo	Drone	7	0.016	0.036	0.042
2021 Laspuña	Drone	12	0.02	0.069	0.092
2021 Escalona	Drone	39	-0.010	0.031	0.037
2021 Escalona	Autogiro	39	0.049	0.051	0.057

The quality of the first cloud (2018 Ésera) was not optimal. The RMSE was greater than 0.50m, while those of subsequent years are between 0.10 and 0.12m. It should be noted that the 2018 campaigns had the fewest GCPs. Data from the Cinca River campaign in 2020 were used to generate the dense point cloud. However, it could have not been post-processed yet (vegetation, noise). These two campaigns were not used in the rest of the thesis.

(v) Water surfaces are affected by the refraction of light at the air-water interface, leading to an underestimation of depths. To correct this bias, an empirical refraction correction model was applied following the procedure of Coutaz (2021) and Woodget et al. (2015). 70% of the CPs surveyed in the submerged zone were used to develop the empirical refraction correction model (Table 2.4 column 5) and the remaining 30% to assess the overall accuracy of the channel bathymetry after correction (Table 2.4 columns 6 to 8).

Table 2.4: Empirical correction model of refraction and altimetric quality of point clouds in wet areas

Flight	Platform	Nb check points Wet area		Empirical refraction correction model	Point cloud Z error (mm) Wet area		
		Trainning	Validation		Bias	MAE	RMSE
2018 Cinca	Autogiro		66	D_{cor}= 1.39 * D_{SfM} + 0.082	0.033	0.152	0.210
2019 Ésera	Autogiro	234	99	D_{cor}= D_{SfM} * 1.800	-0.023	0.142	0.185
2019 Cinca	Autogiro		173	D_{cor}= 1.39 * D_{SfM} + 0.082	-0.042	0.084	0.107
2020 Ésera	Autogiro	186	76	D_{cor} = D_{SfM} * 1.841	-0.017	0.100	0.118
2021 Campo	Drone	20	9	D_{cor} = D_{SfM} * 1.286	-0.019	0.077	0.104
2021 Laspuña	Drone	21	9	D_{cor} = D_{SfM} * 1.511	-0.006	0.091	0.014

The RMSE for the submerged parts covering all the study segments varies between 0.118 and 0.210m.

(vi) The set of corrected dense point clouds were regularised using the ToPCAT algorithm (Brasington et al., 2012; Rychkov et al., 2012) developed by members of the MorphPeak & MorphHab team and fully available in the Geomorphic Change Detection tool developed by Wheaton et al. (2010). A grid of 0.25 × 0.25 m cells was generated and only one point representing the minimum altitude of each cell retained. The point clouds at the scale of the study segments and the more precise point clouds for the study sections are combined together to form hydride point could.

(*vii*) Finally, triangulated irregular networks (TINs) were calculated from the hybrid clouds, and then transformed into DEMs with a desired cell size resolution depending of objectives (0.25 or 0.5m), providing a continuous model of the ground over the study segment, i.e. a DEM.

2.2.2.2 Roughness estimation

Sediment size estimation and riverbed roughness mapping were carried out following the approach developed by Brasington et al. (2012). The aim is to establish correlations between the detrended standard deviation of the bed elevation from the point cloud (dt_{SD}) in a given area and a measure of the grain size of that same area. Correlations depend on the topographic technique (e.g. TLS, SfM), sensor and platform used, data characteristics (e.g. density of observations), bed sediment characteristics (e.g. packing, shape, nesting) (Pearson et al., 2017).

The calibration involved 5 steps:

1) During the topographic campaign carried out in 2021, 3 point clouds of the large Escalona sedimentary bar were acquired using 2 techniques. (i) One cloud with TSL from the ground and two by (aerial) digital photogrammetry. In the case of photogrammetry, in order to assess whether the correlation changed with altitude, flights were carried out respectively at approximately (ii) 350 meters and (iii) 40 meters above ground level, using an autogyro and a drone.

2) During this campaign, 30 patches of 1mx1m with various grain sizes were sampled on the same sedimentary bar by photographic method. The photos were processed with the *PhotoMOB* toolbox in order to extract the GSD (truncated at a low limit of 8 mm) and convert it into GbN form. The D_{50}s ranged from 2.28 to 226 mm. The patches, their location on the bar and their GSDs are shown in Figure 2.13.

3) The dt_{SD} was obtained by decimating the point clouds using the algotithm ToPCAT with a 1 x 1 m grid at the location of the 30 patches.

4) Correlations between each percentile (D_5 to D_{95}) and dt_{SD} were established for each point cloud. Linear regression models, with an intercept set to zero, were used and compared with models already established by previous authors compiled in Pearson et al. (2017) also using dt_{SD} as a predictor. All correlations were significant with r^2s between 0.82 and 0.93. The relationships of the 3 point clouds concerning the estimation of the D_{50} are presented in Table 2.5 and Figure 2.14 **A** and compared with the models of other authors in Figure 2.14 **C**.

Figure 2.13: A Sampled patch. **B** Location of patches on the Escalona sediment bar. **C** GSD of the 30 patches sampled)

Table 2.5: Model for predicting D_{50} from dt_{SD} with associated r^2 and p-value for the 3 point clouds and model performance assessed by repeated K-fold cross-validation.

Flight	Model of D_{50} prediction			Performance assessment by repeated K-fold cross-validation		
	Model	R^2	p value	R^2	MAE	RMSE
PC SfM 350 m	$D_{50} = dt_{SD} * \mathbf{3.62}$	0.86	<0.001	0.87	0.025	0.029
PC SfM 40 m	$D_{50} = dt_{SD} * \mathbf{3.76}$	0.89	<0.001	0.79	0.021	0.025
PC TLS	$D_{50} = dt_{SD} * \mathbf{2.86}$	0.89	<0.001	0.94	0.019	0.022

5) In order to assess the quality of these prediction models, a Repeated K-fold cross-validation was performed (Kassambara, 2018; Sohil et al., 2022). An illustration of the principle followed is available in Figure 2.14 **B**. First, the 30 couples of the dataset were divided into 10 subsets. Secondly, the prediction model was applied to each of the 10 subsets (composed of 3 elements). The quality of the prediction was measured between the original D_{50} values and the predicted using 3 metrics: coefficient of determination (R^2), Mean absolute error (MAE) and Root Mean Squared Error (RMSE). Thirdly, for each metric, the mean value obtained over the ten subsets was calculated. Fourthly, all of the above operations were repeated 3 times, and for each metric, the average of the mean was calculated. This represents the quality of the calibrations performed.

The two point clouds obtained by SfM photogrammetry show almost the same relationship (Figure 2.14 **A**, blue curves), indicating that the correlation is not affected by the altitude at which the photos were taken. The relationship obtained by PC TLS using the methodology of Brasington et al. (2012) is very close to that of these same authors (curve 10, 3 and 4 Figure 2.14 **C**) which suggests that, despite probable variability linked to sediment characteristics, it is possible to use the same processing method for different rivers. The PC SfM 350m correlation was therefore used to obtain a spatially distributed map of the D_{50} at a resolution of 1m x 1m in the two river segments studied.

The RMSE of the SfM 350m model is of 0.029m while that obtained from the TLS is of 0.022m. These errors were considered acceptable given that only 13% of the samples were well or moderately well sorted. In addition, for hydraulic modelling, these spatial particle size estimates were obtained in order to establish a map of broad roughness classes rather than continuous values of particle size, as will be explained below.

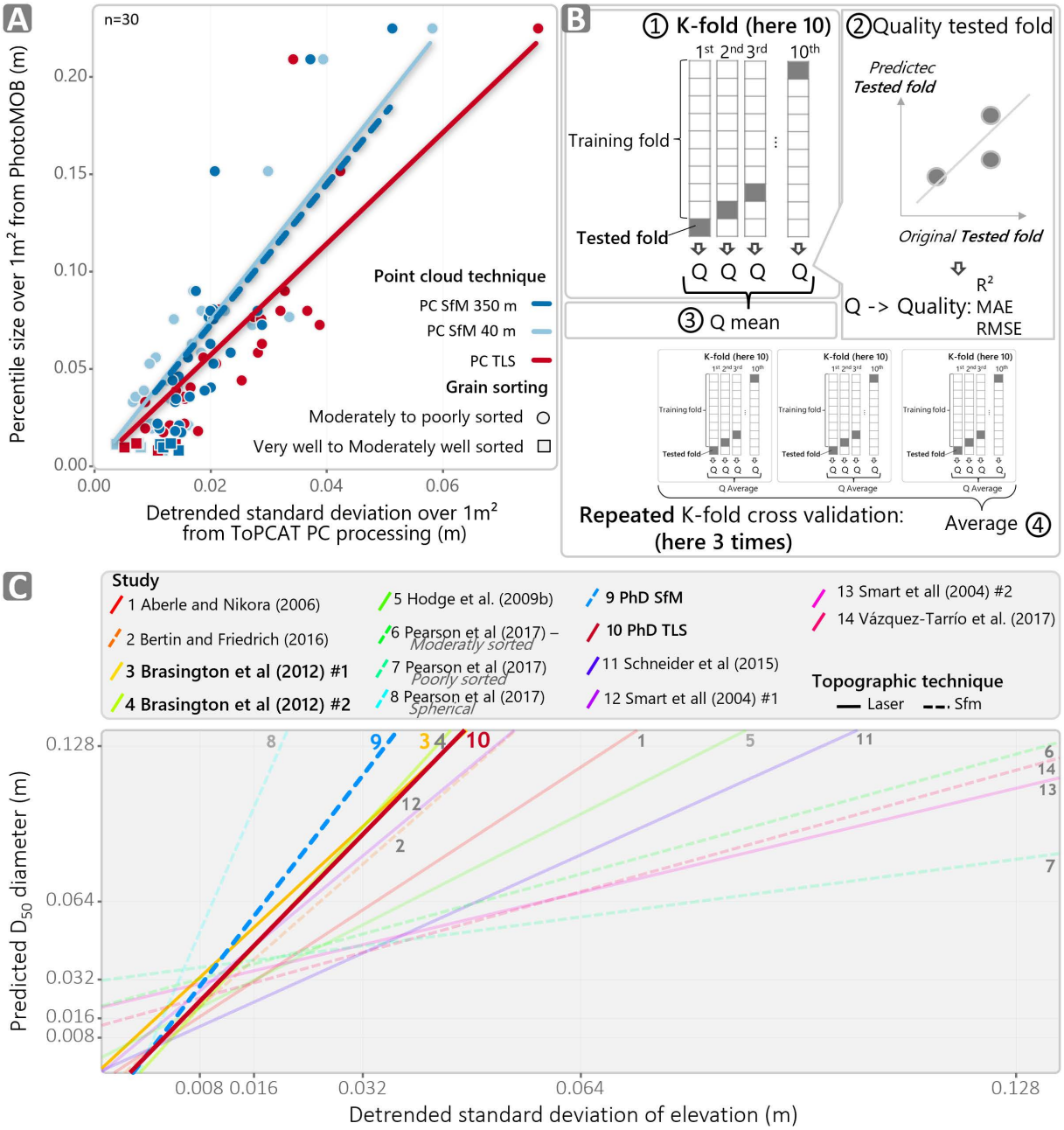

Figure 2.14: A Correlation obtained for the three point clouds. **B** Illustration of the Repeated K-fold cross-validation method used. **C** Comparison of the models obtained with those in the literature compiled by

2.2.2.3 Steady 2D hydraulic model calibration

The use of a 2D hydraulic model and the simulation results enabled to obtain the flow calibration curves (i.e. WSE flow relationship) as well as to estimate the hydraulic forces of incipient motion in Chapter 4. In this PhD the *Iber* hydrodynamic model (Bladé et al., 2014) was used.

The hydraulic models for the Cinca segment were parameterized according to the modalities already used in previous studies, with a size of 1 x 1m and a uniform Manning's roughness coefficient of 0.035. In the case of the Ésera, no hydraulic modelling had previously been carried out in this study segment. The stable hydraulic modelling was calibrated by two sensitivity analyses, (1) mesh size and (2) roughness, at the Santaliestra station, the location for which a greater number of measurements have been acquired over time (i.e. discharge and associated WSE).

(1) Flow conditions of 1.7, 12 and 33 m^3s^{-1} measured by ADCP associated with WSE recorded at SMS, were simulated using different mesh resolutions: 0.5m, 1m, 2m and 4m with a constant Manning's roughness coefficient of 0.025. The value of 0.025 was estimated for the gravel and cobble river bed category from the table in Julien (2002). The simulated WSE models were compared with each other and with the actual WSEs recorded. An illustration of the results is available in Figure 2.15 **A**. The greater the flow, the greater the difference between the WSE given by the 4-meter mesh and the actual WSE. For a flow rate of 12 m^3s^{-1}, the difference between the observed WSE and that modelled is 6 cm, while for a flow rate of 33 m^3s^{-1}, the differences increase to almost 14 cm. This is due to the low spatial resolution, which is not sufficient to reproduce the topography adequately. However, the differences remain similar for meshes of 0.5, 1 and 2 meters. The number of elements for a 0.5-meter mesh exceeds 2 million, whereas it is around 560 000 for a 1-meter mesh, around 142 000 for a 2-meter mesh and only 48 600 for a 4-meter mesh. The calculation time was over 6 days for a 0.5 m mesh, 1 day for a 1m mesh, around 4 hours for a 2 m mesh and only 1.5 hours for a 4m mesh. Consequently, it was decided to use a regular 2 m mesh to propagate the flow and gradually reduce it to 0.5 m at the points of interest (i.e. study reach and monitoring station).

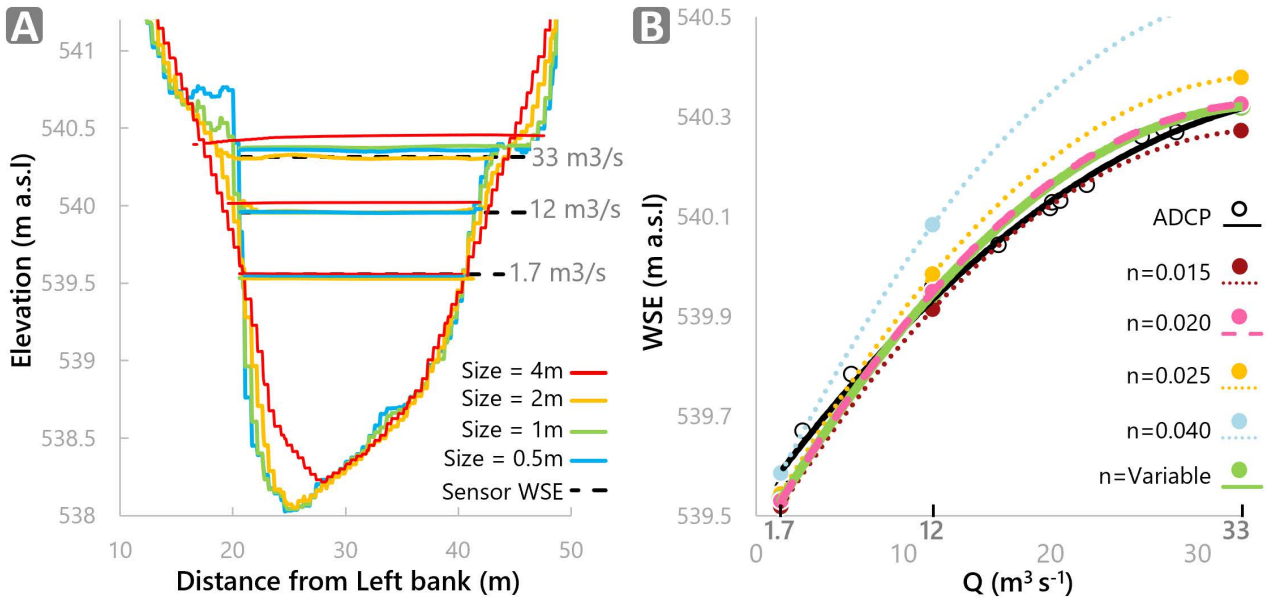

Figure 2.15: A Topography obtained for different mesh sizes and associated simulated WSE models compared to real WSE. B Comparison of the WSE models for tested Manning coefficients (n) with the real WSE.

(2) Then, for the same flow rates with the adopted meshing strategy, a sensitivity analysis of the roughness was performed by varying the Manning's coefficient (n). Uniform values of 0.015, 0.020, 0.025, 0.040 were tested. In addition, in order to study whether spatially varying roughness could improve the simulations, the map of the spatial estimate of D_{50} was reclassified into 4 classes and used to calculate Manning's coefficients using Julien (2002) formula $n = 0.062 * D_{50}^{(1/6)}$. The D_{50} used corresponded to the central value of each class. After simulation of the 3 flows in the 5 roughness configurations tested, the WSE models obtained were compared with the actual WSE recorded (Figure 2.15 **B**). For a uniform value of n = 0.015, the WSE tends to be underestimated for the three simulated flows (4 cm on average). For uniform values of 0.025 and 0.040 the WSE tended to be overestimated, respectively, by an average of 3 and 13 cm. Simulations with a uniform value of n = 0.020 and variable n gave better results, with an average bias of -0.5 and -0.7 cm respectively. According to these results, in steady state, the use of an adapted roughness value, whether uniform or variable, does not seem to have a major impact on the results. The value of 0.020 providing the lowest average residual was selected.

It should be noted that in Chapter 4, the roughness value used for the Ésera was 0.025. When the data was processed in 2019, too few real measurements were available to arrive at the conclusion of 0.020. However, the hydraulic simulations were carried out in order to obtain average values at the scale of the section rather than locally. Consequently, the use of the value 0.025 instead of 0.020 is not considered to call into question the results obtained.

2.2.2.4 Study site physical characterization

2.2.2.4.1 Basin scale

2.2.2.4.1.1 Catchment

The surfaces of the study basins, their upstream sub-basins, their tributaries, the drained areas upstream of each section and monitoring stations, and the longitudinal profiles of the rivers, were delimited by calculating the direction and accumulation of flows from the slopes of the IGN 5m resolution DEM. Figure 2.16 illustrates the different outlet points used.

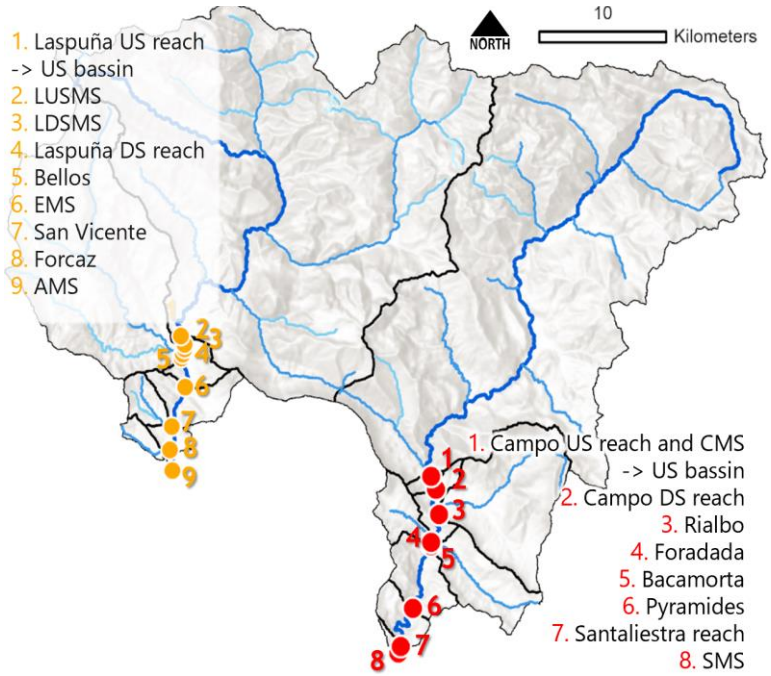

Figure 2.16: Outlet point used to delimit each sub-basin.

2.2.2.4.1.2 Physical context

Data relating to geology, land cover, altitude and slope have been clipped by sub-basin and the distribution of each feature by sub-basin has been calculated. The source of the data was already indicated in the first section.

2.2.2.4.1.3 Climatic data

The 13 rasters representing the annual (1) and monthly (12) averages of temperature and precipitation, taken from the Aragon climatic atlas, were clipped by basins and their minimum, average and maximum values were extracted (Figure 2.8 **B**, p.43). The average volumes of precipitation per basin and sub-basin were estimated by integrating all the water heights accumulated annually or monthly over their entire surface area (Figure 2.8 **A**, p.43). For EMS and CMS, the average volume of runoff at the stations was divided by the average volume of precipitation on their upstream drainage surface to obtain the average annual and monthly runoff coefficient (Figure 2.8 **C**, p.43). Despite taking into account the underestimation of volumes flowed at ESM, these long-term data are accompanied by a degree of uncertainty.

They are presented only as an indication of seasonal trends. Nevertheless, the distributions and amplitudes of variation are consistent with those described by García-Ruiz et al. (1986) in the Central South Pyrenees. Finally, the annual evolution of the climate in the basins since 1950 was established (Figure 2.9 **B**, p.44). Daily rainfall estimates and minimum and maximum temperatures were extracted from the Aragon climatic atlas at various altimetric points in the basins. The daily rainfall was summed to obtain the annual rainfall, while the minimum and maximum temperatures were averaged.

2.2.2.4.2 Segment scale

2.2.2.4.2.1 Longitudinal changes in channel confinement

The degree of channel confinement in the valley, shown in Figure 2.3 A (p.37, was assessed with the O'Brien et al. (2019) geoprocessing approach using the GIS Confinement Tool algorithm written by Whitehead (2017). Three inputs were required. (i) The valley bottom was obtained by manual digitization using orthophotos available on the IGN website and DEM contour lines. (ii) The active channel was also obtained by manual digitisation of water areas and active sediment bars (i.e. non-vegetated or herbaceous vegetation only) as well as (iii) its centerline. Its linear length was divided and classified according to the contact between the active channel and the valley bottom as being confined on both sides, constrained on one side, or unconstrained.

2.2.2.4.2.2 Talweg and annual flood WSE profile

WSE and depth models were obtained by hydraulic simulations for different flows: (i) the base flow (2m/s, corresponding to the ecological flow for both segments), (ii) the mean annual flow (25 and 15 m^3s^{-1} respectively for the Cinca and Ésera), (iii) the maximum flow for which hydropeak forms were detected on the hydrographs (50 and 30 m^3s^{-1} respectively) and for an annual recurrence flood (210 and 100 m^3s^{-1}, respectively). The talweg was extracted in 4 stages as illustrated in Figure 2.17: (1) A centre line passing through the wetted extension at base flow was established. (2) Cross sections to this centre line were created every 20m. (3) Points along these transverse lines were created every 0.5m (i.e. raster resolution covering all segments). (4) The bed elevation at each point was extracted from the DEMs. Only the point with the lowest altitude (Z_{min}) was retained per transect. These points correspond to the talweg. At these same points, the simulated WSEs for an annual flood were extracted. The longitudinal profile of the talweg and the WSE are illustrated in Figure 2.3 **D** (p.37).

2.2.2.4.2.3 Longitudinal changes in channel width and depth

The digitisation of the valley bottom and the wetted extension of the simulated WSE models for the 4 flows mentioned in the previous section were used to assess the geometry of the sections. The cross-sections spaced 20m apart were duplicated in 5 copies, clipped according to the extension of the valley bottom and the 4 WSE models (Figure 2.17), in order to obtain the wetted widths (w) associated with each flow in a quasi-continuous manner (20m) along the segments.

The median and maximum widths per segment were calculated across all the transverse sections. In order to determine the mean depths (d) per section, each cross-sectional line associated with a flow was converted into points spaced 0.5 m apart. The values resulting from the simulated depth models were extracted for each point. The mean value for each transects was calculated, as well as the median and maximum values for each segment (between all the transects). Finally, the median w/d ratio was calculated.

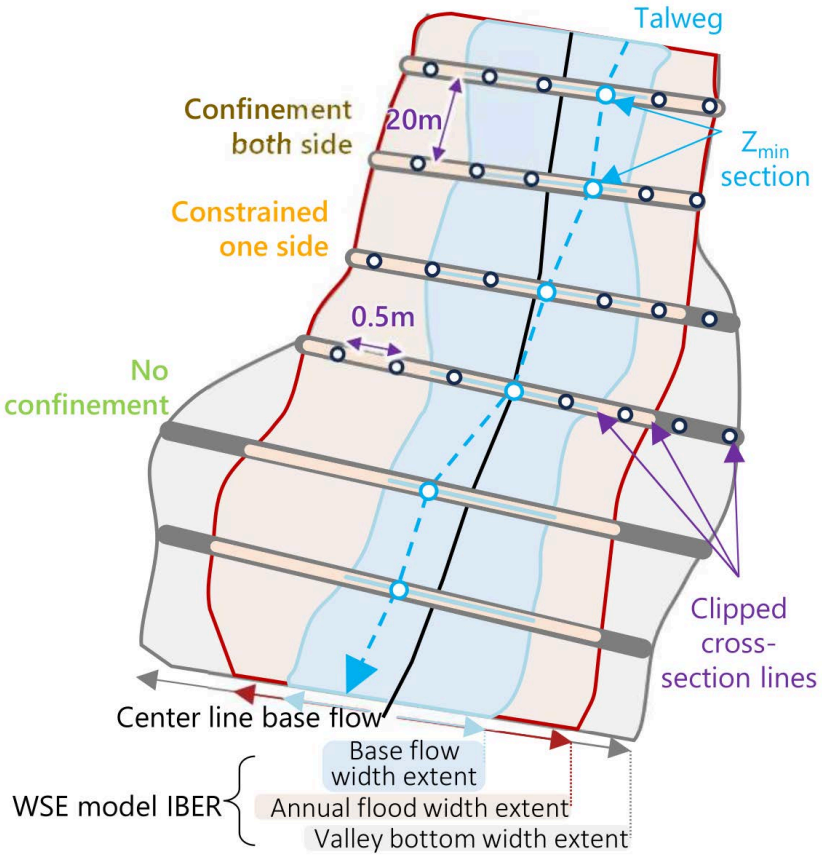

Figure 2.17: Illustration of the spatial analysis to characterize the cross-sections and profile along the study sections.

2.2.2.4.2.4 Longitudinal change in median grain size

The median sediment size (D_{50}) along the segments was derived from the 1m x 1m resolution model representing the spatial distribution of the D_{50} from the detrended standard deviation of elevations (dt_{SD}), as de-scribed previously. Estimates were extracted at each point spaced 0.5 m apart for transects associated with the simulated extent of an annual recurrence flood. The medians for each transect were calculated.

2.2.2.4.2.5 Flood characterization

The analysis of flow magnitudes for different return periods (or probability of occurrence) was based on the long-term hydrological data of annual instantaneous maximums (Q_{ci}) available at the Escalona and Campo stations over a period from 1960 to 2019 (59 years). Some years had missing values, which were estimated by Estrella Carrero as part of her thesis in the RIUS research group. The Gumbel method (Ponce, 1989) was applied to these completed series to characterize the reference floods. Once the flood magnitudes had been obtained, they were normalized by the median annual discharge (Q_{50}). This normalization method was preferred to that of bankfull flood discharge as the main subject of the thesis concerns lower water peaks associated with hydropeaks rather than floods. In chapters 3 (part 2) and 6 the discharges were normalized to this median value. In order to be able to compare the maxima of the normalized hydropeak flows with those of the reference floods, the latter had to be normalized in the same way. Additionally, this allows the comparison between catchments and sites.

2.2.2.5 Flow rating curves

The transformation of the continuous WSE data series (from continuous measurements of water depths as indicated above) obtained from the probe into flow rates required the development of rating curves (i.e. WSE~flow rate relationship), specific to each station. These were elaborated using 2D steady-state hydraulic modelling. The water level measurements from the probe were checked and found to have an average error of 2 cm, which was considered insignificant. At LUSMS, due to dysfunctions, theft and non-optimal positions not allowing the probe to be kept immersed throughout the year, a total of 3 probes positioned at different locations were used during the thesis (Figure 2.18 **A**, **B** and **C**). The whole allowed to obtain a series of continuous data without gaps.

For all the stations except AMS and EMS, the cross-section at the probe points was considered stable over the 2018-2021 study period. The initial and final cross-sections, dashed red curve and continuous grey curve in Figure 2.18 **A**, **B**, **C**, **D**, **G**, **H**, **I** are almost identical. However, Figure 2.18 **E** and **F** illustrate the very dynamic nature of the channels in the second half of the Cinca segment at the ESM and AMS stations. The sections have changed significantly between 2016 and 2020. The probes have been disconnected from the main flow channels. Relationships between the WSE at the probe location and at the main flow channels have been established. However, these stations would have required different rating curves over time in order to obtain quality flow data for the analyses carried out in Chapters 3 (part 2) and 6. Unfortunately, it was not possible to generate all the DEMs and, consequently, the water levels at these stations were not converted to Q.

For both study segments, a series of about forty stepped Q ranging from 0.5 to 600 m^3s^{-1} were simulated, with narrower intervals for low and medium Q in order to best characterize the range of hydropeaks. The WSE at the probe locations was extracted and correlated to each associated modelled Q value. The equations for transforming the WSE into Q were based on polynomial models to best fit the simulated data (black curve, Figure 2.18). To more accurately transform the WSEs into Q over the wide range of simulated Q, 2 to 3 distinct polynomial models were applied for the same probe. Clear changes in cross-sectional shape implied a significant change in the WSE~Q relationship with increasing Q (blue dashed curve in Figure 2.18).

The quality of the rating curves was assessed by comparing the predicted Q for the WSEs for which a Q measurement was carried out using the ADCP (red dot in Figure 2.18). The results are available in Table 2.6.

Table 2.6: Results of the quality assessment of the WSE~Q rating curve

Rivers	Stations	nb point validation	Error assesment in m3/s		
			Bias	MAE	RMSE
Cinca	LUSMS-1	2	-0.56	0.56	0.58
	LUSMS-2	2	-0.08	0.49	0.49
	LUSMS-3	1	0.52	0.52	0.52
	LUDMS	2	3.24	3.24	4.18
Ésera	CMS	7	-0.25	0.33	0.43
	PMS	8	-0.92	1.05	1.28
	SMS	24	-0.46	1.01	1.38

The mean absolute errors are about 0.5 m^3s^{-1} at LUSM and up to 4 m^3s^{-1} at LDSMS. However, limited validation data were available for these stations, between 1 and 2 points, and only at low flow. Nevertheless, the daily Q values obtained are consistent with those provided by the operating company Acciona for the Q released at the Laspuña dam (i.e. LUSMS) and from the power station (i.e. LDSMS). For the Ésera stations, more validation points are available (7 to 24) and over a range of flows covering those of the hydropeaks (0.5 to 34 m^3s^{-1}). The RMSEs are from 0.4 to 1.4 m^3s^{-1}. These values are considered acceptable for analysing the influence of hydropeaks on the dynamics of the study segments. Finally, Figure 2.18 **G** shows the importance of having monitored the CMS station in order to study hydropeaks. The WSE~Q relationship of the SAIH (black dotted line) shows an underestimation of the Q and those in particular on the range of the hydropeaks (i.e. 0.5 to 20 m^3s^{-1}). A flow of 5m^3s^{-1}, for example, is underestimated by around 50%. In order to be able to compare the magnitude of hydropeaks between reaches and rivers, despite such a bias, one possible solution would be to normalize the Q by the annual Q_{50}.

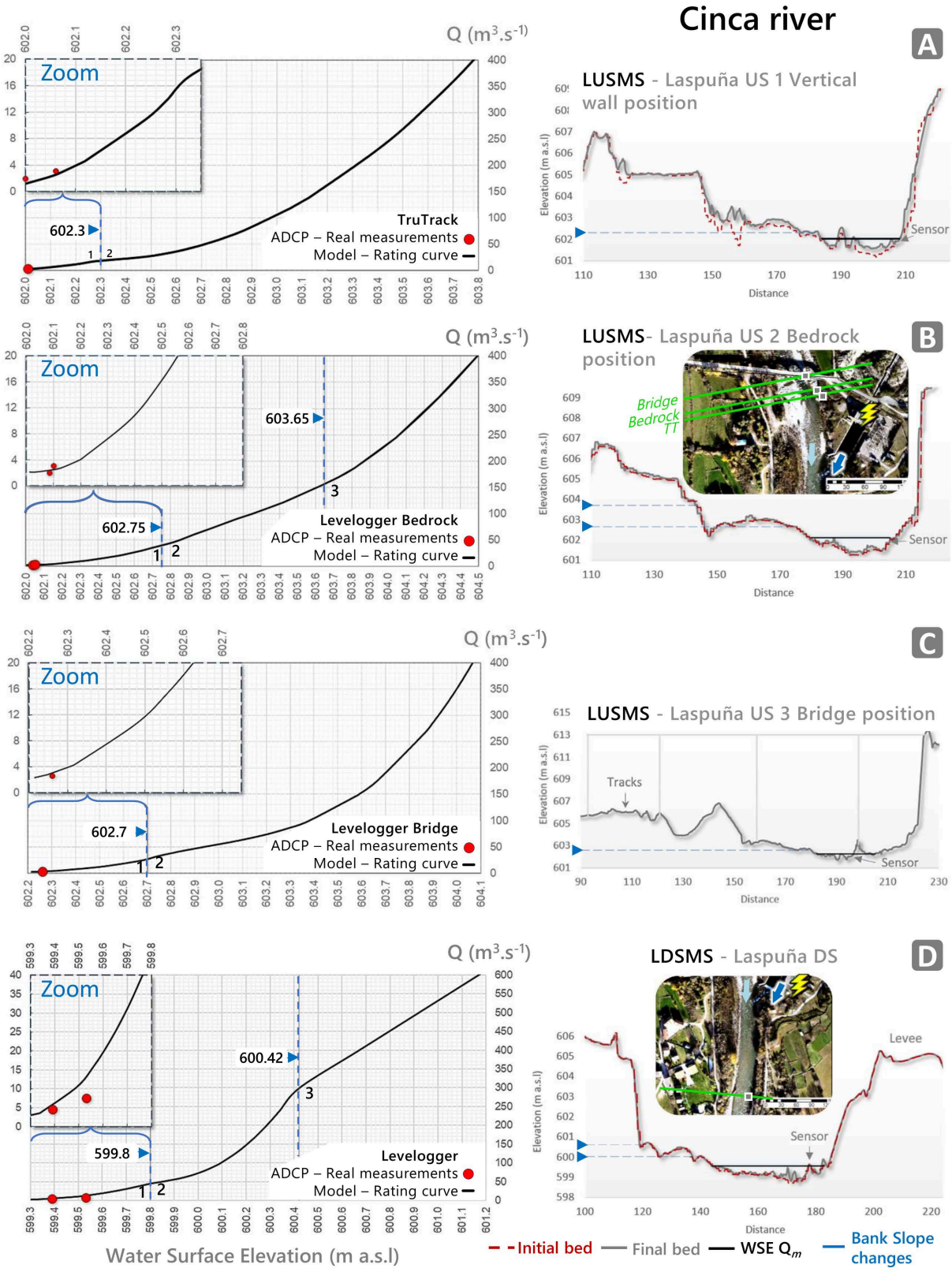
Cinca river
A
LUSMS - Laspuña US 1 Vertical wall position
Zoom
Q (m³.s⁻¹)
602.3
TruTrack
ADCP – Real measurements
Model – Rating curve
Elevation (m a.s.l)
Distance
Sensor
B
LUSMS- Laspuña US 2 Bedrock position
Bridge
Bedrock
TT
603.65
602.75
Levelogger Bedrock
C
LUSMS - Laspuña US 3 Bridge position
Tracks
602.7
Levelogger Bridge
D
LDSMS - Laspuña DS
Levee
600.42
599.8
Levelogger
Water Surface Elevation (m a.s.l)
Initial bed
Final bed
WSE Q_m
Bank Slope changes

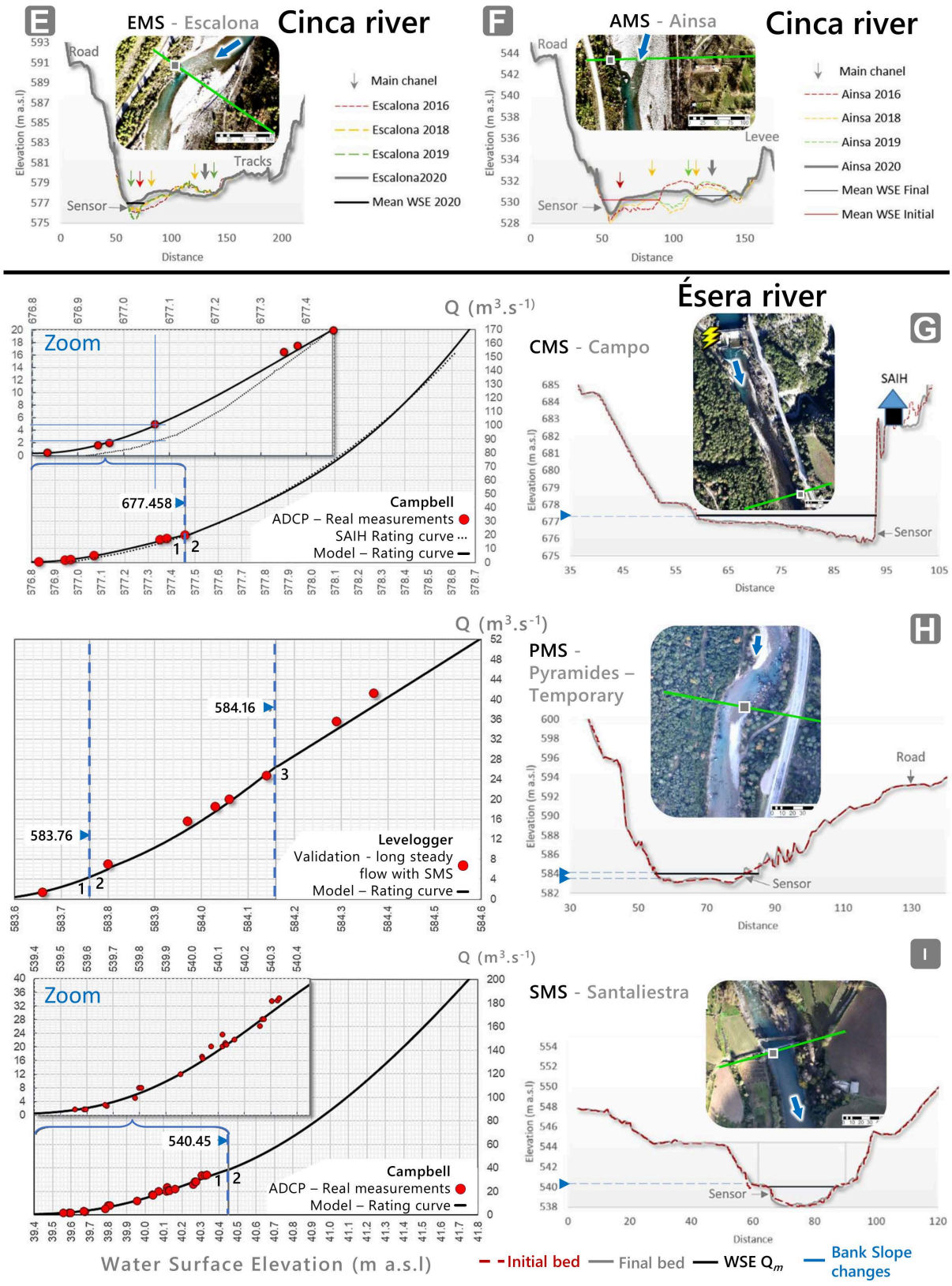

Figure 2.18: Rating curve established for each probe and the associated cross-sectional profile.

2.2.2.6 PhotoMOB: GSD and bed mobility

The *PhotoMOB* GIS toolbox is fully described based in two papers presented in Chapter 5. *PhotoMOB* was used to process the riverbed photos and characterize the sediments and their mobility (Figure 2.19). The first part of the tool allows to identify and create a vector layer (i.e. shapefile) representing the grains visible on the photos, to extract their size (*a*-axis and *b*-axis), their orientation and the proportion of fine and coarse materials in the photographed area. The GSD in AbN can be converted into GbN form for comparison with pebble-count data. The detailed method is available as supplementary material in Chapter 5 Part 1, while the evaluation of GSD and conversion errors is covered in Chapter 5 Part 1. Pre- and post-event photos were processed with the second part of the *PhotoMOB* tool to measure grain mobility dynamics. The method compares the grain shapes between the two images to classify each grain as mobile or immobile. This information is stored in the attribute table of the shapefile. This classification provides information on the disturbed/stable surfaces, the total number of mobile/immobile grains and the number per fraction. This part of the processing and the evaluation of the associated errors is presented in Chapter 5 Part 2.

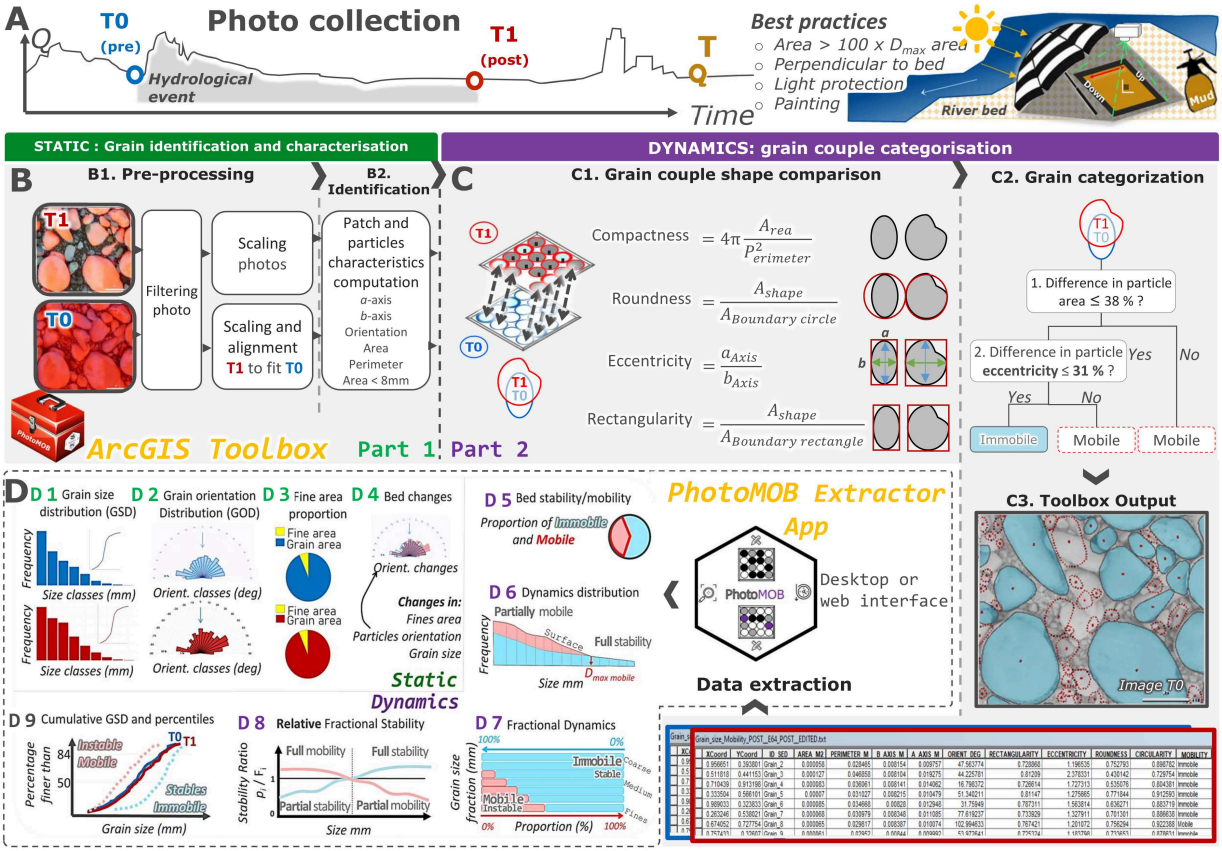

Figure 2.19: Photo processing workflow for the characterization of bed sediments and their mobility using the PhotoMOB method.

REFERENCES

Aberle, J. and **Nikora, V.** (2006) Statistical properties of armored gravel bed surfaces. *Water Resources Research*, **42**, 1–11. DOI:10.1029/2005WR004674

Alatorre, L.C., **Beguería, S.** and **García-Ruiz, J.M.** (2010) Regional scale modeling of hillslope sediment delivery: A case study in the Barasona Reservoir watershed (Spain) using WATEM/SEDEM. *J. Hydrol.*, **391**, 109–123. DOI :10.1016/j.jhydrol.2010.07.010

ARAGON, G.D. (2020) Atlas de ICEARAGON Infraestructura de Conocimiento Espacial de Aragon. https://idearagon.aragon.es/atlas/Clima/info/atlas-climatico-aragon/promedios-1991-2020/promeido-anual-de-temperaturas-medias.

Béjar, M., **Vericat, D.**, **Batalla, R.J.** and **Gibbins, C.N.** (2018) Variation in flow and suspended sediment transport in a montane river affected by hydropeaking and instream mining. *Geomorphology*, **310**, 69–83. DOI:10.1016/j.geomorph.2018.03.001

Bertin, S. and **Friedrich, H.** (2016) Field application of close - range digital photogrammetry (CRDP) for grain - scale fluvial morphology studies. *Earth Surf Processes Landf*, **41**, 1358–1369. DOI:10.1002/esp.3906

Bladé, E., **Cea, L.**, **Corestein, G.**, **Escolano, E.**, **Puertas, J.**, **Vázquez-Cendón, E.**, **Dolz, J.** and **Coll, A.** (2014) Iber: herramienta de simulación numérica del flujo en ríos. *Revista Internacional de Métodos Numéricos para Cálculo y Diseño en Ingeniería*, **30**, 1–10. DOI:10.1016/j.rimni.2012.07.004

Brasington, J., **Vericat, D.** and **Rychkov, I.** (2012) Modeling river bed morphology, roughness, and surface sedimentology using high resolution terrestrial laser scanning: MODELING RIVER BED MORPHOLOGY WITH TLS. *Water Resour. Res.*, **48**, 1–18. DOI:10.1029/2012WR012223

Bunte, K. and **Abt, S.R.** (2001) Sampling surface and subsurface particle-size distributions in wadable gravel-and cobble-bed streams for analyses in sediment transport, hydraulics, and streambed monitoring. *U.S. Department of Agriculture, Forest Service, Rocky Mountain Research Station*, Ft. Collins, CO. DOI:10.2737/RMRS-GTR-74

Choukroune, P. (1992) TECTONIC EVOLUTION OF THE PYRENEES. *Annu. Rev. Earth Planet. Sci.*, **20**, 143–158. DOI:10.1146/annurev.ea.20.050192.001043

Church, M.A., **McLean, D.G.** and **Wolcott, J.F.** (1987) River bed gravels: Sampling and analysis. In: John willey & son (Ed. C. Thorne, J.C. Bathurst, and R.D. Hey), *J. Wiley*, New York, NY, USA, 43–88. ,https://doi.org/10.1002/esp.3290140809

Coutaz, J. (2021) Interactions entre le transport de sédiments , en tresses à lit de galets : le Buëch (Alpes de Haute-Provence, France). Doctoral thesis, Aix-Marseille University

Ebro. Oficina de Planificación Hidrológica, C.H. del (2007) GeoPortal Sitebro. ,http://iber.chebro.es/geoportal/

European Environment Agency (2018) Corine Land Cover (CLC). https://land.copernicus.eu/pan-european/corine-land-cover/clc2018

Galan, F. (2012) CENTRALES HIDROELÉCTRICAS Y PRESAS DEL ALTO ARAGÓN. *Fundation Esteyco*, Madrid, 90 pp.

García-Ruiz, J.M., **Puigdefábregas, J.** and **Novau, J.C.** (1986) La acumulación de nieve en el pirineo central y su influencia hidrológica. *Pirineos*, **127**, 27–72. DOI:http://hdl.handle.net/10261/95396

Graham, D.J., **Rollet, A.-J.**, **Rice, S.P.** and **Piégay, H.** (2012) Conversions of Surface Grain-Size Samples Collected and Recorded Using Different Procedures. *J. Hydraul. Eng.*, **138**, 839–849. DOI:10.1061/(ASCE)HY.1943-7900.0000595

Hassan, M.A. and **Ergenzinger, P.** (2003) Use of tracers in fluvial geomorphology. In: (Ed. G.M. Kondolf and H. Piégay), *John Wiley & Sons, Ltd*, Chichester, UK, 397–423. DOI:10.1002/0470868333.ch14

Hodge, R., **Brasington, J.** and **Richards, K.** (2009) Analysing laser - scanned digital terrain models of gravel bed surfaces: linking morphology to sediment transport processes and hydraulics. *Sedimentology*, **56**, 2024–2043. DOI:10.1111/j.1365-3091.2009.01068.x

Instituto Geográfico de Aragón (1993) Geological map. ,https://idearagon.aragon.es/descargas

Julien, P.Y. (2002) River mechanics, 1st edn. *Cambridge University Press*. DOI:10.1017/CBO9781139164016

Kassambara, A. (2018) Cross-validation essentials in r. ,http://www.sthda.com/english/articles/38-regression-model-validation/157-cross-validation-essentials-in-r/

Llena, M., **Batalla, R.J.**, **Smith, Mw.** and **Vericat, D.** (2021) Do badlands (always) control sediment yield? Evidence from a small intermittent catchment. *CATENA*, **198**, 105015. DOI:10.1016/j.catena.2020.105015

Lobera, G., **Batalla, R.J.**, **Vericat, D.**, **López-Tarazón, J.A.** and **Tena, A.** (2016) Sediment transport in two mediterranean regulated rivers. *Science of The Total Environment*, **540**, 101–113. DOI:10.1016/j.scitotenv.2015.08.018

López Moreno, J.I., **Beguería, S.** and **García-Ruiz, J.M.** (2002) El régimen del río ésera, pirineo aragonés, y su tendencia reciente. *Boletín glaciológico aragonés*, **3**, 131–162.

López-Moreno, J.I., **García-Ruiz, J.M.**, **Vicente-Serrano, S.M.**, **Alonso-González, E.**, **Revuelto-Benedí, J.**, **Rico, I.**, **Izagirre, E.** and **Beguería-Portugués, S.** (2020a) Critical discussion of: "A farewell to glaciers: Ecosystem services loss in the Spanish Pyrenees". *Journal of Environmental Management*, **275**, 111247. DOI:10.1016/j.jenvman.2020.111247

López-Moreno, J.I., **Revuelto, J.**, **Alonso-González, E.**, **Sanmiguel-Vallelado, A.**, **Fassnacht, S.R.**, **Deems, J.** and **Morán-Tejeda, E.** (2017) Using very long-range terrestrial laser scanner to analyze the temporal consistency of the snowpack distribution in a high mountain environment. *Journal of Mountain Science*, **14**, 823–842. DOI:10.1007/s11629-016-4086-0

López-Moreno, J.I., **Soubeyroux, J.M.**, **Gascoin, S.**, **Alonso-Gonzalez, E.**, **Durán-Gómez, N.**, **Lafaysse, M.**, **Vernay, M.**, **Carmagnola, C.** and **Morin, S.** (2020b) Long-term trends (19582017) in snow cover duration and depth in the Pyrenees. *International Journal of Climatology*, **40**, 6122–6136. DOI:10.1002/joc.6571

López-Tarazón, J.A., **Batalla, R.J.**, **Vericat, D.** and **Francke, T.** (2012) The sediment budget of a highly dynamic mesoscale catchment: The River Isábena. *Geomorphology*, **138**, 15–28. DOI:10.1016/j.geomorph.2011.08.020

O'Brien, G.R., **Wheaton, J.M.**, **Fryirs, K.**, **Macfarlane, W.W.**, **Brierley, G.**, **Whitehead, K.**, **Gilbert, J.** and **Volk, C.** (2019) Mapping valley bottom confinement at the network scale. *Earth Surface Processes and Landforms*, **44**, 1828–1845. DOI:10.1002/esp.4615

Pearson, E., **Smith, M.W.**, **Klaar, M.J.** and **Brown, L.E.** (2017) Can high resolution 3D topographic surveys provide reliable grain size estimates in gravel bed rivers? *Geomorphology*, **293**, 143–155. DOI:10.1016/j.geomorph.2017.05.015

Ponce, V.M. (1989) Engineering hydrology: Principles and practices. *Prentice Hall*, Englewood Cliffs, N.J.

Rennie, C.D., **Church, M.** and **Venditti, J.G.** (2018) Rock Control of River Geometry: The Fraser Canyons. *J Geophys Res Earth Surf.* * DOI:10.1029/2017JF004458

Rico, I., **Izagirre, E.**, **Serrano, E.** and **López-Moreno, J.I.** (2017) Superficie glaciar actual en los Pirineos: Una actualización para 2016. *Pirineos*, **172**, 029. DOI:10.3989/Pirineos.2017.172004

Rios Aragues, L.M., **Lanala del Busto, J.M.**, **Rios Mitchell, J.M.** and **Marin Blanco, F.J.** (1982) Mapa geológico de España escala 1:50.000. Bielsa. Hoja 179, 1ª ed. *Instituto Geológico y Minero de España*, Madrid.

Ríos Aragues, L.M., **Galera Fernandez, J.M.**, **Barettino Fraile, D.** and **Hernan martines, F. javier** (2002) Mapa geológico de España escala 1:50.000. Hoja 180 Benasque, 2. serie, 1. ed. *Instituto Geológico y Minero de España*, Madrid. https://info.igme.es/cartografiadigital/datos/magna50/memorias/MMagna0180.pdf

Ríos, L.M., **Beltrán, F.J.**, **Lanaja, J.M.** and **Marin, F.J.** (1979) Contribución a la geología de la zona axial pirenaica, valles del cinca y esera, provincia de huesca. In: *Acta Geológica Hispánica*, 14, 271–279. ,https://api.semanticscholar.org/CorpusID:129513646

Robador Moreno, A. and **Zamorano Cáceres, M.** (2012) Magna. Mapa Geológico de España Escala 1:50.000. Campo. Hoja 212, 1º ed. *Instituto Geológico y Minero de España*, Madrid.

Rychkov, I., **Brasington, J.** and **Vericat, D.** (2012) Computational and methodological aspects of terrestrial surface analysis based on point clouds. *Computers & Geosciences*, **42**, 64–70. DOI:10.1016/j.cageo.2012.02.011

Saz, M., **de Luis, M.** and **Serrano-Notivoli, R.** (2020) ATLAS CLIMÁTICO DE ARAGÓN. ,Gobierno de Aragón. https://icearagon.aragon.es/atlas/Clima/info/atlas-climatico-aragon

Schneider, J.M., **Rickenmann, D.**, **Turowski, J.M.** and **Kirchner, J.W.** (2015) Self - adjustment of stream bed roughness and flow velocity in a steep mountain channel. *Water Resources Research*, **51**, 7838–7859. DOI:10.1002/2015WR016934

Smart, G., **Aberle, J.**, **Duncan, M.** and **Walsh, J.** (2004) Measurement and analysis of alluvial bed roughness. *Journal of Hydraulic Research*, **42**, 227–237. DOI:10.1080/00221686.2004.9728388

Sohil, F., **Sohali, M.U.** and **Shabbir, J.** (2022) An introduction to statistical learning with applications in R: by Gareth James, Daniela Witten, Trevor Hastie, and Robert Tibshirani, New York, Springer Science and Business Media, 2013, $41.98, eISBN: 978-1-4614-7137-7. *Statistical Theory and Related Fields*, **6**, 87–87. DOI:10.1080/24754269.2021.1980261

Spanish National Centre of Geographic Information, C. (2015) Centro de Descargas del CNIG (IGN). ,http://centrodedescargas.cnig.es

Teixell, A., **Zamorano Cáceres, M.**, **Ramírez Merino, J.**, **Navarro Juli, J.J.**, **Rodríguez Santisteban, R.**, **Castaño, R.M.**, **Leyva, F.**, **Ramírez del Pozo, J.**, **Aguilar** and **Robador Moreno, A.** (2016) Mapa geológico de España escala 1:50.000. Graus. Hoja 250, 1ª ed. *Instituto Geológico y Minero de España*, Madrid.

Transición Ecológica y el Reto Demográfico, M. para la (2021) Inventario de Presas y Embalses. ,https://www.miteco.gob.es/es/cartografia-y-sig/ide/descargas/agua/inventario-presas-embalses.aspx

Vázquez-Tarrío, D., **Borgniet, L.**, **Liébault, F.** and **Recking, A.** (2017) Using UAS optical imagery and SfM photogrammetry to characterize the surface grain size of gravel bars in a braided river (Vénéon River, French Alps). *Geomorphology*, **285**, 94–105. DOI:10.1016/j.geomorph.2017.01.039

Vidaller, I., **Revuelto, J.**, **Izagirre, E.**, **Alonso-González, E.**, **Rojas-Heredia, F.**, **Rico, I.**, **López-Moreno, J.I.** and **Serreta, A.** (2021) High spatial resolution thickness changes of Pyrenean glaciers from 2011 to 2020. DOI:10.5281/zenodo.4756351

Wheaton, J.M., **Brasington, J.**, **Darby, S.E.** and **Sear, D.A.** (2010) Accounting for uncertainty in DEMs from repeat topographic surveys: improved sediment budgets. *Earth Surface Processes and Landforms*, **35**, 136–156. DOI:10.1002/esp.1886

Whitehead, K. (2017) Confinement tool, version 2.2.03. Riverscapes Consortium. http://confinement.riverscapes.net/

Wolman, M.G. (1954) A method of sampling coarse river-bed material. *Trans. Am. Geophys. Union*, **35**, 951. DOI:10.1029/TR035i006p00951

Woodget, A.S., **Carbonneau, P.E.**, **Visser, F.** and **Maddock, I.P.** (2015) Quantifying submerged fluvial topography using hyperspatial resolution UAS imagery and structure from motion photogrammetry. *Earth Surf. Process. Landf.*, **40**, 47–64. DOI:10.1002/esp.3613

Zhang, W., **Qi, J.**, **Wan, P.**, **Wang, H.**, **Xie, D.**, **Wang, X.** and **Yan, G.** (2016) An Easy-to-Use Airborne LiDAR Data Filtering Method Based on Cloth Simulation. *Remote Sensing*, **8**, 501. DOI:10.3390/rs8060501

Zingg, T. (1935) Beitrag zur Schotteranalyse. ETH Zurich DOI:10.3929/ETHZ-A-000103455

Chapter 3

Hydrological characterization of hydropeaks

Upstream perspective of the Laspuña monitoring station downstream of the hydroelectric power station, with an upstream view of the Upper Cinca river basin, 04/02/2019. Author: Fanny Ville

Overview

Chapter 3 consists of two parts, both related to the hydrological characterization of hydropeaks, related to the Objective 1 of the thesis. The first, in the form of a published article, provides a temporal characterization of hydropeaks, i.e. analyses the forms and characteristics of the hydropeaks detected on the two river segments in order to classify them and determine their frequency on different time scales. The second part, in the form of a paper in preparation, provides a longitudinal or spatial characterization of hydropeaks, i.e. aiming to examine the changes in hydropeak and flood characteristics along each river segment in order to study flow routing for different forms. Both papers contain an introduction and the specific methodology.

In this chapter the two parts makes the section numbering more complex. The first digit corresponds to the number of the chapter, the second indicates the number of the part (1 or 2) and the following digits refer to the subdivisions.

Part 1 : Temporal characterization

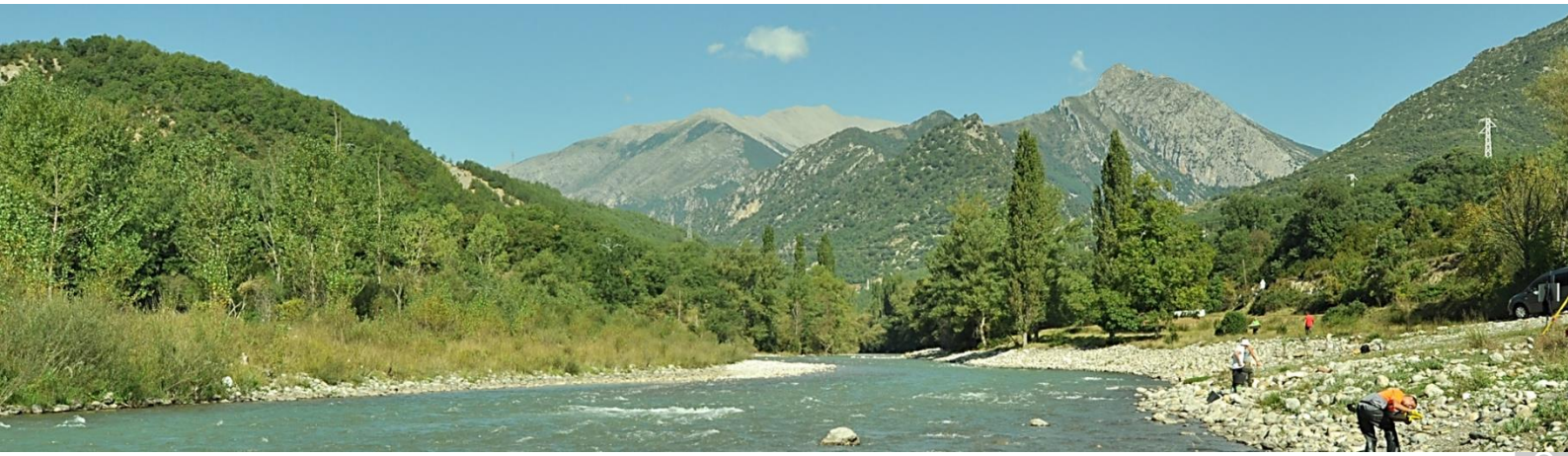

Campo downstream study reach located 1 km from the hydroelectric plant during the 2018 field campaign by the RIUS research group to characterize the impact of hydropeaks. Flow corresponding to a hydropeak with an upstream view of the upper Ésera river basin, 19/09/2018. Author: Unknow

Hydrological characterization of hydropeaks in mountain rivers

(examples from Southern Pyrenees)

This part of the chapter contains the following accepted and already online published paper in the journal River Research and Application. JCR-SCI Impact Factor: 2.796. 2nd Quartile. Tena, A., Ville, F., Reñe, A., Yarnell, S. M., Batalla, R. J., & Vericat, D. (2022). Hydrological characterization of hydropeaks in mountain rivers (examples from Southern Pyrenees). River Research and Applications, 1–21. https://doi.org/10.1002/rra.4058

Abstract: Streamflow in the Ésera and Upper Cinca Rivers (South Central Pyrenees) experiences alterations in the form of rapid pulses, commonly referred to as hydropeaks, associated with highly variable on-demand hydropower production from flowing or stored water. A hydrological characterization of the hydropeaks in these two rivers was carried out to examine their distinct hydropeaking pattern during hydrologically contrasted years. The Ésera demonstrated a hydropeaking regime characterized by a high frequency and magnitude, while the Upper Cinca presented a regime with higher frequency but of lesser magnitude. Additionally, this study classified hydropeaks following the shapes proposed in previous studies and assessed their temporal distribution (frequency), timing, and magnitude. Results indicated that hydropeaks were different in shape and magnitude in both rivers; a Front Step pulse shape dominated in the Ésera whereas a Rectangle pulse shape was the most frequent in the Cinca. The Front Step shape had the highest ramping rates during the rising limb of the hydrograph and the shortest time to the maximum flow; whereas the Rectangle shape had higher duration and a larger volume of water released. Hydropeaks in the Ésera were less frequent (one per day) than in the Cinca (two per day). The river Ésera presented, in general, high-magnitude hydropeaks, with double volume and duration, and three times larger up-ramping rates and time between flow pulses. Overall, hydropeak shapes in the Ésera varied depending on the hydrological year and the season, while in the Cinca, shape distribution followed the same temporal pattern regardless of year and season; thus, hydropeaking in the Ésera appeared to be much more dependent on the annual hydrology (whether the year is wet or dry) than in the Cinca. Hydropeaking regimes were characterized based on three categories of variables: magnitude (flow-based or hydrological variables), timing (duration), and frequency (occurrence).

According to the variability of these variables, a total of three statistically significant groups were obtained in the Ésera, while two groups were identified in the Cinca. Hydropeaks can be statistically classified by their hydrological characteristics that in turn may have a direct effect on sediment entrainment and transport with implications to the ecological functioning of rivers.

Key words: Ebro basin, hydropeak shape and magnitude, hydropeaking, hydropower, mountain rivers, Pyrenees, river Cinca, river Ésera

3.1.1 INTRODUCTION

Rivers and their valleys have been transformed to satisfy water demands for a variety of purposes including, agriculture, navigation, industry, and human consumption. Mountain rivers, in particular, have traditionally been developed to generate electricity via hydropower, owing to their high altitudinal gradients and water availability. Typically, water is stored in reservoirs located at high elevations for flow through hydropower plants (hereafter HP) located at lower elevations for energy production on demand. One of the strengths of HP energy is the ability to immediately respond to changing electricity demands (Jager and Bevelhimer, 2007); however, such versatility results in rapid and regular instream flow fluctuations downstream from the HP plant, which are known as hydropeaks. The range of flow fluctuations is often within the natural range of river flows, though the temporal dynamics are typically different (Bevelhimer et al., 2015). Hydropower is considered a renewable form of energy production, and the global demand for renewables is increasing rapidly as fossil fuels are gradually phased out. However, generating electricity from rivers is not without environmental impacts (Batalla et al., 2021; Hauer et al., 2014a; Schmutz et al., 2015; Valentin et al., 1995; Young et al., 2011), and increased understanding of the pressures imposed by hydropower will help preserve river ecosystems in the decades to come.

A river's flow regime is determined by catchment size, geology and soils, topography, hydro-climatic conditions and vegetation cover, and the interaction between them will result in specific conditions of flow hydraulics, sediment transport, hyporheic exchange, floodplain connectivity, and habitat structure and complexity, among others (Poff et al., 1997). Flow changes associated with hydropeaks can have substantial effects in fluvial systems from changes to the morphological and sedimentary characteristics of the river bed to the composition, structure, and functioning of the aquatic communities (Carolli et al., 2015). HP production schemes often interrupt river continuity through weirs and diversion dams (Fette et al., 2007), which modify the dynamics and continuity of flow and sediment transport that otherwise exists in unaltered fluvial systems.

Broadly, the effects of pulsed flow releases on aquatic biota depend on the interaction between hydraulics, channel morphology, and bed sedimentary structure, with the magnitude and frequency of such releases being a central component of the disturbance. In particular, the availability and characteristics (e.g., grain-size distribution) of the riverbed materials and the competence of hydropeaks to entrain them can directly impact biotic habitat. For instance, Vericat et al. (2020) demonstrated how hydropeaks generated in a river in the Pyrenees mobilized fine and medium gravels, depleting sediment patches in the river bed. The effects of daily entrainment of such sediment fractions are occasionally compensated by natural floods that re-supply sediments from tributaries. However, if gravelly fractions are frequently entrained and transported downstream and not replaced from upstream sources (i.e., dammed rivers), the channel may experience armouring and/or incision. Hydropeaking also affects the finest sediments of the river bed that are transported in suspension (i.e., fine sand, silt, and clay). When fine sediments are available in the channel, hydropeaking can increase water turbidity, which, in turn, may trigger catastrophic or involuntary macroinvertebrate drift (e.g. Béjar et al. 2017).

In addition to impacts on sediment movement, flow fluctuations due to hydropeaking have direct impacts on aquatic biota. One of the main environmental concerns of the pulsed flow releases occurring in hydropeaked rivers relates to the intensity of the ramping rates. The ramping rate is the rate of change of discharge (Q hereafter) per unit of time (i.e., m3/s/h), describing how fast flow increases or decreases (Schmutz et al., 2015). It is widely accepted that sudden changes in flow are significantly linked to responses of aquatic organisms, for instance, by reducing the production of benthic invertebrates, an important food source for river fish (Blinn et al., 1995), or increasing fish stranding and isolation in dewatered areas of the river channel (Irvine et al., 2015; Vanzo et al., 2016b), which may lead to mortality (Casas-Mulet et al., 2015a). Furthermore, hydropeaking has implications on water temperature, often creating cyclical fluctuations termed "thermopeaking" (as per Carolli et al. 2008, Zolezzi et al. 2011). Thermopeaking has been shown to alter the daily, weekly, and seasonal thermal regime of rivers (e.g. Carolli et al. 2012, Fette et al. 2007, Greimel et al. 2018), eventually altering drift patterns of macroinvertebrates (Carolli et al., 2012)

River scientists and basin authorities widely recognize the need to work towards the mitigation of hydropeaking effects. Increased knowledge of the consequences of hydropeaking can support decision makers in defining mitigation strategies that are economically and ecologically sustainable. In Europe, for instance, this increased understanding would help to meet Water Framework Directive requirements to improve the ecological status of the continental water bodies. A key component to understanding hydropeaking consequences is the ability to quantitatively analyse and evaluate sub-daily flow variations and patterns. Several methods are proposed in the literature for flow regime analysis, focused on sub-daily flow variations (Meile et al., 2011; Pfaundler and Keusen, 2007) or other daily parameters (Richter et al., 1997). Fong et al. (2016) analysed and categorized hydropeak shapes as the basis for characterizing the associated morphological and ecological effects of differing hydropeaks. In particular, they found that hydropeak attenuation and ramping rates varied depending on hydropeak shape, thus creating differing impacts within the river system depending on the hydropeaking regime.

Several studies provide detailed examples of quantification of hydropeaking in single rivers (Fette et al., 2007; Leitner et al., 2017; Young et al., 2011), however, a few studies have compared hydropeaking patterns across multiple rivers (Bejarano et al., 2017; Schmutz et al., 2015). Within this context, this study aims to examine the pattern of the hydropeaking regimes in two contrasting mountainous rivers located in the South Central Pyrenees, an area subject to substantial hydropeaking activity. Specifically, the work seeks to classify hydropeaks following the shapes proposed by Fong et al. (2016) and assess their temporal distribution (frequency), timing, and magnitude during hydrologically contrasted years. Results provide a better understanding of the characteristics of hydropeaks, such as shape, magnitude, intensity, and timing. This type of information is never enough to support local environmental management practices aiming at mitigating effects of hydropeaking on rivers' structure and functionality, as well as to extend the knowledge on hydropeaking regimes.

3.1.2 STUDY AREA

This study has been carried out in two morphologically contrasting mountainous catchments, the Ésera and the Upper Cinca, both located in the northernmost part of the Cinca River basin (Figure 3.1, p.77). The Cinca is one of the largest tributaries of the river Ebro, which is the third largest catchment in the Mediterranean basin. At its confluence with the Segre and the Ebro, the Cinca drains a total area of 9,608 km^2, which equates to 11.2% of the total Ebro catchment area.

3.1.2.1 The river Ésera

The river Ésera is a relatively narrow catchment flowing north to south mostly through a confined valley (i.e., mean bankfull and wet channel widths are 38 and 24 m, respectively). The Ésera flows into the Cinca, 45 km downstream from Campo, accounting with a total area of 1 535 km^2 (Figure 3.1 ***a***, p.77)). Flow series registered in the Campo Gauging Station (CGS) provide the hydrological basis for this study (see more details in Section 3.1.3). Upstream from Campo, the Ésera has a catchment area of 567 km^2 (Figure 3.1 ***b***, p.77)). Altitude varies between 3 404 m a.s.l. (the highest elevation in the Pyrenees) and 691 m a.s.l. (in Campo). The catchment has a continental character with Mediterranean influences characterized by important thermal contrasts with drier sunny cold winters (snowfall period at high elevations) and hot stormy summers when torrential rains are frequent (Verdu et al., 2006). The basin shows a notable rainfall gradient ranging from 790 mm $year^{-1}$ in Campo to more than 2 500 mm $year^{-1}$ in the most northern part at higher altitudes (Lobera et al., 2016). The rainfall seasonal pattern in Campo (1997–2021) shows spring and fall as the wettest seasons (255 and 202 mm, respectively), and summer and winter as the driest seasons (179 and 148 mm, respectively).

The hydrology of the Ésera basin is characterized by a nivo-pluvial regime, with high flows in autumn and spring due to abundant rainfalls, which are accentuated in spring due to snowmelt (See Figure 3.3, p.84)). Flash-floods typically occur in summer as a result of intense local storms. The annual runoff (always expressed in this work for the period between October first and September 30th) registered at CGS (operated by the Ebro Water Authorities SAIH-CHE, code A-258, Figure 3.1 p.77)) for the period 1994–2016 ranges between 230 and 831 hm^3 (1 hm^3 = 1 $x10^6$ m3) with an average of 517 hm^3. The mean annual Q for the same period is 17 m^3s^{-1}. Maximum instantaneous recorded Q was 772 m^3s^{-1} (November 1997) representing a return period >25 years. Upstream from Campo, the river is highly regulated for HP production with a series of hydropower plants distributed along the drainage network, accounting with a total installed capacity of 176.8 Mw (Galán, 2012). The HP scheme (Figure 3.1 ***b***, p.77)) includes 35 km of channels and pressure galleries, five run-of-the river HP plants (Eriste, Sesué, Seira, Aragoné, and Campo), and two small reservoirs (Paso Nuevo and Linsoles, both storing ca. 3 hm^3 of water). The impounded ratio (IR; ratio of reservoir capacity divided by mean annual runoff) on the river Ésera is 0.011.

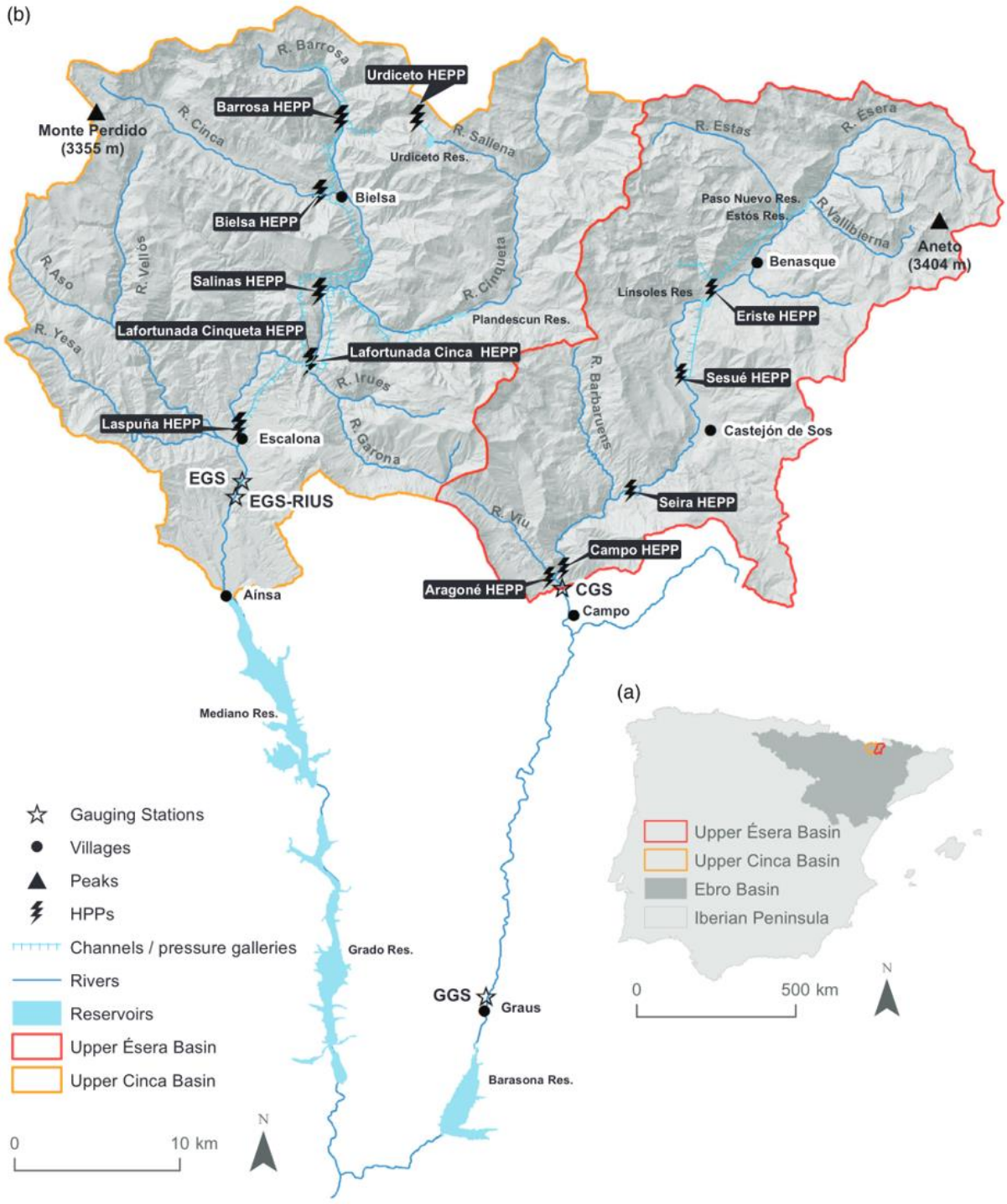

Figure 3.1: (**a**) Location of the Ebro, the Upper Cinca, and the Ésera River basins in the Iberian Peninsula. (**b**) The Upper Cinca and the Ésera River basins. The map shows the hydropower scheme (hydropower plants, reservoirs, channels, and pressure galleries) of both catchments. Note that the downstream ends of the catchments are where the gauging stations used in this study are located: Escalona Gauging Station (EGS) in the Upper Cinca, and Campo Gauging Station (CGS) in the Ésera (Color figure can be viewed at wileyonlinelibrary.com)

3.1.2.2 The upper Cinca

The Upper Cinca basin is located west of the Ésera catchment. It drains an area of approximately 847 km^2 up to the village of Aínsa, which is located at the entrance to the Mediano reservoir (Figure 3.1 **b**, p.77). The valley experiences a steep altitudinal gradient from >3 000 to 1 300 m a.s.l. in barely 3 km (i.e., 40% slope on average). Minimum altitude in the catchment is 569 m a.s.l. in Aínsa. Contrasting with the Ésera, the Cinca flows in a much very wider valley, where mean bankfull and wet channel widths are 238 and 45 m, respectively. The Upper Cinca basin belongs to the same climatic domain as the Ésera (Continental Mediterranean climate) characterized by a great temperature and precipitation contrast between winter and summer; however, the influence of the Atlantic domain produces a larger annual precipitation than the Ésera. As in the Ésera, winter tends to be cold and dry, while summer is hot and stormy with a large number of torrential rainfall episodes (Rubio, 1995). As in the case of the Ésera, the Upper Cinca shows a notable altitudinal rainfall gradient ranging from around 3 000 mm in the summits to a minimum of 801 mm in the lower zones (Béjar et al., 2018), and the same seasonal patterns with maximum in spring and minimum in winter. The hydrology of the basin is again characterized by a nivo-pluvial regime with great interannual variability. Periods of high flows and floods are usually produced in spring, mainly associated with snowmelt and episodes of frontal rains; whereas, at the end of summer and early autumn, floods are usually associated with convective storms (See Figure 3.3, p.84). Mean annual runoff registered at the Escalona Gauging Station (EGS, operated by the SAIH-CHE, code A-051, Figure 3.1, p.77) for the period 1959–2016 is 932 hm^3. The mean annual Q for the same period is 29.6 m^3s^{-1}, while the highest maximum daily flow (Qc) was recorded in November 1982, reaching 1 085 m^3s^{-1}, and representing a return period larger than 100 years (Llena et al., 2020). The Upper Cinca is also highly regulated for HP production accounting in this case with a total installed capacity of 111.2 MW (Galán, 2012). The hydropower scheme includes 58 km of channels and pressure galleries, a network of six run-of-the-river HP plants built along the mainstem river and its tributaries (Urdiceto, Barrosa, Bielsa, Salinas, Lafortunada, and Laspuña, Figure 3.1 **b**, p.77), and two small reservoirs (Urdiceto and Plandescún, with a capacity of 5 and 1 hm^3, respectively; Figure 3.1 **b,** p.77). The IR on the Upper Cinca is 0.007 a value slightly lower than the obtained on the river Ésera.

3.1.3 MATERIALS AND METHODS

This study follows a series of methodological steps: (a) selection and revision of available flow data, (b) identification of hydropeaks based on their shape and magnitude after Fong et al. (2016), (c) characterization of hydropeaking regimes based on three categories of variables: magnitude (hydrological variables), timing (duration), and frequency (occurrence), and (d), identification of groups of hydropeaks based on flow variables in each of the study catchments.

3.1.3.1 Flow series

Data used in this study consist of continuous records of discharge collected at two hydrometric sections in the Ésera and Upper Cinca Rivers. Flow data for the Ésera is registered at CGS located 150 m downstream from Aragoné, the lowermost HP dam (Figure 3.1 **b**, p.77) and consist of continuous flow records at 15-min intervals for the period 1997–2016. Complementary data used for the long-term hydrological analysis and hydropeak shape classification are available at the downstream gauging station in Graus (GGS) (Figure 3.1 **b**, p.77). This station was selected due to the length of the records (i.e., more than 60 years), which provided a better long-term hydrological characterization of the catchment for the particular purposes of the study. Specifically, three years were selected to characterize the hydropeaks in the Ésera. The selection was meant to represent wet, average, and dry years. Years with runoff above the 25th percentile of the long-term series (i.e., $>Q_{25}$) were considered wet; years with annual runoff between the 25th and 75th percentiles (i.e., Q_{25} and Q_{75}) were considered average; and years with runoff greater than the 75th percentile (i.e., $<Q_{75}$) were considered dry (as per Martínez and Fernández, 2010). Selected years for study were WY2013 (wet), WY2014 (average), and WY2016 (dry).

In the case of the Upper Cinca, flow series registered at the EGS-RIUS station operated by the University of Lleida were used. This station is located 3.4 km downstream from the Laspuña HP plant (Figure 3.1 **b**, p.77), where hydropeaks are generated. Flow series at EGS-RIUS are shorter (2014–2016) than those at the official gauging located in Escalona; however, the accuracy of the low flows at Escalona is substantially lower than those measured at the EGS-RIUS. Therefore, and in order to guarantee the quality of the data, the flow record from EGS-RIUS was used. In the case of the Upper Cinca, only two years of data were suitable for the analysis: WY2015 (average) and WY2016 (dry). As in the case of the Ésera, the official period of record (1959–2020) at Escalona was used to assess the long-term hydrology of the river allowing for classification of the targeted years. The aforementioned differences in low flows do not have a significant impact on the annual runoff, which justifies the use of this data set for the hydrological characterization of the study years.

3.1.3.2 Identification and characterization of hydropeaks

All hydropeaks in the study years were identified by segregating the hydropeaks based on ramping rates. The initial and the final discharges of each hydropeak (Q_{in} and Q_{fi}, respectively) were established when the ramping rate (or instantaneous rate of flow change) exceeded a threshold of 0.56 m^3s^{-1} h^{-1} and Q returned to the minimum value or Q_{in}. Instantaneous rate of change is defined here as the maximum rate of change (in both rising and falling limbs) measured over a 15-min interval and expressed in m^3s^{-1} h^{-1}. Once the Q_{in} and Q_{fi} were identified, the shape of each hydropeak was manually classified, and different hydrological variables were extracted for the analysis of the magnitude, timing, and frequency of the hydropeaks.

3.1.3.2.1 Characterization of shape

The classification of hydropeak shape was carried out manually following the categories previously established by Fong et al. (2016). In addition, two new categories (Spike and MultiSpike) were added in this study owing to the shapes identified in the Ésera and Upper Cinca River. Spike is characterized by a single rapid rising limb to Q_{max} followed by a rapid falling limb to baseflow, while MultiSpike is characterized by a rapid rising limb followed by small pulses (more or less of similar magnitude but short duration) until the end of the hydropeak when flow rapidly decreases to baseflow. Thus, hydropeak shapes include: Front Step, Back Step, Rectangle, Spike, MultiSpike, Goalpost, and Tower (see representations of each class in Figure 3.2).

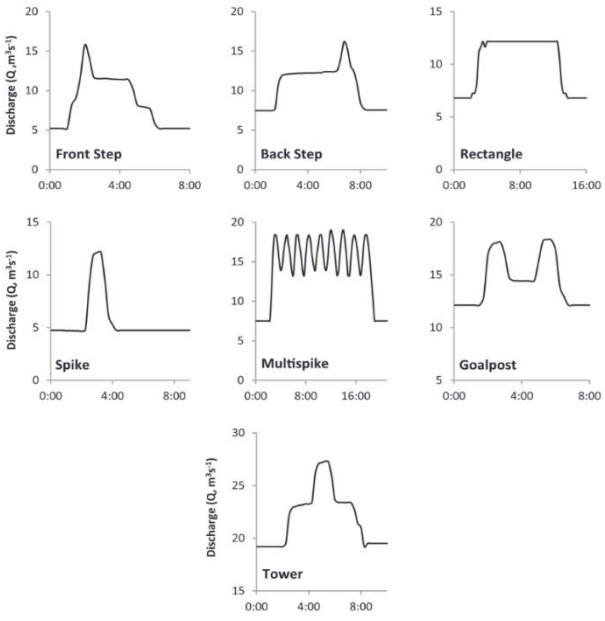

Figure 3.2: Hydropeak shapes used in the classification after Fong et al. (2016)

3.1.3.2.2 Characterization of hydropeaking regime

The analysis of the magnitude, timing, and frequency of hydropeaks consisted of the extraction of a series of relevant variables from each hydropeak then statistically grouping them (clusters), that is, hydropeaks were statistically grouped into clusters based on those hydrological variables. Then, clusters were analysed in order to determine the hydrological characteristics of each group as well as the distribution of shapes in each group in order to analyse if dominant shapes are present in each of them.

3.1.3.2.2.1 Hydrological variables

Twenty-one variables (Table 3.1) were selected to characterize individual hydropeaks. These variables were grouped into three categories related to magnitude, timing, and frequency, similar to those proposed by Richter et al. (1996). Most of these variables had been previously used in the literature (e.g., Hannah et al., 2000; Zolezzi et al., 2011; Meile et al., 2011; Carolli et al., 2015; Sauterleute and Charmasson, 2014; Greimel et al., 2016b; Alonso et al., 2017, Bejarano et al., 2017), with the exception of the time to maximum Q (T_{Qm}), the maximum Q position (P_{Qm}; where position is the location of Q_{max} within the hydropeak), and the hour of the maximum Q (H_{Qm}) that, as far as we know, were not used before in this kind of analyses.

Some of the variables correspond to direct observations of the flow series (as indicated in Table 3.1). Frequency variables, except for the number of peaks per hydropeak (H_{ph}), were directly obtained according to the occurrence of the hydropeak (within month, season, or year). The equations to calculate the rest of variables are indicated in Table 3.1. Specifically, volume (V, Equation 1) represents the volume of water between the start and the end of a single hydropeak. Mean Q (Q_{me}, Equation 2) was calculated as the arithmetic mean of the flow rates between Q_{in} and Q_{fi}. Hydropeak Intensity (Hlin) represents the magnitude of daily flow fluctuations associated with hydropower generation (Hauer et al., 2018b) and was calculated as the ratio of peak flow and baseflow. The range in flow (Q_{range}, Equation 4) was adapted from Hannah et al. (2000) and expresses the maximum amplitude of flow rates in a single hydropeak calculated as the difference between the minimum (Q_{min}) and the maximum discharge (Q_{max}). The maximum flow position (P_{Qm}, Equation 5) indicates the position of maximum discharge (Q_{max}) relative to the duration of the hydropeak (D_{Hp}). The maximum increase (R_{mi}) and decrease ramping rates (R_{md}) were adapted according to Meile et al. (2011) (Equations 6 and 7). The rate of change was defined as the difference in Q between two successive observations divided by the observation time interval as defined by previous equations, where Q_{-1} is the Q in time ti, and Q_{i-1} is the Q in the previous moment t_{i-1} (Meile et al., 2011), that is, positive values represent an increase of Q, while negative values indicate a decrease. The time to maximum Q (T_{Qm}) corresponds to the time elapsed since the beginning of the hydropeak until maximum Q was attained (Equation 8). The hydropeak duration (D_{Hp}, Equation 9) was calculated as the period between initial and final hours (H_{in} and H_{fi}, respectively). The time since the last hydropeak (T_{uh}) is the period between two different single hydropeaks (Equation 10). The number of peaks per hydropeak (H_{ph}) corresponds to the number of peaks attained during a single hydropeak (depending on the shape) and, finally, the number of hydropeak per year (N_{hy}), month (N_{hm}), or season (N_{hs}) corresponds to the number of hydropeaks occurred during a year, month, or season, respectively.

Table 3.1: Variables used for the characterization of the hydropeaks

Category	Variable	Symbol	Units	Equation/data
Magnitude	Volume[a]	V	hm^3	$V = \sum Q_{in+1} + .. + Q_{fi-1} * t$ (1)
	Initial Q	Q_{in}	$m^3 s^{-1}$	Direct observation
	Final Q	Q_{fi}	$m^3 s^{-1}$	Direct observation
	Maximum Q[a]	Q_{max}	$m^3 s^{-1}$	Direct observation
	Minimum Q[a]	Q_{min}	$m^3 s^{-1}$	Direct observation
	Mean Q[a]	Q_{me}	$m^3 s^{-1}$	$Q_{me} = \frac{\sum Q_{in+1} + .. + Q_{fi-1}}{N^{\circ} \text{of records}}$ (2)
	Hydropeak intensity	HI_{in}	–	$HI_{in} = \frac{Q_{max}}{Q_{min}}$ (3)
	Range in flow[a]	Q_{range}	$m^3 s^{-1}$	$Q_{range} = \frac{Q_{max} - Q_{min}}{Q_{min}}$ (4)
	Maximum Q position[a]	P_{Qm}	–	$P_{Qm} = \frac{T_{Qm}}{D_{hp}}$ (5)
Time and duration	Maximum up-ramping rate[a]	R_{mi}	$m^3 s^{-1} h^{-1}$	$R_{mi} = \max \left\lvert \frac{Q_i - Q_{i-1}}{t_i - t_{i-1}} \right\rvert$ (6)
	Maximum down-ramping rate[a]	R_{md}	$m^3 s^{-1} h^{-1}$	$R_{md} = \min \left\lvert \frac{Q_i - Q_{i-1}}{t_i - t_{i-1}} \right\rvert$ (7)
	Initial hour	H_{in}	Hh:Mm	Direct observation
	Final hour	H_{fi}	Hh:Mm	Direct observation
	Maximum Q hour	H_{Qm}	Hh:Mm	Direct observation
	Time to maximum Q[a]	T_{Qm}	Hh:Mm	$T_{Qm} = H_{Qm} - H_{in}$ (8)
	Duration[a]	D_{hp}	Hh:Mm	$D_{hp} = H_{fi} - H_{in}$ (9)
	Time since last event	T_{uh}	Hh:Mm	$T_{uh} = H_{in\,h_{n+1}} - H_{fi\,h_n}$ (10)
Frequency	Number of peaks per hydropeak[a]	N_{ph}	–	Direct observation
	Number of hydropeaks per water year	N_{hy}	–	Direct observation
	Number of hydropeaks per month	N_{hm}	–	Direct observation
	Number of hydropeaks per season	N_{hs}	–	Direct observation

[a]Variables used in the cluster analysis.

[a]Variables used in the cluster analysis.

3.1.3.2.2.2 Cluster analysis: Hydropeaks grouping according to their characteristics

A cluster analysis was carried out following the methodology established by Hannah et al. (2000). A CLARA analysis (Clustering Large Applications, Kaufman and Rousseuw, 1990) was performed using the CLUSTER statistical package in R® version 1.1.423 (Maechler et al., 2018). The objective was to identify groups of hydropeaks based on the variables, which were previously described and listed in Table 3.1. For this, it was necessary to define the number of optimal clusters or number "k" that best suits the data set. Silhouette width (S) is a popular measure for considering such parameter. S is defined as the average distance between data points in the same cluster compared against average distances between data points in other clusters. The result is comprised between 1 and -1, being 1 an indicator of a very good cluster (Rousseeuw, 1987). The CLARA analysis is an implementation of PAM (Partitioning Around Mediods, Halkidi et al., 2001) analysis developed by Kaufman and Rousseuw (1990). The PAM's approach is based on determining a representative object for each cluster; this object, called medoid, is intended to be the most central object within the cluster, and once the medoids have been selected, each unselected object is grouped together with the most similar medoid (Ng and Han, 1994). CLARA is designed to handle large data sets; instead of finding representative objects for the whole set of data, it draws a sample of the dataset and finds the medoids of the sample applying PAM. To obtain the best approach, CLARA draws multiple samples and offers the best clustering as an output (Ng and Han, 1994).

CLARA analysis was performed for the entire hydropeak dataset but using only eleven of the twenty hydrological variables (see variables accompanied by * in Table 3.1). The variable selection was based on a cross-correlation type analysis where one variable from the most highly correlated pairs were dropped thus retaining those that provided more information for the characterization and classification of the hydropeaks.

Finally, the frequency (i.e., percentage) of each (i) hydropeak shape and (ii) hydropeak season was assessed in each cluster to establish the dominant shapes and explore seasonal trends.

3.1.4 RESULTS

3.1.4.1 Hydrological characterization of the study years

Mean water yield in the Ésera at GGS for the period of record (1949-2016) was 608 hm^3 $year^{-1}$. The Q_{25} (726 hm^3 $year^{-1}$) and Q_{75} (473 hm^3 $year^{-1}$) were established to determine if years can be considered wet, average, and dry. Overall, 14 years were classified as wet (annual runoff $> Q_{25}$), 32 were classified as average (between Q_{25} and Q_{75}), and 14 were classified as dry ($> Q_{75}$). The selected years for this study were WY2013 (892 hm^3 $year^{-1}$, that is, wet), WY2014 (526 hm^3 $year^{-1}$, that is, average), and WY2016 (438 hm^3 $year^{-1}$, that is, dry).

In the Upper Cinca, mean water yield for the period of record 1959–2016 at the official gauging station in Escalona (EGS) was 886 hm^3 $year^{-1}$. Percentiles Q_{25} and Q_{75} were 1 117 hm^3 $year^{-1}$ and 714 hm^3 $year^{-1}$, respectively. Overall, 10 years classified as wet,23 as average, and seven as dry. As indicated in the method section, due to the uncertainties of low flow values (< 10 m3 s^{-1}) at EGS, the flow series obtained at the nearby EGS-RIUS during 2014–16 were used for the characterization of the hydropeaks. While uncertainty of the low flow estimations at EGS would not have had a major effect in the annual runoff calculations for the basin, it may have had an effect on the identification of hydropeak shape and the derivation of some of the parameters listed in Table 3.1 (e.g., Q_{min},Q_{range}). Data at EGS-RIUS were previously used by Béjar et al. (2018) to study the variation in flow and suspended sediment transport along a 10-km reach of the Upper Cinca. Additional details about the quality of the flow data is provided in the aforementioned publication. The data from EGS-RIUS were then used for the characterization of the hydropeaks during the two study years (i.e., WY2015 and WY2016). The WY2015 with an annual runoff of 726 hm^3 $year^{-1}$ was classified as average, WY2016 with an annual runoff of 658 hm^3 $year^{-1}$ was classified as dry, and the latter of which was similarly classified as dry in the Ésera.

3.1.4.1.1 River Ésera

Mean discharge (Q_{me}) at CGS for the period of record 1994–2016 was 17 m^3s^{-1}. Table 3.2 shows the main hydrological characteristics of the study years. WY2013 was one of the wettest in the last half century, reaching the largest peak discharge of the twenty-first century on June 18, 2013 (i.e., 461 m^3s^{-1}). Years WY2014and WY2016 were classified as average and dry and had annual runoffs of 526 hm^3 and 438 hm^3, respectively (Figure 3.3 **a**, p.84). Q_{me} registered for the average and dry years differs slightly (ca. 1 m^3s^{-1}), while differences increase to 5 and 6 m^3s^{-1} when compared with the wet one.

Flow frequency curves (Figure 3.4, p.85) were used to summarize the general hydrology of the study years in each basin. WY2014 and WY2016 in the Ésera showed a rather constant flow and a relatively narrow range of discharges (between 0.5 m3 s^{-1} and ca. 100 m3 s^{-1}), which is also reflected in the low standard deviation (SD, 10.7 and 13.3 m^3s^{-1}, respectively) and the coefficient of variation (CV, 0.63 and 0.83, respectively) (Table 3.2). The average year (WY2014) in the Ésera had even a more constant flow regime than the dry year; while in contrast, the wet year (WY2013) was highly variable (Figure 3.4 **a**, p.85). SD in the wet year was 24 m^3s^{-1}, and the CV was close to 1 (Table 3.2).

The fifth, 16th, 50th, 84th, and 95th percentiles (i.e., Q_5, Q_{16}, Q_{50}, Q_{84}, and Q_{95}) were used to calculate the Flow Standard Deviation (FSD; see Batalla et al., 2004, for more details).

This index is calculated as $FSD = |[(Q_{84} - Q_{16}) + (-Q_{95} - Q_5)]/Q_{50}|$ quantifies flow variability within and between years. Flow Standard Deviation (FSD) in the Ésera ranged from 3.1 to 4.5 among the three studied years and was 3.6 for the entire study period; values reflect a low intra and inter annual flow variability (e.g., for comparison, mean FSD values obtained by Batalla et al. (2004) in the Ebro basin were approximately 11.5, while maximum values were 30). Differences between years are accentuated when high flows (e.g., flows equalled or exceeded more than 10% of the time) occur. For example, the difference between the 0.1% exceedance flow of 350 m3 s^{-1} (i.e., large floods) and the 10% exceedance flow of 30 m3 s^{-1} (i.e., high flows) reflects the occurrence of the largest flood in the flow record in June 2013 (Figure 3.4 **a**, p.85).

Table 3.2: Summary of river hydrology at the Campo station (A-258) on the Ésera, during WY2013, WY2014, and WY2016.

Study years	Hydrological Type[a]	Annual Runoff (hm^3)	Mean Q (m^3s^{-1})	Standard Deviation (m^3s^{-1})	Coefficient of Variation	FSD	Maximum Q (m^3s^{-1})	n Floods[b]	N Hydropeaks
WY2013	Wet	894.6	21.85	23.88	1.09	3.8	460.7	11	498
WY2014	Average	526.3	16.89	10.68	0.63	3.1	76.58	6	696
WY2016	Dry	438.1	15.95	13.28	0.83	4.5	88.15	3	582

[a]See methods section for more information. [b]When Q is 1.5 times Q_{me} and verified in the hydrographs. This study considers a flood when the flow is 1.5 times higher than the base flow. This criterion has been widely used in the literature (Tuset et al., 2015; López-Tarazón et al., 2012; Garcia-Ruiz et al., 2005; among others).

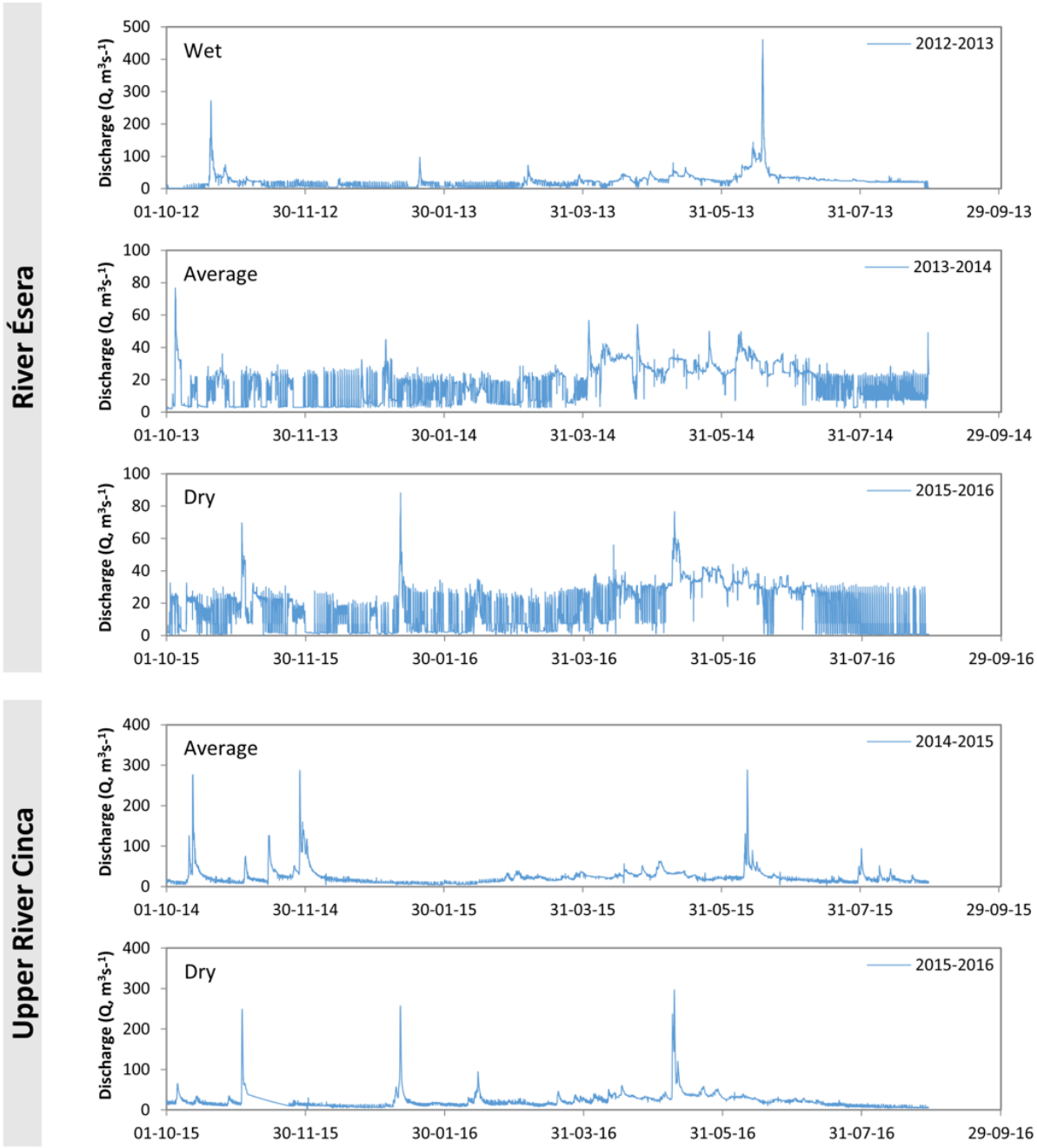

Figure 3.3: Annual hydrographs (a) in the Ésera River (CGS) and (b) in the Upper Cinca River (EGS-RIUS). Note that the scale in the Y-axis varies between years (Color figure can be viewed at wileyonlinelibrary.com)

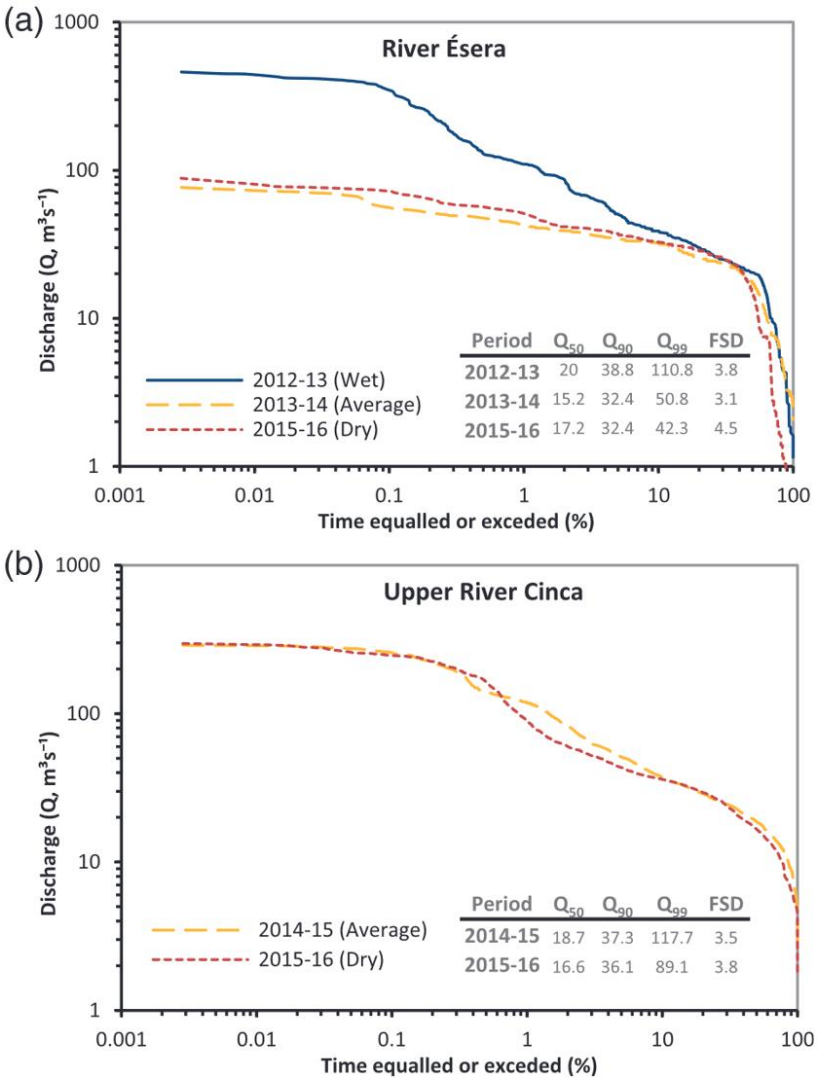

Figure 3.4: Flow frequency curves for the study years in (a) the river Ésera at CGS, and (b) the Upper Cinca at EGS-RIUS; Color figure can be viewed at wileyonlinelibrary .com

3.1.4.1.2 The Upper Cinca

Mean discharge at EGS-RIUS for the study years 2014–2016 was 28 m^3s^{-1}. WY2015 was classified as average and yielded 68.6 hm^3 more annual runoff than WY2016, which was classified as dry (Figure 3.3 **b**, p.84).

Flow frequency curves of the study years in the Upper Cinca (Figure 3.4 **b**, p.85) indicate a similar hydrological behaviour. The two curves show a high variability of flow discharges (SD of 20.9 and 19.7 m^3s^{-1}, and CV of 0.90 and 0.95, for WY2015 and WY2016, respectively) (Table 3.3). Flow variability was less in the dry year, as represented by a lower SD, but the differences between years in the Upper Cinca were less than between the average and dry years in the Ésera. With regard to the FSD, results in the Upper Cinca were similar to those obtained in the Ésera, ranging from 3.5 and 3.8, and with the same value for the whole period (i.e., 3.6), indicating a low intra and inter variability between the study years. Additionally, the magnitude and frequency of floods in the Upper Cinca were similar to those in the Ésera. The 10% exceedance flow was 30 m^3s^{-1} in the Ésera and 35 m^3s^{-1} in the Upper Cinca, while the 0.1% exceedance flow in the Ésera was 350 m3 s^{-1} (i.e., the maximum value observed in the wet year), and 270 m^3s^{-1} (i.e., the maximum value observed during the average year) in the Upper Cinca.

Table 3.3: Summary of the river hydrology registered at EGS-RIUS in the Upper Cinca during WY2015 and WY2016

Study years	Hydrological Type[a]	Annual Runoff (hm^3)	Mean Q (m^3s^{-1})	Standard Deviation (m^3s^{-1})	Coefficient of Variation	FSD	Maximum Q (m^3s^{-1})	n Floods[b]	N Hydropeaks
WY2015	Average	726.4	23.03	20.89	0.90	3.5	288.65	16	776
WY2016	Dry	657.8	20.80	19.74	0.95	3.8	296.54	14	687

[a]See methods section for more information. [b]When Q is 1.5 times Q_{me} and verified in the hydrographs. This study considers a flood when the flow is 1.5 times higher than the base flow. This criterion has been widely used in the literature (Tuset et al., 2015; López-Tarazón et al., 2012; Garcıa-Ruiz et al., 2005; among others).

3.1.4.2 Characterization of hydropeak shape

A total of 2 351 hydropeaks were analysed, with 888 in the Ésera (296 hydropeaks per year) and 1 463 in the Upper Cinca (731 hydropeaks per year). In the following sub-sections, we first present the main shapes identified in both rivers, followed by the intra and interannual variability of them. Five shapes were identified in the two rivers (see Figure 3.2, p.79): Front Step is characterized by the Q_{max} occurring in the first rising limb of the hydropeak, with flow slightly decreasing following the peak to a relatively steady discharge until the end of the hydropeak when flow decreases rapidly to baseflow. Rectangle is characterized by a single rapid rising limb, followed by a prolonged stable period of maximum Q, until the end of the hydropeak when flow rapidly decreases to baseflow at a similar rate to the rising limb. MultiSpike is the most dynamic shape, where following the rapid rising limb, small pulses (more or less of similar magnitude and short duration) occur until the end of the hydropeak when flow rapidly decreases to baseflow. Spike is characterized by a single rapid rising limb to Q_{max} followed by a rapid falling limb to baseflow, and thus is typically of shorter duration than other shapes. Finally, Back Step is characterized by a rapid rising limb, followed by a high stable flow until an additional increase in flow to the Q_{max} occurs at the end of the hydropeak when flow rapidly decreases to baseflow. In addition, two more shapes were identified in the Upper Cinca. First Goalpost, which is characterized by two peaks of similar Q_{max} occurring at the beginning and end of the hydropeak. The other shape is Tower, which is characterized by an initial flow increase to a stable Q followed by a second increase to the Q_{max} and subsequent decreases to baseflow, that mirror the stepped nature of the rising limb.

3.1.4.2.1 Frequency

The most recurrent shape in the Ésera was Front Step (n = 353, 40% of total) followed by Rectangle (n = 178, 20%), MultiSpike (n = 174, 20%), Spike (n = 150, 16%), and Back Step (n = 33, 4%). In the Upper Cinca, Rectangle was the most frequent shape (n = 622, 42.5% of total) followed by Spike (n = 440, 30%), Front Step (n = 233, 16%), Back Step (n = 110, 7.5%), and Goalpost and Tower, both rare with 29 events (2% of total) each. The dominant hydropeak shape differed between the Ésera and the Upper Cinca, Front Step versus Rectangle, respectively, and the frequency of sub-dominant shapes varied between each river with the next three sub-dominant shapes more evenly occurring in the Ésera versus those in the Upper Cinca.

3.1.4.2.2 Temporal variability

In the Ésera, Front Step was the most frequent shape in both dry and wet years (61 and 37%, respectively). The wet year presented more variability in terms of shapes: MultiSpike and Rectangle represented 49% and 29%, respectively, with Spike and Back Step being the least frequent shapes. In the average year, the four most frequent shapes (Spike, Front Step, Rectangle, and MultiSpike) accounted for the 94% of the total hydropeaks and were evenly distributed with regard to their occurrence. The remaining hydropeaks (6%) were Back Step. At the seasonal scale, hydropeaks in autumn and winter were similarly distributed with Front Step as the most frequent followed by MultiSpike and Rectangle (depending on the year). This pattern changed in spring when Rectangle was the dominant shape followed by MultiSpike. In summer, Front Step was on average the most common shape; however, its relative occurrence differed between years, with the highest frequency in the dry year (97% of hydropeaks in summer) and lowest frequency in the average year (4% in summer). The frequency of hydropeaks at a monthly scale was similar to the frequency within seasons, where Front Step was the dominant shape from October to March, and in July and August, whereas from April to June, Rectangle predominated. September was the only differing month when Spike was the most frequent shape observed. The two study years in the Cinca showed nearly identical hydropeaking patterns over time. The dominant shapes were Rectangle (41% and 44% of the total events for the average and dry year, respectively) and Spike (28% and 32% for average and dry years, respectively). The sub-dominant shapes were Front Step (ranging between 15 and 17% in the study years), Back Step (between 7 and 8%), and Tower and Goalpost (between 1 and 3% each). The same distributions were observed at the seasonal and monthly scale.

3.1.4.3 Characterization of hydropeaking regime

3.1.4.3.1 Magnitude, timing, and frequency

3.1.4.3.1.1 River Ésera

Table 3.6 shows the hydrological parameters of the hydropeaks for each of the study years and for all study years combined. The main characteristics of each category (i.e., magnitude metrics, time and duration metrics and frequency metrics) are described.

Some interesting results have been found in magnitude metrics. For instance, the mean volume released during an individual hydropeak was higher in the dry year with an average of 0.89 hm^3. The dry year also included the hydropeak with the largest water volume released (8.82 hm^3). The average year included the greatest number of hydropeaks (348, accounting almost 1 hydropeak per day) but mean volume of releases was smaller (0.56 hm^3).

Water volume released for hydropeaking generation was variable throughout the year. Spring and early summer had the largest runoff due to snowmelt and seasonal rains; however, the generation of hydropeaks was minimal or did not occur. In contrast, hydropeaks occurred throughout summer and autumn when runoff was much less. Across years, catchment water yield dictated the water volume employed for hydropower production, such that the lower the annual runoff, the higher the water volume dedicated to hydropower generation. The dry year had the largest volume dedicated to HP generation (252 hm^3, 57% of annual runoff) followed by the average year (193 hm^3, 37% of annual runoff) and the wet year (164 hm^3, 18% of annual runoff). Consequently, the number of sub-daily fluctuations due to hydropeaking was greater during the dry and average years. The range in flow was variable between years with the highest Q_{range} (21.7 m^3s^{-1}) in the dry year and lower ranges in the wet and average years (15 m^3s^{-1} and 14.5 m^3s^{-1}, respectively) (Table 3.6). The position of the maximum Q in the hydropeak did not show marked differences between years since, and in general, the maximum flow was found at the beginning of the hydropeak owing to the dominant Front Step shape.

Ramping rates for the rising and falling limbs of the hydrographs (for both hydropeaks and flood events) were calculated for each study site. Figure 3.5 **a** and **b** show the accumulated frequency curves of the maximum ramping rates observed during floods and hydropeaks in the river Ésera. Up-ramping rates equalled or exceeded more than the 10% of the time were virtually the same in all the study years, while rates exceeded less than 1% of the time (>50 m3 s^{-1} h^{-1}) were much higher in the average year likely due to natural floods (Figure 3.5 **a**). The maximum flow increase was 162 m3 s^{-1} h^{-1}, observed on June 18, 2013, during a natural flood that reached 461 m^3s^{-1} (ca. 10 years return period flood). In contrast, differences between years in the down-ramping rates (i.e., during the falling limb of the hydrographs; Figure 3.5 **b**) were relatively smaller than those observed for the rising limb. Maximum up and down-ramping rates observed during hydropeaks were 81 and 94 m3 s^{-1} h^{-1}, respectively, both during the dry year (Table 3.6).

Regarding the time and duration metrics, the average duration of hydropeaks was 12 h but varied depending on the year. For example, the longest hydropeaks occurred during the dry year (average of 14 h), while the shortest hydropeaks (average of 10 h) were observed in the average year and moderate duration hydropeaks occurred in the wet year (12 h) (Table 3.6). During the three-year study period, a total of 10 463 h, or 40% of the time, the Ésera was subjected to hydropeaking. The dry year had the most hydropeaking hours (4 100 h, 47% of the time) while the wet year had the least number of hydropeaking hours (3 006 h, 34%). During the average year, despite registering the largest number of hydropeaks (almost one per day), the shorter hydropeak duration was reflected in the total number of hours subjected to flow fluctuation (3 357 h, 40%).

Finally, in terms of frequency, it can be said that the Ésera was subjected to a persistent and high-magnitude hydropeaking regime. The 888 hydropeaks identified in the flow record (i.e., 3 WY) represented an average of 0.81 hydropeaks per day (i.e., 296 hydropeaks per year). Their frequency depended on the hydrology of the study year. Generally, less hydropeaks were generated during the wet year (0.68 hydropeaks per day) than during average and dry years (0.95 and 0.8 hydropeaks per day, respectively). The number of peaks per hydropeak was very high, reaching a maximum of 79 during the dry year. This fact was explained because MultiSpike was one of the most frequent shapes in the Ésera.

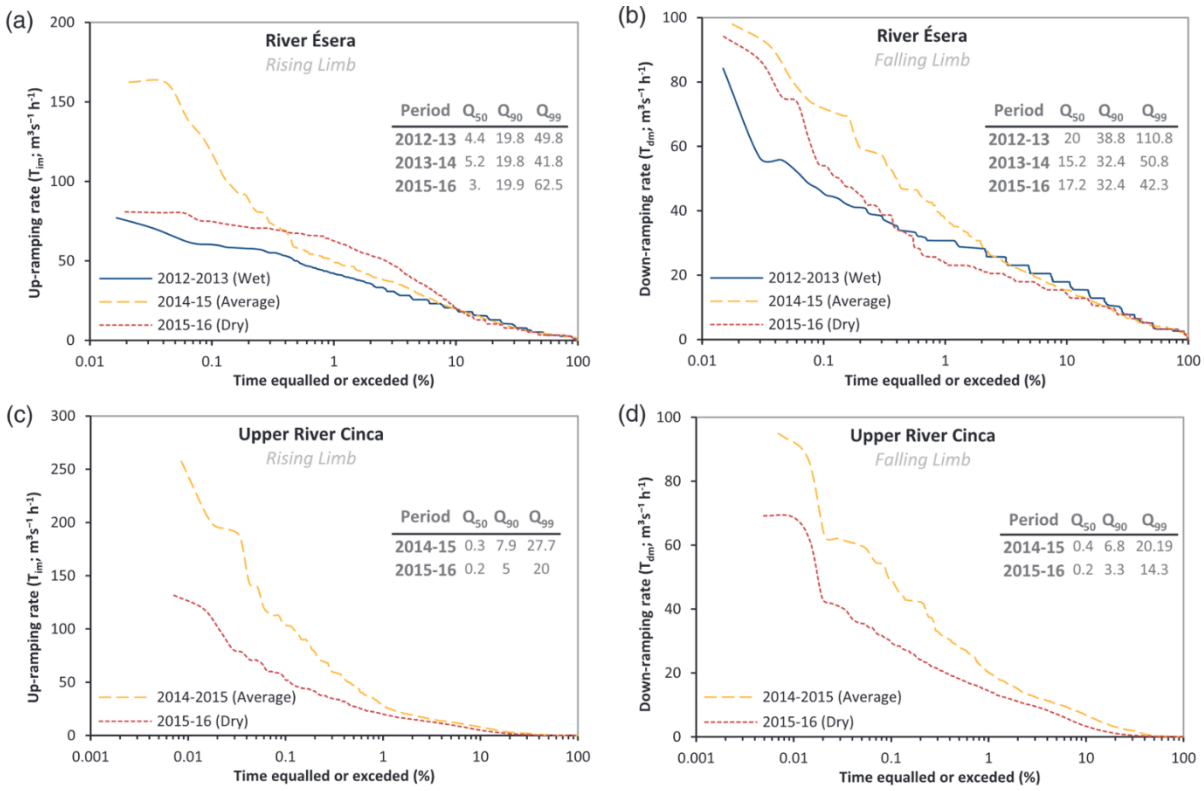

Figure 3.5: Accumulated frequency curves of the maximum ramping rates observed during floods and hydropeaks in the Ésera and the Upper Cinca. (a) and (b) represent the ramping rate during the rising and falling limbs of the hydrographs in the Ésera, respectively. (c) and (d) represent the ramping rate during the rising and falling limbs of the hydrographs in the Upper Cinca, respectively. Note that diagrams also include the ramping rates of natural floods and hydropeaks. Therefore, values differ from those presented in Table 3.6 and Table 3.7, where only the parameters associated with hydropeaks are presented (Color figure can be viewed at wileyonlinelibrary.com)

3.1.4.3.1.2 Upper Cinca River

Table 3.7 shows the hydrological parameters of the hydropeaks for each of the study years and for all years combined. The main characteristics of each category (i.e., magnitude metrics, time and duration metrics and frequency metrics) are described.

Concerning the magnitude metrics, the water volume and average duration of the hydropeaks during the average year were greater (0.36 hm^3 and 5.5 h) than the observed during the dry year (0.25 hm^3 and 4.75 h) (Table 3.7). These values are smaller than the registered in the Ésera; the observed trend also differed; since in the Ésera, the higher volume was observed during the dry year. The hydropeak with greater volume and duration occurred in August of the average year, with 2.96 hm^3 of water released and a duration of 29 h 30 min possibly coinciding with a peak of energy demand during a summer heatwave. The volume of water released during hydropeaks was relatively constant during the studied years with spring and fall registering the highest releases. Runoff associated to hydropeaks in WY2015 was 276.7 hm^3, representing 38% of the annual runoff recorded at EGS; while in WY2016, HP releases only represented 26% of the annual runoff. These values are lower compared to the Ésera.

Ramping rates for the rising and falling limbs of the hydrographs (for both hydropeaks and flood events) in the Upper Cinca (Figure 3.5 **c**) show contrasting trends between the average and the dry years in terms of ramping rates. As in the Ésera, the pattern of up-ramping rates (raising limb) is the same until rates equalled or exceeded more than 1% of the time from where differences increase notably. In the case of the down-ramping rates (falling limb, Figure 3.5 ***d***), patterns are quite different, and in contrast to the up-ramping rates, differences between years are significant from rates equalled or exceeded less than 40% of the time. As in the case of the Ésera, natural floods control differences in the annual distribution. Results also indicate that the average year was the one with the larger ramping rates in both the rising and the falling limbs of the hydrographs (Figure 3.5 ***c***, ***d***). The maximum up and down-ramping rates were 69 and 33 m^3s^{-1} h^{-1}, respectively. The maximum values observed in the cumulated frequency curves occurred during a natural flood registered in October 12, 2014, where the maximum Q increment reached 257 m^3s^{-1} h^{-1} (Table 3.7), 95 m^3s^{-1} h^{-1} higher than the maximum value observed for the Ésera. In total, 63% of the hydropeaks analysed show maximum increases between 5 and 15 m^3s^{-1} h^{-1}. The maximum up- and down-ramping rates registered during hydropeaks in the Cinca River were produced in the average year. The range in flow was similar between years with the highest Q_{range} oscillating between 31.1 m^3s^{-1} and 34.1 m^3s^{-1}, in the average and dry years, respectively (Table 3.7). The position of the maximum Q in the hydropeak did not show marked differences between years and, in general terms, and contrasting with the Ésera, it occurs mainly in the central part of the hydropeak.

In terms of time and duration, the average duration of hydropeaks was slightly greater than 5 h with results varying between study years. The duration of 78% of hydropeaks ranged from 1 and 8 h with 58% between 1 to 4 h and 42% between 4 to 8 h. HP duration in the Cinca was thus much shorter that that observed in the Ésera. The total duration of the 1 463 hydropeaks was almost 7 600 h representing the 43% of the time of the study period with 4 328 h registered in WY2015 and 3 271 h in WY2016 (i.e., 50% and 37% of the total year hours, respectively). Thus, time devoted to HP production in the Upper Cinca was slightly higher than in the Ésera. The average delay from one hydropeak to the next in the average year was 5 h and 45 min, and 7 h and 55 min in the dry year, while the delay in the Ésera was almost three times higher.

Finally, regarding the frequency, as the Ésera, the Upper Cinca was subjected to a very persistent hydropeaking regime but with a slightly lower relative magnitude than in the Ésera. A total of 1 463 hydropeaks were identified and characterized representing an average of approximately two hydropeaks per day. The average year included 776 hydropeaks, averaging 2.1 hydropeaks per day, which was slightly higher than the average of 1.9 hydropeaks per day during the dry year (687 hydropeaks), representing the double than the registered in the Ésera. The number of peaks per hydropeak was very low reaching a maximum of 13 during the average year and four during the dry year. These values are six times lower than the registered in the Ésera explained by the absence of MultiSpike shape in the Cinca.

3.1.4.3.2 Cluster analysis: Hydropeaks grouping according to their characteristics

3.1.4.3.2.1 River Ésera

The optimum number of clusters was established by means of the Silhouette width analysis (Kaufman and Rousseuw, 1990). The Silhouette values for clusters between 2 and 10 (K = 2–10) ranged from 0.26 to 0.39 with the highest value for K = 2, indicating that the optimum number of clusters was 2. However, limiting analysis to two clusters would possibly overlook some important hydropeak characteristics. The value for K = 3 was 0.36 (similar to 0.39 for K = 2), while the value for K = 4 was 0.29, which was a notable decrease in cluster coherence.

Hence, K = 3 was chosen as the optimum number of clusters to be used in the CLARA analysis. Figure 3.6 **a** show the clusters obtained from CLARA, and Table 3.4 presents the main characteristics of the resulting groups. The CLARA analysis describes the 67.8% of the variability of the hydrological parameters.

The season in which each hydropeak was generated is also shown in Figure 3.6 **a** and the occurrence of each season per cluster in Figure 3.6 **b**. Only 14% of the hydropeaks detected in the Ésera took place during spring. Cluster #1 was mainly composed by spring (i.e., 52%) and summer (i.e., 38%) hydropeaks. Cluster #2 was composed by winter (i.e., 60%) and autumn (i.e., 46%) hydropeaks. Finally, cluster 3# was composed by we can observe that autumn and summer hydropeaks (29% and 26%, respectively).

Cluster #1 encompassing 32.5% of all detected hydropeaks was characterized by short duration, low magnitude hydropeaks, as well as by the lowest ramping rates (Table 3.4). Cluster #2, mainly composed by isolated hydropeaks (i.e., 45.8%), was characterized by the hydropeaks with longest durations (at least twice that of cluster #1), highest water volumes, but intermediate ramping rates, although the maximum rate for the falling limb was the largest of the three clusters. Finally, hydropeaks in cluster #3, representing only 21.7% of all hydropeaks, were characterized to have an intermediate duration and volume, but the largest ramping rates of the rising limb of the hydrographs (70% higher than for cluster #2). Cluster #3 also included hydropeaks of greater discharge variability (Q_{range}), with an average maximum discharge of 27.12 m^3s^{-1} (representing almost 200% of the mean annual flow) and a minimum average discharge of 1.6 m^3s^{-1} (corresponding to only 10.5% of the mean annual flow). Additionally, hydropeaks in cluster #3 had the minimum time to maximum discharge and the smaller maximum discharge position compared to the other two clusters.

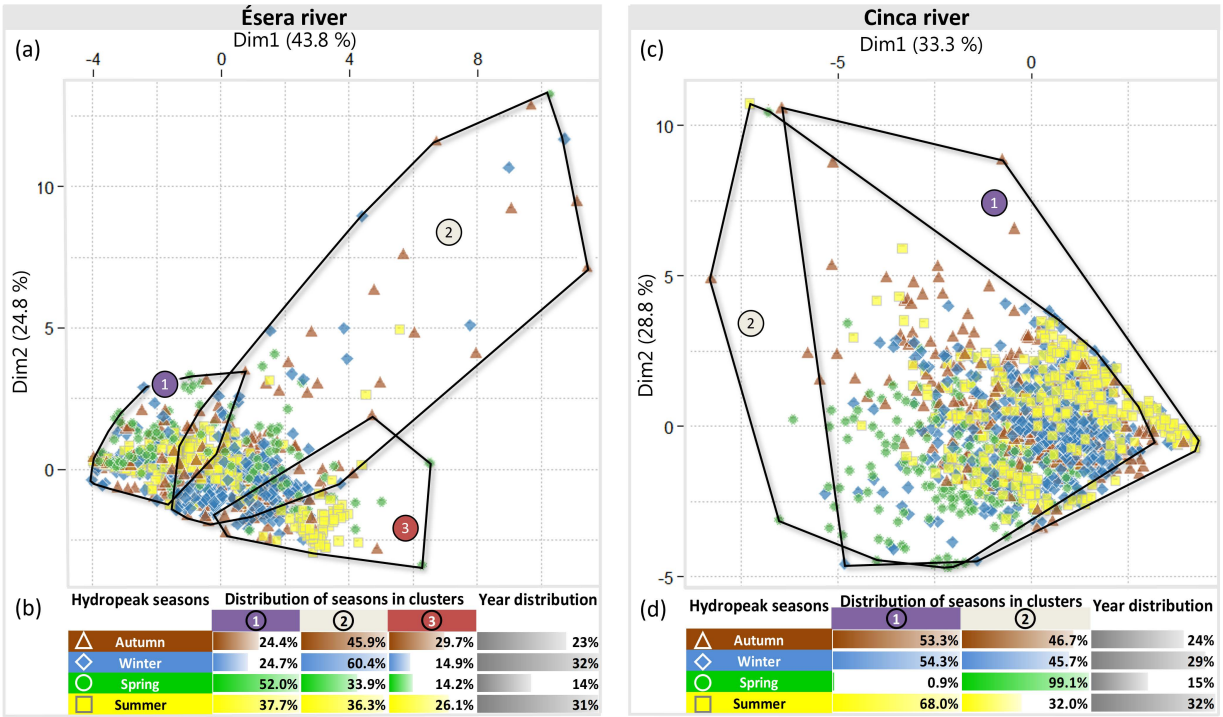

Figure 3.6: Result of CLARA cluster analysis and season distribution per cluster for (**a**, **b**) river Ésera and (**c**, **d**) Upper Cinca River (Color figure can be viewed at wileyonlinelibrary.com)

Table 3.4: Average values of the hydrological parameters of clusters obtained in the river Ésera (#1, #2 and #3), in the Upper Cinca (#1, #2), and in both

Parameter	Symbol	Unit	River sera			Upper Cinca		River Ésera and Upper Cinca		
			Cluster #1	Cluster #2	Cluster #3	Cluster #1	Cluster #2	Cluster #1	Cluster #2	Cluster #3
Duration	Dur	Hh:Mm	06:50	15:03	13:28	05:24	05:00	04:51	06:13	13:40
Volume	V	hm3	0.34	0.88	0.85	0.23	0.38	0.19	0.45	0.8
No. peaks per hydropeaks	N_{ph}	n	2.55	5.37	3.82	1.50	1.36	1.47	1.74	4.66
Maximum up-ramping rate	T_{im}	m^3s^{-1} h^{-1}	13.65	33.24	56.52	10.77	12.77	11.01	11.7	40.98
Maximum down-ramping rate	T_{dm}	m^3s^{-1} h^{-1}	-11.82	-23.89	-22.17	-9.05	-10.74	-9.1	-10.58	-23.37
Maximum Q	Q_{max}	m3s-1	16.08	23.32	27.12	13.93	24.29	13.28	23.31	24.31
Mean Q	Q_{mean}	m^3s^{-1}	12.76	16.48	17.27	12.27	22.31	11.39	21.32	16.5
Minimum Q	Q_{min}	m3s-1	7.8	4.93	1.6	8.54	17.91	7.84	16.51	4.16
Range in flow	Q_{range}	m^3s^{-1}	8.28	18.39	25.52	5.39	6.38	5.44	6.8	20.15
Time to max Q	T_{Qm}	Hh:Mm	2:01	4:31	1:54	3:28	1:30	2:06	2:17	3:22
Max. Q position	P_{Qm}	-	0.36	0.3	0.14	0.39	0.47	0.46	0.41	0.25

Note: Ésera and Upper Cinca (#1, #2 and #3).

3.1.4.3.2.2 Upper Cinca River

The values of the Silhouette width analysis ranged between 0.6 and 0.36 for clusters between two and ten (K = 2–10), with the highest value of 0.6 for K = 2. The value of K = 3 decreased to 0.36, however, suggesting that the consistency of the grouping decreases significantly when K increases to more than two clusters. Therefore, K = 2 was chosen as the optimum number of clusters to be used in CLARA analysis. The CLARA analysis described 62.1% of the variability of the hydrological parameters (Figure 3.6 **c**, Table 3.4). Figure 3.6 **c** shows a certain overlap between the two groups where 51% of the hydropeaks are located in cluster #1 and 49% in cluster #2.

Figure 3.6 **d** shows that the autumn and winter hydropeaks are almost equally distributed between the two clusters. On the other hand, almost all of spring hydropeaks (i.e., 99.1%) are located in cluster #2, while the majority of hydropeaks produced in summer (i.e., 68%) are located in cluster #1. Cluster #2 is only composed by 30% of the hydropeaks generated in the spring season, but this 30% represents the 99.1% of spring hydropeaks. Hence, cluster #2 describes the characteristics of all the hydropeaks in the spring season. Parameters that differed between clusters were water volume, time to maximum Q and maximum Q. Cluster #1 included hydropeaks with water volume, maximum, mean and minimum Q, almost two folds lower than hydropeaks in cluster #2. However, hydropeaks in cluster #2 required more time to reach the maximum Q (average of three hours).

3.1.4.3.2.3 Joint analysis: Ésera and Upper Cinca

In order to search for more general trends in the characteristics of hydropeaks, an additional CLARA analysis was completed on the entire set of hydropeaks from both the Ésera and the Upper Cinca. Both are mountain rivers, so results may shed light on common behaviours in these types of fluvial systems. As in the case of the Ésera, the optimum number of clusters based on means of the Silhouette width analysis was two groups (K = 2, Silhouette value = 0.40); however, we found that using three groups (K = 3; Silhouette value = 0.36) in the CLARA analysis described more variability (71.5%) than using two (69.2%).

Clusters #1 and #2 are essentially composed by Upper Cinca hydropeaks (i.e., 84% and 95%), while cluster #3 is composed by Ésera Hydropeaks (i.e., 99%). Cluster #1 includes summer, autumn, and winter hydropeaks from the Upper Cinca, and a small part of spring and summer hydropeaks of the river Ésera (Figure 3.7). Cluster #2 is mainly composed by spring hydropeaks of the Upper Cinca. Finally, cluster #3 is represented by Ésera hydropeaks; however, no seasonal patterns were found.

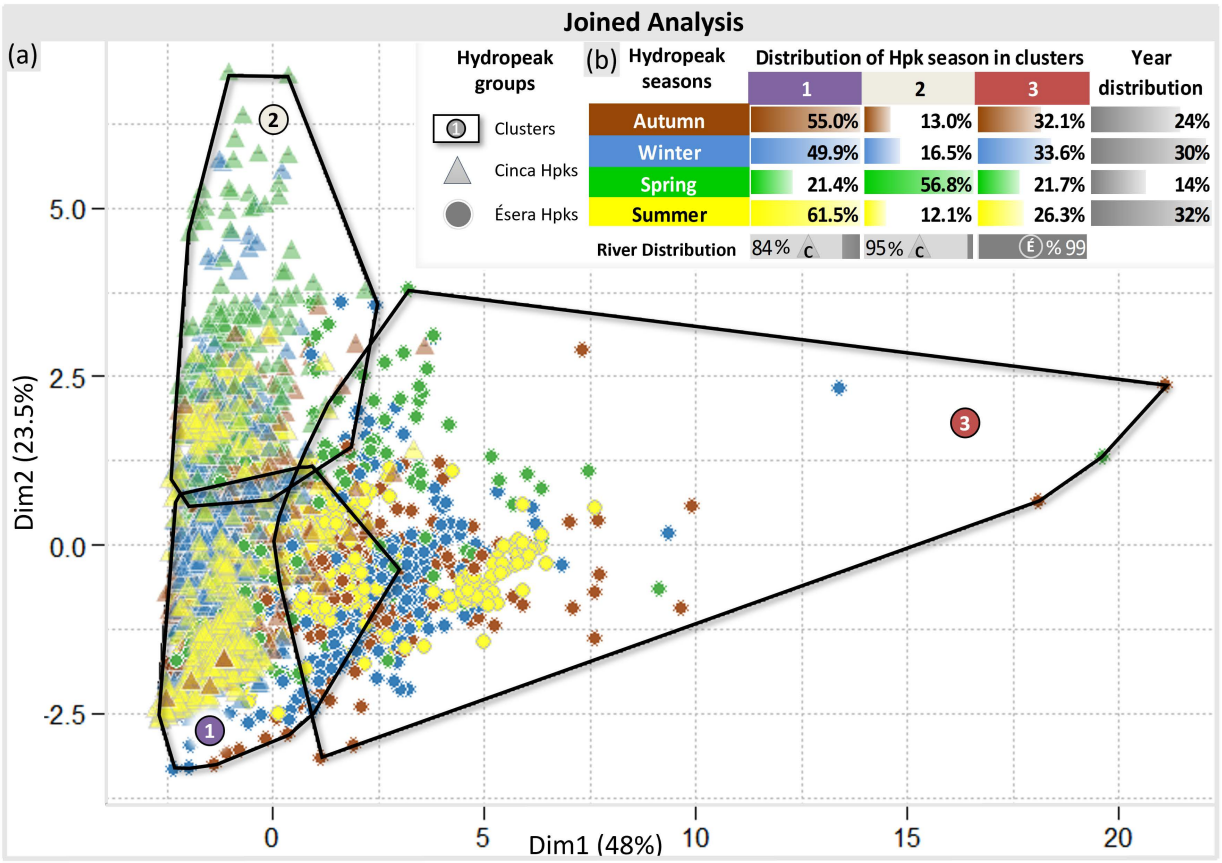

Figure 3.7: Result of CLARA cluster joint analysis and season distribution per cluster of the both the river Ésera and the Upper Cinca River (Color figure can be viewed at wileyonlinelibrary.com)

Results indicated that Cluster #1, representing 51% of all hydropeaks detected on both rivers, was composed of short duration and low magnitude hydropeaks (with maximum, mean and minimum Q, lower than the mean annual river discharge), and with the lowest ramping rates (Figure 3.7, Table 3.4). Cluster #2 is characterized by intermediate duration, water volumes, and ramping rates. This cluster presents the highest minimum, mean, and maximum Q (1.5 times the mean annual river discharge). Finally, hydropeaks in cluster #3, composed by 80% of hydropeaks from the river Ésera, were characterized by the largest values of most variables, including duration, volume, number of peaks, ramping rates, and Q_{range}.

The joint analysis allowed to highlight inter- and intra-river variability. The CLARA analysis grouped all the hydropeaks of the river Ésera in a single cluster, while the hydropeaks of the Cinca River were grouped in the other two clusters. The strong influence of the seasons in the hydrological characteristic of the hydropeaks in the Upper Cinca allows distinguishing two different behaviours in this river (intra-variability). Conversely, the influence of the seasons in the river Ésera hydropeaks is not strongly contrasted. However, their hydropeaks are different enough to be separated from the ones of the Upper Cinca (inter-variability).

3.1.4.4 Relation between the characteristics of the hydropeaks and their shape and timing

Once the characteristics of each cluster in terms of magnitude, timing, and frequency were obtained (Section 3.1.4.3), the relative frequency (i.e., percentage) of each hydropeak shape in each cluster for each river was determined. The objective was to assess if specific characteristics of hydropeaks were given always for the same shape or, contrarily, if different shapes can provide similar characteristics in terms of magnitude, timing, and frequency.

3.1.4.4.1 River Ésera

Table 3.5 shows the percentage distribution of the different shapes in each cluster. The majority of the hydropeaks in cluster #1, representative of spring and summer, were characterized as Spike or MultiSpike (70% of total). These hydropeaks were characterized by relatively rapid flow pulses of short duration, lasting half the duration of other hydropeaks. Despite this rapid flow fluctuation, Q_{max} and Q_{mean}, as well as the ramping rates, were relatively low. Hydropeaks in cluster #2 were strongly representative of autumn and winter hydropeaks, and to a lesser extent of summer hydropeaks. Front Step and Rectangle (78% of total) dominated cluster #2. These hydropeaks typically included the largest volumes of water, average up-ramping rates, and the highest down-ramping rates (Table 3.6). Finally, 89% of hydropeaks in cluster #3, mainly representative of autumn and summer hydropeaks, were characterized as Front Step. These hydropeaks had the highest ramping rates during the rising limb of the hydrographs (53 m3 s^{-1} h^{-1}) and the shortest time to the maximum flow (often less than 2 h). Front Step was the only shape with a relevant presence in both clusters #2 and #3; while the form of the hydropeak was the same, those in cluster #2 were characterized by intermediate magnitude, while those in cluster #3 had the highest peak flows and largest range in flows.

Table 3.5: Percentage distribution of hydropeak shapes for every cluster (CLARA analysis) in the rivers Ésera and Upper Cinca

	Ésera			Upper Cinca	
	Cluster #1%	Cluster #2%	Cluster #3%	Cluster #1%	Cluster #2%
Back step	3.1	5.3	1.5	12	5
Front step	7.5	41.9	86.9	29	9
Rectangle	19.0	36.1	10.6	47	40
MultiSpike	23.1	13.6	1.0	-	-
Spike	47.3	3.0	0.0	3	44
Clavey	-	-	-	4	1
Goalpost	-	-	-	5	1

Note: Note that bold numbers indicate the higher percentage in each cluster.

3.1.4.4.2 Upper Cinca

Table 3.5 also shows the distribution (%) of the different hydropeak shapes in each cluster in the Upper Cinca. The majority of the hydropeaks in cluster #1 were classified as Rectangle and Front Step (76% of total), which had lower durations and water volumes than other shapes. Flow rates as well as the distance between flow peaks were lower in this group compared to cluster #2. Hydropeaks in cluster #2 were mainly Spike and Rectangle (84% of total). They were defined by relatively rapid flow pulses of short duration. Statistically, the value of the hydrologic parameters was very similar between the two clusters, with the exception of flow rates. Differences in the characteristics of each cluster in the Upper Cinca were slight, reflecting the presence of Rectangle in both clusters (40% of hydropeaks in each cluster). In contrast, the characteristics of each cluster in the Ésera was much different, reflecting differing dominant shapes in each cluster.

3.1.5 IMPLICATIONS OF HYDROPEAK SHAPE FOR RIVERS' ECOGEOMORPHOLOGY

Results indicate that the shape of hydropeaks changes during the year, among years, and among catchments. Results also highlighted that those different shapes may yield similar hydrological characteristics. Hydropeaking regimes (shape, frequency, magnitude, and timing) control flow routing, may affect the morphological and sedimentological characteristics and dynamics of the river bed and, ultimately, have an impact on the structure and functioning of aquatic communities, as stated below.

3.1.5.1 How does hydropeak shape interact with flow routing?

It is well-known that channel morphology may affect flow routing. Factors like slope, width, sinuosity, and roughness influence the delay of peak discharges in downstream sections; the response of flow routing on the Ésera and Upper Cinca is also conditioned by their different river-valley morphologies. The Ésera flows mostly through a confined valley whereas the Cinca flows in a much very wider valley. For instance, mean active zone and wet channel widths in the Ésera River are 38 and 24 m, respectively, while in the Upper Cinca are 238 and 45 m, respectively. Other morphological parameters such as sinuosity and slope are more similar with values of approximately 1.07 for sinuosity and 0.007 m m^{-1} for slope. Based on these parameters, it could be expected that flows in the Ésera are transferred downstream faster. The Upper Cinca, with a relatively unconfined valley, presumably experiences a greater proportion of wetted surface area, which may increase roughness, thus favouring a comparably attenuated flood wave.

Hydropeak magnitude and shape interact with channel morphology and thus may also impact flow routing. Preliminary unpublished results (i.e., MorphPeak) of modelling simulations in the Upper Cinca show that depending on the hydropeak shape, flow delay and peak discharge attenuation vary greatly (no such data is available in the Ésera). For instance, when a rectangular pulse is released, the attenuation in the immediate downstream sections is almost negligible, with delays in peak discharge only occurring 2% of the time. These results agree with Fong et al. (2016) who argued that attenuation of Rectangle hydropeaks depended on the hydropeak duration with a durational threshold between 3 and 5 h such that longer durations showed negligible or no attenuation. In contrast, Front Step hydropeaks seem to be the most affected by flow routing, registering a peak delay by approximately 16%, and a peak discharge decrease of approximately 12%. The higher attenuation of the Front Step shape likely occurred because the wave front of the pulse had a greater velocity gradient (Sturm, 2001), in comparison to other hydropeak shapes.

3.1.5.2 How does hydropeak magnitude control sediment entrainment thresholds?

Large up- and down-ramping rates have been suggested to be one of the main factors governing the spatial and temporal distributions of fine sediment in hydropeaked gravel-bed rivers (Béjar et al., 2018; Gailiušis and Kriaučiūnienė, 2009; Hauer et al., 2018b). Riverbed disturbances associated with hydropeaking mainly affect patches of fine sediments; however, depending on the competence of the pulsed flow events, bigger sizes can be entrained (e.g., sporadic entrainment of particles up to 40 mm were reported in the neighbouring Noguera Pallaresa River by Vericat et al. (2020)). Previous studies have related the amount of sediment deposited on the surface gravel layer and in the interstitial space of the gravel bed with hydropeaking intensity (i.e., the ratio of peak flow to baseflow; Hauer et al., 2018b), such that the higher the hydropeak intensity, the greater the amount of fine sediment re-suspended.

Some European states use this ratio to assess impacts, whereby the higher the hydropeaking intensity, the greater the negative impacts in terms of sediment entrainment, stranding of fish and macroinvertebrate drift, and alterations in natural fine sediment dynamics (e.g., Swiss Water Protection Ordinance, WPO).

In Spain, there is no such regulation about hydropeak intensity and, perhaps consequently, the mean peak discharge in the Ésera River was four times the mean base flow (Table 3.6), favouring the entrainment of fine sediment accumulated in the river bed. Lobera et al. (2016) reported increases in suspended sediment concentration up to one order of magnitude during hydropeaks in the river Ésera. Vericat et al. (2020) observed that hydropeaks in the Noguera Pallaresa, displaying a similar hydropeak intensity as the Ésera, had enough competence to entrain an important part of the riverbed materials (i.e., particles up to 40 mm). In contrast, hydropeak intensity in the Upper Cinca was lower with a ratio between peak discharge and base flow of 1.5. Béjar et al. (2017) and Béjar et al. (2018) pointed out that despite mean velocity and water depth increase of 30% and 20%, respectively, during hydropeaks on the Upper Cinca, they were not competent enough to entrain (i.e., hydropeak intensity too low) characteristic grain-sizes of the river bed (i.e., Q_{50} = 67 mm).

Moreover, the sediment availability in both rivers is different, that is, the Upper Cinca experiences sediment exhaustion since few or no sediment comes from the upstream reaches, except the supply during flood events. The main sources of sediment are only the contributions from the river Bellos and, mainly, the San Vicente Creek, an ephemeral stream that drains a badland area in the lowermost part of the study reach far away from hydropeaking action. In the Ésera, however, an extensive area of badlands (Eocene marls) in the central part of the catchment continuously feeds the mainstem river with countless volumes of fine sediments even during low flows (for more details see Lobera et al., 2016). Vericat et al. (2020) stated the importance of the sediment availability in the mobility models proposed for the Noguera Pallaresa, and the main role of the sediment contribution on tributaries in the sedimentary recovery of supply-limited systems, as well as the role of natural flood events re-shaping the structure and texture of the bed, thus changing sediment availability, roughness, protrusion, and hiding that ultimately will determine hydropeaks' capacity and competence. The main difference in terms of sediment entrainment between the Ésera and the Upper Cinca can be primarily attributed to the high competence of the hydropeaks in the Ésera (as stated in the previous section), as a result of factors such as channel geometry and riverbed roughness and texture, but sediment availability also plays a key role and highlights the importance of assessing basin-river relationships to better understand the distinct role of hydropeaking on river dynamics.

3.1.5.3 How does hydropeaking regime potentially affect river habitat?

Flow is a major driver in shaping and maintaining physical habitat in streams, and a major determinant of a river's biotic composition. If the magnitude of hydropeaks is large enough to entrain dominant channel surface sediments, channel structure can be affected by size-selective transport, depleting relevant grain sizes for spawning, which in turn may have an important impact on fish communities. The winnowing of smaller particles favours bed armouring and thus the loss of substrate heterogeneity, which is known to have an important influence on the diversity of organisms (Rempel et al., 2000). Moreover, as reported by Gibbins et al. (2007b), the incipient motion of fine materials, which is common with high hydropeak intensity, can cause massive involuntary macroinvertebrate drift. Fine sediment resuspension, and the inherent increase of turbidity, can affect aquatic biota by reducing the availability of suitable benthic habitat, leading to changes in abundance and composition of invertebrate assemblages (Bilotta and Brazier, 2008; Kjelland et al., 2015). Subsequent suspended sediment deposition may lead to surficial and interstitial cloggings, and reducing the potential habitat suitability for aquatic biota (Kemp et al., 2011). In particular, macroinvertebrate (Crosa et al., 2010) and fish habitats, especially spawning sites (Hauer, 2013; Pulg et al., 2013; Sutherland et al., 2002), may be affected.

In the case of the river Ésera, high suspended sediment concentrations, exacerbated by the high intensity of hydropeaks, may be a limiting factor for aquatic communities. No references about this subject are available for this river. Nevertheless, several publications describe fine sediment dynamics and the relation with aquatic biota in the river Isábena, the main tributary of the river Ésera. As the Ésera, the Isábena experiences large fine sediment loads owing to the presence of extensive badland areas in the central part of the catchment. Results obtained by (Buendia et al., 2013a; Buendia et al., 2013b) were similar to studies on sedimentation effects in anthropogenically modified catchments, showing a decline in species richness, total density, and trait diversity with increasing fine sediment content on the river bed. Sites located close to the badland areas were taxonomically weakened and functionally homogeneous, supporting only 4 taxa and 100 individuals per square meter. The Upper Cinca is also affected by fine sediments loads. Suspended sediment concentrations obtained by Béjar et al. (2018) reached 18 g l^{-1} during a natural flood in June 2015 but remained low in comparison to the 28 g l^{-1} reported by Lobera et al. (2016) in the river Ésera and the 152 g l^{-1} observed by Buendia et al. (2013b) in the river Isábena. In contrast, sediment concentrations associated with hydropeaking are typically around 1 g l^{-1} substantially lower than observed during natural floods (Lobera et al., 2016). In the Cinca, Béjar et al. (2017) found significant relationships between suspended sediment load, and both drift rates and taxon richness in the drift; therefore, not just the magnitude of suspended sediment concentrations is relevant also the total transport (load), a fact that indicates that the shape and duration of hydropeaks may be key in determining their impact.

Changes on flow hydraulics associated to hydropeaking may have a direct impact on habitat suitability for targeted species as well. As it has been stated, mean velocity and water depth in the Cinca increase 30 and 20%, respectively, during hydropeaks. Such changes may alter macroinvertebrates habitat suitability, favouring the homogenization of the community composition, typically dominated by opportunistic taxa tolerant of unstable conditions (Townsend et al., 1997). Besides, the increase of velocity and depth force some species preferring lateral habitats with low flow velocities to a lateral shift, hence increasing the risk of stranding during down ramping periods. River morphology also conditions the potential for stranding; for instance, the wide Cinca valley favours side channels and low gradient bars, enhancing stranding potential in comparison to more homogenous channels as the Ésera. In contrast, morphology may increase the effects of sudden flow increases during hydropeaks with more confined channels experiencing more abrupt changes in water level, that is, in the Ésera, water level increase is three times higher than in the Cinca mostly owing to channel morphology, but also to higher hydropeak intensity (see differences in the hydrographs in Figure 3.3, p.84). Abruptness of flow decrease can be even on greater environmental importance (Greimel et al., 2018). Several studies observed a positive relationship between stranding and down-ramping rate (Bauersfeld, 1978; Bradford et al., 1995; Hunter and Fisheries, 1992), due to fast water level decrease that impairs organisms to shift laterally fast enough to avoid stranding.

3.1.6 CONCLUSION

This study presents a hydrological characterization of hydropeaks in two mountainous rivers of the Pyrenean Range subjected to intense hydropeaking regimes. More than two thousand hydropeaks were classified by their shape, magnitude, timing, duration, and ramping rates, with the aim of determining their main differences during hydrologically contrasted years. The catchments share similar hydroclimatic, geological, and land use characteristics, but their hydropeaking regimes were shown to be different with implications for morphological and ecological conditions. Main conclusions of the work include:

1. Hydropeaks were different in shape and magnitude in the Upper Cinca and the river Ésera basins, but without a clear seasonal trend for the last. A Front Step shape was the dominant hydropeak in the Ésera, while a Rectangle shape was the most frequent in the Cinca. Front Step hydropeaks had the highest ramping rates during the rising limb and the shortest time to maximum flow whereas Rectangle hydropeaks had higher duration and larger volumes of water released.

2. Hydropeaks in the Ésera were less frequent, with an average of one hydropeak per day, than in the Upper Cinca, with an average of approximately two hydropeaks per day. The river Ésera had high magnitude hydropeaks, with double volume and duration, and three times larger up-ramping rates and hydropeak intensity.

3. According to the variability of the hydrological parameters of each hydropeak, a total of three statistically significant groups were obtained in the Ésera, while two groups are identified in the Cinca.

4. Hydropeaks can be statistically grouped based on variables related to magnitude (flow-based or hydrological variables), timing (duration), and frequency (occurrence). Differences between groups are more relevant in the river Ésera.

5. The hydrological characteristics of the Upper Cinca hydropeaks are clearly influenced by the season, while this influence is less evident in the river Ésera.

6. Although dominant shapes are observed in almost all groups and in the two rivers, the presence of all shapes in each group indicate that different shapes may response similarly in terms of magnitude, timing, and frequency. These characteristics will further determine the effect on sediment entrainment and transport with direct implications to the ecological functioning of rivers.

7. Finally, the observed shapes in the Ésera vary depending on the WY and even the season, while in the Cinca, shape distribution follows the same temporal pattern regardless year and season. Therefore, in general, hydropeaking in the Ésera appears to be much more dependent on the annual hydrology (whether the year is wet or dry) than in the Cinca.

A greater knowledge of the potential effects of hydropeaking is needed to design mitigation measures, with the objective to optimize the relationship between economic benefits and ecological status (bio-physical structure and functioning) of hydropeaking river systems. This study provides a quantitative assessment and hydrological characterization of hydropower-induced pulsed flow events and their temporal dynamics, a topic rarely targeted in the literature. Future work should relate these quantitative measures of flow pulses to river morphological and biological responses. However, even in fluvial systems sharing similar physical characteristics, the severity of the impacts may differ, depending on the particular morphology of the system, including valley configuration, channel forms, sediment textures, and the associated flow hydraulics (as recently discussed by Batalla et al., 2021). The determination of technical procedures that would minimize the effects of hydropeaking events is still missing in environmental management research. Emerging data collection methods and analytical and modelling tools will help support the development of hydropower protocols that may limit physical and ecological changes in the reaches downstream. Better understanding of hydropeak characteristics, such as shape, magnitude, intensity, timing, and how pulses may be attenuated in the downstream direction, will help to improve management of hydropower production in such fragile mountain environments.

ACKNOWLEDGEMENTS This work was undertaken thanks to the financial support of the MorphHab (Grant No. PID2019-104979RBI00/AEI/10.13039/501100011033) and the MorphPeak (Grant No. CGL2016-78874-R/AEI/ 10.13039/501100011033) projects funded by the Research State Agency (AEI), Spanish Ministry of Economy and Competiveness, Science and Innovation, and the European Regional Development Fund Scheme. Authors acknowledge the support of the Economy and Knowledge Department of the Catalan Government through the Consolidated Research Group "Fluvial Dynamics Research Group" -RIUS (2017SGR-0459) and the CERCA Program. Damián Vericat is funded through the Serra Húnter Programme (Catalan Government).

DATA AVAILABILITY STATEMENT The data that support the findings of this study are openly available in Fluvial Dynamics Research Group Data Server at https://sites.google.com/view/fluvialdynamics/Home.

ORCID
Alvaro Tena https://orcid.org/0000-0001-8388-6510
Sarah M. Yarnell https://orcid.org/0000-0002-2061-892X

Supplementary material

Table 3.6: Maximum, minimum, mean values and standard deviations of the hydrological parameters calculated to characterize HP in the River Ésera.

Category	Parameter	Symbol	Units	WY2013 (*Wet*)				WY2014 (*Average*)				WY2016 (*Dry*)				All period			
				Mean	Max	Min	SD	Mean	Max	Min	SD	Mean	Max	Min	SD	Mean	Max	Min	SD
Magnitude	Volume	V	hm^3	0.66	2.26	0.02	0.44	0.56	7.63	0.04	0.63	0.89	8.82	0.02	0.85	0.69	8.82	0.02	0.69
	Initial *Q*	Q_{in}	m^3s^{-1}	6.68	23.00	1.61	4.83	6.78	20.30	2.07	2.80	4.21	21.91	0.57	4.29	5.91	23.00	0.57	4.12
	Final *Q*	Q_{fi}	m^3s^{-1}	6.76	21.00	1.61	4.73	6.64	20.30	2.07	3.00	4.16	21.91	0.46	4.35	5.86	21.91	0.46	4.17
	Maximum *Q*	Q_{max}	m^3s^{-1}	20.99	33.60	6.50	4.52	19.55	33.18	7.09	5.51	25.10	41.43	4.25	6.65	21.77	41.43	4.25	6.15
	Minimum Q	Q_{min}	m^3s^{-1}	6.08	20.45	1.61	4.27	5.97	17.10	2.07	2.40	3.34	16.46	0.46	3.51	5.14	20.45	0.46	3.60
	Mean *Q*	Q_{mean}	m^3s^{-1}	15.09	29.56	3.30	4.68	14.49	30.20	6.17	4.53	16.83	36.26	2.93	5.91	15.43	36.26	2.93	5.16
	Hydropeak intensity	HI_{in}	-	3.45	1.64	4.04	1.06	3.27	1.94	3.43	2.30	7.51	2.52	9.24	1.89	4.24	2.03	9.24	1.71
	Range in flow	Q_{range}	m^3s^{-1}	14.91	27.65	2.16	5.51	13.58	29.40	1.69	6.59	21.76	40.05	2.56	8.14	16.63	40.05	1.69	7.76
	Max. *Q* position	P_{Qm}	–	0.29	0.96	0.02	0.22	0.34	0.95	0.01	0.23	0.21	0.87	0.02	0.21	0.29	0.96	0.01	0.22
	Maximum up-ramping rate	T_{im}	$m^3s^{-1}h^{-1}$	28.89	59.32	4.00	13.43	25.17	77.12	2.56	14.94	42.66	80.84	4.40	19.22	31.94	80.84	2.56	17.80
	Maximum down-ramping rate	T_{dm}	$m^3s^{-1}h^{-1}$	19.21	57.28	1.68	8.90	19.65	55.84	1.64	10.47	19.60	94.12	3.68	9.59	19.51	94.12	1.64	9.75
Time and duration	Initial hour	H_{in}	hh:mm	12:25	23:45	0:15	5:32	12:57	23:30	0:00	6:21	11:27	23:15	0:30	5:22	12:19	23:45	0:00	5:51
	Final hour	H_{fi}	hh:mm	9:53	23:45	0:00	6:37	11:35	23:45	0:00	6:57	9:44	23:45	0:00	7:31	10:30	23:45	0:00	7:06
	Time to max. *Q*	T_{Qm}	hh:mm	3:29	25:15	0:30	3:47	3:06	36:15	0:15	4:23	2:47	70:15	0:15	5:33	3:06	70:15	0:15	4:39
	Duration	D_{hp}	–	12:04	48:45	1:00	6:43	10:09	149:15	1:00	11:14	14:05	132:45	1:15	12:48	11:59	149:15	1:00	10:53
	Time since last event	T_{uh}	–	23:08	2049:15	0:00	138:00	15:04	2261:00	0:00	123:01	17:11	1037:15	0:00	68:48	18:01	2261:45	0:00	113:09
Frequency	No. peaks per hydropeak	N_{ph}	–	3.88	25.00	1.00	3.03	3.87	74.00	1.00	5.68	4.53	79.00	1.00	6.66	4.09	79.00	1.00	5.46

Table 3.7: Maximum, minimum, mean values and standard deviations of the hydrological parameters calculated to characterize HP in the Upper Cinca.

Category	Parameter	Symbol	Units	WY2015 (Average)				WY2016 (Dry)				All period			
				Mean	Max	Min	SD	Mean	Max	Min	SD	Mean	Max	Min	SD
Magnitude	Volume	V	hm^3	0.36	2.96	0.02	0.34	0.25	2.08	0.01	0.34	0.31	2.96	0.01	0.29
	Initial Q	Q_{in}	m^3s^{-1}	15.05	34.95	4.23	6.40	12.19	41.27	1.92	6.40	13.71	41.27	1.92	6.33
	Final Q	Q_{fi}	m^3s^{-1}	15.13	34.81	4.23	6.33	12.26	38.90	2.42	6.33	13.78	38.90	2.42	6.23
	Maximum Q	Q_{max}	m^3s^{-1}	20.44	39.21	5.89	6.28	17.45	43.95	5.83	6.28	19.03	43.95	5.83	6.52
	Minimum Q	Q_{min}	m^3s^{-1}	14.45	34.63	4.23	6.20	11.71	38.90	1.92	6.20	13.16	38.90	1.92	6.10
	Mean Q	Q_{mean}	m^3s^{-1}	18.67	37.37	5.83	6.14	15.58	42.22	5.56	6.14	17.22	42.22	5.56	6.32
	Hydropeak intensity	HI_{in}	-	1.41	1.13	1.39	1.01	1.49	1.13	3.04	1.01	1.45	1.13	3.04	1.07
	Range in flow	Q_{range}	m^3s^{-1}	5.99	31.10	0.62	3.12	5.73	34.08	0.62	3.12	5.87	34.08	0.62	3.02
	Max. Q position	P_{Qm}	–	0.41	0.95	0.03	0.22	0.48	0.96	0.03	0.22	0.44	0.96	0.03	0.22
	Maximum up-ramping rate	T_{im}	$m^3s^{-1}h^{-1}$	12.34	69.02	1.66	6.81	11.10	44.34	1.66	6.81	11.76	69.02	1.66	6.84
	Maximum down-ramping rate	T_{dm}	$m^3s^{-1}h^{-1}$	10.59	33.01	10.59	4.92	9.08	33.01	9.08	4.92	9.88	33.01	9.08	5.07
Time and duration	Initial hour	H_{in}	hh:mm	11:22	23:45	0:00	6:29	12:17	5:30	0:00	6:29	11:48	5:30	0:00	6:35
	Final hour	H_{fi}	hh:mm	11:18	23:45	0:00	7:18	11:10	23:45	0:00	7:18	11:14	23:45	0:00	7:14
	Time to max. Q	T_{Qm}	hh:mm	2:06	16:45	0:15	2:15	2:13	22:15	0:15	2:15	2:09	22:15	0:15	2:12
	Duration	D_{hp}	–	5:34	29:30	0:45	4:37	4:45	25:30	0:30	4:37	5:11	29:30	0:30	4:07
	Time since last event	T_{uh}	–	5:42	299:15	0:00	19:10	7:54	1810:00	0:00	19:10	6:44	1810:00	0:00	51:34
Frequency	No. peaks per hydropeak	N_{ph}	–	1.62	13.00	1.00	1.40	1.23	4.00	1.00	1.40	1.43	13.00	1.00	1.10

Part 2 : Longitudinal characterization

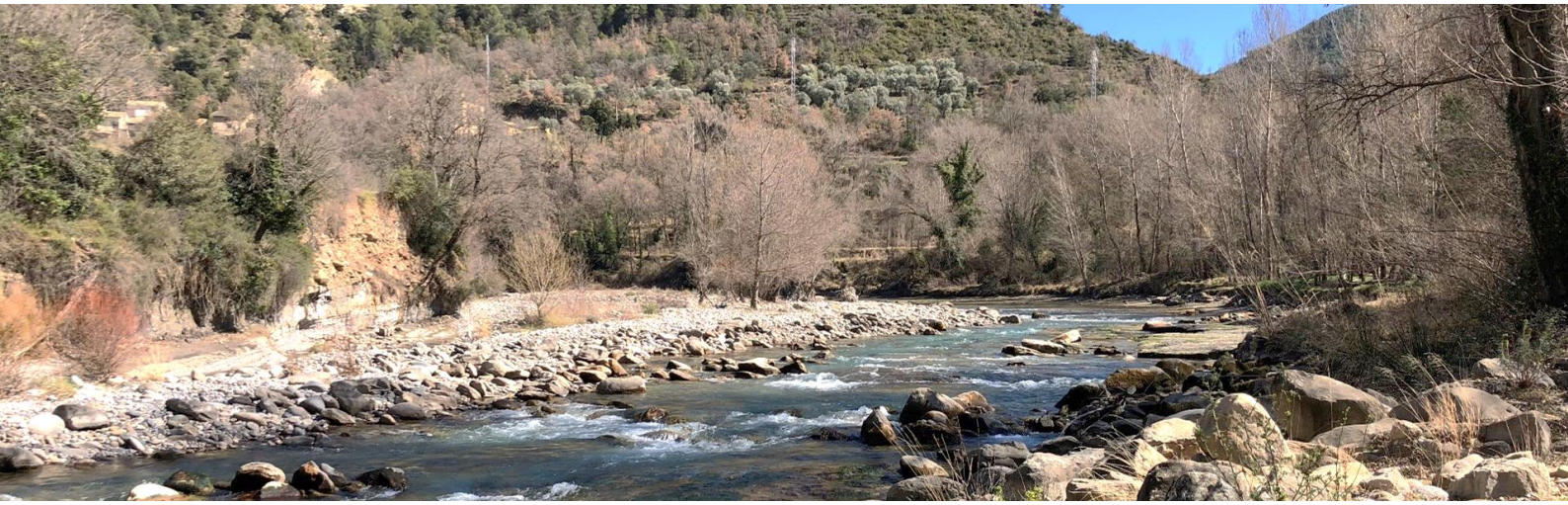

Upper Ésera river near Santaliestra village, 15/07/2019. Author: Fanny Ville

This second part of Chapter 3 presents the results of the longitudinal analysis of hydropeak propagation on the two river segments. This analysis is presented in the form of a paper. However, it is still under development and may be subject to change before submission.

Longitudinal propagation of hydropeaks in contrasting mountain rivers: examples from Southern Pyrenees.

This part of the chapter contains a paper in preparation; therefore, the authors and abstract are not yet provided.

3.2.1 INTRODUCTION

The release of water from Hydroelectric power Plant (HP), known as hydropeaking, artificially induces sudden fluctuations in flow in downstream reaches and according to schemes (i.e. the shape of hydrographs) that can vary between seasons and years (Tena et al. 2022, in Chapter 3 Part 1). These fluctuations cause hydraulic changes such as water depths, velocities and bed shear stress. Aquatic organisms and sediment transport may in turn be affected by these changes. Many studies have focused on characterizing these artificial fluctuations over time from a fixed point in order to assess their potential alteration through time. Hydrographs representing temporal variations in flow and, indirectly, stream power, when coupled with bed or water surface slope, can be analysed on different time scales by wavelet transformation (Zolezzi et al., 2009), on a daily basis (Alonso et al., 2017; Carolli et al., 2015; Meile et al., 2011), or segmented at the scale of hydrological peaks (Fong et al., 2016; Greimel et al., 2016b). Other studies have also examined the difference of the forms and magnitudes of hydropeaks in a single river section (Tena et al., 2022, in Chapter 3 Part1; Bejarano et al., 2017; Greimel et al., 2016b; Tonolla et al., 2023). Greimel et al. (2023) considers this static approach to be equivalent to measuring the bedload passing through a given location per unit time in sediment transport studies.

Simulations in laboratory or numerical 1D or 2D channels (Hauer et al., 2013; Vanzo et al., 2016b) have shown that the magnitude of hydraulic fluctuations can vary spatially. The characteristics of these hydropeak waves can also vary longitudinally as a function of distance from the HP, depending on the existence of tributaries and the morphology of channels or valleys (Greimel et al., 2016b; Hauer et al., 2013). The possible attenuation of these pulses depends on the morphology and characteristics of the rivers. In order to limit the disturbance caused by these artificial pulses, it is important to characterize them and understand their propagation in order to define relevant operational measures and to identify the spatial scales of potential affections. Longitudinal variability can be approached by identifying hydrological events and characterizing them at different points along the river. Greimel et al. (2023) consider this second approach to be comparable to grain tracing in sediment transport studies. Prior to numerical hydraulic modelling of hydropeak routing, a simple method is to use hydrographs distributed longitudinally over segments of affected rivers.

In this study, the distinctive hydrological characteristics of hydropeaks and floods, such as their duration, magnitude and rate of change, are analysed from a longitudinal or spatial perspective for two rivers with different geomorphological contexts. The different forms of hydropeaks generated are also analysed in order to study whether their propagation is similar or not.

3.2.2 MATERIALS AND METHODS

3.2.2.1 Study area and available flow data

The study was carried out in the basins of the Upper Cinca and its main tributary, the Ésera, in the south-central Pyrenees (Figure 3.8 **A**). The two basins have similar altitudinal gradients. The outlet of the Cinca is near the village of Ainsa at an altitude of 526 m a.s.l, while the source of the river is 57.8 km upstream at Monte Perdido at 3 355 m. The outlet of the Ésera is near the village of Santaliestra at an altitude of 539 m a.s.l. The source of the river is 79.9 km upstream at the peak of Aneto at 3 404 m (the highest peak in the Pyrenees).

Both basins have 75% medium to very steep slopes (>16°) and both have about 70% of their surface area above 1,500 m altitude, corresponding to the winter isotherm of 0°C (García-Ruiz et al., 1986). On average, the annual volumes of water precipitated in liquid form are 1 034 and 776 hm^3 respectively in the basins drained by the Cinca and Ésera rivers. These two rivers are characterized by a nivo-pluvial hydrological regime, favoured by high areas suitable for the constitution of a snow pack between winter and spring and the release of meltwater back into the river from mid-spring to the end of the season. The average annual discharge recorded at the Ebro Water Authority stations is 24.8 and 15.8 m^3s^{-1} in the Cinca and Ésera segments, respectively. The steep relief and these water inflows make these basins suitable for hydroelectric generation, but they are sparsely urbanized (< 1%) and sparsely cultivated (3 to 6% respectively). The detailed characterization of these two basins is presented in Chapter 2, Part 1.

In order to characterize the longitudinal variability of hydropeaks, two networks of water level monitoring stations with a temporal resolution of 15 min were installed and maintained by the RIUS research group at the University of Lleida between 2014 and 2021. The two monitored segments are shown in Figure 3.8 **B**. However, not all stations were operated at the same time and continuously. Data series with at least two gap-free years were selected (see table in Figure 3.8 **C** and Figure 3.9). The oldest data (i.e. 2014-2016) come from a study carried out by Béjar et al. (2018), while the most recent (i.e. 2018-2021) are from work carried out during this thesis. The water level series have been processed to convert the level variations into discharge. Briefly, the 2D numerical hydraulic modelling program IBER (Bladé et al., 2014) was used to generate steady-state models to simulate the water level ~ discharge relationship at the probes. This relationship was then applied to the data series. Full details are available in chapter 2 of this thesis and in Béjar et al. (2018).

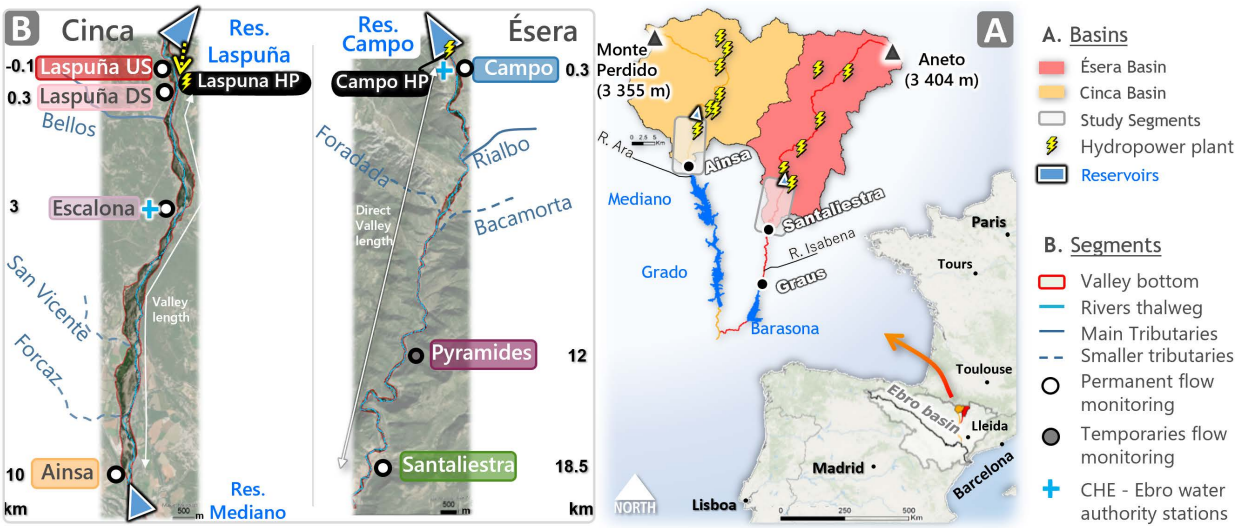

C

River	Cinca				Ésera		
Hydropower							
Power plant	Laspuña				Campo		
Max. turbinable peak flow (m^3s^{-1})	26.0				20.0		
Segment							
Mean annual flow (m^3s^{-1})	24.8				15.8		
Direct valley length (km)[a]	9.2				13.6		
Valley length (Km)	9.5				17.9		
Talweg length (km)	10.0				18.5		
Valley sinuosity (-)[b]	1.03				1.32		
Main river courses sinuosity (-)[c]	1.05				1.03		
Median valley width (m)	197.4				56.7		
Median active width	63.2				34.1		
Slope (%)	0.70				0.73		
Channel morphology	Large bar of different types				Narrow bar of sediment in a position forced by the shape of the valley		
Monitoring station							
Stations	Laspuña US	Laspuña DS	Escalona	Ainsa	Campo	Pyramides	Santaliestra
Distance from HP (km)	-0.1	0.3	3	10	0.3	12	18.5
Drainage area (km^2)	603.4	603.9	796.3	835.3	566.9	719.3	732.9
Elevation (m a.s.l)	601.3	599.1	577.3	529	676	583.5	539
Dataset period Longitudinal central trends	WY2014/15 WY2015/16 WY2018/19 WY2019/20	WY2018/19 WY2019/20	WY2014/15 WY2015/16	WY2014/15 WY2015/16	WY2019/20 WY2020/21	x	WY2019/20 WY2020/21
Dataset period Longitudinal associated events	x	x	x	x	Oct/Nov 2020	Oct/Nov 2020	Oct/Nov 2020

Figure 3.8: Location of the study area. **A** Location of the two basins studied, with the location of the study segments indicated by the grey rectangles. **B** Longitudinal schematic diagram of the study segments (Cinca on the left and Ésera on the right) with the location of the power plants and the reservoirs feeding them, as well as the monitoring stations and their distance from the power plants (coloured rectangle): Laspuña US and DS, Escalona, Ainsa on the Cinca and Campo, Pyramides and Santaliestra on the Ésera). **C** Summary table of the characteristics of the segments studied and the monitoring stations. [a] Direct length of the valley sketched in part B on the Ésera segment. [b] Sinuosity of the valley calculated from the ratio of the length of the valley to the direct length of the valley. [c]Sinuosity of the main channel course calculated from the ratio of the length of the talweg to the length of the valley.

A

Cinca River

Discharge as percentage of Q_{50} (Left log scale) and daily volume of precipitation over the catchment (hm^3 - grey curves - right y axis) from upstream to downstream.

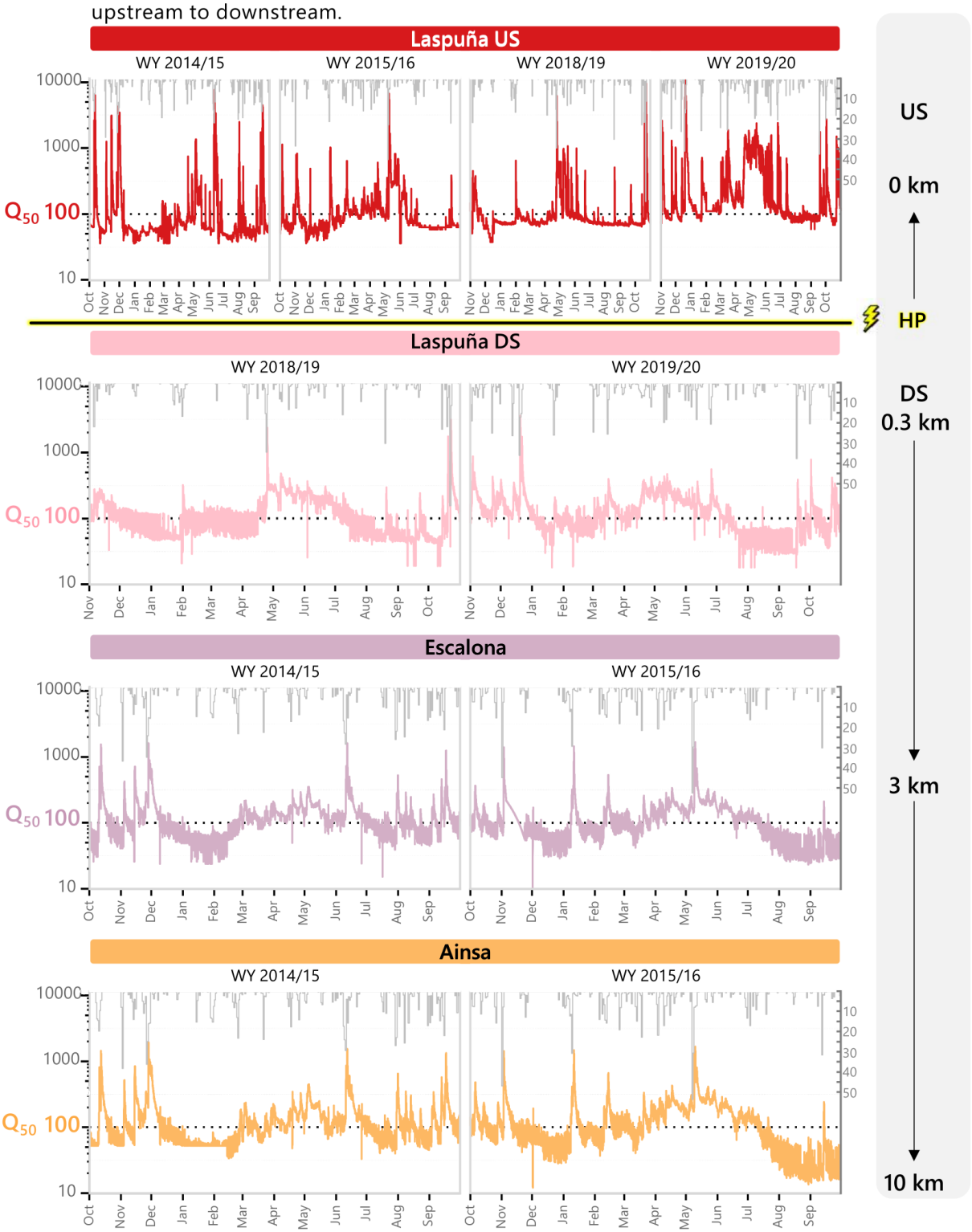

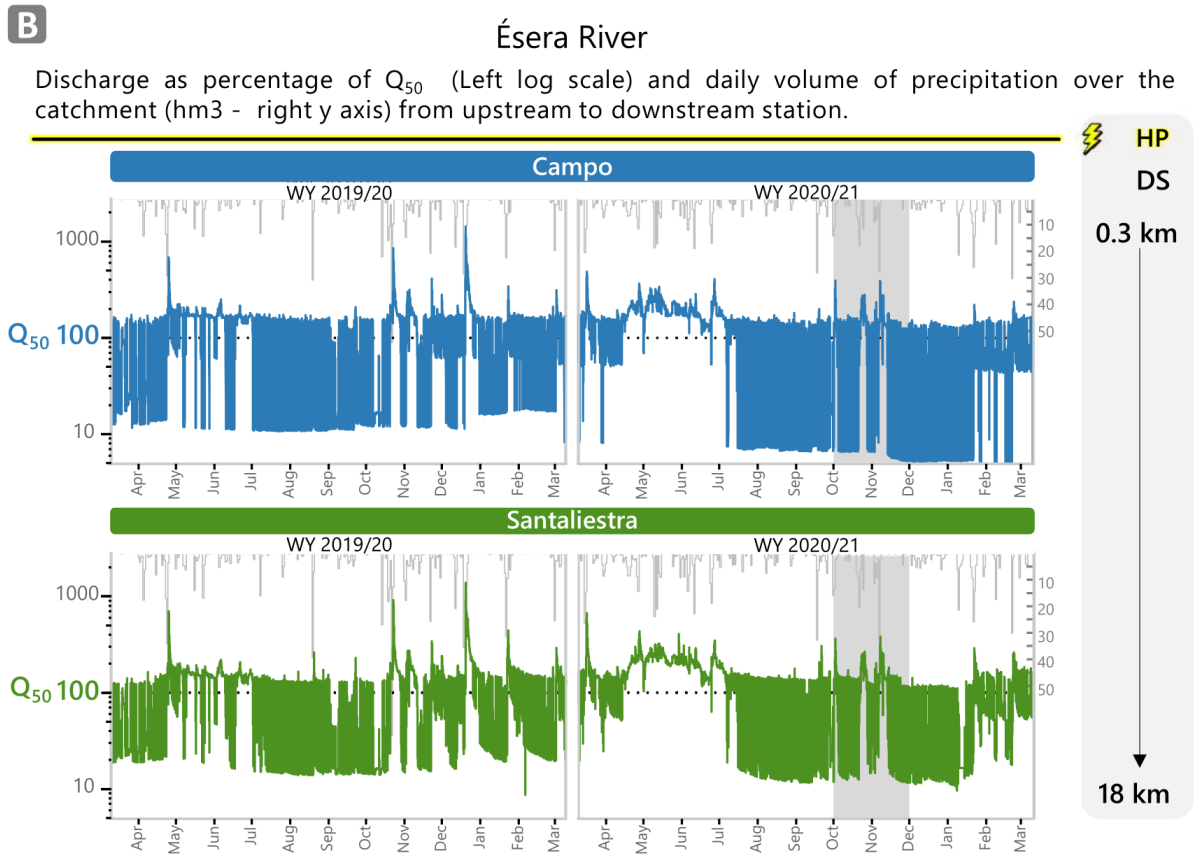

Figure 3.9 (from previous page): Flow data series (15 min) normalized by the median flow (Q_{50}) at each station with its distance from the HP and the daily volume of rainfall on the surface draining to these stations. Data acquisition and processing are described in detail in Chapter 2, Part 2. **A**. River Cinca and **B**. River Ésera. The shaded areas from October to November 2020 for the Ésera River correspond to the dataset used for tracking the associated peaks between hydrographs. See Figure 3.19 for a detailed view.

3.2.2.1.1 The Upper River Cinca

The upper Cinca is occupied by a cascade of 8 Hydroelectric power Plant (HP) with modified run-of-river operation (see Chapter, Section 1.1.2.2.1), which turbine water from small reservoirs with a maximum storage capacity equivalent to 2 days' average runoff (6.3 hm^3). The segment studied, shown in Figure 3.8 **B**, is 10 km long and begins a few meters upstream of the Laspuña HP tail race at 600 m a.s.l and ends at Ainsa at 529 m a.s.l. This section has an average gradient of 0.70%. The river flows in a wide, relatively straight, north-south oriented valley (i.e. average valley width of about 200 m) with a very dynamic, wandering channel morphology (Church, 2006; Fryirs and Brierley, 2013), whose sediment bars change position very frequently. Laspuña Dam is the last dam in the upstream hydroelectric network. It is used to divert water to the HP, which has a maximum turbine flow capacity of 26 m^3s^{-1}.

A network of 4 monitoring stations has been installed on this segment:

(i) The Laspuña US station is located a few meters upstream (-0.1 km) of the HP outlet, corresponding to a bypassed flow. Continuous data were available for the hydrological years WY 2014/15, 2015/16 (i.e. from 01 October to 30 September) and for another two-year period, from 01 November 2018 to 31 October 2020 (i.e. starting from November instead of October). The surface area of the basin at this point is 600.5 km^2.

(ii) Downstream of the HP, the investigated reach receives the entire flow from the reserved flow of the dam, tributaries and hydropeaks. The dam is open during floods. The Laspuña DS station, 0.3

km from the HP outlet, was used to record the flow fluctuations associated with these inflows for the same second period as Laspuña US between 01 November 2018 and 31 October 2020, with no gaps in the series.

(iii) The water of the Bellos tributary is added to those of the Cinca 1 km downstream of the HP. The sum of these flows is measured 3 km downstream of the HP at the Escalona station. The area drained at this point in the basin is 796.3 km². A series of data was available for the hydrological years WY2014/15 and WY2015/16. A monitoring station of the Ebro Water Authority (CHE) is also located at this point. The measurements from this probe ($Escalona_{CHE}$) seem to be underestimated during low flows. They were not used to characterize hydropeaks, but only for the historical hydrological regime.

(iv) Between 6.8 and 8.6 km downstream, the two small rivers San Vicente and Forcaz (10 and 5 km²) join the main course of the Cinca. All these flows are measured at the Ainsa station, 10 km downstream of Laspuña HP. The total area drained is 835.3 km². The available data also correspond to the years WY2014/15 and WY2015/16.

For the latter two stations (i.e. Escalona and Ainsa), more recent continuous water level data (i.e. 2018-2021) were available, but it was not yet possible to convert them into discharge.

3.2.2.1.2 The Upper River Ésera

The upper Ésera is occupied by a cascade of 7 HP operating on a modified run-of-river basis, turbining water from small reservoirs with a maximum storage capacity equivalent to 4 days' average flow (6.3 hm^3). The 18.5 km segment studied, shown in Figure 3.9 **B**, begins at the foot of the Campo dam, where the power station of the same name is located, at an altitude of 676 m a.s.l, and reaches the village of Santaliestra at 539 m a.s.l.

This segment has an average gradient of 0.73%. The river flows through a narrow, tortuous valley (i.e. valley length/direct valley length ratio of 1.3, see Figure 3.9 **B** and **C**) with numerous gorge sections and a median width of about 57 m. The active band, confined to 58% along both margins, has a median width of 34 m. A single straight channel (i.e. talweg length/valley length ratio of 1.03) can be discerned along almost the entire length, following the curves of the valley. The morphology of the valley dictates a sequence of planned bed and pool riffles and frequent exposure of bedrock. The bedforms are stable over time. The Campo dam is the last of the upstream hydroelectric network. It supplies water to the turbines at its foot, which have a total maximum turbine flow capacity of m^3s^{-1}.

A network of 3 monitoring stations has been installed in this segment:

(i) The studied segment receives all the flow from the reserved flow of the dam, the tributaries and the releases from the power station. During floods, the water flows over the spillway and through the bottom gates. The Campo station, 0.3 km downstream of the dam, has been used to record flow fluctuations linked to these inflows for a 2-year gapless period between 10 March 2019 and 09 March 2021, and for a much shorter second period of 45 days between 7 October 2020 and 20 November 2020. The area drained at this point is 566.9 km². There is a measuring station of the Ebro Water Authority (CHE). The measurements collected by this probe ($Campo_{CHE}$) appear to be underestimated during low flow conditions. They have not been used to characterize hydropeaks, but only for the historical hydrological regime.

(ii) The waters of the Rialbo tributary are added to those of the Ésera, 3.9 km downstream of the HP, as well as those of two smaller tributaries, Foradada and Bacamorta, between 6 and 7 km. The sum of these flows is measured 12 km downstream of the power station at the temporary Pyramides station. The area drained at this point in the basin is 719.3 km². This station was used to record flow fluctuations for the same second period as Campo, between 7 October 2020 and 20 November

2020. This short study period corresponds to a campaign of measurements of bed mobility and texture changes presented in Chapters 6 and 8.

(iii) 18.5 km downstream, the entire flow was measured at the Santaliestra station. The total drained area is 732.9 km². The data available for the longitudinal characterization of the hydropeaks are exactly the same as those mentioned for the Campo station.

The two segments, which receive the entire upstream flow without any diversion, have a confluence with 3 tributaries, one main and two minor, with a similar hydrological regime and average bed slope. However, the catchment area of the Cinca River is 13% larger than that of the Ésera and its rainfall is 25% higher. The morphology of their valleys, their channels and their stability are very different.

3.2.2.2 Methods

The study of longitudinal variability was carried out in 4 stages: (1) The first stage consisted of characterizing the hydrological years studied in order to determine whether or not all the peaks were representative of contrasting hydrological years. (2) The second was to identify, isolate and discretize each peak as a flood or hydropeak on the hydrographs. (3) Various characteristics (e.g. shape, magnitude, duration) were then calculated. (4) Finally, the data were analysed using two different methods depending on the data availability periods. (i) The first method consisted of analysing the central tendency of the peak characteristics at each point (i.e. station) of the segments. This analysis was applied to both segments based on a two-year data series. (ii) The second consisted of studying the longitudinal variation of the characteristics of the peaks individually at each point of the segment. This method was applied only to the River Ésera at the three stations over the short period of 45 days. Each identified peak was characterized at the 3 points of the segment and their evolution described by statistical models.

To facilitate comparisons between sections draining different areas (see Figure 3.10) and/or with different river sizes, the set of calculated characteristics describing magnitude can be normalized (e.g. Alonso et al., 2017; Bejarano et al., 2017; Courret et al., 2021; Greimel et al., 2023). In this study, unlike the previous authors and also the paper presented in Part A, the flows were normalized by the median (Q_{50}) and not by the mean hydrological characteristics of the stations in order to study the changes in magnitude relative to the local hydrology of each monitored point in the basins. As this study focuses mainly on artificial pulses associated with hydropower production, the median was chosen as it is less influenced by extreme flow values associated with floods. In addition, normalization reduces the importance of eventual flow estimation errors in the results obtained.

The flow data for the two study years were ranked in descending order and cumulative frequencies calculated. Figure 3.19 **B** shows the flow curves classified at each station. The median of these distributions (Q_{50}) was extracted. The 15 min data set (Q_i) was divided by this value, $Q_{norm_i} = Q_i/Q_{50} * 100$. The normalized data series are shown in Figure 3.9.

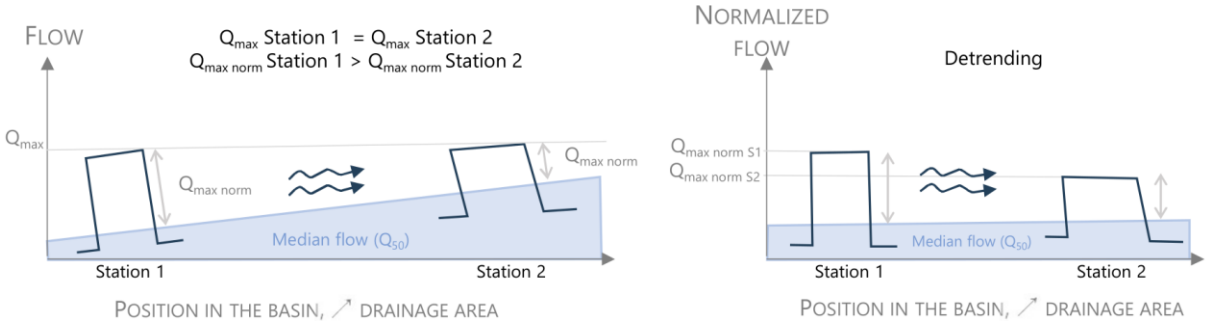

Figure 3.10: Conceptual example of the usefulness of normalization for the longitudinal study of hydropeak propagation

3.2.2.2.1 Classification of water years

The available historical data on the volume of water flowing annually (i.e. water yield) for the period 1951 to 2020 (i.e. almost 70 years) at the CHE stations at $Escalona_{CHE}$ and $Campo_{CHE}$ were used to characterize the hydrological years studied as wet, average or dry. Some years had missing values, which were estimated by the PhD student Estrella Carrero as part of her thesis in the RIUS research group.

The water yield (W_y) obtained from the RIUS probes at Escalona, Laspuña DS and Campo was compared with the percentiles of the historical series. Study years with W_y above the 25th percentile of the long-term series (i.e. $W_{y\ 25}$) were considered wet; those with W_y between the 25th and 75th percentiles (i.e. $W_{y\ 25}$ and $W_{y\ 75}$) were considered average; and those with W_y below the 75th percentile (i.e. $W_{y\ 75}$) were considered dry (following Martínez and Fernández, 2010).

At the $Campo_{CHE}$ station, $W_{y\ 75}$,$W_{y\ 50}$ and $W_{y\ 25}$ are 360, 507 and 623 hm^3 respectively. The two study years available on the Ésera, measured by RIUS probes, show relatively low W_y (363.1 and 387.0 hm^3, Figure 3.11 **A**), but are nevertheless considered average as they remain above the 75th percentile.

At the $Escalona_{CHE}$ station the $W_{y\ 75}$, $W_{y\ 50}$ and $W_{y\ 25}$ are 599, 886 and 1,095 hm^3 respectively. The study years WY2014/15 and WY2015/16 measured by the RIUS probes showed annual W_y of 726.3 and 656.4 hm^3 respectively. These years are therefore considered to be average. Finally, more recent years at the Laspuña DS station on the Cinca River, not taking into account the inflow from the Bellos tributary, were 625.5 and 689.6 hm^3. According to Béjar et al. (2018), the average annual inflow from the Bellos would be 90 hm^3. With this addition, these two years would remain between the 50th and 75th percentiles of the historical series at $Escalona_{CHE}$, i.e. average (Figure 3.11 **A**).

In view of these results, all the periods studied to analyse the longitudinal variability of the peaks are of the average type. Consequently, the hydrological characteristics of all the peaks detected over the two years at each station were merged and not analysed separately for each year.

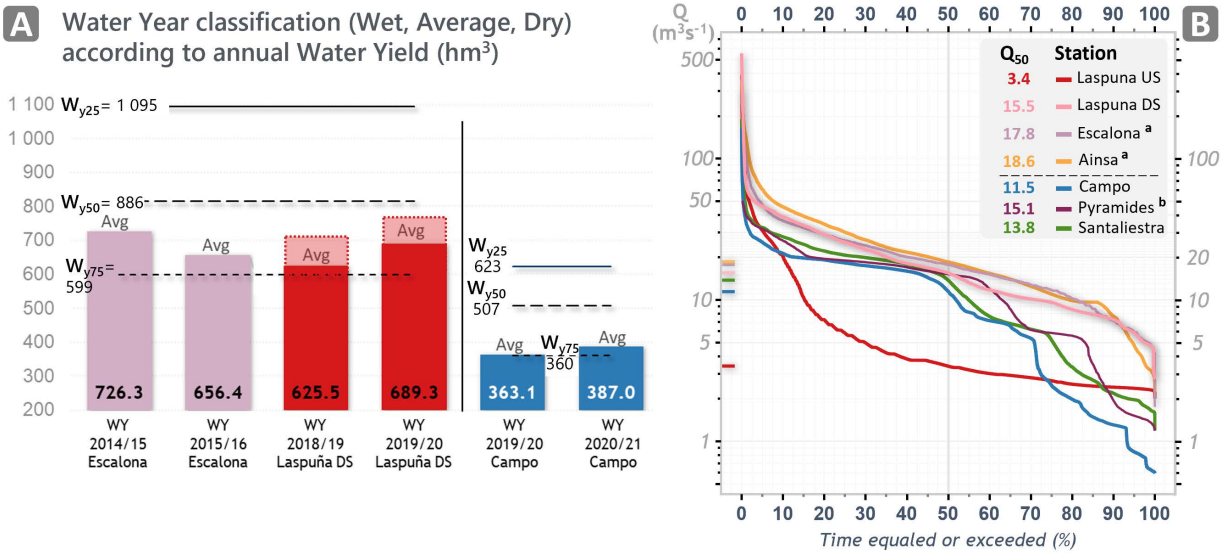

Figure 3.11: Hydrological characteristics of the data used. **A**. Classification of each hydrological year as wet, average or dry. **B** Flow duration curves by station for the period studied. [a] Data from Bejar et al. 2018, [b] Data for 45 days only.

3.2.2.2.2 Segmentation

The shape of a hydropeak can be divided into three phases (Schmutz et al., 2015), namely (**I**) increase (IC), (**II**) plateau and (**III**) decrease (DC), as shown in Figure 3.12 **A**. The two phases of variation of IC and DC may or may not include one or more stages. The segmentation of events is based on the calculation of the differences in normalized flows (Q_{norm_i}) between two consecutive time steps (ts). Continuous time steps with equal trends (increase: $Q_{norm_1} < Q_{norm_2}$, stability $Q_{norm_1} = Q_{norm_2}$, decrease: $Q_{norm_1} > Q_{norm_2}$) are defined as single phases of fluctuation.

IC and DC variations were identified using the method of Courret et al. (2021). This method automatically identifies variation events (i.e. IC and DC) and discretizes between an insignificant variation, a natural variation or a hydropeak. Their discretization model was trained on data sets from 97 gauging stations in French mountain rivers of different sizes, with natural or very slightly altered hydrological regimes. River sizes were classified according to mean annual discharge [<1; 1-3; 3-5; 5-10; 10-15; 15-20; 20-30; 30-50]. For each class, a maximum natural gradient of IC and DC was established. If the gradients of the significant variations (i.e. > 1% of annual mean discharge) detected in the studied hydrographs are higher than the natural ones, these variations are considered as hydropeaks, otherwise as natural. As reported by Courret et al. (2021) and Greimel et al. (2016b) , natural peaks resulting from melting snow or glaciers or from rain events generally have a right-skewed shape with relatively fast rates of increase and slower rates of decrease. The variation detection and discretization method developed by Courret et al. (2021) was implemented in the R language in the context of this thesis. After the detection of each natural or artificial variation, in order to isolate each peak from start to finish (T_{start} to T_{end} Figure 3.12 **A**), the successive significant variations in the same direction (IC or DC) spaced by stages were concatenated if they belonged to the same category (i.e. natural or hydropeak). This is illustrated in Figure 3.12 **A** for two descending phases between 4 green points.

In some cases, peaks were not detected due to undetected increases or decreases. All automatically segmented series were revised to add the missing or poorly defined variations (Figure 3.12 **C**). In order to check these initial results effectively and reproducibly, and to keep a record of the revisions, a CRUD (Create, Read, Update and Delete) application was implemented in *R* using the *tidyverse*, *shiny*, *rshanstable* and *dygraph* packages (Chang et al., 2023a; Owen, 2021a; Vanderkam et al., 2018; Wickham et al., 2019a). This application, illustrated in Figure 3.12 **C**, allows the automatic segmentation results to be dynamically visualized on the hydrographs, the data to be edit, and a new corrected copy of the data to be saved.

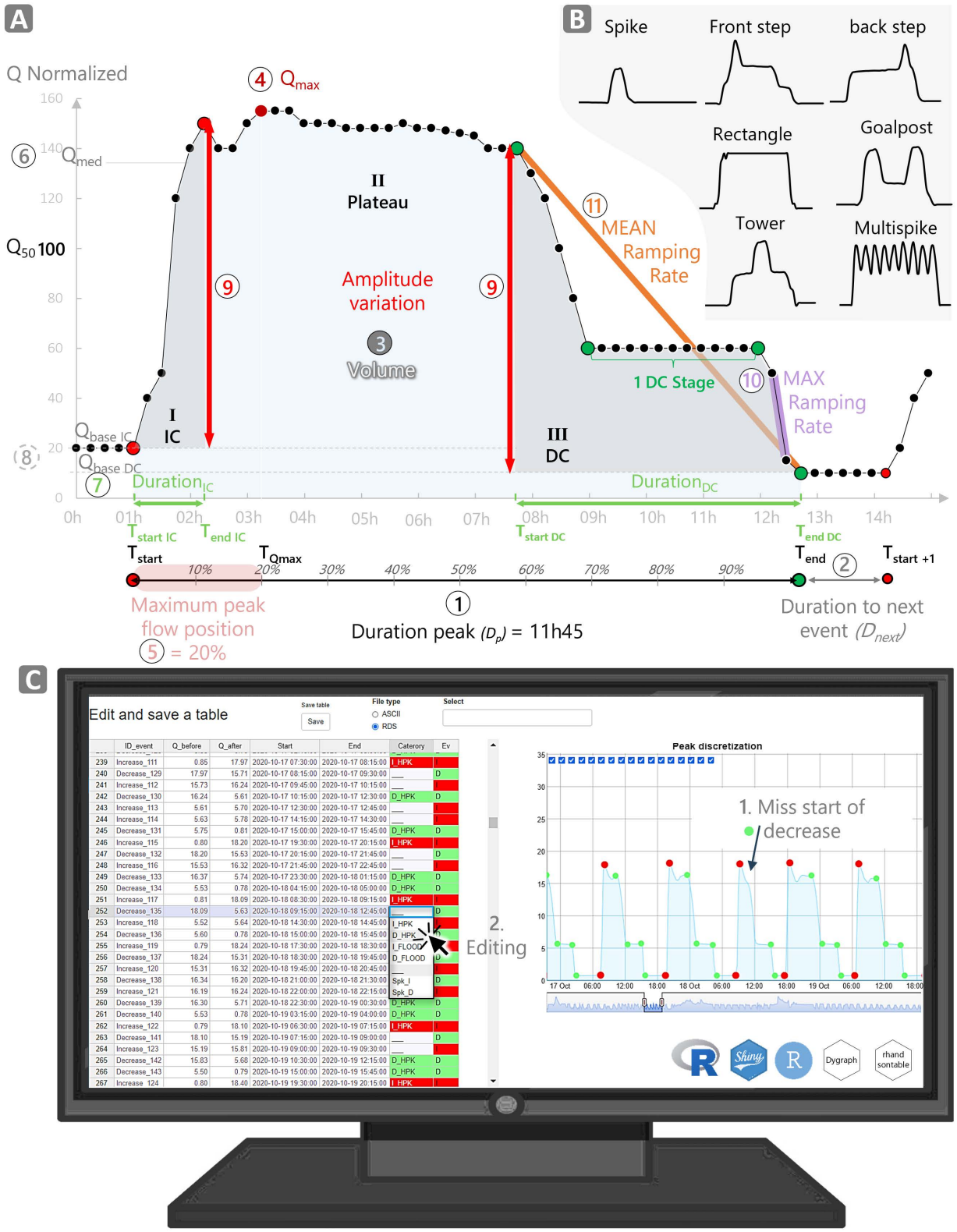

Figure 3.12: Segmentation of hydropeaks. **A** Characteristics of a typical hydropeak. The numbers indicate the characteristics used to isolate and study the hydropeaks. More details in the text and in Table 3.8. **B** Illustration of the different forms of hydropeaks according to Tena et al. (2022), Chapter 3 Part1; based on Fong et al. (2016). **C** Illustration of the application for monitoring the results of the automatic detection of variations of increases (I, red dots) and decreases (D, green dots) with dynamic visualization of hydrographs and editable tables.

Occurrences of superimposed natural and hydropeak phenomena were observed in the data. The intensity of the resulting event is influenced by the sum of the 2, producing an event of greater intensity. Figure 3.13 illustrates the case of a rain event at Laspuña US between 22 and 26 January 2015. As a result, the peak generated by rainfall is interrupted by artificial events. As per Greimel et al. (2016b), this period is therefore associated with artificial fluctuations, while the natural rainfall wave is neglected. The natural decrease that follows is not taken into account because, for an event to be counted, it must have at least one significant phase of increase and decrease without any change in the type of variation (i.e. hydropeak or flood).

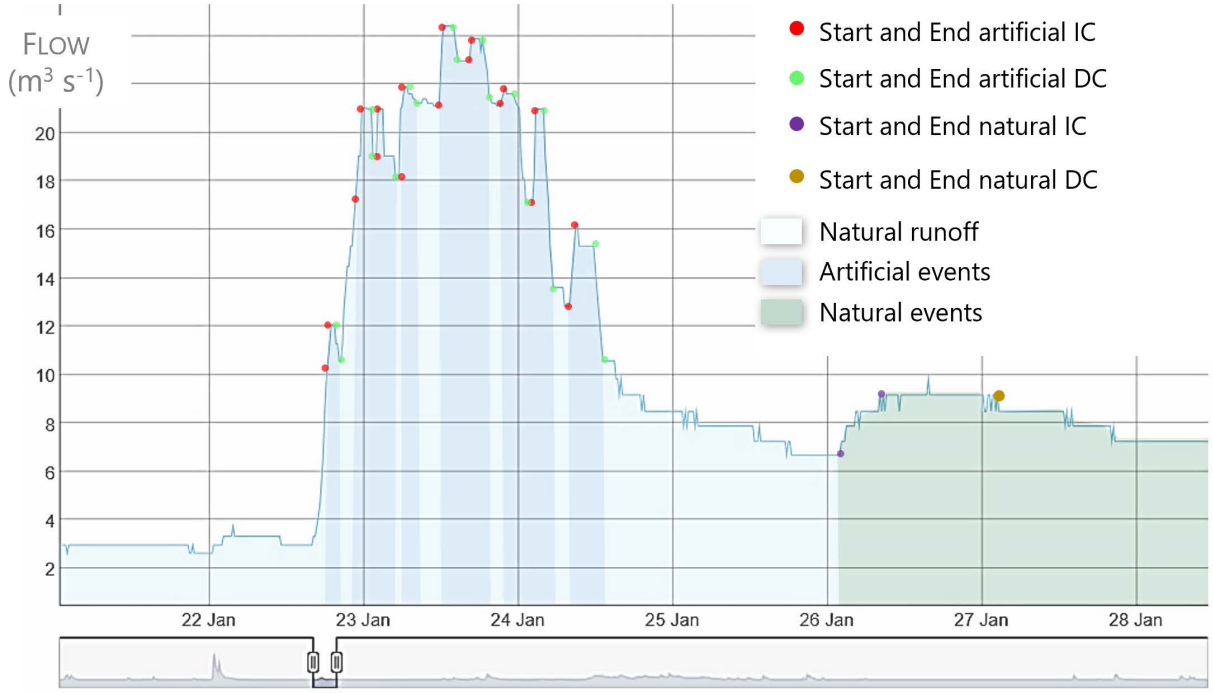

Figure 3.13: Illustration of the superimposition of a rainfall event by hydropeaks in the bypassed reach of Laspuña US between 22 January and 26 January 2015.

3.2.2.2.3 Characterization

3.2.2.2.3.1 Shapes

The classification of hydropeak shapes was based on the same as Tena et al. (2022) after Fong et al. (2016). The shapes are shown in Figure 3.12 **B**: Spike, Front step, Back step, Rectangle, Goalpost, Tower, MultiSpike. They were automatically assigned by conditional branching (i.e. if else statements) for each detected hydropeak as a function of the number of successive increases and/or decreases between stages. The Spike form was assigned to peaks with a duration of 10 h or less, comprising a single variation of increase and decrease without a plateau. In cases where, despite careful manual checking, incorrect automatic detection of IC and DC variations has occurred, the shape assigned may not be appropriate.

3.2.2.2.3.2 Magnitude, timing and frequencies

The number of peaks (hydropeak or flood) was counted by hydrological years and seasons. Then, for each peak, a set of 11 parameters describing their intensity was used, based on those of Courret et al. (2021), Tena et al. (2022), Greimel et al. (2023). The magnitude parameters were calculated for the dimensional and normalized data. They are shown in Figure 3.12 **A** and summarized in Table 3.8. The numbers in brackets in Table 3.8 correspond to the numbers in Figure 3.12 **A**, which show each of the parameters studied. 6 of these parameters characterize the peak as a whole: duration (D_p in hours), duration with the next peak (D_{next}, in hours), total dimensional flow volume (V in hm^3) as well as normalized by the Wy at the station (V_{norm} in % of W_y), the maximum dimensional peak flow (Q_{max}, m^3s^{-1}) and normalized ($Q_{max\ norm}$ in % of Q_{50}), the relative position of Q_{max} (P_{Qmax}, in % of D_p) and the median dimensional flow (Q_{med} in m^3s^{-1}) and normalized ($Q_{med\ norm}$, in % of Q_{50}).

Five other variables were used to characterize the increase (IC) and decrease (DC) variations: the duration of the variation ($D_{IC/DC}$, hours), the base flow before the increase or after the decrease, dimensional ($Q_{base\ IC/DC}$, in m^3s^{-1}) and normalized ($Q_{base\ norm\ IC/DC}$, in % of Q_{50}), the dimensional amplitude ($AMP_{IC/DC}$, in m^3s^{-1}) and normalized ($AMP_{norm\ IC/DC}$, in % of Q_{50}), the maximum ramping rate (i.e. the greatest variation in flow between two instants of time corresponding to the slope of the purple curve in Figure 3.12 **A**) dimensional ($MARR_{ID/DC}$, in $m^3s^{-1}h^{-1}$) and normalized ($MARR_{norm\ IC/DC}$, in % of Q_{50} h^{-1}) and the mean ramping rate (i.e. amplitude of variation divided by its duration, corresponding to the slope of the orange curve in Figure 3.12 **A**) dimensional ($MERR_{ID/DC}$, in $m^3s^{-1}h^{-1}$) and normalized ($MERR_{norm\ ID/DC,}$ in % of Q_{50} h^{-1}). The higher the Ramping Rate (RR) values, the more vertical the purple and orange curves, and vice versa.

3.2.2.2.4 Statistical Analyses

3.2.2.2.4.1 Analysis of central tendencies by station

For each peak shape (i.e. floods and the 7 hydropeak shapes), the distributions of all peaks detected during the two study years for each variable were examined using whisker box plots and, similarly to Carolli et al. (2015), the median values (V_{50}) were extracted as well as the interquartile distance (IQ) (dispersion around the median, $IQ=Q_{75}-Q_{25}$). The presence of outliers is strongly suspected in each of the groups, due to possible poor detection of variations or misclassification of peak shapes that may affect the distributions.

To determine whether the central tendency (i.e. the median) was significantly different between stations and rivers, Mood median tests were performed, followed by post hoc tests to determine which stations were different from the others. The p-value was adjusted using the method of Benjamini and Hochberg (1995) to control for false discovery rate. A p-value of less than 0.05 indicates a significant difference in the observed trend. This test was preferred to the Kruskal-Wallis test, which assumes equal variance. These tests were performed using the *rcompanion* package written by Mangiafico (2023).

Table 3.8: Variable used to characterize hydropeaks. The numbers in brackets correspond to those in Figure 3.12 **A**.

Category	Variable	Symbol	Dimentional Data			Normalized data		
			Units	Equation / data		Units	Equation / data	
Frequency	Number of peak per water year	N_p	–	Direct observation		-	-	
	Number of peak per season	N_{ps}	–	Direct observation		-	-	
Peak	Start time	T_{start}	hh:mm	Direct observation		-	-	
	End time	T_{end}	hh:mm	Direct observation		-	-	
	Duration	D_p	h	$D_{hp} = T_{end} - T_{start}$	(1)	-	-	
	Duration to next peak	D_{next}	h	$D_{hp} = T_{start+1} - T_{end}$	(2)	-	-	
	Volume	V	hm^3	$V = \sum Q_{start+1} + .. + Q_{end-1} * t$	(3)	% of WY	$V_{norm} = [\sum Q_{start+1} + .. + Q_{end-1} * t]/WY$	(3′)
	Maximum peak flow	Q_{max}	m^3s^{-1}	Direct observation	(4)	% of Q_{50}	$Q_{max\ norm} = [Qmax/Q_{50}] * 100$	(4′)
	Time of peak flow (Q_{max})	T_{Qmax}	hh:mm	Direct observation				
	Duration to reach peak flow	D_{Qmax}	h	$D_{Qmax} = T_{Qmax} - T_{start}$				
	Maximum peak flow position	P_{Qmax}	–	$P_{Qmax} = \frac{T_{Qmax}}{D_{hp}}$	(5)	%	$P_{Qmax} = \frac{T_{Qmax}}{D_{hp}} * 100$	(5′)
	Median peak flow	Q_{med}	m^3s^{-1}	$Q_{med} = \left(\frac{n+1}{2}\right)^{th}$, $= \left[\left(\frac{n}{2}\right)^{th} + \left(\frac{n}{2}+1\right)^{th}\right]/2$	(6)	% of Q_{50}	$Q_{med\ norm} = [Qmed/Q_{50}] * 100$	(6′)
Variation IC or DC	Start time variation	$T_{start\ IC/DC}$	hh:mm	Direct observation		-		
	End time variation	$T_{end\ IC/DC}$	hh:mm	Direct observation		-	-	
	Duration variation	$D_{IC/DC}$	h	$D_{IC/DC} = T_{end\ IC/DC} - T_{start\ IC/DC}$	(7)	-	-	
	Base flow	$Q_{base\ IC/DC}$	m^3s^{-1}	Direct observation : Q at T_{start} and T_{end}	(8)	% of Q_{50}	$Q_{base\ norm\ IC/DC} = [Q_{base\ IC/DC}/Q_{50}] * 100$	(8′)
	Amplitude	$AMP_{IC/DC}$	m^3s^{-1}	$AMP_{IC/DC} = Q_{Tend\ IC/DC} - Q_{Tstart\ IC/DC}$	(9)	% of Q_{50}	$AMP_{norm\ IC/DC} = [AMP_{IC/DC}/Q_{50}] * 100$	(9′)
	Maximum ramping rate	$MARR_{IC/DC}$	$m^3s^{-1}h^{-1}$	$MARR_{IC/DC} = \max\left\lvert\frac{Q_i - Q_{i-1}}{t_i - t_{i-1}}\right\rvert$	(10)	% of Q_{50} h^{-1}	$MARR_{norm\ IC/DC} = max\left\lvert\frac{Q_{i\,norm} - Q_{i\,norm\,-1}}{t_i - t_{i-1}}\right\rvert$	(10′)
	Mean ramping rate	$MERR_{IC/DC}$	$m^3s^{-1}h^{-1}$	$MERR_{IC/DC} = AMP_{IC/DC}$ / Duration $_{IC/DC}$	(11)	% of Q_{50} h^{-1}	$MERR_{norm\ IC/DC} = AMP_{normIC/DC}$ / Duration $_{IC/DC}$	(11′)

subscript *i* denote the *i* th time step measurement in the entire serie data

3.2.2.2.4.2 Analysis of associated peaks between stations

The processing to analyse the peaks associated between hydrographs, based on the concept of Greimel et al. (2016a); Greimel et al. (2023), was performed only for the 45-day Ésera dataset. An ID was assigned to each peak detected at the Campo station. The hydrographs from the 3 stations were plotted on the same graph (example Figure 3.19 **B**). Visually, the IDs of the peaks associated with Pyramides and Santaliestra were assigned. Each peak can be individually characterized in the three points of the study segment. The peak shape assigned to each event is the one initially identified in Campo.

Dimensional and normalized flow measurements based on downstream events (Pyramides S2 and Santaliestra S3) were related to those from Campo (S1) and were represented in scatterplots by grouping by hydropeak shape. Linear regression models were then applied between the Campo data (S1) and the Pyramides data (S2) and between the Campo data (S1) and the Santaliestra data (S3), but without taking into account the shape of the peaks. These models make it possible to assess the general correlations between upstream and downstream and possibly predict the propagation of peaks.

3.2.3 RESULTS AND DISCUSSION

3.2.3.1 Analysis of central tendencies by station

3.2.3.1.1 Frequencies

A total of 6 325 peaks were identified, of which 4 728 on the Cinca River and 1 597 on the Ésera, for a total of 14 years analysed. The distribution of the number of peaks per season for each year and station is shown in Figure 3.14. The first row shows all the peaks, the second only those corresponding to natural variations and the third only those identified as hydropeaks. Figure 3.15 shows the volumes of water flowing for each type of flow: base flow, hydropeak and flood. The first row shows the distribution of volumes for each year studied, while the next 4 rows show the distribution by season.

The results show several important points worth highlighting:

1) Artificial peaks have been detected at the Laspuña US station, upstream of the plant (Figure 3.14, third row). Between 15% and 29% of the annual flow is considered unnatural (grey blocks, Figure 3.15, first row). More specifically, it can be seen that during the spring season (4th row), the artificial runoff predominates (31 to 48%). Spring rainfall combined with snowmelt provides a large and constant supply of water. In addition to the reserved ecological flow, this bypassed reach receives volumes of water during floods when the available volume is too great to be stored, diverted or turbined in its totality. The management of the opening of the Laspuña dam gates therefore seems to generate hydrological events similar to hydropeaks (phenomenon already illustrated in Figure 3.13 and Figure 3.15 **B**, blue curve).

2) For all stations downstream of the HP (i.e. all except Laspuña US), the distribution of hydropeaks (Figure 3.14, last row) within the seasons is homogeneous, regardless of the hydrological year studied. It should be noted that the selected years are all considered average hydrological years in terms of water supply. On the other hand, the peaks considered natural ("floods", row 2) occur mainly in spring and autumn for the Cinca River. The volumes discharged during spring floods (Figure 3.15, 4th row) on the Cinca are homogeneous between the studied stations and years (black blocks, between 21 and 34%), whereas those for autumn floods are more heterogeneous between years. This phenomenon is linked to the strong storms that can occur at this time of year, although the occurrence of these storms varies from year to year.

3) There are more hydropeaks on the Cinca (between 600 and 800 per year) than on the Ésera (around 400 per year). However, in terms of annual volume, the Ésera is more dominated by artificial flows (Figure 3.15, 1st row, grey blocks 72 to 76%), even in spring, compared to the Cinca. The base flow represents only 10 to 20% of the annual flow in Campo and Santaliestra. It seems that the daily inflows of spring melt can be stored/modulated to some extent by the reservoirs (maximum 4 days of average daily flow) for peak hydroelectric production. Figure 3.15 **C** shows an extract of the normalized flow data at Campo in spring 2020. Hydropeaks superimposition on the high base level due to meltwater are visible throughout the period. On the other hand, the volumes classified as base flow on the Cinca are slightly higher (white blocks). It seems that the plants on the Cinca can produce hydroelectricity without necessarily generating peaks (see Figure 3.15 **B**, red curve). In spring, they seem to contribute relatively more to the production of base load electricity than to peak load electricity.

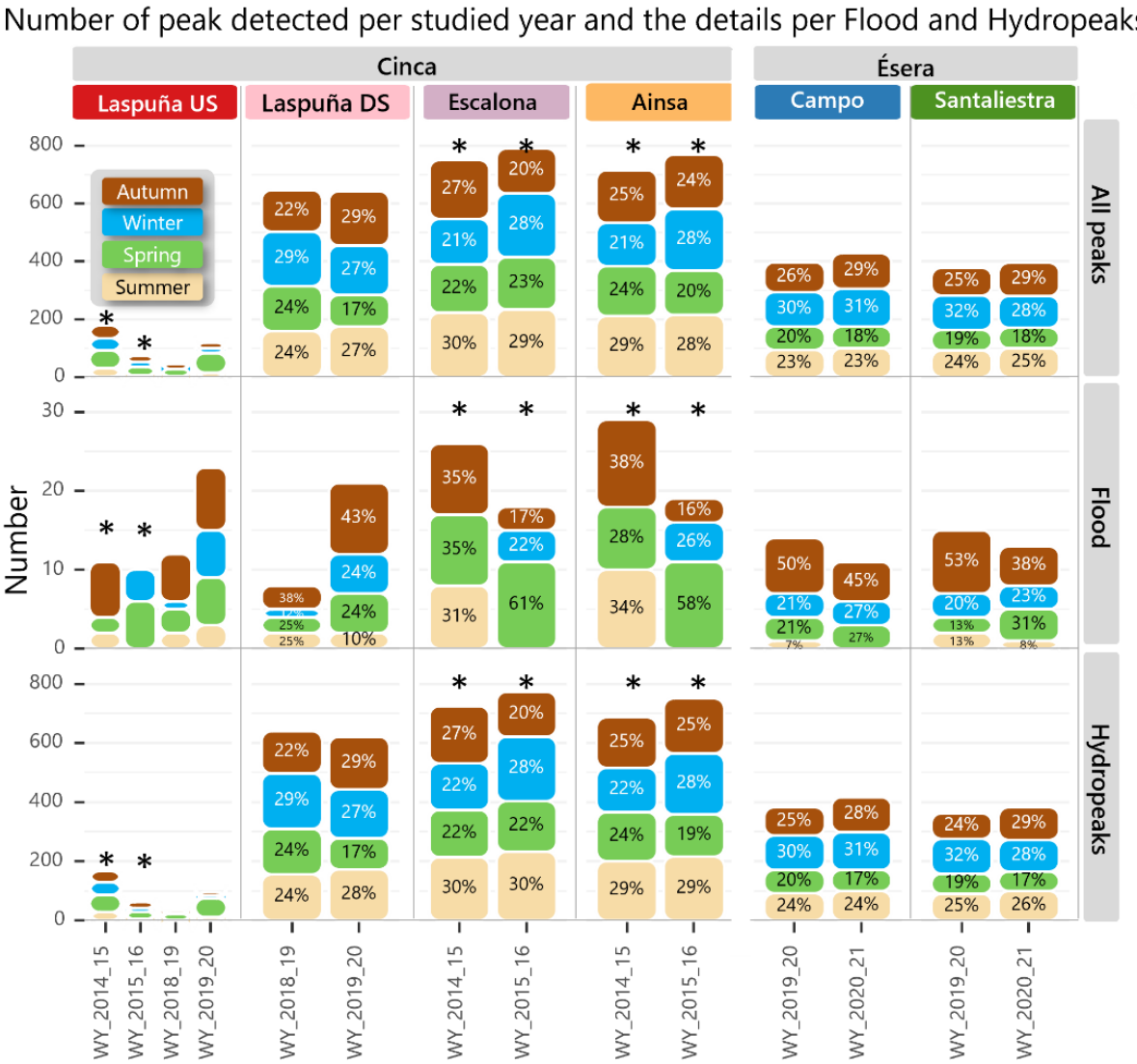

Figure 3.14: Frequency distribution of the peaks. Top, annual and seasonal distribution of all identified peaks. Middle, identified floods and Bottom, hydropeaks. *Dataset from Béjar et al. (2018).

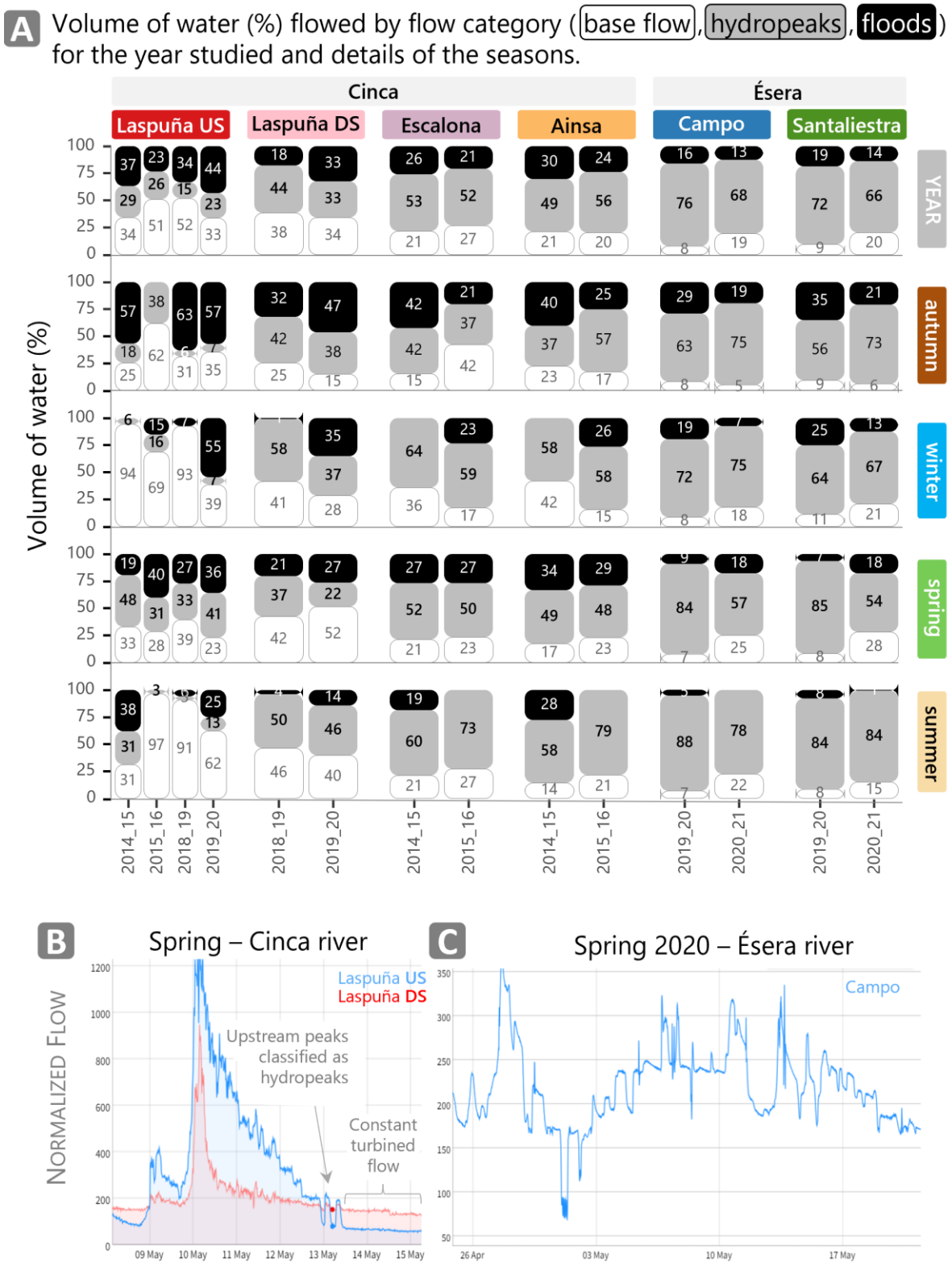

Figure 3.15: A Distribution of volumes classified as base, hydropeak, flood for each station annually and by season. **B** Extract of normalized spring flow data at Laspuña US (blue curve, bypassed reach) showing hydropeaks superimposed on a natural wave and Laspuña DS (red curve, downstream of HP) showing stable flows without peaks. **C** Extract of normalized flow data at Campo in spring 2020 showing a fully artificial hydrograph.

The distribution of hydropeaks by shape is shown in Figure 3.16. The first row shows the annual distribution, while the following rows show the proportion of shapes by season.

The findings underscore several crucial aspects that deserve further attention:

1. The shape of the Cinca River hydropeaks is constant between stations, hydrological years and seasons. The dominant shape is the Spike (from 45% to 66% annually). The Front Step shape is present between 20% and 14%. The occurrence of shapes for the Escalona station is different from that presented in Tena et al. (2022), although based on the same data set. The Rectangle shape was more dominant than the Spike shape. The classification of the peaks was done according to the characteristics described by the previous authors, but here the peaks were classified automatically rather than manually. In addition, no threshold duration was clearly established to define the Spike shape. All hydrological peaks with a duration of less than 10 hours and with a single increase/decrease variation without a significant plateau during these variations were classified as Spikes. Some of the peaks considered as such could have been classified as Rectangles, as they also had only a single increase/decrease (Figure 3.16 **B**). However, considering the results presented in Figure 3.17 for the duration of the Spike hydropeaks, it appears that the distribution is well below the 10 h limit, indicating that this group of peaks has not been truncated.

2. The Goalpost form (with 2 waves) is more present at Escalona and Ainsa than at Laspuña DS upstream (10 to 13% annually compared to 1%). The propagation of the peaks coming from Laspuña DS could be attenuated downstream, which could lead to a convergence of the peaks of certain events occurring at short intervals. However, it should be noted that the data from Escalona and Ainsa do not correspond to the same hydrological years as those from Laspuña DS. The transformation of the water level data into flow at the Escalona and Ainsa stations during the 2018/2021 study period would allow this trend to be confirmed or not.

3. For the Ésera River, the two forms that dominate annually are Front Step (35 to 45%) and Spike (23 to 28%). The occurrence of hydropeak forms shows a greater seasonal variation than on the Cinca River. In autumn (2nd row) Front Step dominates at both stations, followed by Spike. In winter (3rd row), Spike dominates at Campo and Santaliestra (between 38 and 43%). In spring there is no particular predominant shape, but the Rectangle shape seems to be more widespread than in other seasons. Finally, in summer, the Front Step shape is the only predominant shape (48 to 65%).

4. The MultiSpike shape is almost non-existent on an annual scale (only 1 to 4 peaks detected for the Cinca stations and a maximum of 21 at Campo), therefore the distribution of these characteristics was not analysed. The limited number of observations in the central tendency analysis carried out for each shape group and station would have led to unreliable results.

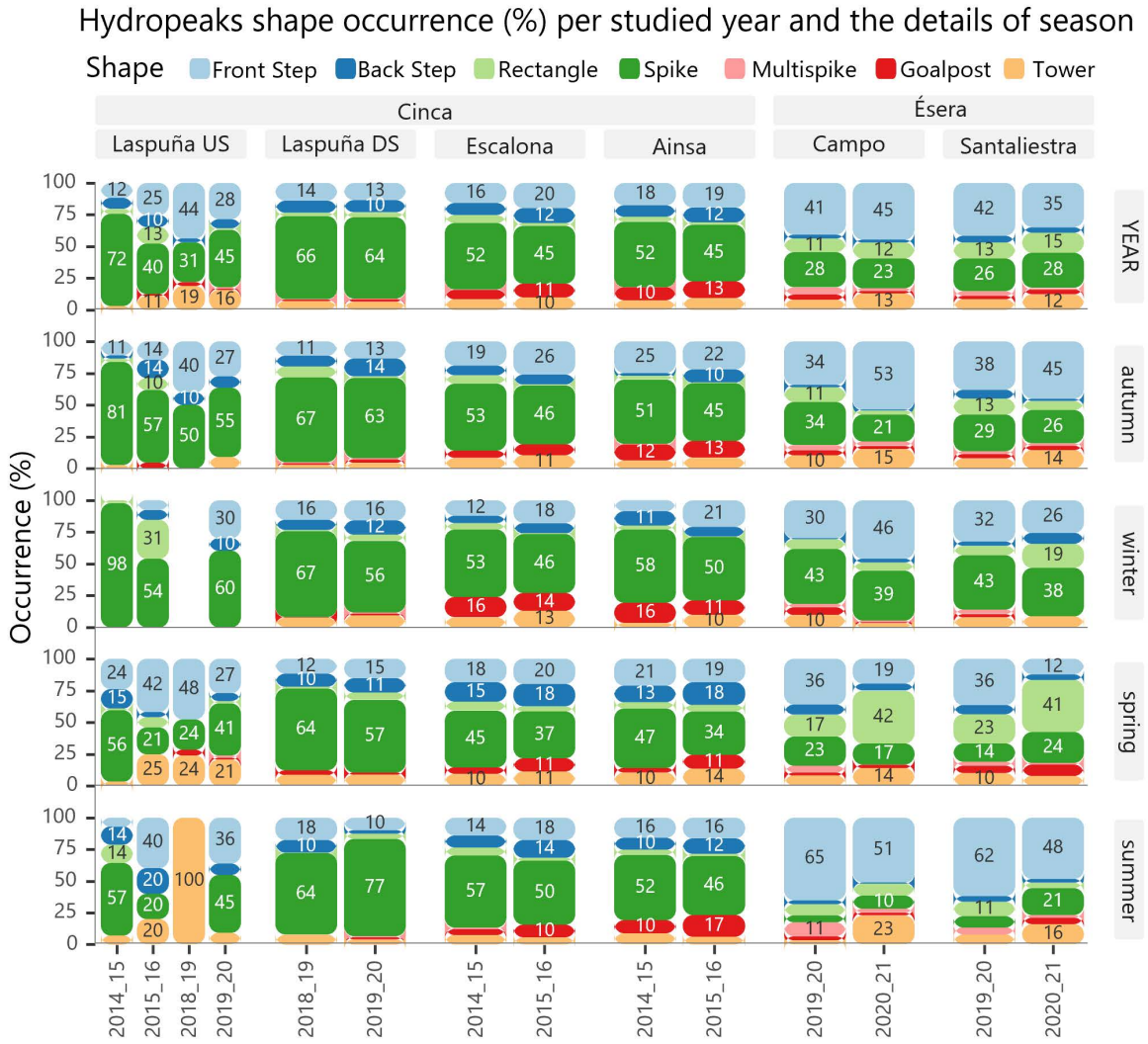

Figure 3.16: Annual and seasonal distribution of peak shapes for each station.

3.2.3.1.2 Peak characteristics

The distributions of the variables describing the peaks (i.e. including the whole period from increase, plateau to the end of the decrease) are shown in Figure 3.17 as whisker boxes for each peak shape at each station. In order to show correctly the central tendencies at the same scale for all distributions presenting sometime large variation between stations and shape of peaks, the ordinate scale has been truncated. Some of the highest extreme values may be not visible. The high values of the distributions, symbolized by the upper grey lines of the boxes, are sometimes truncated. Only the normalized values are shown for the magnitude variables (volume norm, $Q_{max\ norm}$ and $Q_{med\ norm}$). For example, a normalized flow of 150% means that the flow is 150% of the Q_{50} at the station or that it is 1.5 times greater than the Q_{50} at the station. The dominant shapes are represented at the top by a dark grey rectangle (Front Step, Spike and Rectangle for the Ésera) with the number of peaks detected at each station below. The results of the Mood median tests are shown. The presence of dashed black vertical bars between the Cinca and Ésera stations indicates significantly different medians between the two rivers, but not necessarily between stations in the same river. Horizontal bars with stars between stations indicate significantly different medians, while the presence of the symbol ns indicates non-significant differences.

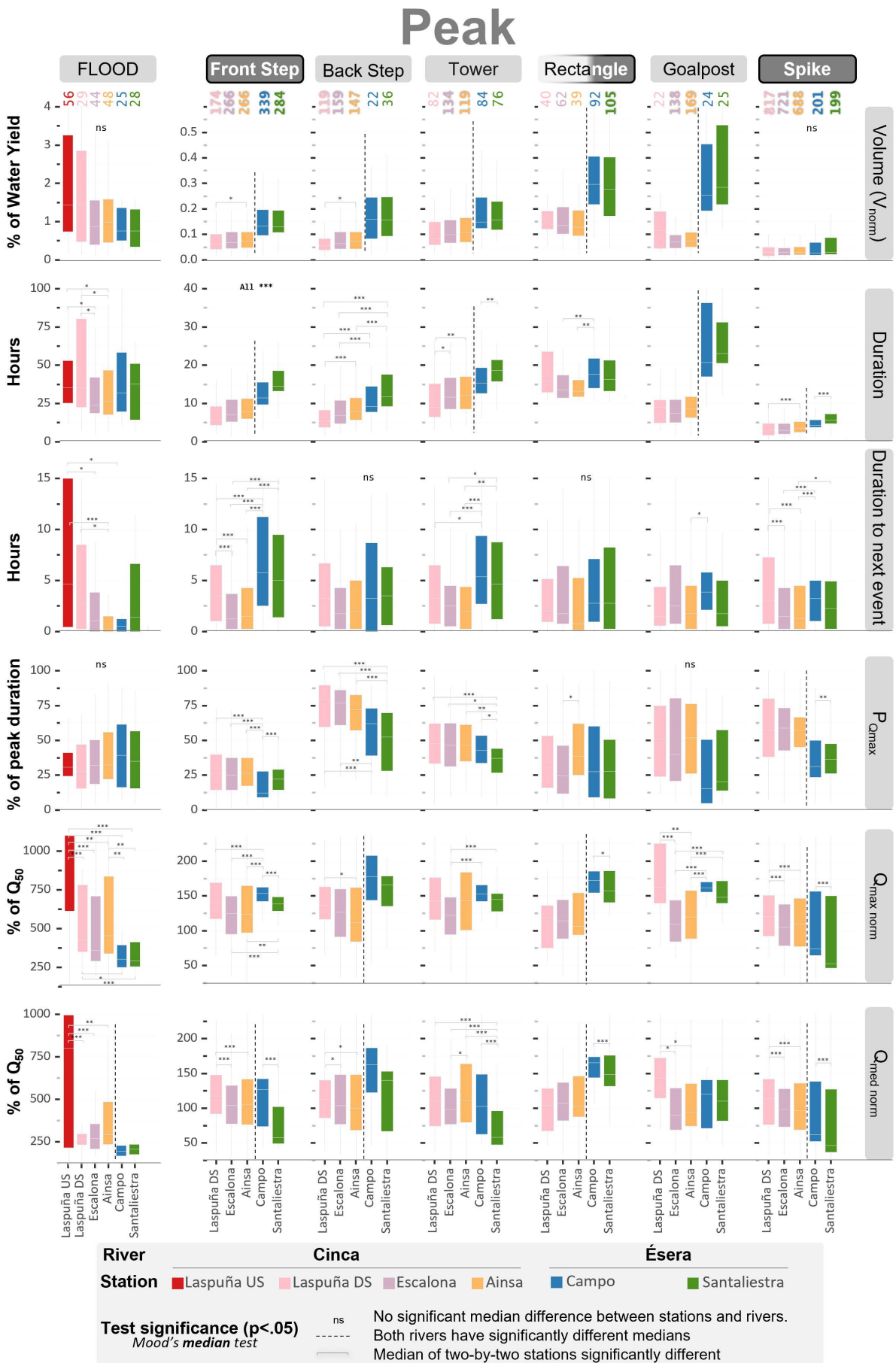

Figure 3.17: Central tendency of the characteristics of the peaks for each station from upstream to downstream on the two river segments studied with the results of the Mood median tests.

The volumes flowing during hydropeaks are relatively stable between stations on the same river downstream. The normalization of the data in relation to the local hydrology of the stations (Figure 3.17, first line) shows that, for all forms of peaks, the volumes of water used to meet peak demand on the Ésera represent a larger proportion of the annual flow than for the Cinca river.

Total hydropeak duration are significantly longer on the Ésera than on the Cinca for almost all shapes (Figure 3.17, blue and green boxes, 2nd row). In addition, both rivers show a significant increase in duration downstream. The Spike form increased from a median duration of 3h at Laspuña DS (0.3 km) to 3h30 at Ainsa (10 km), while the Front Step form increased from 5h45 to 7h45. On the Ésera, the median duration of the Spike shape increases from 4h15 at Campo (0.3 km) to 5h45 at Santaliestra (18.5 km) and that of the Front Step shape from 11h30 to 14h30. The peaks are longer downstream, indicating a certain deceleration of the flow along the rivers.

For the same shape of peak generated by the Campo and Laspuña HPs (Front Step, Back Strep, etc., pink and blue boxes), the position of Qmax within the peak is earlier on the Ésera than on the Cinca (Figure 3.17 4th row, the lower the values, the earlier the peak and vice versa). This position changes slightly downstream for the Ésera, but remains stable for the Cinca. For the Spike shape on the Ésera, its median position is 31% and 36% for Campo and Santaliestra respectively, compared to about 58% for all stations on the Cinca, i.e. almost double. For the Front Step, P_{Qmax} is between 12% (Campo) and 22% (Santaliestra) of the peak on the Ésera and around 26% on the Cinca. It should also be noted that, paradoxically, for the Back Step and Tower forms, for which the power plant turbines the peak flow in the middle or at the end of the peak, the P_{Qmax} is earlier in Santaliestra (downstream) than at Campo. The peak flow is reached earlier than in the hydrograph produced by the Campo HP.

The dimensional peak flows (Q_{max}, m^3s^{-1}) on the Cinca are greater than those on the Ésera. For the Spike form, the median Q_{max} ranges from 18.6 m^3s^{-1} upstream to 20.3 m^3s^{-1} downstream compared to 8 to 7 m^3s^{-1} on the Ésera, and for the Front Step from 21.8 to 23m^3s^{-1} compared to 17.9 to 19.1 m^3s^{-1} on the Ésera. The normalized values (Figure 3.17, 5th line) show that the Q_{max} normalized to the local hydrology tends to decrease downstream. On the Cinca, the two downstream stations of Escalona and Ainsa show lower values than upstream, but similar to each other. After 3 km, the $Q_{max\ norm}$ remained stable until Ainsa (7 km downstream). The $Q_{max\ norms}$ on the Ésera are at least equal to, if not greater than, those on the Cinca, contrary to the dimensional values cited above. The dominant Front Step form shows median $Q_{max\ norms}$ of 154% of Q_{50} at Campo, decreasing to 138% of Q_{50} at Santaliestra, with a low IQ dispersion (20% of Q_{50}), indicating that the peak flows of these peaks are very homogeneous over all the peaks detected.

In summary, a greater relative quantity of water is used on the Ésera to generate electricity during peak demand periods. Compared to the Cinca, the peaks have longer duration, earlier P_{Qmax} and equal or greater relative magnitudes. However, generally speaking, for both rivers and all peak forms, the duration increases downstream, while the normalized Q_{max} decreases by 10 to 20%.

3.2.3.1.3 Increase and Decrease variation characteristics

The distributions of the variables describing the variations (i.e. only IC and DC) are presented in Figure 3.18 in the form of whisker boxes, for each peak shape observed at each station. As in Figure 3.17, the magnitude values presented are the normalized ones, and the results of the median difference tests are indicated. To improve the readability of the figure, the upper parts of the distributions have sometimes been truncated to allow optimum visibility of the central tendencies. When all or almost all the stations differ significantly, three stars appear at the top of the graph instead of horizontal bars. If some stations do not differ significantly, they are indicated by a horizontal line with the ns symbol.

The magnitude of the base flows in dimensional or normalized values ($Q_{base\ norm}$, Figure 3.18, 1st row) at which ICs start (left) and DC end (right) are similar. On the Cinca, for the 3 stations (pink, purple and yellow boxes) the median $Q_{base\ norm}$ are around 80% of the Q_{50} with an IQ of around 55%. These values are similar for all peak shapes.

In comparison, on the river Ésera, they are relatively low with a small IQ distance indicating a homogeneity of $Q_{base\ norm}$ compared to the Cinca. The median $Q_{base\ norm}$ values for the Front Step shape are 11 and 17% of the Q_{50} with an IQ distance $< 10\%$. The Front Step, Tower and Golpost shape, as a result of having very low $Q_{base\ norm}$, have the greatest amplitudes of variation, with medians of 130 to 115% of Q_{50} (Figure 3.18, 1st row vs. 2nd row). These high amplitudes can be clearly seen in Figure 3.18 **B**. Generally, the normalized amplitude of variation decreases significantly downstream on the two study segments for the two dominant Front Step and Spike shapes.

Unlike base flows and amplitudes, Ramping Rates (RR) differ between IC and DC. For IC, normalized max ramping rate ($MARR_{norm}$) and normalized mean ramping rate ($MERR_{norm}$) (Figure 3.18, 3rd and 4th row) show higher values and IQ ranges showing more dispersion than those for DC. Thus, DC variations show RR with homogeneous patterns, whereas IC are more variable. Generally speaking, $MERR_{norm}$ incorporating the entire IC or DC phase follow the same trends as $MARR_{norm}$, but they are weaker (Figure 3.18 row 3 vs. 4). On average, they are 50 to 80% lower.

Only the Laspuña US station (pink box) has a similar RR distribution between IC and DC. The dominant Front Step and Spike shapes show RR decreasing downstream. For the Front Step shape, at Laspuña US, the median $MARR_{norm}$ of IC is 173% of the Q_{50} h^{-1} (i.e. 25 $m^3s^{-1}h^{-1}$) and decreases to Ainsa to 64% of the Q_{50} h^{-1} (10 $m^3s^{-1}h^{-1}$). For the DC, the $MARR_{norm}$ falls from 143 to 34% of the Q_{50} h^{-1} between upstream and downstream (i.e. from 22 to 6.5 $m^3s^{-1}h^{-1}$).

The differences in the Front Step shape are more noticeable on the Ésera between IC and DC and between the two stations. The IC $MARR_{norm}$ are similar at the two stations (blue and green boxes, 3rd row) with a median value close to 300% of the Q_{50} h^{-1} (i.e. approximately 37 $m^3s^{-1}h^{-1}$) and with a wide dispersion (IQ range approximately 125% of the Q_{50} h^{-1}, i.e. 16 $m^3s^{-1}h^{-1}$). They are therefore relatively strong but also highly variable. On the other hand, for DC they are only 118 and 37% of the Q_{50} h^{-1} (i.e. 13 and 5 $m^3s^{-1}h^{-1}$) with IQ ranges reduced to between 30% and 5% of the Q_{50} h^{-1} (i.e. between 5 and 0.8 $m^3s^{-1}h^{-1}$).

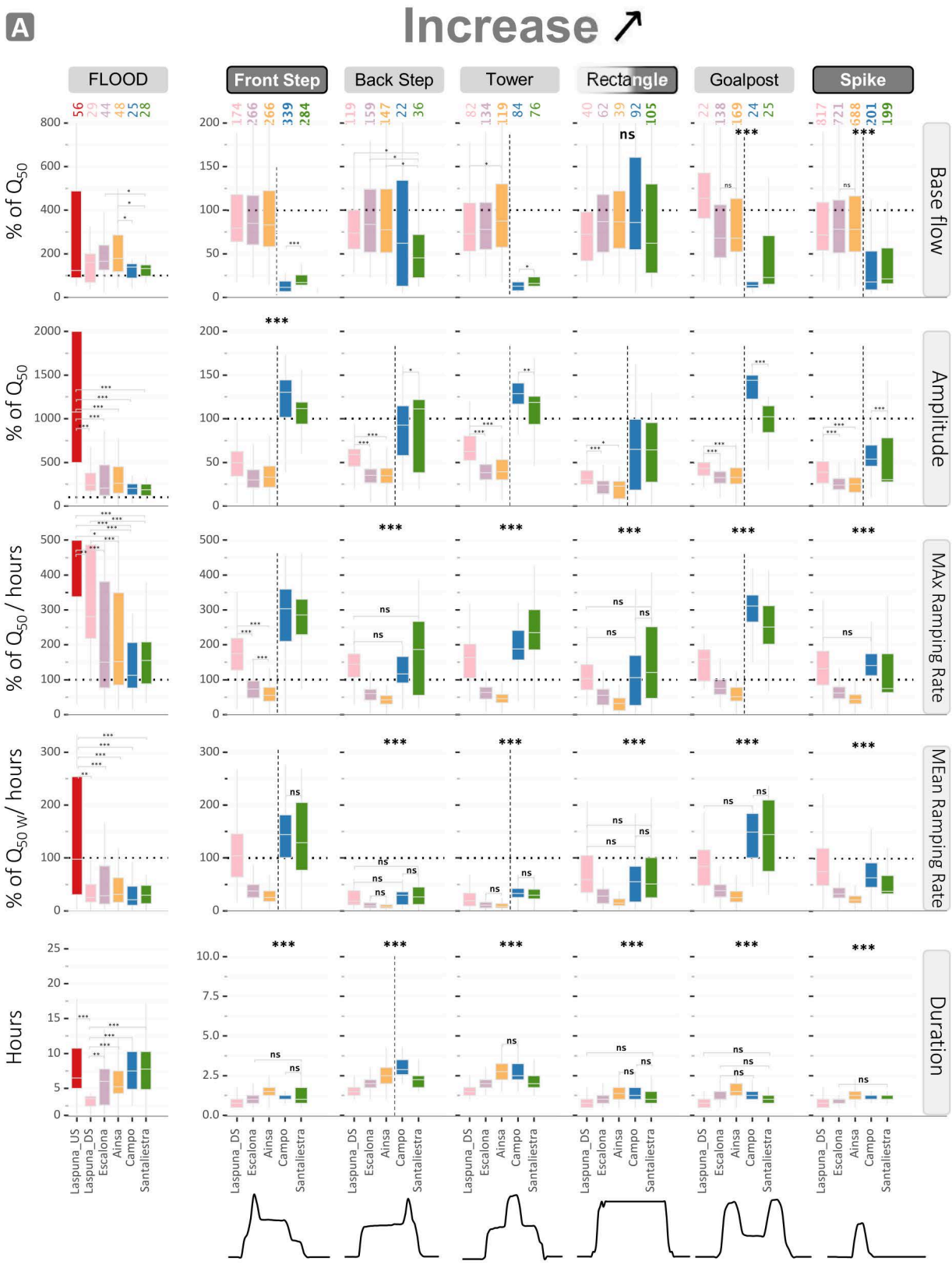

Figure 3.18 (with the following page): Central tendency of the characteristics of increase variation (**A**) and decrease variation (**B**) for each station from upstream to downstream on the two river segments studied with the results of the median Mood tests.


B
Decrease ↘
FLOOD
Front Step
Back Step
Tower
Rectangle
Goalpost
Spike
% of Q50
% of Q50 / hours
Hours
Base flow
Amplitude
MAx Ramping Rate
MEan Ramping Rate
Duration
Laspuña US
Laspuña DS
Escalona
Ainsa
Campo
Santaliestra
River
Cinca
Ésera
Station
Test significance
Mood's median test
ns
No significant median difference between all stations and rivers.
***
Significant median difference between all stations and rivers. Some no significant median can be observed
Both rivers have significantly different medians
*
Median of two-by-two stations significantly different (*p<.05, **p<.01, ***p<.001)
ns
Median of two-by-two stations NOT significantly different, while the rest of the median station are generally significantly different

The variation duration is different for IC and DC. However, both show significant variation duration that are longer downstream. On the Cinca, the Spike shape shows identical median IC and DC duration, from 45 min at Laspuña DS, increasing by 1 hour at Escalona and 1.5 hours at Ainsa. The Front Step shape has the same IC values, but the DC is twice as slow. They increase downstream from 1h30 to 2h and then 3h30 respectively. For the Ésera, the Front Step and Spike shape have identical median IC duration between upstream and downstream of one hour. However, the DC are more than twice as slow downstream. At Campo, the median DC is 1 hour for the Spike and 3.5 hours for the Front Step. At Santaliestra, they increase to 3.5 hours and 8 hours respectively.

Finally, it is worth noting the particular behaviour of the Back Step and Tower shapes on the Ésera. Both have IC duration that decrease significantly downstream, in contrast to what we have just seen for the Spike and Front Step, which are getting longer (Figure 3.18 **A**, left panel, 5th row, columns 3 and 4). The median duration at Santaliestra (2h, green box) are shorter than at Campo (2h30 to 3h, blue box). These shapes also have the lowest $MERR_{norm}$ (4th row) of IC compared with the other shapes. The gradients of IC are much gentler than the others (i.e. the average slopes of rise on the hydrographs are low, see Figure 3.12 **A** point 11 orange curve). Concerning the $MARR_{norm}$ (3rd line), these are the only two shapes to have significantly higher $MARR_{norm}$ downstream than upstream (green box positioned higher than the blue ones).

As a reminder, these are the shapes for which the HP turbines peak flows in the middle or at the end of the peak after stages of lower flows (see Figure 3.18 **A**, shapes below the graph). These two shapes had earlier P_{Qmax} downstream than upstream, as mentioned in the previous section. This suggests that the low flow of the IC stages at the start of these shape is relatively slower to propagate compared to the peak which occurs later. The beginning of these low stages arrives downstream very slowly and is laminated due to the flow resistance of the bed and walls, but is nevertheless detectable on the hydrograph, creating a low $MERR_{norm}$. The peak flow, generated later by the HP, seems to catch up, to some extent, some of the lower intensity flow volumes released earlier. The arrival of these more "concentrated" volumes of water, of these two superimposed waves, implies a significant and relatively rapid change in water level downstream between two measurement instants (15min), creating a strong $MARR_{norm}$, greater than that generated by the power station upstream.

This phenomenon does not occur in the Cinca river, despite the fact that its bed slope is similar to that of the Ésera. The morphology of the river, much wider with large bars and shallow channels, seems to allow greater dissipation of energy. The late peak flows do not seem to catch up with the previous stages.

To summarize, as already reported by Tena et al. (2022), the hydropeak regime in these two rivers is different. The median base flows on the Ésera are 80% lower than on the Cinca and the amplitudes 75% higher. The results also show that their propagation follows different routing, particularly with regard to ramping rates depending on peak shapes.

On the Cinca, whatever the shape and intensity of the peaks, the waves seem to be laminated in the same way. On the Ésera, on the other hand, propagation differs according to peak shape and intensity. For high intensity peaks (i.e. Front Step), the $MARR_{norm}$ of increases does not seem to be significantly attenuated downstream, whereas decreases are. For low-intensity peaks (i.e. Spike), the $MARR_{norm}$ of both increases and decreases are attenuated in a similar way to Cinca.

3.2.3.2 Analysis of targeted peaks between stations

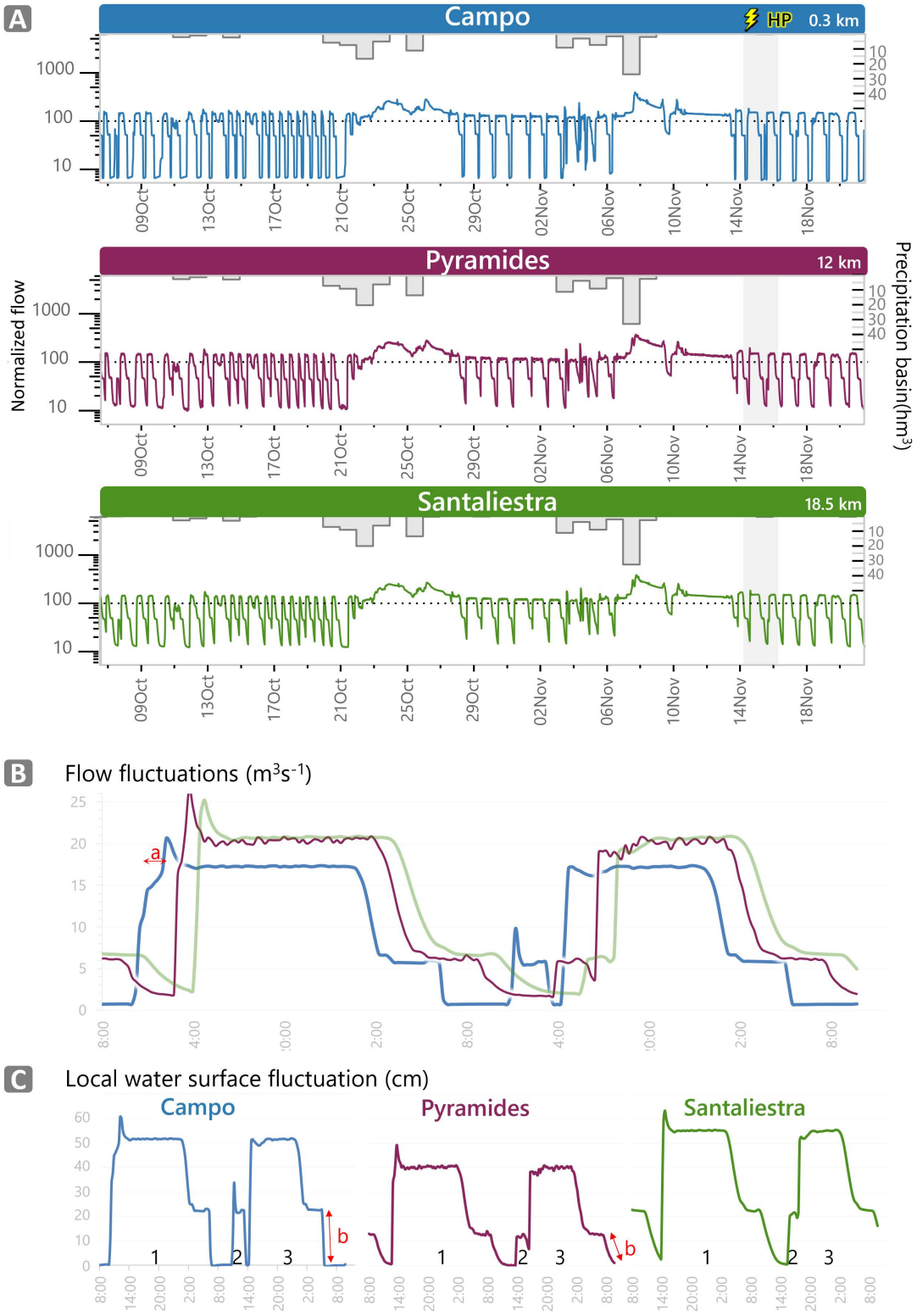

Figure 3.19: **A** Series of flow data (15 min) for peak analysis associated between hydrographs normalized by the median flow at each station with its distance from the HP and the daily volume of rainfall draining to these stations (top). Data acquisition and processing are described in detail in Chapter 2, Part 2. The shaded areas from 14th to 16th November correspond to parts B and C of this figure. **B** Fluctuation of flow for 3 hydropeaks between Campo, Pyramides and Santaliestra. **C** Evolution of the local water level of the stations for these 3 same peaks.

Analysis at peak scale was carried out on the data series between October and November 2020, shown in Figure 3.19 **A**. A total of 56 peaks generated by the Campo HP were monitored downstream at the Pyramides and Santaliestra stations. The characteristics extracted from the two downstream hydrographs are compared with those from Campo by visualizing scatterplots in Figure 3.20.

The x-axis corresponds to the values observed at Campo (S1), while the y-axis represents the characteristics of the same peak but observed at Pyramides (S2) or Santaliestra (S3). The points located on the grey line of equality indicate an identical value between upstream and downstream. The points located in the lower triangle indicate a lower value downstream than at Campo, while the points located in the upper triangle indicate a higher value than at Campo. The variables characterizing the magnitudes are presented in two dimensional and normalized forms.

3.2.3.2.1 Longitudinal characterization of peaks

The total peak duration and the duration to next event (Figure 3.20 **A**) observed at Campo are well correlated with those at the two downstream stations. The R^2 are 0.97 and 0.96. Hydropeaks last about 40 minutes longer at Pyramides and 1 hour longer at Santaliestra than at Campo, and the time between two peaks is reduced by 1h20 at Pyramides and about 2h at Santaliestra.

P_{Qmax} is less well correlated between Campo and downstream (R^2 0.51 and 0.36). A group of points dominated by Front Step show very early P_{Qmax} at Campo, < 12%, for downstream P_{Qmax} ranging from around 25% to almost 75%. However, most of the other points show that downstream peaks start to show a lower (earlier) Q_{max} position when the Q_{max} position at Campo is slightly later (i.e. > 16 and 32%). It can be seen that some Front Steps generated at Campo (blue dots) have a delay greater than this threshold.

This phenomenon is illustrated in Figure 3.19 **B**, on an extract from the data series. The blue curve at Campo for peak no. 1 shows a proto-stage of increase (point a) before the peak flow. This stage disappears almost completely downstream at Pyramides (purple curve) and completely at Santaliestra (green curve). Therefore, the two downstream peaks present an earlier Q_{max} position. In the case of peak no. 2, with a Spike shape of less than 13 m^3s^{-1}, it is gradually caught up at Pyramides and almost integrated with peak number 3 at Santaliestra.

Peak flow magnitudes are well correlated between upstream and downstream stations (R^2 0.92 and 0.87). The $Q_{max\ norm}$ are similar between upstream and downstream (e.g. the linear models in the black curve are close to the grey equality line). On the other hand, the linear models, on dimensional data in m^3s^{-1}, indicate that peak flows are higher for the two downstream stations than at Campo when the latter is approximately greater than 13 m^3s^{-1}. However, at Pyramides (intermediate point), the magnitudes are greater (slope of the black line) than at Santaliestra (downstream point). These results indicate an apparent increase in flow between Campo (upstream) and Pyramides (intermediate), followed by a slight decrease towards Santaliestra (downstream). This can be seen in Figure 3.19 **B**. The purple curve at Pyramides for peak no. 2 shows a higher point flow than that at Campo and Santaliestra. This does not appear to be due to rainfall in the catchment area. Figure 3.19 **A** shows no precipitation in the days preceding this peak.

3.2.3.2.2 Longitudinal characterization of increase and decrease variations

The base flows (Q_{base} Figure 3.20 **B**, left) observed downstream, for both increases/decreases, are well correlated with those at Campo (R^2 0.98 and 0.97). The normalized Q_{base} are similar to those at Campo (e.g. linear models, black curve, close to the grey equality line). However, the dimensional data show slightly higher flows at Pyramides of 1 m^3s^{-1} and 1.4 m^3s^{-1} at Santaliestra. This can be explained by the contribution of tributaries.

Concerning the amplitudes of variation, the dimensional values of IC and DC show that they are practically similar to those of Campo. However, IC amplitudes show more dispersion (R^2 around 0.7) than DC amplitudes (R^2 around 0.87).

The MERR and MARR, as well as the total duration of variation (Figure 3.20 **B**, and **C**, right side), are the variables with the lowest correlation between upstream and downstream, particularly for variations in IC (R^2 only between 0.35 and 0.56). DC are lower than at Campo and the total duration of variation is longer. The DC are slower downstream (phenomenon illustrated by point *b* in Figure 3.19 **C**, gentler slope on the hydropeaks).

On the other hand, total IC duration are shorter downstream and MERR and MARR are higher, particularly at Pyramides (Figure 3.20 **B**, 3rd row). The slopes of the linear regression models for the models on dimensional data are 2 and 1.3 (columns 5 and 7) for Pyramides compared with only 0.95 and 0.78 for Santaliestra. For example, in Figure 3.19 **B**, the purple curve for hydropeak n°1 at Pyramides shows a steeper and faster rise than that at Campo (blue curve).

In summary, the total duration of hydropeaks increases downstream, the P_{Qmax} is earlier and decreases are much more attenuated than increases. At Pyramides, peak flows and IC raping rates appear to rise and then attenuate slightly towards Santaliestra.

Most of the peaks generated at Campo do not immediately reach peak flow. As shown in Figure 3.17, the median P_{Qmax} is 12%. It seems that despite a relatively shorter delay than for the Back Step and Tower shapes, the slightly later peak flow front nevertheless catches up the volumes released earlier with less intensity. This results in earlier P_{Qmax}, higher peak flows and higher ramping rates in the Pyramids and Santaliestra data.

However, it should be noted that the conversion of data into flow is based on the relationship between water level and flow, which means that an increase in water level will result in an estimated increase in flow. These "water level~flow" data were obtained by 2D hydraulic simulation in steady flow. However, it seems that hydropeak IC is a highly unstable phenomenon. The same water level could correspond to different flows (hysteresis). It is possible that the Q_{max} detected at the Pyramides and Santaliestra stations are slightly overestimated due to the detection of relatively high water levels despite potentially lower flow velocities due to retention effect during propagation

Figure 3.20: Scatterplots between the pairs of peaks identified between the Campo station (S1) and the downstream stations of Pyramides (S2) and Santaliestra (S3) **A** the peak characteristics, **B** Increase variation characteristics and **C** Decrease variation characteristics

3.2.3.3 Discussion

The two types of analysis carried out in this study, at the scale of the stations, and of the peaks association between hydrographs, made it possible to examine the propagation of hydropeaks and to establish propagation models. For the same peak shape, these two river segments show different propagation rates.

The model established from the characterization of the median $MARR_{norm}$ for the dominant shape Front Step on the two rivers is illustrated in Figure 3.21.

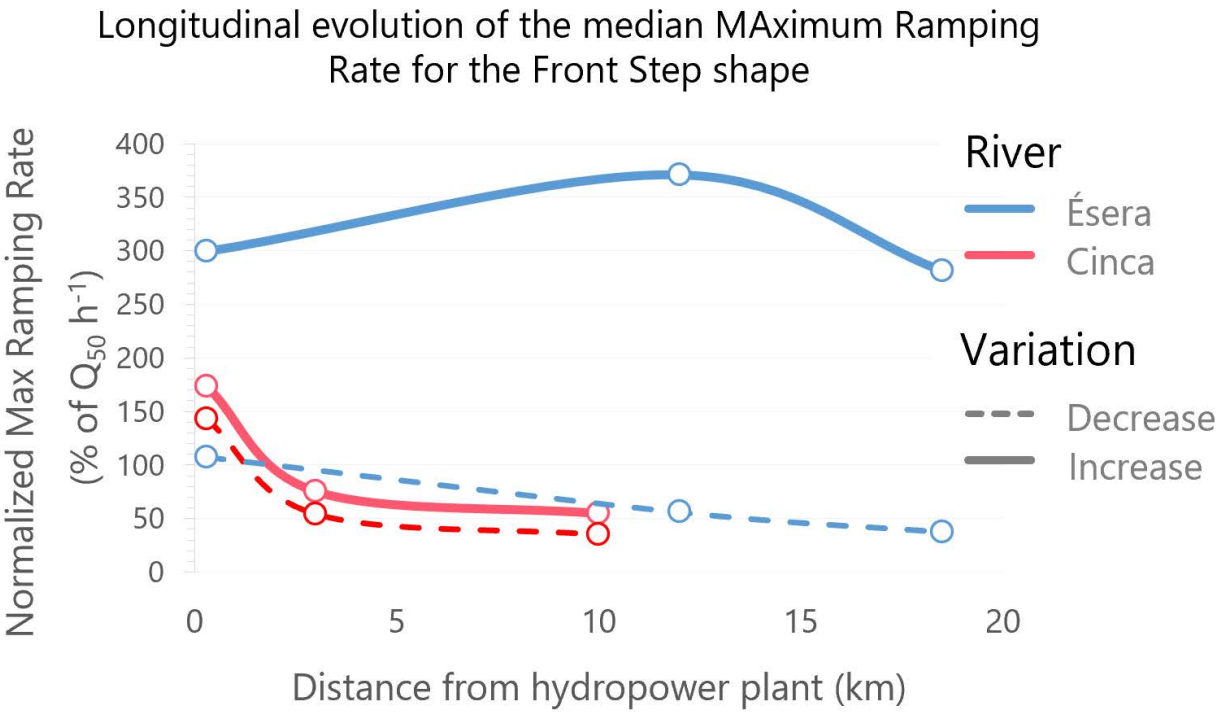

Figure 3.21: Maximum ramping rate propagation model for variations of increase and decrease for the two rivers studied.

The Cinca (red curves) shows similar damping for the IC and DC phases. $MARR_{norm}$ are reduced by an average of 60% for the first 3 km up to Escalona and by only 70% at Ainsa, 10 km downstream of the HP. These attenuations are not linear but of the power type. These results are similar to those of Greimel et al. (2016a) on a 10 km segment on the Ziller river in the Austrian Alpine region.

Decreases on the Ésera appear to diminish linearly (dotted blue curve). On the other hand, this dominant Front Step peak shape on the Ésera River shows IC RR (solid blue curve) that appear to be amplified or at least very weakly laminated over the 18 km studied. Such observations have already been reported by Magilligan and Nislow (2005) and by Fong et al. (2016) concerning confined rivers.

It is certain that the IC variations are not significantly attenuated. However, the apparent increases observed at Pyramides could be explained by its position in the segment (12 km downstream of the HP) and the tortuous morphology of the valley with its many gorges reaches. The segment presents a long reach between the 7 and 12 km from HP almost continuously confined. In confined canyon segments, Rennie et al. (2018) reported possible deceleration of velocities due to high wall friction and secondary circulation generating high roughness, so that flow resistance increases while water surface gradient and mean velocities decrease.

The damping of the first low-intensity wave fronts may be more significant in the gorged sections, allowing the later peak wave fronts, which are also attenuated but less strongly because of their higher velocity gradient, to catch up and be superimposed specifically in this gorges zone. This probably results in relatively high water levels at the exit of the gorges at 12km, at the Pyramides station, for water velocities that are certainly lower. This measuring station could show a significant hysteresis in the water level ~flow relationship linked to the highly unstable nature of the propagation of IC variations

3.2.4 CONCLUSION

The observations in terms of magnitude and timing are consistent with the results previously reported by Tena et al. (2022) in these same rivers, based on previous work by Fong et al. (2016). However, the frequency of appearance of the peak shapes differs. In some cases, it is difficult to compare the results because improvements were made by modifying the method previously used. The magnitude data has been normalized and the floods differentiated from the hydropeaks to better characterize the propagation of the latter without interference from values from natural and/or extreme peaks that could influence the trends. In addition, the median has been used here to describe the central trends instead of the mean in order to exclude any phenomenon or pattern of peaks or duration which may have high or very low values but which occur very rarely as a result, for example, of work on dams or on the HP.

Results demonstrated the importance of isolating each peak and taking into consideration the different peak shapes rather than a simple daily average metric assessment. Such analyses would not capture the multiple daily peaks that can occur, nor the different levels of attenuation downstream of each shape presenting significantly contrasting characteristics.

The central tendency analysis method led to observations that were relatively similar to those obtained by associated peak monitoring between hydrographs. Both showed that the IC phases are more variable than the decreases. Nevertheless, the peak tracking method allows the propagation of each peak to be characterized in detail. Thus, in the case of the development of an operational mitigation measurement strategy, such data is needed to set thresholds and targets to be achieved as a function of position in the basin. In cases where it is too complex to associate peaks between hydrographs, the simple analysis of distributions by station seems satisfactory for study and establishing propagation models for each type of variable analysed bases on normalized data.

Propagation models have clearly shown that the retention effect varies considerably depending on the river and its morphology, and that a complete understanding requires measurements to be taken at several points along the river if it has reaches with distinct morphological styles.

The longitudinal results of the peak characterization may be then coupled with bed mobility measurements to assess the influence of hydropeak regimes on sediment dynamics. In addition, these flow data sets positioned along the course of the river segments could be used to calibrate unsteady 2D hydraulic models.

These simulations would provide a better spatial detailing of the propagation of wave fronts for different fluvial morphologies over the whole of the impacted segments by these artificial pulses downstream of the HP, and verify whether the peak flows are really greater at Pyramides, and therefore the stream power, or whether these greater values than at the other two stations result from a hysteresis in the water level-flow relationship.

REFERENCES

Alonso, C., **Román, A.**, **Bejarano, M.D.**, **Garcia de Jalon, D.** and **Carolli, M.** (2017) A graphical approach to characterize sub-daily flow regimes and evaluate its alterations due to hydropeaking. *Sci. Total Environ.*, **574**, 532–543. DOI:10.1016/j.scitotenv.2016.09.087

Batalla, R.J., **Gibbins, C.N.**, **Alcázar, J.**, **Brasington, J.**, **Buendia, C.**, **Garcia, C.**, **Llena, M.**, **López, R.**, **Palau, A.**, **Rennie, C.**, **Wheaton, J.M.** and **Vericat, D.** (2021) Hydropeaked rivers need attention. *Environmental Research Letters*, **16**, 021001. DOI:10.1088/1748-9326/abce26

Batalla, R.J., **Gómez, C.M.** and **Kondolf, G.M.** (2004) Reservoir-induced hydrological changes in the Ebro River basin (NE Spain). *Journal of Hydrology*, **290**, 117–136. DOI:10.1016/j.jhydrol.2003.12.002

Bauersfeld, K. (1978) Stranding of juvenile salmon by flow reductions at mayfield dam on the cowlitz river, 1976. *State of Washington, Department of Fisheries*. ,https://books.google.es/books?id=uDB4GQAACAAJ

Béjar, M., **Gibbins, C.N.**, **Vericat, D.** and **Batalla, R.J.** (2017) Effects of Suspended Sediment Transport on Invertebrate Drift. *River Res. Appl.*, **33**, 1655–1666. DOI:10.1002/rra.3146

Béjar, M., **Vericat, D.**, **Batalla, R.J.** and **Gibbins, C.N.** (2018) Variation in flow and suspended sediment transport in a montane river affected by hydropeaking and instream mining. *Geomorphology*, **310**, 69–83. DOI:10.1016/j.geomorph.2018.03.001

Bejarano, M.D., **Sordo-Ward, Á.**, **Alonso, C.** and **Nilsson, C.** (2017) Characterizing effects of hydropower plants on sub-daily flow regimes. *J. Hydrol.*, **550**, 186–200. DOI:10.1016/j.jhydrol.2017.04.023

Benjamini, Y. and **Hochberg, Y.** (1995) Controlling the False Discovery Rate: A Practical and Powerful Approach to Multiple Testing. *Journal of the Royal Statistical Society: Series B (Methodological)*, **57**, 289–300. DOI:10.1111/j.2517-6161.1995.tb02031.x

Bevelhimer, M.S., **McManamay, R.A.** and **O'Connor, B.** (2015) Characterizing Sub-Daily Flow Regimes: Implications of Hydrologic Resolution on Ecohydrology Studies: SUB-DAILY STREAM FLOW METRICS. *River Res. Appl.*, **31**, 867–879. DOI:10.1002/rra.2781

Bilotta, G.S. and **Brazier, R.E.** (2008) Understanding the influence of suspended solids on water quality and aquatic biota. *Water Research*, **42**, 2849–2861. DOI:10.1016/j.watres.2008.03.018

Bladé, E., **Cea, L.**, **Corestein, G.**, **Escolano, E.**, **Puertas, J.**, **Vázquez-Cendón, E.**, **Dolz, J.** and **Coll, A.** (2014) Iber: herramienta de simulación numérica del flujo en ríos. *Revista Internacional de Métodos Numéricos para Cálculo y Diseño en Ingeniería*, **30**, 1–10. DOI:10.1016/j.rimni.2012.07.004

Blinn, W., **Shannon, J.P.**, **Stevens, L.E.** and **Carder, J.P.** (1995) Consequences of Fluctuating Discharge for Lotic Communities. *Journal of the North American Benthological Society*, **14**, 233–248. DOI:10.2307/1467776

Bradford, M.J., **Taylor, G.C.**, **Allan, J.A.** and **Higgins, P.S.** (1995) An Experimental Study of the Stranding of Juvenile Coho Salmon and Rainbow Trout during Rapid Flow Decreases under Winter Conditions. *North American Journal of Fisheries Management*, **15**, 473–479. DOI:10.1577/1548-8675(1995)015<0473:AESOTS>2.3.CO;2

Buendia, C., **Gibbins, C.N.**, **Vericat, D.** and **Batalla, R.J.** (2013a) Reach and catchment-scale influences on invertebrate assemblages in a river with naturally high fine sediment loads. *Limnologica*, **43**, 362–370. DOI:10.1016/j.limno.2013.04.005

Buendia, C., **Gibbins, C.N.**, **Vericat, D.**, **Batalla, R.J.** and **Douglas, A.** (2013b) Detecting the structural and functional impacts of fine sediment on stream invertebrates. *Ecological Indicators*, **25**, 184–196. DOI:10.1016/j.ecolind.2012.09.027

Carolli, M., **Bruno, M.C.**, **Siviglia, A.** and **Maiolini, B.** (2012) RESPONSES OF BENTHIC INVERTEBRATES TO ABRUPT CHANGES OF TEMPERATURE IN FLUME SIMULATIONS. *River Research and Applications*, **28**, 678–691. DOI:10.1002/rra.1520

Carolli, M., **Maiolini, B.**, **Silveri** and **Siviglia, A.** (2008) 4th ECRR conference on river restoration. Venezia, 789–796. ,http://hdl.handle.net/10449/16194

Carolli, M., **Vanzo, D.**, **Siviglia, A.**, **Zolezzi, G.**, **Bruno, M.C.** and **Alfredsen, K.** (2015) A simple procedure for the assessment of hydropeaking flow alterations applied to several European streams. *Aquat. Sci.*, **77**, 639–653. DOI:10.1007/s00027-015-0408-5

Casas-Mulet, R., **Alfredsen, K.**, **Boissy, T.**, **Sundt, H.** and **Rüther, N.** (2015) Performance of a One-Dimensional Hydraulic Model for the Calculation of Stranding Areas in Hydropeaking Rivers. *River Research and Applications*, **31**, 143–155. DOI:10.1002/rra.2734

Chang, W., **Cheng, J.**, **Allaire, J.**, **Sievert, C.**, **Schloerke, B.**, **Xie, Y.**, **Allen, J.**, **McPherson, J.**, **Dipert, A.** and **Borges, B.** (2023) Shiny: Web application framework for r. https://CRAN.R-project.org/package=shiny

Church (2006) BED MATERIAL TRANSPORT AND THE MORPHOLOGY OF ALLUVIAL RIVER CHANNELS. *Annual Review of Earth and Planetary Sciences*, **34**, 325–354. DOI:10.1146/annurev.earth.33.092203.122721

Courret, D., **Baran, P.** and **Larinier, M.** (2021) An indicator to characterize hydrological alteration due to hydropeaking. *Journal of Ecohydraulics*, **6**, 139–156. DOI:10.1080/24705357.2020.1871307

Crosa, G., **Castelli, E.**, **Gentili, G.** and **Espa, P.** (2010) Effects of suspended sediments from reservoir flushing on fish and macroinvertebrates in an alpine stream. *Aquatic Sciences*, **72**, 85–95. DOI:10.1007/s00027-009-0117-z

Fette, M., **Weber, C.**, **Peter, A.** and **Wehrli, B.** (2007) Hydropower production and river rehabilitation: A case study on an alpine river. *Environmental Modeling & Assessment*, **12**, 257–267. DOI:10.1007/s10666-006-9061-7

Fong, C.S., **Yarnell, S.M.** and **Viers, J.H.** (2016) Pulsed Flow Wave Attenuation on a Regulated Montane River: Pulsed Flow Wave Attenuation. *River Res. Appl.*, **32**, 1047–1058. DOI:10.1002/rra.2925

Fryirs, K.A. and **Brierley, G.J.** (2013) Geomorphic analysis of river systems: an approach to reading the landscape, 1. publ. *Wiley-Blackwell*, Chichester.

Gailiušis, B. and **Kriaučiūnienė, J.** (2009) Runoff Changes in the Lithuanian Rivers Due to Construction of Water Reservoirs. In: *Rural development 2009*, *Rural development: Proceedings of the International Scientific Conference*, Akademija, Kaunas region, Lithuania, 4, 24–28. ,https://hdl.handle.net/20.500.12259/254504

Galán, F. (2012) CENTRALES HIDROELÉCTRICAS Y PRESAS DEL ALTO ARAGÓN. *Fundation Esteyco*, Madrid, 90 pp.

García-Ruiz, J.M., **Puigdefábregas, J.** and **Novau, J.C.** (1986) La acumulación de nieve en el pirineo central y su influencia hidrológica. *Pirineos*, **127**, 27–72. DOI:http://hdl.handle.net/10261/95396

Garcıa-Ruiz, J.M., **Arnaez, J.**, **Begueria, S.**, **Seeger, M.**, **Martı-Bono, C.**, **Regues, D.**, **Lana-Renault, N.** and **White, S.** (2005) Runoff generation in an intensively disturbed, abandoned farmland catchment, Central Spanish Pyrenees.

Gibbins, C., **Vericat, D.**, **Batalla, R.J.** and **Gomez, C.M.** (2007) Shaking and moving: Low rates of sediment transport trigger mass drift of stream invertebrates. *Canadian Journal of Fisheries and Aquatic Sciences*, **64**, 1–5. DOI:10.1139/f06-181

Greimel, F., **Grün, B.**, **Hayes, D.S.**, **Höller, N.**, **Haider, J.**, **Zeiringer, B.**, **Holzapfel, P.**, **Hauer, C.** and **Schmutz, S.** (2023) PeakTrace : Routing of hydropeaking waves using multiple hydrographsA novel approach. *River Research and Applications*, **39**, 326–339. DOI:10.1002/rra.3978

Greimel, F., **Schülting, L.**, **Graf, W.**, **Bondar-Kunze, E.**, **Auer, S.**, **Zeiringer, B.** and **Hauer, C.** (2018) Hydropeaking Impacts and Mitigation. In: (Ed. S. Schmutz and J. Sendzimir), *Springer International Publishing*, Cham, 91–110. DOI:10.1007/978-3-319-73250-3_5

Greimel, F., **Zeiringer, B.**, **Hauer, C.**, **Holzapfel, P.**, **Fuhrmann, M.** and **Schmutz, S.** (2016a) LONGITUDINAL ASSESSMENT OF HYDROPEAKING IMPACTS AND EVALUATION OF MITIGATION MEASURES. *11th International Symposium on Ecohydraulics*, Melbourn, Autralia,

Greimel, F., **Zeiringer, B.**, **Höller, N.**, **Grün, B.**, **Godina, R.** and **Schmutz, S.** (2016b) A method to detect and characterize sub-daily flow fluctuations: Sub-Daily Flow Fluctuations - Austria. *Hydrol. Process.*, **30**, 2063–2078. DOI:10.1002/hyp.10773

Halkidi, M., **Batistakis, Y.** and **Vazirgiannis, M.** (2001) On Clustering Validation Techniques. *Journal of Intelligent Information Systems*, **17**, 107–145. DOI:10.1023/A:1012801612483

Hannah, D.M., **Smith, B.P.G.**, **Gurnell, A.M.** and **McGregor, G.R.** (2000) An approach to hydrograph classification. *Hydrol. Process.*, **14**, 317–338. DOI:10.1002/(SICI)1099-1085(20000215)14:2<317::AID-HYP929>3.0.CO;2-T

Hauer, C., **Blamauer, B.**, **Mühlmann, H.** and **Habersack, H.** (2014) Morphodynamische Aspekte der Ökohydraulik und Habitatmodellierung im Kontext der rechtlichen Rahmenbedingungen. *Österreichische Wasser- und Abfallwirtschaft*, **66**, 169–178. DOI:10.1007/s00506-014-0151-5

Hauer, C., **Leitner, P.**, **Unfer, G.**, **Pulg, U.**, **Habersack, H.** and **Graf, W.** (2018) The Role of Sediment and Sediment Dynamics in the Aquatic Environment. In: (Ed. S. Schmutz and J. Sendzimir), *Springer International Publishing*, Cham, 151–169. DOI:10.1007/978-3-319-73250-3_8

Hauer, C., **Schober, B.** and **Habersack, H.** (2013) Impact analysis of river morphology and roughness variability on hydropeaking based on numerical modelling: RIVER MORPHOLOGICAL IMPACTS ON HYDROPEAKING PROCESSES. *Hydrol. Process.*, **27**, 2209–2224. DOI:10.1002/hyp.9519

Hauer, G.U.H.H.(Wien/Österreich),.U.P.(Bergen/Norwegen). und J.S.(München). (2013) Bedeutung von Flussmorphologie und Sedimenttransport in Bezug auf die Qualität und Nachhaltigkeit von Kieslaichplätzen. *Bedeutung von Flussmorphologie und Sedimenttransport in Bezug auf die Qualität und Nachhaltigkeit von Kieslaichplätzen*, **2013**, 189–197. DOI:10.3243/kwe2013.04.002

Hunter, M.A. and **Fisheries, W.(State).D. of** (1992) Hydropower flow fluctuations and salmonids: A review of the biological effects, mechanical causes, and options for mitigation. *State of Washington, Department of Fisheries, Habitat Management Division*. https://books.google.es/books?id=HKoiywAACAAJ

Irvine, R.L., **Thorley, J.L.**, **Westcott, R.**, **Schmidt, D.** and **DeRosa, D.** (2015) Why do fish strand? An analysis of ten years of flow reduction monitoring data from the Columbia and Kootenay rivers, Canada: Analysis of ten years of Columbia and Kootenay fish stranding data. *River Res. Appl.*, **31**, 1242–1250. DOI:10.1002/rra.2823

Jager, H.I. and **Bevelhimer, M.S.** (2007) How Run-of-River Operation Affects Hydropower Generation and Value. *Environmental Management*, **40**, 1004–1015. DOI:10.1007/s00267-007-9008-z

Kaufman, L. and **Rousseuw, P.J.** (1990) Finding Groups in Data: An Introduction to Cluster Analysis. *Biometrics*, **47**, 788. DOI:10.2307/2532178

Kemp, P., **Sear, D.**, **Collins, A.**, **Naden, P.** and **Jones, I.** (2011) The impacts of fine sediment on riverine fish. *Hydrological Processes*, **25**, 1800–1821. DOI:10.1002/hyp.7940

Kjelland, M.E., **Woodley, C.M.**, **Swannack, T.M.** and **Smith, D.L.** (2015) A review of the potential effects of suspended sediment on fishes: potential dredging-related physiological, behavioral, and transgenerational implications. *Environment Systems and Decisions*, **35**, 334–350. DOI:10.1007/s10669-015-9557-2

Leitner, P., **Hauer, C.** and **Graf, W.** (2017) Habitat use and tolerance levels of macroinvertebrates concerning hydraulic stress in hydropeaking rivers – A case study at the Ziller River in Austria. *Sci. Total Environ.*, **575**, 112–118. DOI:10.1016/j.scitotenv.2016.10.011

Llena, M., **Vericat, D.**, **Martínez-Casasnovas, J.A.** and **Smith, M.W.** (2020) Geomorphic adjustments to multi-scale disturbances in a mountain river: A century of observations. *CATENA*, **192**, 104584. DOI:10.1016/j.catena.2020.104584

Lobera, G., **Batalla, R.J.**, **Vericat, D.**, **López-Tarazón, J.A.** and **Tena, A.** (2016) Sediment transport in two mediterranean regulated rivers. *Science of The Total Environment*, **540**, 101–113. DOI:10.1016/j.scitotenv.2015.08.018

López-Tarazón, J.A., **Batalla, R.J.**, **Vericat, D.** and **Francke, T.** (2012) The sediment budget of a highly dynamic mesoscale catchment: The River Isábena. *Geomorphology*, **138**, 15–28. DOI:10.1016/j.geomorph.2011.08.020

Maechler, M., **Rousseeuw, P.**, **Struyf, A.**, **Hubert, M.** and **Hornik, K.** (2018) Cluster: Cluster analysis basics and extensions. ,https://CRAN.R-project.org/package=cluster

Magilligan, F.J. and **Nislow, K.H.** (2005) Changes in hydrologic regime by dams. *Geomorphology*, **71**, 61–78. DOI:10.1016/j.geomorph.2004.08.017

Mangiafico, S.S. (2023) Package rcompanion: Functions to support extension education program evaluation.

Martínez, C. and **Fernández, J.A.** (2010) Indices de alteración hidrológica (IAHRIS 3.0): Manual de referencia metodológica. *Universidad Politécnica de Madrid*. https://www2.montes.upm.es/dptos/digfa/Investigaci%C3%B3n/Para%20WEB%20Departamento/IAHRIS%203.0_Manual%20de%20referencia%20metodologica_20211024.pdf

Meile, T., **Boillat, J.-L.** and **Schleiss, A.J.** (2011) Hydropeaking indicators for characterization of the Upper-Rhone River in Switzerland. *Aquat. Sci.*, **73**, 171–182. DOI:10.1007/s00027-010-0154-7

Ng, R.T. and **Han, J.** (1994) Proceedings of the 20th VLDB Conference. Santiago, Chile, https://citeseerx.ist.psu.edu/document?repid=rep1&type=pdf&doi=375c3b4753410b642cd404b9625ecedde043bd1b

Owen, J. (2021) Rhandsontable: Interface to the 'handsontable.js' library. ,https://CRAN.R-project.org/package=rhandsontable

Pfaundler, M. and **Keusen, M.** (2007) Veränderungen von Schwall-Sunk. Hydrologische Datenanalyse zur Charakterisierung von Schwall-Sunk Phänomenen in der Schweiz. *Bundesamt für Umwelt BAFU*.

Poff, N.L., **Allan, J.D.**, **Bain, M.B.**, **Karr, J.R.**, **Prestegaard, K.L.**, **Richter, B.D.**, **Sparks, R.E.** and **Stromberg, J.C.** (1997) The Natural Flow Regime: A paradigm for river conservation and restoration N. *BioScience*, **47**, 769–784. DOI:10.2307/1313099

Pulg, U., **Barlaup, B.T.**, **Sternecker, K.**, **Trepl, L.** and **Unfer, G.** (2013) RESTORATION OF SPAWNING HABITATS OF BROWN TROUT (SALMO *TRUTTA*) IN A REGULATED CHALK STREAM. *River Research and Applications*, **29**, 172–182. DOI:10.1002/rra.1594

Rempel, L.L., **Richardson, J.S.** and **Healey, M.C.** (2000) Macroinvertebrate community structure along gradients of hydraulic and sedimentary conditions in a large gravel-bed river. *Freshwater Biology*, **45**, 57–73. DOI:10.1046/j.1365-2427.2000.00617.x

Rennie, C.D., **Church, M.** and **Venditti, J.G.** (2018) Rock Control of River Geometry: The Fraser Canyons. *J Geophys Res Earth Surf*. DOI:10.1029/2017JF004458

Richter, B., **Baumgartner, J.**, **Wigington, R.** and **Braun, D.** (1997) How much water does a river need? *Freshw. Biol.*, **37**, 231–249. DOI:10.1046/j.1365-2427.1997.00153.x

Richter, B.D., **Baumgartner, J.V.**, **Powell, J.** and **Braun, D.P.** (1996) A Method for Assessing Hydrologic Alteration within Ecosystems. *Conserv. Biol.*, **10**, 1163–1174. DOI:10.1046/j.1523-1739.1996.10041163.x

Rousseeuw, P.J. (1987) Silhouettes: A graphical aid to the interpretation and validation of cluster analysis. *Journal of Computational and Applied Mathematics*, **20**, 53–65. DOI:10.1016/0377-0427(87)90125-7

Rubio, V. (1995) Dinámica fluvial del río ara (pirineo aragonés). PhD thesis,https://repositorio.uam.es/handle/10486/6520?show=full

Sauterleute, J.F. and **Charmasson, J.** (2014) A computational tool for the characterisation of rapid fluctuations in flow and stage in rivers caused by hydropeaking. *Environ. Model. Softw.*, **55**, 266–278. DOI:10.1016/j.envsoft.2014.02.004

Schmutz, S., **Bakken, T.H.**, **Friedrich, T.**, **Greimel, F.**, **Harby, A.**, **Jungwirth, M.**, **Melcher, A.**, **Unfer, G.** and **Zeiringer, B.** (2015) Response of fish communities to hydrological and morphological alterations in hydropeaking rivers of austria. River Research and Applications. DOI:10.1002/rra.2795

Sturm, T.W. (2001) Open channel hydraulics. *McGraw-Hill*, Boston.

Sutherland, A.B., **Meyer, J.L.** and **Gardiner, E.P.** (2002) Effects of land cover on sediment regime and fish assemblage structure in four southern Appalachian streams. *Freshwater Biology*, **47**, 1791–1805. DOI:10.1046/j.1365-2427.2002.00927.x

Tena, A., **Ville, F.**, **Reñe, A.**, **Yarnell, S.M.**, **Batalla, R.J.** and **Vericat, D.** (2022) Hydrological characterization of hydropeaks in mountain rivers (examples from Southern Pyrenees). *River Research & Apps*, rra.4058. DOI:10.1002/rra.4058

Tonolla, D., **Dossi, F.**, **Kastenhofer, O.**, **Doering, M.**, **Hauer, C.**, **Graf, W.** and **Schülting, L.** (2023) Effects of hydropeaking on drift, stranding and community composition of macroinvertebrates: A field experimental approach in three regulated Swiss rivers. *River Research and Applications*, **39**, 427–443. DOI:10.1002/rra.4019

Townsend, C.R., **Scarsbrook, M.R.** and **Dolédec, S.** (1997) Quantifying Disturbance in Streams: Alternative Measures of Disturbance in Relation to Macroinvertebrate Species Traits and Species Richness. *Journal of the North American Benthological Society*, **16**, 531–544. DOI:10.2307/1468142

Tuset, J., **Vericat, D.** and **Batalla, R.J.** (2015) Evolución morfo-sedimentaria del tramo medio del río Segre. *CIG*, **41**, 23–62. DOI:10.18172/cig.2707

Valentin, S., **Wasson, J.G.** and **Philippe, M.** (1995) Effects of hydropower peaking on epilithon and invertebrate community trophic structure. *Regulated Rivers: Research & Management*, **10**, 105–119. DOI:10.1002/rrr.3450100207

Vanderkam, D., **Allaire, J.**, **Owen, J.**, **Gromer, D.** and **Thieurmel, B.** (2018) Dygraphs: Interface to 'dygraphs' interactive time series charting library. https://CRAN.R-project.org/package=dygraphs

Vanzo, D., **Zolezzi, G.** and **Siviglia, A.** (2016) Eco-hydraulic modelling of the interactions between hydropeaking and river morphology. *Ecohydrology*, **9**, 421–437. DOI:10.1002/eco.1647

Verdu, J.M., **Batalla, R.J.** and **Martinez-Casanovas, J.A.** (2006) Estudio hidrologico de la cuanta del rio Isabena (cuenta del Ebro). I: Variabilidad de la precipitation. **13**, 10.

Vericat, D., **Ville, F.**, **Palau-Ibars, A.** and **Batalla, R.J.** (2020) Effects of hydropeaking on bed mobility: Evidence from a pyrenean river. *Water*, **12**, 178. DOI:10.3390/w12010178

Wickham, H., **Averick, M.**, **Bryan, J.**, **Chang, W.**, **McGowan, L.D.**, **François, R.**, **Grolemund, G.**, **Hayes, A.**, **Henry, L.**, **Hester, J.**, **Kuhn, M.**, **Pedersen, T.L.**, **Miller, E.**, **Bache, S.M.**, **Müller, K.**, **Ooms, J.**, **Robinson, D.**, **Seidel, D.P.**, **Spinu, V.**, **Takahashi, K.**, **Vaughan, D.**, **Wilke, C.**, **Woo, K.** and **Yutani, H.** (2019) Welcome to the tidyverse. *Journal of Open Source Software*, **4**, 1686. DOI:10.21105/joss.01686

Young, P.S., **Cech, J.J.** and **Thompson, L.C.** (2011) Hydropower-related pulsed-flow impacts on stream fishes: a brief review, conceptual model, knowledge gaps, and research needs. *Reviews in Fish Biology and Fisheries*, **21**, 713–731. DOI:10.1007/s11160-011-9211-0

Zolezzi, G., **Bellin, A.**, **Bruno, M.C.**, **Maiolini, B.** and **Siviglia, A.** (2009) Assessing hydrological alterations at multiple temporal scales: Adige River, Italy: HYDROLOGICAL ALTERATIONS OF THE ADIGE RIVER. Water Resour Res. DOI:10.1029/2008WR007266

Zolezzi, G., **Siviglia, A.**, **Toffolon, M.** and **Maiolini, B.** (2011) Thermopeaking in Alpine streams: event characterization and time scales. *Ecohydrology*, **4**, 564–576. DOI:10.1002/eco.132

Chapter 4

Bed-material entrainment in a mountain river affected by hydropeaking

Downstream view of the Upper Ésera River flowing in the Santaliestra study section during a small flood, 09/11/2020. Author: Fanny Ville

This chapter contains the following accepted and already online published paper in the journal Science of the Total Environment. JCR-SCI Impact Factor: 10.909. 1st Quartile (Environmental Sciences) . López, R., Ville, F., Garcia, C., Batalla, R.J., Vericat, D., 2023. Bed-material entrainment in a mountain river affected by hydropeaking. *Science of The Total Environment* 856, 159065. https://doi.org/10.1016/j.scitotenv.2022.159065

Abstract: Hydropeaking, by artificially generated flow peaks, influences hydro-sedimentary dynamics on rivers and, consequently, affects bed material entrainment and transport. This study examines the onset of motion of sediment particles in four sections of a Pyrenean gravel-to-cobble bed river exposed to frequent hydropeaking (once per day, on average). Five criteria of particle entrainment have been used to assess the prediction of the initiation of grain motion in each section. Theoretical entrainment conditions were validated using real observations of mobility by means of tracers. It was found that the maximum flow discharged by the hydropower plant mostly affects the furthest downstream section, located almost 17 km downstream, in which the finer fractions of the bed are entrained. The mobile grain sizes include up to coarse gravels (≈ 30 mm). Differences in sediment supply (imposed by tributaries), the value of the bed slope and the structure of the coarse surface layer decisively control the downstream variability of incipient particle motion between sections. Results from a 17 km study segment indicated that hydropeaking generate partial transport, that is, a partially size-selective transport that occurs downstream from the hydropower plant and winnows the sand and small gravel further downstream, increasing armouring and depleting fine sediments.

Keywords: Sediment motion threshold, Bed-mobility, Tracer particle, Partial transport, Hydropower plant, Hydropeak

4.1 INTRODUCTION

Hydropower (hereafter HP) is presently perceived as a major sustainable alternative for renewable energy generation. However, this type of production typically affects the physical structure and process of the fluvial systems hosting HP stations. The generation of energy by means of turbines (whether they are associated to dams and weirs, or placed in run-of-the river production schemes, or both) causes sudden pulses, called hydropeaks, to river flow. These pulses are controlled by the demand for electric power. Hydropeaking alters the hydrological regime and flow hydraulics, hence habitat availability, therefore influencing the overall ecology of the river (see examples in Hauer et al., 2014b; Schmutz et al., 2015; Vanzo et al., 2016a; Smokorowski, 2022; and a complete review in Hayes et al., 2022). Sediment dynamics (river-bed structure, transport) are arguably amongst the processes affected by hydropeaking. Therefore, the need arises to keep analysing the effects of hydropeaks on multiple features of river processes, including sediment transport, with the aim of achieving the best possible coexistence between hydroelectricity generation and preservation of fluvial environments. The effect of hydropeaks on sedimentary processes, particularly bed-material entrainment, has not been extensively investigated (see some of the few examples in López et al., 2020 and Vericat et al., 2020). Scarcity of observational data is likely the main reason for this, and the absence of data and their transferability impede generalisation of results in comprehensive assessment of the impacts of hydropeaks on river behaviour.

Naturally, river bed particles are consecutively entrained, transported and deposited in river channels on the occasion of competent flow events (Church, 2006). The balance between the flow and weight destabilizing forces (which tend to put particles into motion) and resisting or stabilizing forces (function of variables such as particle grain-size and density, angularity, hiding or protrusion of grains, and packing) determines the critical condition for incipient sediment motion (e.g. see Julien, 2002 and Garcia, 2008 for further details), which controls the frequency and magnitude of changes in channel geometry and form.

Bed material transport in gravel bed streams commonly occurs at low rates. In this condition, the bed is only partially mobilized, a flow condition in which a portion of the grains on the bed surface are actively transported (Wilcock and McArdell, 1993), and much of the bed material, mainly the coarser, remains in place for extended periods of time (Hassan and Church, 2000).

River-bed sediments are commonly variable in both the vertical (in depth) and cross-sectional channel dimensions, as well as longitudinally (downstream). Vertically, the coarse surface layer is typically well sorted (i.e. greater selection of size classes, less scattered), while subsurface sediments typically show poorly sorted distribution, which leads to a wider grain size range (e.g. Parker and Klingeman, 1982; Vericat et al., 2006; Wilcock and DeTemple, 2005). The result is a coarse surface layer (i.e. armour) protecting subsurface sediments, which comprises the majority of the fractions present in the bed surface but also a substantial proportion of fine fractions (e.g. sand and fine gravel) not observed in the surface. This non-uniformity in grain sizes (sediment mixtures and depth variability) implies a greater conceptual and practical complexity to determining thresholds of sediment motion.

Mobility, furthermore, is conditioned by bed structure, which has a direct effect on particle hiding and protrusion (White, 1982). This implies that, compared to uniform grain size beds, fine particles may require a higher threshold and coarser grains a lower one. Comparatively finer particles are protected by the larger ones, which protrude over the bed; under such grain-size and bed structural conditions, an increase of flow discharge (hereafter Q) does not necessarily imply a proportional increase in sediment mobility, hence, bed-material transport. The structure of sediment mixtures works to equalize the threshold shear stress required for the motion of all grains or equal-threshold scenario in opposition to the size-independence (hiding-free) limiting case where the initiation of transport of sediment mixtures would be highly selective based on grain size (Parker, 2008).

After reaching the mobility threshold, the bed begins to destabilize. Flows high above the threshold of sediment motion can unchain a larger destabilization, which, if it endures, may even cause changes in whole river morphology (e.g. effects on channel geometry and forms, and grain-size distribution). These dynamics also depend on the upstream supply of sediment, a process that is significantly affected in the presence of a dam. Streams with large sediment supply have finer textures, poorly developed surface structures and higher sediment transport rates (e.g., Lisle and Madej, 1992). When the sediment supply is low the development of a well-structured, coarse-textured bed significantly reduces the sediment transport rates (Church et al., 1998; Dietrich et al., 1989). It is important to characterize sediment motion thresholds, to understand the occurrence and the magnitude of events causing bed destabilization. In the particular case of hydropeaked rivers, such processes must be related to the competence, frequency and magnitude of such artificial flow pulses.

In addition, clogging of river bed surface by fines (silt, clay, fine sand) often carries collateral deleterious effects in hydropeaked rivers, especially in those affected by run-off-the river schemes, where by-passed river reaches are depleted from discharges capable to keep the transport of fines in suspension, thus favouring sedimentation. Fine sediment infiltration within the bed matrix has an impact on primary production, causing decreased variety and abundance of benthic macroinvertebrates (Wood, 1997), also affecting salmonid reproduction (Coulombe-Pontbriand and Lapointe, 2004); moreover the loss of porosity and permeability alter water exchanges between surface- and ground-waters (Brunke, 1999), and chemical interactions such as water temperature (Packman and MacKay, 2003).

River-bed sediments also vary spatially, in the cross-sectional channel dimensions and along river reaches and segments. Surface patches of fine sediment are also common in gravel-bed rivers. Patches are formed by accumulations of sand and gravel around particles of larger diameter, which provide a protective effect on the surrounding particles and favour sedimentation (e.g. Garcia et al., 1999). They occupy small proportions of river channels and the entrainment and transport of sediment from these structures hardly modify channel morphology (Vericat et al., 2008c), but their mobilisation can be the cause of significant impacts on river ecological processes. For example, Gibbins et al., (2007a) found that incipient bedload discharge from patches unchains involuntary macroinvertebrate drift in gravel-bed rivers.

Processes of partial bed mobility impelled by sediment mobilization from patches are frequent in human-impacted river sites. This is the case in reaches exposed to hydropeaking in which flow discharge is artificially raised without a sediment supply from upstream. Fine grain fractions (i.e. sand, granules, fine and medium gravel), which are essential to a suite of river processes (e.g. fish spawning, invertebrate refugia), can be then entrained and depleted during competent events, unchaining for instance massive involuntary drift of fauna (also known as catastrophic drift i.e. disturbances such as floods physically dislodge animals) (e.g. Gibbins et al. 2007a). The mobilisation of grains in these areas, even the mere particle agitation, can trigger such processes (Batalla et al., 2010; Vericat et al., 2008c). Fine grains offer stimulating spots for fish spawning and refugia for juveniles, given that hydraulics tends to be less intense (i.e. lower shear stress) in those depressed areas in comparison to the surrounding protruding particles. The integrity of the particle architecture in gravel-bed rivers appears to be an essential factor in assuring the integrity of physical habitat.

Mobilisation of sand and fine gravel appears to be quite an effective and frequent process downstream from HP plants; however, the insufficiency of studies precludes simple generalisations on the effects of such artificial flows onto sediment dynamics. As has been recently discussed by Batalla et al. (2021), it is thus essential to search for empirical evidence and model simulations to improve knowledge of the magnitude of the effects of these fluctuating flows on river structure and processes. Naturally (i.e. dam absence), floods transfer bedload from upstream, favouring the presence of patches of fine sediments (sand, fine gravel); in contrast, hydropeaking favours the exhaustion of fine sediments and the loss of such river bed structures (Vericat et al., 2020). Generally, gravel augmentation downstream dams has been used to ameliorate adverse effects of dams on river functioning (see initial works in Kondolf, 1997), as well more recent experiences (e.g. Chardon et al., 2021); with increasing interest in by-passed reaches on rivers affected by hydropeaking (e.g. Arnaud et al., 2017).

As stated, despite previous studies analysing the environmental effects of hydropeaking (see early works by Cushman, 1985; Moog, 1993; Cereghino and Lavandier, 1998), there is still a lack of studies examining their influence on river sedimentary dynamics and, in particular, on bed-material entrainment (see Aigner et al., 2017; López et al., 2020; Vericat et al., 2020) as some few recent examples). From a broad perspective there are still numerous research questions that have not been fully addressed in the field of sediment transport in hydropeaked rivers such as (i) how does hydropeaking might affect bed armouring? (ii) what are the effects of hydropeaking on the removal and depletion of fines which are, in turn, essential for a variety of river biophysical processes? and (iii) what are the downstream effects of mobilization of deposited sediment in hydropeaked rivers? All these questions have in common the need to examine the onset of particles from the bed. Within this context, the objective of this work is to further address these fundamental questions by analysing the changes on the entrainment of bed particles in a segment of a Central Pyrenean river subjected to a hydropeaking. Theoretical approaches (i.e. formulae, hydraulic estimations, entrainment predictions, see Section 4.3.6 for more details) were contrasted with particle tracer data, obtained in several sections regularly exposed to such flow pulses, in order to investigate downstream changes of threshold of sediment motion.

4.2 STUDY AREA

The study was carried out in the River Ésera (Central Pyrenees, Figure 4.1 **A**), over a 17-km long river segment between the Campo dam and the village of Santaliestra and San Quílez (Figure 4.1 **B**). The catchment area at the outlet of the study reach is 733 km². The basin has an elongated shape and the length of the main channel is around 75 km. Altitude varies between 3400 m and 540 m asl, with 85% of the catchment located at altitudes higher than 1000 m asl. More than 70% of the area has slopes between 30% and 100%, and almost 10% of the area has slopes above 100%. Catchment relief makes this basin a poorly populated region. Almost 53% of its surface is occupied by herbaceous stratum vegetation or is without vegetation cover (bare soils), while the remaining 41% is covered by forests, and 6% is used for agricultural purposes.

The mean annual runoff registered at the gauging station of Campo (operated by the Ebro Water Authorities SAIH-CHE, code A-258, Figure 4.1) for the period 1994-2016 is 517 hm^3 (i.e. 1 hm^3 = 10^6 m^3), yielding a mean annual discharge of 16 $m^3\ s^{-1}$. Mean annual maximum instantaneous discharge (i.e. annual flood) reaches 200 $m^3\ s^{-1}$, while less frequent floods (e.g. 10-year return period) can attain 470 $m^3\ s^{-1}$. The River Ésera is subjected to several impacts related to changes in land use (mostly natural afforestation), damming, and hydropeaking. The water flow at the inlet of the study segment is regulated by a network of seven hydropower plants that became operational in the first half of the 20th century. The cumulative capacity of the production units is 177 MW. The Eriste and Sesué HP plants (both located upstream of the study reach) have reservoirs with a capacity of 3.15 hm^3 and 2.17 hm^3, respectively, providing daily flow regulation (Galán, 2012). The rest of the downstream HP plants (Seira, Argoné, and Campo) operate with run-of-the-river schemes associated with weirs and small dams built in the river course and 35 km of galleries, which allow the water to be diverted to the production unit.

The maximum turbine discharge at the Campo HP plant (inlet of the study reach) is 20 $m^3\ s^{-1}$. On average, one hydropeak is generated per day, with a mean duration of 12 h and a mean discharge around 15.4 $m^3\ s^{-1}$ (Tena et al., 2022). Hydropeaking is also conditioned by the needs of recreational uses (e.g. rafting). The magnitude of the floods is little affected by the dam, due to their evacuation through the spillway and bottom outlet; however, the dam has a direct effect on trapping sediments; virtually all bedload is trapped while an important proportion of the suspended load is retained. This indicates that sediment supply at the inlet of the study segment is negligible and it is controlled by downstream sources such as direct hillslope erosion or tributaries. Hillslopes are composed by coarse formations like the alluvial terrace and conglomerates (44%), mudstones, marl and sandstones (32%) and limestones (15%). The most important tributaries downstream are the rivers Rialbo, Bacamorta and Foradada, composed of allochemical formations (limestone and dolomite: 50%), coarse loose formations (conglomerate, colluvium: 30%) and fine friable formations (mudstones marl and sandstone: 20%). Therefore, bed-material dynamics in the study segment will be directly influenced by bed structure (degree of armouring), in-channel sediment availability and the supply from the aforementioned sources or tributaries.

The bed is characterized as a gravel-to-cobble channel bed. The channel presents entrenched and meandering riffle-pool river reaches. The valley is highly confined due to topographical and geological context. Mapping of the valley bottom confinement using the GIS tool developed by O'Brien et al. (2019b) indicates that 58.5% of the length is confined (lateral confinement of both banks) and 36.5% is confined to one side. Only 4.5% of the main channel is open (see confinement map in Figure 4.1 **B** for more details). The active width ranges between 18 m and 178 m, while the mean channel gradient is 0.7%. The average median bed surface material is 77 mm (see more information on the spatial variability of surface materials in the results section). It should also be noted that there are patches of fine materials consisting of fine gravel, sand, clay and silt. The size of these structures varies through time, influenced by the supply of sediment from tributaries and hillslopes.

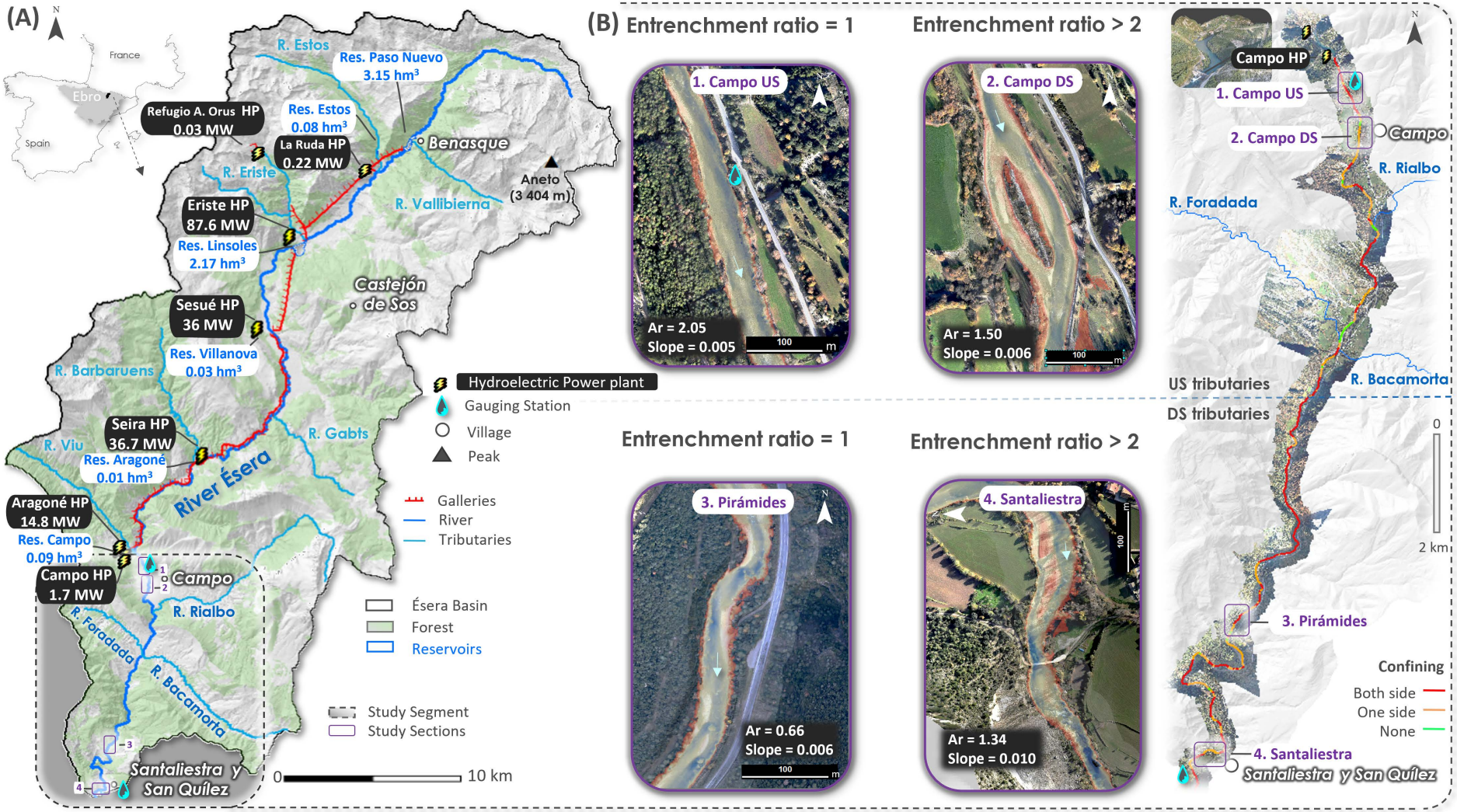

Figure 4.1: (**A**) Location of the Ésera catchment, the study segment and the study sections. (**B**) Aerial photography of each section with general characteristics. The configuration of the study segment and the study sections can be seen in the aerial photographs, together with the location of hydropower plant and tributaries. The spatial variability of the confinement is also indicated by a colour scale. Ar is the armouring ratio.

Four study sections, referred to as Campo Upstream, Campo Downstream, Pirámides and Santaliestra (from upstream to downstream, Figure 4.1) have been selected. All study sections are situated downstream of the HP plant outlet. The first two sections are located between the Campo HP plant and the confluence with the main tributaries. The river bed presents an armouring ratio (i.e. the quotient between the surface and subsurface median particle size) of 2.05 in Campo Upstream; hence, the bed can be qualified as armoured. The armouring ratio in Campo Downstream is smaller (i.e. 1.50) than the one observed near the dam. In both sections the armour is broken-up during annual competent floods. Campo Upstream is the studied section with the largest armouring value. This attributed to the proximity to the dam and the negligible sediment supply form upstream. These two sections are contrasted in terms of confinement. The entrenchment ratio (i.e. ratio of the valley width to the active width, as per Rosgen David L., 1994) is 1 for Campo Upstream and 2.4 for Campo Downstream. The Pirámides and Santaliestra sections are located downstream of the tributaries, and bed armouring ratio is 0.66 and 1.34, respectively (hence, not armoured). Pirámides has an entrenchment ratio of 1 and a mean slope of 0.6%, while Santaliestra is steeper (geological control), with a slope of 1%, and wider, with an entrenchment ratio equal to 2.0.*

4.3 MATERIAL AND METHODS

4.3.1 Channel topography

Channel topography was acquired by high-resolution topography, obtained by means of digital photogrammetry, specifically through Structure from Motion and Multi View Stereo Digital Photogrammetry (hereafter SfM) algorithms. Overall, SfM photogrammetry allow extracting high resolution orthophotomosaics and point clouds from a given number of images with overlapping scene (e.g. James and Robson, 2012; Westoby et al., 2012; Carrivick and Smith, 2019). A set of 1 240 aerial photographs were taken from an autogiro at a flight altitude of approximately 350 m above the ground (Figure 4.2 **A**). An SLR Nikon D750 (28 mm Lens) camera was used. Digital photographs were processed with *Agisoft Photoscan Professional 1.2.2*. In order to georeference, calibrate the cameras and get a correct scaling (i.e. registration), a total of 154 Ground Control Points (GCPs) were placed along 17 km of the river on both banks. Their GPS coordinates were recorded through an RTK-GNSS system (Leica Viva GS15) allowing 3D quality below 5 cm. Of the 154 GCPs, 77 GCPs were used to register the point cloud while the other 77 points were used as check points to quantify the errors. The 2D horizontal error (root mean square error) was 0.056 m, while the vertical error was 0.13 m on dry areas and 0.25 m in the submerged areas. The point cloud in wet surfaces is affected by refraction of light at the air-water interface. After the correction of the refraction in the submerged areas, the vertical error decreased to 0.185 m. This correction is fully described below. An orthophotomosaic with a resolution of 0.1 m and a terrain point cloud with a mean density of 46 points m^{-2} (Figure 4.2 **A**) were generated over an area of 14.2 km^2.

As indicate, the point cloud in wet surfaces is affected by refraction of light at the air-water interface. This effect causes an underestimation of the depths (e.g. Figure 4.2 **B**) because light rays passing through an air-water interface are shifted and depths, and thus elevation, are biased. To correct this bias, an empirical refractive correction model was applied to the data following the procedure of Woodget et al. (2015): $d = n_1 d_a$, where the real depth (d) can be estimated by knowing the apparent water depth (d_a) and the refractive index or coefficient (n_1). A set of 644 check points was collected during the day before the flight (Figure 4.2 **A**); 286 of these in exposed sediments and 358 in the submerged channel perimeter (from 0 to 1.3 m depth). Water flow on the day of the flight was the same as the day the check points were surveyed. Check points in the submerged zoned allowed both to develop the empirical refractive model and to evaluate the general accuracy of the channel bathymetry. A set of 70% of the submerged points was used to fit the empirical refractive correction model. The remaining 30%, called the test data set, were used to evaluate the accuracy of the data

once corrected. Each elevation value (m asl) of the submerged check points (Z_{ChP}) was transformed to water depth (d). In order to make this transformation, a model of the water surface elevation (Z_{WSE}) needed to be developed, as will be explained. The water depth of each point was obtained by subtracting the elevation of the submerged check points from the water surface elevation (i.e. $d = Z_{WSE} - Z_{ChP}$, see Figure 4.2 **B** for a graphical representation of this transformation).

To generate the water surface elevation (hereafter WSE) model, an un- corrected Digital Surface Model, computed from *Agisoft Metashape Professional 1.6.5*, and a uniform Manning's roughness coefficient value of 0.025 s $m^{-1/3}$ were used to run a series of flow simulations along the study segment, by means of the Iber 2D hydraulic model (see Section 4.3.4 for details in terms of modelling). This value of Manning's coefficient (n_M) has been estimated for the category of cobble-bed rivers from table (Julien, 2002), graph (Ferguson, 2010) and the formula of Henderson (1966) : $n_M = 0.038 D_{75}^{1/6}$ (D_{75} of the bed surface material in m). The value of flow discharge was modified until the water surface extension of the simulation fitted with the water surface extension observed in the orthomosaic. When this was achieved, the WSE model from this simulation was exported. The submerged checkpoints were intersected with the WSE model in order to extract the elevation of the water surface in each point (Z_{WSE}). The difference between Z_{WSE} and Z_{ChP} provided the depth of each point, considered the real depth (d). Additionally, all elevation values in the wet channel obtained through SfM and Z_{SfM} were also transformed to apparent water depth (d_a), following the same procedure. A statistical relationship between d and d_a was obtained (grey points in Figure 4.2 **C**). Then, a correction coefficient was calibrated to minimize the differences between the apparent depth and what was considered the real depth. From a cross-validation calculation (jackknife), an optimum coefficient was obtained, which yielded the refraction correction model. Evaluation of the quality of the refraction correction model was performed on a validation set consisting of 99 points (Figure 4.2 **D**). The average error was reduced from − 0.200 m to − 0.020 m and the root mean square error from 0.250 m to 0.185 m.

Before to correct water refraction the point cloud was filtered in order to remove all errors caused by water turbulence and shadows. Points in shaded zones and those located in turbulent areas were removed by means of a classification of the aerial image obtained through the digital photogrammetry process. Apparent water depth points for the whole wet channel were subsequently corrected, applying the equation shown in Figure 4.2 **C**. After, the corrected depth points (m) were transformed to elevations (m asl), i.e. the corrected depths were subtracted from the water surface elevation model ($Z_{corrected} = Z_{WSE} - d_{corrected}$). These corrected wet points were combined with the point cloud for the dry points to generate a hybrid DEM as follows. The entire corrected dense point cloud was regularized by means of the ToPCAT algorithm (Brasington et al., 2012a; Rychkov et al., 2012). ToPCAT is freely available from the Geomorphic Change Detection software as an ArcMap tool, see http://gcd.riverscapes.xyz/ and Wheaton et al. (2010) for details of the methodological developments. The minimum elevations within a 0.5 × 0.5 m grid cell were extracted and were considered to represent the ground elevation of each grid. Vegetation was filtered out through the orthomosaic and, lastly, triangulated irregular networks were calculated from the filtered minimum observations, from which a 0.5 m resolution hybrid DEM was computed, providing a continuous model of the ground along the 17-km long segment.

4.3.2 Bed material characterization

The grain-size characterization of the bed surface sediment was carried out through the pebble-count method (Wolman, 1954). Bed-surface particles were collected along transects at each section. This method is indicated for gravel and cobble-bed streams, as it is difficult to pick up particles smaller than 8 mm. Grain-size samples were collected during a field campaign in September 2018. Bed-surface particles were sampled in morphological equivalent units. Between 120 and 200 particles were measured at each of the four studied sections, and grain-size distributions (hereafter GSD) were truncated, considering only material ≥8 mm (Figure 4.3).

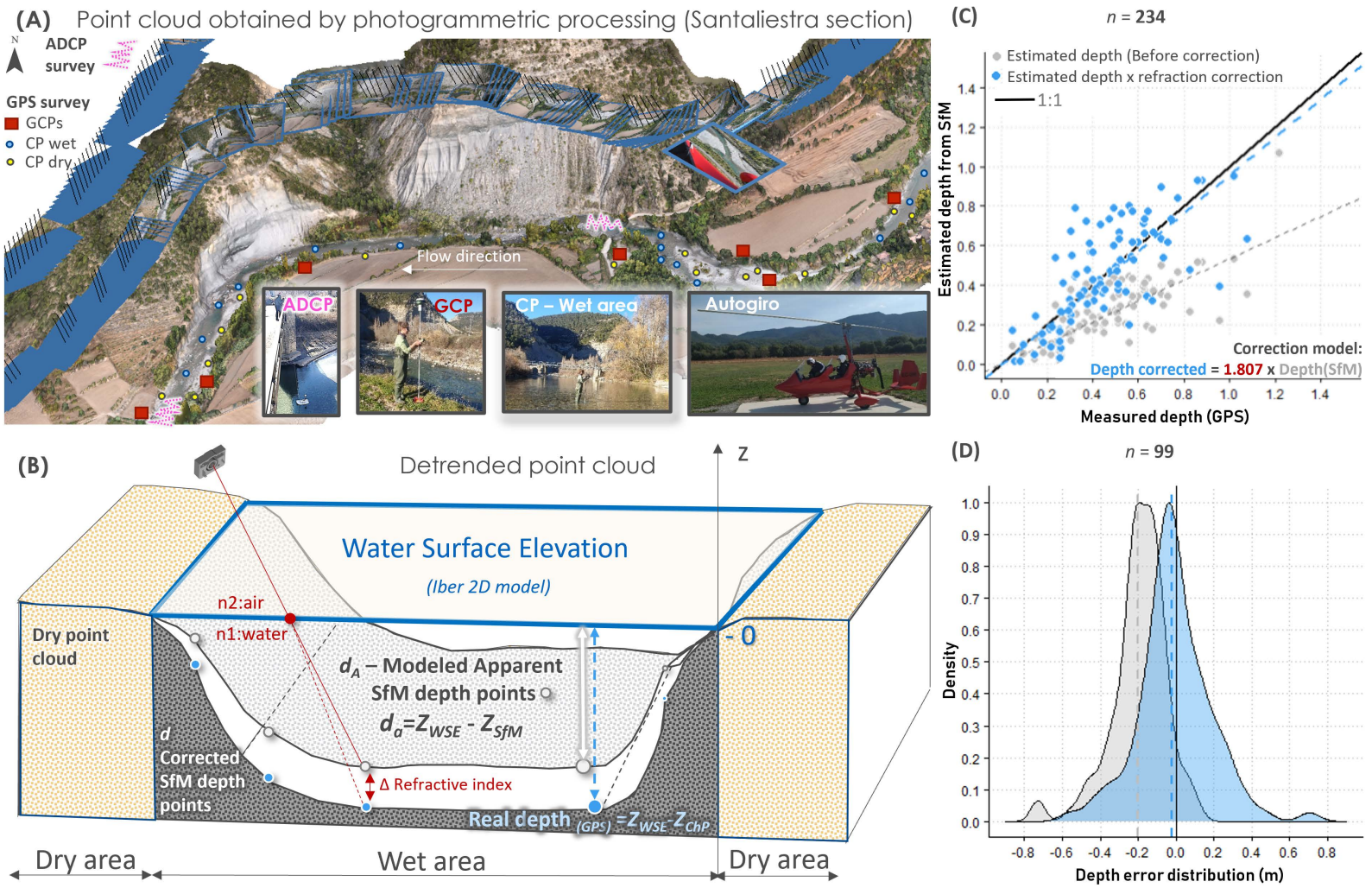

Figure 4.2: Generation of a High Resolution Digital Elevation Model. (**A**) Example of a 3D view of the point cloud obtained through digital photogrammetry (SfM algorithms) superposing the network of Ground Control Points (GCPs) and Check Points (CP), both obtained in the dry or exposed channel (CP dry) and those in the submerged channel (CP wet). (**B**) Schematic drawing of the light refraction issue. (**C**) Development of the refraction correction model based on survey observations; the grey are uncorrected values while the blue are the points after correction. (**D**) Evaluation of errors before and after correction based on the test data set of the Check Points (see text for more details).

4.3.3 Field assessment of particle mobility

Particle mobility was assessed during autumn 2018 in the four study sections using two different tracer techniques: (i) lines of individual painted particles, and (ii) painted pebble squares. It should be noted that, in this work, the field assessment of particle mobility was intended to contrast the tracer data with the predictions of the selected criteria for estimating the sediment motion threshold, a way to validate the theoretical approach selected (see Section 4.3.6 for more details on these selected criteria). Consequently, a complete analysis of bed mobility is out of the scope of this research. Tracers have been widely used to study bed mobility in fluvial geomorphology (see the review by Kondolf and Piégay, 2005). In the case of the tracer lines, tracer particles were chosen from the bed material to rep- resent a range of grain sizes between 16 mm and 181 mm. The selected particles were first measured and then painted. Once dried, particles were placed in the wet part of the bed along a single transverse line with a spacing of 1 m between particles. The length of these lines ranged from 20 m to 25 m. Two lines were established in the Pirámides and Santaliestra sections and only one line in both of the Campo sections. Two painted pebble squares of 1 × 1 m were located in exposed low bars in each of the study sections. The corners of these areas were surveyed by an RTK-GNSS system (Leica Viva GS15).

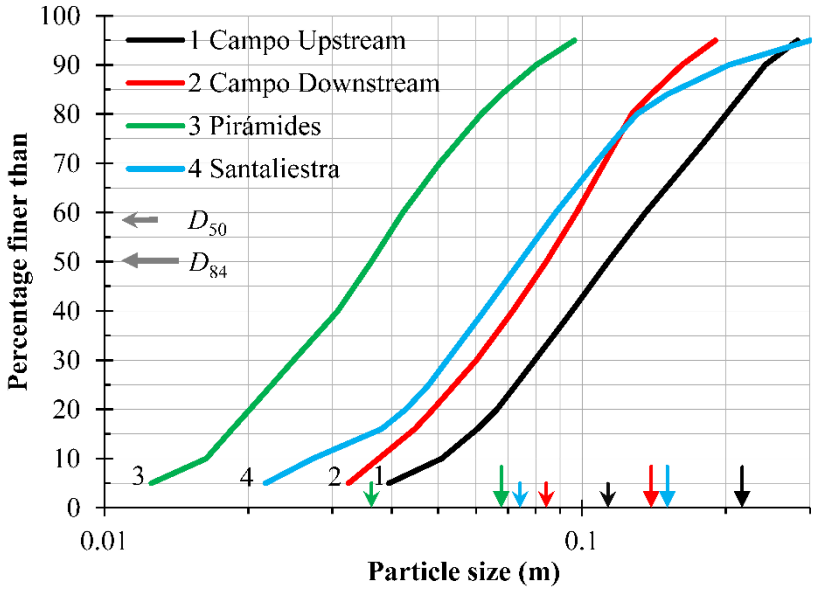

Figure 4.3: Grain size distributions of the bed surface sediment for the four studied sections. Particle size is represented between D_5 and D_{95} grain size percentiles for each section. As a visual reference, the D_{50} and D_{84} grain size percentiles have been marked on the *x*-axis.

Three flow episodes allowed the assessment of particle mobility, two of which corresponded to hydropeaks and one to a flood event. Hydropeaks were recorded on two consecutive days, 19th and 20th September 2018, with maximum Q reaching 19 $m^3 s^{-1}$, and 17 $m^3 s^{-1}$, respectively. The flood event occurred on 15th October 2018, with a peak Q of 57 $m^3 s^{-1}$ at the Campo gauging station and 102 $m^3 s^{-1}$ at the Santaliestra gauging station (both around 1.25 years recurrence interval). The difference in maximum discharge between these two stations was due to the contributions of the tributaries that flow between the Campo Downstream and Pirámides sections (Figure 4.1). The mobility of the tracers was surveyed after each flow pulse episode. Three different scenarios were considered with regard to the mobility analysis of the traced particles: (i) particles found in their initial position (no motion), (ii) particles found to be displaced downstream (mobile particle), and (iii) particles not found (large downstream displacements, burial, overturning on the painted side or paint deterioration). Painted pebbles observed downstream from the source areas (single lines or painted squares) were measured (the intermediate axis, i.e. the *b*-axis), and their position was surveyed in order to calculate the step length (displacement). In the case of painted squares, the initial position of the tracers was always considered to be the centroid of each area; therefore, uncertainties of ±0.5 m are implicit in this approach. Detailed information on the tracer particles recovered is given in Section 4.4.2.

4.3.4 Hydraulic modelling

Flow hydraulics associated with targeted Q were simulated along the whole river segment using the Iber 2D hydraulic model (Bladé et al., 2014). A regular mesh of 1.25 m was generated by importing the 0.5 × 0.5 m DEM resolution (see Section 4.3.1). The size of the mesh was stablished by optimizing the computational time and providing acceptable results at-a- section scale, the scale in which entrainment is analysed (see Section 4.3.5). Although finer meshes may have a direct impact on maximum and minimum values of hydraulic variables trough a given reach, preliminary sensitivity analyses in the study site indicated that these differences are not significant at the cross-sectional scale. Surface roughness was parameter as spatially uniform with a Manning's roughness coefficient value of 0.025 s m $^{-1/3}$ (see Section 4.3.1). The model was run at steady flow for each target Q. Targeted Q were 2, 5, 10, 15, 20, 25, 30, 35, 40, 50, 60, 70, 80, 90, 100, 150, 200, 222, 250, 300, 355, 400, 477, and 600 m3 $^{-1/3}$ (see a visual representation of several of the simulations in Figure 4.4).

The assessment of model performance was made using spatially distributed surveys from an acoustic Doppler current profiler (SonTek RiverSurveyor M9) coupled to an RTK-GNSS system. Water depth, water surface elevation and mean flow velocity was surveyed at different Q (2, 5, 8, 17, and 20 m^3 s $^{-1}$) in Campo Upstream, Campo Downstream and Santaliestra (providing >4600 real observations). The Mean Absolute Error (MAE) between observed and modelled data was computed as:

$$MAE = \frac{1}{n}\sum_{i=1}^{n}\left|x_{obs_i} - x_{mod_i}\right| \qquad (4.1)$$

in which x_{obs_i} = observed i value of the variable x; x_{mod_i} = modelled i value of the variable x; n = number of data; and x represented independently the following three variables: (i) mean flow velocity (m^3 s $^{-1}$); (ii) water depth (m) and (iii) water surface elevation (m asl). Therefore, three MAE were calculated for each Q. The MAE of flow velocity ranged between 0.12 m s $^{-1}$ and 0.20 m s $^{-1}$ (with an average value in terms of relative error of 32 %) for low flows (i.e. 2, 5 m^3 s $^{-1}$ and 8 m^3 s $^{-1}$), and between 0.14 m s $^{-1}$ and 0.22 m s $^{-1}$ (mean value of the relative error of 30 %) for medium Q (i.e. 17 m^3 s $^{-1}$ and 20 m^3 s $^{-1}$). The MAE for water depth oscillated between 0.13 m and 0.21 m (mean relative error of 25 %) for low Q and between 0.15 m and 0.24 m (mean relative error of 15 %) for medium Q. The water surface elevation MAE for low and medium flow are between 0.13 and 0.14 m asl and 0.13 and 0.16 m asl, respectively (note that in this case, the values in terms of relative error are very low since water surface elevation is >500 m asl).

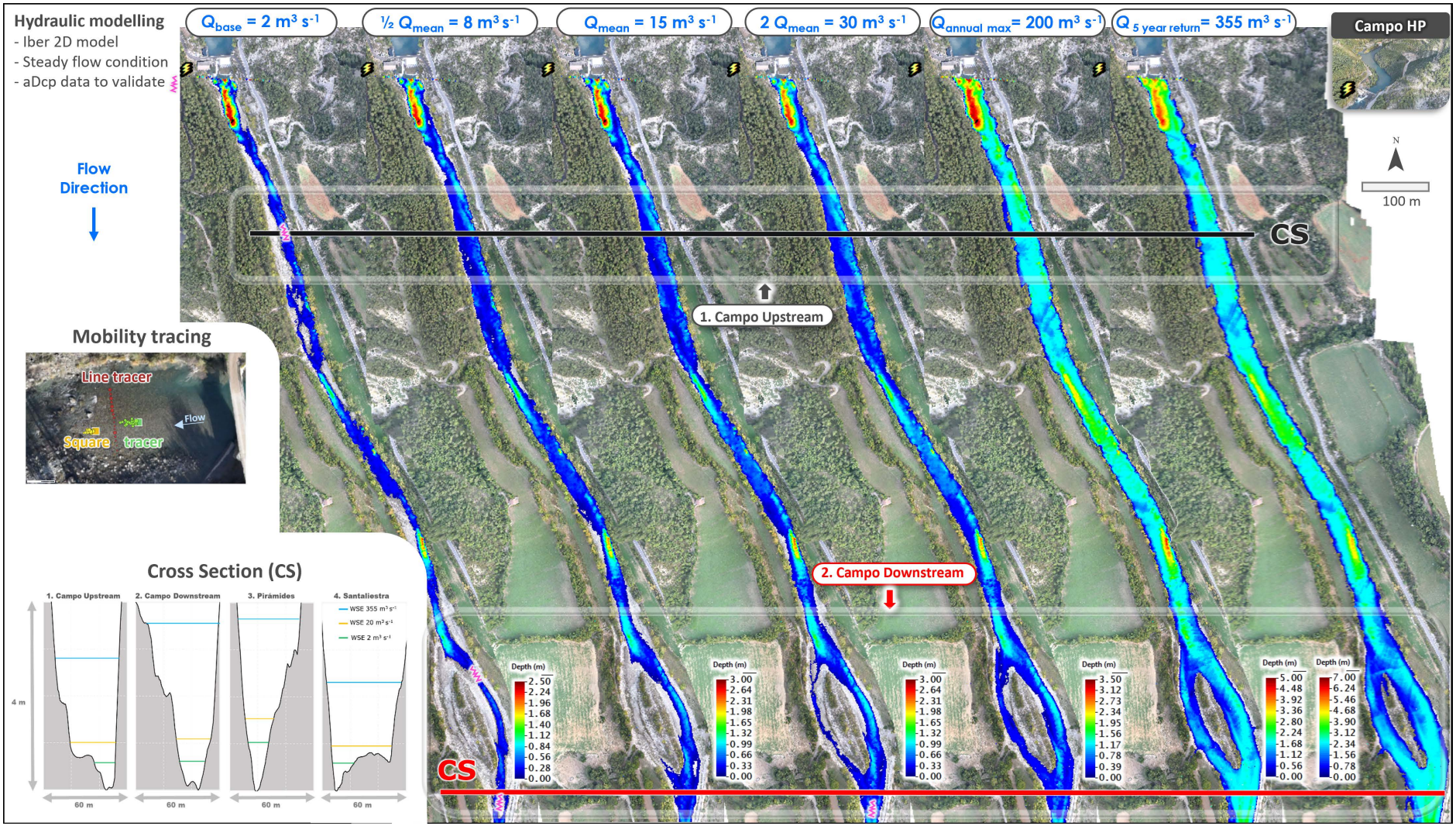

Figure 4.4: Example of the results of the hydraulic models developed in this study. On the left side is an example of the painted line and square tracer used for field assessment of particle mobility. Where aDcp is the acoustic Doppler current profiler.

4.3.5 Estimation of shear stress

By considering the equilibrium of forces on a control volume for one-dimensional steady gradually varied flow in a wide-open channel (i.e. R ≈ y), the mean boundary shear stress in a cross-section (τ) can be estimated as:

$$\tau = \rho g y S_f \qquad (4.2)$$

in which ρ = density of water; g = acceleration due to gravity; y = mean water depth; R = hydraulic radius; and S_f = friction slope or energy gradient.

However, the Iber model allowed us to estimate the shear stress distribution on the channel boundary for two-dimensional flow throughout the whole river reach for any of the modelled Q (i.e. the same list as that specified in Section 4.3.4). Nevertheless, it should be pointed out that, in this work, sediment entrainment was predicted at-a-section scale (i.e. one-dimensional) for each of the four studied sections. A transect was determined for each section, about perpendicular to the main channel direction. It should be remembered that these transects are not, strictly speaking, cross sections to the flow, since the flow simulation is not one- dimensional. Iber supplies the value of the integral of shear stress distribution on the channel boundary in these transects for each of the modelled Q. The mean shear stress exerted by the flow in each section and for any Q was determined by dividing that integral value by the wetted perimeter. Hence, a set of 21 points (corresponding to the same number of targeted flows) with values (Q, τ) was obtained for each section, and a simple power law regression was applied to these points:

$$\tau = aQ^b \qquad (4.3)$$

in which τ = mean boundary shear stress; Q = flow discharge; a = coefficient; and b = exponent. A power law function was adopted because, given a section, the mean depth (y) and flow discharge (Q) can be correlated by a simple power law, according to the at-a-station hydraulic geometry concept (Dingman and Afshari, 2018; Leopold and Maddock, 1953) and due to the relationship between the mean boundary shear stress (τ) and the mean water depth (y) (i.e. Eq. 4.2).

4.3.6 Prediction of particle entrainment

The resistance of a sediment particle to be entrained was assessed by the dimensionless critical shear stress (θ_{ci} or the critical value of the Shields number) needed to set in motion a particle of size D_i and was estimated as:

$$\theta_{ci} = \frac{\tau}{g\rho_s - \rho)D_i} \qquad (4.4)$$

in which D_i = size of particle median axis for which i % of the particles are finer; τ_{ci} = critical shear stress for D_i ; and ρ_s = sediment density. Due to the relatively low value of the mean bed slope in the studied reach (Section 6.2), the analytical correction that takes into account the effect of high slopes on the Shields number (e.g. Armanini (2018)) has not been applied. The condition for incipient motion of sediment (i.e. threshold of motion) was determined by establishing equality between critical shear stress of a particle of size D_i (τ_{ci}) and the mean boundary shear stress of the cross section (τ). So, to unify the notation and avoid confusion, Eq. 4.3 is expressed as:

$$\tau = aQ_{ci}^b \qquad (4.5)$$

in which τ_{ci} = critical mean boundary shear stress forD_i; Q_{ci} = critical discharge for D_i ; a = coefficient; and b = exponent. In coarse river beds of poorly sorted size distribution, the so-called hiding-exposure effect was observed, i.e. the process in which small particles are hidden from the flow by larger and more exposed particles (e.g. Garcia, 2008; Bathurst, 2013).

This effect makes the prediction of the beginning of the particle's motion more difficult. The hiding-exposure effect over the dimensionless critical shear stress can be estimated as:

$$\theta_{ci} = \theta_{cr}\left(\frac{D_i}{D_r}\right)^a \qquad (4.6)$$

in which subscript *r* refers to the reference particle size that is not influenced by the hiding-exposure effect. In this work it has been assumed, as usually, that this reference particle size corresponds to D_{50} of the bed surface material. The exponent α or hiding factor represents the dependence of the dimensionless critical shear stress on relative particle size. If the hiding factor is zero ($\alpha = 0$), this means that the relative size effects are not decisive, and critical shear stress is a function of absolute grain size (constant critical value of the Shields number). On the contrary, if $\alpha = -1$, equal mobility is assumed (i.e. grains of different sizes begin their motion at the equal mean shear stress).

Table 4.1:

Values of θc~50 and~ α in $\theta_{ci} = \theta c_{50(Di/D}50_{)}\ \alpha$

Reference	Equation	θc_{50} (-)	α (-)
Miller et al. (1977); Yalin and Karahan (1979)	(4.7)	0.045	0
Komar (1987)	(4.8)	0.045	-0.60
Dey and Ali (2019)	(4.9)	0.057	-0.76
Wilcock and Crowe (2003) [a]	(4.10)	0.036[b]	$-1+\frac{0.67}{1+exp(1.5-D_i/D_{50})}$
This study (data compiled rivers worldwide)	(4.12)	0.045	-0.77
This study (River Ésera tracer data)	(4.13)	0.018	-0.54

[a] as presented in McCarron et al. (2019)

[b] In this equation the value of θc_{50} is a function of the proportion of sand in the surface layer GSD. In this study it was assumed to be zero.

Five different criteria were used to estimate the values of the coefficient and exponent of Eq. 4.6. First, the Miller et al. (1977) and Yalin and Karahan (1979) criterion was used (hereafter designated M-Y&K) as representative of purely size-selective entrainment (i.e. $\alpha = 0$) (Eq. 4.7 in Table 4.1). This equation was determined by the mentioned authors for hydraulically rough turbulent flow from a selection of databases acquired in flumes with beds of non-cohesive particles. The second criterion was proposed by Komar (1987) and was validated with >150 measurements in different fluvial and marine environments (with particle sizes varying between very fine gravel to boulders and D_i/D_{50} between 0.3 and 30). The proposed empirical equation (Eq. 4.8 in Table 4.1) has a hiding factor (α) of $-$ 0.6 (i.e. between 0 and -1) and implies a medium dependence of critical shear stress on particle size; it can be classified as partially size-selective entrainment. The third criterion was the equation fitted by Dey and Ali (2019) to a large database (about 500 data, with D_i/D_{50} varying between 0.03 and 20), compiled with both field and flume data from several sources (Eq. 4.9 in Table 4.1). The fourth criterion was obtained by fitting Eq. 4.6 to an extensive database compiled specifically for this study from publications by various researchers. Data obtained in the field (gravel or coarse bed material rivers) and agreeing with the flow competence method (largest particle mobilized) were selected. See results and more detailed information on the selected database and the fitted equation in Section 4.4.2 and Figure 4.5. Lastly, a fifth criterion was adopted in which it is assumed that the hiding and exposure effects are different and that, therefore, the α value in Eq. 4.6 is variable with the D_i/D_{50} ratio. Specifically, the equation of Wilcock and Crowe (2003) was adopted, which was proposed from the application of the reference method to flume data (Eq. 4.10 in Table 4.1).

However, it should be noted that results of the reference and flow competence methods are different (Buffington and Montgomery, 1997), as it was observed in studies in which both have been applied to the same sites (e.g. Ashworth et al., 1992; Wathen et al., 1995; Batalla and Martín-Vide, 2001). Indeed, expressed in absolute value, the exponent α of Eq. 4.6 is between 15 % and 35 % higher using the reference method.

To choose a single equation of bed entrainment (i.e. the equation that best represents the conditions of the study segment), prediction of the five equations or criteria mentioned above was contrasted with the values (D_i/D_{50}, θ_{ci}) obtained from the tracer data available for the four sections studied (Section 4.3.3). The equation (or criterion) of bed entrainment finally chosen was the best fit on the tracer data. Therefore, this equation was subsequently used as the only criterion for predicting downstream changes at the onset of sediment motion. Finally, a simplified equation for the calculation of bed entrainment was obtained by combining Eq. 4.4, Eq. 4.5 and Eq. 4.6 taking g = 9.81 m s^{-2}, ρ_s = 2650 kg m^{-3} and ρ = 1000 kg m^{-3} and considering the dimensionless critical stress (θ_{ci}) equation chosen. The resulting equation is a simple power law (see Supplementary material A):

$$Q_{ci} = cQ_i^d \qquad (4.11)$$

in which Q_{ci} = critical discharge needed to set in motion a particle of size D_i; D_i = size of particle median axis for which i % of the particles are smaller; c = coefficient; and d = exponent.

4.4 RESULTS AND DISCUSSION

4.4.1 Mean boundary shear stress

Table 4.2 shows the power law regression between Q and mean boundary shear stress (τ) for each section, as well as the value of the coefficient of determination for each regression (R^2) (third and fourth columns, respectively). For the four sections, the goodness-of-fit of the power law regression can be considered acceptable (R^2 varies between 0.96 and 0.98) and statistically significant (in all cases p-value < 0.0001). The regression equation corresponding to Pirámides section diverges the most from the rest. This is due to the fact that for, lower flows, the mean shear stress predicted in this section is comparatively lower than for the rest of the sections and, in contrast, the shear stress for the four sections tend to converge for the highest flows.

4.4.2 Dimensionless critical shear stress

Figure 4.5 shows the relationship between dimensionless critical shear stress (θ_{ci}) and relative particle size (D_i/D_{50}), both for the measured entrainment using traced particles and for the five criteria adopted to estimate the values of the coefficient and exponent of Eq. 4.6, as explained in detail in Section 4.3.6. Measured entrainment in River Ésera, composed by six observations (Figure 4.5), was determined by the flow competence method; that is, matching the diameter (b-axis) of the coarsest particle mobilized with the maximum discharge occurring between periods the tracers were recovered (see Section 4.3.3). The 15th October 2018 flood was the only episode in which tracer mobilization was observed in all four study sections. In terms of mobilization during hydropeaking, the only detected bed disturbance after the hydropeak on 19th October 2018 was a patch of fine gravel deposited on one of the painted squares in the Campo Downstream section. The largest particle of this patch was measured. In the case of the hydropeak on 20th September 2018, only the mobilization of a tracer particle from a painted square in the Santaliestra section was observed. A regression is fitted based on these six points (i.e. River Ésera data regression). For comparison purposes, the five entrainment observations from the neighbouring River Cinca presented in López et al. (2020) have also been represented. Finally, the curves corresponding to the M-Y&K, Komar (1987), Wilcock and Crowe (2003) and Dey and Ali (2019) equations and the mobility observations together with the regression equation corresponding to the field database compiled in this study have also been represented.

Table 4.

Regression equations according to $\tau_{ci} = aQ_{ci}^{b}$ model, Eq. (5), their coefficient of determination for regression (R^2) and $Q_{ci} = cD_i^d$ type equations, Eq. (11), based on Eq. (13), for the studied sections.

Section name	Section number	$\tau_{ci} = aQ_{ci}^{b}$	R^2	$Q_{ci} = cD_i^d$
Campo Upstream	1	$\tau_{ci} = 1.07Q_{ci}^{0.768}$	0.97	$Q_{ci} = 319.8D_i^{0.599}$
Campo Downstream	2	$\tau_{ci} = 1.17Q_{ci}^{0.701}$	0.96	$Q_{ci} = 388.7D_i^{0.656}$
Pirámides	3	$\tau_{ci} = 0.337Q_{ci}^{0.945}$	0.96	$Q_{ci} = 191.8D_i^{0.487}$
Santaliestra	4	$\tau_{ci} = 1.41Q_{ci}^{0.790}$	0.98	$Q_{ci} = 143.8D_i^{0.582}$

[a] Q_{ci} in m^3s^{-1} and τ_{ci} in Pa.
[b] D_i in m and Q_{ci} in m^3s^{-1}

The database is composed of a total of 491 entrainment observations, taken from 15 bibliographic references (see Supplementary material B and from 22 unpublished data obtained after a reassessment of bedload measurements in the rivers Tordera (Garcia et al., 1999) and Ebro (López et al., 2014). The D_{50} ranged between 14 mm and 128 mm and D_{max}/D_{50} (where D_{max} is the maximum grain size transported) between 0.014 and 5.3. Despite the scatter in the cloud associated with the compiled database (for a given value of D_i/D_{50}, the dimensionless critical shear stress (θ_{ci}) varies over a broad range), a general trend of decreasing θ_{ci} value within creasing D_i/D_{50} is clearly evident in Figure 4.5. The regression equation fitted to that database according to Eq. 4.6 is Eq. 4.12 showed in Table 4.1 .

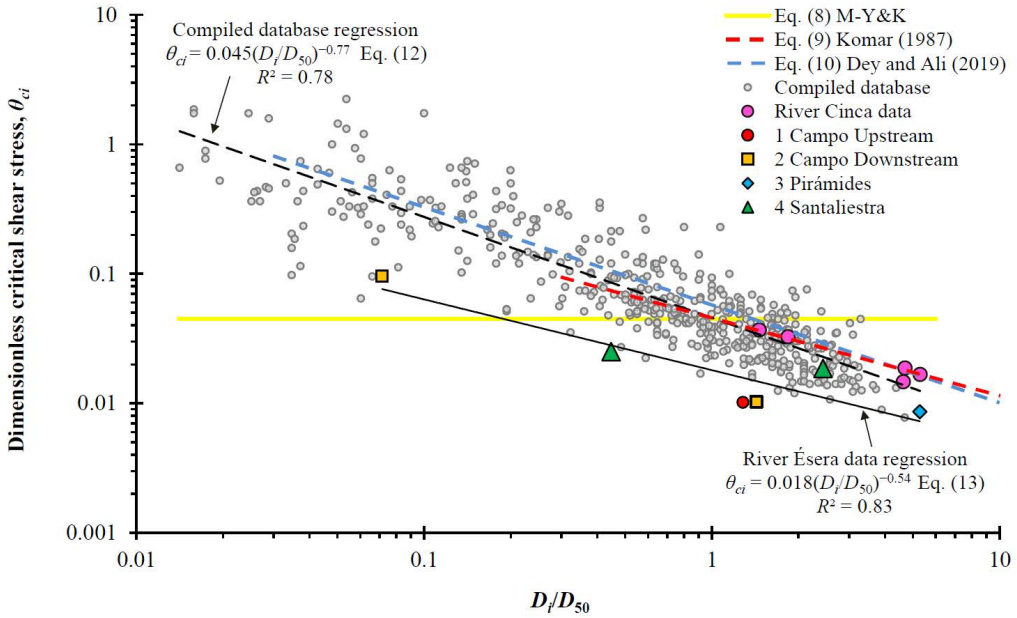

Figure 4.5: Dimensionless critical shear stress (θ_{ci}) against relative particle size (D_i/D_{50}), where D_{50} is the median size of the bed surface material. Regression relationships according to Eq. 4.6 are compared with tracer particle data from River Ésera (Campo Upstream, Campo Downstream, Pirámides, and Santaliestra sections) and River Cinca. The complete point cloud corresponding to the database of various rivers worldwide compiled in this study and equal mobility equation (i.e. with $\alpha = -1$ and assuming $\theta_{c50} = 0.045$) are also shown for visual reference.

The value of the coefficient of Eq. 4.12 ($\theta_{c50} = 0.045$) coincides with that of Eq. 4.8, by Komar (1987), and the exponent ($\alpha = -0.77$) is very similar to Eq. 4.9, from Dey and Ali (2019). Figure 4.5 shows that the predictions are quite similar over the D_i/D_{50} range covered by these three equations, Eq. 4.8, Eq. 4.9 and Eq. 4.12. However, in comparison, the points of the tracer particles associated with the River Ésera describe a trajectory with much lower values of the dimensionless critical shear stress.

The same can be said about Eq. 4.10, even though it sets a variable α value. In fact, with the exception of one of the points (belonging to the Santaliestra section), the data align practically matching with the lower envelope of the compiled database. That is, Eq. 4.8 - Eq. 4.10 and Eq. 4.12 predict a threshold of sediment motion clearly higher than that measured by the tracer particles in the River Ésera. These equations predict that the mean boundary shear stress required to mobilize a particle of diameter D_i is much higher than that estimated from the tracer particles. In contrast, the position of the points defined by the tracer particles of the River Cinca fitted much better to the curves of the previous equations plotted, especially Eq. 4.8. Entrainment measurements also show that the River Ésera does not have purely size-selective entrainment conditions, represented by Eq. 4.7. Therefore, Eq. 4.7 - Eq. 4.10 and Eq. 4.12 are not suited to predict the threshold of sediment motion in the four sections studied in the River Ésera. As an alternative, the regression equation fitted to the tracer particle data from the River Ésera was adopted. The fitted equation is Eq. 4.13 (R^2 = 0.83, p = 0.012) showed in Table 4.1 and also represented in Figure 4.5. As can be seen in Figure 4.5, the plot of Eq. 4.13 practically coincides with the lower envelope of the point cloud belonging to the compiled database. This is due to the low value of the coefficient (θ_{c50} = 0.018). The value of exponent (hiding factor (α) = − 0.54), indicating a medium dependence of critical shear stress on particle size, is similar to that obtained by Whitaker and Potts (2007) (α = − 0.59), based on regression analysis of flow competence data (bedload samples) in a gravel-bed stream.

Finally, the equation used to estimate the threshold of sediment motion in the four sections in the River Ésera was the version of Eq. 4.11 obtained by combining Eq. 4.4, Eq. 4.5 and Eq. 4.13. This equation for each of the four study sections is presented in the last column of Table 4.2 (in which the value of D_{50} has already been substituted for each section).

4.4.3 Downstream changes on the onset of sediment entrainment

Figure 4.6 shows the equations of threshold of sediment motion for the four study sections, presented in the last column of Table 4.2. It is important to note that these equations have been plotted in the D_i interval between D_5 and D_{95} of the grain size distribution of each section (Figure 4.3). This is why the four curves cover a range of representation that, in absolute terms, is different for each one (the limits of the curves depend on the particular GSD of each section). Therefore, the four curves share only the particle size range between 0.04 m and 0.1 m. The value of the exponent of the four equations (Table 4.2) varies in a relatively narrow range (between 0.5 and 0.7), so the slope of the corresponding curves shown in Figure 4.6 is similar. The major difference among these four equations is due to the value of the coefficient, c in Eq. 4.11, which varies between 144 and 389 (Table 4.2).

For comparison purposes, the equations of the first two upstream sections (i.e. Campo Upstream and Downstream) can be considered as a single set, given the similarity of their curves (Figure 4.6). In this group, when setting the value of D_i, the predicted Q_{ci} value is comparatively high (more flow is required to entrain a D_i compared to downstream sections). That is, it shows a higher threshold of sediment motion than the rest of the two downstream sections (i.e. Pirámides and Santaliestra). This is mainly explained by the fact that the bed surface layer in the two Campo sections is coarser (even armoured in the uppermost section) than in the two downstream sections, for most of the GSD range (see Figure 4.3). In contrast, in the case of the Santaliestra equation (the furthermost section), when setting the value of D_i, the predicted Q_{ci} value is comparatively low (less flow is required to entrain a D_i compared to all other upstream sections). That is, it shows a lower threshold of sediment motion than the rest of the sections (see Figure 4.6). The main reason for this is that, given a flow rate Q, the value of the mean boundary shear stress predicted by the equation fitted to the Santaliestra section is comparatively higher than the rest of the upstream sections (see third column of Table 4.2). This is because the value of the mean longitudinal bed slope in the Santaliestra section is almost double the bed slope of the rest of the upstream sections.

Finally, the plot of the equation associated with the Pirámides section is located below the trajectory of the equations of the Campo sections and above the curve of the Santaliestra section (although closer to the plot of the curves of the Campo sections). The size of the bed surface material in the Pirámides section is significantly smaller than in the other sections. This could have caused the threshold of sediment motion predicted for the Pirámides section to be comparatively lower than for the other sections. However, as seen above, its critical flow rate curve of incipient sediment motion occupies a relatively high position (Figure 4.6). This is because the value of the mean shear stress predicted in the Pirámides section (Table 4.2) is significantly lower than the corresponding value in the other sections for discharge below 100 $m^3 s^{-1}$.

For the purpose of comparing the four curves, the prediction of Q_{ci} can be contrasted by setting the same value of Di for all sections. In this case D_i = 77 mm (small cobble), which is the median value of D_{50} in the four sections. Accordingly, for the Campo sections curves, to initiate the movement of a 77 mm diameter particle, a mean Q_c value of 71 $m^3 s^{-1}$ would be required. However, a Q_c of only 32 $m^3 s^{-1}$, is required in the Santaliestra section. Finally, for a D_i = 77 mm, the Pirámides section entrainment equation predicts a value of Q_c of 55 $m^3 s^{-1}$.

4.4.4 Bed-material entrainment during floods and hydropeaking

We have assumed two well-differentiated sediment entrainment conditions during floods, driven by the distinct coarsening of the river bed; a lower limit based on the critical shear stress for D_{84} particle size and an upper limit for a shear stress equivalent to two times the critical shear stress of the D_{84}. These limits were considered to predict phase 2 of bedload transport in armoured beds (Recking, 2010) and to establish the dynamically stable phase in a conceptual model of channel stability in gravel-bed rivers (MacKenzie et al., 2018).

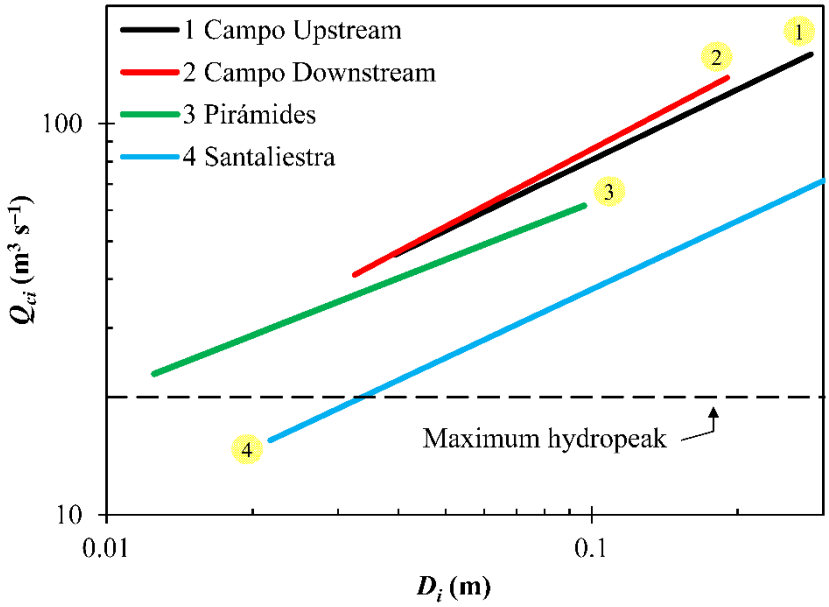

Figure 4.6: Incipient motion prediction for maximum hydropeak discharge. The relationships between critical flow discharge (Q_{ci}) and particle size (D_i) according to Eq. 4.13 for all studied sections (last column in Table 4.1) are compared with maximum value of hydropeak discharge (Q_{ci} = 20 $m^3 s^{-1}$). Particle size (D_i) is represented between D_5 and D_{95} grain size percentiles for each section.

For the Santaliestra curve (Figure 4.6), the lower (D_{84} = 151 mm) and upper limits are predicted under a Q_c of 48 $m^3 s^{-1}$ and 115 $m^3 s^{-1}$, respectively. Both values are lower than the peak Q associated with annual floods. It should be recalled that the Santaliestra section shows a more mobile bed, i.e. less flow required to entrain a given D_i. For the Campo sections, with a comparatively more stable bed, lower limit (D_{84} is 216 mm for Campo Upstream and 140 mm for Campo Downstream) is predicted under an average Q_c of 118 $m^3 s^{-1}$ (varying between 107 $m^3 s^{-1}$ and 128 $m^3 s^{-1}$).

These values are also lower than the peak Q associated with annual floods. The upper limit is predicted under an average Q_c of 302 m^3s^{-1} (varying from 288 m^3s^{-1} to 316 m^3s^{-1}), a condition reached during floods with a recurrence interval between four and five years. Finally, lower (D_{84} = 68 mm) and upper limits in the Pirámides section requires only Q_c values of 52 m^3s^{-1} and 108 m^3s^{-1}, respectively. Both values are lower than the peak Q associated with annual floods and similar to those predicted for the Santaliestra section. This is mainly due to the low value of D_{84} for the Pirámides section.

Summarising, with regard to entrainment conditions of coarser bed material during floods, results indicate that the studied reach of the River Ésera has a frequently mobilized bed. However, in relative terms, a downstream change in mobility has been detected, i.e. from a more stable bed where mobility is less frequent in sections close to the hydropower station to a more mobile and frequently mobilized bed in the further downstream sections.

Hydropeaks reach a maximum Q of 20 m^3s^{-1}. So, in this study, this value is adopted as the maximum entrainment capacity caused by hydropeaks for the entire river segment. In an initial analysis, base flows and reduced peak flow due to downstream routing of the hydrograph were ignored. Figure 4.6 shows hydropeaking Q as a parallel line to the *x*-axis. The intersection point of this line with the particle entrainment curves determines the maximum grain size for the incipient motion (D_i) at each study section associated with the maximum hydropeaking Q, i.e. when Q_{ci} = 20 m^3s^{-1}.

Figure 4.6 shows that the only intersection of the horizontal line (Q_{ci} = 20 m^3s^{-1}) occurs in the Santaliestra section, the most downstream section. In this case, the initiation of motion is predicted for a sediment particle size less than or equal to 34 mm (approximately equivalent to D_{14} of the bed surface in this section, Figure 4.3). Since the Santaliestra section is the furthest from the outlet of the Campo hydropower plant (Figure 4.1), it is of interest to assess the attenuation effect of maximum Q of the hydropeaks in this section due to the propagation of the hydrograph (e.g. Hauer et al., 2013). From the analysis of recorded hydropeaks at the study reach and the simulation of typical hydropeaks (2D modelling at unsteady-flow conditions using Iber), it has been concluded that the attenuation effect is very moderate; it has been estimated that the maximum value of the hydropeak at Santaliestra decreases to 18 m^3s^{-1}. In this case, the threshold of motion is predicted for a grain size less than or equal to 28 mm (approximately equivalent to D_{10} of the bed surface in this section, Figure 4.3). Therefore, results indicate that the entrainment of sediment in the Santaliestra section caused by hydropeaks would only affect the smaller fractions of the surface GSD (Figure 4.3).

For the remaining sections located upstream (Campo Upstream and Downstream and Pirámides), peak flows associated with hydropeaking (Q_{ci} = 20 m^3s^{-1}) are not able to entrain a significant D_i of the surface GSD. It is worth remembering that in Figure 4.6, D_i was represented only in the interval between D_5 and D_{95} of the surface GSD of each section. According to the power laws (last column of Table 4.2) of these sections, the maximum particle size corresponding to the threshold of sediment motion for a discharge of 20 m^3s^{-1} would be about 10 mm (medium gravel) for all three sections; the size is close to the lower limit of detection in the method used to sample surface sediment (Section A.3.2). Nevertheless, these are the size fractions that are prevalent in patches of fine materials in fluvial environments similar to the River Ésera (e.g. Garcia et al., 1999; Vericat et al., 2008c; Vericat et al., 2020) and would therefore entrain, if present. Within this context, in those sections where the presence of fine particles is considered significant, combining pebble-count and area by weight samples (Kellerhals and Bray, 1971) may provide a GSD representative of the full spectrum of sizes on the bed (e.g. Vericat et al., 2006). Combined surface grain size distributions can be generated according; for instance, Fripp and Diplas (1993) and Rice and Haschenburger (2004).

Generally, sediment transport induced by hydropeaking in the studied segment can be interpreted as phase I transport (e.g. Jackson and Beschta, 1982; Ryan et al., 2002) that involves the transport of fine grains over the coarser particles constituting the bed. The range of mobile grain sizes in Santaliestra is larger than in the upstream sections and includes up to very coarse gravel (<34 mm). This is a consequence of a much higher slope (about double that of the other sections) and smaller particle size corresponding to the lower percentiles of the GSD (regarding the upstream Campo sections). So, in relative terms, we conclude that in the River Ésera, the maximum hydropeak Q from the Campo HP plant should be competent to mobilising the finer size fractions of the bed, even 17 km downstream, a condition termed partial transport (Wilcock and McArdell, 1997).

Similar conclusions were drawn from an analogous study in another Pyrenean river (the Upper Cinca) under frequent hydropeaking (López et al., 2020); of five sections downstream of the HP plant, only the one closest to the plant was predicted to have significant sediment movement caused by the maximum hydropeak (its associated threshold of motion corresponds to D_{10} = 20 mm). For the rest of the downstream sections, the threshold of sediment motion corresponded to values much lower than D_5 of the surface GSD (varying between 0.5 mm and 11 mm). In contrast, in the present study of the River Ésera, it is precisely the section furthest downstream that is most affected. This is explained by the particular characteristics (geomorphology and bed surface sediment) of both sections. In the case of the Upper Cinca, the most mobilized section presented a narrower channel, high bed slope and a finer grain-size distribution than in the other downstream sections. As shown above, in the River Ésera, how- ever, the Santaliestra section has a comparatively much higher slope and smaller particle size (for the lowest percentiles of the GSD) with respect to the upstream sections. This was also observed in the Upper Noguera Pallaresa, another of the many Pyrenean rivers affected by hydropeaking, in which sand and fine gravel, stored in patches, and medium and coarse pebbles are winnowed by hydropeaked flows (Vericat et al., 2020) until natural floods provide fresh fine sediment from upstream.

In the particular case of the River Ésera, tributaries downstream from the Campo Downstream section supply relevant amounts of water and, eventually, sediment. As has been introduced before, as an example, the flood registered on 15th October 2018 had a peak of 57 m^3 s^{-1} at the Campo gauging station and 102 m^3 s^{-1} at the Santaliestra gauging station. This difference is mainly attributed to the role of tributaries. In the same way, tributaries supply sediment and will have a major role on supplying sediment in the downstream sections, thus controlling sediment availability. However, in other gravel-bed streams exposed to hydropeaking, bed stability (i.e. scarce or null mobility) can be reinforced by hydropower regulation and extended downstream from the dam (e.g. Sear, 1995).

The impact of a dam associated with a hydroelectric power plant on bedload sediment transport is decisive for the formation of a coarse surface layer. In our case, flow releases are controlled by a system of four reservoirs located upstream of the Campo sections (the furthest one is about 40 km away and the volume of the reservoirs varies between 0.01 hm^3 and 3.1 hm^3), a fact that has a direct impact on the supply of sediment from upstream. Lastly, despite peak Q corresponding with hydropeaking in the River Ésera and the Upper Cinca having a low impact on the coarse surface layer, as described by Vericat et al. (2020) in the Noguera Pallaresa River, the condition of partial mobility that is attained (i) in reaches close to the HP plant, (ii) in reaches showing finer grain sizes (e.g. immediately downstream from tributaries), and/or (iii) during other periods or conditions (e.g. after flood events supplying fine materials from upstream) is significant in determining the frequency and extent of benthic disturbance (e.g. Gibbins et al., 2007a; Wilcock et al., 2009; Schülting et al., 2016). Hence, it should not be neglected when assessing the effects of such flow pulses on the overall ecosystem behaviour.

4.5 CONCLUSIONS

This study brings valuable knowledge regarding the spatial variability of bed-material entrainment caused by hydropeaking along a 17-km channel segment of the River Ésera. The use of three equations of particle entrainment, representing different conditions of initiation of motion (i.e. purely size-selective entrainment and different levels of partially size-selective entrainment) plus an equation developed by means of 491 entrainment observations allowed the critical analysis of the threshold of sediment motion in four study sections. The entrainment observations corresponded to an extensive database of various rivers worldwide, compiled for this study. The comparison between these predictions and six real entrainment observations in the River Ésera, acquired from traced particles, indicates that the analysed models considerably overestimate the threshold of motion compared to real mobility conditions. These real mobility observations are aligned following the lower envelope of the cloud given by the entrainment observations of the extensive database. Therefore, the regression equation fitted to the tracer data obtained in this study is chosen as alternative predictor. This equation shows partially size-selective entrainment, in which only the finer size fractions of the bed are mobilized during hydropeaking, and this condition is only reached in the section furthest to the hydropower plant (Santaliestra).

Channel geometry and relative location of the sections in the reach are key aspects when assessing downstream changes of sediment entrainment. Our study shows the effect of channel slope on mobilization of bed material. The steepest section is capable of reaching the threshold of motion of the coarser bed material during relative low floods (lower than the annual flood), while more gentle reaches require less frequent (higher than the annual flood) but larger peak flows to reach this condition. Hydropeaking in the River Ésera impacts the steepest and the furthest section from the hydropower plant and, as stated, affects only the finer fraction of grain-size distribution. The fine sediments eventually supplied by the floods of the intermediate tributaries are gradually entrained by the continuous action of the hydropeaks, thus establishing cycles that oscillate between different levels of availability and depletion of the fine sediment. So, mobility resulting from hydropeaking has a low impact on the coarser particles of the bed surface and the overall bedload flux of the river, but entrainment of the finest grains may help explain the extent of benthic disturbance in hydropeaked rivers, as has been reported elsewhere. Future research in the study reach will be carried out to address questions beyond those presented here with the objective to study spatial and temporal changes on river-bed dynamics (i.e. armouring, imbrication, porosity) associated to hydropeaking, and also to determine the role of the shape of the hydropeaks on channel hydraulics and mobility along the 17 km channel segment.

Supplementary data to this article can be found online at https://doi.org/10.1016/j.scitotenv.2022.159065

Supplementary material A

Derivation of Eq. 4.11

Combining Eq. 4.4, Eq. 4.5 and Eq. 4.6 and isolating Q_{ci} results:

$$Q_{ci} = \left[\frac{\theta_{c_{50}}}{a}\left(\frac{1}{D_{50}}\right)^{\alpha} g(\rho_s - \rho)\right]^{1/b} D_i^{(1+\alpha)/b}$$

if

$$c = \left[\frac{\theta_{c_{50}}}{a}\left(\frac{1}{D_{50}}\right)^{\alpha} g(\rho_s - \rho)\right]^{1/b}$$

and

$$d = (1 + \alpha)/b$$

finally

$$Q_{ci} = cD_i^d$$

Supplementary material B

This supplementary material cites the bibliographic sources consulted to compile the database together with the number of data (*n*) selected from each reference. Andrews (1983) (n = 14); Ashworth and Ferguson (1989) (n = 33); Ashworth et al. (1992) (n = 83); Batalla et al. (2010) (n = 10); Church and Hassan (2002) (n = 56); Ferguson et al. (1989) (n = 94); Hammond et al. (1984) (n = 33); Komar and Carling (1991) (n = 66); López et al. (2020) (n = 5); Marion and Weirich (2003) (n = 27); Núñez-González et al. (2018) (n = 17); Thompson and Croke (2008) (n = 4); Vázquez Tarrío (2013) (n = 5); Vericat et al. (2020) (n = 8); Whitaker and Potts (2007) (n = 14)

CRediT authorship contribution statement
Raúl López: Data curation, Formal analysis, Visualization, Writing - original draft, Writing - review & editing. Fanny Ville: Data curation, For- mal analysis, Visualization, Writing - original draft, Writing - review & editing. Celso Garcia: Data curation, Formal analysis, Writing - original draft, Writing - review & editing. Ramon J. Batalla: Conceptualization, Investigation, Supervision, Writing - review & editing. Damià Vericat: Conceptualization, Methodology, Investigation, Supervision, Writing - review & editing.

Data availability
The data that has been used is confidential.

Declaration of competing interest
The authors declare that they have no known competing financial interests or personal relationships that could have appeared to influence the work reported in this paper.

Acknowledgments
This research was undertaken under the MorphHab (PID2019-104979RB-I00/AEI/10.13039/501100011033) and MorphPeak (CGL2016-78874-R/AEI/10.13039/501100011033) research projects funded by the Spanish State Research Agency (Ministry of Science and Innovation) and the European Regional Development Fund Scheme (FEDER). The last author is a Serra Húnter Fellow at the University of Lleida. We also acknowledge all support provided by the Ebro Water Authorities (CHE), including the Automatic Hydrologic Information System of the Ebro river basin (SAIH) and the company Acciona for providing information regarding hydropeaks.

REFERENCES

Aigner, J., **Kreisler, A.**, **Rindler, R.**, **Hauer, C.** and **Habersack, H.** (2017) Bedload pulses in a hydropower affected alpine gravel bed river. *Geomorphology*, **291**, 116–127. DOI:10.1016/j.geomorph.2016.05.015

Andrews, E.D. (1983) Entrainment of gravel from naturally sorted riverbed material. *Geological Society of America Bulletin*, **94**, 1225. DOI:10.1130/0016-7606(1983)94<1225:EOGFNS>2.0.CO;2

Armanini, A. (2018) Principles of River Hydraulics. *Springer International Publishing*, Cham. DOI:10.1007/978-3-319-68101-6

Arnaud, F., **Piégay, H.**, **Béal, D.**, **Collery, P.**, **Vaudor, L.** and **Rollet, A.-J.** (2017) Monitoring gravel augmentation in a large regulated river and implications for process-based restoration. *Earth Surface Processes and Landforms*, **42**, 2147–2166. DOI:10.1002/esp.4161

Ashworth, P.J. and **Ferguson, R.I.** (1989) Size-selective entrainment of bed load in gravel bed streams. *Water Resour. Res.*, **25**, 627–634. DOI:10.1029/WR025i004p00627

Ashworth, P.J., **Ferguson, R.I.**, **Ashmore, P.E.**, **Paola, C.**, **Powell, D.M.** and **Prestegaards, K.L.** (1992) Measurements in a Braided River chute and lobe: 2. Sorting of bed load during entrainment, transport, and deposition. *Water Resour. Res.*, **28**, 1887–1896. DOI:0043-1397/93/92WR02748

Batalla, R.J., **Gibbins, C.N.**, **Alcázar, J.**, **Brasington, J.**, **Buendia, C.**, **Garcia, C.**, **Llena, M.**, **López, R.**, **Palau, A.**, **Rennie, C.**, **Wheaton, J.M.** and **Vericat, D.** (2021) Hydropeaked rivers need attention. *Environmental Research Letters*, **16**, 021001. DOI:10.1088/1748-9326/abce26

Batalla, R.J. and **Martín-Vide, J.P.** (2001) Thresholds of particle entrainment in a poorly sorted sandy gravel-bed river. *CATENA*, **44**, 223–243. DOI:10.1016/S0341-8162(00)00157-0

Batalla, R.J., **Vericat, D.**, **Gibbins, C.N.** and **Garcia, C.** (2010) Incipient bed-material motion in a gravel-bed river: field observations and measurements. *US Geol. Surv. Sci. Investig. Rep*, **5091**, 15. https://pubs.usgs.gov/sir/2010/5091/papers/Batalla.pdf

Bathurst, J.C. (2013) Critical conditions for particle motion in coarse bed materials of nonuniform size distribution. *Geomorphology*, **197**, 170–184. DOI:10.1016/j.geomorph.2013.05.008

Bladé, E., **Cea, L.**, **Corestein, G.**, **Escolano, E.**, **Puertas, J.**, **Vázquez-Cendón, E.**, **Dolz, J.** and **Coll, A.** (2014) Iber: herramienta de simulación numérica del flujo en ríos. *Revista Internacional de Métodos Numéricos para Cálculo y Diseño en Ingeniería*, **30**, 1–10. DOI:10.1016/j.rimni.2012.07.004

Brasington, J., **Vericat, D.** and **Rychkov, I.** (2012) Modeling river bed morphology, roughness, and surface sedimentology using high resolution terrestrial laser scanning: MODELING RIVER BED MORPHOLOGY WITH TLS. *Water Resour. Res.*, **48**, 1–18. DOI:10.1029/2012WR012223

Brunke, M. (1999) Colmation and Depth Filtration within Streambeds: Retention of Particles in Hyporheic Interstices. *International Review of Hydrobiology*, **84**, 99–117. DOI:10.1002/iroh.199900014

Buffington, J.M. and **Montgomery, D.R.** (1997) A systematic analysis of eight decades of incipient motion studies, with special reference to gravel-bedded rivers. *Water Resources Research*, **33**, 1993–2029. DOI:10.1029/96WR03190

Carrivick, J.L. and **Smith, M.W.** (2019) Fluvial and aquatic applications of Structure from Motion photogrammetry and unmanned aerial vehicle/drone technology. *WIREs Water*, **6**, e1328. DOI:10.1002/wat2.1328

Cereghino, R. and **Lavandier, P.** (1998) Influence of hypolimnetic hydropeaking on the distribution and population dynamics of Ephemeroptera in a mountain stream. *Freshw. Biol.*, **40**, 385–399. DOI:10.1046/j.1365-2427.1998.00353.x

Chardon, V., **Schmitt, L.**, **Arnaud, F.**, **Piégay, H.** and **Clutier, A.** (2021) Efficiency and sustainability of gravel augmentation to restore large regulated rivers: Insights from three experiments on the Rhine River (France/Germany). *Geomorphology*, **380**, 107639. DOI:10.1016/j.geomorph.2021.107639

Church (2006) BED MATERIAL TRANSPORT AND THE MORPHOLOGY OF ALLUVIAL RIVER CHANNELS. *Annual Review of Earth and Planetary Sciences*, **34**, 325–354. DOI:10.1146/annurev.earth.33.092203.122721

Church, M. and **Hassan, M.A.** (2002) Mobility of bed material in Harris Creek: MOBILITY OF BED MATERIAL IN HARRIS CREEK. *Water Resour. Res.*, **38**, 19-1-19-12. DOI:10.1029/2001WR000753

Church, M., **Hassan, M.A.** and **Wolcott, J.F.** (1998) Stabilizing self-organized structures in gravel-bed stream channels: Field and experimental observations. *Water Resour. Res.*, **34**, 3169–3179. DOI:10.1029/98WR00484

Coulombe-Pontbriand, M. and **Lapointe, M.** (2004) Geomorphic controls, riffle substrate quality, and spawning site selection in two semi-alluvial salmon rivers in the Gaspé Peninsula, Canada. *River Research and Applications*, **20**, 577–590. DOI:10.1002/rra.768

Cushman, R.M. (1985) Review of Ecological Effects of Rapidly Varying Flows Downstream from Hydroelectric Facilities. *North American Journal of Fisheries Management*, **5**, 330–339. DOI:10.1577/1548-8659(1985)5<330:ROEEOR>2.0.CO;2

Dey, S. and **Ali, S.Z.** (2019) Bed sediment entrainment by streamflow: State of the science. *Sedimentology*, **66**, 1449–1485. DOI:10.1111/sed.12566

Dietrich, W.E., **Kirchner, J.W.**, **Ikeda, H.** and **Iseya, F.** (1989) Sediment supply and the development of the coarse surface layer in gravel-bedded rivers. *Nature*, **340**, 215–217. DOI:10.1038/340301a0

Dingman, S.L. and **Afshari, S.** (2018) Field verification of analytical at-a-station hydraulic-geometry relations. *Journal of Hydrology*, **564**, 859–872. DOI:10.1016/j.jhydrol.2018.07.020

Ferguson, R. (2010) Time to abandon the Manning equation? *Earth Surf. Process. Landforms*, **35**, 1873–1876. DOI:10.1002/esp.2091

Ferguson, R.I., **Prestegaard, K.L.** and **Ashworth, P.J.** (1989) Influence of sand on hydraulics and gravel transport in a braided gravel bed river. *Water Resources Research*, **25**, 635–643. DOI:10.1029/WR025i004p00635

Fripp, J.B. and **Diplas, P.** (1993) Surface Sampling in Gravel Streams. *Journal of Hydraulic Engineering*, **119**, 473–490. DOI:10.1061/(ASCE)0733-9429(1993)119:4(473)

Galán, F. (2012) CENTRALES HIDROELÉCTRICAS Y PRESAS DEL ALTO ARAGÓN. *Fundation Esteyco*, Madrid, 90 pp.

Garcia, C., **Laronne, J.B.** and **Sala, M.** (1999) Variable source areas of bedload in a gravel-bed stream. *Journal of Sedimentary Research*, **69**, 27–31. DOI:10.2110/jsr.69.27

Garcia, M. (ed) (2008) Sedimentation Engineering: Processes, Measurements, Modeling, and Practice. *American Society of Civil Engineers*, Reston, VA. DOI:10.1061/9780784408148

Gibbins, C., **Vericat, D.** and **Batalla, R.J.** (2007) When is stream invertebrate drift catastrophic? The role of hydraulics and sediment transport in initiating drift during flood events. *Freshwater Biol*, **52**, 2369–2384. DOI:10.1111/j.1365-2427.2007.01858.x

Hammond, F.D.C., **Heathershaw, A.D.** and **Langhorne, D.N.** (1984) A comparison between Shields' threshold criterion and the movement of loosely packed gravel in a tidal channel. *Sedimentology*, **31**, 51–62. DOI:10.1111/j.1365-3091.1984.tb00722.x

Hassan, M.A. and **Church, M.** (2000) Experiments on surface structure and partial sediment transport on a gravel bed. *Water Resources Research*, **36**, 1885–1895. DOI:10.1029/2000WR900055

Hauer, C., **Schober, B.** and **Habersack, H.** (2013) Impact analysis of river morphology and roughness variability on hydropeaking based on numerical modelling: RIVER MORPHOLOGICAL IMPACTS ON HYDROPEAKING PROCESSES. *Hydrol. Process.*, **27**, 2209–2224. DOI:10.1002/hyp.9519

Hauer, C., **Unfer, G.**, **Holzapfel, P.**, **Haimann, M.** and **Habersack, H.** (2014) Impact of channel bar form and grain size variability on estimated stranding risk of juvenile brown trout during hydropeaking. Earth Surface Processes and Landforms. DOI:10.1002/esp.3552

Hayes, D.S., **Schülting, L.**, **Carolli, M.**, **Greimel, F.**, **Batalla, R.J.** and **Casas-Mulet, R.** (2022) Hydropeaking: Processes, Effects, and Mitigation. *Elsevier*, 134–149. DOI:10.1016/B978-0-12-819166-8.00171-7

Henderson, F.M. (1966) Open channel flow. *MacMillan Publishing Co*, New York.

Jackson, W.L. and **Beschta, R.L.** (1982) A model of two-phase bedload transport in an oregon coast range stream. *Earth Surface Processes and Landforms*, **7**, 517–527. DOI:10.1002/esp.3290070602

James, M.R. and **Robson, S.** (2012) Straightforward reconstruction of 3D surfaces and topography with a camera: Accuracy and geoscience application. *Journal of Geophysical Research: Earth Surface*, **117**, 2011JF002289. DOI:10.1029/2011JF002289

Julien, P.Y. (2002) River mechanics, 1st edn. *Cambridge University Press*. DOI:10.1017/CBO9781139164016

Kellerhals, R. and **Bray, D.I.** (1971) Sampling Procedures for Coarse Fluvial Sediments. *J. Hydraul. Div.*, **97**, 1165–1180. DOI:10.1061/JYCEAJ.0003044

Komar, P.D. (1987) Selective gravel entrainment and the empirical evaluation of flow competence. *Sedimentology*, **34**, 1165–1176. DOI:10.1111/j.1365-3091.1987.tb00599.x

Komar, P.D. and **Carling, P.A.** (1991) Grain sorting in gravel-bed streams and the choice of particle sizes for flow-competence evaluations. *Sedimentology*, **38**, 489–502. DOI:10.1111/j.1365-3091.1991.tb00363.x

Kondolf, G.M. (1997) Hungry Water: Effects of Dams and Gravel Mining on River Channels. *Environmental Management*, **21**, 533–551. DOI:10.1007/s002679900048

Kondolf, G.M. and **Piégay, H.** (eds) (2016) Tools in fluvial geomorphology. *Wiley*.

Leopold, L.B. and **Maddock, T.** (1953) The hydraulic geometry of Stream Channels and Some Physiographic Implications. Washington, D.C. DOI:10.3133/pp252

Lisle, T.E. and **Madej, M.A.** (1992) Spatial variation in a channel with high sediment supply. In: (Ed. P. Billi, R.D. Hey, C.R. Thorne, and P. Tacconi), *John Willey*, Hoboken, NJ, USA, 277–291.

López, R., **Garcia, C.**, **Vericat, D.** and **Batalla, R.J.** (2020) Downstream changes of particle entrainment in a hydropeaked river. *Science of The Total Environment*, **745**, 140952. DOI:10.1016/j.scitotenv.2020.140952

López, R., **Vericat, D.** and **Batalla, R.J.** (2014) Evaluation of bed load transport formulae in a large regulated gravel bed river: The lower Ebro (NE Iberian Peninsula). *Journal of Hydrology*, **510**, 164–181. DOI:10.1016/j.jhydrol.2013.12.014

MacKenzie, L.G., **Eaton, B.C.** and **Church, M.** (2018) Breaking from the average: Why large grains matter in gravel-bed streams: Breaking from the average. *Earth Surf. Process. Landforms*, **43**, 3190–3196. DOI:10.1002/esp.4465

Marion, D.A. and **Weirich, F.** (2003) Equal-mobility bed load transport in a small, step-pool channel in the Ouachita Mountains. *Geomorphology*, **55**, 139–154. DOI:10.1016/S0169-555X(03)00137-5

McCarron, C.J., **Van Landeghem, K.J.J.**, **Baas, J.H.**, **Amoudry, L.O.** and **Malarkey, J.** (2019) The hiding-exposure effect revisited: A method to calculate the mobility of bimodal sediment mixtures. *Mar. Geol.*, **410**, 22–31. DOI:10.1016/j.margeo.2018.12.001

Miller, M.C., **McCAVE, I.N.** and **Komar, P.D.** (1977) Threshold of sediment motion under unidirectional currents. *Sedimentology*, **24**, 507–527. DOI:10.1111/j.1365-3091.1977.tb00136.x

Moog, O. (1993) Quantification of daily peak hydropower effects on aquatic fauna and management to minimize environmental impacts. *Regulated Rivers: Research & Management*, **8**, 5–14. DOI:10.1002/rrr.3450080105

Núñez-González, F., **Rovira, A.** and **Ibàñez, C.** (2018) Bed load transport and incipient motion below a large gravel bed river bend. *Advances in Water Resources*, **120**, 83–97. DOI:10.1016/j.advwatres.2017.07.026

Packman, A.I. and **MacKay, J.S.** (2003) Interplay of stream-subsurface exchange, clay particle deposition, and streambed evolution. *Water Resources Research*, **39**, 2002WR001432. DOI:10.1029/2002WR001432

Parker, G. (2008) Transport of Gravel and Sediment Mixtures. In: *Sedimentation Engineering*, *American Society of Civil Engineers*, Reston, VA, 165–251. DOI:10.1061/9780784408148.ch03

Parker, G. and **Klingeman, P.C.** (1982) On why gravel bed streams are paved. *Water Resources Research*, **18**, 1409–1423. DOI:10.1029/WR018i005p01409

Recking, A. (2010) A comparison between flume and field bed load transport data and consequences for surface-based bed load transport prediction. *Water Resour. Res.*, **46**, 1–16. DOI:10.1029/2009WR008007

Rice, S.P. and **Haschenburger, J.K.** (2004) A hybrid method for size characterization of coarse subsurface fluvial sediments. *Earth Surface Processes and Landforms*, **29**, 373–389. DOI:10.1002/esp.1043

Rosgen David L. (1994) A Classification of Natural Rivers. *Catena*, **22**, 169–199. DOI:10.1126/science.61.1573.191

Ryan, S.E., **Porth, L.S.** and **Troendle, C.A.** (2002) Defining phases of bedload transport using piecewise regression. *Earth Surface Processes and Landforms*, **27**, 971–990. DOI:10.1002/esp.387

Rychkov, I., **Brasington, J.** and **Vericat, D.** (2012) Computational and methodological aspects of terrestrial surface analysis based on point clouds. *Computers & Geosciences*, **42**, 64–70. DOI:10.1016/j.cageo.2012.02.011

Schmutz, S., **Bakken, T.H.**, **Friedrich, T.**, **Greimel, F.**, **Harby, A.**, **Jungwirth, M.**, **Melcher, A.**, **Unfer, G.** and **Zeiringer, B.** (2015) Response of fish communities to hydrological and morphological alterations in hydropeaking rivers of austria. River Research and Applications. DOI:10.1002/rra.2795

Schülting, L., **Feld, C.K.** and **Graf, W.** (2016) Effects of hydro- and thermopeaking on benthic macroinvertebrate drift. *Science of The Total Environment*, **573**, 1472–1480. DOI:10.1016/j.scitotenv.2016.08.022

Sear, D.A. (1992) Impact of hydroelectric power releases on sediment transport processes in pool-riffle sequences. In: (Ed. P. Billi, R.D. Hey, C.R. Thorne, and P. Tacconi), *John Wiley; Sons*, 629–250.

Sear, D.A. (1995) Morphological and sedimentological changes in a gravel-bed river following 12 years of flow regulation for hydropower. *Regulated Rivers: Research & Management*, **10**, 247–264. DOI:10.1002/rrr.3450100219

Smokorowski, K.E. (2022) The ups and downs of hydropeaking: a Canadian perspective on the need for, and ecological costs of, peaking hydropower production. *Hydrobiologia*, **849**, 421–441. DOI:10.1007/s10750-020-04480-y

Tena, A., **Ville, F.**, **Reñe, A.**, **Yarnell, S.M.**, **Batalla, R.J.** and **Vericat, D.** (2022) Hydrological characterization of hydropeaks in mountain rivers (examples from Southern Pyrenees). *River Research & Apps*, rra.4058. DOI:10.1002/rra.4058

Thompson, C. and **Croke, J.** (2008) Channel flow competence and sediment transport in upland streams in southeast Australia. *Earth Surface Processes and Landforms*, **33**, 329–352. DOI:10.1002/esp.1558

Vanzo, D., **Siviglia, A.**, **Carolli, M.** and **Zolezzi, G.** (2016) Characterization of sub-daily thermal regime in alpine rivers: quantification of alterations induced by hydropeaking. *Hydrological Processes*, **30**, 1052–1070. DOI :10.1002/hyp.10682

Vázquez Tarrío, D. (2013) Transporte de sedimento como carga de fondo en la cuenca del río Narcea (vertiente Norte de la Cordillera Cantábrica). PhD thesis, Universidad de Oviedo

Vericat, D., **Batalla, R.J.** and **Garcia, C.** (2006) Breakup and reestablishment of the armour layer in a large gravel-bed river below dams: The lower Ebro. *Geomorphology*, **76**, 122–136. DOI:10.1016/j.geomorph.2005.10.005

Vericat, D., **Batalla, R.J.** and **Gibbins, C.N.** (2008) Sediment entrainment and depletion from patches of fine material in a gravel-bed river. *Water Resour. Res.*, **44**, 1–15. DOI:10.1029/2008WR007028

Vericat, D., **Ville, F.**, **Palau-Ibars, A.** and **Batalla, R.J.** (2020) Effects of hydropeaking on bed mobility: Evidence from a pyrenean river. *Water*, **12**, 178. DOI:10.3390/w12010178

Wathen, S.J., **Ferguson, R.I.**, **Hoey, T.B.** and **Werritty, A.** (1995) Unequal Mobility of Gravel and Sand in Weakly Bimodal River Sediments. *Water Resour. Res.*, **31**, 2087–2096. DOI:10.1029/95WR01229

Westoby, M.J., **Brasington, J.**, **Glasser, N.F.**, **Hambrey, M.J.** and **Reynolds, J.M.** (2012) 'Structure-from-Motion' photogrammetry: A low-cost, effective tool for geoscience applications. *Geomorphology*, **179**, 300–314. DOI:10.1016/j.geomorph.2012.08.021

Wheaton, J.M., **Brasington, J.**, **Darby, S.E.** and **Sear, D.A.** (2010) Accounting for uncertainty in DEMs from repeat topographic surveys: improved sediment budgets. *Earth Surface Processes and Landforms*, **35**, 136–156. DOI:10.1002/esp.1886

Whitaker, A.C. and **Potts, D.F.** (2007) Analysis of flow competence in an alluvial gravel bed stream, Dupuyer Creek, Montana. *Water Resources Research*, **43**, 2006WR005289. DOI:10.1029/2006WR005289

White, R.W. (1982) Transport of graded gravel bed-material. In: (Ed. J.C. Hey, J.C. Bathurst, and C.R. Thorne), *John Wiley*, New York, 181–223.

Wilcock, P., **Pitlick, J.** and **Cui, Y.** (2009) Sediment transport primer: estimating bed-material transport in gravel-bed rivers. Ft. Collins, CO. DOI:10.2737/RMRS-GTR-226

Wilcock, P.R. and **Crowe, J.C.** (2003) Surface-based Transport Model for Mixed-Size Sediment. *J. Hydraul. Eng*, **129**, 120–128. DOI:10.1061/ASCE0733-94292003129:2120

Wilcock, P.R. and **DeTemple, B.T.** (2005) Persistence of armor layers in gravel-bed streams. *Geophysical Research Letters*, **32**, 2004GL021772. DOI:10.1029/2004GL021772

Wilcock, P.R. and **McArdell, B.W.** (1993) Surface-based fractional transport rates: Mobilization thresholds and partial transport of a sand-gravel sediment. *Water Resour. Res.*, **29**, 1297–1312. DOI:10.1029/92WR02748

Wilcock, P.R. and **McArdell, B.W.** (1997) Partial transport of a sand/gravel sediment. *Water Resour. Res.*, **33**, 235–245. DOI:10.1029/96WR02672

Wolman, M.G. (1954) A method of sampling coarse river-bed material. *Trans. Am. Geophys. Union*, **35**, 951. DOI:10.1029/TR035i006p00951

Wood, P.J. (1997) Biological Effects of Fine Sediment in the Lotic Environment. *Environmental Management*, **21**, 203–217. DOI:10.1007/s002679900019

Woodget, A.S., **Carbonneau, P.E.**, **Visser, F.** and **Maddock, I.P.** (2015) Quantifying submerged fluvial topography using hyperspatial resolution UAS imagery and structure from motion photogrammetry. *Earth Surf. Process. Landf.*, **40**, 47–64. DOI:10.1002/esp.3613

Yalin, M.S. and **Karahan, E.** (1979) Inception of Sediment Transport. *Journal of the Hydraulics Division*, **105**, 1433–1443. DOI:10.1061/JYCEAJ.0005306

Chapter 5

PhotoMOB: Automated GIS method for estimation of fractional grain dynamics in gravel bed rivers.

Pyramides reach river bed (Upper Ésera River), 07/03/2019. Author: Fanny Ville

Overview

Chapter 5 consists of two parts, each in the form of an article submitted to *Earth Surface Processes and Landforms* (under review. The pair papers present PhotoMOB, an automated photographic processing GIS-based method developed as part of the thesis. The first paper presents the surface bed grain characterization method and its associated errors. The second presents the mobility characterization method and its associated errors.

In this chapter the two parts makes the section numbering more complex. The first digit corresponds to the number of the chapter, the second indicates the number of the part (1 or 2) and the following digits refer to the subdivisions.

Part 1: Grain size

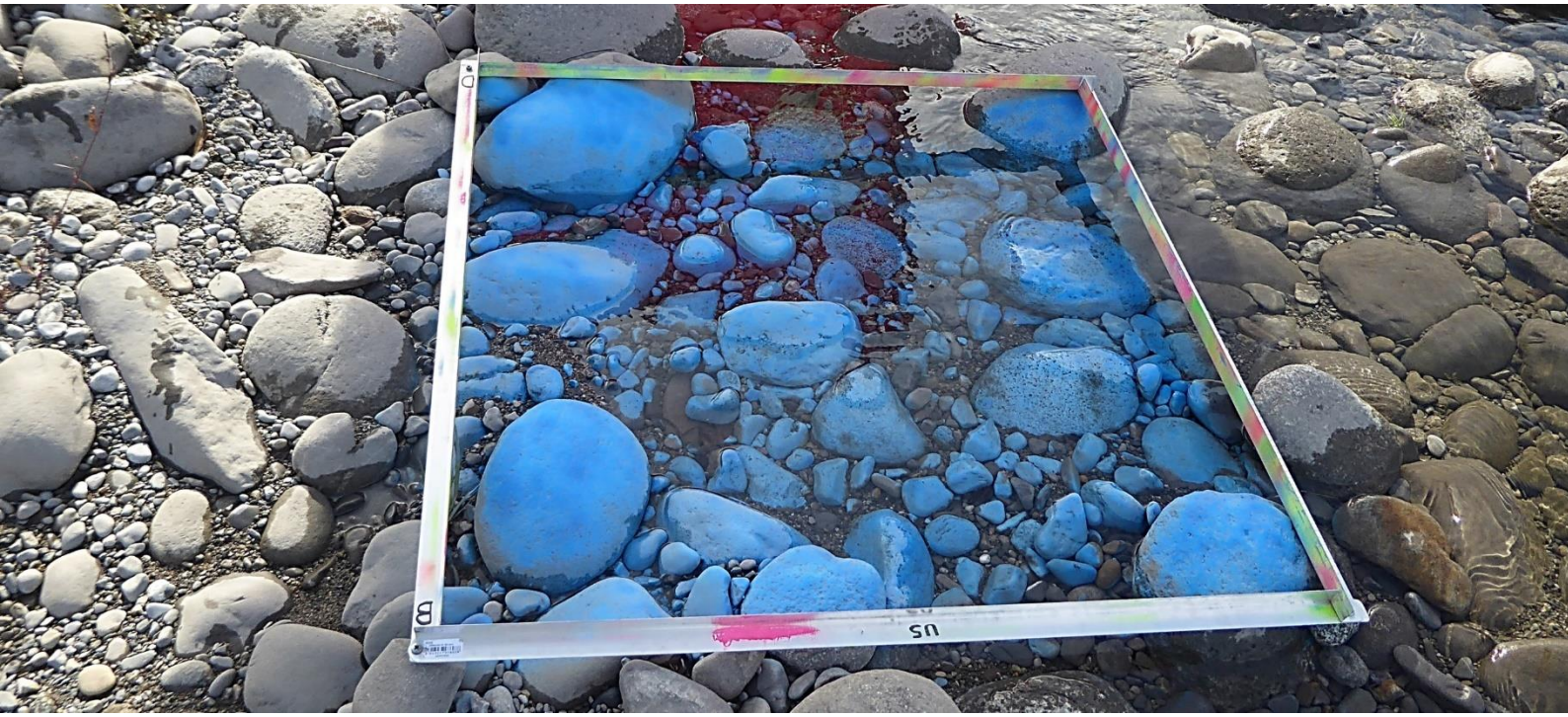

Bed grain size characterization of coarse bed at Laspuña reach (Upper Cinca River), 0.6 km downstream of hydropower plant. The size of the metal frame is 1m², 01/11/2020. Author: Fanny Ville

This part 1 contain the following submitted and under review paper by the journal Earth Surface Processes and Landforms. IF (JCR-SCI):3.941, Q1(2022). Ville, F., Vericat, D., Batalla, R. J., & Rennie, C. (2023). Photomob: automated gis method for estimation of fractional grain dynamics in gravel bed rivers. Part 1: grain size [Preprint]. Earth Sciences. https://doi.org/10.31223/X5K67D

Abstract

Particle entrainment intensity is spatially and temporally variable, making it a complex phenomenon to measure. This paper is the first of a pair, in which we present an automated image processing procedure (*PhotoMOB*) for monitoring the mobility/stability of gravel river beds. The method is based on local comparison of the shape of the grains identified at the same coordinates between successive photos to identify coincident and new grains. For each grain fraction, the proportion of grains that remained immobile and the proportion of grains newly identified in the study area can be calculated. In this part 1 paper, we present only the GIS-based procedure for identifying and characterizing grain shapes in digital images of bed patches to derive a reliable surface Grain Size Distribution (GSD), and for subsequent analyses of bed mobility. The procedure is compatible with different forms of sampling (Area-by-Number i.e., AbN, and Grid-by-Number i.e., GbN) and types of measurements (*continuous* or real measures of the axes and *discrete* square holes measurements of the axes). The performance of the GIS procedure is evaluated by comparing estimated percentiles against manually delineated grains in ten 40x40cm image samples, as well as against the real bed grain sizes from the same patches measured with a Pebble-Box (*continuous* axis value) and two samples measured with a template (*discrete* axis value). Under optimal condition, the average root mean squared error (RMSE) of the manual procedure compared to the real measurement is 8.2% in AbN and 16.3% in GbN, while PhotoMOB performance is similar with RMSE of 9.5% in AbN and 16.6% in GbN.

The paper also analyses how the tool performs when compared to *discrete* procedures such as measurement with templates. We found that in AbN, the under-estimation of the apparent size due to the imbrication effect is of the same order of magnitude as the under-estimation of the grain size measured by template. In GbN form, results emphasize the need of converting grain axis as a function of the average grain flatness for compatibility with *discrete* measurement, as coarse grains have more weight in the distribution and are often flatter in shape, hence are more often retained in inferior classes than smaller more spherical particles. A sufficiently large and appropriate sample area could reduce all the above mentioned RMSE by a third for AbN and by half in GbN.

Keywords: Photographic-method, Image processing, GIS, Grain delineation, Area- and Grid-by-Number

5.1.1 INTRODUCTION

Bed-material dynamics (mobility or stability), is a process controlled by different factors, notably, bed structure, sediment supply, flow hydraulics, and bed texture, i.e., the shape, size and the position of the grains that compose the river bed (e.g. Cassel et al., 2021; Church et al., 1998; Deal et al., 2023; Dietrich et al., 1989). Depending on the importance and combination of these factors, and the history of stress (e.g. Mao, 2012, 2018; Ockelford et al., 2019; Ockelford, 2011; Ockelford and Haynes, 2013), gravel riverbeds can be subject to varying degrees of mobility in time and space. This makes it a complicated process to measure and qualify. A common indirect method of tracing grain dynamics consists of painting a surface area of the bed and then surveying after a hydrological event. This method avoids alteration of the natural packing of the particles without limitation of the size of the traced grain. If entrained painted particles can be located downstream, then transport distances can also be measured (e.g. Brenna et al., 2019; Church and Hassan, 1992; Hassan and Ergenzinger, 2003; Mao et al., 2017; Vázquez-Tarrío et al., 2019b; Vericat et al., 2020).

However, this technique has several limitations (see Text **S** Section 5.1.6.1), among which is that a large amount of information from the original patch location is not further analyzed such as the proportion and size of immobile particles. A solution can be to compare successive images of the bed surface taken at the same location (Cerney, 2010; Peckarsky et al., 2014; Vericat et al., 2008a). Information related to grain dynamics can be extracted by a spatial grain-by-grain inter-analysis of the particles present in the two photographs. In this case, a semi- or fully-automated image processing procedure is extremely useful. This enables photographing and subsequent analysis of many different areas of the bed, such that the spatial and temporal variability of bed particle entrainment and transport can be examined. As far as we know this has not been yet fully developed. Until now, several automated procedures have been developed only for detecting particles in images and measuring them to extract the Grain Size Distribution (GSD) of the photographed surface (e.g. Butler et al., 2001; Chang and Chung, 2012; Detert and Weibrecht, 2013 ; Graham et al., 2005a, 2005b; Ibbeken and Schleyer, 1986; Purinton and Bookhagen, 2019; Sime and Ferguson, 2003).

We present in this pair of papers, a GIS-based photographic processing procedure *PhotoMOB* for first characterizing the grain-size of the surface bed-materials (this paper i.e., Part 1) and quantify the changes in bed surface sediments (texture) for individual targeted patches and individual and/or sequential hydrological events. We do not aim to merely promote a new automatic image processing procedure for extracting the GSD of gravel bed river surfaces, but to go one step further. We developed a second part to determine the proportion of the bed disturbed and grain mobility by fractions (Chapter 5, Section 5.2.1). Instead of estimating the transport distance of recovered tagged particles, this method focuses on a given square of a bed with the objective of quantifying for each grain fraction, the proportion of grains (number or area) that has remained stationary and the proportion that is occupied by particles that were not originally detected in this area. In addition, new particles deposited on the study surface will be included in the analysis of the next hydrological event without having made additional effort in the field other than the acquisition of a new photo.

This initial paper presents the workflow under GIS environment to perform grain shape identification and characterization. The tool is capable of deriving *continuous* reliable surface grain size distributions (GSD) in Area-by-Number (AbN) (i.e., a number of grains on a given area) as well as in a Grid-by-Number form (i.e., sampling of a predetermined number of grains according to a grid of sampling points), and also a *discrete* size measurement that can be compared to pebble count data (Wolman, 1954). We present the results of an evaluation of the performances with a photo-set showing different characteristics of surface heterogeneity (i.e., grain size, lithology, painted or unpainted grains, direct sunlight or shaded, wet or dry particles). The performances of *PhotoMOB* are discussed and compared with the ones obtained with other available tools. Finally, we address the limits of the method as well as the compatibility of the obtained results with other non-photographic methods. In the course of this article, all the references to "Text **S**", and "Figure **S**" followed by a number indicate the location of the element in question in the supplementary information.

5.1.2 THE PHOTOMOB WORKFLOW

Figure 5.1 represents the entire workflow of the *PhotoMOB* GIS toolbox. The objective of the procedure is to identify and characterize the grains observed in a photo and, ultimately, to simply compare two photos, of the exact same bed area, acquired before and after a hydrological period in order to estimate fractional grain dynamics. The first stage Figure 5.1 **B** consists of scaling the photos and then detecting and characterizing each particle in the images (i.e., size, shape and orientation characteristics). This allows extraction, Figure 5.1 **C**, of the grain size distribution, the cumulative distribution as well as percentiles, distribution of grains' orientation, proportion of the area occupied by fine material (the finest limit is defined by the operator). Only a brief presentation of the procedure will be given here. The reader is invited to read the supplementary material Text **S** Section 5.1.6.2 for a detailed view of the developed procedure. The second part, Figure 5.1 **D**, represented by the shaded area and fully developed in the companion paper (Chapter 5, Section 5.2.1), consists in comparing the two photos, called here, pre (T0) and post-event (T1) photos. The shape (area, *a*-axis and *b*-axis) of each grain positioned between the two photos at the same coordinates are compared in order to classify them as possibly identical (i.e., immobile particle) or not (i.e., particle is different between images and therefore indicates new particle). This grain-by-grain analysis allows an estimate of the proportion of the bed was disturbed and the fractional mobility within the patch Figure 5.1 **E**.

5.1.2.1 Image collection

Once a sufficiently large target area has been selected, a frame (see Text **S** Section 5.1.6.2.1) with known exact internal dimensions is placed on the riverbed to delineate the area. The distance between each internal corner will be used to locally scale the images. The photo is recommended to be taken facing against the flow direction, with nadir view (perpendicular to the riverbed), and with the area protected from direct sunlight to avoid brightness changes within the photo. In general, the more homogeneous the area is in terms of light and colour, the easier is to detect the particles automatically. Finally, the positions of the four corners of the frame can be marked and/or surveyed by a topographic method to enable finding again the location for a subsequent photo collection. Once the area is re-visited, the frame is placed back on the bed, and the second photo is taken following the same protocol. This last field phase can be repeated for the same area successively according to successive flow events (as show in Figure 5.1 **A**).

5.1.2.2 Bed particle detection and characterisation

Once the pre- and post-event photos have been acquired, the objective of the first part of the GIS procedure is the transformation of the images (i.e., raster data type) into vector data layers (polygon type), reproducing the contour of each particle present on the photos. In this manuscript, we use the words segmentation, digitalization, delimitation and delineation as synonyms. This process is based on the assumption that the boundaries between particles correspond to the darkest pixels in the image, Figure 5.1 **B1**. Grain detection and characterization is done in five steps represented also in Figure 5.1 **B**: image pre-processing (B.1), and the image processing steps of image classification (B.2), image binarization (B.3), boundary adjustment (B.4), and grain characterization (B.5).

5.1.2.2.1 Image pre-processing

In order to facilitate good detection of the particles, the photos are first filtered externally to GIS in GIMP (Team, 2019), a free image manipulation software, to smooth the intra-grain noise while preserving edges. Afterwards, the filtered images are loaded into GIS. The four internal corners of the frame are marked manually and used as local reference points to scale the photo and correct the perspective of the image by applying a projective transformation. Finally, the second (or post-event) photo has to be aligned manually with the first one with a further projective transformation. All of these steps are developed in much greater detail in Text **S** Section 5.1.6.2.2.1.

5.1.2.2.2 Image processing

In this section we only briefly present the steps, all the thresholds and precise parameters are available in Text **S** Section 5.1.2.2.2. The scaled filtered images are transformed into a grey scale image (intensity level). Then these grey scale images have to be transformed into binary images, where the foreground would correspond to the particles (high intensity, white) and the background to the boundary of the particles and gaps (low intensity, black). To generate this binarization, a *threshold of dark intensity* must be selected to perform the partition. The selection of the threshold value to partition the image is based on the method of moments thus relies on use of the histogram of the frequency distribution of the grey levels of the pixels Figure 5.1 **B3**. The whole process can be *supervised* by the operator or be performed *automatically* through a threshold prediction model developed in this study. A fully detailed description of the prediction model is available in Text **S** Section 5.1.6.2.2.3. The prediction is based on a visual approximation of the areal proportion of material finer than pebbles (<16 mm) covering the study area correlated with the optimal grey level binarization threshold.

This model was trained on 67 photos representing three different light and colour conditions (C1: painted, C2: not painted, C3: not painted and with light variation) with a total of 34246 grains manually digitalized to extract the % area finer than 16 mm. In parallel, each of the same images was processed in the tool. For each of them, 22 threshold grey levels were tested, not taken as an absolute value but relative to the mean of the pixel distribution, and a single operator selected the one that provided the best segmentation. Figure 5.2 **C** shows the prediction models of the binarization threshold established with these pairs of information. A validation set of 11 patches photographed in the three conditions with proportions of area below 16 mm ranging from 15% to 71% was collected. The mean absolute error of prediction (average distance between the model line and the validation point for each photo condition on Figure 5.2 **C** was 1 grey level for photo conditions C1 and C2, but 2 grey levels for C3.

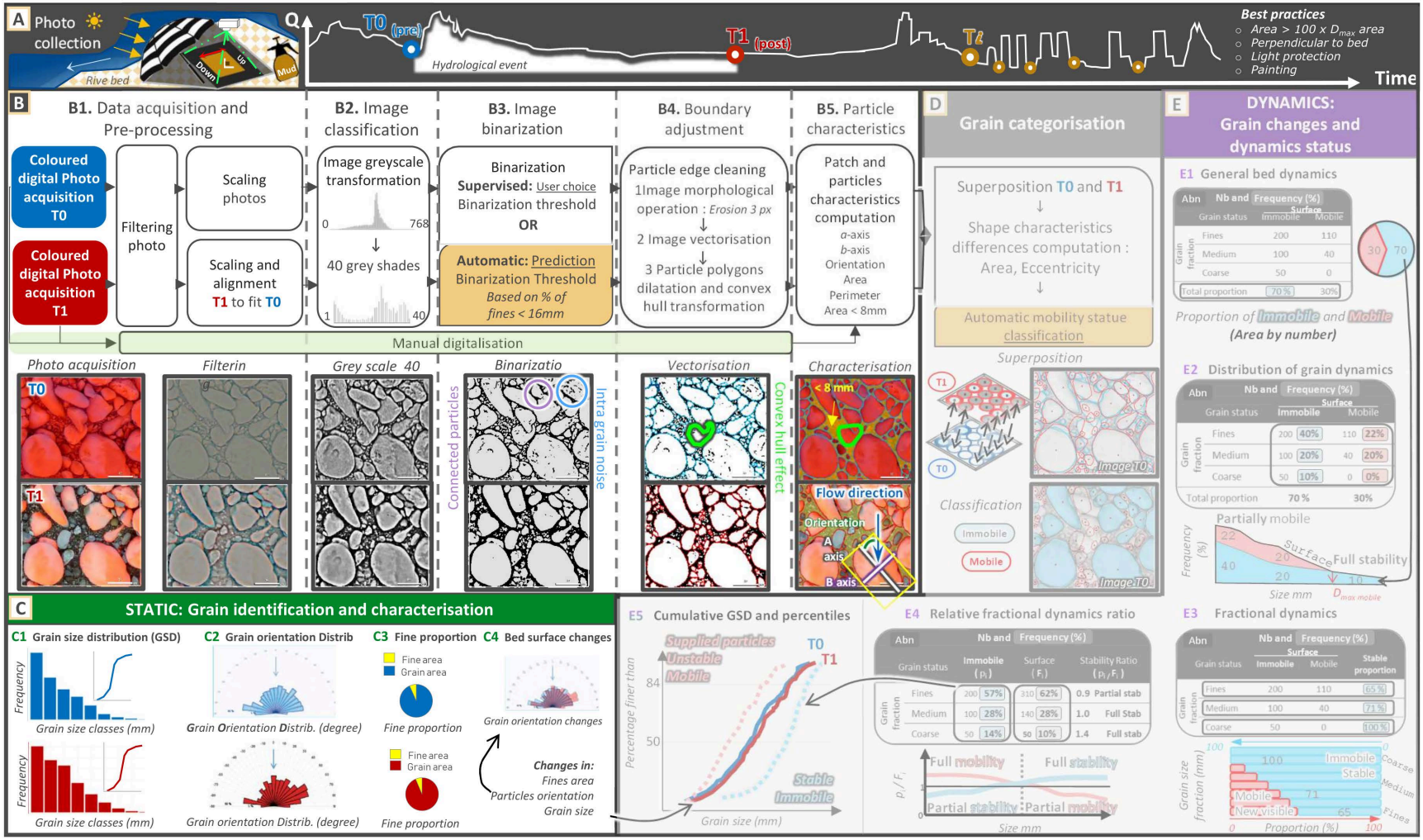

Figure 5.1: Illustration of the entire workflow required to sample and characterize the bed surface (developed in this paper) and sediment dynamics (shaded blocks representing what will be further analyzed in Part 2). (**A**) Photo acquisition. (**B**) Extraction of grain and patch characteristics. (**C**) Possible output after patch surface characterization. (**D**) Characterization of grain dynamics and (**E**) possible output from characterization. The yellow boxes represent the developed models (i) of dark threshold prediction (see text) and (ii) of particle classification. Note the effect of the convex hull transformation on the green particle in the center of the two images in the Vectorisation and Characterization columns. In the Characterization column, the second image shows the sketch explaining how particle characteristics are derived.

Then, the white pixel areas are converted from raster to polygons, vector features, yielding the outline of each particle Figure 5.1 **B4**. A succession of boundary adjustments and a convex envelope are applied. An example can be seen between the images in Figure 5.1 **B4** Vectorisation and Figure 5.1 **B5**, which present the raw delimitation and the convex envelope (note the highlighted particle in the centre). Once this convex hull is generated, it is possible to extract six characteristics of the patch. The (i) area and (ii) perimeter of each detected particle are directly acquired from the convex hull. For (iii) the longest axis (*a*-axis) and (iv) the intermediate axis (*b*-axis), on each particle, a minimum bounding rectangle box delimiting its smallest width is generated. The length of this rectangle corresponds to an estimate of the particle's *a*-axis, while its width corresponds to the particle's *b*-axis. Furthermore, the angle of the longest axis with north gives us information about (v) the orientation of the particle (see Figure 5.1 **B5** and **C**). Finally, (vi) an estimate of the area covered by fine material is obtained by subtracting from the total study area the summed area of particles with *b*-axis larger than a fine limit specified by the operator (by default 8mm).

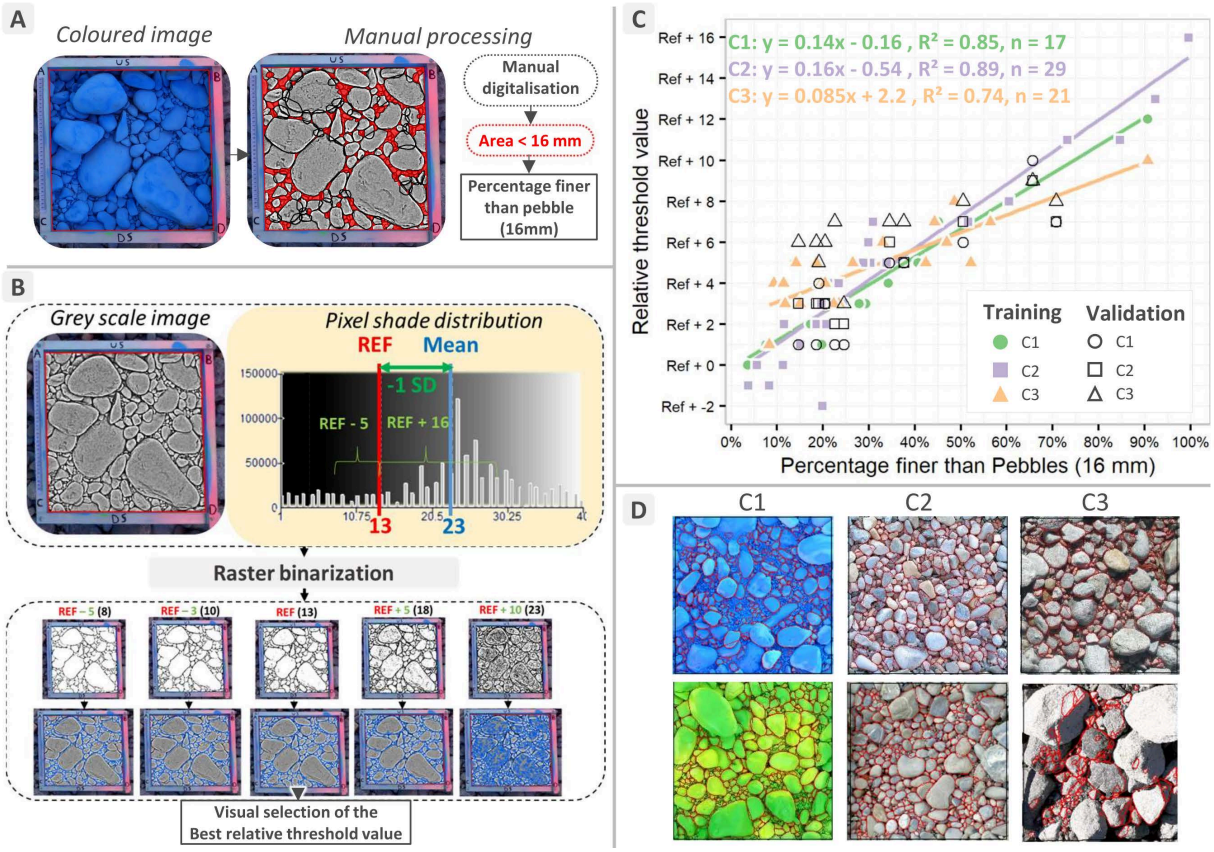

Figure 5.2: Training data sets used to build the dark threshold prediction model for the 3 photo conditions (n=68). (**A**) Percentage area covered by particles finer than pebbles derived from manual digitisation. (**B**) Relative value of binarisation threshold tested (22) and visual selection of the best threshold leading to an optimal delineation to build the (**C**) threshold prediction model for the 3 photo conditions. (**D**) Example of grain delineation generated by the best selected threshold for the 3 photo conditions and from different river beds.

5.1.3 METHOD FOR PERFORMANCES AND COMPATIBILITY ASSESSMENT

Two questions guide the performance analysis:

(1) How good is the automatic detection of objects (grain) in the image? For this, we will compare the GSDs from the automated segmentation results, with GSDs from manual digitalization (what we consider the *gold standard*, the best we can expect for grain identification).

(2) How well do the manual and automated procedures reproduce the grains present on the surface of the bed? That is, the combined error of the segmentation procedure developed here and the errors inherent in the photographic method. To do this, we will compare the GSDs of grains identified (automatically or manually) on the images with those within the target areas extracted using the *paint-and-pick* protocol to collect all surface grains (e.g., Graham et al., 2005b) and then measured in the laboratory.

The photographic method allows sampling in the form of a number of particles (analysis method) per area (sampling method) and extracting quantitative real values (i.e., *continuous* type variables) per each grain. In order to analyse the performance of the tool, a control data set is needed, of the same form as the data to be compared (i.e., Area-by-Number (AbN)). This data set will avoid errors that would be linked to the method of data acquisition. Both manual digitalization and real data from *paint-and-pick* corresponds to AbN form (Bunte and Abt, 2001) and were preferred to grid sampling of digitalized grain on the images or the common pebble count method (Wolman, 1954) corresponding to a Grid-by-Number form (GbN).

Additionally, to the above-mentioned questions, the analysis of the compatibility of data from the photographic method with other forms and methods is guided by two other questions:

(3) How well the photographic method produces correct data in GbN form? We will transform the tested data from the images (manual and automatic) as well as the control data (*paint-and-pick*) from the AbN form to the GbN to evaluate the deviation between the test and control data in the latter form.

(4) How well the photographic method provides data compatible with data obtained by other non-photographic methods? Generally, of the GbN form and with *discrete* square holes measurements of the axes. The compatibility is analysed by comparing the GSD resulting from the automatic and manual image procedures extracted as GbN form with control data (*paint-and-pick* sampling) measured by a square holes template (binned *b*-axis sizes).

5.1.3.1 Control dataset

5.1.3.1.1 Control data set acquisition

A control dataset was used to evaluate the performance and reproducibility of the image processing procedure to produce corrected grain identification and associated GSD and as well as providing compatible data compare with other methods. The control dataset was obtained in two rivers of the South Central Pyrenees (Cinca and Ésera) to introduce lithological, shape, and imbrication variability. Moreover, at each site, the choice of patches to be photographed was guided to also introduce variations in general GSD (coarse, fine, intermediate) and possible factors leading to error of particle detection by creating complexity on images: e.g., partially wet surface, heterogeneous lithology.

A Panasonic DMC-TZ60EG© digital camera with a maximum image resolution of 4896 × 3672 (18 MP) was used to take the pictures perpendicular to the surface of the bed at a height of about 1.70 m from the ground, which gives an average image resolution of 0.4 mm after scaling. The detection limit of the particles was therefore on average 5.2 mm *b*-axis (ca. 13x13 pixels). Ten sediment patches of 0.16 m² square (40 cm × 40 cm) were photographed. According to Diplas and Fripp (1992) and Graham et al. (2005a), to be able to represent an accurate GSD with a 0.16 m² area, the size of the larger *b*-axis particle should be about 40 mm. However, it is worth to remark that the aim here was not to fully represent the bed surface but to understand how well the photographic method reproduces it.

On each targeted area, a metal frame was placed and oriented in an upstream-downstream direction to (i) ensure a constant sampling area, (ii) orient the photo with respect to the flow direction, (iii) serve as a stencil for painting the area and (iv) allow scaling via the 4 inner corners of the frame. A first photo was acquired, corresponding to condition C3, and a second photo was acquired while shielding the area from direct sunlight with a beach umbrella, corresponding to photographic condition C2. Finally, the area inside the frame was painted and then photographed again while protected from direct sunlight. The latter corresponds to condition C1, expected to be optimal for *PhotoMOB* procedure. All these photographs are shown in **S** Figure 5.10.

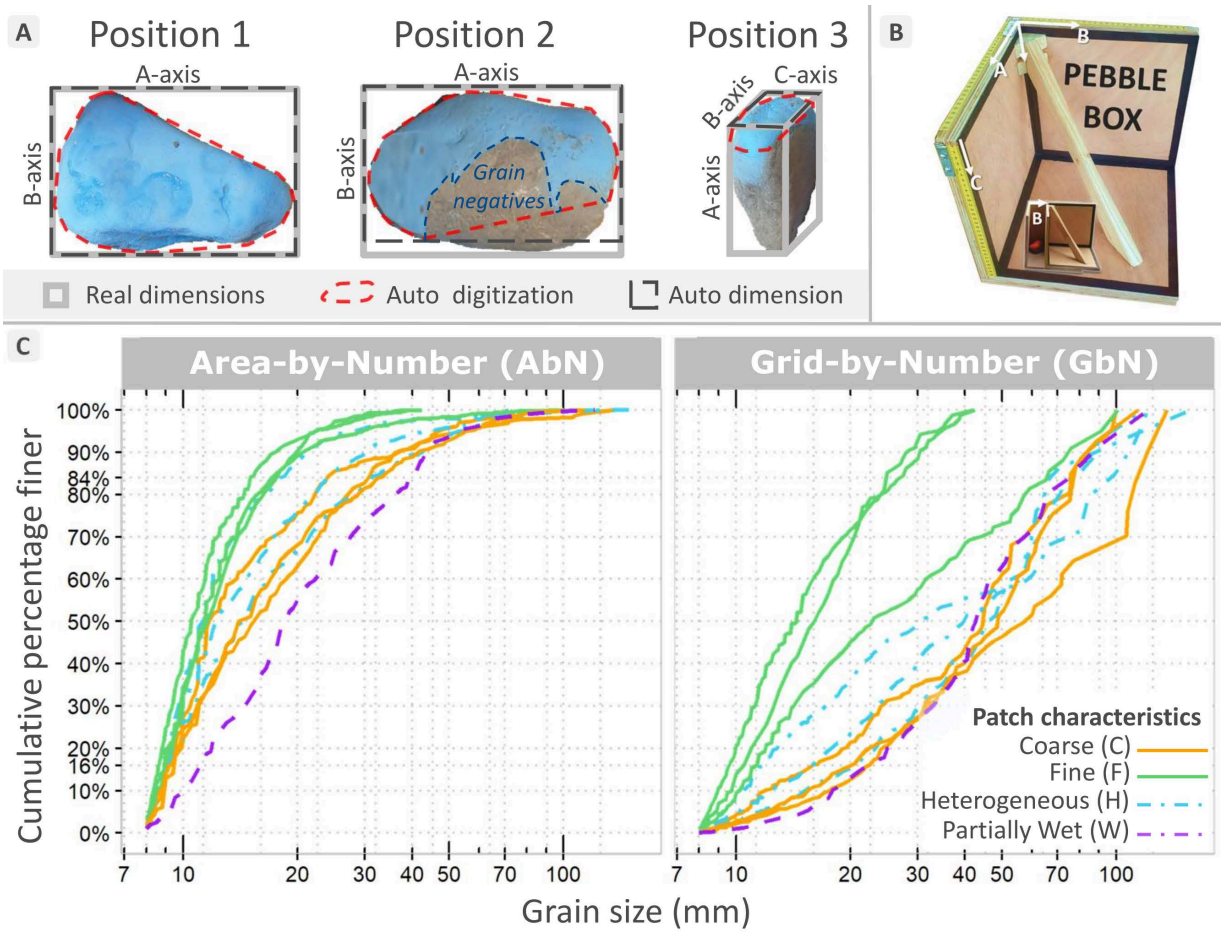

Figure 5.3: (**A**) Illustration of the position and orientation of the particles on the bed according to the projection of the paint on their surface. (**B**) Illustration Pebble-Box manual device (Ibbeken and Denzer, 1988) used to measure particle size axis. (**C**) Validation dataset used to test the particle detection image-processing procedure. Cumulative *b*-axis grain size distribution curves for the 10 patches and their main characteristics. Data are for AbN (*paint-and-pick* samples) truncated at 8 mm and converted to GbN using the method of Kellerhals and Bray (1971).

After taking the last picture, the metal frame was removed and all painted or semi-painted particles that were in contact with the edge were carefully collected and stored in a container. Then, all painted particles completely inside the area that were not in contact with the edges were collected and stored in a second container. Both containers were returned to the laboratory.

For each of the ten samples, the position orientation on the bed of each grain was estimated and classified into three categories based on the projection of the paint on their surface (Figure 5.3). Position 1 (P1) particles rest in a stable position with the longest and intermediate axes exposed on the surface and fully painted. These particles should be correctly characterized by our procedure. This position can be compared to the work of Ibbeken and Schleyer (1986), **S** Figure 5.10. Position 2 (P2) particles have the same orientation as P1 but are partially covered by one or more other particles. The painted surface shows the negative of other particles. In these conditions, the *b*-axis may be under-estimated and the aspect ratio distorted. However, if the hidden portion is less than half of the particle, the under-estimation will be minimal. Finally, Position 3 (P3) particles are orientated such that the surface exposure and thus paint is not projected onto the side showing the *a*- and *b*-axes. The size of the axes may be then under-estimated. Additionally, particles with only a small and light trace of paint were assumed to come from the sub-surface and were discarded.

The actual three orthogonal axes of each particle were then measured manually using a Pebble-Box (Bunte and Abt, 2001; Ibbeken and Denzer, 1988) (*b*-axis > 8 mm) or with a caliper (*b*-axis < 8 mm). The use of the Pebble-Box Figure 5.3 **B** allows for fast and consistent measurement of the orthogonal axes as all three axes can be measured by manipulating the particle once without re-manipulating it. The accuracy of the measurement is in the range of ½ to 1 mm. About 6800 particles were manually measured and classified. In addition to being able to establish the size distribution of the *b*-axis, the measurement of the three axes allows the shape of each particle to be determined via the Zingg classification (Zingg, 1935). These samples are considered the real control grains (mentioned as *paint-and-pick* reference). Finally, for two samples, representing a total of 1000 grains, each particle, before being measured in the Pebble-Box, was passed through a template with several sieve-sized square-holes *D* with 0.5 ψ -increment (ψ = log2[*b*]) to obtained binned *b*-axis sizes.

5.1.3.1.2 Control data set characteristics

The characteristics of each sample are presented in Table 5.1, while the GSDs are presented in Figure 5.3 **C** and the particle shape and position are available in Figure 5.11. Cumulative particle size distributions are presented as Area-by-Number directly from the *paint-and-pick* sampling and also as a Grid-by-Number via the Kellerhals and Bray (1971) conversion method by multiplying the frequency of all particles-size D_i by an exponent of 2 (D_i^2).

The sediments of the Cinca consisted mainly of coarse-grained white granite (increasing the complexity of the photographed surface to be segmented) and pale limestone. The Ésera sediments were dominated by dark sandstone with varying degrees of metamorphism. The particle shapes of the two coarse samples S2 and S10 from this river were significantly different from the other seven with predominantly discoidal shapes (41 and 49% respectively)

The sampled patches were divided into four groups based primarily on grain size and lithology. Samples 1 through 3 were grouped as having a coarse particle size distribution (D_{50} in GbN form ranging between 44 mm to 57 mm). Samples 4 through 6, all coming from the Cinca, were grouped as having heterogeneous surfaces. Samples 4 and 5 were heterogeneous in terms of lithology, while sample 6 showed a low grain sorting coefficient (Folk and Ward, 1957) of 1.3 (poorly sorted). Samples 7 through 9 were representative of fine patches composed of between 38 and 71% material finer than pebbles (16 mm) and with D_{50} in GbN form between 14 to 22 mm. Finally, the last sample S10, was collected because it had a partially wet surface that may generate issues for grain

delineation. As 49% of the sample was disc-shaped (flat and circular) and dominated at 38% by particles in position P2, it will be difficult to characterize correctly by photographic methods.

It should be noted that all samples showed a similar evolution of the median shape with increasing size (*b*-axis). The coarser the particles, the flatter they tended to be. A more complete description of these trends and of the characteristics of the control samples in general is available in the supplementary Text **S**3.1.2 and Figure 5.11 .

Table 5.1

	Sample	River	Fines (%)[a]	Grain number	D_{max} (mm)	Ratio: sample area/ d_{max} area	Number (nb) and frequency (%) of grains per classes	8 11.3	11.3 16	16 22.6	22.6 32	32 45.3	45.3 64	64 90.5	90.5 128	128 >	GSD form[b]	Percentiles in mm D5	D16	D50	D84	D95	Sorting[c]
Coarse	S1	Cinca	15	233	136	9	*nb*	70	48	44	39	15	8	4	4	1	AbN	8.7	9.6	15.8	31.3	58.0	1.1 Poorly
							%	30%	21%	19%	17%	6%	3%	2%	2%	0%	GbN	12.6	22.3	57.4	113.5	128	
	S2	Ésera	19	383	114	12	*nb*	158	95	58	28	21	15	6	2		AbN	8.3	9.4	15.2	33.7	57.0	0.9 Moderately
							%	41%	25%	15%	7%	5%	4%	2%	1%		GbN	11.9	20.1	48.8	75.9	95.8	
	S3	Cinca	20	260	100	16	*nb*	81	63	50	21	22	15	7	1		AbN	8.5	9.3	12.0	24.4	48.1	1.1 Poorly
							%	31%	24%	19%	8%	8%	6%	3%	0%		GbN	10.4	15.9	44.6	77.1	97.0	
Heterogeneous	S4	Cinca	23	354	156	7	*nb*	141	82	63	38	12	13	4		1	AbN	8.4	9.0	12.7	24.8	46.4	1.1 Poorly
							%	40%	23%	18%	11%	3%	4%	1%		0%	GbN	10	15.9	39.7	67	117.1	
	S5	Cinca	19	313	120	11	*nb*	104	74	48	38	24	15	9	1		AbN	8.3	9.2	14.7	32.1	56.7	0.9 Moderately
							%	33%	24%	15%	12%	8%	5%	3%	0%		GbN	11.4	20.7	46.1	76.2	97.1	
	S6	Cinca	35	519	121	11	*nb*	259	147	70	24	7	4	5	3		AbN	8.3	9.0	11.3	18.5	28.5	1.3 Poorly
							%	50%	28%	13%	5%	1%	1%	1%	1%		GbN	9.3	11.7	30.8	96.6	114.8	
Fines	S7	Cinca	38	719	101	16	*nb*	348	225	87	30	15	8	4	2		AbN	8.3	9.1	11.5	17.6	30.2	1.1 Poorly
							%	48%	31%	12%	4%	2%	1%	1%	0%		GbN	9.2	11.3	22.8	65.4	90.9	
	S8	Cinca	71	838	42	91	*nb*	481	236	77	38	6					AbN	8.2	8.7	10.6	15.1	23.2	0.6 Moderately well
							%	57%	28%	9%	5%	1%					GbN	8.5	9.6	14.4	24.8	33.6	
	S9	Ésera	66	717	42.5	89	*nb*	326	232	126	23	10					AbN	8.2	9.0	12.0	18.0	22.9	
							%	45%	32%	18%	3%	1%					GbN	8.8	10.5	16	27	34.6	
Partially wet	S10	Ésera	25	203	121	11	*nb*	31	38	54	30	32	12	4	2		AbN	9.3	11.5	19.0	41.1	58.5	0.9 Moderately
							%	15%	19%	27%	15%	16%	6%	2%	1%		GbN	15.1	22.5	42.6	74.9	101.5	

[a] Areal fraction finer than pebbles (16mm) obtained my manual digitization (see Figure 5.2), [b] Grain size distribution in Area-by-Number form (AbN) (*paint-and-pick* samples) truncated at 8 mm and converted to Grid-by-Number (GbN) using the method of Kellerhals and Bray (1971). [c] Sorting from Folk and Ward (1957) on GbN distribution.

5.1.3.2 PhotoMOB assessment

5.1.3.2.1 Assembling of the dataset

Photos of the 10 patches were scaled and digitized by hand. Manual digitization was only carried out on the photos in C1 condition. This data set is considered the best delineation that can be expected from the image i.e., the *gold standard*. Sometimes some grains were partially covered by others to a small extent, so their presumed shape was drawn.

In order to evaluate the performance of our image processing procedures (*supervised* or *automated*) on different photographic conditions, the 30 photos (10 samples × 3 photographic conditions) were (i) processed in a *supervised* way (selection of the best binarization threshold by the same operator) and (ii) processed automatically. The automatic form of this procedure requires an estimation of the areal proportion of material finer than pebbles in the image as mentioned in Section 5.1.2.2.2 and Text **S** Section 5.1.6.2.2.3. By manual digitization, the proportion of the sampling area composed of particles finer than 16 mm is known. But to account for the fact that the user would need to estimate this proportion, we made a survey form asking to a total of 335 random participants the surface proportion of fine material (<16 mm) on 20 photos from the dataset corresponding to conditions C1 and C2 (the survey is available at: https://docs.google.com/forms/d/e/1FAIpQLSdWh0IRbPQqwZ7TvqZfTVRBwGa3kw7uE_BYqGkbe6NRNEL6Q/viewform?usp=sf_link).

The mean accuracy error (MAE) of the 335 participants is 15% in C1 and 13.5% in C2 with a similar standard deviation for both conditions (14%). We processed the photos automatically by assuming for the proportion of material finer than pebbles (<16 mm) the median of the respondents' estimates for C1 and C2. We used the responses from C2 to process the photos in condition C3. The particles identified at the edge were removed from the analysis due to the metallic frame visible in the photographs. Only grains entirely within the frame were retained for the purpose of this performance analysis to allow a comparison with the *paint-and-pick* on the same exact grain population.

Figure 5.4 presents an overview of the digitization results obtained in a *supervised* manner (i.e., using the segmentation tool but with the binarization threshold selected by the operator) in the three photographic conditions (columns) for a sample from each group (rows). Some particles are left out of the count (labelled U_e) because they are under-segmented (i.e., joined to other particles) and bounded by a polygon touching the edges. In other cases, over-segmentations can be generated because of image complexity (intra grain colour variation). The more the photographic condition deteriorates (from C1 to C3), the more anomalies appear. This image is discussed more in Text **S** Section 5.1.6.3.2.1.

To allow for comparison, the 30 photos were also additionally processed through two other available tools to derive GSDs form imagery, *Basegrain*^{TM} a free and stand-alone tool developed by Detert and Weibrecht (2013), and *Sedimetrics Digital Gravelometer*^{TM}software (Graham et al., 2005a, 2005b). Both tools were applied using the default parameters.

The data were homogenized via truncation at 8 mm when assessing the performance of the procedures, as for each photo and each procedure the lower limit of particle detection may vary slightly. In addition, truncation eliminates from the control data set very small particles that may originate from the subsurface rather than the surface. Additionally, particles smaller than 8 mm were not measured with the Pebble-Box but with a calliper, which makes these measurements less reliable.

5.1.3.2.2 GSD computation and percentiles extraction

5.1.3.2.2.1 Continuous measurement or real measure of grains

For each of the 30 images (10 samples ∗ 3 photo conditions), a real GSD (*paint-and-pick* grains collection followed by Pebble-Box axis measurements), a manual digitized distribution (*gold standard*), and four estimated distributions by each of the automated image processing procedures (*PhotoMOB* either *supervised* or *automated*, *Basegrain* and *Sedimetrics*) of *continuous* measurement are available in AbN and GbN form. It should be noted that the cumulative distribution and percentile estimates are calculated from *continuous b*-axis data and not, as is usually the case, from *discrete* size class data (i.e., binned *b*-axis sizes). The method of percentiles extraction in the form of Area-by-Number (number of grains of identical *b*-axis size) and Grid-by-Number (summed grain area of identical *b*-axis size), following the principles explained by Bunte and Abt (2001) and Graham et al. (2012), is fully described in section Text **S** Section 5.1.6.3.2.2. Also, this supplementary section describes examples of limitations for the GbN GSD. More analyses are also developed in Section 5.1.4.2.1 and Section 5.1.4.2.2 of this paper.

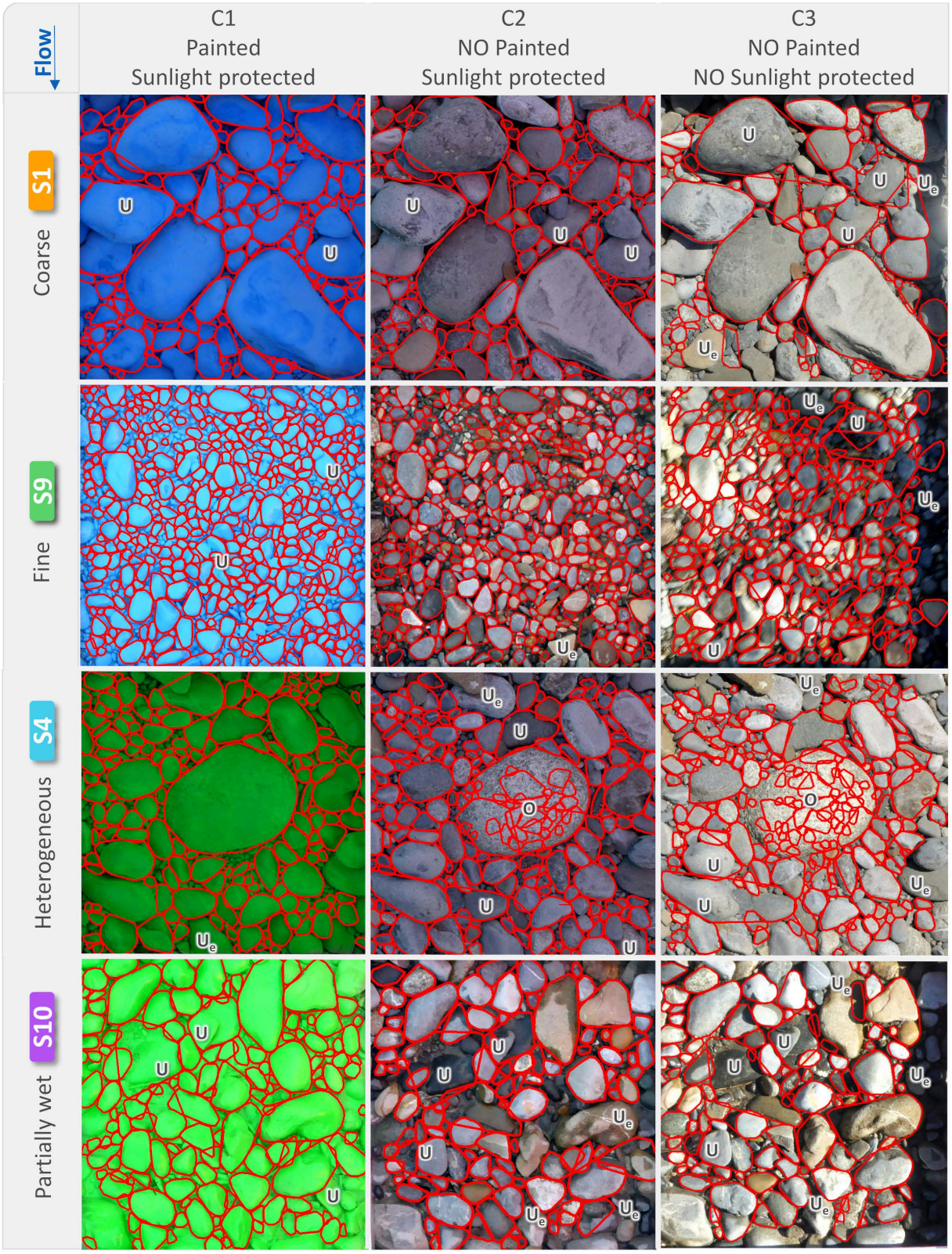

Figure 5.4: Particle detection results by supervised image-processing procedure. The 4 main patch characteristics (from top to bottom: coarse, fine, heterogeneous, partially wet) are represented for each of the 3 photographic conditions. The image patches represent approximately 40cm×40cm and show detected particles >8mm. The *U* label denotes examples of under-segmentation issues, the *O* label denotes examples of over-segmentation issues and the label U_e denotes examples of under-segmentation leading to *non-real* large particles along the edge that were thus subsequently not taken into account.

5.1.3.2.2.2 Discrete measurements or binned b-axis sizes

For the 2 samples, sampled in AbN form (*paint-and-pick* protocol), but with particles also measured by the template (*discrete* square holes measurement of the axes), the extraction of percentiles for the GSDs was carried out using the common method indicated by Bunte and Abt (2001). The conversion to the GbN form was carried out according to the Kellerhals and Bray (1971) conversion method by multiplying the frequency of all particles-size D_i by an exponent of 2 (D_i^2).

5.1.3.2.3 Performance and compatibility assessment

From the 360 *continuous* grain size distributions [6 procedures (real, manual,4 automated) × 10 samples × 3 photo conditions × 2 GSD forms] and 72 *discrete* grain size distribution (6 procedures × 2 samples × 3 photo conditions × 2 GSD forms), we extracted 2 variables, (i) Nb_i, the number of grains per grain fraction, with i being the lower limit in mm from each 0.5 ψ unit interval grain size class [where $\psi=\log_2(b)$], where b is the size of the b-axis in mm and (ii) D_i, corresponding to 15 percentiles of grain diameters in millimetres, (i indicates percentile number, $D_{5, 10, 16, 20, 25, 30, 40, 50, 60, 70, 75, 80, 84, 95}$). We will only present the results that we consider to be of interest to the community.

The residuals and the relative residuals between the estimated i-values and the control i-values for each combination between the photographic condition (C1, C2, C3), the GSD form (AbN or GbN), and the type of measurement (*continuous* or *discrete*) were computed. The relative residuals express the error of the estimated variable i as a percentage of the control variable i (manual or real).

Following Sime and Ferguson (2003) and Buscombe (2013) , using the residuals, four metrics were applied to quantify the estimation error and relative estimation error for each individual Nb_i and D_i. The *bias (B)*, indicating whether the evaluations were on average over- or under-estimated, is defined as:

$$B_{Var\ i} = \frac{1}{n}\sum(Residuals_i) \qquad (5.1)$$

where n represents the number of patches (10). The mean absolute error (MAE), corresponding to the reducible error or the error of accuracy, indicating how far from the correct value are the estimates, is given as:

$$MAE_{Var\ i} = \frac{1}{n}\sum(|Residuals_i|)) \qquad (5.2)$$

The root means square error, representing the combination of the systematic error (bias) and the random error (irreducible random error) is calculated as:

$$RMSE_{Var\ i} = \frac{1}{n}\sum\sqrt{(Residuals_i)^2)} \qquad (5.3)$$

And the precision error denoting the dispersion around the bias, also called irreducible random error, is:

$$e_{Var\ i} = \sqrt{RMSE_i{}^2 - B_i{}^2} \qquad (5.4)$$

Finally, the general error of the procedures with respect to the control data (manual digitization or *paint-and-pick)* was quantified by calculating for the four above mentioned metrics, its average over all percentiles:

$$Procedure\ performance_{metrics} = \frac{1}{n} * \sum\left(Metrics_{D_5} + Metrics_{D_{10}} + \ldots + Metrics_{D_{95}}\right) \qquad (5.5)$$

where n represents the number of studied percentiles (15).

5.1.4 RESULTS AND DISCUSSION

5.1.4.1 Performances

5.1.4.1.1 Grain's detection - Comparison to manual grain distribution or *Gold standard*

Figure 5.21 presents the bias, accuracy and precision for each photo condition (rows) to reproduce the manual delineation. The performances of each procedure, obtained from Eq. 5.5, are shown in Table 5.2. Figure 5.5 **A** displays the mean bias of grain number detection per grain size class for our *supervised* and *automated* procedures as well as for *Basegrain* and *Sedimetrics* procedures. The vertical shaded areas mark the 10% error limits. The curves in Figure 5.5 **B** represent the relative bias (%) along the percentiles estimates (an average curve passing between the residuals in Figure 5.5 **C** for each procedure. Figure 5.5 **C** shows the dispersion of the 10 relative residuals for the 15 percentiles estimates. The shape and colour of the dots represent the 4 groups of samples. Finally, part **D** of Figure 5.5 illustrates, for the 4 procedures compared to manual delineation, the average accuracy and precision error obtained for each individual percentile (coloured dots) as well as the overall performance of each procedure (black square, values reported in Table 5.2). On the ordinate is the relative MAE (%) for each percentile, i.e., the mean absolute deviation of the residuals from the grey line of equality in parts B and C, while on the abscissa is the irreducible error (*e*) (precision error), which indicates the dispersion of the residuals among themselves for each percentile.

5.1.4.1.1.1 Condition 1 – Painted and Sunlight protected

The *supervised* and *automated PhotoMOB* procedures present similar trends concerning bias of the detected number of grains (Figure 5.5 **A**, orange and green bars) and percentiles estimates compared to manual delineation. The number of particles between 8 and 16 mm is constantly under-estimated by -15% to -25% (negative bias). Grains may have shifted to lower class or discarded (detected below 8 mm) due to the contour enhancement in the pre-processing step (see Text **S** Section 5.1.6.2.2.1). Then from 32 mm the trends are less constant (shaded horizontal rectangles areas in Figure 5.5 **A**) but generally there is an over-detection of grain number (positive bias). Due to the low number of particles present in these fractions (see Table 5.1), a few erroneous particle detections will quickly lead to high percentage of error compared to the reference number. Figure 5.5 **B** first row, *supervised* and *automated PhotoMOB* (orange and green curves) shows low or no bias and then a progressive positive bias from D_{60} to D_{95} reaching +9.7% (i.e., bias of +3 mm at D_{95}). In C1 only the end of the distribution is deviated from *gold standard* due to under-segmentation (union of grains) errors creating large polygons (see Figure 5.4). However, all percentiles are estimated with an accuracy error and a precision error lower than 10% (all points are located in the shaded area on Figure 5.5 **D** (first row, first and second columns).

The *Basegrain* procedure is the least biased in C1 (Figure 5.5 **B**, first row, brown line) but with a higher residual dispersion than for the two *PhotoMOB* procedures (Figure 5.5 **C**, first row, 3rd

column). For *Sedimetrics*, grain detection is more under-estimated for fine grain classes (grey segment on Figure 5.5 **A**, first row) resulting in a positively biased percentile estimation due to the lack of small grains. (Figure 5.5 **B**, first row, grey line). The residuals are much more scattered with a general irreducible error of 9% (Figure 5.5, part **C** and **D** last column).

5.1.4.1.1.2 Condition 2 – Not Painted but Sunlight protected

The *supervised* and *automated PhotoMOB* procedures present, again, similar trends between them in C2 condition (second row). Grain detection is under-estimated in classes between 8 and 22.6 mm. As a reminder, for our 10 samples, between 60 and 95% of particles belong to these classes (see Figure 5.3). For particles larger than 22.6 mm the bias is generally low (<10%, i.e., inside shaded vertical area). Percentiles estimates are more scattered and positively biased as the percentiles increase than in C1 (Figure 5.5 **C** second row, first and second columns and Figure 5.5 **B** orange and green curves), reaching a maximum positive relative bias of 14% (i.e., +2.8 mm error on the D_{75} estimate). Then the percentile estimate bias is constant until the end of the distribution. This behaviour is due to more frequent grain union over a wider range of grain sizes, as can be seen in Figure 5.4. Each percentile of sample S10 is over-estimated (Figure 5.5 **C** second row, first and second column, triangle points). This is because of under-segmentation (unified grains), especially in the wet area (see Figure 5.4, last row), resulting in a coarser GSD.

However, *PhotoMOB* gives similar GSD to a manual digitalization, with average accuracy and precision procedure performance errors between 6.8 et 7.5% (see black squares in Figure 5.5 **D** second row ,1st and 2nd columns and Table 5.2. Only the percentiles of the D_{75} to D_{90} are estimated with mean errors greater than 10% (between 10 and 14.5%).

In contrast, for *Basegrain* and *Sedimetrics*, the percentiles of the sample S10 are under-estimated (Figure 5.5 **C** second row, 3rd and 4th columns, triangle points), the general percentiles bias is negative (Figure 5.5 **B** second row, brown and grey curves) and show larger disparity between the sample's residuals, also represented in Figure 5.5 **D** (second row, 3rd and 4th columns) by higher precision error or *e*. The general average precision error of these procedures is greater than 10% (black squares are outside of the shaded area).

Figure 5.5: Performance assessment of image processing procedures compared to manual digitization (*gold standard* expected from photographic method). (**A**) Relative bias of grain detection number per grain size classes under the three photo conditions for the *supervised* and *automated PhotoMOB* procedure as well as for *Basegrain* free stand-alone tool from Detert and Weibrecht (2013) and *Sedimetrics Digital Gravelometer*™ from Graham et al. (2005a, 2005b).

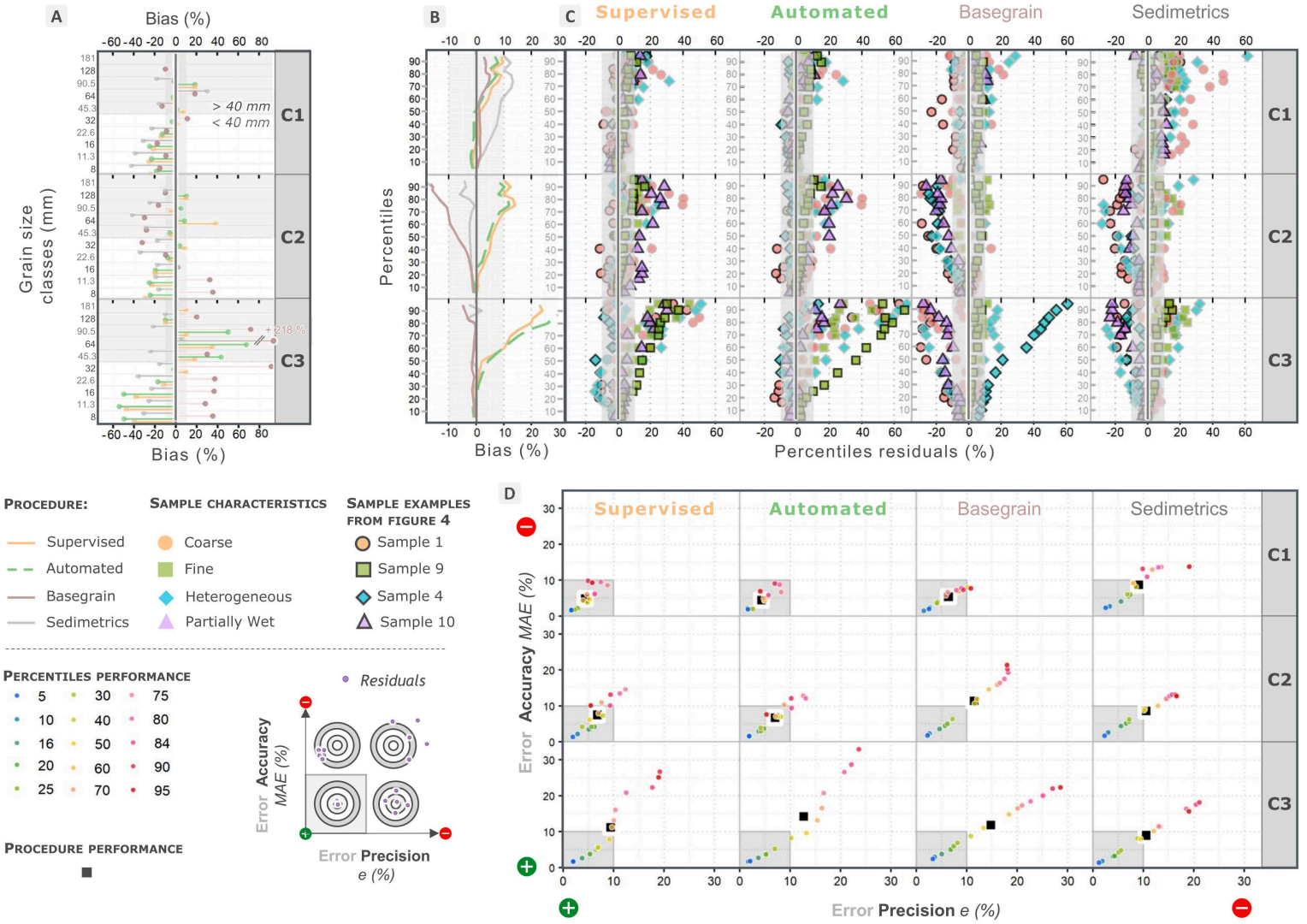

(**B**) Relative bias of percentiles estimation for each procedure. Bias is calculated over residuals of the 10 samples. (**C**) Distribution of the 150 relative residuals of percentiles estimation (15 percentiles ∗ 10 samples) for the 4 automated procedures. The residuals are coloured according to the 4 main patch characteristics (coarse, fine, heterogeneous, partially wet). Samples taken as example in Figure 5.4 are represented here by symbols with black outline. (**D**) Average relative performance for the individual estimation of each percentile (coloured point) as well as the average general performance of the procedures (black square). The shaded vertical areas in A, B, C and D mark the 10% error limits.

5.1.4.1.1.3 Condition 3 – Not Painted and Not Sunlight protected

In C3 (3rd row in Figure 5.5 **A**) the two *PhotoMOB* procedures differ in that the biases in the grain size estimates and the dispersion of the residual percentiles are greater for the *automated* procedure than for the *supervised* procedure. For both, procedure difference in performance between groups of samples is remarkable. Percentile precision error reaches more than 20% for high percentiles (Figure 5.5 **D** last row, 1st and 2nd columns). Sample S4 with heterogeneous lithology (blue diamonds with dark boundary) and some of the coarse samples (orange circles; S1) have under-estimated sizes (due to over segmentation) while for the other groups our procedures over-estimate the percentiles because of the creation of large coarse *non-real* or *fictitious* particles.

Basegrain and *Sedimetrics* show deviation from the *gold standard* (manual delineation) in a similar way to C2 (Figure 5.5 **C** second and last rows, 3rd and 4th columns). Their percentiles estimated average MAE are almost equal in C2 and C3 (Table 5.2 around 11 and 9%).

Overall, for C1 and C2 our procedures reproduce the manual GSD (*gold standard*) with a good precision and accuracy (Figure 5.5 **D** 1st and 2nd row and column) but with a tendency to over-estimate the percentiles with an average bias procedure performance of up to +6.3% (Table 5.2). All procedures show that the error compared to manual delineation is percentile dependent, with low error for the small percentiles (blue dots in Figure 5.5 **D** and progressively larger errors for larger percentiles (red dots in Figure 5.5 **D)**.

5.1.4.1.2 Photographic method performance - Comparison to real bed distribution or *Paint-and-pick*

The photographic method, even manual procedure, provides an estimate of GSD from a surface, where the detected particle size is limited by its visible surface. Conversely, for the *paint-and-pick* sampling, the particles are taken out of the bed to be measured. It has already been shown by previous authors that the photographic method may tend to under-estimate the real particle size distribution (Butler et al., 2001; Graham et al., 2005b; Sime and Ferguson, 2003).

Figure 5.6 presents the performances taking the *paint-and-pick* (i.e., real data) as the reference. Part A1 presents the dispersion of the 10 relative residuals for the 15 percentiles estimates from the *gold standard* (manual). The shape and colour of the dots represent the 4 groups of samples. The curves in Figure 5.6 **A2** represent the relative bias (%) along the percentiles (the mean curves passing between the residuals) for the five image processing procedures in photo condition C1. The dispersion of the residuals of percentiles estimates for the four automatic procedures as well as the bias evolution under the 3 conditions are available as supplementary material **S** Figure 5.13. Part A3 and B of Figure 5.6 illustrate, for the manual and for the four automated procedures, the average performance (accuracy and precision) obtained for each percentile (coloured dots) as well as the overall performances of the procedures (black square). On the ordinate is given the relative MAE (%) for each percentile, thus the absolute deviation of the residuals from the grey equality line in parts A1 and A2, while on the abscissa is represented the irreducible error (*e*, i.e., precision), denoting the dispersion of the residuals among themselves for each percentile. Finally, parts C and D present the mean bias of grain number detection per grain size class under each photo condition (rows) for automated and manual procedures respectively.

Table 5.2: General procedure performances - Deviation from manual digitization and real measurements

Reference	Photo Condition	Procedure	Procedure Bias (B) [a]				Procedure Irreducible error (e) [a]				Procedure Accuracy error (MAE) [a]				Procedure RMSE [a]			
			mm	(sd)	%	(sd)	mm	(sd)	%	(sd)	mm	(sd)	%	(sd)	mm	(sd)	%	(sd)
Manual digitization [b]	C1	Supervised	0.9	(1.2)	3.3	(4.2)	1.0	(0.9)	4.3	(2.2)	1.0	(1.1)	4.8	(3.1)	1.4	(1.4)	6.1	(3.8)
		Automatic	0.6	(0.9)	1.8	(3.8)	0.9	(0.7)	4.3	(2.3)	0.9	(0.9)	4.5	(2.5)	1.2	(1.1)	5.6	(3.1)
		Basegrain [d]	0.2	(0.3)	1.8	(1.5)	1.3	(1.1)	6.3	(3.0)	1.0	(0.8)	5.3	(2.3)	1.3	(1.1)	6.7	(3.1)
		Sedimetrics [e]	1.4	(1.2)	7.4	(4.7)	1.7	(1.5)	9.0	(4.2)	1.6	(1.4)	8.7	(4.1)	2.2	(1.9)	11.9	(5.8)
	C2	Supervised	1.3	(1.4)	6.3	(5.0)	1.4	(1.1)	6.7	(2.9)	1.5	(1.3)	7.5	(4.3)	2.0	(1.7)	9.5	(5.2)
		Automatic	1.1	(1.2)	4.6	(4.8)	1.5	(1.2)	6.9	(3.6)	1.4	(1.2)	6.8	(3.9)	1.9	(1.6)	8.8	(5.2)
		Basegrain [d]	-2.3	(2.8)	-7.8	(6.3)	2.8	(2.8)	11.4	(6.1)	2.8	(2.9)	11.4	(7.0)	3.7	(4.0)	14.0	(8.5)
		Sedimetrics [e]	-0.9	(1.0)	-2.3	(1.4)	2.5	(2.3)	10.6	(5.0)	1.9	(1.7)	8.6	(4.0)	2.6	(2.5)	10.9	(5.0)
	C3	Supervised	2.0	(2.7)	8.4	(9.9)	2.0	(2.2)	9.4	(5.6)	2.4	(2.8)	11.2	(8.9)	2.9	(3.4)	13.5	(10.2)
		Automatic	2.7	(4.2)	11.6	(14.0)	2.5	(3.0)	12.6	(8.3)	3.1	(4.0)	14.2	(12.4)	3.9	(5.0)	18.1	(15.1)
		Basegrain [d]	-0.9	(1.2)	-1.6	(1.5)	3.6	(3.9)	14.8	(9.0)	2.8	(3.0)	11.8	(7.2)	3.7	(4.1)	14.9	(9.0)
		Sedimetrics [e]	-0.6	(0.8)	-0.6	(1.3)	2.5	(2.7)	10.6	(6.9)	2.0	(2.1)	9.0	(5.9)	2.6	(2.8)	10.6	(6.9)
	Manual – Gold standard		**-0.7**	**(0.8)**	**-2.6**	**(1.6)**	**1.9**	**(1.4)**	**7.6**	**(2.6)**	**1.3**	**(1.0)**	**5.8**	**(2.3)**	**2.0**	**(1.6)**	**8.2**	**(2.7)**
Paint-and-pick [c]	C1	Supervised	0.1	(0.6)	0.5	(3.6)	2.1	(1.7)	8.9	(3.7)	1.5	(1.2)	6.9	(3.1)	2.2	(1.7)	9.5	(3.8)
		Automated	-0.2	(0.5)	-0.9	(3.3)	2.1	(1.6)	8.7	(3.5)	1.5	(1.2)	6.6	(2.6)	2.2	(1.5)	9.4	(3.3)
		Basegrain [d]	-0.5	(0.7)	-1.0	(1.6)	2.0	(1.7)	8.7	(3.7)	1.5	(1.4)	6.7	(3.1)	2.1	(1.8)	8.8	(3.7)
		Sedimetric [e]	0.7	(0.8)	4.6	(4.4)	2.7	(2.5)	12.1	(6.1)	2.2	(2.0)	10.1	(5.6)	2.9	(2.6)	13.2	(6.9)
	C2	Supervised	0.6	(0.9)	3.2	(4.5)	1.7	(1.5)	7.6	(4.8)	1.4	(1.2)	6.5	(3.8)	1.9	(1.7)	8.9	(5.6)
		Automated	0.4	(0.8)	1.6	(4.3)	1.8	(1.6)	8.3	(4.1)	1.3	(1.2)	6.2	(2.9)	2.0	(1.6)	9.3	(4.5)
		Basegrain [d]	-3.0	(3.5)	-10.4	(6.9)	3.2	(3.0)	11.6	(5.7)	3.2	(3.6)	12.0	(7.6)	4.4	(4.6)	15.7	(8.8)
		Sedimetric [e]	-1.6	(1.7)	-5.0	(2.2)	3.0	(2.6)	11.9	(4.9)	2.3	(2.2)	9.6	(4.3)	3.4	(3.0)	13.0	(5.1)
	C3	Supervised	1.3	(2.1)	5.4	(9.2)	2.7	(2.8)	11.4	(7.1)	2.6	(2.9)	11.5	(8.4)	3.1	(3.3)	14.1	(9.7)
		Automated	2.0	(3.5)	8.5	(13.0)	3.4	(3.7)	14.6	(9.2)	3.2	(3.8)	14.3	(11.4)	4.1	(4.9)	18.5	(13.8)
		Basegrain [d]	-1.6	(1.9)	-4.0	(2.6)	4.3	(4.1)	17.2	(8.5)	3.5	(3.4)	14.0	(7.5)	4.6	(4.5)	17.8	(8.6)
		Sedimetric [e]	-1.3	(1.5)	-3.2	(1.7)	3.2	(3.2)	12.3	(7.0)	2.4	(2.6)	9.8	(6.2)	3.5	(3.5)	12.8	(7.0)

[a] For each of the 15 extracted percentiles, the 4 performance parameters were calculated on the 10 sample residuals. Then, each of the parameters was averaged over the 15 percentiles to give a general error for the procedure estimate. The standard deviation is given to illustrate the inter percentiles estimation performance variation; [b] General deviation from manual digitization; [c] General deviation from the *paint-and-pick* bed surface sampling; [d] *Basegrain* free stand-alone tool from Detert and Weibrecht (2013) and *Sedimetrics Digital Gravelometer*™ from Graham (2005a, 2005b). Note that *Gold standard* (highlighted in orange) is based on manual digitization and is compared with real percentiles (i.e., *paint-and-pick*).

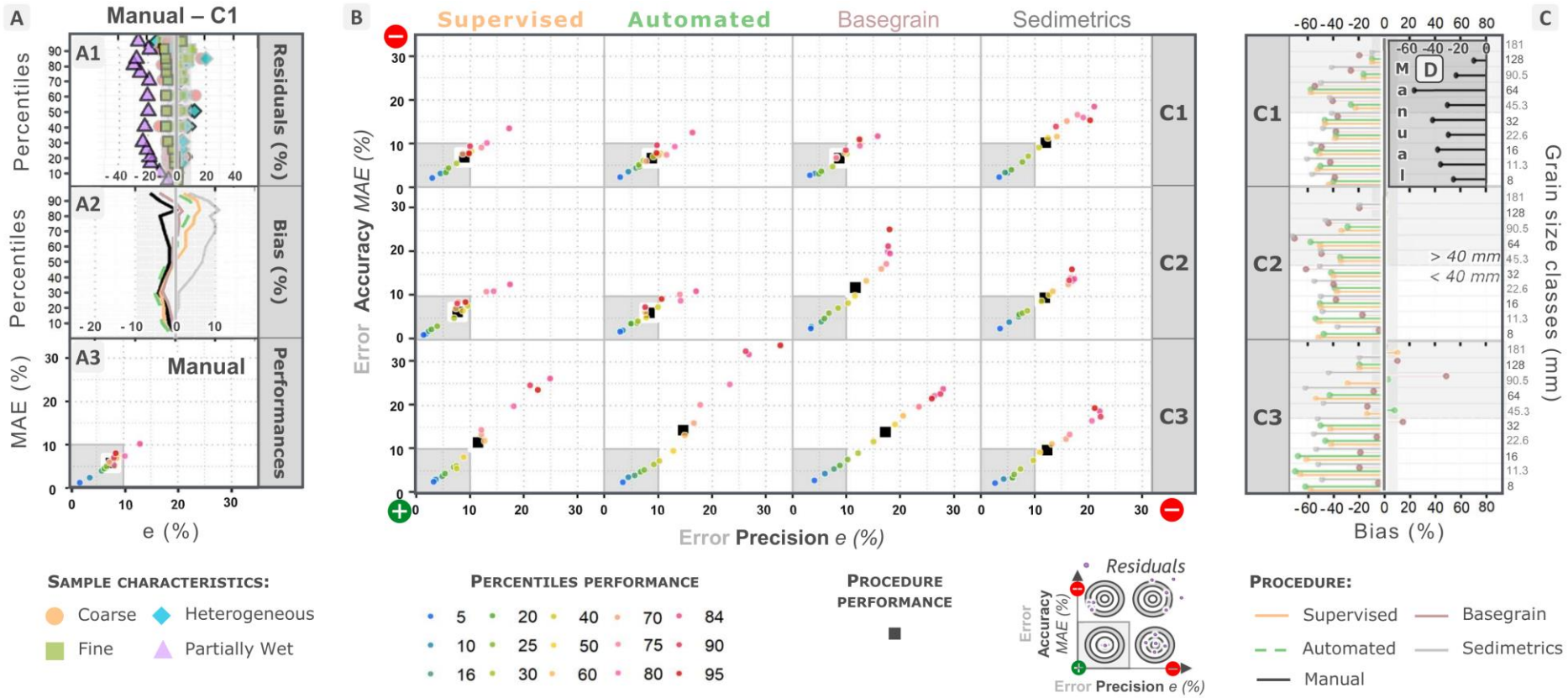

Figure 5.6: Performance assessment of image processing procedures compared to paint-and-pick bed surface sampling. (**A**) Manual digitization performances. Manual digitization was performed only on painted photos (C1). (A1) Distribution of the 10 relative residuals of each sample for the 15 percentile estimates for manual digitization. The residuals are coloured according to the 4 main patch characteristics (coarse, fine, heterogeneous, partially wet). Samples taken as example in Figure 5.4 are represented here by symbols with black outlines. (A2) Relative bias of percentiles estimation in C1 photo condition for the manual procedure, the supervised and automated PhotoMOB procedures as well as for Basegrain free standalone tool from Detert and Weibrecht (2013) and *Sedimetrics Digital Gravelometer*™ from Graham et al. (2005a; 2005b). Bias is calculated over residuals of the 10 samples. (A3) Average relative performance (accuracy and precision) for the estimation of each percentile (coloured dots), as well as the overall performance (black square) of manual digitalisation and (**B**) four automatic procedures. (**C**) Relative bias of grain detection number per grain size classes for the 4 image-based procedures and for the three photo conditions and (**D**) manual procedure. The vertical shaded areas mark the 10% error limits.

5.1.4.1.2.1 Manual delineation

Figure 5.6 **D** (black segment, first row) shows that the number of grains identified in C1 by manual digitization is lower in all classes than that collected in the *paint-and-pick* samples. Classes from 8 to 22.6 mm are under-predicted with a mostly increasing trend, then from 32 mm onward the negative bias decreases with increasing size. An exception is visible in the class 64 mm where the number of particles detected is strongly negatively biased at almost -60%. This class contains many disk-shaped (flat) particles (54.5 %) leading to the class with the most particles in the P2 overlapped position (over 57%). Particles may therefore be mistakenly categorized in the smaller classes. The residuals of percentile estimates are quite clustered with the exception of sample S10 (Figure 5.6 **A1**). This is the sample which has the most discoid (flat) particles (see Figure 5.11 **B** and **C**) and for which the 11 mm (D_{20}) to 16 mm class is the most dominated (at 50%) by P3 oriented particles. Thus, all these particles will tend to be identified as finer. This has the effect of refining the distribution from the D_{20} percentiles onwards. This behaviour is not related to the partially wet nature of the sample but to the shape and position of the particles in the bed (called the fabric effect by Graham et al., 2010). The manual bias is almost constant (Figure 5.6 **A2** black segment). Percentiles are generally underestimated in average by -2.6% (or -0.7 mm) (see Table 5.2). The accuracy and precision errors over percentiles range between 2 and 13% (0.1 to 4.7 mm) (see Figure 5.6 **A3**).

5.1.4.1.2.2 Automated delineation

In C1 and C2 (Figure 5.6 **C**, 1st and 2nd rows), the *PhotoMOB* procedures show the same behaviour between them (as mentioned in Section 5.1.4.1.1.1), similar to the manual procedure. There is underestimation or a negative bias of the number of particles up to 22.6 mm and then, as the size increases, the bias is reduced. As with manual delineation, there is an exception with a larger underestimate of around 60% between 64- and 90.5-mm. Figure 5.6 **A2** shows that percentiles bias estimates are similarly negative as the manual procedure up to D_{50}, then overestimated. Percentiles from D_{70} to D_{84} are estimated with more than 10% accuracy or precision error (out of the shaded area on Figure 5.6 **B**, first row, 1st and 2nd column). This is a consequence of the union of grains (under-segmentation), which implies the appearance of *non-real* coarse grains and the diminution of finer grains in the estimated GSD. Finally, the error decreases for the D_{90} and D_{95} percentiles.

For *Basegrain*, the number of grains from 8 to 22 mm is much less under-estimated in C2 and C3 (bias only between 0 and -40%, Figure 5.6 **C** 2nd and 3rd rows, brown bars) than by the other procedures, even manual (Figure 5.6 **D**). *Basegrain* over-estimates the number of grains visible on the picture due to a large amount of over-segmentation. By compensation, the bias of number of detected grains is low even if the photographic method cannot detect all the real grains present in the patch.

The average accuracy (i.e., MAE) and precision errors (i.e., irreducible error *e*) of *PhotoMOB* procedures in C1 and C2 are between 6 and 9 % (1.3 to 2 mm, Table 5.2). In C1 errors are basically the same magnitude as with the *Basegrain* (Figure 5.6 **B** 1st row, 1st, 2nd and 3rd columns) or the manual procedure (Figure 5.6 **A3**). In C2, our procedures are the ones with the lowest error compare to the real GSD (Table 5.2, Figure 5.6 **B**, second row). In C3 however, our procedures reproduce the *paint-and-pick* (real bed GSD) method with less good performance (Figure 5.6 **B**, 1st and 2nd columns, last row).

Finally, although *Sedimetrics* is the procedure that best reproduces the *paint-and-pick* method in the relatively challenging C3 condition (Figure 5.6 **B**, last row, last column), it should be noted that *Sedimetrics* had similar performance for all three photographic conditions. For all three conditions, the mean precision was around 12%, while the average accuracy was 10%. These stable results over the three conditions (Figure 5.6 **B** last column, see black square constant position) confirm that the tool developed by Graham (2005a, 2005b) performs acceptably well regardless of condition (lithology, grain texture, lighting).

5.1.4.1.3 Limitations and further developments

5.1.4.1.3.1 Limitations

The *supervised* and *automated PhotoMOB* procedures have shown satisfactory performance. Average percentiles estimate error are less than 10% in both conditions C1 and C2, taking either the manual digitization (*gold standard*) or real grain size distribution as reference (Figure 5.5 **D**, and Figure 5.6 **B** 1st and 2nd rows and columns). The GSDs are relatively similar to those found by manual delimitation (i.e., *gold standard*), not due to compensation, but due to correct delimitation especially in condition C1 where image complexity (Purinton and Bookhagen, 2019) is reduced by paint, which avoids the problems caused by intra granular colour variation, veins, fractures, and shadow variations. Moreover, there was no marked difference between the different groups of samples (coarse, fine, heterogeneous, partially wet), indicating the tool can be applied to a variety of river beds.

However, in C1 and C2 we detected a positive bias for coarser particles in our *PhotoMOB* procedure. During the development of the binarization threshold process development, under-segmentation errors (union of two or more particles) were preferred to over-segmentation errors. This resulted in a greater number of coarse *non-real* or *fictitious* particles resulting, in case of C2, an over-estimated of the D_{75} to D_{84}. As the accuracy error ranges between 10 and 15% (i.e., accuracy from 90 to 85%) for these percentiles, it will not be necessary to correct the *non-real* particle delimitation if the operator accepts this margin of error in the estimation of the coarsest percentiles. However, if the GSD is to be expressed in GbN, these erroneous delimitations will have a greater weight (detailed discussion in Section 5.1.4.2.1 below), or if the user intends to use the second part of *PhotoMOB* to characterize grain dynamics (detailed in the companion paper, a correction will be necessary. Poorly delineated or segmented particles will result in an over-estimation of mobile particles, because if incorrectly delineated particles overlap between the two images, even if they are the same, there is a high chance that they are classified as different (i.e., mobile or new particles). It will then be preferable to correct them. Nevertheless, these particle unions are easily visible. An operator will tend to see these very coarse visible errors more easily than fictitious small polygons (*non-real*). Finally, in C3 the prediction threshold for the binarization threshold is less performant and *PhotoMOB* was not developed to perform in this photographic condition where the use of only one binarization threshold is not suitable for images with varying intensity.

5.1.4.1.3.2 Methodological improvements for image acquisition and processing

First, in C2 and C3, to avoid partially wet area issues, a solution to the problem of darker wet areas would be to humidify the whole patch to reduce the colour variation between the wet and dry areas. Correct delineation is more generally obtained with C1 type photos (e.g., painted and protected from the sun), but if it is not possible to protect the area from the sun (C3) and/or if the area cannot be painted with common spray paint (C2), several recommendations are offered here to reduce grain identification errors and the subsequent manual correction effort. In order for *PhotoMOB* to best identify grains, a first solution could be to prepare a highly concentrated simple mixture of clay and water and applied it to the bed area with a gardening spray. This reduces the complexity of the image and reflectance of the surface by its colour and matte texture.

Secondly, very recently, a new open-source software library based on convolutional neural networks, called *ImageGrains* was released by Mair et al. (2023) with the possibility in the near future to be implemented for GIS. A second solution could be to implement *ImageGrains* in the *PhotoMOB* workflow to reduce the correction effort and then carry out the second part of the protocol. We tested *ImageGrains* and *PhotoMOB* on a challenging patch containing grains with varied lithology that could cause strong over-segmentation in conditions C2 (shaded but not painted) and C1 (shaded and painted with a clay solution).

The percentiles are estimated by *ImageGrains* with a bias close to 0% in both C2 and C1 compare to a manual delineation. The use of clay paint reduces the estimation bias for the *PhotoMOB* procedure from -12% to -3%.

More details on these two solutions are provided in Text **S** Section 5.1.6.4.1.3 and **S** Figure 5.14. In general, following numerous tests on different images (not presented in this paper), *ImageGrains* enables very satisfactory grain segmentations on photos taken under C3 and C2 conditions but not in C1 for which it has not been trained. In the future, it is expected to train *ImageGrains* with our painted images manually digitized. Our digitalization will be available. Finally, as this tool seems to be flexible in terms of training, it might also be possible to train it on underwater photos. This would make it possible to track mobility, or at least the proportion of stable and perturbed bed area, even in areas that are still in the water.

Errors will always remain regardless of the procedure used (*PhotoMOB*, *Basegrain*, *Sedimetrics*, *ImageGrains*) but the two mentioned improvements could reduce drastically segmentation error and the effort of correction. As *PhotoMOB* is developed under GIS, the manual correction of persistent errors is facilitated. All the output of our image processing procedure is in the form of a vector file, which makes it easy to manipulate the results for a GIS user, hence giving a surplus of flexibility to our tool.

5.1.4.2 Compatibility with existing GbN data

5.1.4.2.1 GbN performances

Most of the existing data on GSD for more than half a century comes from a surface count of the particles via a Grid-by-Number (as Wolman method, Wolman, 1954) or from a subsurface volume by weight method (bulk sampling). As we pointed out in Text **S** Section 5.1.6.3.2.2 and **S** Figure 5.12, Grid-by-Number form seems to be more sensitive than Area-by-Number form to over-estimation of the coarser fractions due to the low number of coarse grains present in the sample. This reflects the need to have a sufficiently large area to characterize the whole distribution correctly.

We conducted a sensitivity analysis to understand how the performance of the photographic-based procedures depend on the choice of size of the sampled area and on the distribution form, AbN or GbN. The sample area size was assessed by varying GSD truncation to vary the representation of the coarsest analyzed fraction in the image (i.e., Diplas and Fripp (1992) criterion for the minimum extension of the analyzed area). Specifically, we present performance calculations for (1) AbN with only a low truncation at 8 mm, as well as five other GSD forms: (2) AbN truncated between 8 mm and 40 mm (40 mm allowing to respect the Diplas criterion in accordance with the sampled area), (3) AbN with low truncation at 11 mm, (4) AbN truncated between 11.3 and 40 mm, (5) GbN with low truncation at 8 mm, and (6) GbN truncated between 8 mm and 40 mm to meet the Diplas criterion. Figure 5.7 **A** shows, for each image processing procedure, the performance average RMSE (Eq. 5.5) calculated over the 15 percentiles mean RMSE and their standard deviation (corresponding to the last column in Table 5.2 but for different distribution truncation) with *paint-and-pick* measurements taken as reference. The lower the average RMSE values, the less error there is in the overall percentile estimate compared to the 'real' *paint-and-pick* data. Furthermore, the closer the values of the automatic procedures (*PhotoMOB supervised* or *automated*, *Basegrain* and *Sedimetrics*) are to the value of the manual (black) procedure, the more likely it is that the automatic delineation obtained corresponds to what the operator would expect visually.

A low truncation (8 or 11.3 mm, (1) and (3) on the X- axis) used in AbN has little influence on performance. A lower truncation at 11.3 mm (3) reduces errors by only 10% compared to an 8 mm truncation (1) regardless of the photographic condition and image procedure used. When an upper truncation (40 mm here) is used to meet the Diplas and Fripp (1992) criterion, the results get better. Average RMSEs are reduced by a third in all photographic conditions and for all procedures [(1)

vs. (2) and (3) vs. (4)]. It should be noted that none of our 10 samples had a ratio *area sampled/area* $D_{max} \geq 100$ (see Table 5.1).

In C1 and C2 our procedures (orange and green points) are very close to the manual process (black points) and remain below 10% error regardless of the truncation performed (all points are inside the shaded area). On the other hand, the errors of automated procedures under GbN GSDs with only lower truncation at 8 mm (5) are large (between 15 and 20% in C1, 15 and 35% in C2 and 25 and 50% in C3), while the use of upper truncation (6) reduces the errors to below 10% for the manual procedure and our *supervised* and *automated* procedures in C1 and C2.

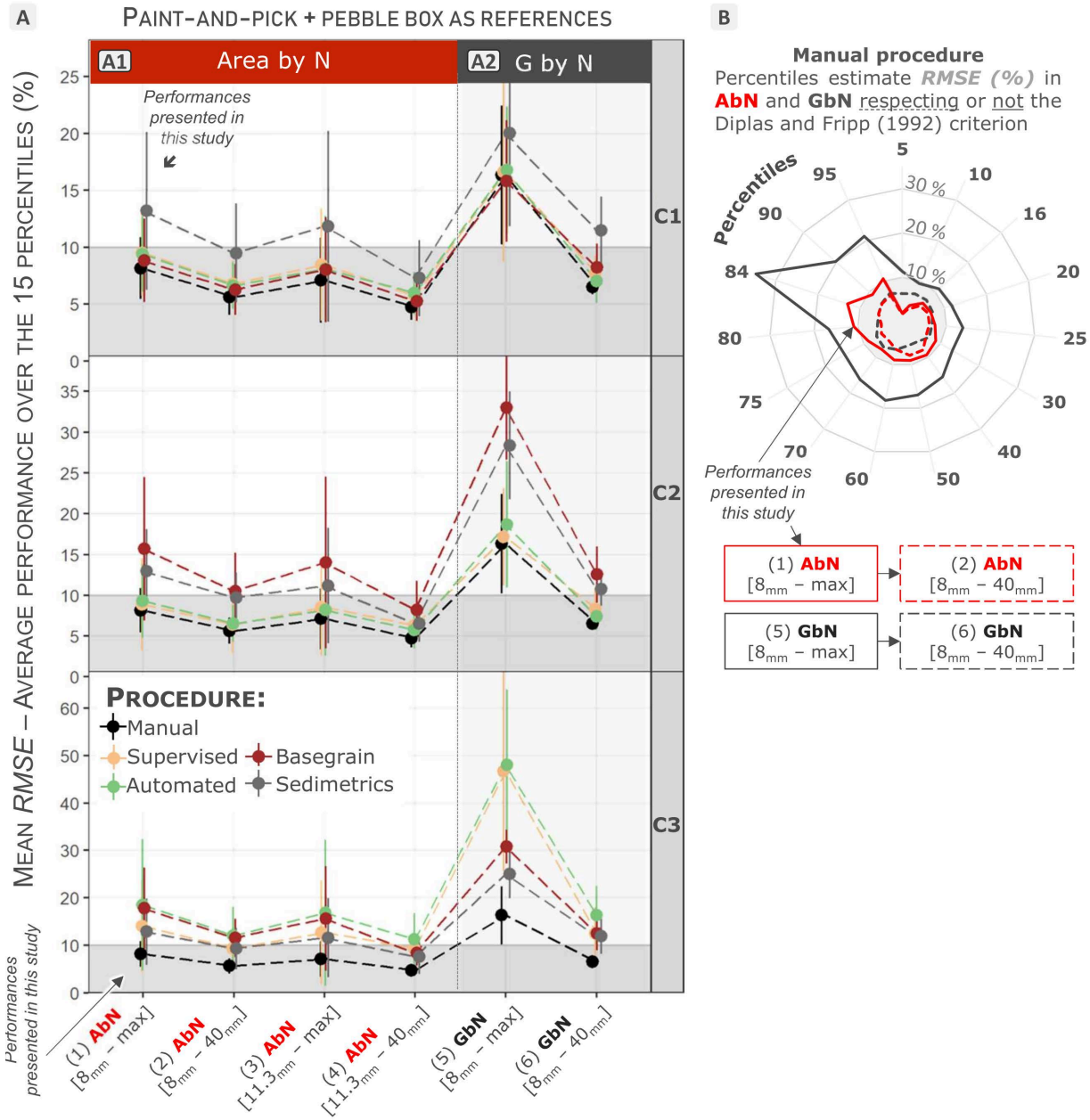

Figure 5.7: (**A**) Evolution of the overall performance of each image processing procedure as a function of low and high truncation (respecting the Diplas and Fripp (1992) criterion) in the form of (**A1**) Area-by-Number and (**A2**) Grid-by-Number. The dots represent the average RMSE of each procedure (average of the RMSEs calculated for each of the 15 percentiles estimate (based on the 10 residuals)). The bars represent the standard deviation around the mean RMSE (scatter of the RMSE of the 15 percentiles). (**B**) Estimate RMSE of each of the 15 percentiles from Manual delimitation (gold standard) for grain size distribution in Area-by-Number (red curves) and Grid-by-Number form (black curve) with (dashed curve) and without (solid curve) high truncation at 40 mm to respect the Diplas and Fripp (1992).

Figure 5.7 **B** shows in more detail the RMSE in condition C1, for each percentile estimate between the manual delineation (*gold standard*) and the real grain size distribution (*paint-and-pick*). The respect of the criterion (i.e., ratio *area sampled/area* $D_{max} \geq 100$) in AbN (dashed red curve compared to solid red curve) allows to reduce the error of the D_{50} estimation from 9 to 7.8% and the error on the D_{84} from 13 to 5.6%. In GbN, compliance with the criterion (black dashed curve compared to solid black curve) reduces the error of the D_{50} estimate from 17 to 5.6% and the error of the D_{84} estimate from 35 to 5.6%. The same behaviour and order of magnitude of error reduction for *PhotoMOB supervised* is showed in supplementary material Text **S** Section 5.1.4.2.2 and **S** Figure 5.16.

Respecting the Diplas and Fripp (1992) criterion allows a better estimation of the percentiles and especially the largest ones (from the D_{80}). Respecting the criterion ensures the same performance whether distributions are expressed in AbN or GbN forms (black and red dashed line superposed). These specific performance gains may not be generalizable to other rivers, as here we did not perform this experiment by sampling a larger study area but by performing a truncation. However, we reiterate that if the GSDs obtained via photographic processing are to be derived in GbN form for comparison with other data or for use in sediment transport equations, then it is imperative that the extent of the photographic area is at least 100 times greater than the area of the largest grain. If the frame size is not adjustable then it may be possible to take several photographs of the site to be characterized so that the total area under study converges to the Diplas criterion and then combine all the particles identified into a single composite sample.

5.1.4.2.2 Compatibility between *continuous* and *discrete* square holes measurements

We chose the Pebble-Box approach to measure the actual size, *b*, of each particle ≥ 8 mm, which yields *continuous real* values of the axis, as the Photographic method gives also *continuous b*-axis sizes. Most of the existing data on GSD are from surface count of the particles via a Grid-by-Number (often called Wolman count, Wolman (1954)) or from a subsurface volume-by-weigh method (bulk sampling) with *b*-axis size measured by template or sieve device. Sometimes, the only information available in GbN are a few percentiles from a previous study or from other authors where the original database is no longer available. Also, percentile could be used in sediment transport equations that have been established mostly using GbN data measured by square holes. Below we examine the compatibility of GSDs obtained from photographs with GSDs obtained from sieves or template.

For sample S2 (dominated by coarse and discoid or flat particles) and S9 (fine and spherical particles), each particle, before being measured in the Pebble-Box, was passed through a template with several sieve-sized square-holes *D* with 0.5 ψ -increment (ψ = $\log_2$(b)) to extract *discrete* binned *b*-axis sizes. The retained sizes recorded via the template, *D*, are influenced by the grain flatness (*c/b*) as described by Church et al. (1987) via the relationship $D/b = 1/\sqrt{2} * [1 + (c/b)^2]^{0.5}$. Graham (2005b, 2010) reported for 500 measured particles (*a*, *b* and *c* axes) a *D/b* ratio ranging from 0.79 to 0.82. Graham (2005b, 2010) therefore transformed the apparent *b'* axes obtained by the photographic method with a factor of 0.79 (*c/b* =0.51) and 0.8 (*c/b*=0.71) respectively in order to compare them to the control set obtained by sieving. Stähly et al. (2017), showed a *D/b* ratio ranging from 0.83 to 0.86 on 2245 clasts. Similarly, to these last authors, our 10 samples (6800 particles) show a median theoretical ratio *D/b* ranging from 0.837 to 0.892 (corresponding to a flatness index ranging from 0.634 to 0.768) with an average of 0.872. However, we noticed a significant disparity in the ratio value between particles smaller and larger than 16 mm (see **S** Figure 5.15).

As mentioned in the description of the samples, and visible in Figure 5.11 , the particles of the 8/11.3 mm and 11.3/16 mm classes, in addition to representing almost 50% or more than of the total particles (see Table 5.1 and Figure 5.3 **C**), are the ones with the highest flatness index while the rest of the particles (larger than 16 mm) present lower *c/b* ratios. This has the effect of under-estimating the real size *b* of the larger particles (smaller in number) by allowing them to pass through the sieve more often due to their smaller thickness. Figure 5.8 shows the GSD in AbN (A1) and GbN (B1) from different measurement procedures (Pebble-Box, template, manual photo-delineation) while Tables A2 and B2 in Figure 5.8 show the average bias (average of the 15 residual percentiles) between procedures for each sample. In both A1 and B1, the solid red curve (template GSD) is localized to the left of the black solid curve (Pebble-Box GSD), with the template GSD being 5% (15%) finer on average than the Pebble-Box GSD in AbN form (GbN form). The way the control set is measured is therefore important, and it is more or less important depending on the form of the expressed GSD (AbN or GbN).

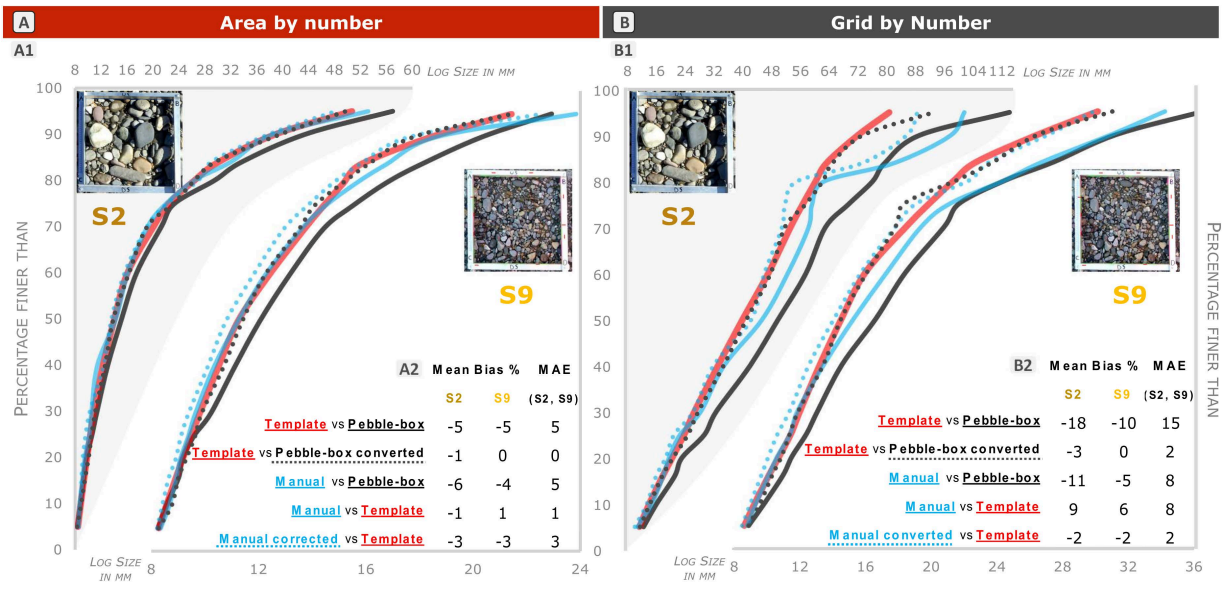

Figure 5.8: Comparison of the control sampling procedure (Pebble-Box or template/sieving) and its effect on the performance found for percentile estimation with the manual photographic method. Are represented as a curve, the 15 percentiles ($D_{5,\ 10,\ 16,\ 20,\ 25,\ 30,\ 40,\ 50,\ 60,\ 70,\ 75,\ 80,\ 84,95}$) in AbN form (**A1**) and GbN form (**B1**) of sample S2 and S9 according to (i) Pebble-Box measurement (black solid line), (ii) template measurement (red solid line), (iii) Pebble-Box converted to sieve form (black dashed line) via the *D/b* ratio (Church et al., 1987), (iv) manual digitisation (blue line) and (v) manual digitisation converted to sieved form (blue dashed line) via the *D/b* ratio (Church et al., 1987). In the lower right part of the plots, are annotated with corresponding colours, the mean bias over the 15 percentiles estimates with the two forms (AbN – **A2** and GbN – **B2**) of control dataset taken as reference (Pebble-Box or template) for each sample.

For our two samples S2 and S9, we know the median *D/b* ratio of particles smaller and larger than 16 mm, respectively 0.843 and 0.815 for S2, 0.864 and 0.837 for S9. A binary conversion factor, one for particles < 16 mm and a second for particles > 16 mm, was used to convert the control GSD obtained from a *continuous* measurement (Pebble-Box, black dashed curve) to the control GSD obtained from sieved measurement (Template, red solid curve). In both AbN and GbN, the black dashed curve converges to the red *continuous* curve. This conversion seems to be suitable for our study sites as the average bias falls between -1% and 0% in AbN and -3 and 0% in GbN.

On the two samples S2 and S9 in AbN, Figure 5.8 **A1**, the apparent GSDs obtained by manual delineation (blue solid curve) show an under-estimation compared to the Pebble-Box (black solid curve) of about 5%, as do the GSDs obtained from the template (blue and red curve overlap quite well). The average Manual vs. Template bias varies between -1 and +1% (MAE=1%). Such observations have already been made by Stähly et al. (2017). In their study, they found a constant *b'/b* ratio (photographic apparent size *b'*/actual measured size *b*) of 0.86. Here, we found a *D/b* ratio of 0.87. Therefore, the *D/b'* ratio should be close to 1.

This means that the impact of the fabric effect, minimising the apparent *b'* axis by photographic method compared to the real measurement (*b'/b*), is of the same order of magnitude as the reduction of the GSD by sieving compared to the real measurement *b* (*D/b*). We therefore make the same conclusion as Stähly et al. (2017), the GSD obtained by manual delineation is directly comparable to the GSD obtained by sieving. However, these conclusions are not valid in GbN. The same analyses were performed for the *supervised PhotoMOB* procedure (MAE=3%) and reach the same conclusion but not presented here for lack of space.

In GbN, the representativeness of the particles is proportional to the surface area of the grains. The shape of the GSD is therefore controlled by the largest particles (even if they are smaller in number). As these coarser particles are more often under-estimated by sieving than the fines by virtue of being flatter, the sieved GSD (retained hole size *D*) becomes finer than the apparent size from manual delimitation GSD (*b'*). The red solid curve in B1 is localized on the left of the blue solid curve whereas in A1 they were superposed. The manual GSD is on average 8% larger than the template. In this context, a conversion may be necessary if one wants to compare the photographic GSD (blue) with a sieved/template GSD (red).

It is difficult to estimate the average *D/b* ratio of each patch photographed, let alone the ratio for particles smaller than 16 mm and those larger. This would involve taking a number of particles of different sizes and measuring their *c* and *b* axes. The two-factor conversion applied here to the Pebble-Box records is actually impractical. Furthermore, the manual delineation (blue solid curve) under-estimates the GSD of the Pebble-Box (black solid curve) by about 8%. Using a binary factor, which works well to convert the Pebble-Box GSD (black dashed line) to a template/sieved GSD (red solid curve) would produce a converted manual GSD finer than the template (-6% on average, manual delimitation curve converted with double factor is not presented in this figure for better clarity).Using a factor of 0.8 as proposed by Graham et al. (2005b) would also be too large, producing a converted manual GSD finer than the template by -8% on average (manual delimitation curve converted with 0.8 factor are not presented in this figure for better clarity). Using the average *D/b* ratio of 0.87 calculated on our ten samples, allows us to reduce the bias between the manual delineation converted (blues dashed curve) and the template (red solid curve) to -2% for both samples despite their significantly different shapes and grain sizes. We have reached the same conclusion for the *PhotoMOB Supervised* procedure delineation, applying the conversion factor allows to reduce the MAE from 24% to 12%. It should be noted that for these results mentioned here, the sampled area does not meet Diplas's criterion, the distributions have not been truncated. Once truncated the percentile deviation for both manual and *supervised* procedure are of 6%. A graph summarizing the percentile RMSEs for the manual and *supervised* procedures based on GSD in AbN and GbN, without and with high truncation as well as without and with *b'* axis conversion is available in **S** Figure 5.16 - Part **B**

5.1.4.2.3 Intended purpose

The acquisition of data by photographic methods and their processing must be conditioned by the use that will be made of them in order to obtain a correct level of precision in the characterization of the real grains of the river bed. Below we list recommendations for using data from the photographic method:

(1) If the *PhotoMOB* derived GSDs are to be of *continuous* form and AbN, then they can be used as they are. The percentiles in the AbN form with the manual procedure are estimated with an average error of less than 10%. However, the percentile estimate is not constant, it is little higher than 10% for the largest percentile. A minimum area equal to 100 times the coarsest grain seems to reduce the error to about 5% in average in our case.

(2) If the *PhotoMOB* derived GSDs are to be compared with GSDs in AbN of *discrete* form obtained by sieving or passing through a template (e.g., areal sampling + sieving measurement), they can be used as they are as long as the extent area is large enough to characterize the whole grain size range. The under-estimation of grain size via photo due to the fabric effect is similar to the under-estimation of the actual grain size when measured through a template due to the degree of flatness leading which may to a classification in a lower fraction.

(3) If the *PhotoMOB* derived GSDs are to be compared with the GSDs in GbN form with *continuous* values (e.g., pebble count with a calliper to measure sizes) then the ratio of the sampled area to the area of the largest particle must be at least 100. In this study we found that, under good photographic conditions (C1), the average error in estimating the percentiles could be reduced from 15-20% to 5-10%.

(4) Finally, if the *PhotoMOB* derived GSDs are to be compared with GSDs in GbN form with *discrete* values (e.g., pebble count sampling + template measurement or bulk sample + sieving) then it will be necessary to (i) respect the criterion of a sampled area at least 100 times the size of the largest particle and (ii) convert the apparent grain size as a function of the flatness index. This will have the effect of making the GSD finer, as a sieve tends to minimize the actual grain size of particles that are relatively flat. However, a flatness index cannot be generalized to all rivers. In our case, we found that the flatness indexes used by Graham (2005b, 2010) were not suitable for our samples. A conversion factor of 0.87 for the rivers Ésera and Cinca seems to be appropriate to compare the photographic GSD with real sieved data. It may be worthwhile to sample the *c*- and *b*-axis of a sample of grains to obtain an average flatness ratio on a particular river or section. This little effort will enable more precise results to be obtained in the perspective of spatial and temporal tracking using photographic methods.

5.1.4.3 Final discussion

For several reasons, it is difficult to compare the performance data of this paper with previous authors who have already worked on this topic (e.g., Buscombe, 2008, 2013; Butler et al., 2001; Chang and Chung, 2012; Detert and Weibrecht, 2013; Graham et al., 2005a, 2005b; Ibbeken and Schleyer, 1986; Purinton and Bookhagen, 2019; Sime and Ferguson, 2003; Stähly et al., 2017; Strom et al., 2010; Warrick et al., 2009) . Many have provided (i) the results not in millimetre units but in psi (ψ) units and (ii) the relative errors (%) are not always fully reported. Additionally, (iii) performance is presented for different lower truncations and sometimes, (iv) the control data set varies between a manual delimitation on a photo taken as a reference or the actual grains taken from the bed as the reference. In the latter case (v) the tested data sets were sometimes obtained in GbN form so the photographic distributions (AbN form) were converted to Grid-by-Number, by taking only a few particles from the photos along a grid or via the Kellerhals and Bray (1971) conversion method or even by the area of segmented particles as described previously in this paper with the help of Text **S** Section 5.1.6.3.2.2 and **S** Figure 5.12. One last parameter makes it difficult to compare the performance with the other works mentioned above: (vi) once the real grain size constitutes the control sets, grains are systematically measured by sieving, generally square holes, and then the number of grains per particle size classes is counted, which generates *discrete* values. The percentile values are then estimated by interpolation, either linear or spline, between the particle size classes. This has a direct impact on the control distribution and, consequently, to the error estimates. If we had acquired our control set only by sieving, as almost all other studies on this topic, we would have obtained lower errors.

Figure 5.8 showed that in AbN, the average bias of the manual delimitation was -5% with the Pebble-Box as reference, but it goes down to -1/1% when taking the GSD by sieving as reference. In GbN, the average bias of the manual delimitation was -8% with the Pebble-Box as reference, yet it goes down to -2% with the GSD by sieving as reference if the conversion factor is well adapted. So, if the authors previously cited had used a Pebble-Box, they may have found somewhat larger errors.

5.1.5 CONCLUSION

This paper is the first (Part 1) of a pair of connected papers in which we present an automated image processing procedure for measure grains and monitoring the mobility/stability (bed dynamics) of gravel river beds from photographs. We present here only the GIS-based procedure for identifying and measuring grains in order to derive a reliable surface Grain Size Distributions (GSD) together with additional information form the texture of the bed. The main conclusions of the paper are as follows:

(1) The *PhotoMOB* procedure identifies grain contours in a very similar way to those obtained by a manual delineation, with an efficiency to estimates percentile better or comparable to existing procedures as *Basegrain* and *Sedimetrics* when the bed area is painted and protected from the sun during photo acquisition (i.e., C1, RMSE of 6.1 – 5.6% compare to 6.7-11.9%). PhotoMOB also performs better when the bed is not painted but still protected from the sun (i.e., C2, RMSE of 9.5-8.8% compare to 14.0-10.9%).

(2) The study of the shape of the particles sampled in the Cinca and Ésera rivers showed that there is a slight tendency to flatten with increasing size between 16 and 64 mm. The coarsest sample (S10) having 60% of its grains in this size range and having the most discoidal shape and overlapped particle was most strongly under-estimated by manual delineation (on average at -20%). Therefore, in some cases, the fabric effect (shape and imbrication) on GSD accuracy may be significant.

(3) Despite the impact of the fabric effect, the photographic method provides reliable percentile estimates. Over the 10 sample studied, the manual delineation shows an RMSE of 8.2% (corresponding to an RMSE of 2 mm) in relation to the measured grain which were actually present on the surface of the bed. Similarly, *PhotoMOB* both, *supervised* and *automated*, provides RMSEs of 8.9-9.5% (around 2.2 mm) for photo conditions C1 and C2.

(4) The GSDs extracted from the photographic method (AbN sampling, *continuous* axis measures) can be compatible with different sampling and measurement methods (GbN - sieved). The 2 square holes sieved samples studied, indicate that respecting a sufficiently large sampling area to cover the whole grain size range properly and taking into account the mean grain flatness, allows an average MAE error in percentile estimation by the photographic method (manual of PhotoMOB delineation) of 6%.

(5) The use of photography allows for a reduction in field time workload, monitoring over time without artificially altering the bed surface, and the technique does not require mandatory use of aerosol paint to mark particles but can of course be coupled to particle travel distance measurements.

(6) Finally, the accuracy of the delineation not just affects the GSDs, it I also fundamental to decrease errors when paired photos are compared to analyse bed dynamics (companion paper). In order to increase the speed of the whole process and to avoid the operator having to work too hard to correct under- or over-segmented particles, the photographed area should be protected from direct sunlight and painted if possible (C1 photo condition). A future enhancement to the tool could be the use/integration of the model developed by Mair et al. (2023) into the workflow to reduce the correction effort that is working very well on C2 and C3. *PhotoMOB* has the advantage of running under GIS, making it easier for the large community of ArcGIS® users to verify, correct and manipulate the results.

Code availability.

The processing of the images with the ArcGIS desktop toolbox PhotoMOB part 1 and 2 generates shapefile with for each grain, in pre- and post-event, its shape characteristics (area, perimeter, *a*-axis, *b*-axis, orientation, rectangularity, eccentricity, roundness, compactness) as well as its classification (immobile/mobile). The attribute table of these layers is also saved in text format. A web and desktop application based on R language and shiny package (Chang et al., 2023b; R Core Team, 2021), called PhotoMOB Extractor, has been developed to analyse the data from the text files and to allow the user to quickly and easily obtain the outputs mentioned in Figure 5.17 (C1, C2, C4, E1, E2, E3, E4, E5) in both AbN and GbN form. The actual and future version of the PhotoMOB toolbox as well as the PhotoMOB Extractor App are available with documentation at https://shiny.fannyville.com/PhotoMOB_Tool.html. The toolbox is currently only available for ArcGIS desktop, but will be soon converted to ArcGIS Pro and, additionally, our intention is to convert to the open source QGIS.

Acknowledgements

This research was undertaken under the MorphHab (PID2019104979RB-I00/AEI/10.13039/501100011033). It has also benefit from the research undertaken in the background of MorphPeak (CGL201678874-R/AEI/10.13039/501100011033) research projects funded by the Spanish State Research Agency (Ministry of Science and Innovation) and the European Regional Development Fund Scheme (FEDER). The first author has a grant funded by the Ministry of Economy, Industry and Competitiveness, Spain (BES-2017-081850). Damià Vericat is a Serra Húnter Fellow at the University of Lleida. All authors are part of the Fluvial Dynamics Research Group –RIUS, a consolidated group recognized by the Generalitat de Catalunya (2021 SGR 01114). We thank Alexandre Moron for building the square frame and the Pebble-Box device and his assistance, as well as Meritxell Puig and Estrella Carrero, for their assistance during the fieldwork campaigns and grains' measurement. Finally, we thank Jonathan Coutaz and Daniel Vázquez Tarrío for sharing training photos from the Buëch and Vénéon rivers.

Credit authorship contribution statement

Fanny Ville: Conceptualization, Methodology, Investigation, Data curation, Formal analysis, Visualization, writing original draft, Writing – review & editing.
Damià Vericat: Funding acquisition, Methodology, Supervision Writing – review & editing.
Ramon J. Batalla: Funding acquisition, Methodology, Supervision, Writing – review & editing.
Colin Rennie: Methodology, Supervision, Writing – review & editing.

Data availability statement

Dataset of measured grain from field (from *paint-and-pick*), as well as manual grain digitalisation and automated grain delineation from *PhotoMOB* either *supervised* or *automated*, *Basegrain* and *Sedimetrics* are available under: https://zenodo.org/records/10038313

Declaration of competing interest:

The authors declare that they have no conflict of interest.

S-5.1.6 SUPPORTING INFORMATION PART 1

Supporting Information for:

PhotoMOB: Automated GIS method for estimation of fractional grain dynamics in gravel bed rivers.

Part 1: Grain size

Contents of this file:

This document provides supplementary material. It is structured using the same headings as the main article to help readers find what they are interested in reading more about. Title followed by the word "none" indicate that no supplementary information is provided for that section.

S-5.1.6.1 Introduction

To characterize and quantify mobilized sediment intensities, direct sediment sampling methods can be deployed (e.g., Helley and Smith, 1971 ; Bunte et al., 2007; Bunte and Abt, 2001) as well as indirect methods via for examples the use of targeted tracer stones (e.g., Church and Hassan, 2002; Hassan and Ergenzinger, 2003; Vázquez-Tarrío and Batalla, 2019). The use of a painted plot is a commonly used indirect technique which involves painting a zone of the bed to use the coloured grains as a tracer. This method avoids alteration of the natural packing of the particles without limitation of the size of the traced grain. If entrained painted particles can be located downstream, then transport distances can also be measured (e.g., Brenna et al., 2019; Church and Hassan, 1992; Hassan and Ergenzinger, 2003; Mao et al., 2017; Vázquez-Tarrío and Batalla, 2019; Vericat et al., 2020).

However, the use of painted patches has several limitations (i) Firstly, the use of aerosols to ensure good paint adhesion may contaminate river surroundings. (ii) The paint must be applied to a dry substrate and allowed to dry before re-wetting. These conditions of use are not always available, as for example in rivers subject to hydropeaking, where water is released rapidly and large areas of the bed are frequently (daily, hourly) and quickly inundated. (iii) The measurements are focused on visually recovered downstream particles while the mobilized painted particles may deposit paint side down and/or be subsequently buried, resulting in a low recovery rate as reviewed by Hassan and Roy, (2016). (iv) Finally, a large amount of information from the original patch location is not further analysed such as the proportion and size of immobile particles. A solution can be to compare successive images of the bed surface taken at the same location (Cerney, 2010; Peckarsky et al., 2014; Vericat et al., 2008a). Information related to grain stability and mobility can be extracted by a spatial grain-by-grain inter-analysis of the particles present in the two photographs. In this case, a semi- or fully-automated image processing procedure is extremely useful. To meet this objective, we have developed an ArcGIS® toolbox to automate image processing in two distinct phases. The first part consists of identifying and characterizing all the grains present in the photos. This makes it possible to extract the size of the grains, their shape, their orientation and to estimate the proportion of the area covered by fine material. The second part compares the shape of the grains positioned at the same coordinate between the photos in order to categorize them as immobile or mobile.

S-5.1.6.2 The PhotoMOB workflow

S Figure 5.9 **A** represent the photo acquisition procedure while **S** Figure 5.9 **B** represents the workflow of the *PhotoMOB* GIS toolbox Part 1.

S-5.1.6.2.1 Image collection

Once a target area has been selected, a frame with known exact internal dimensions is placed on the riverbed to physically delineate the area. The distance between each internal corner will be used to scale the images. In order to facilitate fieldwork and the subsequent scaling of the photos, a metal frame consisting of L-shaped side elements that are fixed together at their ends by a screw system can be used. The repetitive task of scaling the photos one after the other is facilitated by an area of interest of constant shape and surface, without any variation. The frame could include a measuring scale and a marker indicating upstream direction so that during office work the operator can quickly orientate the photo. The size of the area should be a function of the largest particle i.e., Diplas and Fripp (1992) proposed that the area to be sampled must be at least 100 times larger than the area of the largest particle. This would give an accuracy equivalent to a 100-grain Grid-by-Number sample, such as a pebble-count.

Finally, the photo is recommended to be taken facing against the flow direction, the more possible perpendicular to the riverbed, and with the area protected from direct sunlight to avoid brightness changes within the photo. In general, the more homogeneous the area is in terms of light and colours, the easier is to detect the particles automatically. Finally, the positions of the four corners of the frame can be marked and/or surveyed by a topographic method to enable to find back the location for a subsequent photo collection. Even if the precision of the method used to survey the corners of the frame is not the appropriate (i.e., cm) to scale the images, these coordinates will enable to return to the same location for subsequent photo collection.

Once the area is re-visited, the frame is placed back on the bed, and the second photo is taken following the same protocol. This last field phase can be repeated for the same area successively according to successive flow events (as show in **S** Figure 5.9 **A**).

S-5.1.6.2.2 Bed particle detection and characterization

Grain detection and characterization is done in five steps represented in **S** Figure 5.9 **B**. These five steps are grouped in two main processing tasks, which are fully described below. (i) Image pre-processing and (ii) image processing: (B.2) image classification, (B.3) image binarization, (B.4) boundary adjustment and (B.5) grain characterization.

S-5.1.6.2.2.1 Image pre-processing

In order to facilitate good detection of the particles, the photos are first filtered externally to GIS in GIMP (Team, 2019), a free image manipulation software, to smooth the intra-grain noise while preserving edges. A high-pass filter is applied to the area inside the frame to sharpen the boundary of the particles which correspond to areas of rapid tonal change. It is a frequency filter that (i) preserves high frequencies via a first parameter named *standard deviation* that controls the level of detail preserved and (ii) increases them via the *contrast* parameter. This first filter depends strongly on the sunlight condition and the homogeneity of the surface. For fully painted photos with homogenous light (i.e., homogenized surface, low complexity) it is not necessary to use a high standard deviation value because the image contains few details (i.e., details correspond only to the particle edges) that are easily visible. For each photo in these conditions, a constant value of 5 for the *standard deviation* and 2.5 for the *contrast* parameter are used. On the other hand, for unpainted photos or a variable lighting photo condition, is necessary to keep a higher level of detail in order to make the contours appear more clearly.

A constant value of 10 for the *standard deviation* and 2.5 for *contrast* parameters are used. Then, for all conditions, a noise reduction filter with a constant *strength* of 10 is applied twice in succession, in order to attenuate the intra-grain noise. All these parameters were established by evaluating the performance of different values.

Afterwards, the filtered images are loaded into GIS. The four internal corners of the frame are marked manually. They are used as Cartesian reference points on a local plan to scale the photo. For example, for a square frame with 1m sides (internal), points A, B, C and D receive the coordinates 0.1; 1.1; 0.0; 1.0 respectively. Then to correct the perspective of the image a projective transformation is applied. As it is difficult to get a perfect tilt free photographs without structure, this transformation removes the tilt and link the image to the ground for more accurate grain measurements.

In the case of partial or selective transport (i.e., when a certain proportion of the study area has remained stationary) the second or post event photo has to be aligned with the first one with a further projective transformation. This alignment is done manually by identifying identical points between the two photos. When all bed was disturbed and no reference points are found, the corner frame can be located at the same position of the first photo. In this case all grain will be new when compared to the precedent or first photo.

S-5.1.6.2.2.2 Image processing

The scaled filtered images, are transformed into a grey scale image (intensity level) by simply summing the three bands (i.e., Red, Green and Blue). Each band can contain pixels with values ranging from 0 to 255. The grey scale image can thus finally present shades ranging from 0 (black) to 768 (white).

The next step is to transform these grey scale images into binary images, where the foreground would correspond to the particles (high intensity, white) and the background to the boundary of the particles and gaps (low intensity, black). To generate this binarization, a threshold of dark intensity must be selected to perform the partition. However, it is difficult to determine a threshold value out of 768 possibilities. Therefore, the grey scale levels are reduced (i.e., reclassified) from 768 to 40 levels *(ca. 5% of 768)*, and the threshold is identified from those 40 possibilities. This reduction allows the contour effect to appear (Tyagi, 2018). The selection of the threshold value relies on the use of the histogram of the frequency distribution of the grey levels of the pixels (method of moments corresponding of part B2 in Figure 5.9). The whole process can be *supervised* by the operator or be performed *automatically* through a threshold prediction model developed in this study and presented in Section 5.1.6.2.2.3.

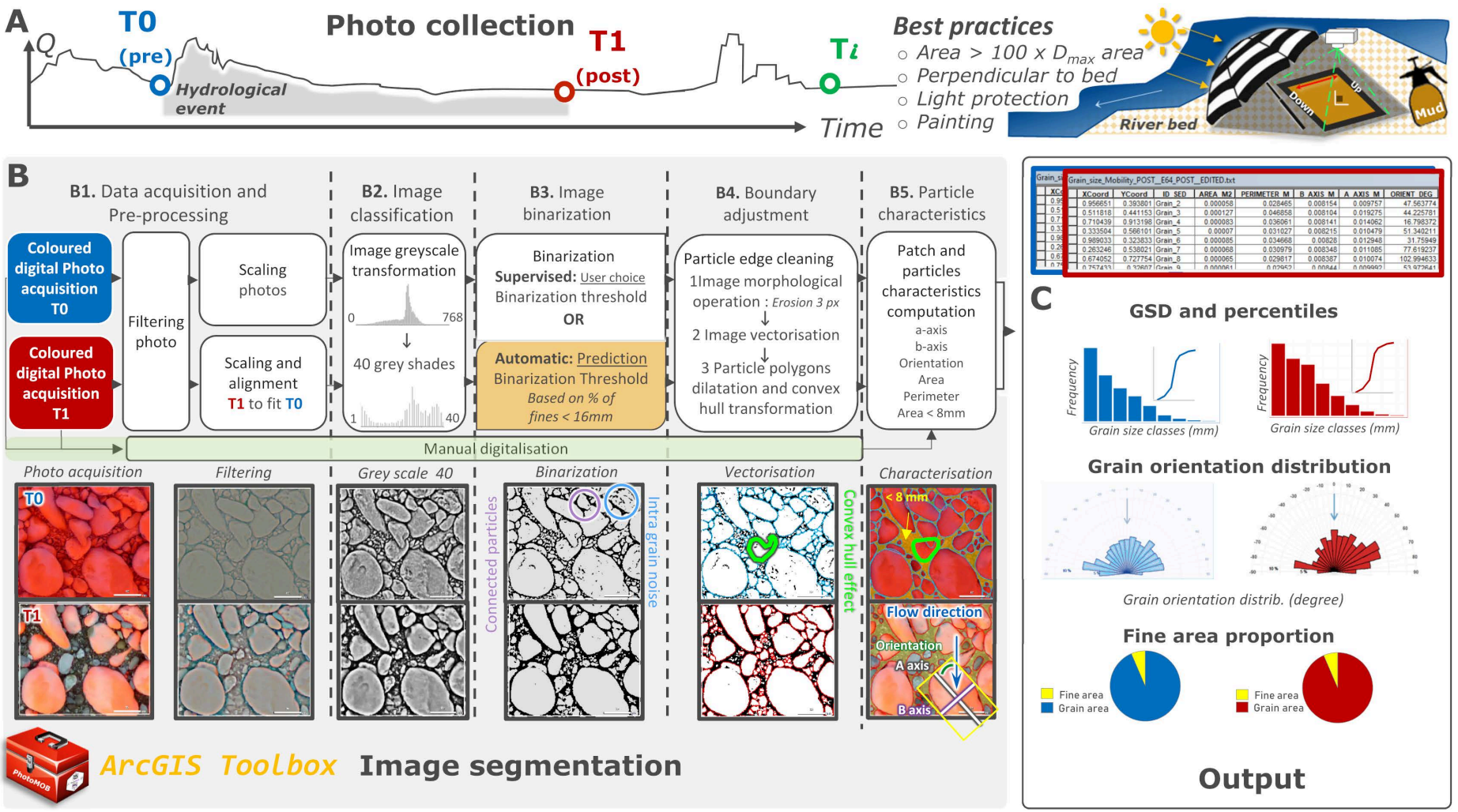

S-Figure 5.9: Illustration of the image segmentation workflow required to sample and characterize the bed surface. (**A**) Photo acquisition. (**B**) Extraction of grain and patch characteristics. (**C**) Possible output after patch surface characterization. The yellow boxes represent the developed models of dark threshold prediction (see Text **S** Section 5.1.6.2.2.3). Note the effect of the convex hull transformation on the green particle in the centre of the two images in the Vectorisation and Characterization columns. In the Characterization column, the second image shows the sketch explaining how particle characteristics are derived

The boundaries of the particles in the binary images are not completely segmented. Sometimes there is still a chain-of-connection of some white pixels between two particles (shown in the **S** Figure 5.9 **B3**. To remedy this, a morphological erosion operation is performed (Tyagi, 2018). This consists of increasing the black background area by a certain size and shrinking the white foreground area. It was established in this study, following multiple visual checks on different images, that an erosion of three pixels was optimal. Sime and Ferguson (2003) have also shown that a three pixel value allows for correct segmentation without amplifying too much the intra-grain noise. Then, the white pixel areas are converted from raster to polygons, vector features, yielding the outline of each particle (see **S** Figure 5.9 **B4**). However, as these areas have been previously eroded, a dilation of the polygons is necessary in order to return to the original particle size. This dilation distance corresponds to three times the resolution of the raster (three times the pixel size of the image). Then, to smooth the rough contours of the particles and obtain a more realistic particle shape, a convex envelope is applied. This corresponds to an envelope passing uniquely through the extremities of the raw contour and eliminating any concavities. An example can be seen between the images in **S** Figure 5.9 **B4** and **B5** (*Vectorisation* and *Characterisation*) which present the raw delimitation and the convex envelope (note the highlighted particle in the center).

Once this convex hull is generated, it is possible to extract six characteristics of the sediment patch. The (i) area and (ii) perimeter of each detected particle are directly acquired from the convex hull. For (iii) the longest axis (*a*-axis) and (iv) the intermediate axis (*b*-axis), on each particle, a minimum bounding rectangle box delimiting its smallest width is generated. The length of this rectangle corresponds to an estimate of the particle's *a*-axis, while its width corresponds to the particle's *b*-axis. Furthermore, the angle of the longest axis with north gives us information about (v) the orientation of the particle (see **S** Figure 5.9 **B5** and **C**). Finally, an estimate of the area covered by fin material is obtained by subtracting from the total study area, the summed area of particles with *b*-axis larger than fine limit defined by the operator (by default 8mm).

S-5.1.6.2.2.3 Training of a dark binarization threshold prediction model

Butler et al. (2001) had already noted that this threshold depends on several factors such as (i) the sunlight condition, (ii) the scale of the photo, (iii) the source (camera), (iv) the texture (particle sizes). Since the photos are taken with the same camera under controlled light conditions and with fixed frame size, the most important factor for determining the optimal threshold is the general grain size of the study riverbed area. This phenomenon was captured by Sime and Ferguson (2003) using the term "image porosity". This term refers to the proportion of the image representing edges and gaps, which present low grey intensity levels (darker areas). The finer the grain size of the study area, the more edge pixels there are, and therefore the greater number of black pixels there are in the image. Conversely, the coarser the grains, the fewer the number of pixels representing contours, and the fewer the number of black pixels. The method followed in this study is based on the intensity distribution histogram shape and statistical properties (Burger and Burge, 2016) (see Figure 5.2 *main text*). We assume that all photos, taken under the conditions described in the **S** Figure 5.9 **A** and Section 5.1.6.2.1, present a similar general shape of histogram, which is a skewed distribution toward the left side, i.e., toward low intensity (Figure 5.2 **B** *main text*). The binarization threshold for partitioning the image between particles (foreground) and interstices/boundary (background) will therefore be located towards the left of the histogram. Each image has a unique GSD and therefore a different proportion of interstice for the same study extent. It cannot be an absolute fixed value valid for all images. If the approximate proportion of pixels representing the background is known, then the binarization threshold could be set to this percentile. However, it appears difficult to give a visual estimation of the fraction of the image only occupied by the gaps and contours. Moreover, having only 40 grey levels, the percentile approach would be too sensitive. A bad estimate of ±15% would cause a change in the threshold value of ±6 levels. This would strongly change the delimitation.

Instead, we propose to develop a prediction model based on a visual approximation of the areal proportion of material finer than pebbles (<16 mm) covering the study area correlated with the optimal binarization threshold expressed not as a percentile but as a relative grey level value to a reference grey level value:

$$Reference\ grey\ level = mean\ value\ of\ the\ grey\ pixels\ level - 1\ SD\ (\ grey\ pixels\ levels) \quad (5.6)$$

The prediction model was developed from a dataset of 68 surface river bed photos from five different rivers [Cinca (Spain), Ésera (Spain), Vénéon (France), Buëch (France) and Blanco-Este (Chili)] covering areas from 0.16 to 1 m². Since it was not always possible to paint the area or to protect it from direct sunlight, we have created a training dataset divided into three groups corresponding to different photo conditions (see Figure 5.2 **D** *main text*). Condition C1, corresponds to painted areas protected from the sun (optimal condition). Condition C2 corresponds to unpainted areas but still protected from the sun (degraded condition). Finally, condition C3, corresponding to unpainted areas and not protected from the sun (inadvisable condition). The photos were scaled and digitized by hand (Figure 5.2 **A** *main text*). This is the *gold standard* i.e., the best delineation that can be expected. In total, 34246 particles were delineated manually. These delineation layers were fed into the tool to perform step B5 on Figure 5.9 (Particle characterization). The *b*-axis size of each particle could be calculated. All areas of the image covered by polygons representing particles with a *b*-axis greater than 16 mm were subtracted from the study area; this allows us to know the area covered by finer materials than pebbles.

In parallel, each of the same images was processed in the tool. For each of them, 22 grey levels were tested as a threshold for binarization. In total, 1496 delineation proposals were generated (68 photos × 22 tested thresholds). The 22 binarization thresholds tested are expressed as a relative value to the reference value as illustrated in Figure 5.2 **B** (*main text*) and Eq. 5.6. Then, from these 22 delineations, a single operator selected the best delineation. In order to remain consistent on the comparison of all these particle layers, for each photo, the delineations were compared two by two, from the lowest threshold level (*Reference value - 5*) to the highest (*Reference value + 16*), preferring to keep a layer with a few under-delineations rather than a layer with a large number of over-delineations for two main reasons: (i) because if a manual edge correction (edition) is desired, a few polygons to segment is a faster operation than removing a large number of small polygons and then re-delineating them correctly; and, (ii) furthermore, by using the Area-by-Number form to establish the particle size distribution, each particle present has the same representativeness in the sample. Adding a large number of false small particles will have more impact on the final result than keeping a few large false particles.

The result of all these steps is (i) the proportion of the photo covered by material smaller than 16 mm and (ii) the optimal binarization threshold. Figure 5.2 **C** (*main text*) shows the prediction models of the binarization threshold established via these pairs of information, specific to each photo condition (C1, C2, C3). The R-square of 0.74 (*p*-value <0.001) for the C3 predicting model is lower than the ones for C1 and C2 respectively 0.85 (*p*-value <0.001) and 0.89 (*p*-value <0.001). In condition C3 the optimal threshold is less conditioned by the GSD than by the variation in image brightness. To obtain an order of magnitude of the error of these prediction models, a validation set of 11 patches photographed in the three conditions with proportions of area below 16 mm ranging from 15% to 71% was collected. The mean absolute error of prediction is 1 grey levels for photo condition C1 and C2, whereas in C3 it is of 2 (average distance between the model line and the validation point for each photo condition on Figure 5.2 **C**, *main text*).

S-5.1.6.3 Method of performances and compatibility assessment

S-5.1.6.3.1 Control dataset

S-5.1.6.3.1.1 Control data set acquisition

The data set consists of 10 patches, seven from Cinca river and three from Ésera river. Each of the 10 patches was photographed in 3 different conditions (see Figure 5.10 part A below). Once the patches had been painted and the last photo taken, all the whole grains inside the frame were collected and their position on the bed estimated and classified into three categories based on the projection of the paint on their surface (Figure 5.3 *main text*). This position can be compared to the work of Ibbeken and Schleyer (1986), see Figure 5.10, part B below.

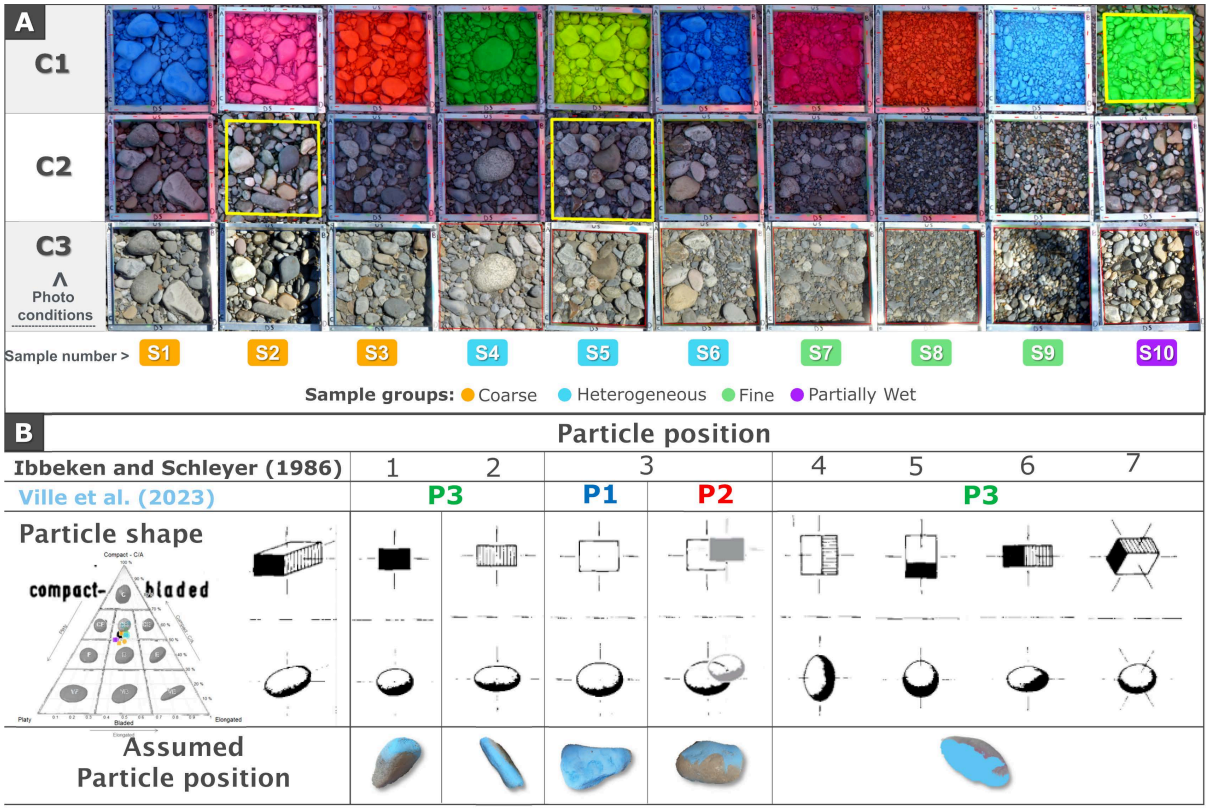

S-Figure 5.10: (**A**) Illustration of the 10 40*40 cm samples for the 3 photo conditions. C1: painted and protected from the sun, C2: unpainted but protected from the sun and C3: unpainted and unprotected from the sun. Samples were divided into three groups according to grain size and lithology. (**B**) Classification of grain position (indicative of degree of imbrication) based on the work of Ibbeken and Schleyer (1986) (modified after Ibbeken and Schleyer., 1986).

S-5.1.6.3.1.2 Control data set characteristics

According to the Zingg classification **S** Figure 5.11 **A** the median shape of the sampled particles from both rivers is spherical. However, the lithology and shape of all these particles varies between rivers i.e., the sediments of the Cinca consist mainly of coarse-grained white granite (increasing the complexity of the photographed surface to be segmented) and pale limestone. The seven samples from this river as well as sample S9 (from Ésera River) are composed approximately of 50% spherical particles, then 30% discoidal particles (quite flat), and about 10% bladed and rod-like particles (elongated) (**S** Figure 5.11 **B** and **C**). The Ésera sediments are dominated by dark sandstone with varying degrees of metamorphism. The particle shapes of the two coarse samples S2 and S10 from this river are significantly different from the other seven with predominantly discoidal shapes (41 and 49% respectively), followed by spherical shapes at 30%.

Samples 1 through 3 were grouped as having a coarse particle size distribution (D_{50} in GbN for ranging between 44 mm to 57 mm). Samples S1 and S2 were dominated at 38% and 37% by particles in the P1 position (fully visible) while S3 is the only sample dominated by particles in the P3 position (39%). Samples 4 through 6 were dominated by articles in P2 position (i.e., overlapped, between 39% and 45%), all from the Cinca, and were grouped as having heterogeneous surfaces. Samples 4 and 5 were heterogeneous in terms of lithology, while sample 6 has a low grain sorting coefficient (Folk and Ward, 1957) of 1.3 (poorly sorted). Samples 7 through 9 were representative of fine patches composed of between 38 and 71% material finer than pebbles (16 mm) and with D_{50} in GbN form between 14 to 22 mm. S7 has similar proportions of particle in P1 and P2 (around 35%), while samples S8 and S9 are largely dominated by particle in P1 position (fully visible) at 48 and 49%. Finally, the last sample S10, was collected because it had a partially wet surface. As 49% of the sample is disc-shaped (flat and circular) and dominated at 38% by particle in position P2, it will be difficult to characterise correctly by photographic methods.

In spite of notable differences in size and shape between rivers and groups of samples, all samples show a similar evolution of the median shape with increasing size (*b*-axis) visible in **S** Figure 5.11 **B**. This can be broken down into 3 phases: (i) First, between 5.66 and 11 mm there is a significate progressive decrease in elongation and an increase in sphericity (p-value < 0.5) while the flatness remains stable. The p-values of the statistical Mann-Whitney tests between size classes are given in **S** Figure 5.11 **D**. (ii) Secondly, between 11 and 45 mm, the median shape of the particles becomes progressively more elongated and flatter towards a bladed shape. (iii) Finally, there is an abrupt change in trend for the particles above 45 mm, when they become more compact with a discoidal tendency.

In addition, all the samples are composed of particles of similar shape in P1 and P2, while all of them present particles in P3 with a significantly more spherical shape (less elongated and less flat). The proportion of P3 particles (necessarily under-estimated by photographic method) varies between 12 and 40% within the 10 samples. In a study comparing the photographic method with the more traditional pebble-count method, Strom et al. (2010) observed at six different sites with little or no particle imbrication, a proportion of P3 particles varied between 10 and 22%. The proportion of P3 in our study appears to be consistent, although some of our samples show lot of imbrications.

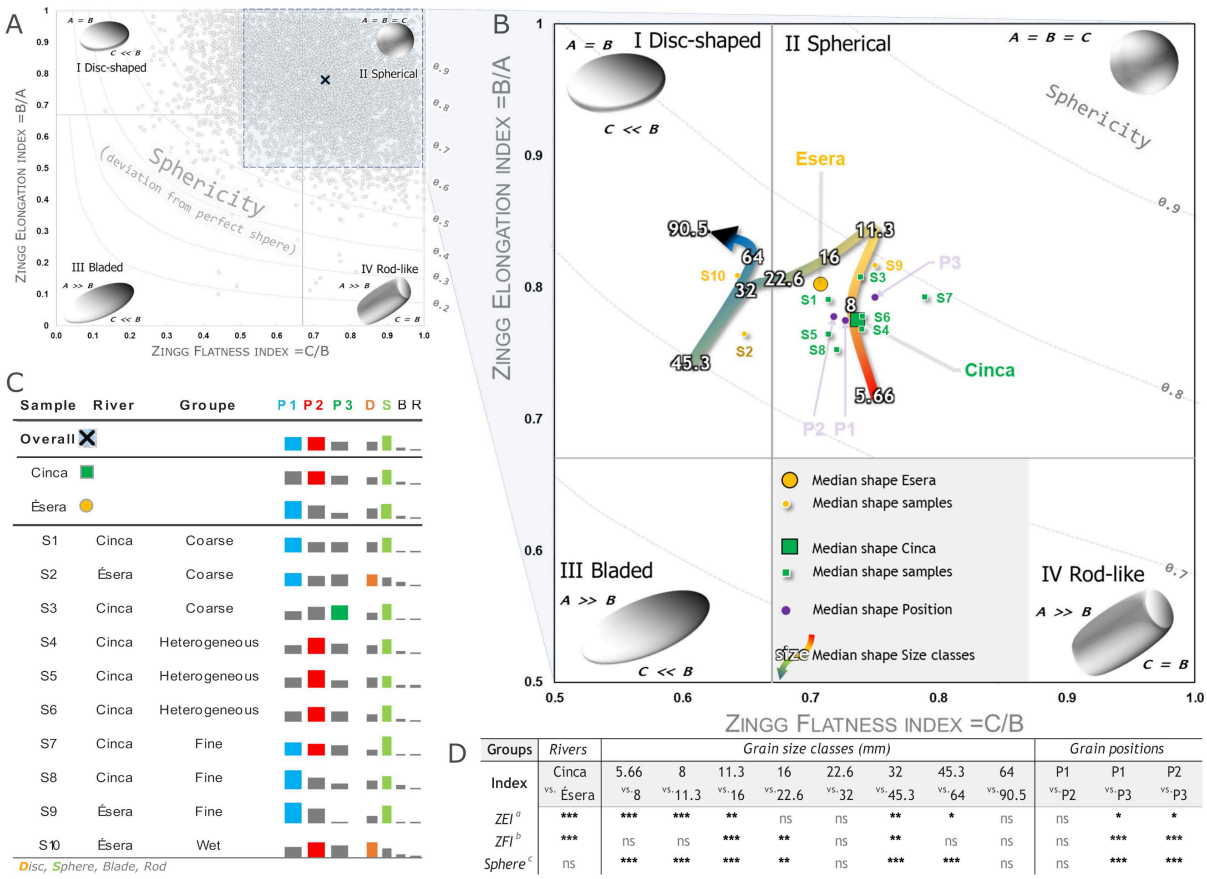

S-Figure 5.11: Characteristic of control particles. (**A**) Classification of the shape of each particle according to the classification of Zingg (1935) and the overall median shape. (**B**) Median Zingg flatness and elongation index by (i) rivers (Ésera in yellow circle and Cinca in green square), (ii) samples (S1-S10), (iii) size classes (warm to cold colour gradient) and (iv) position on the bed (purple circle). (**C**) Proportion and dominant (coloured bar) proportion of particle position and shape by groups (D) Mann-Whitney test of statistical significance of the shape disparity between the rivers, consecutive grain size classes and positions of the bed particles: * significant test on α=0.05, ** significant test on α=0.01, *** significant test at all levels, ns: insignificant test, [a] Zingg Elongation Index (b/a), [b]Zingg Flatness Index (c/b), [c]Krumbein shpericity index $\left((b*c)/a^2\right)(1/3))$ (Krumbein, 1941)

S-5.1.6.3.2 PhotoMOB assessment

S-5.1.6.3.2.1 Assembling of the dataset

Figure 5.4 (*main text*) presents an overview of the digitization results obtained in a supervised manner (i.e., using the segmentation tool but with the binarization threshold selected by the operator) in the three photographic conditions (columns) for a sample from each group (rows). The particles at the edge are removed from the analysis due to the metallic frame visible in the photographs. Only the particles entirely within the frame were retained for the purpose of this performance analysis to allow a comparison with the *paint-and-pick* on the same exact grain population.

In condition C1, the samples show some under-segmented particles (labelled U in Figure 5.4 first column), mainly concerning large overlapped particles. The contrast is not strong enough to separate them well. In addition, some particles are left out of the count (labelled U_e) because they are under-segmented (i.e., joined to other particles) and bounded by a polygon touching the edges.

The under-segmentation is due to the pixel foreground still being connected despite the morphological erosion operation in step B4 Boundary adjustment.

In C2 condition there is generally a little more under-segmentation (Figure 5.4, second column); this time it concerns to the wider range of grains. This will result in the loss of some intermediate grains and the detection of some very large *non-real* particles. The two heterogeneous samples S4 and S10 show more anomalies (Figure 5.4, second column, 3rd and 4th row). In S4 the large centre particle is very over segmented because of its mineralogy whereas in S10 a large number of particles are grouped to form large false particles. The wet areas, such as the area labelled U in the upper left or the two Ue on the right, are not well segmented because they are formed by a set of pixels that are darker than the rest of the image forming relatively lighter areas that are dry. Such a partially wet condition causes the same problem as in condition C3.

In C3 (Figure 5.4, last column), the delineation process is less efficient; many particles are under-segmented and a large part of the image is discarded. Further, for the heterogeneous sample S4 there is more over-segmentation of the large central granitic particle than in C2.

S-5.1.6.3.2.2 GSD computation and percentiles extraction

Continuous measurement or real measure of grains

The extraction of percentiles in the form of Area-by-Number and Grid-by-Number for the image-based GSD and for the control data measured with the Pebble-Box (all giving *continuous* measurement axis) was carried out following the principles explained by Bunte and Abt (2001) and Graham et al. (2012) as follows:

1) In each data table representing a sample where each line represents the attributes of a given detected grain, a *b axis* column indicating the *b*-axis value and an *Area* column indicating the area of each particle were used. For the distribution from the Pebble-Box, the surface area of the particles was estimated by calculating the area of an ellipse by knowing the *a* and *b* axis ($Area = \left(\frac{a}{2}\right) * \left(\frac{b}{2}\right) * \pi$). Within each sample, *b*-axis grains smaller than 8 mm have been excluded.

2) It can sometimes happen that some grains have exactly the same size, especially in the control data from the Pebble-Box. The grains were grouped by identical *b*-axis size value.

3) A column *Nb* was added to calculate the number of grains for each single *b*-axis size value. An example of such a table is shown in **S** Figure 5.12 **A1** for sample S4.

4) A *Total area* column has also been added (**S** Figure 5.12 **A2**) to calculate the sum of the surface area occupied by the grains of strictly identical size.

5) The table was sorted in ascending order from column *b axis*.

6) A *Frequency* column was created to calculate the frequency of occurrence (Nb) of each unique grain size within the sample.

7) Finally, a *Cumulative Frequency* column was created to calculate the percentage of grains in the sample below each unique size detected. In order to follow the method described in Bunte and Abt (2001), for the extraction of percentiles, this column accumulates the values of the Frequency column with a lag of 1 so that 0% of the distribution is below the value of the finest particle encountered. It was therefore necessary to add a last row at the bottom of the table to arrive at a total accumulation of 100%. In this last row, we have indicated in the column *b axis,* the maximum size encountered +0.001 mm. In the case of the Area-by-Number analysis, this does not lead to any problems. Despite the small number of relatively large particles, the penultimate row of the cumulative frequency column always contains values above 99%. This does not lead to any errors in the analysis of the comparison of the different Area-by-Number particle size distributions depending on the acquisition procedure.

A

A1 Area by Number				A2 Grid by Number			
b axis (mm)	Nb	Freq. (%)	Cumulative Freq. (%)	*b* axis mm	Total Area (mm²)	Freq. Area (%)	Cumulative Freq. Area (%)
8.0	10	2.8	0.0	8.0	724	0.4	0.0
8.1	1	0.3	2.8	8.1	70.6	0.0	0.4
8.2	5	1.4	3.1	8.2	349	0.2	0.4
		...				...	
11.5	15	4.2	40.1	38.5	2009	1.1	46.4
11.7	1	0.3	44.4	39.5	127	1.0	47.5
12.0	13	3.7	44.6	40.0	2026	1.1	48.5
12.5	13	3.7	48.3	**40.5**	2228	1.1	49.6
13.0	6	1.7	D_{50} 52.0	**44.0**	872	1.1	D_{50} 50.7
13.5	6	1.7	53.7	45.5	1044	1.2	51.8
14.0	7	2.0	55.4	48.5	1280	3.0	53.0
		...				...	
64.0	1	0.3	98.6	64.0	4523	2.4	77.7
66.0	2	0.6	98.9	66.0	8086	4.4	80.1
70.5	1	0.3	99.4	70.5	5426	2.9	D_{84} 84.5
156.0	1	0.3	99.7	156.0	23401	12.6	D_{90} 87.4
156.001	0	0.0	100.0	156.001	0	0.0	D_{95} 100.0

B

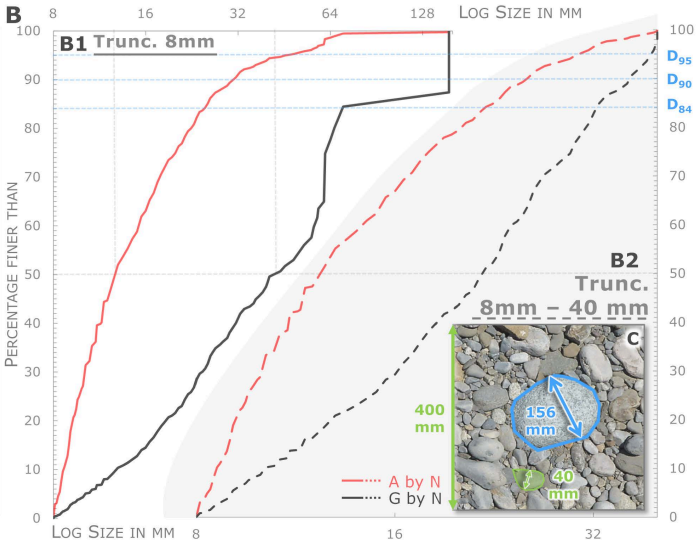

Figure 5.12: (**A**) Illustration of the procedure for extracting cumulative particle size distributions and percentiles, with the example of the sample S4 in (**A1**) AbN and (**A2**) GbN. (**B**) Grain size distribution of sample 4. (**B1**) Distribution in the form of Area-by-Number (in solid red) and Grid-by-Number (in solid black) with low truncation at 8 mm. Note the problematic shape of the end of the Grid by Number distribution. (**B2**) Distribution in the form of Area-by-Number (in dashed red) and Grid-by-Number (in dashed black) with a low truncation at 8 mm and a high truncation at 40 mm. The value of 40 mm corresponds to the value of the theoretical maximum *sampleable* diameter for this 400 mm long square. (**C**) Illustration of sample S4.

To estimate the distribution in Grid-by-Number form:

8) A *Frequency Area* column was created, where the percentage of area represented by each grain size was calculated.

9) In a column *Cumulative Frequency Area* the cumulative sum of the column *Frequency Area* was calculated. Here too, a shift of one row was made.

10) For both forms of distribution, the percentiles were obtained by interpolation only between two grain sizes located on either side of the desired percentile.

It should be noted that the estimation of percentiles in Grid-by-Number (GbN) form (solid left black curve) compare to Area-by-Number (AbN) form (solid red left curve) **S** Figure 5.12 **B1** can be subject to errors if the criterion proposed by Diplas and Fripp (1992) is not met, because the relative weight of the particles in the distribution is proportional to their surface area. As in the example in **S** Figure 5.12 **B1** and **C**, a single large particle impacts the end of the GbN GSD (left solid black curve) and thus the estimation of the largest percentiles (here probably from the D_{75} but strongly visible from the D_{84} onwards). **S** Figure 5.12 **B2** illustrates the shape of the cumulative GSD for the same sample in AbN (right dashed red curve) and GbN (right dashed black curve) but with this time a high truncation at 40 mm allowing to respect the criterion of Diplas and Fripp (1992) by excluding the largest particles too few to be correctly characterized. The value of 40 mm corresponds to the value of the theoretical maximum *sampleable* diameter for this 400 mm long square. A detailed evaluation of the effect of expressing the GSD from the photos as GbN form and the importance of respecting a minimum sampled area based on the largest clast is presented in section 4.2 of the *main text*.

S-Discrete measurements or binned b-axis sizes

None

S-5.1.6.3.2.3 Performance and compatibility assessment

None

S-5.1.6.4 Results and discussion

S-5.1.6.4.1 Performances

S-5.1.6.4.1.1 Grain's detection - Comparison to manual grain distribution or Gold standard

None

S-Condition 1 – Painted and Sunlight protected

None

S-Condition 2 – Not Painted but Sunlight protected

None

S-Condition 3 – Not Painted and Not Sunlight protected

None

S-5.1.6.4.1.2 Photographic method performance - Comparison to real bed distribution or Paint-and-pick

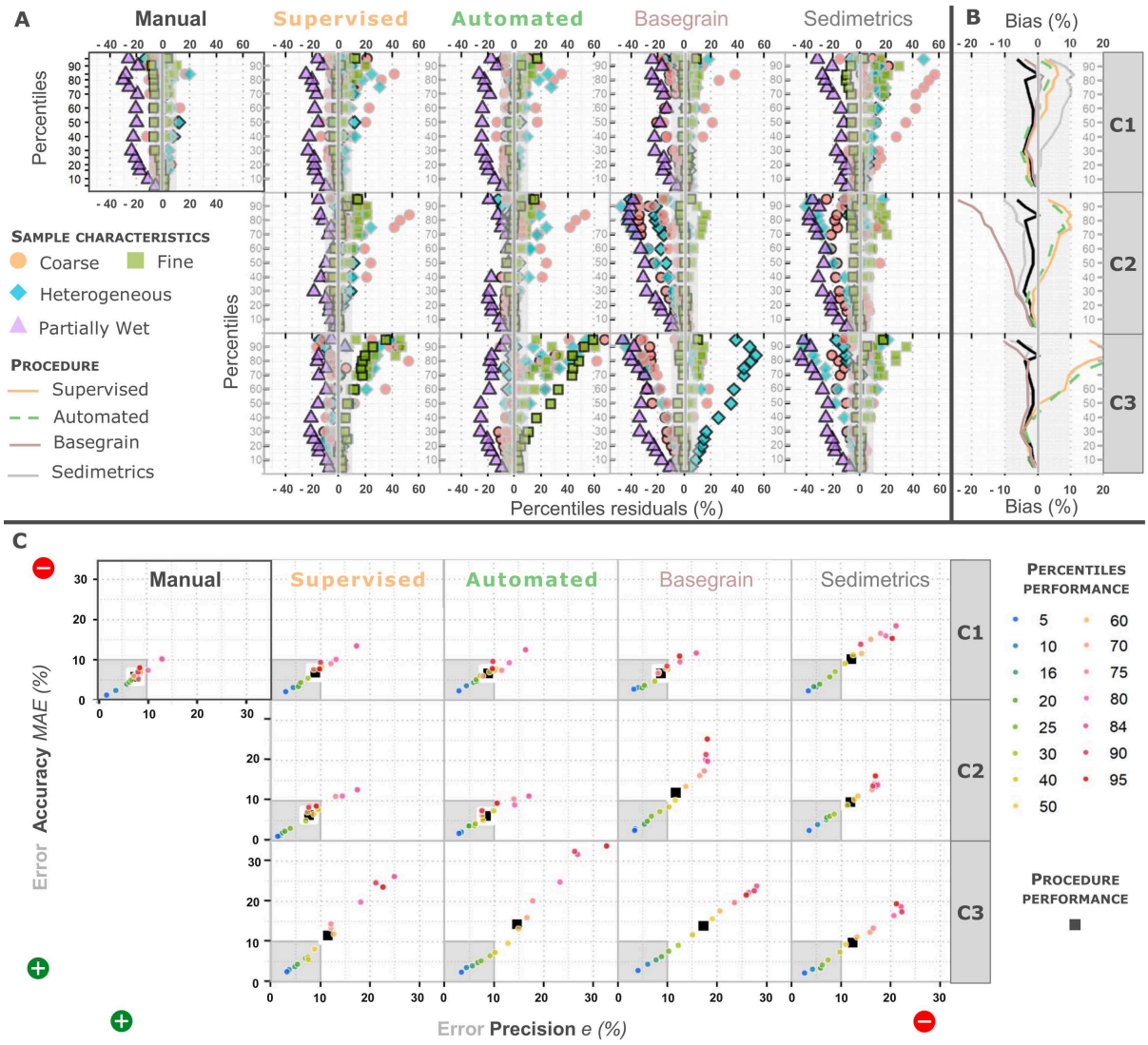

S-Figure 5.13: Performance assessment of image processing procedures compared to *pain-and-pick* bed surface sampling. (**A**) Distribution of the 150 relative residuals of percentiles estimation (15 percentiles ∗ 10 samples) under the three photo conditions for the manual, *supervised* and *automated PhotoMOB* procedure as well as for *Basegrain* free stand-alone tool from Detert and Weibrecht (2013) and *Sedimetrics Digital Gravelometer*™ from Graham (2005a, 2005b). Manual digitization was performed only on painted photos (C1). The residuals are coloured according to the 4 main patch characteristics (coarse, fine, heterogeneous, partially wet). Samples taken as example in (Figure 5.4 4 *main text*) are represented here by symbols with black outlines. (B) Relative bias of percentiles estimation for each procedure. Bias is calculated over residuals of the 10 samples. (**C**) Average relative performance (accuracy and precision) for the estimation of each percentile (coloured dots), as well as the overall performance (black square) of the 5 procedures. The vertical shaded areas mark the 10% error limits.

S-Manual delineation

None

S-Automated delineation

None

S-5.1.6.4.1.3 Limitations and further developments

S-Limitations

None

S-Methodological improvements for image acquisition and processing

Figure 5.14 shows photos example without (C2) and with the clay solution (C1 clay) on a sample with a large number of particles that can cause over-segmentation (coarse mineral, veined...). The automated digitization obtained by *PhotoMOB* on the photo painted with our solution (C1 clay) shows almost no over-segmentation compare to C2 (Figure 5.14 - **B**, top and bottom images in *PhotoMOB* column). The graph on the bottom (Figure 5.14 - **C**) shows the positive impact of adding the clay solution. In case of C2 (solid red curve), despite the number of grains detected (1327) being very close to the manual procedure (1388), there is an under-estimation of the entire GSD due to an over-segmentation of the grains as can be seen in Figure 5.14 - **B**. The C1 Clay painted automated delimitation (red dashed curve) is closer to the manual delineation (black curve) except for the coarse grain sizes where D_{95} is over-estimated due to the under-segmentation (union) of some grains. However, the error in estimating the D_{50} was reduced from -12.2% to -3%. Therefore, the use of a clay solution allows a homogenization of the photographed scene. There is a reduction of the complexity of the image, the only details (dark pixel) correspond to the edge of the grain (almost no detail intra grain left). Moreover, the clay reduces the reflectance of the surface by its colour and matte texture which absorbs the light instead of re-emitting it and this even better than the spray paint. The use of this solution and the performance of our procedure in C1 are very encouraging. Good quality delineations will require little time and effort for correction by the operator to proceed to the next stage of mobility characterization. We also tested the new software developed by Mair et al. (2023). This new procedure makes it possible to obtain very correct delineation in condition C2 and also in C3 (C3 not shown in this image for lack of space). We also tested it on fluorescent spray-painted images (condition C1). Unfortunately, the algorithm was not trained on painted sediment (C1). However, these results are very encouraging, and in the near future it may be possible to train their procedure with our manually digitized data on photos painted or partially painted. This will greatly reduce the boundary correction effort.

S-Figure 5.14: Illustration of solution for a better grain segmentation (**A**) Application of the clay/water solution to the study area. (**B**) Example of grain segmentations in the study area for both conditions C2 (top) and C1 with clay paint (bottom). Left, original images and, middle and right, *PhotoMOB* and *ImageGrains* (Mair et al. 2023) segmentation results.

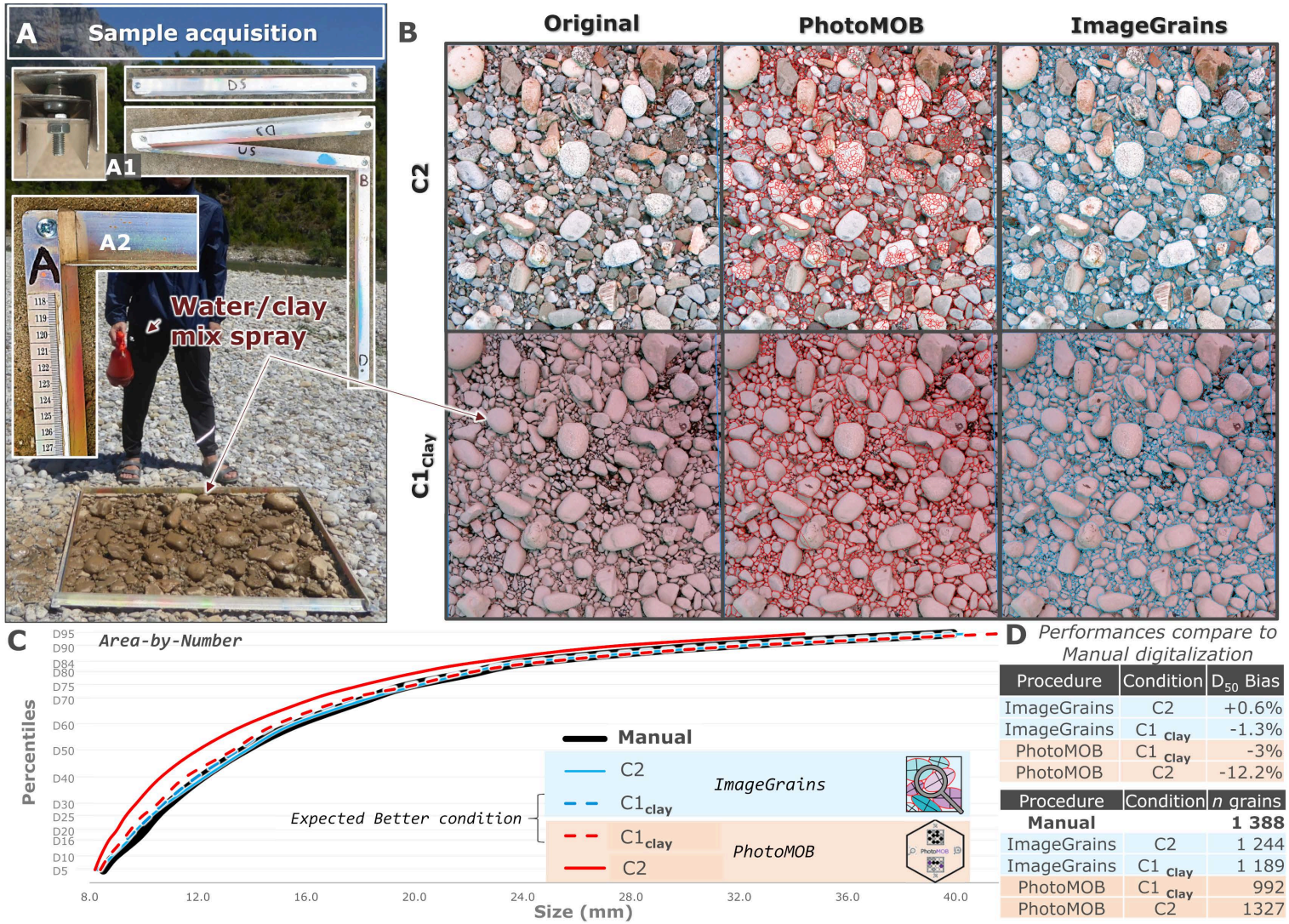

Procedure	Condition	D_{50} Bias
ImageGrains	C2	+0.6%
ImageGrains	$C1_{Clay}$	-1.3%
PhotoMOB	$C1_{Clay}$	-3%
PhotoMOB	C2	-12.2%

Procedure	Condition	*n* grains
Manual		**1 388**
ImageGrains	C2	1 244
ImageGrains	$C1_{Clay}$	1 189
PhotoMOB	$C1_{Clay}$	992
PhotoMOB	C2	1327

(**C**) Percentiles from manual digitalization (black curve) compared to automated procedures in C2 condition (solid curves) and in C1 Clay painted condition (dashed curve). (**D**) Performance for D50 estimation and grain number estimation. Finally, in (**A2**), note the L-shape of the metal frame elements fixed together at their ends by a screw system (**A1**). This allows the frame to be folded on itself to not be cumbersome and to have a strict square shape that is always identical between each photo thanks to the stop in the corners formed by the L shape. The repetitive task of scaling the photos one after the other is facilitated by an area of interest of constant shape and surface, without any variation.

INDEX

S-5.1.6.4.2 Compatibility with existing GbN data

S-5.1.6.4.2.1 GbN performances

None

S-5.1.6.4.2.2 Compatibility between continuous and discrete square holes measurements

For sample S2 (dominated by coarse and discoid (flat) particles) and S9 (fine and spherical particles), each particle, before being measured in the Pebble-Box, was passed through a template with several sieve-sized square-holes *D* with 0.5 ψ -increment (ψ = log2(b)) to replicate a sieving machine. The median shape of the samples is visible in **S** Figure 5.11 **B**. The *D/b,* of both samples, per grain size classes is presented in Figure 5.15, below. Particles smaller and coarser than 16 mm (pebble limits) have different flattening index, resulting in markedly different *D/b* ratios.

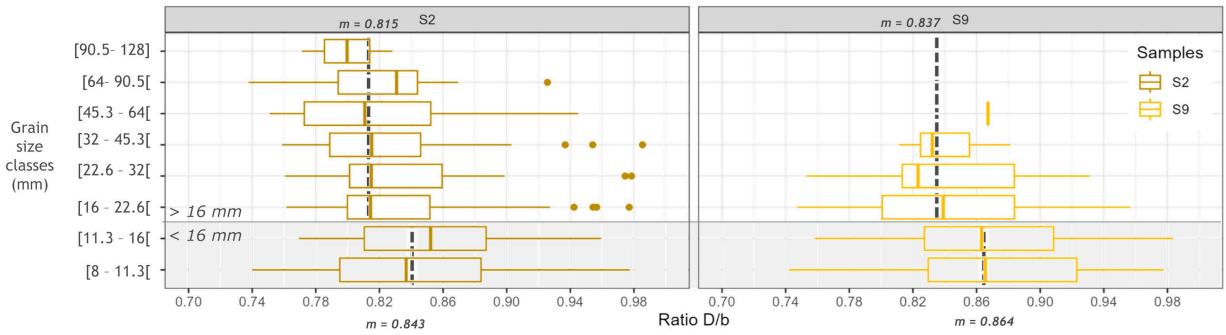

S-Figure 5.15: Dispersion of *D/b* ratio per grain size classes for the 2 sample (S2 and S9) with *b*-axis measured with the template and Pebble-Box. Black dashed vertical lines indicate median *D/b* ratio per particle < and > to 16 mm.

Finally, Figure 5.16 shows the impact of compliance with the Diplas criterion and the axis measurement method for the manual and supervised *PhotoMOB* procedures

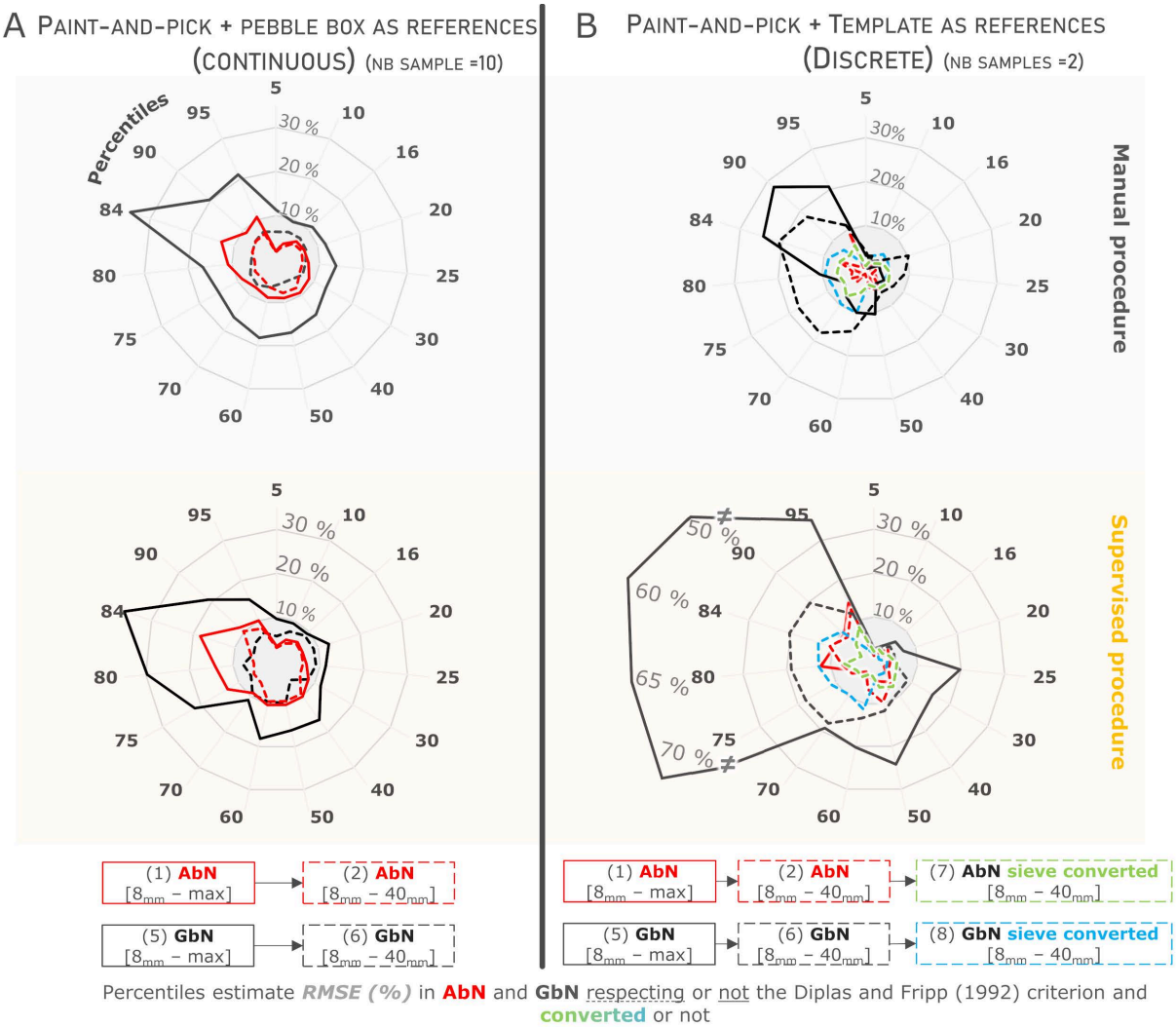

S-Figure 5.16: RMSE for the estimation of the 15 percentiles analysed in relation to the grain actually present in the bed. Top for manual procedure, bottom for supervised *PhotoMOB* procedure. (**A**) Data from photos compared with *paint-and-pick* grains measured with the Pebble-Box. (**B**) Data from photos compared with *paint-and-pick* grains measured by the template. The numbers in brackets in the legend refer to the mean RMSE presented in Figure 5.7 of the *main text*. Solid curve represents the percentile from GSD with only low truncation at 8 mm for AbN (red (1)) and GbN (black (5)) while dashed line represent GSD with low and high truncation (8 mm to 40 mm) to meet the Diplas criterion (2 and 6). Finally, the truncated and converted distribution according to average flatness of Cinca and Ésera river (7) and (8). The shaded areas mark the 10% error limits.

This figure illustrates the important points to consider when using the data from the photographic method, summarized in section 4.2.3 of the main text, by following the arrows of the boxes in the legend. On the first (part A) column are the RMSE for percentiles estimates for the manual (top) and supervised *PhotoMOB* procedure (bottom) for C1 condition. The condition for the one *PhotoMOB* was developed. It shows the deviation from the real control set measured with *continuous* data (Pebble-Box). Solid line represents the GSD of all the grain $\leq 8mm$ in AbN (red) and GbN (black) while the dashed line represents the errors with truncated GSD at 40 mm to meet the Diplas criteria. The gain of performance is visible. Dashed line (red (2) and black (6)) are below 10% RMSE. AbN error are reduced by one third while GbN by half. The top and bottom plot are quite similar reflecting the good performance of *PhotoMOB* to reproduce the gold standard behaviour.

The second column (B) is the deviation from the real control set but measured with *discrete* data (square holes' template). This only concerns the two samples S2 and S9. Again, solid red and black line represent the GSD from all the apparent grain on the image with the manual (top) and supervised procedure (bottom). In GbN we can observe large error for estimates of high percentiles. With the truncation at 40mm (dashed black lines), the error stayed below 20%. Problem of under-segmentation take lot of importance in GbN specially when they are small in term of number and area sampled not adequate.

Then the red solid (1) and red dashed (2), high truncation, are overlapped showing no strong impact of sampling a too small area in AbN. In green (7) is represented the AbN GSD truncated to meet the Diplas criteria and converted to sieve data (via Church equation and by average flatness ratio). The green dashed line is localized close to the red solid and dashed lined. Under estimation of percentile from photos because of fabric effect is of the same amount than the measure bias of the sieving method. This make directly comparable AbN size from the photo with size from template.

In blue (8) is represented the GbN GSD truncated to meet the Diplas criteria and converted to sieve data (via Church equation and my average flatness ratio). The blue dashed line in localised below or close to 10%. This indicate that in GbN, converting the *b*-axis size reduce by half the deviation between size measurement from the photo and size measured with *discrete* square holes method (template, sieve). Common Wolman data and photo data will have a deviation of 10% in average if the sampled area criteria are respected and data converted.

S-5.1.6.4.2.3 Intended purpose

None.

S-5.1.6.4.3 Final discussion

None

S-5.1.6.5 Conclusion

None

Part 2: Bed stability and fractional mobility

Bed grain mobility characterization at Ainsa reach (Upper Cinca River) 10 km downstream of hydropower plant, 01/11/2020. Author: Fanny Ville

This part 2 contain the following submitted and under review paper by the journal Earth Surface Processes and Landforms. IF (JCR-SCI):3.941, Q1(2022). Ville, F., Vericat, D., Batalla, R. J., & Rennie, C. (2023). PhotoMOB: Automated GIS method for estimation of fractional grain dynamics in gravel bed rivers. Part 2: Bed Stability and Fractional Mobility [Preprint]. Earth Sciences. https://doi.org/10.31223/X5Q108

Abstract

Bed mobility and stability are spatially and temporally variable, making it a complex phenomenon to study. This paper is the second of a pair, in which we present an automated image processing procedure for monitoring the mobility/stability of gravel river beds. The method is based on local comparison of the shape of the grains identified at the same coordinates between successive photos to identify coincident and new grains. From this categorization in a given study area, several variables can be extracted, such as: the general proportion of *mobile* or *immobile* grains (number or area), the maximum *mobile* or *immobile* diameters, the proportion per grain fraction of grains that remained *immobile* (stable) and grains newly identified. Additionally, percentiles of the surface Grain Size Distribution (GSD) before and after a target hydrological event, as well as the *immobile* and *mobilized* GSD (which could be used as a proxy for bedload GSD) can be computed. In this part 2 paper, we present the entire GIS-based procedure for identifying the shape of each grain in digital images of bed patches to then classify their dynamic status (*mobile*/*immobile*), and derive a reliable result compatible with different forms of sampling (Area-by-number, Abn, and Grid-by-number, Gbn) and types of measurements (continuous and discrete square holes grain size reading). The performance of the GIS procedure is evaluated for the mentioned above variables over a control set composed of ten 1×1m paired before/after image samples representing different field conditions.

The automatic classification applied on a perfect (*manual*) grain delineation yields Mean Absolute Errors (MAE) lower than 3% in both Abn and Gbn, while the automatic classification applied on an *automated* delineation with 10 min of manual boundary *revision* shows MAE around 8% and presents a larger MAE of 29% for only the estimation of the *mobile* percentile.

Keywords: Particle dynamics, Bed stability, Fractional mobility, GIS, Fluvial monitoring, River habitat

5.2.1 INTRODUCTION

Riverbed stability and mobility, referring to the bed surface that remains stable or not (MacKenzie et al., 2018), varies over time and space. The understanding, characterization, and prediction of bed surface dynamics related to sediment transport is important for geomorphologists (e.g., estimation of transported or deposited volume) and ecologists (e.g., the timing and intensity of bed instability determines the disturbance of aquatic substrate habitats and thus controls the presence and resilience of aquatic organisms (e.g., Cobb et al., 1992; Gibbins et al., 2005, 2007a; Matthaei and Townsend, 2000).

A first approach to evaluate the mobility (or the loss of stability) of grains is based on the competence of the flow (Gilbert, 1914) by estimating the force of the water required to set into motion grains present on the bed (e.g., Ashworth et al., 1992; Dey and Ali, 2019; Komar, 1987; Miller et al., 1977; Parker, 2008). For a given force exerted on the bed, (i) the mobility can be defined as equal when all the grain fractions are movable independently of their size (ii) while it is selective when only certain grain fractions enter into motion. The mobilization is generally positively dependent on the grain size (an increase in force will progressively mobilize coarser grains). This approach is commonly based on the observation and measurement of the coarsest clasts mobilized for different competent hydrological events (Andrews and Parker, 1987). Although this method is sometimes also used by ecologists (e.g., Downes et al., 1997; Duncan and Suren, 1999; Lorang and Hauer, 2003), it has a disadvantage as a *mobile* grain of a given size does not necessarily mean that all grains of that size are mobilised.

Another approach to characterizing substrate mobility, based on the proportion of surface and bedload grain fractions, has been introduced by Wilcock and McArdell (1993) and further used by, for instance, Wathen et al. (1995), Wilcock (1997), Mao and Lenzi (2007). When the proportion of a grain fraction of diameter *i* present in the bedload is the same to that of the bed surface, then the term full mobility can be used. When the proportion of a given size fraction present in the bedload is less than of the bed the surface, then the mobility can be termed partial.

To feed these two cited examples approaches, one inexpensive method, with respect to both instrument cost and fieldwork effort, is the use of tracers such a painted bed area (see summary in Hassan and Roy, 2016). A representative area of the bed is painted and photographed. After a hydrological event, a repeated photograph of the initial patch can be taken and the entrained painted grains can be eventually located downstream and transport distances measured, as well as their size (e.g., Brenna et al., 2019; Church and Hassan, 2002; Hassan and Ergenzinger, 2003; Mao et al., 2017; Vázquez-Tarrío et al., 2019a; Vericat et al., 2008a, 2020). This method avoids altering natural grain imbrication and packing without limitation of tracer size.

However, mobilized painted grains can be transported over varying distances and may settle on the paint side down and/or be subsequently buried, resulting in a low recovery rate. For example, in the context of a hydropeaked river generating limited mobility (i.e. intensity and size range) particularly in the finest fractions (López et al. 2023), the mobility of the latter downstream, which are more difficult to detect visually than coarse fractions with large painted surfaces, may consequently be poorly characterised (size and distance). Furthermore, the number of grains found in relation to the number of grains initially painted is not known.

Most measurements focus on the downstream particles, while a large amount of information from the original spot location is usually not exploited, such as the proportion of the bed surface that is stable (*immobile*) or not (*mobile*) for each grain size fraction.

This information is present on the photographs; hence, an analysis based on all the grains present in the photos (before and after), not just on the few grains found downstream, would greatly increase the number of particles studied and potentially improve the accuracy of deduced trends of dynamics.

To our knowledge, this information has not been systematically extracted. There is thus the need for an automated systematic photographic measurement method that is reproducible and easily implemented to quantify fractional stability and mobility (e.g., Gibbins, 2015, Peckarsky et al., 2014, Quinlan et al., 2015). Photographs collected from many different areas of the bed (bar head, low and high bar, secondary channels) would then enable examination of the spatial and temporal variability of bed grain stability or entrainment and transport by fraction. In addition, new particles deposited on the study surface may be included in the analysis of the next hydrological event without having made any additional effort in the field other than the acquisition of a new photo. In order to draw on the data set provided by repeated photographic acquisition (Cerney, 2010) of patches, we developed a GIS-based method that allow a spatial grain-by-grain inter-analysis of the particles present in the two sets of photographs.

This paper is the second of a pair of papers in which we describe and evaluate this methodological procedure. The first paper dealt with the workflow under GIS environment to perform identification and characterization of grains in digital images of gravel river beds, to derive reliable surface Grain Size Distributions (GSD) (Part 1, Section 5.1.1). In this second paper, we first describe the workflow to categorize the dynamics of each grain, then we present a performance evaluation with a non-optimal photo set corresponding to various complex field conditions (limited time available, imperfect photo shooting, partially wet surface due to flooding or hydropeak, etc.). Finally, we discuss the application of the method, as well as limitations and recommendations to extract the most accurate results. In the course of this article, all the references to "Text **S**", "Table **S**", and "Figure **S**" followed by a number indicate the location of the element in question in the supplementary material section.

5.2.2 THE COMPLETE PHOTOMOB WORKFLOW

The objective of the PhotoMOB procedure is to compare two photos, of the exact same river bed area, acquired before and after a hydrological event (or a succession of events when it is impossible to access the area – Figure 5.17 **A**). The process consists of two parts: i) the first, the grain detection; only a brief description of the identification procedure is given below (for a detailed explanation, the reader is referred to Section 5.1.1); ii) the second step, the categorization, allows the classification of each particle as *mobile* or *immobile* by a spatial grain-by-grain comparison (Figure 5.17 **D**).

5.2.2.1 Grains' detection

The photos are (i) first filtered with the successive use of a high pass filter and two noise reduction filters using GIMP (Team, 2019), an image manipulation program, to improve edges contrast and smooth the intra-grain noise. This first step improves the detection of the particles. (ii) Then, the initial filtered photo (pre-event) is loaded into ArcGIS© to be manually scaled using the distance between the four internal corners of the frame as reference points. A projective transformation is applied. The second photo (post-event) is then georeferenced to the first.

This alignment is done manually by identifying identical points between the two photos. This step should be done as accurately as possible. Again, a projective transformation is applied.

It is mandatory that the images are well aligned with each other, as a slight misalignment may not allow a correct superposition of the grains, which may result in a *mobile* grain classification even in the case of the same grain in the identical position. (iii) The two photos are then automatically processed with the *PhotoMOB toolbox part 1* to extract the contour of each grain as a polygon shapefile (see companion paper).

(iv) At this stage, if the photos present some complexity (e.g., variation of sunlight, partially wet, heterogeneous lithology, partially painted, presence of vegetation), it is advisable to check the result of the grain delimitation and edit them manually, if necessary, as errors of delimitation are likely to occur. From this image processing it is then possible, at each time step, to know the surface GSD of the *a* and *b* particle axes as *continuous* data and not by class, the orientation with respect to the north of the photo, as well as the proportion of fine material (fine limit defined by the operator).

5.2.2.2 Characterization of grain dynamics

The second part of the method classifies each detected particle as (i) *mobile* or (ii) *immobile* by comparing the superposed pre (T0) and post-event (T1) photos on a grain-by-grain basis (Figure 5.17 **D** and **S** Figure 5.29 **C**). This is carried out in two steps: (i) calculation of a geometric shape descriptor at pre- and post-event times, and (ii) classification of the mobility status.

5.2.2.2.1 Hypothesis and rationale

Categorization is based on the following hypothesis: if two particles, sharing approximately the same *xy* coordinate on the two pre- and post- event images, are identical, then they are considered to be the same *immobile* particle i.e., not having been mobilized during the hydrological event. On the other hand, if their shapes are relatively different (according to a certain threshold) then they are not the same, which may indicate particle *mobilization* during the hydrological event.

With the classification, from the pre-event time (T0) photo, *stable immobile* particles can be identified that are still in place (still visible), as well as the *unstable* area formed by the particles that are no longer visible on the surface and which correspond either to particles mobilized (eroded) during the event or covered by new ones. Similarly, from the post-event photo (T1), *stable immobile* grains during the event (i.e., identical particle between both images) can be identified, and new particles that are now visible on the surface either because they were mobilized and deposited in the study area or because they were uncovered due to localized erosion of the surface. As such, if the particle is not the same between the pre-event (T0) and post-event (T1) photos, then either or both of the particles visible in images T0 and T1 were mobilized during the event.

Of course, the categorization has limitations that the user should keep in mind, concerning our basic hypothesis and the classification terminology used (*immobile*/*mobile*), which may be wrong in some cases. The concept of stability/instability can by more attributed to the description of the sampled surface, while the concepts of immobility/mobility to the grain. By clarifying the notion of stability/instability, immobility/mobility, Section 5.2.5.2 will show that this criticism can be in some way minimised.

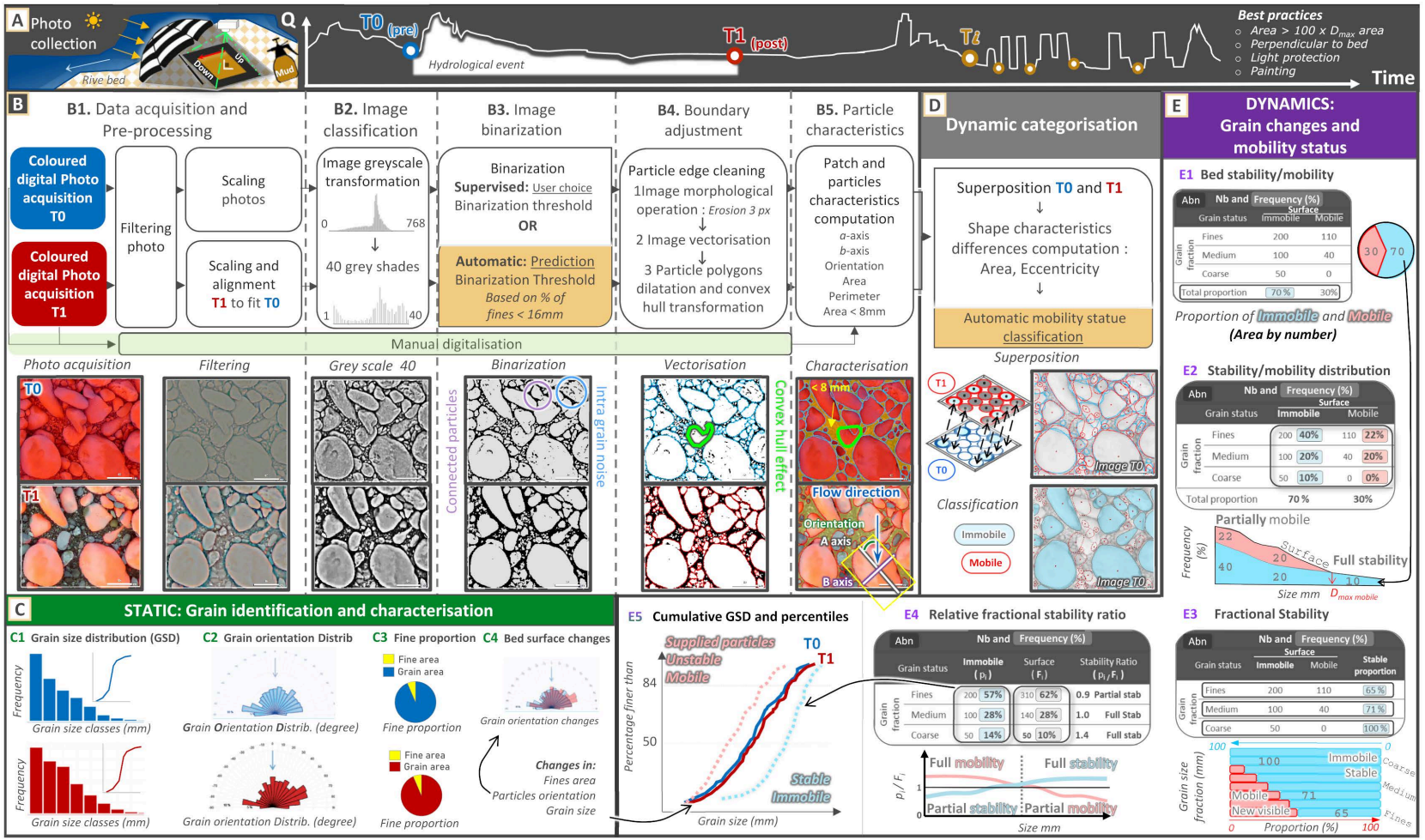

Figure 5.17: Illustration of the entire workflow required to characterize bed surface (see companion) and sediment dynamics (developed in this paper). (**A**) Photo acquisition. (**B**) Detection of grain and patch characteristics. (**C**) Possible output after patch surface characterisation. (**D**) Characterisation of dynamics and (**E**) conceptual example of possible output from dynamics characterization. The rounded black-edged rectangles in the tables represent the whole on which the proportions are calculated. For example, the 200 fine immobile particles represent 40% of all visible surface particles (E2), 65% of all fine fraction surface particles (E3), and 57% of all immobile particles (E4). The yellow boxes represent the developed models (i) of dark threshold prediction (companion paper) and (ii) of particle classification (see in text).

5.2.2.2.2 Workflow

A unique ID is assigned to each grain in the two layers. Then, each pair of superposed particles is selected Figure 5.17 **D**. For this purpose, the centre of the polygon particle at T1 is marked with a point, still containing T1 shape information. Then, to this point layer, is coupled by spatial join, the information of the T0 particle polygon layer of which this point is located above. If a T1 particle is not coupled to any T0 particle, then it is considered to be *mobile* (*newly arrived*). At this stage, the analysis consists of a layer of points with the attributes of both pre- and post- particles present at the same location. The particles are classified according to their relative degree of likeness. The classification of the dynamics status of each particle as *mobile* or *immobile* is done automatically from a classification model developed over ten pairs of 40 x 40 cm photos where 1704 grain pairs were identified, classified, and used to train the model (details in Text **S** Section 5.2.7.2.2 and **S** Figure 5.29). The classification tree of dynamics is shown in Figure 5.18. If two paired particles have a difference in area greater than 38%, then they are considered to be different (*mobile*). If not, if the difference in eccentricity is greater than 31%, then they are considered to be mobile, otherwise they are identical (*immobile*).

From the point layer containing the classification, the dynamics status is returned to both polygon layers via an attribute-based join based on the grain identifiers. If no match is found for a particle at T0 then it is considered *mobile*.

Once the particles have been classified, it is possible to derive different types of information. These data can be expressed as the number of grains in the sampled area, i.e., Area-by-number (Abn), or in terms of grain area in the sampled area. The latter is equivalent to the Grid-by-number (Gbn) data form commonly obtained by the pebble-count method (Wolman, 1954). The reader is invited to refer to Figure 5.17 **E** and Text **S** Section 5.2.7.2.2 for a conceptual example of the data that can be obtained from the photo pair analysis.

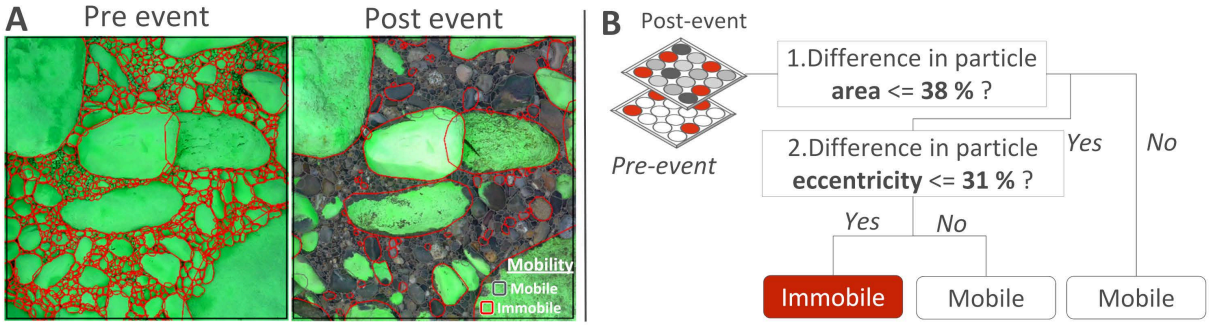

Figure 5.18: Classification tree of dynamics, developed on 1704 visual grain comparison. (**A**) Example of one of the sample patches used to build (**B**) the decision tree. The two photos were digitized manually and a visual mobility classification was then carried out on the second photo.

5.2.3 PERFORMANCE ASSESSMENT

The goodness of the dynamics characterization is highly dependent on (i) the classification model we have developed and (ii) the correct grain boundary delimitation. The objective is to obtain an automated classification of all particles as *immobile* or *mobile* as it could be done by the eyes of a human operator, but much faster. In this section we will present a control data set and quantify the errors on the E1 to E5 outputs shown in Figure 5.17.

In addition, we also wish to quantify how much of the error is due to the classification model and how much is due to boundary errors detection.

5.2.3.1 Control dataset

The control data-set was obtained from two gravel-bed rivers of the South Central Pyrenees (Cinca and Ésera). The sedimentary characteristics of these rivers are detailed in the companion paper. Pre- and post- image pairs for hydrological events of various magnitudes (natural floods, hydropeaks), and different from the training set of the classification model, were selected in order to introduce variability in particle lithology, shape, interlocking and mobility degree. All of the control data images were collected at similar elevation and with direct sunlight protection. Figure 5.19 **A** shows the set of 10 pairs of photos taken with direct sunlight protection but with a mixture of photo conditions (painted and unpainted, partially wet, partially painted). The pairs of photos T0 and T1 never correspond to the same condition and sometimes the paint on the painted patch photos got relatively dissolved which allows the asperities of the particles to show through (S4 or S6). It should be noted that these photos are from previous field campaigns and were not acquired specifically for developing *PhotoMOB*.

For each pair of photo samples (a small view shown in Figure 5.19 **A**), an area of interest of 1 m^2 was defined. As shown in the classification model, all particles present within these zones were delimited by hand. This represents a total of 15080 particles. Partially buried particles were included where it was possible to identify them with certainty between the two photos. The overlapping particles at T1 and T0 were listed in a point shapefile. Finally, a single operator visually assigned the status (*immobile* or *mobile*) to each listed T1 particle. Approximately 7 480 visual pairwise comparisons were conducted. If the centroid of a particle at T1 was located above more than one T0 polygon, which could occur because a convex hull was applied to smooth the contours of the particles, then the T1 particle was deemed to be *mobile* only if it differed from all associated particles in T0. The control data set was therefore acquired with a *manual* delineation followed by a visual classification. The characteristics of the sampled area of the post-surface truncated at 8 mm are presented in Table 5.3 while the cumulative GSDs of the pre-surface, post-surface, *mobile* and *immobile* are presented in Figure 5.19 **B** and the frequency distribution per grain fraction in Figure 5.19 **C**.

Figure 5.19: Control dataset used to test the particle dynamics image-processing procedure, obtained by manual delimitation and visual classification of each grain. (**A**) Zoom on a portion of 1m^2 squares of T0 (pre-event) and T1 (post-event) of the ten samples. (**B**) Cumulative grain size distribution of each sample in Area-by-number (Abn, first row) and Grid-by-number (Gbn, second row) truncated at 8 mm. The solid black and grey curves indicate the GSD at T0 and T1 respectively. The dashed red and blue curves indicate the *mobile* and *immobile* GSD respectively.

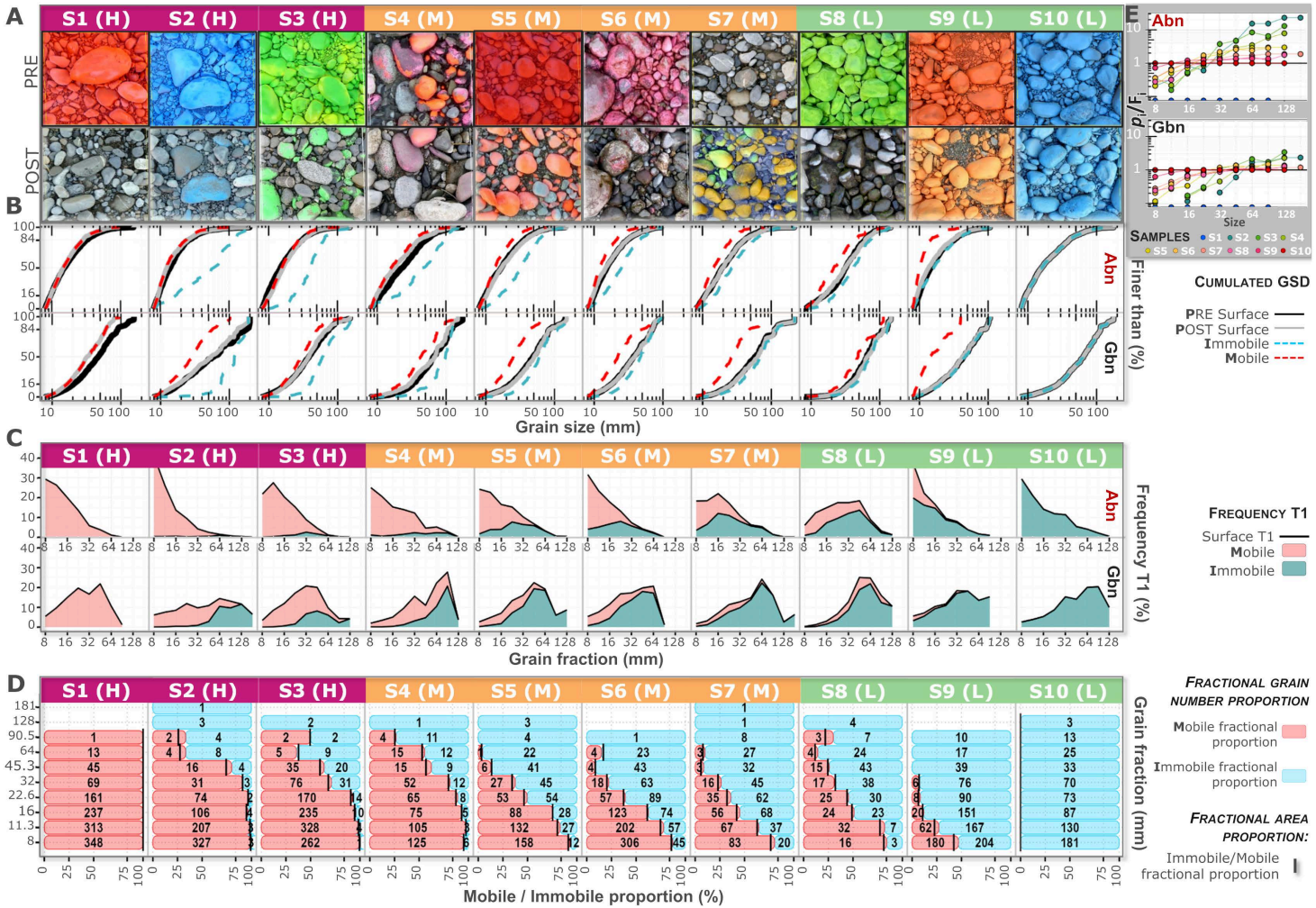

(**C**) Stacked distribution frequency of *mobile* (red area) and *immobile* (blue area) grains in each grain fraction of size 0.5ψ, based on the classification obtained with the T1 layer; the black line at the top thus represents the distribution frequency of all surface grains visible at T1. The first row corresponds to the data in Abn form and the second in Gbn. (**D**) Fractional dynamics. Percentage of *mobile* (red) and *immobile* (blue) particles number found on the post-event surface for each grain fraction. The numbers in bold correspond to the number of grains of each status in each fraction. The black vertical marks indicate the *mobile* and *immobile* proportion area for each fraction. Relative fractional stability in Abn (top) and Gbn (bottom). Stability ratio $p_{i\ immobile}$ /F_i as a function of grain fraction. Where p_i is the proportion of each size fraction *i* present in the whole *immobile* grain category and F*i* is the proportion of each size fraction *i* in the whole surface bed sediment.

INDEX

Table 5.3

Sample	River	Photo condition		$D_{84\,immo}/D_{84\,surf}$	D_{max} (mm)	Stability %	
		Pre[a]	Post[a]			Grain	Area
S1 (H)	Cinca	C1	C2	Inf	93	0	0
S2 (H)	Cinca	C0	Mix C1C1	4.6	190	4	43
S3 (H)	Ésera	C0	Mix C1C1	2.1	152	8	29
S4 (M)	Ésera	Mix C1C2 WET	Mix C1C2	1.9	149	13	44
S5 (M)	Cinca	C0	Mix C1C1	1.6	150	34	73
S6 (M)	Ésera	C1	Mix C1C1	1.5	98	36	68
S7 (M)	Ésera	Mix C1C2	Mix C1C2 WET	1.4	217	53	84
S8 (L)	Ésera	C1	C2 WET	1.2	146	57	78
S9 (L)	Cinca	C0	Mix C1C1	1.1	107	73	93
S10 (L)	Cinca	C1	C1	1	177	100	100

Mobility Status[c]	Nb total	Grain fraction (mm)										Percentiles (mm)[d]									
		8 11.3	11.3 16	16 22.6	22.6 32	32 45.3	45.3 64	64 90.5	90.5 128	128 181	181 <	D5 Abn	D5 *Gbn*	D16 Abn	D16 *Gbn*	D50 Abn	D50 Gbn	D84 Abn	D84 *Gbn*	D95 Abn	D95 *Gbn*
$Surface_{T1}$	1187	348	313	237	161	69	45	13	1	0	0	9	11	10	16	15	32	28	60	45	77
Immobile	0	0	0	0	0	0	0	0	0	0	0	-	-	-	-	-	-	-	-	-	-
Mobile	1187	348	313	237	161	69	45	13	1	0	0	9	11	10	16	15	32	28	60	45	77
$Surface_{T1}$	802	330	210	110	76	34	20	12	6	3	1	8	11	9	18	12	54	25	132	46	190
Immobile	35	3	3	4	2	3	4	8	4	3	1	9	52	17	75	59	119	118	187	166	190
Mobile	767	327	207	106	74	31	16	4	2	0	0	8	10	9	13	12	28	23	57	36	96
$Surface_{T1}$	1206	263	332	245	184	107	55	14	4	2	0	9	12	10	18	16	38	31	73	48	113
Immobile	93	1	4	10	14	31	20	9	2	2	0	16	31	23	39	41	60	64	120	88	152
Mobile	1113	262	328	235	170	76	35	5	2	0	0	9	11	10	16	15	30	27	51	40	80
$Surface_{T1}$	523	131	108	80	73	64	24	27	15	1	0	9	16	10	29	18	68	39	106	74	133
Immobile	67	6	3	5	8	12	9	12	11	1	0	9	33	20	59	45	98	98	123	120	149
Mobile	456	125	105	75	65	52	15	15	4	0	0	9	13	10	22	16	43	34	78	56	114
$Surface_{T1}$	701	170	159	116	107	72	47	23	4	3	0	9	14	10	24	17	51	38	84	61	146
Immobile	236	12	27	28	54	45	41	22	4	3	0	11	24	16	35	32	60	59	111	80	150
Mobile	465	158	132	88	53	27	6	1	0	0	0	8	10	10	14	14	25	24	44	36	62
$Surface_{T1}$	1109	351	259	197	146	81	47	27	1	0	0	9	11	10	18	15	39	30	70	51	82
Immobile	395	45	57	74	89	63	43	23	1	0	0	10	18	12	26	25	47	46	73	67	87
Mobile	714	306	202	123	57	18	4	4	0	0	0	8	9	9	12	12	22	21	49	31	71
$Surface_{T1}$	564	103	104	124	97	61	35	30	8	1	1	9	16	11	27	19	64	41	113	72	217
Immobile	301	20	37	68	62	45	32	27	8	1	1	11	20	15	32	27	69	56	121	82	217
Mobile	263	83	67	56	35	16	3	3	0	0	0	9	10	10	14	14	26	26	48	38	76
$Surface_{T1}$	315	19	39	47	55	55	58	28	10	4	0	11	25	15	37	31	66	62	125	86	141
Immobile	179	3	7	23	30	38	43	24	7	4	0	16	28	22	44	41	74	72	128	106	146
Mobile	136	16	32	24	25	17	15	4	3	0	0	10	16	12	28	21	48	46	93	65	113
$Surface_{T1}$	1030	384	229	171	98	82	39	17	10	0	0	8	11	9	19	14	43	30	81	52	103
Immobile	754	204	167	151	90	76	39	17	10	0	0	9	13	10	21	16	46	35	93	57	103
Mobile	276	180	62	20	8	6	0	0	0	0	0	8	9	9	10	10	14	14	34	23	40
$Surface_{T1}$	615	181	130	87	73	70	33	25	13	3	0	8	14	9	28	16	64	39	114	70	166
Immobile	615	181	130	87	73	70	33	25	13	3	0	8	14	9	28	16	64	39	114	70	166
Mobile	0	0	0	0	0	0	0	0	0	0	0	-	-	-	-	-	-	-	-	-	-

[a] Photographic condition, *C1*: protected from the sun and fully painted, *C2*: Protected from the sun and not painted, *WET*: area partially wet, *Mix C1C2*: protected from the sun and partially painted. [b] ratio of the D84 for the *immobile* grain and the bed surface at T1 in Abn. [c] presentation of all grains composing the surface in T1, those identified as *immobile* and those *mobile*. [d] percentiles in Area-by-number and Grid-by-number. Grid-by-number extraction from the identified grains follows the method described in Graham et al. (2005b) and in the companion paper

The 10 samples were classified into 3 groups according to their degree of bed disturbance (see Table 5.3. Samples 1 to 3 were classified as having high mobility intensity with a ratio $D_{84\ Immobile}/D_{84\ Surface} > 2$. There were no or very few particles that remain *immobile*, with mostly large particles making up the *immobile* group. Samples 4 to 7 were classified as having a medium mobility intensity with a ratio of $1.2 < D_{84\ Immobile}/D_{84\ Surface} < 2$. Finally, samples 8 to 10 were classified as having low mobility, as few or no *mobile* particles were identified. The ratio $D_{84\ Immobile}/D_{84\ Surface} < 1.2$ indicates a surface almost identical to the *immobile* grains. The samples are presented from highest to lowest degree of mobility.

Figure 5.19 **B** shows that some samples, such as S5, S6, S7 and S8, do not have significantly different pre and post GSDs (black and grey solid curve Figure 5.19 **B**) (p-value of K-S test > 0.05) although surface changes have occurred. The distributions are presented as both Abn and Gbn to demonstrate the importance of the choice of distribution form. Furthermore, for a given sample, the calculated stable bed proportion (blue area in Figure 5.19 **C**) is not the same whether one uses the number of *immobile* grains (Abn) or the area covered by *immobile* grains (Gbn). For example, sample S4 contains 13% of *immobile* grains whereas in terms of surface area covered by *immobile* grains, the stability is 44% (see Table 5.3).

The fractional dynamics of each sample is shown in Figure 5.19 **D**. The red horizontal columns represent the proportion of the number of *mobile* grains for each fraction. The *immobile* proportion is represented by the blue columns. The boundary between these two columns thus indicates the distribution of grains as *mobile* or *immobile* within each fraction. Regardless of the sample and the corresponding intensity, the few grains above 128 mm are fully *immobile*. The vertical black bars indicate the proportion of *mobile* and *immobile* grains in terms of surface area. These black bars are located at very near the red and blue column boundaries (on average 2% difference), because Abn and Gbn distributions are essentially the same for fractional mobility since all particles within a narrow grain size class are of the same size.

Finally, an overview of the relative fractional stability is presented in Figure 5.19 **E**. In Abn, this figure shows that for high intensity events (S1 to S4) the grains larger than 32 mm are very over-represented in the *immobile* group. The ratio is between 5 and 25. In comparison, grains smaller than 16 mm are very under-represented or even absent, indicating they were very *mobile*. In Gbn, the four high intensity samples show grains over-represented only for fractions > 64 mm, with ratios between 1 and 3. This figure shows that in Gbn only large fractions can be classified as relatively fully stable, whereas in Abn, intermediate size fractions are also considered as relatively fully stable with larger ratios than in Gbn. In contrast to fractional stability, relative fractional stability is dependent on the form of the chosen distribution (Abn or Gbn).

5.2.3.2 Performance assessment approaches

To evaluate the performance of *PhotoMOB*, we applied our classification model to three particle delimitation procedures.

(1) The classification model was applied to our *manually* delineated control data set. The control particles and the *manual* tested particles are exactly the same. This evaluates only performance of the classification model, on a different data set from the one used to train the classification model.

(2) The automatic classification was applied to *automatically* delineated particles (Part 1 of the toolbox, developed in the companion article). The proportion of images occupied by material smaller than 16 mm, an input required to run the process fully automatically, was derived from the *manual* delineation. The operator is not expected to know the proportion of material smaller than 16 mm, but must make a visual estimate (we were looking for consistency in the delimitation process). Our classification model was then applied to these *automated* delineations. This permit assessing the magnitude of the combined errors of the delimitation and the classification model.

It should be noted that with *automated* delineation the control particles and the tested particles are not the same. The number of *automated* detected particles differs from the number of control particles by about 20% as already described in the performance analysis of the companion paper.

(3) Finally, in order to understand the positive impact that a fast correction of the *automated* delineations by an operator could have, a correction of the *automated* delineation in a maximum time of ten minutes for each of the 20 images was performed by a single operator. This correction consisted mainly in (i) eliminating the over-segmentation areas by selecting then deleting the incorrect multiple small polygons and then redrawing correctly as single polygons, and (ii) fixing under-segmented areas by quickly segmenting as many polygons representing clusters of grains as possible within the time limit. The classification model was then applied to these *reviewed* delineations.

Figure 5.20 shows an overview of the *automated* particle delineation results at T0 (before-event) and T1 (after-event) (columns A and B), as well as the result of applying the classification model to the *automated* delineation at T1, with the photo at T0 in the background (column C). This figure shows the challenge of the different image conditions. The slightest error in delineation, if not identical on the two photos T0 and T1, will inevitably cause more particles to be classified as *mobile*. On the S4 sample (first row), both photos show partially removed paint and wet areas. The granitic particle in the upper left is present in both photos, but in T1 it is poorly delineated, over-segmented (O). This lead to the classification of a large number of small *mobile* particles which in reality do not exist (M). Sample 6 (second row), shows in T1 the paint was almost completely removed, leaving the problematic asperity of some particles, as well as partially wet areas (W), respectively creating over- and under-segmentation. Finally, sample S9 (last row) shows better photographic conditions, even if in T1 the photo is only partially painted. Nonetheless, some particles are united (U). This problem of under-segmentation comes from the fact that the contrast of the overlapping particles is not strong enough. During classification, this problem may add a higher proportion of *mobile* particles compared to the control set, mainly in the large fractions. The same figure but with the *reviewed* delimitation is available in Text **S** Section 5.2.7.3.2 and **S** Figure 5.30.

For the 10 control post-event (T1) distributions, and for the three tested image processing procedures, we calculated different variables in Abn and Gbn form:

(E1) the proportion (%) of bed stability (inversely proportional to bed mobility), corresponding to output E1 in Figure 5.17 **E**.

(E2) the frequency distribution (%) in grain fractions ($F_{8,\ 11.3,\ 16,\ 22.6,\ 32,\ 45.3,\ 64,\ 90.5,\ 128,\ 181}$) per mobility status ($F_{i\ Immobile}$, $F_{i\ Mobile}$), corresponding to output E2 in Figure 5.17 **E** and visible in Figure 5.19 **C**.

(E3) for each size fraction, the proportion that was classified as *immobile* and *mobile* ($P_{i\ Immobile}$, $P_{i\ Mobile}$), corresponding to output E3 in Figure 5.17 **E** and in Figure 5.19 **D**.

(E4) the relative stability and mobility ratio for each grain fraction ($R_{i\ Immobile}$, $R_{i\ Mobile}$), corresponding to output E4 in Figure 5.17 **E**.

(E5) 15 common percentiles ($D_{5,\ 10,\ 16,\ 20,\ 25,\ 30,\ 40,\ 50,\ 60,\ 70,\ 75,\ 80,\ 84,\ 90,\ 95}$) of the *immobile* and *mobile* grain size distribution have been extracted ($D_{i\ Immobile}$, $D_{i\ Mobile}$), corresponding to output E5 in Figure 5.17 **E**. The method of the extraction of percentiles in the form Gbn is developed in the companion paper.

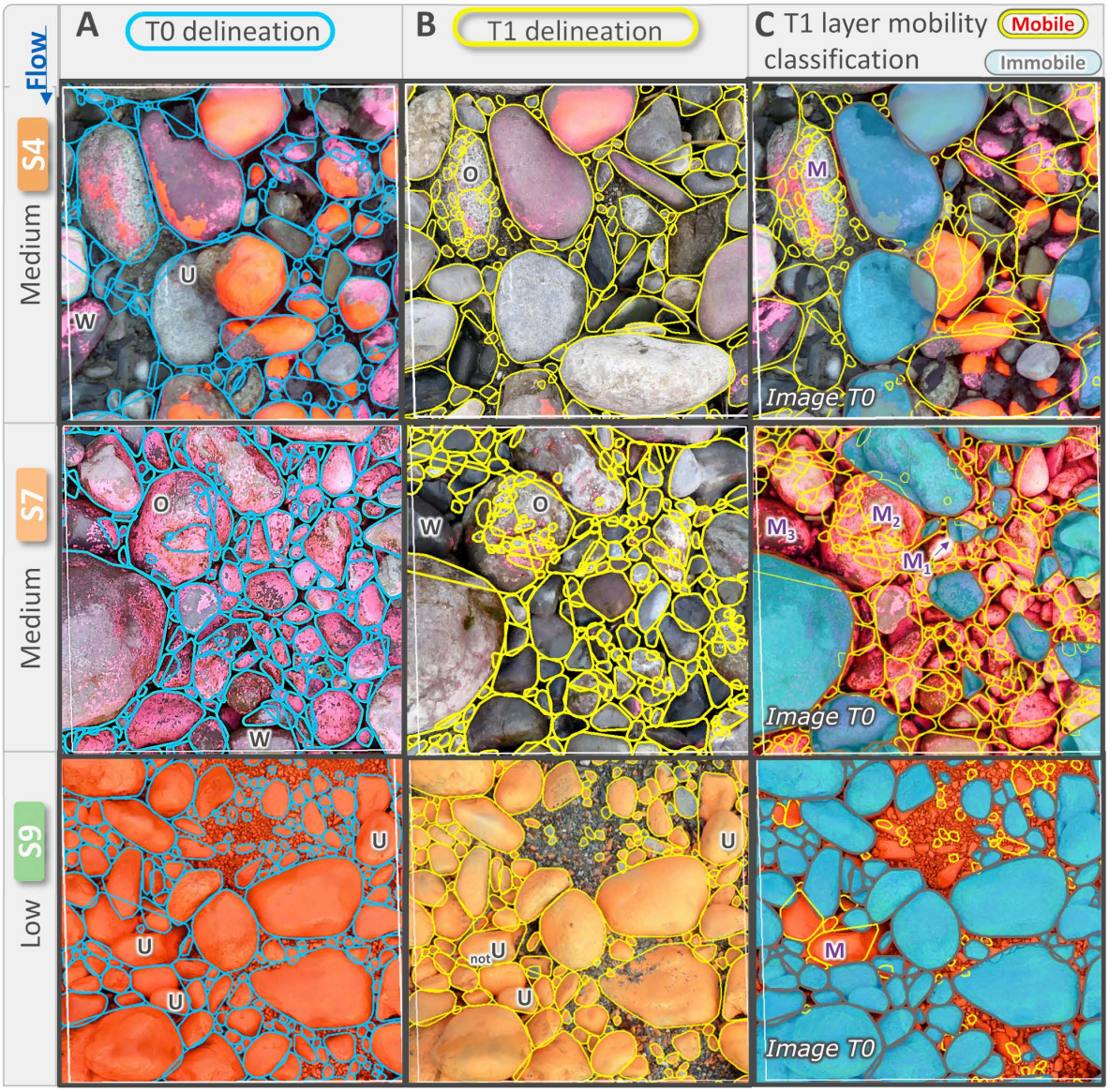

Figure 5.20: Particle delineation results at T0 (**A**) and T1 (**B**) by automated image-processing procedure. (**C**) Automated particle classification as *immobile* or *mobile* based on T1 classification. The image patches represent approximatively 0.4×0.4 m and show detected particles > 8mm. The *U* labels denote examples of under-segmentation issues, the *O* labels denote examples of over-segmentation issues, the label *w* denotes examples of wet surface generating under-segmentation leading to *non-real* large particle and the label *M* shows misclassification examples. *M1* corresponds to a misclassification as *immobile* due to similar shape; *M2* corresponds to misclassification of many *non-real* small particles as *mobile*; and *M3* corresponds to a larger *non-real* particle misclassified as *mobile*.

We chose to evaluate the performance using the classification obtained with the post-event layer (T1), but it would also have been possible to perform this analysis based on the classification obtained in pre-event (T0). This aspect is discussed in Section 5.2.5.2 and Section 5.2.5.3.

Residuals between control and tested value ($Residuals = Var_{i\ predicted} - Var_{i\ control}$ have been calculated for the approaches E1 to E3, error ratios $Error\ Ratio = Var_{i\ predicted}/Var_{i\ control}$) for the E4 approach, and finally the relative residuals ($Relative\ Residuals = \left(Var_{i\ predicted} - Var_{i\ control}\right) \times 100/Var_{i\ control}$) regarding percentile estimates (E5).

As in the companion paper using the residuals and relative residuals (E1, E2, E3 and E5), four metrics were applied to quantify the estimation error over the 10 samples: the root mean square error, the irreducible random error, the bias (B), indicating whether the evaluations were on average over- or under-estimated, defined as : $B_{Var\ i} = \frac{1}{n}\sum(Residuals_i)$, where *n* represents the number of patches (10) and the mean absolute error (MAE), corresponding to the reducible error or the error of accuracy, indicating how far from the correct value are the estimates, given as: $MAE_{Var\ i} = \frac{1}{n}\sum(|Residuals_i|)$). For the error ratios concerning the E4 approach, only an average of the error ratios for each of the 10 grain size fractions is calculated. Finally, the error of the procedures for each approach (E1 to E5) was quantified by calculating for each metric its average over all variable elements *Var* i:

$$Procedure\ performance_{metrics} = \frac{1}{n} * \sum\left(Metrics_{Var_i} + Metrics_{D_{Vari+1}} + \ldots + Metrics_{D_{Vari+n}}\right)$$

where *n* represents the number of studied elements (10 for grain fractions and 15 for percentiles).

The procedure performances in Abn and Gbn for each approach are summarized in Figure 5.21 . For clarity only the average MAE is presented in this paper. The columns (grey, white and black) represent the average MAE. The dots indicate the average MAE for each sample intensity group. This is indicative of the residuals dispersion of results across groups. Average performance procedure metrics (RMSE, e, Bias, MAE) are available Text **S** Section 5.2.7.4.

When evaluating the average MAE for fractional stability/mobility (E3) and relative fractional stability/mobility (E4) we made the decision to not consider the two extreme samples S1 and S10 presenting respectively *immobile* and *mobile* P_i proportion equal to zero. Moreover, for the percentile estimate average MAE we decided not to consider samples with *immobile* or *mobile* particle size distributions with less than 100 particles (See Table 5.3). We have thus considered only the 5 samples S5, S6, S7, S8, S9. The reason is that for *immobile* or *mobile* fractions containing little or no grains, inclusion or exclusion of a single particle from a set result in large outlier residuals when compared to the control set, which generates large average percentage errors without reflecting any real trend. However, the behaviour of each procedure on all samples (S1 and S10 included) can be seen in the set of Figure 5.22 to Figure 5.24 and dots of average MAE for each sample intensity group take all samples into account in Figure 5.21 .

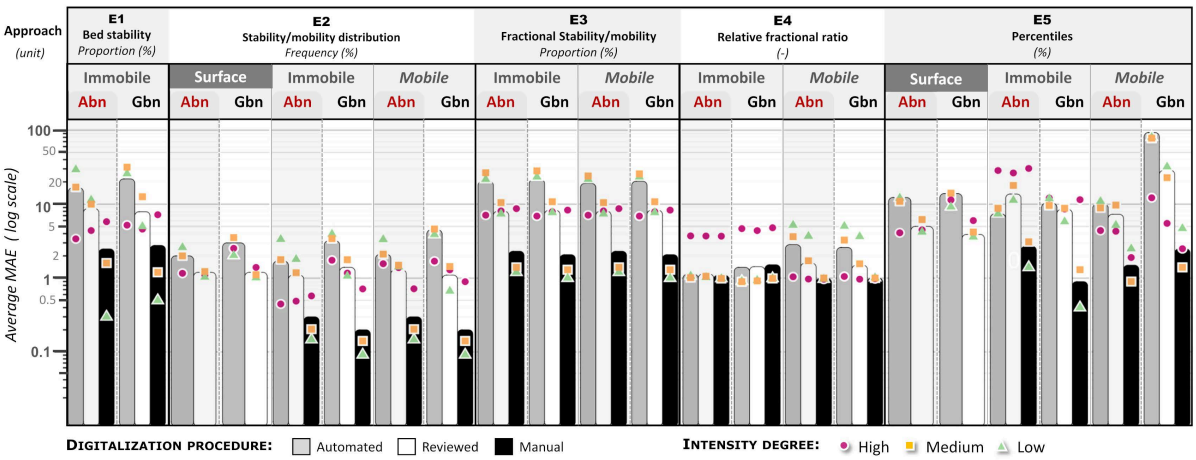

Figure 5.21: Accuracy and precision performance for the three delineation procedures followed by automatic grain classification for each approach E1 to E5. The performance is presented for each grain category (Surface, *Immobile*, *Mobile*) and in the two forms Abn and Gbn. The colour of the bars corresponds to the delineation procedure (*automated*, *reviewed*, *manual*). The evaluation of the accuracy of the procedures is represented by the average bed stability error between the 10 samples (**E1**), the average MAE of all grain fractions between the 10 samples (**E2**) and between the 8 samples S2 to S9 (**E3**), the average of the mean error ratio of all fractions between the 8 samples S2 to S9 (**E4**), and finally the average of the relative MAE of all 15 percentiles calculated between the five samples S5 to S9. The assessment of the precision of the procedures is given by the dispersion of the average MAE (E1, E2, E3, E5) or the average error ratio (E4) between the groups of intensity samples. The shape and colour of the dots correspond to the three degrees of mobility (high, medium and low).

5.2.4 RESULTS OF PERFORMANCE ASSESSMENT

5.2.4.1 General bed dynamics

Figure 5.22 shows the degree of agreement of the bed proportion of the number (Abn) and area (Gbn) of particles classified as *immobile* (or conversely *mobile*) per sample, between the control data (manual delineation + visual classification) and the three delineation procedures (*manual*, *automated*, *reviewed*) followed by the automatic classification. The *manual* delimitation procedure (Figure 5.22 **A)** shows good agreement for all samples with the control data, for both Abn and Gbn forms. The general MAE taking into account the 3 sample groups is 2.6% (Figure 5.21 **E1** black column). The *automated* procedure presents a less good fit (Figure 5.22 **B**). Bed stability is well estimated for high intensity events. However, there appears to be a larger scatter for samples with lower degrees of mobility. MAEs are more important in Gbn than in Abn, especially for medium intensity events, rising from 17% to 32%. These photos have a high complexity, as for example S4 and S6 in Figure 5.20, causing coarse *non-real* particles. These *non-real* particles are not present in both paired pictures, so they appear *mobile*. This is more problematic in Gbn because the coarser the particle the more weight it has, whereas in terms of Abn the *immobile/ mobile* partition is not weighted by the grain surface. Finally, with the *reviewed* delineation, the errors for the medium and low intensity samples are reduced, in both Gbn and Abn, by more than half. The rapid correction of the delineation is obviously localized on the larger polygon's boundaries i.e., coarser *non-real* particles being the most visible.

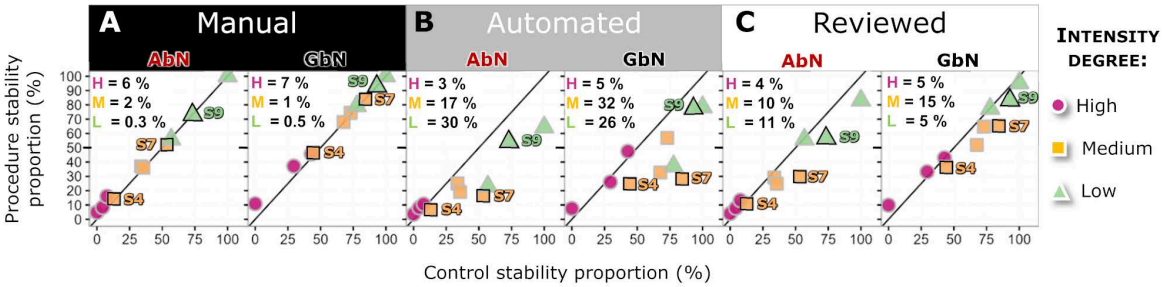

Figure 5.22: Comparison of the total proportion of grains, in term of number (Abn) and area (Gbn), classified as *immobile* (inversely proportional to *mobile*) for (**A**) *manual*, (**B**) *automated* and (**C**) *reviewed* image-delimitation processing procedure compared to the control. The reference control grain proportion was obtained by a manual digitalization followed by visual classification. The shape and colour of point correspond to the three mobility degrees (High, Medium Low). Samples taken as examples in Figure 5.20 are represented here by black contour. The equality line is shown with a solid bold line. The MAE per sample group is quoted for each procedure.

5.2.4.2 Distribution per dynamics status

The frequency distribution prediction errors from the three procedures with the control dataset are presented in Figure 5.23 , and the percentiles estimates, in both Abn and Gbn form, of the three procedures are shown in Figure 5.24. Surface percentile estimates for *automated* and *reviewed* procedure at post-event times are shown in Figure 5.24 **A**. The *manual* procedure estimate is not presented as the control surface and the manual surface were both obtained manually and thus are composed of the same grains. In part B is presented the *immobile* percentile estimates, and in part C, the *mobile* percentile estimates of the three procedures compared to the control data. The red solid line represents the control data (manual delineation + visual classification), while the black, grey and white points correspond to the predictions obtained via the *manual*, *automated* and *reviewed* delineation procedures respectively followed by automatic dynamics classification.

5.2.4.2.1 Identification of surface grains

The errors in the frequency distribution of the grains within each subset ($F_{i\ Immobile}$ and $F_{i\ Mobile}$) are firstly conditioned by a correct delineation of all the surface grains. Figure 5.23 **A** shows the post-event surface frequency residuals of each grain fraction for the two forms Abn and Gbn, taking the whole surface sediment as a whole, and Figure 5.24 **A** presents percentiles estimation. There appear to be no major differences between the group samples (mobility degrees). The better or worse performance in reproducing the surface distribution is mostly related to the complexity of the photos.

In Abn, the *automated* delineation shows maximum bias of grain frequency of +8% for the particles < 16 mm. Consequently, the particle size distribution of the surface will then tend to be finer than the control due to the presence of small *non-real* particles at the beginning of the distribution, which shifts the distribution towards finer sizes. This phenomenon is illustrated in Figure 5.24 **A**. The first row shows the 15 percentile estimates extracted in Abn form for the *automatic* delineation (grey dots) and *reviewed* (white dots) compared to the control set (red solid curve). The grey points tend to lie to the left of the solid curve. The automated procedure average MAE of the percentile estimate is 12.3% (Figure 5.21 - **E5** - Surface -Abn). Eight of the samples have both partially wet and partially painted areas, which creates a large heterogeneity in pixel colour. This average MAE indicates similar performance found in the companion paper for C3 condition (not protected from the sun and not painted), where the average MAE was from 11.2- 14.2%.

In Gbn (Figure 5.23 **A** second row Gbn), the *automated* procedure reproduces fairly well frequencies until 64 mm, above which there is more scatter and progressively over-estimation by up to 18%. The high surface percentiles will therefore be over-estimated. In Figure 5.24 **A Gbn** (second row), the grey points of the percentiles above D_{75} are often positioned to the right of the red control line. The *automated* procedure average MAE of the surface percentile estimate is 14%. This example shows the importance of the choice of the form to represent the data. The Abn form is likely to have errors in the first fraction while in Gbn the errors seem to be more in the coarse fraction.

The *reviewed* delineation reduces the errors. The *reviewed* procedure average MAE for surface fraction frequency for each sample group in Abn or Gbn is less than 1.4% (see Figure 5.21 **E2** - Surface - white bar), resulting in a *reviewed* procedure average MAE for surface percentile estimate of less than 5%, in both Abn and Gbn (Figure 5.21 **E5** - Surface - white bar). These errors are similar to those found in the companion paper in C1 condition (4.5 to 4.8%).

5.2.4.2.2 Stability/Mobility

Figure 5.23 **B** and **C** show the residuals of the grain frequency distribution estimations for each grain fraction per dynamics status, $F_{i\ Immobile}$ and $F_{i\ Mobile}$, concerning the three delineation procedures, while Figure 5.24 **B** and **D** present *immobile* and *mobile* percentiles estimates.

5.2.4.2.2.1 Manual procedure performance

It should be remembered that in the *manual* procedure (manual delineation + automatic classification) it is exactly the same grains that are being compared with the control set since this one was obtained via manual delineation + visual classification. Consequently, errors are solely due to the classification model. The *immobile* and *mobile* frequency estimation residuals in Abn and Gbn are between 2.5 and -2.5% (Figure 5.23 **B** and **C** - Manual). The samples with the highest error are the 'highest mobility' samples (S1 to S4). These samples are composed of between 87% and 100% newly deposited *mobile* particles. Sometimes a new particle is deposited in a location where previously a particle had a similar shape and size although it is not the same. Unfortunately, the difference in area and shape is too small to be considered as different (i.e., *mobile*), and they are therefore misclassified as *immobile*. The residuals of the other group samples (medium and low) are lower because there is less turnover of particles and therefore the error due to similar shape is less likely to occur. On the other hand, *immobile* particles are only rarely misclassified as *mobile* in the manual delineation.

5.2.4.2.2.2 Immobile Distribution

Percentiles from the *manual* delineation procedure are under-estimated for high intensity events. In Figure 5.24 **B** - Abn, for samples S1 to S3, the black points are shifted to the left compared to the continuous solid red line (control data). This is because there are very few *immobile* particles in these control samples (between 0 and 13%, Table 5.3 and Figure 5.19 **C** Abn blue area) and they are often of relatively large size; however, the procedure will identify small *immobile* particles in fractions between 8 mm and 32 mm due to similar shape, so the *immobile* GSD will be refined by adding fines at the beginning of the distribution. The *manual* procedure average MAE of *immobile* percentile estimates (visible in Figure 5.21 **E5** Immobile - black bar) for the high intensity samples is 30% while for medium and low intensity samples it is 1.4-3%.

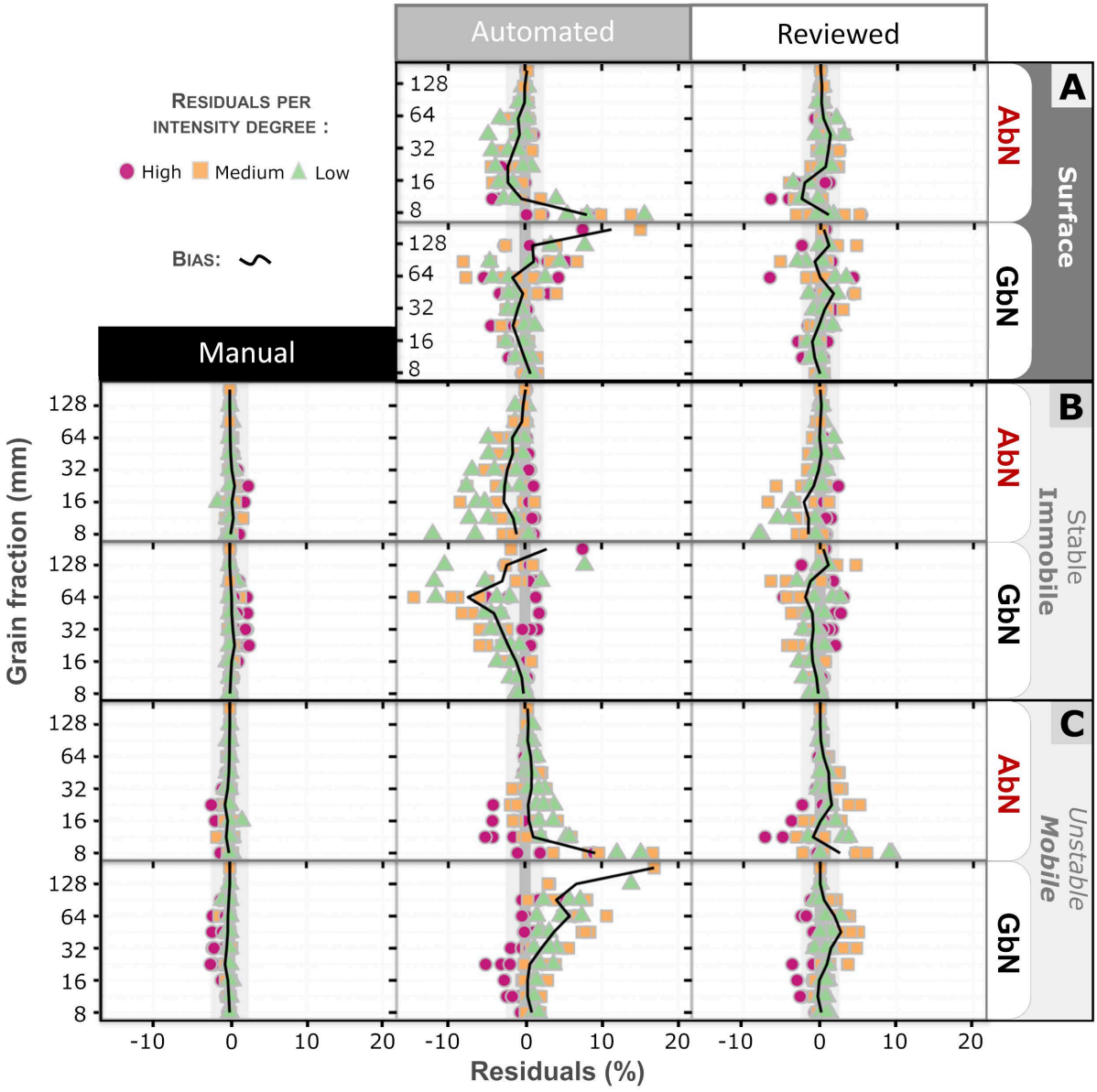

Figure 5.23: (**A**) Distribution of the 100 relative post-event surface frequency estimation residuals for the *automated* and *reviewed* delineation procedure (10 samples per 10 grain size fractions). (**B**) Distribution of the *immobile* and *mobile* (**C**) Frequency estimation residuals for the *manual*, *automated*, and *reviewed* delineation procedures. The residuals are shown for the forms Abn and Gbn. The shape and colour of point correspond to the three mobility degrees (High, Medium and Low). The bias (mean error across 10 residuals) along grain fraction (%) is shown with the bold black curve.

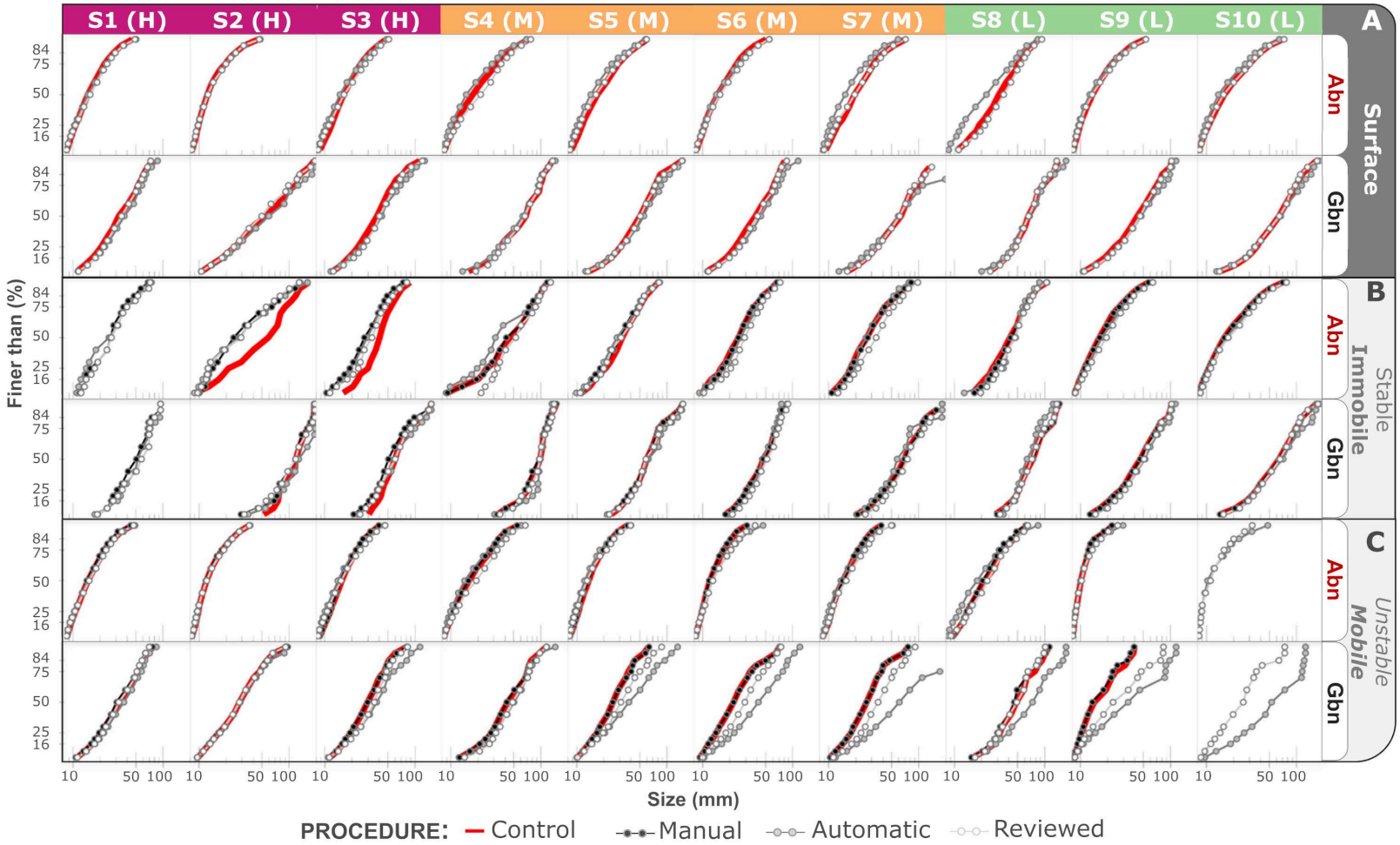

Figure 5.24: Performance evaluation of the extracted 15 percentile estimates in Abn and Gbn. The 15 points representing the percentile estimates are connected by lines, but the information presented here is not the cumulative distribution frequency. Therefore, the last point at the end of the lines in Abn and Gbn does not correspond to the same size on the *x*-axis. The last point corresponds to the D_{95} and not the Dmax (100 %). (**A**) Surface visible grain percentiles estimates for automated (grey dots) and reviewed (white dots) delineation procedures compared to control data (red solid line). Data in Abn (top) and Gbn (bottom). (**B**) *Immobile* and *mobile* (**C**) grain percentiles estimate for *manual* (black dots), *automated* (grey dots), and *reviewed* (white dots) delineation procedures compared to control data (red solid line). Data in Abn (top) and Gbn (bottom)

INDEX

In Gbn, the maximal 2.5% of over-estimation and under-estimation is more likely to be in the intermediate fraction between 22 mm and 64 mm instead of 8 mm to 32 mm as for Abn. The distributions of high intensity events will be less impacted than in Abn from the beginning of the distribution. In Figure 5.24 **B-Gbn**, Sample S1 to S3, the black points are much closer to the solid red curve in Gbn than in Abn. The *manual* procedure average MAE *immobile* percentile estimate for high intensity samples in Gbn is 11.5% (two and a half times less than in Abn) while for medium and low intensity samples it is from 0.4-1.3%.

5.2.4.2.2.3 Mobile distribution

On the other hand, the estimation of the *manual* procedure *mobile* percentiles associated to high intensity events will not be affected by large errors because the 2.5% under-estimation for *mobile* grains between 8 and 32 mm or between 22 to 64 mm has little influence on a grain set composed almost exclusively of *mobile* grains (See Figure 5.19 **C** - Abn red area, S1 to S4). There is no strong disparity between the samples subject to different intensity. In Figure 5.24 **C** - Abn and Gbn, the black points are relatively close to the red solid line. The *mobile* percentiles are estimated with a manual average MAE of 1.5% in Abn, and of 2.5% in Gbn.

5.2.4.2.3 Automatic and reviewed procedure performance

5.2.4.2.3.1 Immobile

In Abn, the *automated* delimitation procedure shows disparity between the mobility intensity groups. At lower intensity there is under-estimation of fine *immobile* particles because poor particle delineation will often lead to the classification of *non-real* particles as *mobile*. This problem therefore affects medium to low intensity events in a progressive manner. The *reviewed* delineation shows the same pattern (Figure 5.24 **B** - Reviewed - Abn) for the fine fraction, but with lower bias. *Immobile* percentile estimate for medium and low intensity events will tend to be slightly over-estimated as the absence of fine particles results in a GSD containing fewer fine fractions, and will shift the start of the distribution towards coarser sizes. However, the high intensity samples show the same error as the *manual* procedure (see Figure 5.24 **B**, Abn, grey and white points). Sometimes small, *immobile* grains are detected due to very similar shapes. The distribution is deviated from the beginning towards finer sizes.

In Gbn, under- or over-estimation of frequencies affects coarser grain size classes than in Abn. The percentile estimate will be biased, but only from high percentiles. This time, the *reviewed* delineation reduces the bias and there is less disparity between the sample groups. The *reviewed* distribution in Gbn has more reliable *immobile* percentiles estimation than the *automated* delineation and also than the *reviewed* delineation in Abn. In Figure 5.21 **E5** - Immobile - Abn, the white column (*reviewed* delineation procedure) shows an average MAE of almost 14% while the *automated* delineation shows a lower average MAE of only 7.5%. In Gbn, the MAE for the *reviewed* delineation decreases to 8.7%, and is similar for the 3 groups of samples. There was insufficient time in the rapid 10 min review correction to deal with small particles, while in Abn it is their presence that controls the GSD. They are present in greater numbers than the coarser particles (see Figure 5.19 **C**). The frequency of the fine *immobile* fractions up to 16 mm are under-estimated causing a coarser estimate of the beginning of the distribution, then due to the boundary correction process splitting the coarse union of *non-real* intermediate and coarse grains, the rest of the distribution is less under-estimated, so the whole distribution is shifted towards the coarse sizes. The white points in Figure 5.24 **B**, Abn are positioned to the right of the red curve for samples S4, and S6 to S10, while in Gbn these are more superposed to the solid red control curve. The *automated* delineation, due to an under-estimation of the fine fraction, will also present a relatively coarse beginning of the cumulative distribution, but as the other fractions are still under-estimated, there will be less over-estimation of the percentile sizes.

5.2.4.2.3.2 Mobile

In Abn, the estimation of *mobile* grain frequencies with *automated* delineation shows disparity between the sample groups (Figure 5.23 **C** - Automated - Abn). The lower the intensity, the higher the over-estimation of the grain frequency as *mobile* for grains < 11 mm. In addition to poor particle delineation creating directly *mobile* classification, if there is a misalignment of the two photos, then the small grains in T1 will not necessarily be superimposed on the same *immobile* small grain present in T0, and will be classified as *mobile*. The small grains are therefore more likely to experience this problem. The larger the grain size, the less important the image shift is, as the *immobile* grains always have some portion of the surface overlapping, allowing the centroid of the reference layer (T1) to be located in the polygon of the compared layer (T0). The *reviewed* delineation does not seem to have completely reduced this phenomenon affecting the finest grains. As already mentioned, the review focuses on the coarse grains first. The first percentiles would tend to be under-estimated due to the addition of small *non-real mobile* particles at the beginning of the distribution.

In Gbn, the *automated* delineation (Figure 5.23 **C** - Automated - Gbn) shows increasingly over-estimated mobility with increasing grain size up to 17%. The *reviewed* procedure (Figure 5.23 **D** - Reviewed - Gbn) seems to allow a better estimation of the distribution frequencies. The *mobile* percentile derived from the fully automated procedure will be highly over-estimated. In Figure 5.24 **C**- Gbn, grey dots are strongly shifted to the right, to larger sizes, as the intensity of the event decreases (from S1 to S10). The *reviewed* delineation correction, focusing on the coarse particles to be segmented, strongly reduces these over-estimates (white dots). The *reviewed* delineation procedure reduces the average MAE of the *automated* delineation from 93% to 29%.

Finally, Figure 5.24 **B** shows that all three procedures detected *immobile* particles for sample S1, whereas in the control set, 100% of the grains are *mobile*. For the three procedures, the *non-real immobile* grains in question represent between 4 and 5% of the total grain number, with size ranging from 11 to 93 mm and with median size of 25 mm. Opposite, Figure 5.24 **C**, sample S10, shows that the *automated* and *reviewed* procedures detected *mobile* grains, whereas in the control set 100% of the grains were *immobile*. This time the *non-real mobile* grains represent between 18 and 38% of the total grain number, a wider range of sizes (8 to 74mm (reviewed) and to 128mm (automated) with a finer median size of 10 mm. The misclassification seems to have involved a lot of small grains, probably due to image misalignment but also a wide range of grain sizes. In Gbn just some few coarse *non-real* and associated misclassified grains will have a lot of influence creating a very coarse *mobile* distribution when no grain is really moving.

To recap, the error in estimating the frequencies of each grain size fraction varies from 0.2-0.3% for *manual* delineation, from 1-1.5% for *reviewed* delineation and from 2-5% for *automated* delineation. The error on the estimation of percentiles is greater due to the accumulation of frequency errors and varies depending on the form of the distribution and the intensity of the event. In Abn the error on percentile estimate will be higher for the low percentiles and decrease for high percentiles. Meanwhile, Gbn will have more error on the high percentiles. The average MAE (corresponding to the D_{50} percentile MAE) varies from 0.9-2.7% for the *manual* procedure (all percentiles are evaluated with a MAE below 10%), from 7.3-29% for the *reviewed* procedure and from 7.4% to 93% for the *automated* delimitation. Finally, there are less errors when estimating *immobile* grain-size distributions (i.e., stable parts of the bed) than *mobile* ones.

5.2.4.3 Fractional dynamics

The fractional stability corresponds, for a given fraction, to the proportion of grains or surface area that remains *immobile* and, complementary, the fractional mobility corresponds to the *mobile* proportion. The grains of the given fraction have similar surface areas, so the *mobile* and *immobile* proportions are almost identical to those calculated in terms of the number of grains (Abn). As the fractional study only focuses on each individual grain fraction, the estimates of the *immobile* proportion and *mobile* proportion are inversely proportional.

In Figure 5.21 **E3**, for each procedure, the average error is almost identical between the Abn or Gbn forms and between fractional *mobility* or *immobility*. The predictions of the three procedures are shown only in Abn in Figure 5.25 **A**. The red solid line represents the control data. It corresponds to the boundary of the red and blue columns from Figure 5.19 **D**, while the black, grey and white points correspond to the predictions obtained via the *manual*, *automatic* and *reviewed* procedures respectively.

5.2.4.3.1 Manual procedure performances (classification model only)

The average MAE of the *manual* procedure for low and medium intensity samples is 1.3% (Figure 5.21 **E3** Immobile – Abn). The black dots in Figure 5.25 **A** for samples S4 to S10 are almost perfectly superimposed on the continuous control curve. In contrast, the high intensity samples show an under-estimation of the *mobile* proportion and conversely an over-estimation of the *immobile* proportion. The black points are shifted to the right of the red reference curve. The average MAE for this group is of 8.7%. The reason for this is the same as mentioned before i.e., newly deposited particles may be of similar shape to those present before the event, leading to a classification as *immobile* instead of *mobile*. The average MAE of the *manual* procedure is 2.3%.

5.2.4.3.2 *Automated* and *reviewed* performance

With *automated* delineation (Figure 5.25 **A** - grey dots), the *mobile* proportions of low and medium intensity samples are over-estimated. The grey points are shifted to the right with respect to the red solid reference curve. This phenomenon is more important for grain fractions above 45 mm. The very large errors in the coarse fractions do not accurately reflect the true amount of error. Very few particles are present in the coarse fractions (see Table 5.3 or Figure 5.19 **D**), so the presence or absence of a single grain yields very large errors. *Mobile* over-estimation of coarse grains is explained by the coarse *non-real* particles' identification. If these delineation errors are not the same between the two images, very coarse polygons may be superimposed on smaller real particles in the other image. This has the effect of artificially increasing the number of *mobile* coarse and intermediate grains. For high mobility intensity samples, it is the opposite, the *mobile* particles proportions are under-estimated. As mentioned above, these samples contain very few *immobile* particles i.e., the appearance of a particle misclassified as *immobile* rapidly increases the percentage of errors. Furthermore, the large number of new particles increases the probability in which new and old particles have similar shapes although they are not actually the same particles. The *automated* procedure average MAE over all samples is 20.3%.

The *reviewed* procedure shows the same patterns (e.g., over-estimation of *mobile* proportion for low and medium intensity events and under-estimation of high intensity events) but with lower residuals (smaller distance between red curve and white dots). The coarser fractions no longer show errors, thanks to the boundary correction mainly made on the most visible large grains. The *reviewed* procedure average MAE is 8%.

Once again, grains are considered *mobile* in sample S10, whereas the control set does not show any. The error decreases with increasing grain size. With the revised delineation, up to 25% of the small grains are considered *mobile*. This finding is discussed later in the text.

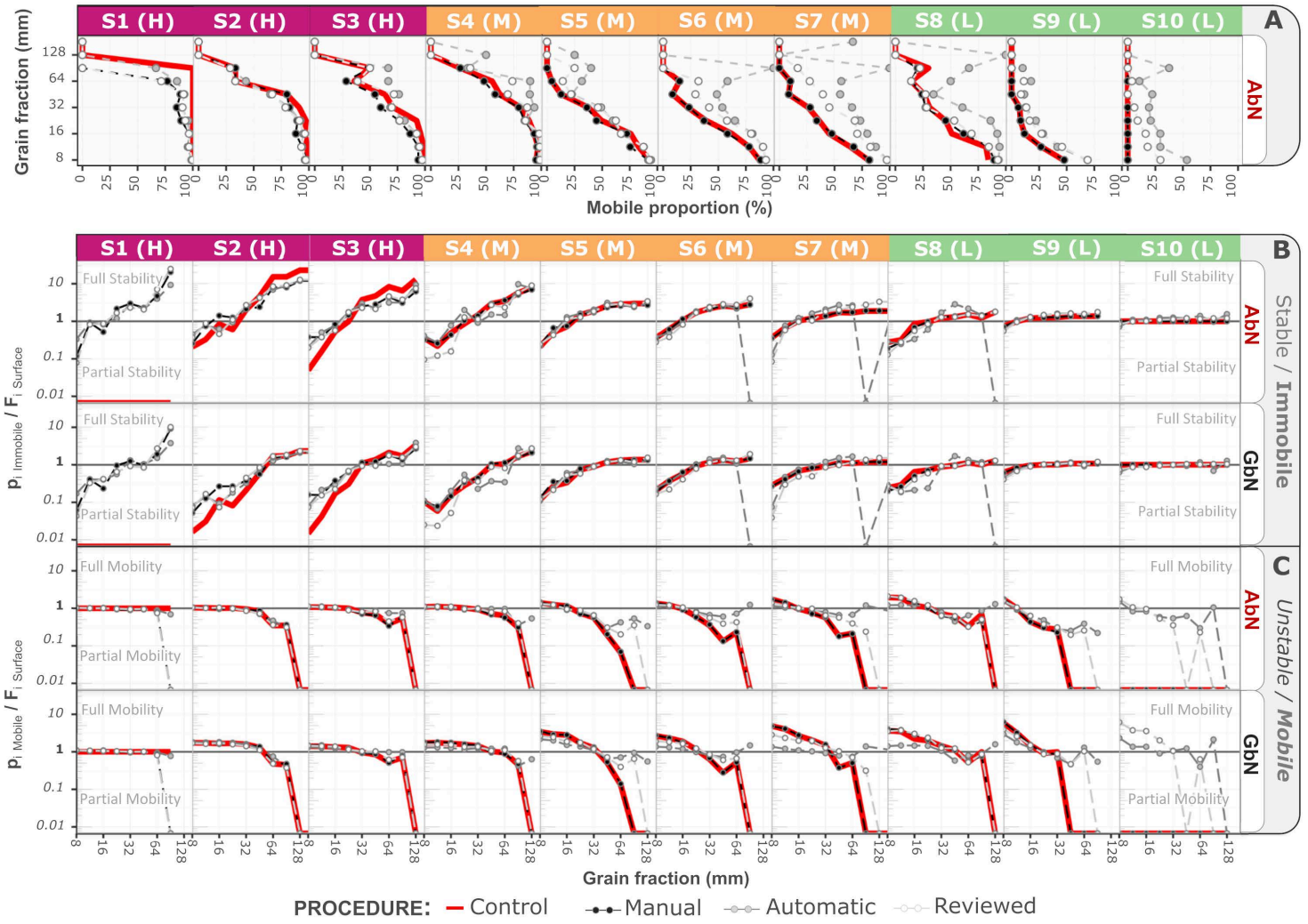

Figure 5.25: (**A**) Fractional *mobility / immobility* proportion estimate in Abn for *manual* (black dots), *automated* (grey dots) and *reviewed* (white dots), delineation procedure compared to control data (red solid line). The red solid line corresponds to the boundary of the red and blue columns from Figure 5.19 D. Data are only in Abn due to similarity with Gbn. (**B**) Relative fractional *stability* (immobility) ratio estimates and (**C**) relative fractional mobility (instability) ratio estimates. Where, $p_{i\ Immobile}$ is the proportion of each size fraction *i* present in the whole *immobile* surface grain category and $p_{i\ Mobile}$ in the whole *mobile* surface grain category, F_i is the proportion of each size fraction *i* in the whole surface bed sediment. Data in Abn (top) and Gbn (bottom).

INDEX

5.2.4.4 Relative fractional dynamics

The relative stability (or mobility) ratio corresponds, for a given fraction, to the proportion that this fraction represents in all the *immobile* (or *mobile*) grains, divided by the proportion that this fraction represents in all the grains forming the surface (*immobile* + *mobile*). If the ratio is equal to or greater than 1, the grain fraction is considered fully stable (or fully *mobile*) while when the ratio is less than 1 the fraction is considered partially stable (or partially *mobile*). The predictions, in both Abn and Gbn form, of the three procedures are shown in Figure 5.25 **B** for relative bed stability (*immobility*) and Figure 5.25 **C** for relative bed *mobility*. Again, the red solid line represents the control data (manual delineation + visual classification), while the black, grey and white points correspond to the predictions obtained via the *manual*, *automated* and *reviewed* procedures respectively.

5.2.4.4.1 Relative stability ratio

The three procedures, *manual*, *automated* and *reviewed*, show the same patterns in Abn and Gbn (Figure 5.25 **B**) and performances (Figure 5.21 – E4 – Immobile). The high intensity samples are the least well estimated. The fine fractions are estimated to be more stable than in the control set (dots higher than control curve), while the coarse fractions are estimated to be less stable than in the control set (dots lower than control line). In Gbn, deviation from the control set shows the same pattern as in AbN but with a higher deviation from the control curve (dots are more distant from the control line than in Abn).

It should be noted that despite the difference in ratios compared to the control set, the classification as partially *immobile* (<1) and fully *immobile* (≥1) is still good. The *manual* procedure provided a correct stability categorization (full/partial) in Abn in 91% of the relative grain fraction stability estimates, and 94% in Gbn. The *automated* procedure provided a correct stability categorization (full/partial) in Abn of 84% and 77% in Gbn. The *reviewed* procedure provided a good stability categorization (full/partial) in Abn of 88% and 87% in Gbn.

5.2.4.4.2 Relative mobility ratio

Unlike the immobility ratio, the mobility ratio performance estimates are variable across the three procedures but each procedure produces similar performance in either Abn or Gbn (Figure 5.21 – E4 – Mobile, Abn and Gbn area almost identical). The *manual* procedure worked well: the black dots in Figure 5.25 **C** are almost perfectly aligned with the control curve, and the *manual* procedure provided a correct *mobility* categorization (full/partial) in 91% of the relative grain fraction mobility estimates in Abn and 93% in Gbn. The *automated* and *reviewed* procedures showed good estimates in both Abn and Gbn for high intensity events (grey and white dots close to control line for S1 to S4). In contrast, for the medium intensity events, the small fractions are considered relatively less *mobile* (grey points below the control curve) while the larger fractions are considered relatively more *mobile* (grey points above the control curve). The *reviewed* procedure (white points) shows less difference with the control curve. Overall, the *automated* procedure provided a correct *mobility* categorization (full/partial) in 82% of the relative grain mobility estimates in Abn and 75% in Gbn, while the *reviewed* procedure provided a correct *mobility* categorization (full/partial) in 88% in Abn and 87% in Gbn.

5.2.5 DISCUSSION

5.2.5.1 Performance limitation and recommendation

5.2.5.1.1 Manual procedure

The *manual* delineation + automatic classification, assessing only classification error, yielded good performances compared to the control dataset for all approaches E1 to E5. The MAE averages (for approaches E1, E2, E3 and E5) are between 0.2 and 2.5%. Other metrics are given in supplementary material **S** Table 5.4 to **S** tbl-p2table-S4. Whether the data are expressed as Abn or Gbn, the performances are similar.

The surface area and eccentricity shape likeness thresholds have been set in PhotoMOB based on a trained data set, but can be user-defined. If the PhotoMOB procedure is to be used on another river, it may be possible to carry out two or three pairs of control photos (with *manual* delineation + visual classification) in order to establish whether the automatic classification model we provide is capable of providing similarly acceptable results with respect to a new control set.

It should be noted that the analysis developed in this paper does not provide information on the possible differences between what the operator can measure by the photographic method and the actual or real stability/mobility. An experiment in a controlled environment would be required to obtain a real dataset. Here, the control dataset was elaborated with what was visible from the photo, i.e., it is a visual photo interpretation, the best that can be expected from the photographic method.

5.2.5.1.2 Automatic procedure

The fully *automated* procedure (*automated* delineation followed by automatic classification) represents the total error of the procedure in achieving correct grain segmentation and classification. The MAE averages for the approaches E1, E2, E3 and E5 are between 2 and 93%. There is a disparity in performance between the different samples (error of precision) and errors are always greater in the Gbn form, with high impact from large polygons unifying several grains. It should be noted that the photo pairs used in this study (see Figure 5.19 **A** - post) were not optimal and came from a set of old photos not acquired for this particular analysis. For instance, *PhotoMOB* has not been developed to perform on partially painted or partially wetted photos creating areas of differing brightness and colours within a photo. A partially painted photo has the same order of magnitude of error as a photo not protected from direct sunlight (see companion paper for further details on this).

As already discussed in the companion paper, two solutions can drastically improve *automated* grain delineation, and therefore the subsequent revision effort: (1) Before photographing the square at post-event time, it can be advisable to paint the area again so that both photos are painted. The aim is to reduce the complexity of the photo, i.e., to reduce the details of the image to only grain boundaries. (2) In the near future we plan to implement the new open-source software library ImageGrains (Mair et al., 2023) in the *PhotoMOB* workflow. An example of the performance of the application of this new library on our photos is available in the supplementary materiel of the companion paper. For the moment, this new algorithm has not been trained on partially painted photos, but we have a dataset to do so. This would further facilitate the protocol we are proposing. However, despite adequate paint and/or implementation of this new grain segmentation algorithm, some error will inevitably remain.

5.2.5.1.3 *Reviewed* procedure

The *reviewed* procedure (*automated* delimitation corrected in 10 minutes followed by boundary revision + automatic classification), shows average MAEs for E1, E2, E3 and E5 between 1 and 29%. Other performance metrics are given in supplementary material from **S** Table 5.4 to **S** Table 5.8.

A 10-minute correction per photo greatly reduce the errors. The performance gains (compared to the fully *automated* procedure i.e., white vs grey columns Figure 5.21) are stronger in the Gbn form. Errors are reduced by 60% in Gbn and by 30% in Abn. There is a disparity in performance between different intensity groups. Due to small sample sizes, there were exceptionally large percentage errors on fractions with small numbers of particles, such as the percentage of *immobile* particles in high intensity samples. This had a strong impact on the average error shown in Figure 5.21. In reality, these classification errors concern only a few grains. In order to solve this problem, after the automatic classification of the grains, the user can symbolize with a certain colour the few grains classified as *immobile* as in Figure 5.26. In this way, the user can quickly walk around the image and locate these particles and change the attribute field from *immobile* to *mobile*. The inverse *mobile/immobile* way can be applied to low mobility intensity samples.

Figure 5.26 shows samples S1 and S10 with the two pre- and post- photos in transparency on top of each other, where 6 types of errors are pointed out. Recommended strategies during the boundary revision to reduce the 6 errors are available in Text **S** Section 5.2.7.5.1.3

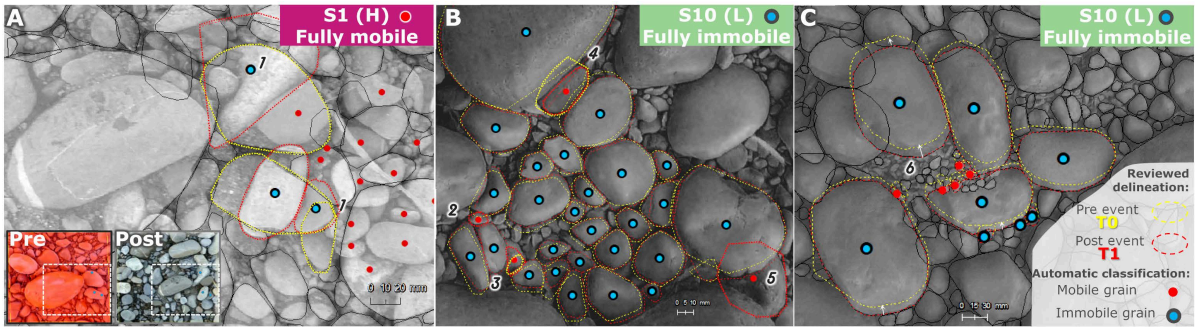

Figure 5.26: Example of misclassification of grains (**A**) Error due to the classification model giving *immobile* particles (*1:* similarity threshold too large and maybe not enough shape descriptor used). (**B**) Misclassification due to *automated* boundary and revision delineation giving *mobile* particle (*2*: small grain found only in a single layer, *3*: relatively small grain identified with slightly different shapes between the two photos, *4*: grain modified by user only in one of the two layers, *5*: user forgets to redraw a grain in one of the two layers. (**C**) Misclassification due to photo misalignment (*6*: the centroid of the small grain in T1 is not superimposed on the grain in T0 although they are indeed the same). This photo alignment is not the one reported in this study, it is just an example to show the effect of a bad alignment.

However, respecting the best practices during photo collection phase i.e., (i) painting the square before each shot, (ii) protecting the area to be photographed from direct sunlight, (iii) taking the photos as perpendicular to the ground as possible, contributes to an easier, faster and good photo alignment and allows *PhotoMOB* to generate quite good automatic delimitation, thus reducing the effort of boundary correction afterwards. Moreover, correcting the pre and post polygon layers simultaneously, rather than 10 minutes one after the other, could further reduce errors thanks to consistent shape correction between the two layers.

Organizing data, applying filters in GIMP, scaling, aligning the photos, applying the *PhotoMOB toolbox part 1*, correcting the grain boundaries, applying the *PhotoMOB toolbox part 2*, equates to 1-hour desk work per set of paired photos. The objective of the *PhotoMOB* procedure is to automate all of the individual subsequent steps that an operator would have to perform to produce grain delineation and classification in a GIS. Part 1 of *PhotoMOB* described in the companion paper corresponds to the automation of more than 260 successive actions, while Part 2 presented in this paper corresponds to the automation of more than 100 successive actions. The processing of two photos automated by the *PhotoMOB* toolbox to quantify the dynamics represents more than 620 successive actions. These actions should be repeated for each pair of photos per event.

The realisation of this procedure in GIS allows the user to control all processes and to check the quality of the results and make corrections. Finally, we believe that implementing the ImageGrains (Mair et al., 2023) algorithm would reduce the processing time for both pre- and post-event images to well under an hour and perhaps even eliminate the need to paint the patches (see example in companion paper).

5.2.5.2 Immobility, Stability, Mobility, and Instability

The stability of the bed corresponds to the undisturbed, unchanged area. That is, the area that does not exhibit deposition or erosion as a result of a hydrological event. Once the *immobile* grains have been identified, the proportion of the stable zone and the distribution frequency of its *immobile* grain fractions can be determined. The concept of stability/instability is more attributed to the description of the sampled surface, while the concepts of immobility/mobility are attributable to the grain. Care must be taken because with the method we are describing, subtle difference between stability and immobility may exist. It can happen that a particle is considered *immobile* while the area is unstable.

Let's take the example of Figure 5.27 **A**. The hydrological event caused entrainment of four small particles present in T0, which have therefore become part of the bedload, and the appearance of a new relatively large particle in T1 (classified as *mobile*). In terms of stability (grey area) and instability (red area), the classification of the pre- and post-event layers are valid, both layers show instability at this location. But looking at the competence of the flow and understanding what (size) grains are *mobile* and *immobile*, then there is a problem. The large particle was slightly visible at T0, so it could be considered as part of the surface sediment. It was not part of the bedload and deposited, but appeared due to bed scour.

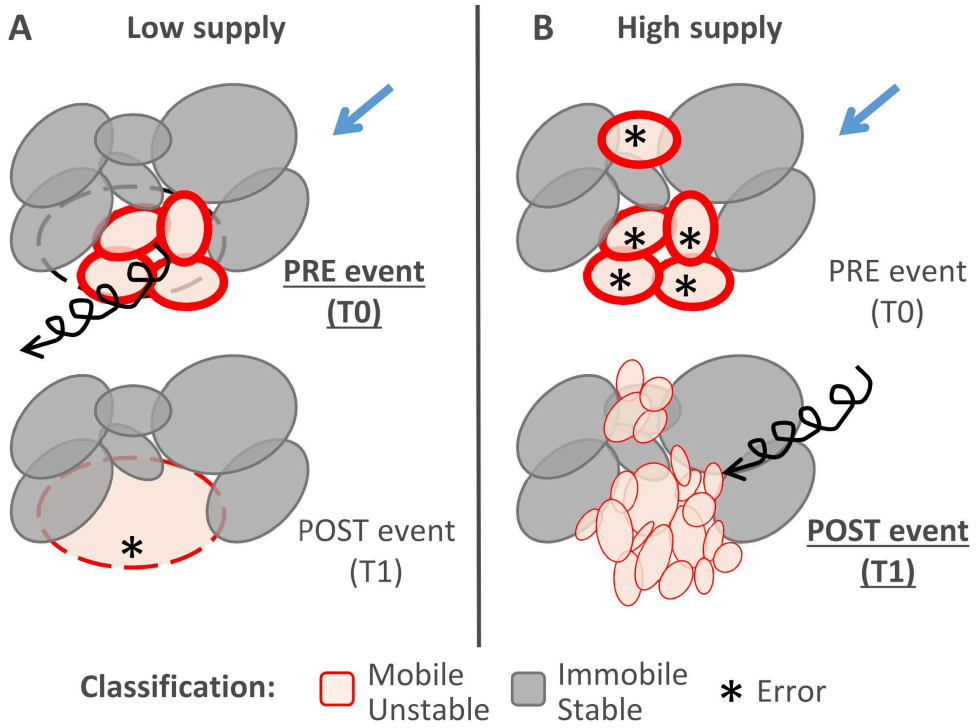

Figure 5.27: Sketch illustrating probable misjudgements of grain dynamics. (**A**) In the context of low sediment supply, grains newly appearing in T1 due to surface erosion are classified as *mobile*. The use of the T0 layer classification is recommended for analysing the sediment dynamics. (**B**) In a context of significant sediment supply, grains previously apparent in T0 can be classified as *mobile*, although it is not certain that they have been transported, perhaps simply covered. The use of the T1 classification is recommended to analyse the sedimentary dynamics.

Assuming that the *automated* delineation will be corrected by the operator, two situations are possible. In the first one, the coarse grain could only be delineated in the post-event layer (T1). The result will be a classification as *mobile*, which is "false". In the second case, the operator might want to make this large particle also appear in the pre-event layer since it is guessable in T0 and perfectly visible in T1. In this case, this grain will end up classified as *immobile*, which is "true". In both cases, it is problematic to rely on the post-event layer (T1). In the first case, the large grain is classified as *mobile*, which is not true. It will strongly influence the GSD of the *mobile* grains (which can be used as a proxy for the GSD of the bedload). This will lead to a strong over-estimation of the size of the high *mobile* percentiles, even more so if the results are expressed as Gbn. This is one of the factors that explains the highest error in the *reviewed* procedure for the Gbn form (white dots in Figure 5.23 **C** and white columns in Figure 5.21 **E5**). In the second case, it will be classified as *immobile* (grey instead of red), which is the "reality". But this will lead to the area being considered as stable (undisturbed), which is not true since some grains were eroded.

In the context of low sediment supply, whether from the point of view of stability/instability or immobility/mobility, it would be preferable not to draw the large particle at T0 and to rely on the classification obtained with this pre-event layer (T0) since it does not seem to present any problem. The four small grains are well *mobile* and contribute to bedload, while represent an unstable surface.

In the context of a greater sediment transport rate, schematically represented in Figure 5.27 **B**, other subtleties appear. The five small particles present in T0 are no longer visible in T1. Whether one relies on the classification of the pre- or post-event layer, the area is considered unstable, which is "true". On the other hand, it is not certain whether the five small particles in T0 were *mobile* as part of the bedload, or that they remained *immobile* and were covered by new ones. In T1, however, the new visible grains are likely to have been part of the bedload, and to have been deposited here. In the context of significant sediment supply, it will be necessary to rely on the classification obtained from the post-event layer (T1) to quantify both stability/instability and immobility/mobility correctly.

5.2.5.3 Use of data

In order to study the sediment dynamics as quickly and reliably as possible, the procedure to be followed and the recommendations listed here and in the rest of this paper are summarized in Figure 5.28. The processing of the images with the GIS *toolbox PhotoMOB part 1 and 2* generates a shapefile with information for each grain, in pre- and post-event, of its shape characteristics (area, perimeter, *a*-axis, *b*-axis, orientation, rectangularity, eccentricity, roundness, compactness) as well as its classification (*immobile*/*mobile*). The attribute table of these layers is also saved in text format. A web or desktop application based on R language and shiny package (Chang et al., 2023b; R Core Team, 2021) , called *PhotoMOB Extractor*, has been developed to analyse the data from the text files and to allow the user to quickly and easily obtain the outputs mentioned in Figure 5.17 (C1, C2, C4, E1, E2, E3, E4, E5) in both Abn and Gbn form. Depending on the objectives of the study for which the photographic method can be used and the data with which it can be coupled, either the Abn or Gbn form may be preferable.

From a stability/instability point of view, perhaps more related to ecological studies, it will probably be preferable to think in terms of stable or unstable surfaces and therefore use the Gbn form. From a sediment transport dynamics point of view, both forms seem to be useful, the choice will depend on the objectives sought. However, it seems that the Abn form is adequate if the photographic observations are to be linked to mobility or travel distance observation of tracer grains from a pre-defined (painted) patch area. This is because the tracer particles available to be entrained and thus subsequently traced are pre-selected as all surface particles within a pre-defined area. On the other hand, if the dynamics observed via photographs are to be related to other data such as pebble counts, bulk samples, bedload samples obtained by in situ sampling, then the Gbn form would be the most appropriate.

Moreover, percentile values may be used in sediment transport equation that have been generally established using Gbn data measured by square holes. In case the compared Gbn data are coming from square holes binned *b*-axis measurement (template, sieve), the apparent *continuous b'*-axis value obtained by the photographic method should be converted based on the flatness of the grains of the studied river (see details in companion paper).

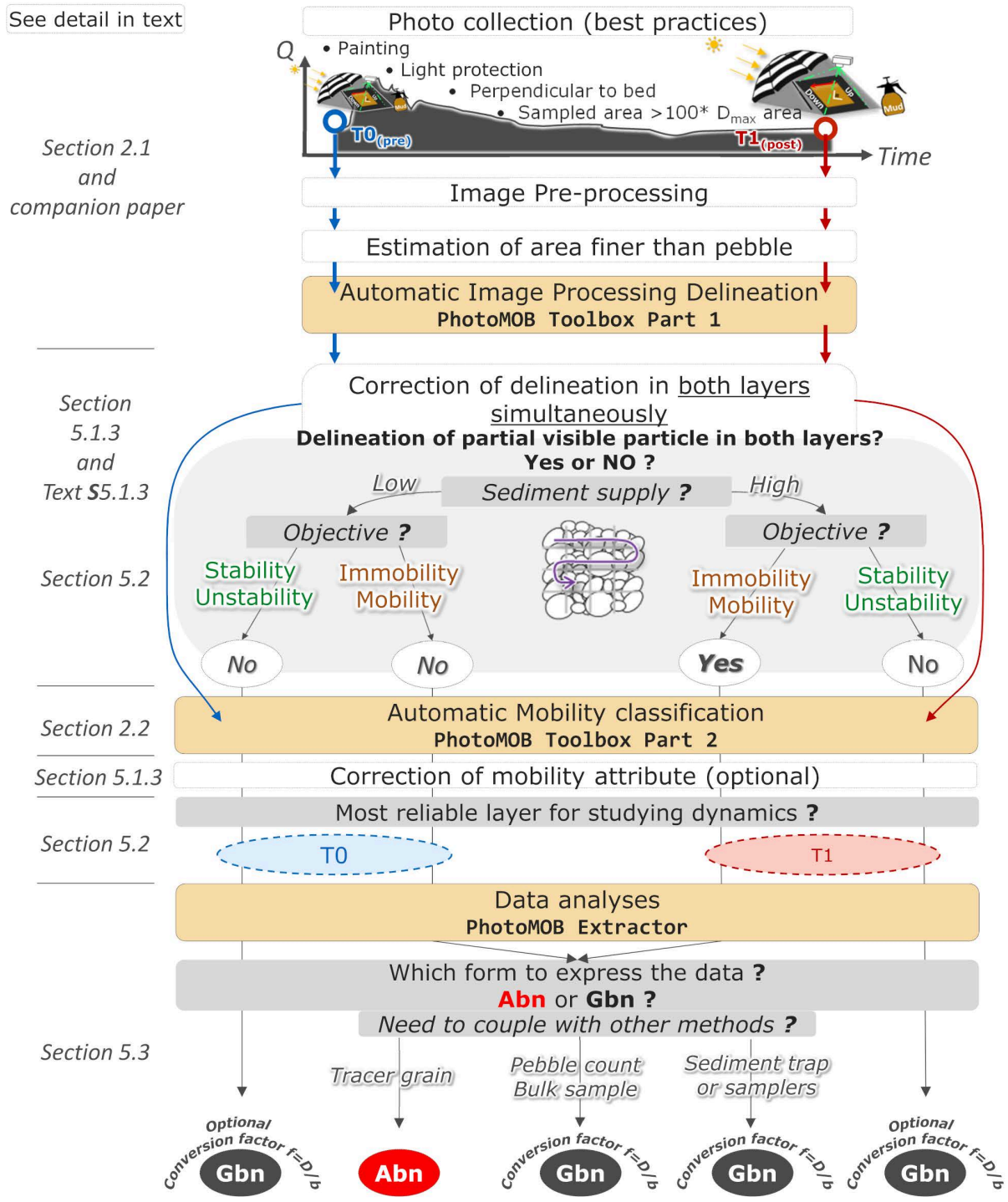

Figure 5.28: Illustration of the successive stages and recommendations required to extract grain size and dynamics data from photographic method. The yellow boxes represent the automated steps developed in the pair of paper.

5.2.6 CONCLUDING REMARKS

The performance analysis of *PhotoMOB* to characterize particle dynamics in gravel bed rivers shows an acceptable agreement with the control data set. The classification error (mean absolute error) due only to the classification model on perfectly delineated particles (*manual* procedure) is less than 3% for all the outputs examined. The *reviewed* procedure (automated delineation manually revised in 10 min + automated classification) gives a general bed and fractional grain dynamics (stability/mobility) estimates with a mean absolute error of around 8% in both Area-by-number and Grid-by-number GSD form. The relative fractional dynamic as partial or full is well estimated at 87-88% (Abn-Gbn). *Mobile* and *immobile* percentiles are estimated with MAE ranging between 13.7 - 7.3% in Abn and between 8.5 and 28.7% in Gbn.

The photographic method we present has several advantages:

(1) It provides information on bed *mobility* as well as bed *stability*. The latter is generally not covered by other methods.

(2) The data extracted from the photos can be compared with other existing studies thanks to the availability of the data in Gbn form. However, it is important to ensure a large enough sampled area and use *b*-axis size adequate conversion, based on the average grain flatness, in order to compare data from photos and data from measurements using square holes' template or sieves.

(3) If the sampled surfaces are large enough to represent the entire grain-size distribution, even the coarsest fractions, then it will be possible to correctly assess the fractional dynamics of coarse fraction and the maximum *mobile* diameters. Moreover, repeated photographic observations of the same area for hydrological events of different intensity can allow the development of mobility models for each grain size fraction. For a given fraction, the incipient motion threshold can be determined when a hydrological event generates a given minimum *mobile* proportion of the grains in that fraction. Whereas the full mobility threshold can be determined when an event causes 100 % of the *mobile* grain of that fraction or its relative mobility ratio is ≥ 1.

(4) After 1-hour processing (single operator), a lot of information is available (output Figure 5.17 **C** and **E**). This is faster than the pebble count method (Wolman, 1954), which requires two operators to work at least one hour two different days to just get surface GSD. The estimation of the *mobile* proportion of each grain fraction is faster and more reliable than the time effort to search for *mobile* grains downstream of a painted patch by two operators having to locate and measure all visible grains, where often the return rate is very low.

(5) *PhotoMOB* can be coupled with other types of observations and measurements (painted tracer, pebble count, sediment traps, pit tags) to compensate some of their limitations.

(6) Obtaining the correct categorization of grains can be improved by implementing new algorithms for better grain segmentation.

(7) The protocol is flexible as the grain boundary can be easily corrected and the grain classification too. The user is therefore free to analyse the texture and dynamics of all the grains or to select and create subsets of the grains in the study area and extract their characteristics by group.

Following the steps developed in this pair of papers and the recommendations summarised in Figure 5.17 and Figure 5.28, *PhotoMOB* provides an aid to the observation and analysis of sediment dynamics, in a consistent manner, across time and space at the scale of the grain and morphological unit

Code availability

The actual and future version of the PhotoMOB toolbox as well as the PhotoMOB Extractor App are available with documentation at https://shiny.fannyville.com/PhotoMOB_Tool.html. The toolbox is currently only available for ArcGIS desktop, but will be soon converted to ArcGIS Pro and, additionally, our intention is to convert to the open source QGIS.

Acknowledgements

This research was undertaken under the MorphHab (PID2019104979RB-I00/AEI/10.13039/501100011033) and MorphPeak (CGL201678874-R/AEI/10.13039/501100011033) research projects funded by the Spanish State Research Agency (Ministry of Science and Innovation) and the European Regional Development Fund Scheme (FEDER). The first author has a grant funded by the Ministry of Economy, Industry and Competitiveness, Spain (BES-2017-081850). Damià Vericat is a Serra Húnter Fellow at the University of Lleida. The Fluvial Dynamics Research Group –RIUS is a consolidated group recognized by the Generalitat de Catalunya (2021 SGR 01114). We thank Alexandre Moron for building the square frame and María Eugenia Benito for providing feedback concerning the development of the PhotoMOB toolbox and Extractor application user interface.

Credit authorship contribution statement

Fanny Ville: Conceptualization, Methodology, Investigation, Data curation, Formal analysis, Visualization, writing original draft, Writing – review & editing.
Colin Rennie: Methodology, Supervision, Writing – review & editing.
Ramon J. Batalla: Funding acquisition, Methodology, Supervision, Writing – review & editing.
Damià Vericat: Funding acquisition, Methodology, Supervision Writing – review & editing.

Data availability statement

Control, manual, automated and reviewed dataset made of identified and classified grains used in *PhotoMOB* error assessment, as well as example files to use in the *PhotoMOB Extractor app* are available under: https://zenodo.org/records/10038313

Declaration of competing interest:

The authors declare that they have no conflict of interest.

S-5.2.7 SUPPORTING INFORMATION PART 2

Supporting Information for:

PhotoMOB: Automated GIS method for estimation of fractional grain dynamics in gravel bed rivers.

Part 2: Bed stability and fractional mobility

Contents of this file:

This document provides supplementary material. It is structured using the same headings as the main article to help readers find what they are interested in reading more about. Title followed by the word "none" indicate that no supplementary information is provided for that section.

S-5.2.7.1 Introduction

Bed mobility can be assessed by direct methods such as the *Helley Smith sampler,* Helley and Smith (1971) and *sediment traps*, Bunte and Abt (2001) , and indirect approaches as for instance *tracers* (Church and Hassan, 2002; Hassan and Ergenzinger, 2003; Vázquez-Tarrío and Batalla, 2019) and those based on *visual estimation* (moss, algae's development; Pfankuch, 1975) and on *organism density changes* (Schwendel, 2012). All these methods or approaches have limitations in terms of applicability, ease of implementation or accuracy. One inexpensive method, is the use of a painted bed area (i.e. painted tracers, see summary in Hassan and Roy, 2016). A representative area of the bed is painted and then usually photographed to identify each grain and derive the pre-event surface GSD using automated tools such as *Sedimetrics Digital Gravelometer©* (Graham, 2005a, 2005b) or *Basegrain* (Detert and Weibrecht, 2013). Following a hydrological event, the entrained painted grains can be located downstream and transport distances measured. This method avoids altering natural grain imbrication without limitation of tracer size. However, the majority of measurements generally focus on the downstream particles, while a large amount of information from the original spot location has not been exploited, such as the proportion of the bed surface that is *stable* (*immobile*) for each grain size fraction. It should be noted that in only few studies (e.g., Mao et al., 2017; Mao and Surian, 2010; Vericat et al., 2008a), the overall proportion of the bed surface that remained *stable* has been estimated, either visually by changes in painted surface between two photos or by analysing the proportion of pixels that still have paint in a post-event photo. This technique yields the proportion of the sampled bed area that has remained *stable* (not scoured and/or filled), but it can be unreliable if the paint washes off, and it has not as of yet taken into account grain size. Although information on the fractional mobility of each grain size fraction is present in the photo, to our knowledge this has not previously been extracted systematically. Within this context and limitations, we have developed a semi-automated method for quantifying the stability and mobility of bed grains, based on photographic methods and GIS processing. The paper quantifies its performance.

S-5.2.7.2 The complete PhotoMOB workflow

The objective of the procedure is to compare two photos, of the exact same river bed area, acquired before and after a hydrological event (or a succession of events when it is impossible to access the area).

S-5.2.7.2.1 Grains' detection

None

S-5.2.7.2.2 Characterization of grain dynamics

The categorization (see **S** Figure 5.29 – B below), by comparing grain located at the same coordinates between the pre- and post-event photo, will be done on sediments from the same section of the river, the two grain shapes are likely to be similar. In order to overcome this problem, five particle shape descriptors were tested (Chaki and Dey, 2019). It is necessary to establish which shape descriptors are most relevant and then to evaluate the relative difference thresholds of these criteria in order to decide whether particles are identical or not. We constructed a training dataset consisting of 10 pairs of pre- (T0) and post- event (T1) photos coming in equal proportions from two rivers of the South Central Pyrenees (Cinca and Ésera). The sedimentary characteristics of these rivers are detailed in the companion paper. Each photo was scaled and a projective transformation applied, then the T1 photo was aligned with the T0 photo using control points (identical points between the two photos).

All the particles were manually delimited in the form of polygon shapefiles. More than 12100 particles were delineated. For each particle, we extract five shape descriptors (see **S** Figure 5.29 – **B** and **C** above).

(i) The surface area, (ii) the compactness which represents the relationship between the area and the perimeter of the particle:

$$Compactness = 4\pi \times \frac{Area}{Perimeter^2} \qquad (5.7)$$

Next, (iii) the roundness is obtained using the minimal circle envelope box, in which the roundness is the proportion the particle fills its minimal circle:

$$Roundness = \frac{Area_{Particle}}{Area_{Circle}} \qquad (5.8)$$

The next two descriptors are obtained using the minimal rectangle bounding box. By creating this box, the length of the axes of the particle is known, which allows the calculation of the (iv) eccentricity which corresponds to the aspect ratio:

$$Eccentricity = \frac{A_{axis}}{B_{Axis}} \qquad (5.9)$$

Then, (v) the rectangularity which indicates in which proportion the particle is rectangular, i.e. in which proportion the particle fills its minimal rectangle:

$$Rectangularity = \frac{Area_{Particle}}{Area_{Rectangle}} \qquad (5.10)$$

The polygons delimiting the particles at T1 have been transformed into a point layer, materializing their centroid. This point layer still contains the shape characteristics information at post event time. This T1 point layer has been superimposed on the polygon layer materializing the particles at T0. The T0 shape information (area, compactness, roundness, eccentricity, rectangularity) has been attached to the T1 point overlay.

At this stage, the T1 centroid point layer has the paired shape information from T1 and T0 (**S** Figure 5.30). Then the grain degree of likeness is evaluated. For each shape descriptor, the percentage difference is calculated by taking pre-event time as a reference:

$$Shape\ likeness = \frac{Descriptor_{post} - Descriptor_{pre}}{Descriptor_{pre}} \times 100$$

If a T1 particle is not coupled to any T0 particle, then it is considered to be *mobile* (newly arrived). A single operator visually assigned the dynamics status (*immobile* or *mobile*) to each T1 particle listed in the T1 point layer. In total 5479 pairwise particle comparisons were performed. As the particle detection limits may vary slightly between photos or if an operator is using a lower resolution camera, we decided to truncate the particles to 8 mm, decreasing the number of retained comparisons to 4202.

We then used R Core Team (2021) software and the *rpart* package developed by Therneau and Atkinson (2019) to build a classification decision tree model. Among the 4202 pairs, 852 represented *immobile* particles while 3350 represented *mobile* particles. In order not to influence the classification results we randomly eliminated particles classified as *mobile* from our training set to obtain equal proportions of both classes. Of the remaining 1704 particles we used 70% to train different classification trees and kept 30% to test models and select the best one. The simplest tree with good accuracy was preferred. The selected classification model is shown in **S** Figure 5.29 – C2 above. The testing accuracy was 87%. The two relevant descriptors are (i) particle area and (ii) eccentricity. The surface area seems to be the first intuitive descriptor. Finally, eccentricity makes sense because even if the images are rotated, translated, with a slightly different scale, the eccentricity ratio should remain similar. If two paired particles have a difference in area greater than 38%, then they are considered to be different (*mobile*). If not, if the difference in eccentricity is greater than 31%, then they are considered to be *mobile*, otherwise they are identical (*immobile*).

Once the particles have been classified, it is possible to derive different types of information. This data can be expressed as the number of grains in the sampled area, i.e. Area-by-number (Abn), or in terms of grain area in the sampled area. The latter is equivalent to the Grid-by-number (Gbn) data form commonly obtained by the pebble-count method (Wolman, 1954). **S** Figure 5.29 - D shows a conceptual example of the possible data that can be obtained from the analysis of photo pairs.

• Taking the surface sediment as a whole (out of 100 %) and the mobility classification or status of each particle (i.e. *mobile* or *immobile*), it is possible to calculate the *immobile* proportion (i.e., bed stability) and the *mobile* proportion (i.e., bed instability) in term of grain number or area (see **S** Figure 5.29 – D5)

• Additionally, because each particle is classified as *mobile* or *immobile*, it is also possible to know frequency distribution of each grain fraction per dynamics status composing the new bed surface (see **S** Figure 5.29 – D6).

• The relative fractional stability (or relative fractional mobility) can also be examined with the ratio p_i/F_i (see **S** Figure 5.29 – D8). In this expression, p_i is the frequency of the *immobile* particle in a given i^{th} size fraction. F_i is the frequency for the given fraction i taking all surface grains as a whole (*immobile* + *mobile*). A value less than 1 indicates partial mobility or stability, depending if p_i is based on the *mobile* or *immobile* grains, whereas a ratio $p_i/F_i \geq 1$ indicates full mobility or stability of the fraction i.

• Finally, taking as two distinct sets the *mobile* and *immobile* particles, it is possible to calculate for each status the frequencies of each fraction, to derive the cumulative frequency and to estimate the percentiles (see **S** Figure 5.29 – D9).

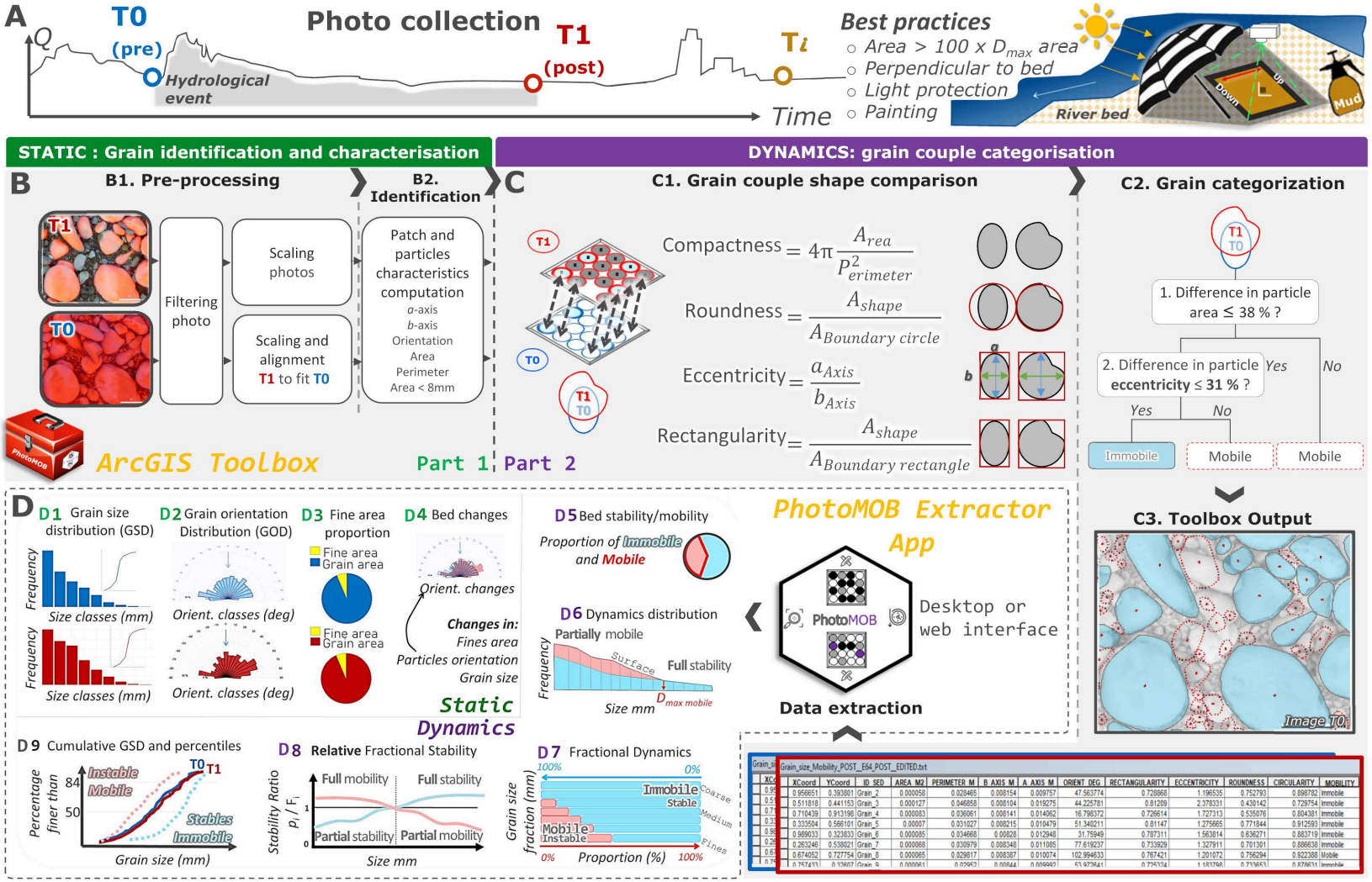

S-Figure 5.29: Illustration of the workflow required to samples and characterize bed surface (see companion paper) and sediment dynamics (developed in this paper). (**A**) Photo acquisition. *PhotoMOB* toolbox Part 1 for (**B**) detection of grain and shape characterization and Part 2 for (**C**) grain couples' comparison and categorization. (**D**) Extraction of different possible types of data (static views in green D1 to D4, and dynamic views in purple D5 to D8) facilitated by the *PhotoMOB* Extractor application.

S-5.2.7.2.2.1 Hypothesis and rationale

None

S-5.2.7.2.2.2 Workflow

None

S-5.2.7.3 Performance assessment

None

S-5.2.7.3.1 Control dataset

None

S-5.2.7.3.2 Performance assessment approaches

S Figure 5.30 shows an overview of the *reviewed* particle delineation at T0 and T1 (columns A and B), as well as the result of applying the classification model to the *reviewed* delineation at T1, with the photo at T0 in the background (column C). The correction of delineations can still cause classification errors. In the case of *automated* delineation errors and a correction made only on one of the two layers, the shapes of the grains still remain different, leading to misclassification as *mobile* (see **S** Figure 5.30 – M_2). This error is also covered in the *main text* and latter in this document Text **S** Section 5.2.7.5.1.3.

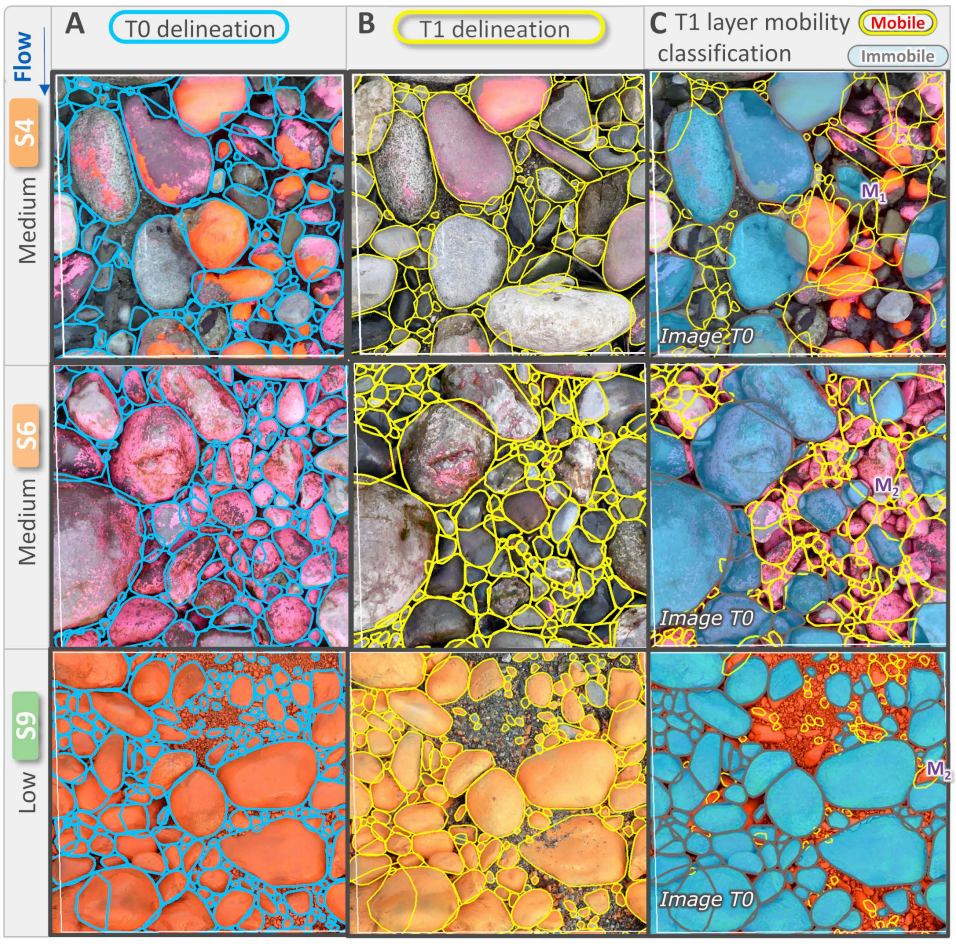

S-Figure 5.30: Particle *reviewed* delineation results at T0 (**A**) and T1 (**B**). (**C**) Automated particle classification as *immobile* or *mobile* based on T1 classification. The image patches represent approximatively 40 cm x 40 cm and show delineated particles > 8mm. The label *M* is showing misclassification example. *M1* correspond a miss classification as immobile due to similar shape. *M2* correspond to a misclassification as *mobile* due to shape correction only in one layer (T0 or T1) leading to different shapes while the particles were *immobile*.

S-5.2.7.4 Results of performance assessment

Average performance procedure metrics (Bias, e, MAE, RMSE) are available below

S-5.2.7.4.1 General bed dynamics

Table 5.4: Bed stability performances (S Figure 5.29 – D5)

Distribution [a]	Delineation procedure [b]	Procedure Bias (B) [c]		Procedure Irreducible error (e) [c]		Procedure Accuracy error (MAE) [c]		Procedure RMSE [c]	
		Abn %	Gbn %	Abn %	Gbn %	Abn %	Gbn %	Abn %	Gbn %
Bed stability	Manual	2.1	2.7	2.9	3.5	**2.5**	**2.8**	3.6	4.4
	Reviewed	-6.1	-5.1	9.6	8.3	**8.7**	**7.9**	11.4	9.8
	Automated	-14.6	-19.5	15.5	19.0	**16.6**	**21.9**	21.3	27.3

[a] The bed stability proportion (number - Abn or area - Gbn) is inversely proportional to bed mobility. The bias for bed mobility will have the opposite sign to those shown here for bed stability. Other metric values will be equal for bed stability or mobility. [b] The *manual* procedure corresponds to *manual* delineation + automatic grain categorization, *automated* procedure corresponds to *automated* delineation + automatic grain categorization, and *reviewed* procedure correspond to *automated* delineation followed by 10 min of boundary correction + automatic grain categorization. [c] Average of the bed stability/Instability proportion estimates error over the 10 samples, corresponding to the general procedure errors for each procedure (*manual*, *automated*, *reviewed*). [d] Theses value correspond to the column in Figure 5.21 (*main text*).

S-5.2.7.4.2 Distribution per dynamics status

Table 5.5

Distribution [a]	Delination procedure [b]	Procedure Bias (B) [c,d]		Procedure Irreducible error (e) [c]		Procedure Accuracy error (MAE) [c,e]		Procedure RMSE [c]	
		Abn % *(sd)*	Gbn % *(sd)*	Abn % *(sd)*	Gbn % *(sd)*	Abn % *(sd)*	Gbn % *(sd)*	Abn % *(sd)*	Gbn % *(sd)*
Surface	Reviewed	0 *1.3*	0.1 *0.9*	1.1 *0.9*	1.4 *0.9*	**1.2** *1*	**1.2** *0.7*	1.5 *1.2*	1.6 *0.9*
	Automated	0 *3*	0.9 *3.8*	1.6 *1.4*	2.3 *1.4*	**2** *2.3*	**3** *3.1*	2.4 *2.7*	3.4 *3.3*
Immobile	Manual	0.2 *0.2*	0.2 *0.2*	0.4 *0.4*	0.3 *0.3*	**0.3** *0.3*	**0.2** *0.2*	0.4 *0.4*	0.4 *0.3*
	Reviewed	-0.6 *0.8*	-0.6 *0.9*	1.3 *1*	1.5 *0.9*	**1.1** *0.9*	**1.4** *0.8*	1.5 *1.3*	1.8 *1*
	Automated	-1.4 *1*	-2.1 *2.7*	1.8 *1.2*	2.8 *1.7*	**1.7** *1.1*	**3.2** *2.1*	2.3 *1.5*	4 *2.5*
Mobile	Manual	-0.2 *0.2*	-0.2 *0.2*	0.4 *0.4*	0.3 *0.3*	**0.3** *0.3*	**0.2** *0.2*	0.4 *0.4*	0.4 *0.3*
	Reviewed	0.6 *1*	0.7 *1*	1.4 *1.4*	1.1 *0.7*	**1.3** *1.2*	**1.1** *1*	1.7 *1.6*	1.4 *1.1*
	Automated	1.5 *2.7*	4.2 *5*	1.8 *1.7*	2.3 *1.5*	**2.1** *2.7*	**4.5** *4.8*	2.5 *3.1*	5.2 *4.8*

[a] Distribution of surface grains, *immobile* and *mobile*, for the 3 delineation procedures tested. For the surface, the manual and control grains are the same. [b] The manual procedure corresponds to *manual* delineation + automatic grain categorization, *automated* procedure corresponds to *automated* delineation + automatic grain categorisation and *reviewed* procedure correspond to *automated* delineation followed by 10 min of boundary correction + automatic grain categorization. [c] Average of grain frequency errors, for each metric, over the 10 grain fractions, corresponding to the general procedure errors for each procedure (*manual*, *automated*, *reviewed*) and each distribution (surface, *immobile*, *mobile*). The sd represent the standard deviation around the average. A low value indicates a constant error of prediction along grain fraction while greater value indicates disparity of performance estimation along grain fraction. [d] The procedure bias corresponds to the average of the black line in Figure 5.23 (main text) while *sd* indicate how constant or not are the black line along grain fractions. [e] The procedure MAE in black bold correspond to the value of the column in Figure 5.21 (*main text*)]

Table 5.6

Distribution [a]	Delination procedure [b]	Procedure Bias (B) [c]				Procedure Irreducible error (e) [c]				Procedure Accuracy error (MAE) [c, d]				Procedure RMSE [c]			
		mm (sd)		% (sd)		mm (sd)		% (sd)		mm (sd)		% (sd)		mm (sd)		% (sd)	
		Abn	Gbn	Abn	Gbn	Abn	Gbn	Abn	Gbn	Abn	Gbn	Abn	Gbn	Abn	Gbn	Abn	Gbn
Surface [e]	Reviewed	0.8 *0.8*	0.6 *1.2*	2 *2.7*	2.3 *2.4*	1.3 *0.7*	2.1 *2.0*	5.2 *1.6*	3.4 *1.5*	1.3 *0.7*	2.1 *1.5*	**5.0** *1.0*	**3.9** *1.6*	1.6 *0.9*	2.5 *1.9*	6.1 *1.3*	4.6 *1.8*
	Automated	-2.8 *1.1*	9.3 *13.0*	-11.0 *4.1*	9.5 *12.7*	3.2 *1.5*	10.3 *14.8*	10.2 *1.6*	12.4 *10.2*	3.2 *1.5*	10.6 *12.1*	**12.3** *2.9*	**13.9** *8.9*	4.3 *1.7*	14.6 *19.1*	15.2 *3.6*	17.7 *13.9*
Immobile	Manual	0.0 *0.3*	-0.1 *0.2*	0.2 *1.1*	-0.3 *0.5*	1.0 *0.4*	0.5 *0.3*	3.3 *1.9*	1.1 *0.9*	0.8 *0.3*	0.4 *0.2*	**2.7** *1.6*	**0.9** *0.7*	1.0 *0.4*	0.6 *0.3*	3.4 *1.9*	1.2 *1.0*
	Reviewed	3.6 *1.4*	3.9 *3.5*	12.5 *3.0*	7.6 *4.4*	3.0 *1.2*	4.7 *5.3*	9.8 *2.2*	6.6 *3.0*	4.0 *1.4*	4.8 *3.2*	**13.7** *3.4*	**8.5** *3.9*	4.7 *1.7*	6.4 *6.0*	16.0 *3.2*	10.3 *4.8*
	Automated	0.0 *1.3*	-0.3 *5.0*	1.5 *3.2*	1.3 *4.5*	2.9 *1.9*	9.2 *8.2*	8.4 *2.9*	11.3 *4.9*	2.5 *1.5*	8.1 *6.8*	**7.4** *2.5*	**10.3** *4.0*	3.1 *2.1*	9.9 *8.9*	9.0 *3.2*	12.1 *5.1*
Mobile	Manual	-0.4 *0.4*	-0.6 *0.6*	-1.4 *1.1*	-1.6 *1.1*	0.6 *0.6*	1.5 *1.5*	1.6 *1.3*	3.1 *2.4*	0.4 *0.4*	1.0 *1.0*	**1.5** *1.1*	**2.5** *1.8*	0.7 *0.7*	1.6 *1.6*	2.1 *1.7*	3.6 *2.5*
	Reviewed	1.4 *1.8*	7.6 *6.0*	5.8 *6.8*	27.0 *13.3*	1.0 *1.0*	6.8 *6.5*	5.1 *2.5*	23.0 *14.1*	1.6 *1.7*	8.8 *7.2*	**7.3** *5.5*	**28.7** *14.0*	1.9 *2.0*	10.4 *8.7*	8.7 *6.0*	36 *18.6*
	Automated	0.8 *3.5*	35.5 *33.9*	1.1 *###*	92.5 *63.4*	1.8 *1.3*	19.4 *21.7*	9.0 *2.2*	53.6 *45.9*	2.2 *2.9*	35.5 *33.9*	**10.1** *6.7*	**92.6** *63.3*	2.7 *3.1*	40.7 *40.0*	12.7 *6.9*	107.5 *77.3*

[a] Distribution of surface grains, *immobile* and *mobile*, for the 3 delineation procedures tested. For the surface, the manual and control grains are the same. [b] The manual procedure corresponds to *manual* delineation + automatic grain categorization, *automated* procedure corresponds to *automated* delineation + automatic grain categorization and *reviewed* procedure correspond to *automated* delineation followed by 10 min of boundary correction + automatic grain categorization. [c] Average of percentiles estimate errors, for each metric, over the 15 extracted percentiles, corresponding to the general procedure errors for each procedure (*manual*, *automated*, *reviewed*) and each distribution (surface, *immobile*, *mobile*). The sd represent the standard deviation around the average. A low value indicates a constant error of prediction along percentiles while greater value indicates disp arity of performance estimation along percentiles. [d] The procedure MAE in black bold correspond to the value of the column in Figure 5.21 (*main text*). The procedure bias corresponds to the average of the black line in Figure 5.23 (*main text*) while the sd indicate how constant or not are the black line along grain fractions. [e] The performance of the *automated* and *reviewed* procedures for estimating surface percentiles can be compared with the performance data presented in the companion paper.

S-5.2.7.4.3 Fractional dynamics

Table 5.7

Mobility[a]	Delination procedure[b]	Procedure Bias (B)[c]		Procedure Irreducible error (e)[c]		Procedure Accuracy error (MAE)[c,d]		Procedure RMSE[c]	
		Abn	Gbn	Abn	Gbn	Abn	Gbn	Abn	Gbn
		% *(sd)*	% *(sd)*	% *(sd)*	% *(sd)*	% *(sd)*	% *(sd)*	% *(sd)*	% *(sd)*
Immobile	Manual	1.6 *1.5*	1.4 *1.3*	3.1 *1.9*	2.7 *1.9*	**2.3** *1.7*	**2.1** *1.7*	3.6 *2.2*	3.1 *2.2*
	Reviewed	-5.7 *3.4*	-6.2 *3.7*	8.3 *4.8*	8.2 *4.8*	**8** *4.6*	**8.3** *4.9*	10.2 *5.6*	10.4 *5.9*
	Automated	-18.4 *11.7*	-20 *11.6*	20.1 *11.3*	20.8 *11.1*	**20.3** *11.1*	**21.6** *11.1*	27.8 *15.1*	29.6 *14.5*
Mobile	Manual	-1.6 *1.5*	-1.4 *1.3*	3.1 *1.9*	2.7 *1.9*	**2.3** *1.7*	**2.1** *1.7*	3.6 *2.2*	3.1 *2.2*
	Reviewed	5.7 *3.4*	6.2 *3.7*	8.3 *4.8*	8.2 *4.8*	**8** *4.6*	**8.3** *4.9*	10.2 *5.6*	10.4 *5.9*
	Automated	17.2 *10.4*	18.8 *10.6*	19.4 *9.9*	20.1 *9.8*	**19.1** *10*	**20.4** *10.2*	26.5 *13.1*	28.3 *12.6*

[a] The *manual* procedure corresponds to *manual* delineation + automatic grain categorization, *automated* procedure corresponds to *automated* delineation + automatic grain categorization, and *reviewed* procedure correspond to *automated* delineation followed by 10 min of boundary correction + automatic grain categorization. [b] Average of the fractional dynamic estimate's errors, for each metric, over the 10 grain fractions, corresponding to the general procedure errors for each procedure (*manual*, *automated*, *reviewed*) and each distribution (*immobile*, *mobile*). The sd represent the standard deviation around the average. A low value indicates a constant error of prediction along grain fractions while greater value indicates disparity of performance estimation grain fraction. [c] The procedure MAE in black bold correspond to the value of the column in Figure 5.21 (*main text*)

S-5.2.7.4.4 Relative fractional dynamics

Table 5.8

Mobility[a]	Delination procedure[b]	Procedure Accuracy error[c]	
		Abn	Gbn
		ratio *(sd)*	ratio *(sd)*
Immobile	Manual	**1.10** *0.40*	**1.52** *0.94*
	Reviewed	**1.14** *0.29*	**1.43** *0.82*
	Automated	**1.13** *0.47*	**1.40** *0.97*
Mobile	Manual	**1.00** *0.03*	**1.01** *0.03*
	Reviewed	**1.60** *0.91*	**1.50** *0.91*
	Automatied	**2.84** *2.08*	**2.60** *2.19*

[a] Groups of *immobile* and *mobile* grain, for the 3 delineation procedures tested. [b] The *manual* procedure corresponds to *manual* delineation + automatic grain categorization, *automated* procedure corresponds to *automated* delineation + automatic grain categorization, and *reviewed* procedure correspond to *automated* delineation followed by 10 min of boundary correction + automatic grain categorization. [c] Average of the relative fractional dynamic error ratio over the 10 grain fractions, corresponding to the general procedure errors for each procedure (*manual*, *automated*, *reviewed*) and each distribution (*immobile*, *mobile*). The sd represent the standard deviation around the average. A low value indicates a constant error of prediction along grain fractions while greater value indicates disparity of performance estimation grain fraction. Theses value correspond to the column in Figure 5.21 (*main text*)

S-5.2.7.5 Discussion

S-5.2.7.5.1 Performance limitation and recommendation

S-5.2.7.5.1.1 Manual procedure

None

S-5.2.7.5.1.2 Automatic procedure

None

S-5.2.7.5.1.3 Reviewed procedure

S-Recommendation for the revision of the grain contour

Figure 5.26 **A** (*main text*) is a localized view of the result of the *reviewed* procedure obtained on sample S1. The black outline represents the T0 or PRE event grain (see small Pre square on the left). The background image represents the T1 or POST event grain (see in T1 the small square on the right). The dots (blue and red) represent some examples of comparison results. Only *mobile* grains are expected (red dot). However, the classification results in *immobile* grains (blue dot). Here, the grains concerned were correctly delineated. The yellow and red layers highlight the pre- and post-event misclassified contours of the grains. The shapes of these grains are too similar to be considered as different. In this case, the correction of the grain boundaries will never correct these errors. The surface and eccentricity likeness thresholds are too large in these cases, perhaps the addition of another shape descriptor could have allowed a correct classification. After the classification, a check and correction of the attribute field can be considered to inverse the classification results.

Figure 5.26 **B** (*main text*) shows errors, which this time are theoretically avoidable in the *reviewed* procedure. The picture shows the sample S10 where only *immobile* grains are expected (blue dot), but the classification gave some grains as *mobile* (red dot). The point numbered 2 represents a small particle detected in the post-event (red contour). However, this small particle does not appear in the pre-event layer (no yellow contour). The image processing leading to the amplification of the edges by the application of filters and the image binarization (see companion paper) resulted in the detection of a particle identified as smaller than 8mm, therefore discarded. This small particle, present only in the post-event, is therefore considered *mobile* (i.e., new). The operator could either delete this small red polygon to avoid creating a *mobile* particle or add a small yellow polygon. Point 3 represents a particle detected in both photos but whose shapes are too different to be classified as identical. The operator would have to modify one of them to allow classification as identical. These two types of error, 2 and 3, are related to the *automated* delimitation and to the lack of time of the operator who preferred to correct larger, more visible particles and did not linger on the small grains.

Point 4 corresponds to a particle identified in both layers. However, it seems that in the pre-event layers (yellow outline), the particle has been entirely redrawn by hand by guessing its part hidden under the adjacent much larger particle in the upper left. In the post-event layer (red outline), the particle has not been modified. This has generated polygons of too different shapes to be considered as one and the same particle. This time, the misclassification comes from the operator's correction and not from the original *automated* delimitation. Similarly, point 5 shows a grain that in both the T0 and T1 automatic delineations was joined to the adjacent larger grain. During the review process, grains were separated and the grain at point 5 was only redrawn in the T1 image, which mistakenly resulted in a *mobile* interpretation. As for error in point 4, it is therefore advisable to first

generate the *automated* delineation of the grains of the two photos to then display both to correcting them at the same time with consistency to avoids such errors (4 and 5) and allows to run through both layers at the same time rather than one after the other, which is a time grain.

In order to be efficient during this correction work, it is advisable to apply a virtual grid to the photos and to carry out the correction line by line (or column by column). We believe that the implementation of the ImageGrains algorithm (Mair et al., 2023) for grain detection could greatly eliminate these problems.

Finally, Figure 5.26 **C** (main text) shows a type of error that is not related to the *automated* delimitation or its correction. Once again, the image corresponds to sample S10 where all the grains are *immobile* (blue dot). However, some small grains are given *mobile* (red dot). The grains appear in both pre and post layer and are correctly delimited by the *automated* delimitation. However, the post image is not correctly aligned with the pre image. It is possible to see the shift on the coarse grain with small white arrows. The yellow outlines are shifted upwards with respect to the red outline. The offset is between 5 and 10 mm. The centroids of T1 polygons are therefore no longer superimposed on the small yellow polygons. They are considered *mobile*. This alignment between the pair of photos of S10 is not the one presented in this paper. During the alignment of these photos, we saved the two not fully aligned photos and then generated the automatic delineation and correction in 10 minutes to see the impact of the misalignment. Misalignment can increase the fractional mobility of fine grain fractions by 2/3. For example, the well aligned sample S10 (presented in this paper) showed a proportion of *mobile* grain between 8 and 11 mm of more than 25% (*main text*, Figure 5.24 **A**, S10). With less well aligned photos, as seen in Figure 5.26 **C**, this fraction of grain can show a *mobile* proportion of more than 75%. As a reminder, 0% was expected. A correct photo alignment is essential to obtain accurate data on fractional stability/mobility, especially for small fractions. Worth to notice that such a small grain may constitute marginal bedload that may have a role in rivers affected by frequent low-intensity flows such as for instance hydropeaks, hence putting the entrainment threshold very low, but in any case, with ecosystemic implications (Gibbins et al., 2007a). It can sometimes seem difficult to align the photos properly. Often this is because the photos are not taken from the same point of view, especially when images are not perfectly nadir. Two different angles of view make it difficult to get a correct uniform alignment on the entire image. It might be possible to add a small spirit level to the camera. This could be a less cumbersome and quicker alternative for operators than a structure or a tripod to get a correct perpendicular picture from the ground.

S-5.2.7.5.2 Immobility, Stability, Mobility, and Instability

None

S-5.2.7.5.3 Use of data

None

S-5.2.7.6 Concluding remarks

None

REFERENCES

Andrews, E.D. and **Parker, G.** (1987) Formation of a coarse surface layer as the response to gravel mobility. In: John Wiley & Sons (Ed. C.R. Thorne, J.C. Bathurst, and R.D. Hey), 269–325. ,https://cir.nii.ac.jp/crid/1574231874050281856

Ashworth, P.J., **Ferguson, R.I.**, **Ashmore, P.E.**, **Paola, C.**, **Powell, D.M.** and **Prestegaards, K.L.** (1992) Measurements in a Braided River chute and lobe: 2. Sorting of bed load during entrainment, transport, and deposition. *Water Resour. Res.*, **28**, 1887–1896. DOI:0043-1397/93/92WR02748

Brenna, A., **Surian, N.** and **Mao, L.** (2019) Virtual Velocity Approach for Estimating Bed Material Transport in Gravel-Bed Rivers: Key Factors and Significance. *Water Resour. Res.*, **55**, 1651–1674. DOI:10.1029/2018WR023556

Bunte, K. and **Abt, S.R.** (2001) Sampling surface and subsurface particle-size distributions in wadable gravel-and cobble-bed streams for analyses in sediment transport, hydraulics, and streambed monitoring. *U.S. Department of Agriculture, Forest Service, Rocky Mountain Research Station*, Ft. Collins, CO. DOI:10.2737/RMRS-GTR-74

Bunte, K., **Swingle, K.W.** and **Abt, S.R.** (2007) Guidelines for using bedload traps in coarse-bedded mountain streams: Construction, installation, operation, and sample processing. *USDA For. Serv. - Gen. Tech. Rep. RMRS-GTR*, 1–97.

Burger, W. and **Burge, M.J.** (2016) Digital Image Processing. An Algorithmic Introduction Using Java. *Springer London*, London, 812 pp. DOI:10.1007/978-1-4471-6684-9

Buscombe, D. (2008) Estimation of grain-size distributions and associated parameters from digital images of sediment. *Sediment. Geol.*, **210**, 1–10. DOI:10.1016/j.sedgeo.2008.06.007

Buscombe, D. (2013) Transferable wavelet method for grain-size distribution from images of sediment surfaces and thin sections, and other natural granular patterns. *Sedimentology*, **60**, 1709–1732. DOI:10.1111/sed.12049

Butler, J.B., **Lane, S.N.** and **Chandler, J.H.** (2001) Automated extraction of grain-size data from gravel surfaces using digital image processing. *J. Hydraul. Res.*, **39**, 519–529. DOI:10.1080/00221686.2001.9628276

Cassel, M., **Lavé, J.**, **Recking, A.**, **Malavoi, J.-R.** and **Piégay, H.** (2021) Bedload transport in rivers, size matters but so does shape. *Sci Rep*, **11**, 508. DOI:10.1038/s41598-020-79930-7

Cerney, D.L. (2010) The Use of Repeat Photography in Contemporary Geomorphic Studies: An Evolving Approach to Understanding Landscape Change: Repeat photography use in geomorphic studies. *Geogr. Compass*, **4**, 1339–1357. DOI:10.1111/j.1749-8198.2010.00376.x

Chaki, J. and **Dey, N.** (2019) A Beginner's Guide to Image Shape Feature Extraction Techniques. *CRC Press*, 147 pp. DOI:10.1201/9780429287794

Chang, F.-J. and **Chung, C.-H.** (2012) Estimation of riverbed grain-size distribution using image-processing techniques. *J. Hydrol.*, **440–441**, 102–112. DOI:10.1016/j.jhydrol.2012.03.032

Chang, W., **Cheng, J.**, **Allaire, J.**, **Sievert, C.**, **Schloerke, B.**, **Xie, Y.**, **Allen, J.**, **McPherson, J.**, **Dipert, A.** and **Borges, B.** (2023) shiny: Web application framework for r. **Error! Hyperlink reference not valid.**

Church, M.A., **McLean, D.G.** and **Wolcott, J.F.** (1987) River bed gravels: Sampling and analysis. In: John willey & son (Ed. C. Thorne, J.C. Bathurst, and R.D. Hey), *J. Wiley*, New York, NY, USA, 43–88. ,https://doi.org/10.1002/esp.3290140809

Church, M. and **Hassan, M.A.** (1992) Size and distance of travel of unconstrained clasts on a streambed. *Water Resour. Res.*, **28**, 299–303. DOI:10.1029/91WR02523

Church, M. and **Hassan, M.A.** (2002) Mobility of bed material in Harris Creek: MOBILITY OF BED MATERIAL IN HARRIS CREEK. *Water Resour. Res.*, **38**, 19-1-19-12. DOI:10.1029/2001WR000753

Church, M., **Hassan, M.A.** and **Wolcott, J.F.** (1998) Stabilizing self-organized structures in gravel-bed stream channels: Field and experimental observations. *Water Resour. Res.*, **34**, 3169–3179. DOI:10.1029/98WR00484

Cobb, D.G., **Galloway, T.D.** and **Flannagan, J.F.** (1992) Effects of Discharge and Substrate Stability on Density and Species Composition of Stream Insects. *Can. J. Fish. Aquat. Sci.*, **49**, 1788–1795. DOI:10.1139/f92-198

Deal, E., **Venditti, J.G.**, **Benavides, S.J.**, **Bradley, R.**, **Zhang, Q.**, **Kamrin, K.** and **Perron, J.T.** (2023) Grain shape effects in bed load sediment transport. *Nature*, **613**, 298–302. DOI:10.1038/s41586-022-05564-6

Detert, M. and **Weibrecht, V.** (2013) User guide to gravelometric image analysis by basegrain. *Adv. Sci. Res.*, **ISBN 978-1**, 1789–1795.

Dey, S. and **Ali, S.Z.** (2019) Bed sediment entrainment by streamflow: State of the science. *Sedimentology*, **66**, 1449–1485. DOI:10.1111/sed.12566

Dietrich, W.E., **Kirchner, J.W.**, **Ikeda, H.** and **Iseya, F.** (1989) Sediment supply and the development of the coarse surface layer in gravel-bedded rivers. *Nature*, **340**, 215–217. DOI:10.1038/340301a0

Diplas, P. and **Fripp, J.B.** (1992) Properties of Various Sediment Sampling Procedures. *J. Hydraul. Eng.*, **118**, 955–970. DOI:10.1061/(asce)0733-9429(1992)118:7(955)

Downes, B.J., **Glaister, A.** and **Lake, P.S.** (1997) Spatial Variation in the Force Required to Initiate Rock Movement in 4 Upland Streams: Implications for Estimating Disturbance Frequencies. *Journal of the North American Benthological Society*, **16**, 203–220. DOI:10.2307/1468252

Duncan, M.J. and **Suren, A.M.** (1999) Assessment of Streambed Stability in Steep, Bouldery Streams: Development of a New Analytical Technique. *Journal of the North American Benthological Society*, **18**, 445–456. DOI:10.2307/1468377

Folk, R.L. and **Ward, W.C.** (1957) Brazos River bar [Texas]; a study in the significance of grain size parameters. *Journal of Sedimentary Research*, 3–26. DOI: https://doi.org/10.1306/74D70646-2B21-11D7-8648000102C1865D

Gibbins, C. (2015) Coupling Biological and Physical Processes: The Ecological Significance of River Channel Hydraulics and Fluvial Dynamics. In: *Rivers – Physical, Fluvial and Environmental Processes* (Ed. P. Rowiński and A. Radecki-Pawlik), *Springer International Publishing*, Cham, 479–496. DOI:10.1007/978-3-319-17719-9_19

Gibbins, C., **Scott, E.**, **Soulsby, C.** and **Mcewan, I.** (2005) The relationship between sediment mobilisation and the entry of Baetis mayflies into the water column in a laboratory flume. *Hydrobiologia*, **533**, 115–122. DOI:10.1007/s10750-004-2401-1

Gibbins, C., **Vericat, D.** and **Batalla, R.J.** (2007) When is stream invertebrate drift catastrophic? The role of hydraulics and sediment transport in initiating drift during flood events. *Freshwater Biol*, **52**, 2369–2384. DOI:10.1111/j.1365-2427.2007.01858.x

Gilbert, G.K. (1914) The Transportation of Debris by Running Water. *California Water Science Center, U.S. Geological Survey*. DOI:10.3133/pp86

Graham, D.J., **Reid, I.** and **Rice, S.P.** (2005a) Automated Sizing of Coarse-Grained Sediments: Image-Processing Procedures. *Math. Geol.*, **37**, 1–28. DOI:10.1007/s11004-005-8745-x

Graham, D.J., **Rice, S.P.** and **Reid, I.** (2005b) A transferable method for the automated grain sizing of river gravels. *Water Resour. Res.*, **41**, 1–12. DOI:10.1029/2004WR003868

Graham, D.J., **Rollet, A.-J.**, **Piégay, H.** and **Rice, S.P.** (2010) Maximizing the accuracy of image-based surface sediment sampling techniques. *Water Resour. Res.*, **46**, 1–15. DOI:10.1029/2008WR006940

Graham, D.J., **Rollet, A.-J.**, **Rice, S.P.** and **Piégay, H.** (2012) Conversions of Surface Grain-Size Samples Collected and Recorded Using Different Procedures. *J. Hydraul. Eng.*, **138**, 839–849. DOI:10.1061/(ASCE)HY.1943-7900.0000595

Hassan, M.A. and **Ergenzinger, P.** (2003) Use of tracers in fluvial geomorphology. In: (Ed. G.M. Kondolf and H. Piégay), *John Wiley & Sons, Ltd*, Chichester, UK, 397–423. DOI:10.1002/0470868333.ch14

Hassan, M.A. and **Roy, A.G.** (2016) Coarse particle tracing in fluvial geomorphology. In: *Tools in Fluvial Geomorphology*, 1st edn. (Ed. G.M. Kondolf and H. Piégay), *Wiley*, 306–323. DOI:10.1002/9781118648551.ch14

Helley, E.J. and **Smith, W.** (1971) Development and calibration of a pressure-difference bedload sampler. *Water Resour.Div, U. S. Geol. Surv.*, Menlo Park, Calif, https://pubs.usgs.gov/of/1973/0108/report.pdf

Ibbeken, H. and **Denzer, P.** (1988) Clast measurement: A simple manual device and its semiautomatic electronic equivalent. *J. Sediment. Res.*, **58**, 751–752. DOI:10.1306/212f8e36-2b24-11d7-8648000102c1865d

Ibbeken, H. and **Schleyer, R.** (1986) Photo - sieving: A method for grain - size analysis of coarse - grained, unconsolidated bedding surfaces. *Earth Surf. Process. Landf.*, **11**, 59–77. DOI:10.1002/esp.3290110108

Kellerhals, R. and **Bray, D.I.** (1971) Sampling Procedures for Coarse Fluvial Sediments. *J. Hydraul. Div.*, **97**, 1165–1180. DOI:10.1061/JYCEAJ.0003044

Komar, P.D. (1987) Selective gravel entrainment and the empirical evaluation of flow competence. *Sedimentology*, **34**, 1165–1176. DOI:10.1111/j.1365-3091.1987.tb00599.x

López, R., **Ville, F.**, **Garcia, C.**, **Batalla, R.J.** and **Vericat, D.** (2023) Bed-material entrainment in a mountain river affected by hydropeaking. *Science of The Total Environment*, **856**, 159065. DOI:10.1016/j.scitotenv.2022.159065

Lorang, M.S. and **Hauer, F.R.** (2003) Flow competence and streambed stability: An evaluation of technique and application. *Journal of the North American Benthological Society*, **22**, 475–491. DOI:10.2307/1468347

MacKenzie, L.G., **Eaton, B.C.** and **Church, M.** (2018) Breaking from the average: Why large grains matter in gravel-bed streams: Breaking from the average. *Earth Surf. Process. Landforms*, **43**, 3190–3196. DOI:10.1002/esp.4465

Mair, D., **Witz, G.**, **Do Prado, A.H.**, **Garefalakis, P.** and **Schlunegger, F.** (2023) Automated detecting, segmenting and measuring of grains in images of fluvial sediments: The potential for large and precise data from specialist deep learning models and transfer learning. *Earth Surface Processes and Landforms*, esp.5755. DOI:10.1002/esp.5755

Mao, L. (2012) The effect of hydrographs on bed load transport and bed sediment spatial arrangement. *J. Geophys. Res. Earth Surf.*, **117**, 1–16. DOI:10.1029/2012JF002428

Mao, L. (2018) The effects of flood history on sediment transport in gravel-bed rivers. *Geomorphology*, **322**, 196–205. DOI:10.1016/j.geomorph.2018.08.046

Mao, L. and **Lenzi, M.A.** (2007) Sediment mobility and bedload transport conditions in an alpine stream. *Hydrol. Process.*, **21**, 1882–1891. DOI:10.1002/hyp.6372

Mao, L., **Picco, L.**, **Lenzi, M.A.** and **Surian, N.** (2017) Bed material transport estimate in large gravel-bed rivers using the virtual velocity approach. *Earth Surf. Process. Landf.*, **42**, 595–611. DOI:10.1002/esp.4000

Mao, L. and **Surian, N.** (2010) Observations on sediment mobility in a large gravel-bed river. *Geomorphology*, **114**, 326–337. DOI:10.1016/j.geomorph.2009.07.015

Matthaei, C.D. and **Townsend, C.R.** (2000) Long-term effects of local disturbance history on mobile stream invertebrates. *Oecologia*, **125**, 119–126. DOI:10.1007/PL00008883

Miller, M.C., **McCAVE, I.N.** and **Komar, P.D.** (1977) Threshold of sediment motion under unidirectional currents. *Sedimentology*, **24**, 507–527. DOI:10.1111/j.1365-3091.1977.tb00136.x

Ockelford, A.-M. (2011) **Ockelford, A.-M.** (2011) The impact of stress history on non cohesive sediment bed stability and structure. PhD thesis, University of Glasgow ,http://theses.gla.ac.uk/id/eprint/2577

Ockelford, A.M. and **Haynes, H.** (2013) The impact of stress history on bed structure. *Earth Surf. Process. Landf.*, **38**, 717–727. DOI:10.1002/esp.3348

Ockelford, A., **Woodcock, S.** and **Haynes, H.** (2019) The impact of inter-flood duration on non-cohesive sediment bed stability. *Earth Surf. Process. Landf.*, **44**, 2861–2871. DOI:10.1002/esp.4713

Parker, G. (2008) Transport of Gravel and Sediment Mixtures. In: *Sedimentation Engineering*, *American Society of Civil Engineers*, Reston, VA, 165–251. DOI:10.1061/9780784408148.ch03

Peckarsky, B.L., **McIntosh, A.R.**, **Horn, S.C.**, **McHugh, K.**, **Booker, D.J.**, **Wilcox, A.C.**, **Brown, W.** and **Alvarez, M.** (2014) Characterizing disturbance regimes of mountain streams. *Freshwater Science*, **33**, 716–730. DOI:10.1086/677215

Pfankuch, D. (1975) Stream reach inventory and channel stability evaluation, Northern Region Forest Service, US Department of Agriculture, Washington, DC. ,https://wildlandhydrology.com/resources/docs/Assessment/Pfankuch_1975.pdf

Purinton, B. and **Bookhagen, B.** (2019) Introducing PebbleCounts: A grain-sizing tool for photo surveys of dynamic gravel-bed rivers. *Earth Surf. Dynam.*, **7**, 859–877. DOI:10.5194/esurf-7-859-2019

Quinlan, E., **Gibbins, C.**, **Malcolm, I.**, **Batalla, R.**, **Vericat, D.** and **Hastie, L.** (2015) A review of the physical habitat requirements and research priorities needed to underpin conservation of the endangered freshwater pearl mussel Margaritifera margaritifera. *Aquatic Conservation: Marine and Freshwater Ecosystems*, **25**, 107–124. DOI:10.1002/aqc.2484

R Core Team (2021) R: A Language and Environment for Statistical Computing. ,https://www.R-project.org/

Schwendel, A.C. (2012) Measurement of Stream Bed Stability Characteristics Relevant to Lotic Ecosystems. In: *Management of Mountain Watersheds* (Ed. J. Krecek, M.J. Haigh, T. Hofer, and E. Kubin), *Springer Netherlands*, Dordrecht, 113–122. DOI:10.1007/978-94-007-2476-1_9

Sime, L.C. and **Ferguson, R.I.** (2003) Information on Grain Sizes in Gravel-Bed Rivers by Automated Image Analysis. *J. Sediment. Res.*, **73**, 630–636. DOI:10.1306/112102730630

Stähly, S., **Friedrich, H.** and **Detert, M.** (2017) Size Ratio of Fluvial Grains' Intermediate Axes Assessed by Image Processing and Square-Hole Sieving. *J. Hydraul. Eng.*, **143**, 06017005. DOI:10.1061/(ASCE)HY.1943-7900.0001286

Strom, K.B., **Kuhns, R.D.** and **Lucas, H.J.** (2010) Comparison of Automated Image-Based Grain Sizing to Standard Pebble-Count Methods. *J. Hydraul. Eng.*, **136**, 461–473. DOI:10.1061/(ASCE)HY.1943-7900.0000198

Team, T.G.D. (2019) GIMP. https://www.gimp.org

Therneau, T. and **Atkinson, B.** (2019) Rpart: Recursive Partitioning and Regression Trees. ,https://CRAN.R-project.org/package=rpart

Tyagi, V. (2018) Understanding Digital Image Processing. *CRC Press*. DOI:10.1201/9781315123905

Vázquez-Tarrío, D. and **Batalla, R.J.** (2019) Assessing Controls on the Displacement of Tracers in Gravel-Bed Rivers. *Water*, **11**, 1598. DOI:10.3390/w11081598

Vázquez-Tarrío, D., **Fernández-Iglesias, E.**, **Fernández García, M.** and **Marquínez, J.** (2019a) Quantifying the Variability in Flow Competence and Streambed Mobility with Water Discharge in a Gravel-Bed Channel: River Esva, NW Spain. *Water*, **11**, 2662. DOI:10.3390/w11122662

Vázquez-Tarrío, D., **Recking, A.**, **Liébault, F.**, **Tal, M.** and **Menéndez-Duarte, R.** (2019b) Particle transport in gravel-bed rivers: Revisiting passive tracer data: Particle transport in gravel-bed rivers. *Earth Surf. Process. Landforms*, **44**, 112–128. DOI:10.1002/esp.4484

Vericat, D., **Batalla, R.J.** and **Garcia, C.** (2008) Bed-material mobility in a large river below dams. *Geodinamica Acta*, **21**, 3–10. DOI:10.3166/ga.21.3-10

Vericat, D., **Ville, F.**, **Palau-Ibars, A.** and **Batalla, R.J.** (2020) Effects of hydropeaking on bed mobility: Evidence from a pyrenean river. *Water*, **12**, 178. DOI:10.3390/w12010178

W. C. Krumbein (1941) Measurement and Geological Significance of Shape and Roundness of Sedimentary Particles. SEPM JSR. doi: 10.1306/D42690F3-2B26-11D7-8648000102C1865D DOI:10.1306/D42690F3-2B26-11D7-8648000102C1865D

Warrick, J.A., **Rubin, D.M.**, **Ruggiero, P.**, **Harney, J.N.**, **Draut, A.E.** and **Buscombe, D.** (2009) Cobble cam: Grain-size measurements of sand to boulder from digital photographs and autocorrelation analyses. *Earth Surf. Process. Landf.*, **34**, 1811–1821. DOI:10.1002/esp.1877

Wathen, S.J., **Ferguson, R.I.**, **Hoey, T.B.** and **Werritty, A.** (1995) Unequal Mobility of Gravel and Sand in Weakly Bimodal River Sediments. *Water Resour. Res.*, **31**, 2087–2096. DOI:10.1029/95WR01229

Wilcock, P.R. (1997) The components of fractional transport rate. *Water Resour. Res.*, **33**, 247–258. DOI:10.1029/96WR02666

Wilcock, P.R. and **McArdell, B.W.** (1993) Surface-based fractional transport rates: Mobilization thresholds and partial transport of a sand-gravel sediment. *Water Resour. Res.*, **29**, 1297–1312. DOI:10.1029/92WR02748

Wolman, M.G. (1954) A method of sampling coarse river-bed material. *Trans. Am. Geophys. Union*, **35**, 951. DOI:10.1029/TR035i006p00951

Zingg, T. (1935) Beitrag zur Schotteranalyse. Doctoral thesis, ETH Zurich DOI:10.3929/ETHZ-A-000103455

Chapter 6

Longitudinal mobility dynamics

Detail of the Riverbed in the Pyramides reach (Upper Ésera River) after a high magnitude hydropeak superimposed on a natural wave, showing a large particle mobilized over few metres from a painted patch and deposited as a cluster. The white arrow indicates the direction of flow, 09/11/2020. Author: Damià Vericat

Chapter 6 presents a paper in preparation; therefore, the authors and abstract are not yet provided. PhotoMOB is applied in two geomorphologically contrasted mountain rivers subjected to hydropeaks and floods in order to study downstream changes on bed mobility.

Tentative title:

Longitudinal mobility patterns in two mountain hydropeaked rivers (Southern Pyrenees)

6.1 INTRODUCTION

The release of water from a Hydropower Plant (HP) to generate electricity during peak demand, known as hydropeaking, artificially induces sudden fluctuations in flow in downstream river reaches. These hydropeaks are manifested by the propagation of a wave that rapidly inundates the lateral margins of the channels and causes hydraulic changes such as water depth, velocity and bed shear stress (Hauer et al., 2013; Le Coarer et al., 2023; Vanzo et al., 2016b). Once the energy peak demand has passed, the turbines are switched off and, in the case of storage or modified run-of-river schemes (see Section 1.1.2.2.1), only a small flow reserved for ecology (ecological flow) is maintained, leading to a rapid withdrawal of water from the margins and a decrease in the magnitude of hydraulic variables (velocity, depth, shear stress). The hydrological characteristics of hydropeaks (i.e. magnitude, frequency, duration, timing) can vary according to the type of hydropower system and according to hydrograph forms that can vary between seasons and years (Tena et al., 2022, Section 3.1.1; this thesis). The morphology of rivers and their valleys can also influence the propagation of these waves by favouring or not the longitudinal attenuation of peak flows, velocity gradients and duration (Section 3.2.1).

These physical variations (abiotic environment) can affect the biotic environment. Physical aquatic habitats are highly dependent on water depth, current velocity, bed forms and substrate size, structure and stability (Jowett et al., 1991, 1991; Quinn and Hickey, 1994). During hydropeaks, habitat availability changes (Bätz et al., 2023) and organisms intentionally move to other parts of the channel and lateral margins, known as *ramping areas*, to find better conditions (Boavida et al., 2017). In some cases, the abundance and diversity of aquatic communities, particularly benthic invertebrates, can be drastically reduced by catastrophic drift (unintentional displacement) when shear rates are too high, or even higher when they cause bed destabilization in channels or ramping areas (Béjar et al., 2017; Gibbins et al., 2007a). The ramping areas are at the interface between the aquatic, terrestrial and avian ecosystems, where different species, such as aquatic insects, depending on their stage of development (egg, larva, adult) and the time of year, can be more or less disturbed by the mobilization of the substrate, also affecting the entire food chain above them (Hauer et al., 2016; Kennedy et al., 2016).

In natural or less and non-modified systems, river bed particles are sequentially entrained, transported and deposited in the channel during competent flow events (Church, 2006). The frequency and intensity of their displacement depends, in addition to the hydraulic forces acting, on their shape, weight and arrangement with each other (Dey, 2014; Dey and Ali, 2019; Yager et al., 2018). The sediment mobility threshold corresponds to the transition between a stable state of the grains and the moment when sufficiently important hydraulic forces are reached to set them in motion. Flow competence (Gilbert, 1914) can be assessed by examining the coarsest grain sizes set in motion for given flow rates (Komar, 1987; Mao and Lenzi, 2007). However, these mobilized sizes do not imply that all grains in these fractions were mobile, as some may have remained stable (i.e. immobile). The degree of destabilization/mobilization of the bed for a given flow rate can be approximated by assessing the unstable proportion in relation to the bed as a whole or in relation to the unstable proportion per individual grain fraction (Haschenburger and Wilcock, 2003; MacKenzie et al., 2018; Wilcock and McArdell, 1993).

In practice, the degree of mobility is defined in relation to a reference value (Haschenburger and Wilcock, 2003). When less than 10% of the bed area or fraction entrains, the is considered stable and the transport *marginal*. When this proportion reaches 10%, mobility can be defined as partial, while a proportion above 90% represents full mobility. In addition, the relative degree of mobility per fraction can be expressed as the ratio between the proportion p_i of a given fraction in all transported grains (i.e. bed material transport) and its initial proportion on the bed surface F_i. When the proportion of a fraction i in the bed material transport is over-represented or at least equal to its proportion on the surface, it can be described as a fully mobile condition ($p_i/F_i \geq 1$). When it is under-represented ($p_i/F_i < 1$), it can be qualified as partially mobile (Wilcock and McArdell, 1993).

Previous studies on various Pyrenean rivers affected by hydropeaking, using the flow competence method, have shown that hydropeaks can be sufficiently competent to mobilize up to medium gravels ($< 20\ mm$) in the River Cinca with a wandering gravel bed pattern, and coarse gravels ($\approx 30\ mm$) in the River Ésera with a very narrow valley and pool-riffle succession. Contrarily, hydropeaks can entrain very coarse gravels (62 mm), as is the case of in the River Noguera Pallaresa, also with a pool-riffle configuration but with a steeper channel (López et al. 2020; López et al. (2023) corresponding to Chapter 4 and Vericat et al. 2020 in the Annex A of this thesis). However, the grain sizes that appeared to be mainly movable were close to the lower detection limit of the methods used to sample surface sediments and examine their mobility (pebble count, (Wolman, 1954) and tracing of individual painted grains (Hassan and Ergenzinger, 2003). In addition, these methods do not allow the degree of bed disturbance or its frequency to be quantified.

From a general perspective, taking into account river beds support aquatic habitats, several research questions have not yet been fully addressed for a biologically relevant characterization of the effect of hydropeaks on the dynamics of bed sediment mobility (Hayes et al., 2023): How do hydropeaks affect changes on bed grain composition in terms of sorting and particle size distribution? What key hydrological characteristics of hydropeaks can explain their effects on sediment mobilization? To what extent (competence/intensity) do hydropeaks affect substrate stability/mobility and how often compared to natural events (floods)? How do these effects evolve longitudinally? (i.e. downstream trends). How do hydropeaks affect the dynamics of sediment mobility in rivers with contrasting geomorphological contexts? (e.g. different degrees of confinement, channel with, grain size).

In order to tackle these questions, the influence of floods and hydropeaks on the dynamics of mobility in ramping areas is investigated. Downstream or longitudinal changes on mobility are assessed on two segments of about 10 km each in mountain rivers with contrasting geomorphological contexts. The recent *PhotoMOB* tool, which allows photographic sampling of bed sediment size and mobility (developed in Chapter 5, this Thesis), is used. Firstly, the grain size distributions obtained from the photographs were compared with those obtained from a traditional method (pebble count) to check their compatibility and thus allow future comparisons. Then, the rest of the study aims to answer the previously formulated questions.

6.2 MATERIAL AND METHODS

6.2.1 Study area and available data

6.2.1.1 The basins

The study was carried out in the basins of the Upper Cinca and its main tributary, the Upper Ésera, in the south-central Pyrenees (Figure 6.1 **A**). The two basins have similar altitudinal gradients. The outlet of the Cinca is near the village of Ainsa at an altitude of 526 m a.s.l, while the source of the river is 57.8 km upstream at Monte Perdido at 3 355 m a.s.l. The outlet of the Ésera is near the village of Santaliestra at an altitude of 539 m a.s.l. The source of the river is 79.9 km upstream at the peak of Aneto at 3 404 m a.s.l (the highest Pyrenean summit).

C River	Cinca			Ésera	
Hydropower					
Power plant	Laspuña			Campo	
Max. turbinable peak flow (m^3s^{-1})	26.0			20.0	
Segment					
Mean annual flow (m^3s^{-1})	24.8			15.8	
Direct valley length (km) [a]	9.2			13.6	
Valley length (Km)	9.5			17.9	
Talweg length (km)	10.0			18.5	
Valley sinuosity (-) [b]	1.03			1.32	
Main river courses sinuosity (-) [c]	1.05			1.03	
Median valley width (m)	197.4			56.7	
Median active width	63.2			34.1	
Slope (%)	0.70			0.73	
Channel morphology	Large bar of different types			Narrow bar of sediment in a position forced by the shape of the valley	
Study reaches					
Reaches	Laspuña US	Laspuña DS	Ainsa	Campo DS	Pyramides
Position:					
Distance from HP (km)	-0.1	0.3	10	1	12
Drainage area (km^2)	603.4	603.9	835.3	569.6	719.3
Elevation (m a.s.l)	601.3	599.1	529	671.5	583.5
Flow:					
Q_{50} (m^3 s^{-1})	3.4	15.5	18.6	11.5	13.8 [d]
$Q_{1y\ flood}$ (m^3 s^{-1}, % of Q_{50})	210 – 6 170%	210 – 1 355%	210 – 1 130%	100 – 870%	100 – 725%
Max_{hpk} Q_{max} (m^3 s^{-1}, % of Q_{50})	-	60 – 387%	67 – 360%	30 – 260%	36 – 260%
Med_{Hpk} Q_{max} (m^3 s^{-1}, % of Q_{50})	-	22 – 140%	23 – 124%	18 – 154%	19 – 138%
Geometry:					
Area sedimentary bar (m^2)	2 907.12	1 015.56	2 153.18	2 396.21	737.56
Base flow width (m)	15	35	34	15	15
Active width (m)	50	44	120	67	28
Slope (%)	0.86	0.82	0.70	0.6	0.6
Grain size distribution:					
D16 (mm)	15.2	28.7	19.6	28.2	24
D50 (mm)	34.6	114	41.2	61.3	51.6
D84 (mm)	69.7	215.8	77	117.9	102.4
Sorting ($\sigma_{F\&W}$)	2.1	2.7	2	2	2.1

Figure 6.1: Location of the study site. **A** Location of the two basins studied with the location of the study segments indicated by the grey rectangles. **B** Longitudinal schematic representation of the study segments (on the left the Cinca, and on the right the Ésera) with the position of the power stations and the reservoirs feeding them, as well as the water level measurement stations and the reaches studied with their distance from the power stations (coloured rectangle: Laspuña US and DS, Ainsa on the Cinca river and Campo DS, Pyramides on the Ésera river). **C**. Summary table of the characteristics of the segments and the reaches. [a] Direct length of the valley shown in part B for the Ésera segment. [b] Sinuosity of the valley calculated by the ratio of length of the valley to direct length of the valley. [c] Sinuosity of the main course calculated by the ratio of length at the thalweg to length of the valley. [d] Value calculated at the Santaliestra station with a longer data series of 2 years representative of Pyramides.

Both basins have 75% medium to very steep slopes (> 16°) and both have about 70% of their surface area above 1 500 m altitude, corresponding to the winter isotherm of 0 °C (García-Ruiz et al., 1986). On average, the annual volumes of water precipitated in liquid form are 1 034 and 776 hm^3 respectively in the basins drained by the Cinca and Ésera rivers. These two rivers are characterized by a nivo-pluvial hydrological regime, favored by high areas suitable for the constitution of a snow pack between winter and spring and the release of meltwater back into the river from mid-spring to the end of the season. The average annual discharge recorded at the Ebro Water Authority stations is 24.8 and 15.8 $m^3\ s^{-1}$ in the Cinca and Ésera segments, respectively, while the 1-year flood is of 210 et 100 $m^3\ s^{-1}$. The steep relief and these water inflows make these basins suitable for hydroelectric generation, but they are sparsely urbanized (< 1%) and sparsely cultivated (3 to 6% respectively). The detailed characterization of these two basins is presented in Chapter 2, Section 2.1.1 of this Thesis.

In order to characterize the effect of floods and hydropeaks on the dynamics of bed material (size and mobility) and its evolution as a function of distance from the HP and the presence of tributaries, three study reaches were selected on the Upper Cinca River and two others on the Upper Ésera River. These areas were chosen for the presence of sediment bars representative of ramping areas, at relatively low elevations compared to the base flow, being frequently flooded during hydropeaks. Mobility in these areas was monitored between 2019 and 2020. Water level stations with a temporal resolution of 15 minutes were installed and maintained between 2014 and 2021 in these reaches or in more distant locations that are still representative of their hydrology. Data from historical stations in each segment ($Escalona_{CHE}$ and $Campo_{CHE}$) from the EBRO water authority (CHE) network were also used to characterize flood frequency and magnitude. All these water level data were used to characterize the flows and, in Chapter 3, Section 3.2.1, to extract the median and maximum trends in the hydrological characteristics of the hydropeaks (e.g. peak flow (Q_{max}), ramping rate, duration) for each of these reaches. The magnitude of the events (floods and hydropeaks) observed by the photographic method in this study are characterized according to 3 reference flows: the median value of the hydropeak peak flows ($Med_{Hpk}\ Q_{max}$), the maximum value of the detected hydropeak peak flows ($Max_{hpk}\ Q_{max}$) and the value of the magnitude of an annual flood ($Q_{1y\text{-}flood}$).

6.2.1.2 The Upper Cinca

The upper Cinca is occupied by a cascade of 8 hydroelectric plants with modified run-of-river systems (see Chapter 1, Section 1.1.2.2.1), which turbine water from small reservoirs with a maximum storage capacity equivalent to 2 average runoff days (6.3 hm^3). The segment studied, shown in Figure 6.1 **B**, is 11 km long and begins a few meters upstream of the Laspuña power station outlet at an altitude of 600 m and ends at Ainsa at 529 m. This section has an average gradient of 0.70%. The river flows in a wide, relatively straight, north-south oriented valley (i.e. average valley width of about 200 m) with a very dynamic, wandering channel morphology (Church, 2006; Fryirs and Brierley, 2013), whose sediment bars change position very frequently. Laspuña Dam is the last dam in the upstream hydroelectric network. It is used to divert water to the power station, which has a maximum turbine flow capacity of 26 $m^3\ s^{-1}$.

On this segment, 3 study reaches were monitored:

i) The Laspuña US reach is located 1 km upstream (- 1 km) of the HP outlet, corresponding to the bypass flow. A water level sensor representative of the flow in this reach is located further downstream, a few meters upstream of the HP outlet (-0.1 km). This reach receives the *ecological* flow released from the dam. During floods, the dam is opened, allowing water and sediment to pass. The median annual discharge (Q_{50}) is 3.4 $m^3\ s^{-1}$. The wetted width at base flow is 15 m, while the active width of the river is 50 m. The monitored area corresponds to a bar head with a surface area of approximately 2 900 m^2 (see Figure 6.2 **A**). Mobility measurements were obtained in 2019 and 2020.

ii) Downstream of the HP at 0.6 km, the Laspuña DS reach receives all of the flow from upstream. A water level sensor located 0.3 km between the HP and this point was used to record flow fluctuations. The Q_{50} is 15.5 $m^3 s^{-1}$, while the Med_{hpk} Q_{max} is 22 $m^3 s^{-1}$. During small floods associated with rainfall or snowmelt, the 26 $m^3 s^{-1}$ turbined flow can be superimposed on these natural waves, producing peak flows (Max_{Hpk} Q_{max}) of up to 60 $m^3 s^{-1}$. The surface area of the basin at this point is 603.9 km^2 and the main wetted channel occupies most of the active width (35 m for an active width of 44 m) as shown in Figure 6.2 **B**. The grain size is very coarse. The D_{50} is 3 to 4 times coarser than the other two reaches on this river (114 mm compared to 34.6 mm upstream and 41.2 mm downstream, more details in Section 6.3.2).

iii) The last reach, Ainsa, is 10 km downstream of the Laspuña HP. Between this last reach and that of Laspuña DS, the waters of the Bellos tributary and the two small rivers San Vicente and Forcaz join the main course of the Cinca 1, 6.8 and 8.6 km downstream of the HP respectively. The total area drained at this point is 835.3 km^2, i.e. 1/3 larger than at Laspuña, and the reach is twice as wide (i.e. 120 m compared to 44 to 50 m). Flow fluctuation data for 2019-2020 are not available at this point in the segment. Instead, flow data from the $Escalona_{CHE}$ station, located 3 km downstream of the HP, measuring the sum of flows from Laspuña DS and the main Bellos tributary, were used. These flow data are considered to be representative of the Ainsa hydrology. The hydrological analysis carried out in Chapter 3, Section 3.2.1 of this thesis showed a very similar hydrology between Escalona and Ainsa, particularly in terms of magnitude (i.e. peak flow and velocity gradient). Mobility measurements were only carried out in the autumn of 2020 on the bar shown in Figure 6.2 **C**.

Figure 6.2: Overview of surveyed areas and aerial photographs. **A**. Laspuña US, -1 km from the HP (Upper Cinca). **B** Laspuña DS, 0.6 km and downstream of the HP (Upper Cinca). **C** Ainsa, 10 km downstream of the HP (Upper Cinca). **D** Campo DS, 1 km downstream of the HP (Upper Ésera) and **E** Pyramides 12 km downstream of the HP (Upper Ésera).

6.2.1.3 The Upper Ésera

The upper Ésera is occupied by a cascade of 7 hydroelectric power stations operating in a modified run-of-river mode, turbining water from small reservoirs with a maximum storage capacity equivalent to 4 days' average run-off (6.3 hm^3). The 12 km segment studied, shown in Figure 6.1 **B**, begins at the foot of the Campo dam, on which the power station of the same name is located, and ends at the Pyramides point. A temporary water level probe was installed at this point in 2020. The mobility observations made in 2019 were correlated with the flow fluctuations measured at Santaliestra, 18.5 km downstream of the Campo HP. The hydrological analysis carried out in Chapter 3, Section 3.2.1 showed that the hydrology between Pyramides and Santaliestra is very similar, with little damping of the flux, particularly in terms of magnitude (i.e. peak flow and ramping rate).

This segment has an average gradient of 0.73%. The river flows through a narrow, tortuous valley (i.e. direct valley length/valley length ratio of 1.3, see Figure 6.1) with numerous gorge sections and an median width of about 57 m. The active channel, 58% confined to these two margins, has a median width of 34 m. A single straight channel (i.e. talweg length /valley length ratio of 1.03) can be seen along almost the entire length of the valley following its curves. The morphology of the valley imposes a sequence of planned bed and riffle pools, as well as the frequent appearance of bedrock. The bedforms are stable over time. The Campo dam is the last of the upstream hydroelectric network. It supplies water to the turbines at its foot, which have a total maximum turbine flow capacity of 20 $m^3\ s^{-1}$.

Two reaches were monitored and followed in this segment:

i) The Campo DS study reach, located 1 km downstream of the Campo HP, receives all the instream flow and water releases from the HP. The dam does not allow coarse sediment to pass. During floods, water flows over the spillway and through the bottom gates. The Campo station, 0.3 km from the dam, records flow variations. The Q_{50} is 11.5 $m^3\ s^{-1}$. The area drained at this point is 569.6 km^2. Mobility was monitored exclusively in the autumn of 2020 at the head of a bar of about 2 400 m^2 located on the margin of an island. At this point, the river is relatively wide compared to the rest of its course, with an active width of 67 m (wider than the median width of the valley bottom). At low flow, the flow is concentrated in a channel on the left bank (see Figure 6.2 **D**), which is about 15 m wide. During hydropeaks, the secondary channel on the right bank of the island becomes flooded. The hydrological analysis carried out in Chapter 3, Section 3.2.1 showed that the $Med_{hpk}\ Q_{max}$ on this part of the segment was 18 $m^3\ s^{-1}$. Hydropeaks superimposed on natural waves were observed up to 30 $m^3\ s^{-1}$ ($Max_{Hpk}\ Q_{max}$).

ii) 12 km downstream of the HP is located the Pyramides reach. Between this latter and the Campo reach, the waters of the main tributary Rialbo and the secondary tributaries Foradada and Bacamorta join those of the Ésera at 3.9, 6 and 7 km respectively downstream of the HP. The area drained at this point in the basin is 719.3 km^2, 1/4 more than at Campo DS. The river is confined by steep valley margins. The active width is 28 m, while the wetted width at low flow is 15 m. The representative Q_{50} observed at Santaliestra is 13.8 $m^3\ s^{-1}$, while the $Med_{hpk}\ Q_{max}$ is 19 $m^3\ s^{-1}$. Mobility observations were carried out in 2019 and 2020.

In summary, the two segments subject to hydropeaking downstream of the HPs, which receive the entire upstream flow without diversion, have a confluence with 3 tributaries, one main and two minor, with a similar hydrological regime and average gradient. However, the catchment area of the Cinca River is 13% larger than that of the Ésera and its rainfall is 25% higher. The morphology of their valleys, their channels and their stability are considerably different (Figure 6.1).

6.2.2 Methods

The longitudinal characterization of the effects of flood and hydropeaks on the bed material dynamics was carried out in four stages: (1) The first stage consisted of characterizing the size of the grains on the bed surface at each site, mainly using a photographic method, and then carrying out measurements to quantify mobility, again using the same method, by photographing the same area PRE- and POST-hydrological events. (2) The pairs of photographs (before and after) were then processed using the PhotoMOB tool to determine the maximum mobile diameter and the mobile proportions (of the whole bed or of the grain fractions). (3) The flow data series (i.e. hydrographs) were segmented to isolate each peak (flood and/or hydropeak) and extract its hydrological characteristics. Between each PRE and POST instant, considered as an event (i.e. comparison between 2 photos), the hydrological peak(s) that occurred and their characteristics were correlated with the mobility observations. (4) Finally, all the mobility/hydrology data pairs were analysed using different methods described in Section 6.2.2.4, in order to achieve the objectives mentioned in the introduction.

6.2.2.1 Field measurements of bed materials and their mobility

The bed materials of the Laspuña US, Campo DS and Pyramides reaches were characterized by two different methods in order to compare the compatibility of the results obtained: the commonly used pebble-count, or Grid-by-Number method (Wolman, 1954), and the photographic method (Bunte and Abt, 2001; Graham et al., 2005b; Mair et al., 2023) using *PhotoMOB* (the full description of the tool is available in Chapter 5). The Laspuña DS and Ainsa sites were only characterized using the PhotoMOB.

For the Grid-by-Number or pebble count method, more than 100 grains were collected along a grid with a spacing at least one times greater than the coarsest particle, to avoid measuring the same particle twice. Their *b*-axis was measured by passing the grain through a template consisting of several square holes divided into $^{1}/_{2}\phi$ intervals, based on the Wentworth scale (where $\phi = -log_2 D$, D is the size of the particles in millimetres). The number of grains identified in each interval is used to compute frequency and characterize the grain size distribution (GSD) on the bed surface. This method was applied only once per site at the beginning of the mobility monitoring campaigns. In the rest of the manuscript, the different grain fractions are designated by the lower limit of the interval (e.g. 8 mm for grains belonging to the fraction $]8\ mm - 11.3\ mm]$).

The photographic method corresponds to an Area-by-Number, which allows indirect characterization of grain size after treatment without altering their structural arrangement. This method was used for each site on 2 to 4 patches in order to be able to take into account of spatial grain size variation along the reach. All photographs were taken according to the principles described in Chapter 5, Section 5.1.1.

The patches were then painted in order to easily find their position and extent during subsequent visits, and to use the grains as tracers (to carry out future studies of their travel distance). New photos (POST) were taken on subsequent visits. The POST photos of one event become the PRE photos of the nth subsequent event. These successive photos make it possible to obtain updated GSDs of the areas monitored after each event, in order to assess the impact of the peaks on the textural (grain size) composition of the bed, as well as to determine the absence or presence of mobile grains and to quantify their proportion if this is the case.

6.2.2.2 Characterization of bed materials and their mobility

The GSD and mobility of the monitored patches were obtained by processing the PRE- and POST-event photo pairs with the *PhotoMOB* GIS tool developed in *ArcGIS®* in the framework of the thesis. The functioning of the tool and the processing steps are fully detailed in Chapter 5. Briefly, the PRE-event photos were manually scaled using the boundaries of a metal frame previously placed on the ground to delimit the zones when the photos were taken. The POST-event photos were then locally georeferenced to the PRE-event photos by identifying identical fixed (i.e. stable) points between the two shots. The two PRE and POST photos of each event were processed with the first part of the tool to obtain the delineation of each grain present in the form of a polygon-type shapefile with the grain shape characteristics in the attribute table (e.g. *a*-axis, *b*-axis, *area*). All these grain layers were carefully checked visually. In the case of errors in grain identification, the geometries were manually edited. Each pair of photographs was then processed using the second part of the PhotoMOB tool. The shapes of the grains positioned at the same Cartesian coordinates (x, y) at the PRE- and POST-event times were compared. Depending on the degree of similarity, the grains were classified as identical, i.e. immobile, or non-identical, i.e. mobile. This new mobility information was also stored in the attribute table. A careful inspection of the automatic classification results was carried out to detect any errors related to grains classified as identical due to similar shapes despite an obvious difference visible to the naked eye, or conversely, grains classified as mobile (e.g. non-identical) due to different shapes detected, often linked to the angle of view of the images, but which nevertheless appear to be the same. The attribute tables were edited as shown in Figure 6.3 **A**.

The data (i.e. attribute tables of the shapefiles) were processed with a *PhotoMOB Extractor* developed in the background of this thesis to be able to use the PhotoMOB outcomes and optimize analyses (https://shiny.fannyville.com/photomob_extractor.html). This application extractor tool was implemented under the R language using various packages (cowplot, Wilke (2024); DT, Xie et al. (2023); ggh4x, van den Brand (2024); ggtext, Wilke and Wiernik (2022); grid, R Core Team (2023); htmlwidgets, Vaidyanathan et al. (2023); janitor, Firke (2023); lemon; Edwards (2023); moments, Komsta and Novomestky (2022); qdapRegex, Rinker (2023); rhandsontable, Owen (2021b); shiny, Chang et al. (2023b); shinybusy, Meyer and Perrier (2023); shinydashboard, Chang and Borges Ribeiro (2021); shinydisconnect, Attali (2023); shinyjs, Attali (2021); shinyWidgets, Perrier et al. (2024); skimr, Waring et al. (2022); wesanderson, Ram and Wickham (2023); writexl, Ooms (2023); tidyverse, Wickham et al. (2019b) (See Figure 6.3 **B**). This application was used to extract:

– The PRE-event GSDs

– The POST-event GSDs

– GSDs of grains only classified as mobile following a competent event (i.e. proxy of the bedload GSD)

– The GSD of grains only classified as immobile

– The relative mobility (i.e. null, partial or full) per grain size fraction by comparing their frequency in the mobile GSD p_i with their frequency of occurrence at the surface in the PRE-event GSD F_i.

– The proportion stable/mobile over all the zones in terms of grain surface area or number of grains

– The immobile/mobile proportion for each grain size fraction.

The general grain size of each site studied was determined by creating a "composite" sample of all the grains detected on all the photographed patches (between 2 and 4 patches).

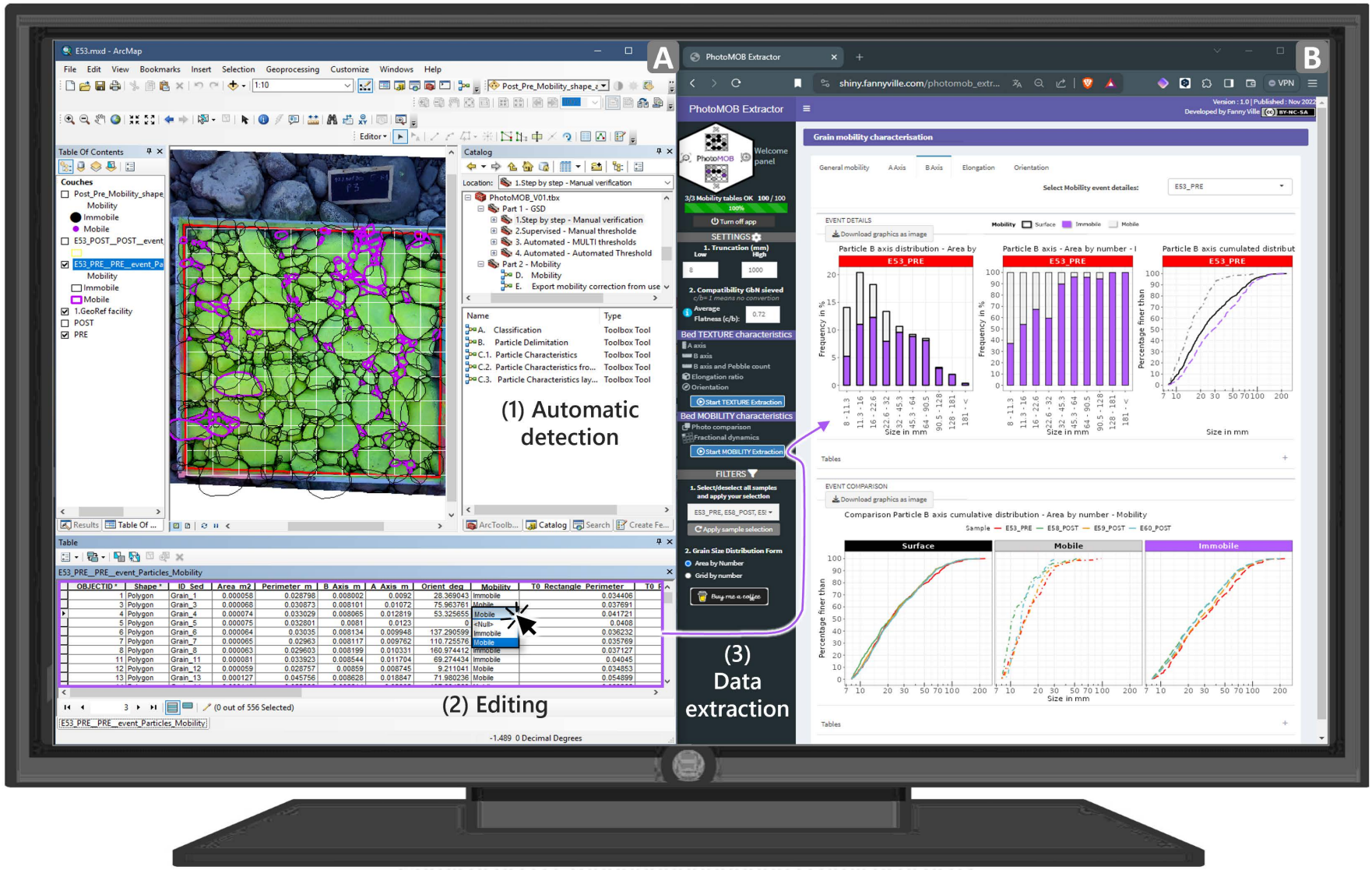

Figure 6.3: Illustration of the *PhotoMOB* photographic processing method. **A** Overview of the results of automatic grain detection and classification (1) and the content of the editable attribute table (2). **B** Overview of the *PhotoMOB Extractor* application for calculating grain characteristics and mobility, with the possibility of parameterization (i.e. truncation, Area-by-Number or Grid-b-Number form, conversion to discrete measurement methods).

In order to allow comparison of the results obtained in this study with those of previous work or future studies carried out on other rivers using predominantly traditional methods (e.g. in situ mobile grain sampling and sieving), a low truncation of 8 mm was set when calculating all grain size and mobility variables. The results of the grain size distributions were expressed in Grid-by-Number form using the method presented in Chapter 5, Section 5.1.1, which is based on that developed by Graham et al. (2012), before being converted as a function of the average grain flatness coefficient (*c*-axis/*b*-axis ratio = 0.72). The results of these conversions are presented and discussed in Section 6.3.1.

In agreement with the arguments developed in Chapter 5, Section 5.2.1, for all sites except Campo DS, the mobility of all monitored events is based on the classification obtained from the POST-event layers. At Campo DS, mobility is based on the PRE-event layer due to the potentially low sediment supply from upstream because of the dam. Most of the new grains visible would probably not come from upstream but rather from the subsurface, while the grains in the PRE-event photo that are no longer visible are more likely to have been mobilized downstream rather than covered by new grains. For flood events, on the other hand, mobility was characterized in the same way as for the other sites, using the POST-event classification.

A total of 75 events were processed, representing 150 georeferenced photos and more than 128000 particles, the edges and classification of which were meticulously checked.

6.2.2.3 Hydrological characterization

In order to facilitate comparison between sections draining different areas and/or river sizes, all the calculated characteristics describing the magnitude of the peaks, in addition to being presented in dimensional form (m^3s^{-1}), can be normalized (Alonso et al., 2017; Bejarano et al., 2017; Courret et al., 2021; Greimel et al., 2023). In this study, as in the one carried out in Chapter 3, Section 3.2.1, the flows were normalized by the median hydrological characteristics of the stations in order to take into account the particular river hydrology: $Q_{norm_i} = Q_i/Q_{50} * 100$

The hydrological characteristics of the peaks occurring between two photographic observations (i.e. PRE and POST) were obtained by segmenting the hydrographs. The method is described in detail in Chapter 3, Section 3.2.1. Briefly, the hydropeak shapes can be divided into three phases (Schmutz et al., 2015), namely (**I**) increase (IC), (**II**) plateau and (**III**) decrease (DC), as shown in Figure 6.4. The isolation of each peak, from the beginning of the increase phase (IC) to the end of the decrease phase (DC), is based on the differences in normalized flow rates (Q_{norm_i}) between two consecutive time steps (ts). The method of Courret et al. (2021) was used to identify significant increasing or decreasing variations and to classify them as natural or artificial according to their rate of change. Finally, successive significant variations in the same direction (IC or DC), spaced by stages, were concatenated if they belonged to the same category (i.e. natural or hydropeak). This is illustrated in Figure 6.4 for two descending phases between 4 green points.

For each peak, a set of 5 parameters, based on those of Tena et al. (2022); Courret et al. (2021); Greimel et al. (2023), that could potentially explain the competence of the flow (maximum movable grain size) and the degree of destabilization (mobile proportion) were used. They are illustrated in Figure 6.4: the duration (D_{peak} in hours), the total dimensional runoff volume (V in hm^3) and that normalized by the annual water yield at the station (W_y) (V_{norm} in % of W_y), the maximum dimensional peak flow (Q_{max} , m^3s^{-1}) and the normalized one (Q_{max} in % of Q_{50}), the relative position of Q_{max} (P_{Qmax} in % of D_{peak}) and the maximum ramping rate (i.e. the greatest variation in flow between two instant of time corresponding to the slope of the purple curve in Figure 6.4) in dimensional ($MARR_{ID/DC}$, in $m^3s^{-1}h^{-1}$) and normalized ($MARR_{norm\ IC/DC}$, in % of Q_{50} h^{-1}). The greater the Ramping Rate (RR) value, the more vertical the purple curve and vice versa.

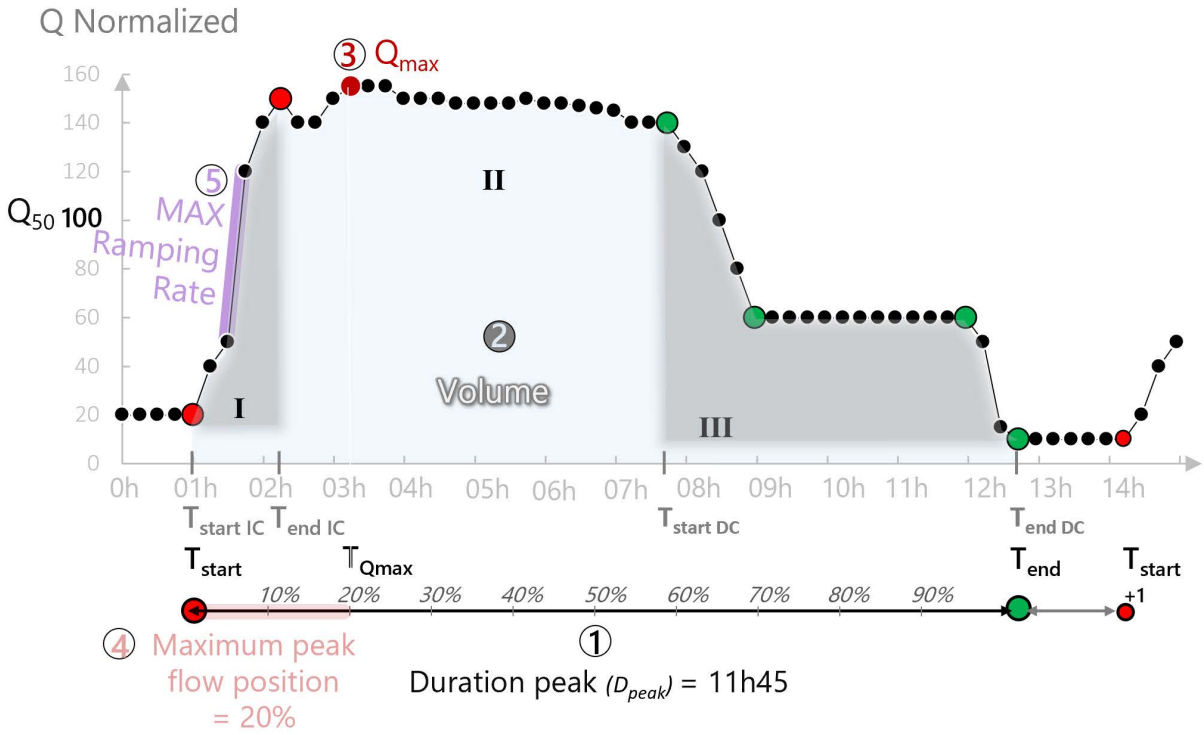

Figure 6.4: Segmentation of hydropeaks and characteristics of a typical hydropeak. The numbers indicate the characteristics used to isolate and study hydropeaks. See text for more details.

These hydrological characteristics were coupled with the mobility information obtained previously. However, all pairs of photographs covered periods corresponding to successions of peaks (ranging from 2 to 56 peaks with a median of 7). Figure 6.5 **A** illustrates the periods covered by the photographic observations. The vertical blue lines indicate the dates on which the photographs were taken.

For the 2020 campaign on the Ésera, field visits were made almost daily. POST photos were only taken when degradation of the paint was visible after a hydrological peak. For each period between the PRE and POST photos, only the values of the variables Q_{max}, P_{Qmax} and $MARR_{IC}$ corresponding to the largest peak were retained. If the largest peak corresponded to a flood, the mobility extracted from the photos is considered representative of a flood, if not of a hydropeak. With regard to duration and volume, the total duration and all volumes flowing during the peaks of the monitored period were summed.

The distribution of the 75 photographic observations between study reaches, photographed patches and event types (base, hydropeak and flood) is shown in Figure 6.4 **B**. Figure 6.4 **C** shows the different dimensional and normalized magnitudes (Q_{max} and $Q_{max\ norm}$ of the events analyzed for each site. The grey horizontal lines represent the reference flows ($Max_{Hpk}\ Q_{max}$; and $Q_{1y-flood}$). There were more photographic events observed (i.e. 75) than peak magnitudes studied (i.e. 28). This is explained by the multiple zones photographed at each site (between 2 and 4), representative of the same hydrological event. Of these 75 observations, 38 corresponded to flood events, 36 to hydropeaks and only 1 to a base flow with no hydrological peak. In the Cinca River, the majority of observations corresponded to floods. In the Ésera River, about 50% of the observed events were hydropeaks and the remaining 50 were floods. The magnitude of these natural peaks is less than an annual flood, but greater than the maximum peak that hydropeaks can reach.

The entire dataset can be viewed dynamically in the form of a dashboard available at this link: https://www.arcgis.com/apps/dashboards/9fc1fd7bbd4e4cfb8831e903dfaa908d

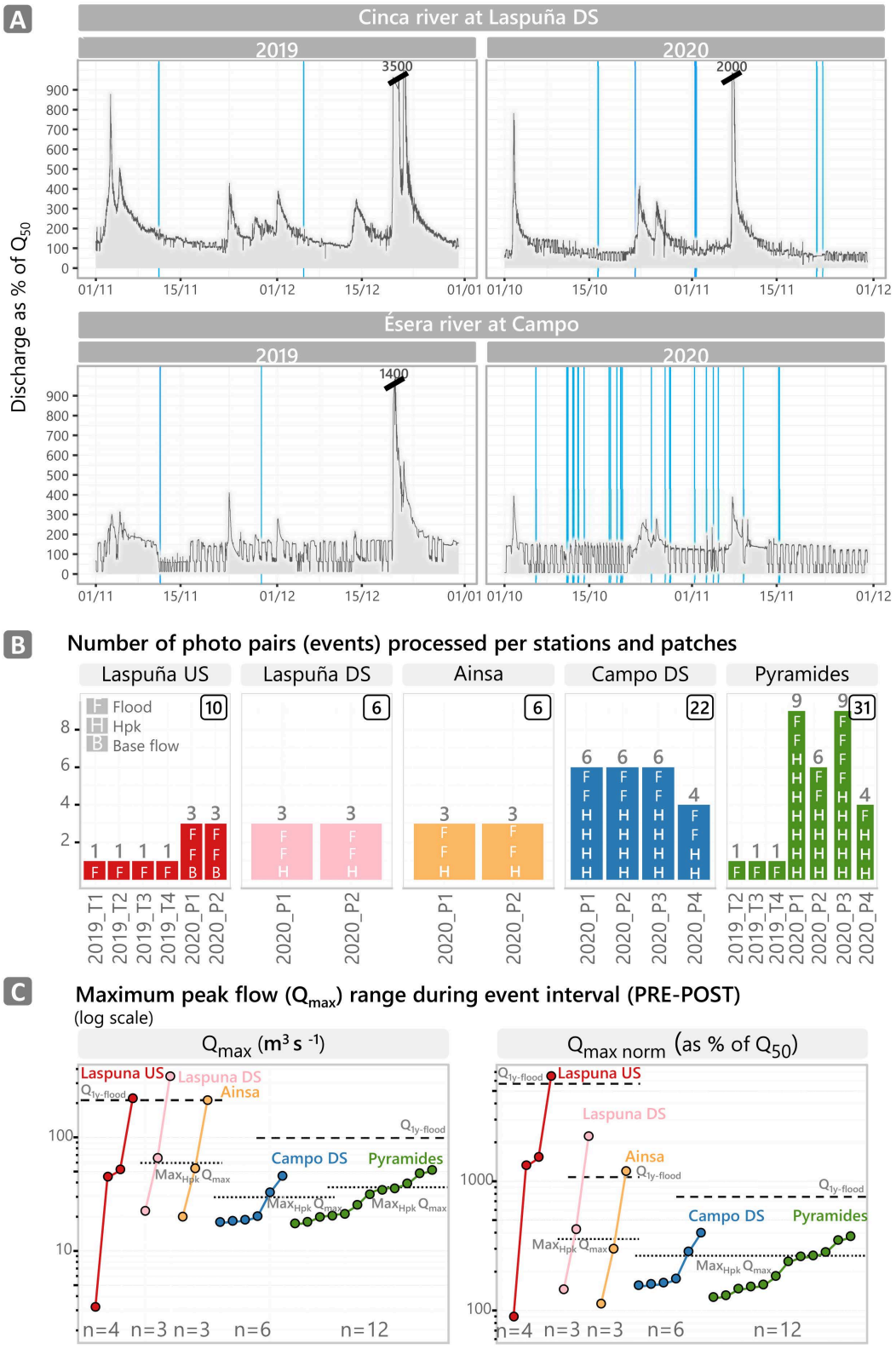

Figure 6.5: Summary of the monitored hydrological events. **A** Series of flow fluctuations during the mobility monitoring campaigns. The blue lines indicate the times at which the photographs were taken. **B** Distribution of the number of mobility observations per study reach and patch according to the type of event (flood, hydropeak and base flow). **C** Range of flows associated to mobility observations for each reach in dimensional (left) and normalized (right) values. The horizontal lines show the 2 reference flows: the annual flood ($Q_{1y\text{-}flood}$) and the maximum peak flow of the detected hydropeaks (Max_{Hpk} Q_{max}). Note that the periods in 2019 are indicated as 2019_Ti, where i is the Id of the patch, while in 2020 they are indicated as Pi.

6.2.2.4 Statistical analysis

The results of the GSD calculations were compared between the two methods used (pebble-count vs. Photographic). Next, the hydrological/mobility data pairs were examined in 4 different ways to answer the questions posed in the introduction.

6.2.2.4.1 Comparison of GSD measurement methods

The GSDs obtained by the pebble-count method (Wolman, 1954) and that obtained by photographic composite sampling were compared. The differences between the D_{16}, D_{50} and D_{84} percentile values obtained by the two methods were calculated in dimensional (mm) and relative (%) terms.

6.2.2.4.2 Effect of hydropeaks and floods on the composition of the riverbed

Possible changes in GSDs after each hydrological event were examined by comparing PRE and POST GSDs. Kolmogorov-Smirnov tests were performed to compare PRE-POST GSD pairs to determine whether significant patch changes had occurred. GSDs were considered significantly different for a p value < 0.05.

6.2.2.4.3 Key hydrological hydropeak variables explaining mobility

The five extracted peak characteristics listed in Section 6.2.2.3 and shown in Figure 6.4 were correlated to (i) the proportion of mobile grains, (ii) the relative maximum mobile diameter (D_{max}/D_{50}). The D_{50} corresponds to that obtained at the PRE-event time.

Linear and power regression models were used to quantify the significance of the correlations. These models were run on the observations corresponding to the hydropeaks only, and then on all observations (flood + hydropeak). This analysis was only carried out for the Ésera river due to the small number of observations associated with hydropeaks in the Cinca. Only the correlations with power-type models, which most often gave the best correlation coefficients (R^2), are presented and discussed in Section 6.3.4.

6.2.2.4.4 Longitudinal evolution of hydropeak competence compared to floods

The maximum relative diameters mobilized ($D_{max}/D_{50\ pre}$) were correlated with the $Q_{max\ norm}$ for the associated event. These data pairs were presented in a scatterplot grouped by study reach. Normalization of the data allowed the competence of the events to be compared between the two river segments and between the upstream and downstream reaches of the same river. Power-type models were applied to each reach to predict flow competence and to study its longitudinal variability.

6.2.2.4.5 Longitudinal trends in the degree of bed destabilization associated with hydropeaks compared to floods

The proportions of mobilized patches, in terms of area and number of grains, were related to the magnitude of the events observed for each reach. Polynomial regression models of order 2 were applied to predict the proportion of the bed potentially mobilized for a given peak flow. Polynomial models were chosen because they provided the best fit for all the different reaches, some of which had very few observations (e.g. Laspuña DS and Ainsa). For each reach, the models were used to estimate the critical flow inducing a mobility of at least 10% (i.e. the critical flow for partial mobility, $Q_{cr\ partial}$) and 90% (i.e. the critical flow for full mobility, $Q_{cr\ full}$) in terms of number or surface area of grains.

The same analyses were carried out for each grain size fraction individually. Mobility prediction models were then established per each fraction. The critical flows for partial and full mobility can be extracted. Only those concerning the classes to which the D_{16}, D_{50} and D_{84} of each reach belong are discussed in Section 6.3.6.

6.2.2.4.6 Frequency and timing of bed destabilization due to hydropeaks and floods

The timing of river bed mobility is a crucial factor for aquatic habitat in fluvial ecosystems. Mobility generated by artificial and even natural peaks can lead to reductions in benthic macroinvertebrate densities (Gibbins et al., 2007a; Power et al., 2008; Robinson et al., 2004). In order to study the temporal and frequency variations of partial or full mobility events between the two river segments and between upstream and downstream, associated with hydropeaks on the one hand and floods on the other, the $Q_{cr\ partial}$ and $Q_{cr\ full}$ of the D_{16}, D_{50} and D_{84} percentiles obtained from the previous analyses were applied to the multidecadal (1997-2023) flow time series available at the $Escalona_{CHE}$ (representative of the Ainsa reach) and $Campo_{CHE}$ stations. The data from these stations has a time resolution of 15 minutes. The maximum daily values were extracted.

In order to assess the estimated bed destabilization in the other reaches of Laspuña US, Laspuña DS and Pyramides, the flow time series were reconstructed. Daily peak flows from the medium-term time series installed in these reaches by the RIUS research group were used and related to those from the CHE stations (i.e. Laspuña US and DS with $Escalona_{CHE}$ and Santaliestra/Pyramides with $Campo_{CHE}$). Generalized additive models (GAM) were fitted between $Q\ max\ day\ CHE$ and $Q\ max\ day\ RIUS$. This processing was carried out using the package *mgcv* (Wood, 2011).

Finally, for each reach, a time series of daily peak flows ($Q\ max\ DAY$) was available or reconstructed. For each of them and for each of the 3 percentiles D_{16}, D_{50} and D_{84}, their potential daily stability/destabilization history was estimated and classified into 4 classes: (1) When $Q_{max\ DAY} < Q_{cr\ partial\ Di}$, the grains corresponding to the given Di were considered stable. (2) When $Q_{max\ DAY} > Q_{cr\ partial\ Di}$ but less than the reference flow $Max_{Hpk}\ Q_{max}$, the grains were considered likely to exhibit partial mobility due to hydropeaks. (3) When $Q_{max\ DAY} > Q_{cr\ partial\ Di}$ and greater than the reference flow $Max_{Hpk}\ Q_{max}$ but still less than $Q_{cr\ full\ Di}$, the grains were considered likely to exhibit partial mobility due to natural events. (4) Finally, when $Q_{max\ DAY} > Q_{cr\ full\ Di}$, the grains were considered likely to be fully mobile.

6.3 RESULTS AND DISCUSSIONS

6.3.1 Compatibility of bed material characterization methods.

Figure 6.6 **A** shows the difference between the GSD obtained by the pebble count method (blue curve) and the composite GSD obtained from *PhotoMOB* (dashed red curve), expressed in GbN, for only one site on each river (Laspuña US on the Cinca and Campo DS on the Ésera). The estimate of the pebble count GSD is finer than that of the composite GSD due to the tendency to underestimate grain sizes according to their degree of flatness. The latter, when measured with a template of their *b*-axis, can be counted in a lower class if they are relatively flat. In order to obtain comparable results between these two methods, the GSDs of the photographic composite samples expressed in GbN form were converted as a function of the median grain flatness coefficient. The median grain flatness coefficient, 0.722, was measured on grains coming in different proportions from the two rivers Cinca and Ésera (more details in Chapter 5, Section 5.1.1). Figure 6.6 **B** shows the converted composite GSDs. The difference between the two GSDs is reduced.

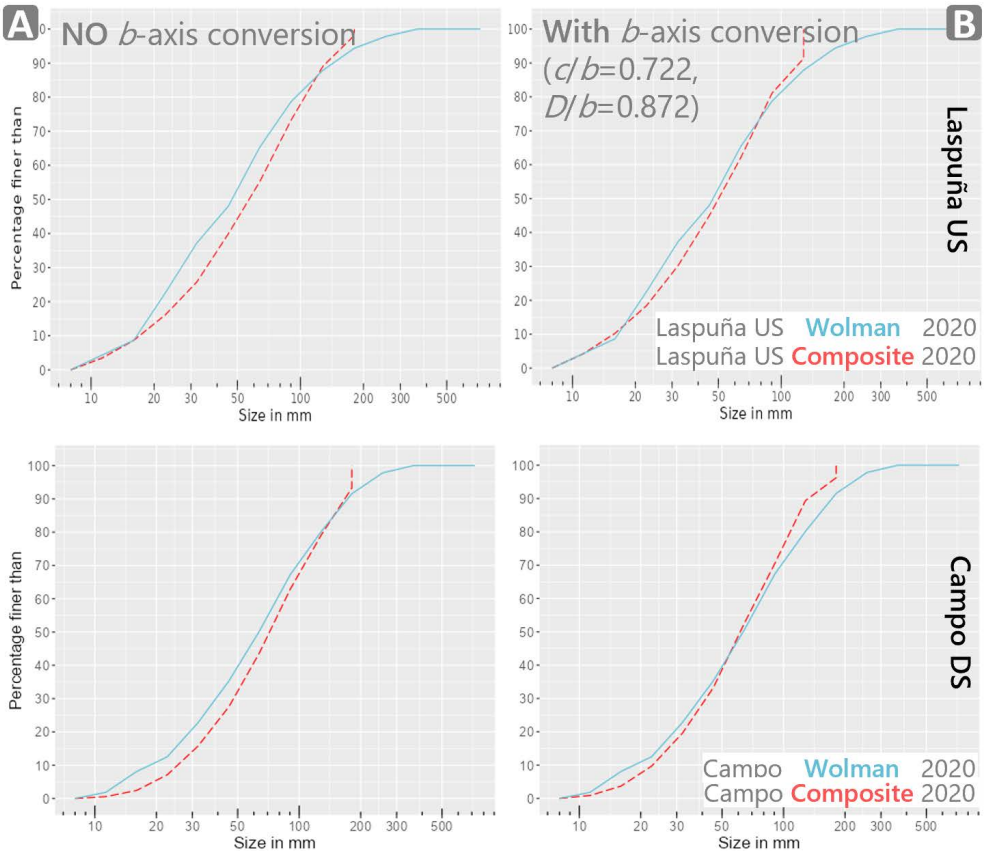

Figure 6.6: Cumulative distribution of the *b* axis at Laspuña US, above, (upper Cinca River) and at Campo DS, below, (upper Ésera River) for both pebble count and photographic methods. **A** GSD composite without conversion and **B** with conversion to account for grain flatness.

Figure 6.7 shows the difference between the GSDs for the 4 available pebble-count measurements (black dots) and those for the converted GbN composite samples (colored dots). The composite GSDs show D_{16} and D_{50} close to those of the pebble-count, with differences ranging from 0.9 to 3.3 mm (i.e. between -3.5 and 9.3% difference) for the measurements carried out at Laspuña US in 2020, Campo DS in 2020 and Pyramides in 2019 (Figure 6.7 **A**, **B** and **C**). The differences for D_{84} are greater (between 10 and 20%). Note the large difference between the two methods for the measurements at Pyramides in 2020 (Figure 6.7 **D1**).

This can be explained by the fact that the sampled area is 1.3 to 4 times smaller than that used in the other reaches and shows a certain spatial variability in grain size (Figure 6.7 **D2**). In 2020, the Pyramides patches were positioned very close to the channel (coarse surface) in order to be sure that these areas were flooded and to examine, at best, the mobility associated with the hydropeaks (see Figure 6.2 **E**). The areas sampled between the two methods do not correspond exactly to the same facies (i.e. pebble-count with a larger sampled area).

These results do not in any way assess the potential error of either the photographic or the pebble-count method. They consolidate those previously presented in Chapter 5, Section 5.1.1 on this new dataset by simply showing that the GSDs obtained from these two methods are comparable with adequate conversion (generally low deviation) and that the photographic method can allow a more detailed characterization of small areas of specific interest, depicting the spatial variability of particle size in gravel bars.

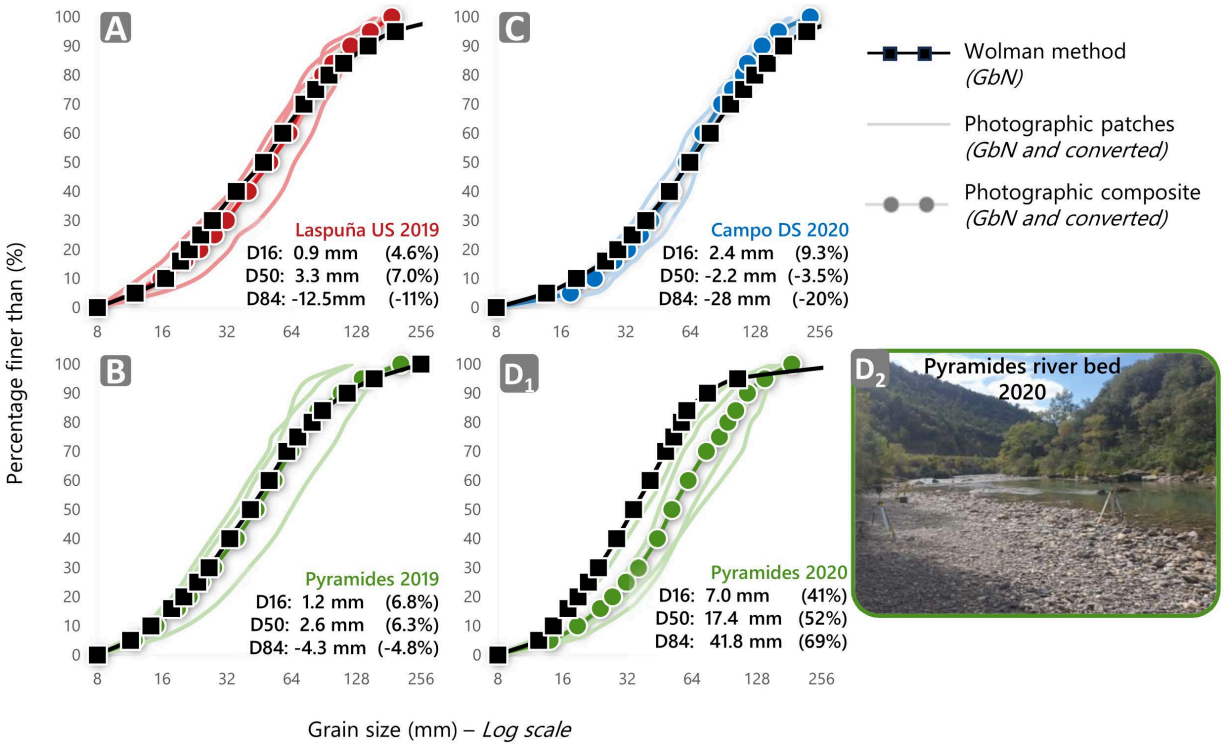

Figure 6.7: Grain Size Distributions (*b*-axis) in 2019 for (**A**) Laspuña US and (**B**) Pyramids and in 2020 for (**C**) Campo DS and (**D1**) Pyramides. The black squares represent the GSDs obtained by the pebble-count method. The coloured circles represent the composite GSDs obtained by the photographic method in GbN converted according the grain flatness, and the coloured curves represent those of the patches individually. The differences between the methods for the D_{16}, D_{50} and D_{84} percentiles are given in mm and as in percentage. (**D2**) Note the high spatial variability Pyramids over a small area.

6.3.2 River bed grain size characterization

The GSDs considered in this study are those obtained using the composite photographic method and are shown in Figure 6.8. The D_{16}, D_{50} and D_{84} percentile values are shown in Figure 6.1 **C**. On the Ésera, the GSD at Campo DS (blue curve) is 15% coarser than that at Pyramides (green curve), with D_{50} values of 61.3 and 51.6 mm respectively (very coarse gravel). The two reaches have similar, very poorly sorted grain size distributions, with sorting coefficients of 2.1 and 2 (Folk and Ward, 1957). On the Cinca, the GSD of Laspuña US (red curve) and Ainsa (yellow curve) are the finest of the 5 reaches with D_{50} of 34.6 and 41 mm (coarse gravel). Conversely, the Laspuña DS reach (pink curve), located 0.6 km from the Laspuña HP, has a much coarser grain size than any of the other sites, with a D_{50} of 114 mm (small cobbles) and a sorting coefficient of 2.7.

In summary, in the reaches affected by the hydropeaks, those close to the HP (0.6 km Laspuña DS on the Cinca and 1 km Campo on the Ésera) have coarser grain sizes than those downstream of the HP and the confluences with the tributaries (10 and 12 km, see Figure 6.1), the latter being able to supply additional finer sediment.

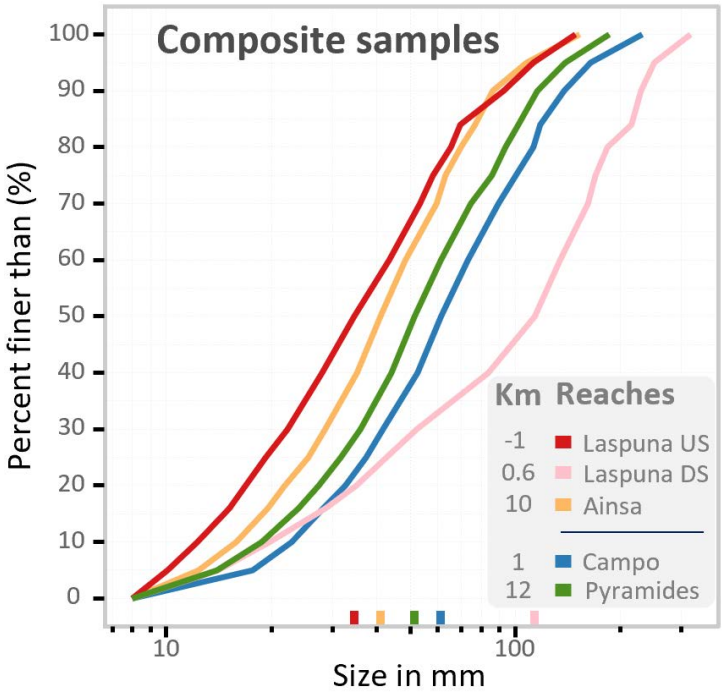

Figure 6.8: Grain size distribution of study reaches on the Upper Cinca and Upper Ésera Rivers

6.3.3 Effects of hydropeaking and flooding on river bed composition

Figure 6.9 shows, for each event studied, the significance or not of the differences between the PRE and POST surface GSDs as a function of the $Q_{max\ norm}$ and the proportion of the number of mobile grains. The red dots indicate a significant difference between the PRE and POST GSDs. Only 20% of the analysed events showed a significant change. Observations obtained on the Ésera (triangular points) show that events with magnitudes close to the $Med_{Hpk}\ Q_{max}$ (dotted line) were able to mobilise up to 25% of the grains without inducing a significant change in the surface GSD.

Furthermore, for event magnitudes greater than $Max_{Hpk}\ Q_{max}$ (i.e. just above the grey area), observations on the two rivers (all point shapes) show PRE and POST GSDs that are not significantly different (grey points), despite mobility of 75 to 90% of the grains. These results suggest that most of the hydropeaks and some small frequent certain floods do not cause significant changes in the surface grain size distribution in the short term.

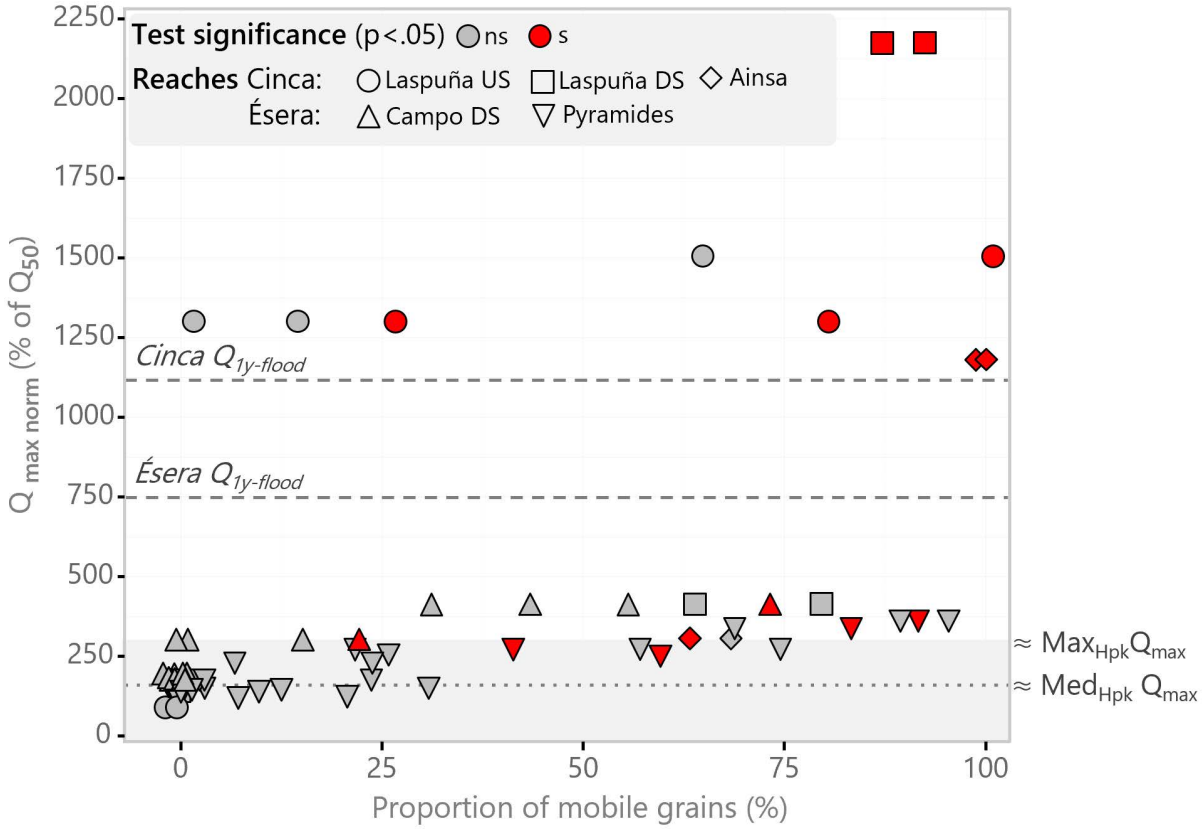

Figure 6.9: Results of Kolmogorov-Smirnov test between PRE- and POST-event surface GSD. Red dots indicate a significant difference in GSD between the two time instants. The horizontal lines indicate the reference flows: median of the peak flows ($Med_{Hpk}\ Q_{max}$), the maximum value of the peak flows detected $Max_{Hpk}\ Q_{max}$ and the value of the magnitude of an annual flood ($Q_{1y\ flood}$).

The results show also how simple measurements of the GSD PRE- and POST-event, even at high spatial resolution using photographic methods (i.e. multiple samples), are not sufficient to study the effect of hydropeaks on river bed. Analysing mobility at the patch-scale between photographs seems more relevant to characterize the bed destabilization associated with hydropeaks. Here, on the River Ésera, it has been shown that the majority of peak flows from hydropeaks located on either side of the $Med_{Hpk}\ Q_{max}$ show mainly partial transport (up to about 30% of the grains) without significant changes in the surface GSD; i.e. the 30% of the is destabilized but the GSDs are not statistically different.

6.3.4 Hydropeak characteristics explaining partial bed mobility (competence and degree of destabilization)

Figure 6.10 shows the correlations only for the River Ésera (numerous observations of hydropeaks available) between the five hydrological characteristics of the hydropeaks and (i) the proportions of the number of grains mobilized (left) and (ii) the relative maximum diameter mobilized (right). Coloured dots and black lines represent hydropeaks. The white filled points represent flood, while the grey lines represent the models for all points (hydropeaks + floods). Only the most significant correlation coefficients R^2 are shown in the top left. The strongest correlation concerning the proportion of grain mobilized for hydropeaks is found with the ramping rate of increase. The relative mobile D_{max} is more strongly correlated with the $Q_{max\ norm}$.

The models developed with all points show a stronger correlation, especially for $Q_{max\ norm}$, which has an R^2 of 0.54 and 0.64 for mobile proportions and mobile D_{max} respectively.

The correlations are weak, especially for the hydropeaks alone. There is a large scatter of points. It should be noted that up to 4 observations were made for the same flow. The hydrological characteristics presented here only correspond to average values for a variety of GSDs and local hydraulic conditions. In addition, these differences between points could be explained by the fact that the threshold for setting the grains in motion may vary according to the stress history effect. Studies have shown that prolonged flow near the motion threshold can modify grain arrangement and increase bed stability (Ockelford et al., 2019; Ockelford and Haynes, 2013; Pender et al., 2007). This rearrangement can be disrupted by floods and then gradually reconstituted, causing hysteresis in grain mobility dynamics (Mao, 2018).

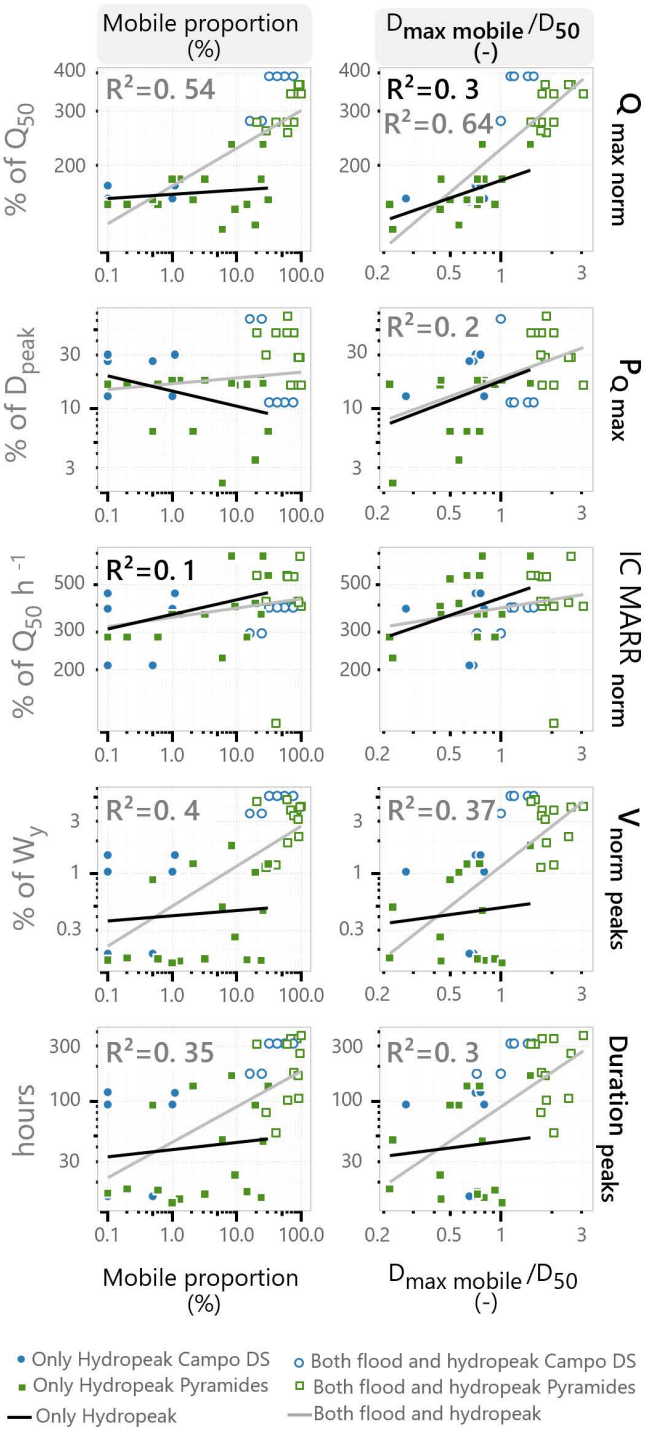

Figure 6.10: Relationship for the Upper Ésera River between the mobile proportion (left) and the relative maximum mobilized diameter (right) with the five extracted hydrological characteristics. The black and grey curves represent the power type models for hydropeak only and hydropeak + flood, respectively. The most significant R^2 correlation coefficients are shown in the upper left, with the respective colors of the straight lines. $Q_{max\ norm}$ is the peak flow of the event normalized by the Q_{50} , P_{Qmax} is the relative time where occur the peak flow relative to the entire duration of the peak (%), IC MARR $_{norm}$ is the maximal increase ramping rate representing the fasted discharge change between to measurement (15 min) normalized by Q_{50} , $V_{norm\ peaks}$ is the volume released from the HP during the peak normalized by the annual water yield, Duration $_{peak}$ correspond to the entire duration from the start of the increase to the end of the decrease.

6.3.5 Longitudinal evolution of hydropeak competence compared to floods

Figure 6.11 shows the relationship between the normalized peak flow ($Q_{max\ norm}$) and the relative maximum diameters mobilized (D_{max}/D_{50})

On the Cinca River, at the Laspuña DS reach, 0.6 km downstream of the HP, of the 3 flows observed, only 1 was associated with a hydropeak. This was of 22 $m^3\ s^{-1}$ (i.e. 142% of Q_{50}), corresponding exactly to the $Med_{Hpk}\ Q_{max}$ for this reach. Two photo comparisons were available. No mobile grains were detected. The intermediate intensity flood visible on the graph, of about 400% of Q_{50} (i.e. 64 $m^3\ s^{-1}$), mobilized a relative D_{max} of 0.44 to 0.50 (i.e. 56 to 57 mm, very coarse gravel) and the greater than annual flood D_{max} of 0.9 and 1.4 (i.e. 103 to 154 mm, small to large cobbles).

Downstream at Ainsa, two of the flows analysed were associated with hydropeaks and a third was greater than an annual flood. Two photographic observations were available for each. The smallest hydropeak (110% of Q_{50}, i.e. 19.6 $m^3\ s^{-1}$) did not mobilize any grains. The second, associated with a higher intensity hydropeak closer to $Max_{Hpk}\ Q_{max}$ (293% of Q_{50}, i.e. 52$m^3\ s^{-1}$, visible on the graph), mobilized normalized D_{max} between 1.5 and 1.7 (i.e. between 65 and 67 mm, small cobbles), while the flood mobilized D_{max} larger than the D_{50} of 3.1 to 3.5 (i.e. 118 to 155 mm, small to large cobbles).

Finally, the floods observed at Laspuña US in the bypassed reach seem to show, for the same flow, a great variability in the normalized D_{max} mobilized between the 8 photographic observations available.

In the Cinca, only the high magnitude hydropeaks at Ainsa appear to be competent to entrain grains. Furthermore, for a given flow, the movable dimensional D_{max} is similar upstream and downstream. However, in relation to the local grain size, it is 3 times lower close to the HP at Laspuña DS than downstream at Ainsa.

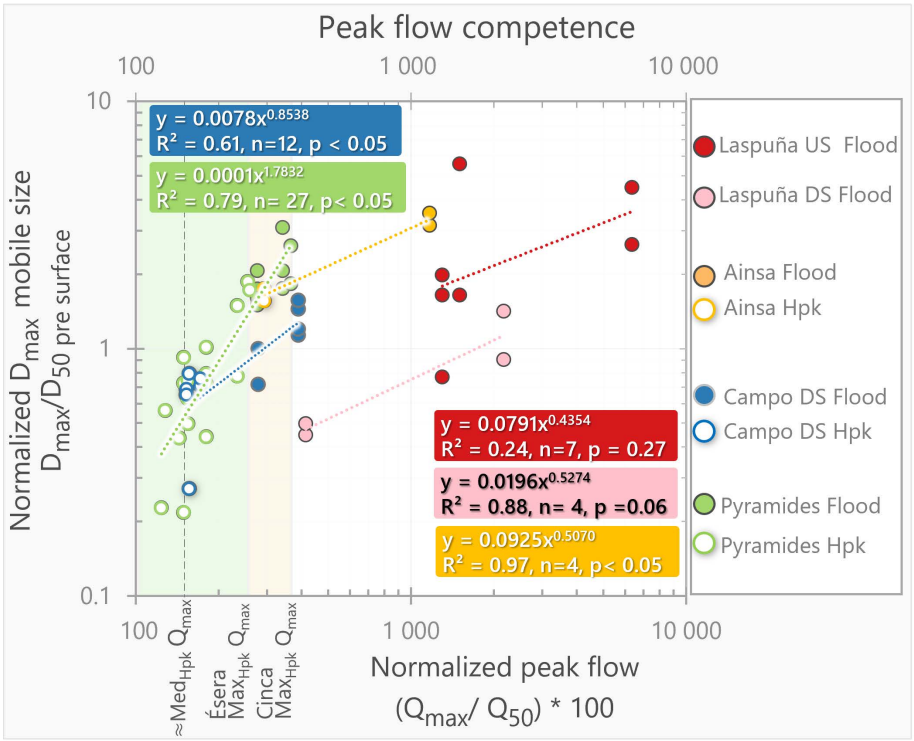

Figure 6.11: Regression relationship between the normalized peak discharge and the maximum mobile grain diameter relative to the D_{50} of the bed surface materials at the PRE-event time. Points filled in white correspond to observations associated with hydropeaks and those in color to floods.

On the Ésera, at Campo located 1 km downstream of the HP, 14 photographic observations associated with 4 different but similar hydropeak magnitudes (between 152 and 172% of the Q_{50}, i.e. between 17 and 20 m^3 s^{-1}), roughly equivalent to the Med_{Hpk} Q_{max} (154% of the Q_{50}) were available. For a given flow rate, some patches showed mobile grains while others did not (spatial variability). For a given patch with variable mobility across the range of flow, it was not necessarily the higher flow rates that mobilize the greater number of grain (temporal variability). D_{max} does not increase distinctly with increasing Q_{max}. In total, 6 of the 14 observations showed mobility with normalized D_{max} ranging from 0.27 to 0.79 (i.e. 16.5 mm to 46 mm, coarse to very coarse gravel).

Two flood-related events were also analysed. For each, 4 photographic observations were available. The lowest flood had a magnitude slightly greater than the Max_{Hpk} Q_{max} (276% of the Q_{50}, i.e. 32 m^3 s^{-1}). Only two of the patches showed mobilization with normalized D_{max} between 0.7 and 1 (i.e. between 44 and 54 mm, very coarse gravel). The second, with a magnitude of 389 % of Q_{50} (i.e. 45 m^3 s^{-1}) mobilized normalized D_{max} between 1.1 and 1.5 (i.e. 76 to 98 mm, small cobbles) on all 4 patches photographed.

Downstream at Pyramides, 21 observations corresponded to hydropeaks of 7 different magnitudes. Four of these were close to Med_{Hpk} Q_{max} (dotted line) between 123 and 155% of Q_{50} (i.e. between 17 and 21 m^3 s^{-1}). 2/3 of the patches showed mobility with a normalized D_{max} between 0.21 and 0.91 (i.e. 14 to 45 mm, medium to coarse gravel). The 3 other magnitudes, corresponding to higher magnitude hydropeaks of 180 to 250 % of Q_{50} (i.e. 24 to 35 m^3 s^{-1}), induced mobility on all the patches with normalized D_{max} between 0.4 and 1.8 (i.e. 19 to 123 mm, coarse gravel to small cobbles).

Finally, 3 magnitudes corresponding to floods with 12 photographic observations were available. The peak flows, ranging from 276 to 366% of the Q_{50} (i.e. 38 to 50.5 m^3 s^{-1}), induced mobility on all the patches with normalized D_{max} between 1.5 and 3 (i.e. 72 to 123 mm, small cobbles).

On the Ésera, for a given hydropeak flow, the dimensional and normalized D_{max} size are similar upstream and downstream. On the other hand, floods of a given magnitude seem to mobilize larger sizes at Pyramides. The strongest hydropeaks are competent enough to mobilize grain sizes similar to those of floods with a return period shorter than one year.

In general, on both rivers, hydropeaks with the highest magnitudes are often associated with natural waves or pulses, on which they are often superimposed. They are then detected as an artificial event of high magnitude. However, these peaks are truly artificial and show very rapid gradients of increase and decrease as illustrated in Figure 6.12. It is therefore appropriate to consider these observations of mobility as being associated with artificial peaks.

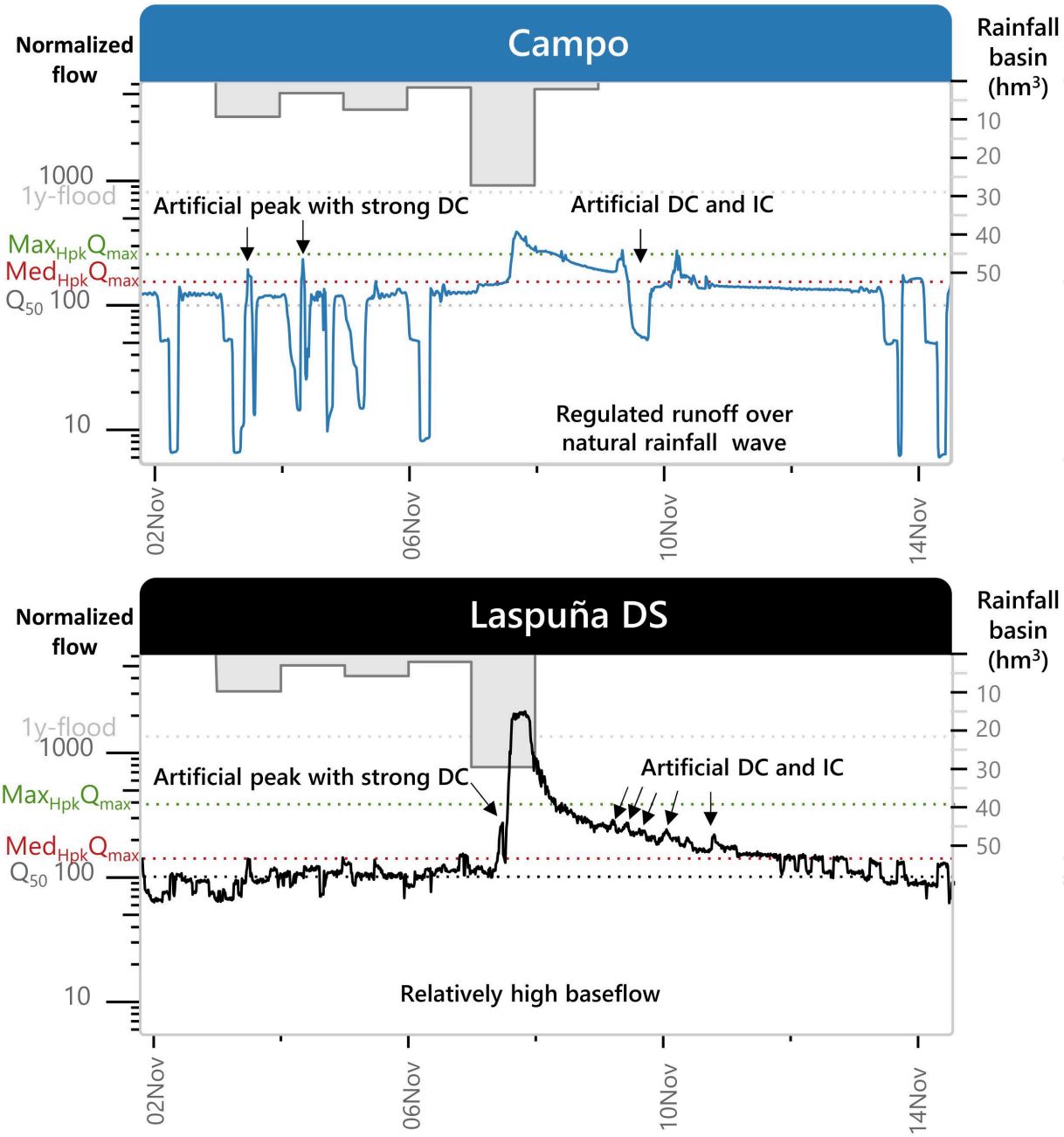

Figure 6.12: Example on the Ésera (top) and Cinca (bottom) of hydropeaks superimposed on rainfall-driven events over a 12-day interval, between 02 and 14 November 2020, during the mobility observation campaign. The left-hand axis represents the fluctuations in flow normalized by the Q_{50}, and the right-hand axis the integration of rainfall volumes over all the drainage basins. Reference flows are indicated by horizontal dotted lines. Note that the scales are identical in both graphs.

6.3.6 Longitudinal trend in the degree of bed destabilization linked to hydropeaks compared with floods

Figure 6.13 shows the relationship between the proportion of mobile grains in terms of area (1st line) and number (2nd line) in relation to the normalized peak flow, while Figure 6.14 **A** shows the mobile proportion by grain fraction. Polynomial models of order 2 are represented by the curves passing between the points. In Figure 6.14 **A**, a model has been fitted for each grain fraction. The fractions to which the D_{16}, D_{50} and D_{84} percentiles belong are highlighted by dashed curves. Proportions equal to zero indicate zero mobility (or total stability), while proportions $< 10\%$ indicate very low, marginal mobility (white zone below). Proportions between 10 and 90% (light grey area) are considered to indicate partial mobility on the photographed patches or grain fractions, while mobility greater than 90% (dark grey area) is considered to be full mobility. The vertical long dashed lines indicate the $Max_{Hpk}\ Q_{max}$ for each reach. Observations (points) and models (curves) positioned at least 10% (in the intermediate grey area) and located to the left of this line, indicate mobility generated by hydropeaks. To the right of this curve, mobility is therefore linked to natural events (i.e. flooding). In these graphs, only normalized magnitudes are shown. However, the same analysis has been carried out on dimensional data ($m^3\ s^{-1}$).

The classification of the degree of stability/destabilization of the bed may differ depending on the criterion used, whether it is based on the proportion of mobile grains or the surface area they occupy. For example, in Figure 6.13, for Laspuña DS, a flow rate of about 375% of Q_{50} results in a destabilized grain surface area of 10 to 20% (1st line), while this represents between 60 and 80% of mobile grains (2nd line). For Pyramides, a flow rate of 366% of Q_{50} can produce a mobility of more than 90% of the grains (therefore considered full, 2nd row), while this represents a disturbed surface area of only about 70% (which can be considered partial). This can be explained by the fact that relatively small grains are mobilized and the surface area they occupy on the bed is relatively small compared to their number.

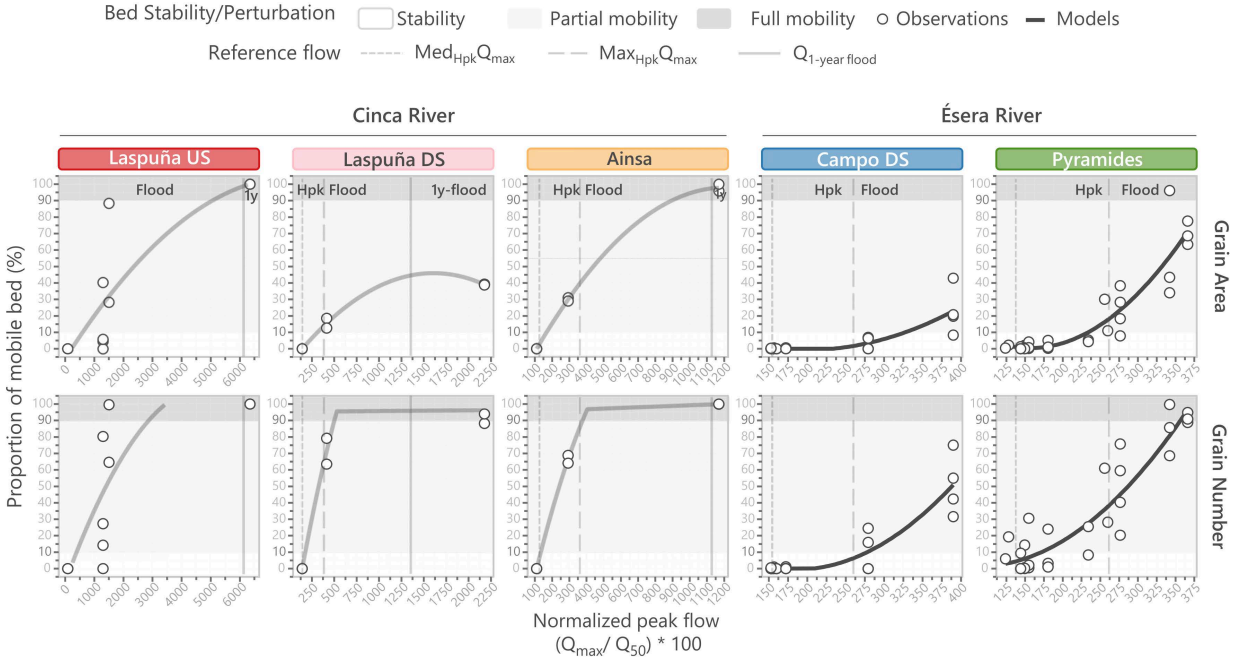

Figure 6.13: Regression relationship between the normalized peak flow and the proportion of mobile bed grains in terms of surface area (top) and number (bottom) for each reach. The points correspond to the mobility observations from the photos, and the curves to the polynomial models fitted between the points. The vertical lines indicate the reference flows, and the shaded areas from light to dark indicate the different degrees of mobility (Null or marginal in white, partial in light grey and full in dark grey).

Figure 6.14 **A** shows that for the Laspuña DS, Ainsa and Pyramides reaches, the hydropeaks can partially mobilize the grains corresponding to D_{16}. The short-dashed curves intersect the partial mobility zone to the left of the $Max_{Hpk}\ Q_{max}$ limit. At Campo DS, only the 8 mm fraction appears to have been partially mobilized by the hydropeaks. For Ainsa and Pyramides (i.e. the two most downstream reaches), the D_{50} curve (long dash) also intersects the partial mobility zone, indicating that the hydropeaks can partially mobilize the D_{50}. None of the reaches show partial mobility for D_{84}. None of the hydropeaks observed generated full mobility of the D_{16}, D_{50} and D_{84} percentiles. None of the dashed/dotted curves intersect the full mobility zone (dark grey) to the left of the $Max_{Hpk}\ Q_{max}$.

From the models established between the observed mobility and the magnitude (dimensional and normalized), it is possible to estimate, for each reach, the critical threshold flows generating partial mobility $Q_{cr\ partial}$ and those critical generating full mobility ($Q_{cr\ full}$). This is shown by the flows for which the model curves intersect the various shaded areas on the graphs. The prediction models for partial and full mobility, for the proportion of surface area with mobile grains, for the number of mobile grains and for the fractions to which the D_{16}, D_{50} and D_{84} percentiles belong are presented in Table 6.1 for normalized data and Table 6.2 for dimensional data.

Two important considerations should be made regarding these models:

– all the p values of the models are not significant ($p\ value > 0.05$). Once again, this can be explained by the high variability of mobility observations between patches for the same flow on a given reach. Nevertheless, these observations give insights and are representative of the spatial variability of grain size on the bars (see Figure 6.7, individual GSD of the patches), and of the temporal variability of mobility for magnitudes that are often similar but observed at different times (i.e. different sequences of hydropeaks interspersed between floods, see Figure 6.5). It therefore seems that these models can represent an average estimate of mobility dynamics, or at least orders of magnitude between rivers and reaches of the same river for ramping area zones.

– Estimates of the $Q_{cr\ partial}$ and $Q_{cr\ full}$ of the mobile area proportions are very similar to those for the fractions corresponding to D_{50} (intermediate grey lines in Table 6.1 and Table 6.2), while estimates of the Q_{cr} of the mobile grain number proportion are very similar to those for the fractions corresponding to D_{16} (white lines in the tables). For example, in Table 6.2, for Pyramides, the $Q_{cr\ full}$ for D_{16} is 50.4 $m^3\ s^{-1}$, similar to that for the number of mobile grains, which is 49.2 $m^3\ s^{-1}$. Or again, at Ainsa, the $Q_{cr\ partial}$ for D_{50} is 31.8 $m^3\ s^{-1}$ similar to that for the proportion of partially mobile areas of 29.8 $m^3\ s^{-1}$. These results therefore seem to suggest that, on the rivers studied in the ramping areas, although it is not possible to carry out a complex study of mobility by fraction, the stability/mobility of the grains corresponding to D_{16} and D_{50} can be estimated by simply examining the proportion of the number of mobile grains and the surface area that this represents.

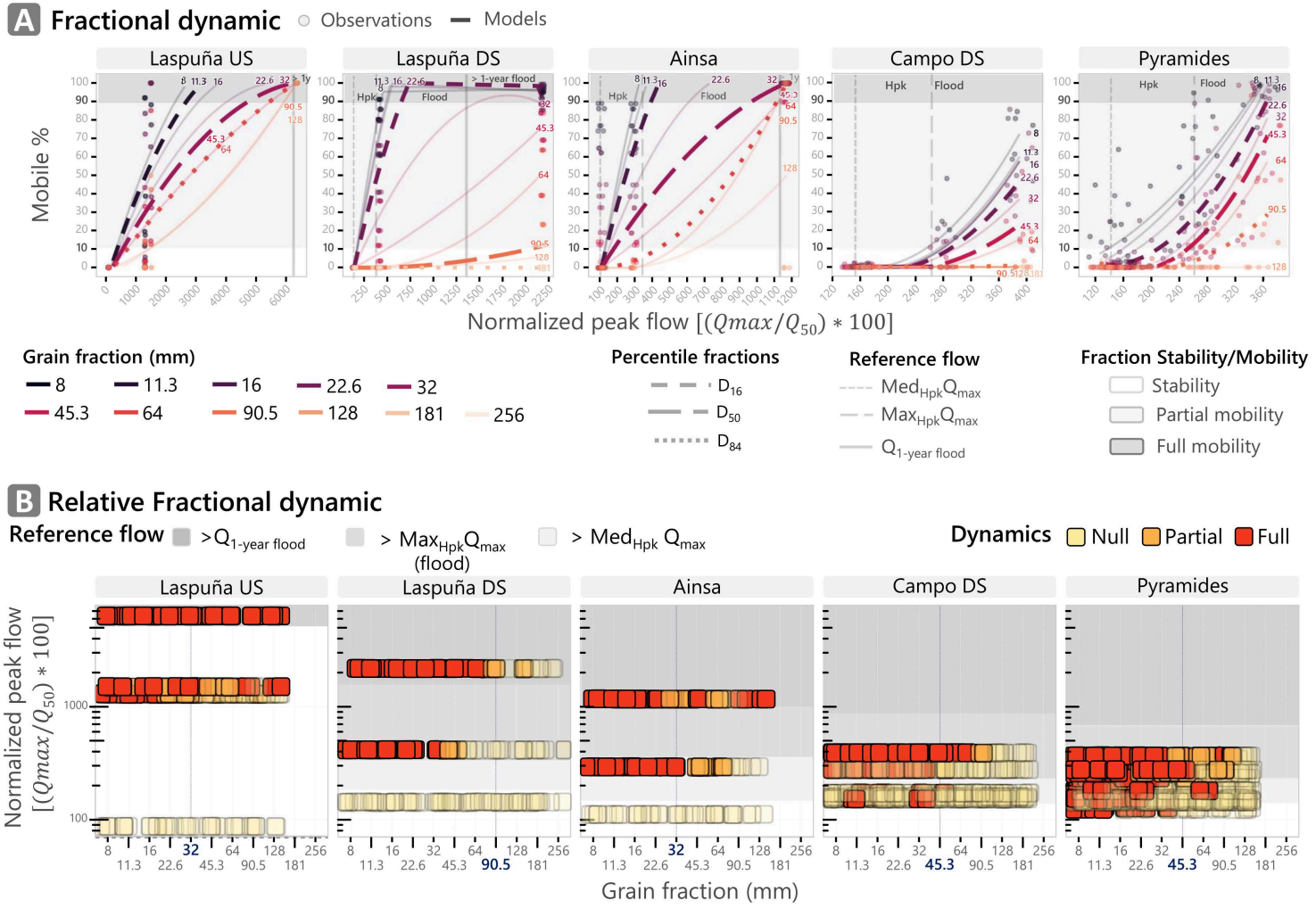

Figure 6.14:
Bed mobility. **A** Regression relationship between the normalized peak flow rate and the proportion of mobile grains per fraction. The points correspond to the mobility observations from the photographs, and the curves to the polynomial models fitted between the points. The dashed and dotted curves represent the models for the fractions to which the D_{16}, D_{50} and D_{84} belong. The vertical lines indicate the reference flows, and the shaded areas from light to dark indicate the different degrees of mobility (Null or marginal in white, partial in light grey and full in dark grey) **B**. Fractional relative mobility as a function of normalized peak flow. The colors of the squares indicate the degree of relative mobility. The vertical lines indicate the fraction of D_{50}.

Figure 6.14 **B** shows the fractional relative mobility (Wilcock and McArdell, 1997). The points are superimposed transparently and slightly offset from left to right in order to visualise the data from different patches obtained for a given flow rate. A fraction i is considered to have zero mobilization (yellow squares) if none of the grains belonging to this given fraction have been mobilized. If the proportion of a fraction p_i is under-represented in the set of mobile grains compared with its initial surface proportion F_i , then it is considered to be relatively partially mobile ($p_i/F_i < 1$, orange squares). Conversely, if it is over-represented or in equal proportion, it is considered fully mobile ($p_i/F_i \geq 1$, red squares). The fraction corresponding to D_{50} is indicated by a dark vertical line. The light grey areas denote the rank between the peak flow of the hydropeaks $Med_{Hpk}\ Q_{max}$ and $Max_{Hpk}\ Q_{max}$, the intermediate grey areas represent frequent floods, and the dark grey areas represent floods with a return period of more than one year. In addition to obtaining the maximum mobile diameter (D_{max}), the data acquired by photographic methods, particularly during low-intensity transport events (partial mobility), make it possible to assess whether all the smaller fractions are mobilized in the same way. The floods examined on the Cinca river show only partial mobility (orange squares in Figure 6.14 **B**) for certain classes below the coarsest mobilized. It should also be noted that some of the hydropeaks on the Ésera at Campo and Pyramides caused the mobility of fractions sometimes greater than D_{50}, without mobilizing, even partially, smaller fractions. It is difficult to know whether this phenomenon occurs on the Cinca River, as only one hydropeak with mobility was observed at Ainsa. However, it did not exhibit this behavior.

Table 6.1: Partial and full mobility critical discharge prediction from the 2 order polynomial models with their coefficient (α , β_1 , and β_2), coefficient of correlation (R^2) and p value, for the proportion of surface area of mobile grains, the number of mobile grains and the fractions to which the D_{16}, D_{50} and D_{84} percentiles belong and the associated **normalized** threshold critical flows generating partial mobility ($Q_{cr\ )partial}$ and those generating full mobility ($Q_{cr\ full}$).

Reaches	Bed mobility variable	Mobile proportion = $\alpha + \beta_1 Q + \beta_2 Q^2$					$Q_{cr\ partial}$ (10%) bed mobility (% of Q_{50})	$Q_{cr\ full}$ (90%) bed mobility (% of Q_{50})
		R^2	p value	α	β_1	β_2		
Laspuña US	D_{84}	0.53	0.404	-5.96	0.02	-0.000001	735.5	5484.5
	Area proportion (%)	0.61	0.234	-5.87	0.03	-0.000002	590.8	5042.0
	D_{50}	0.52	0.257	-6.83	0.03	-0.000002	569.2	4751.0
	Number proportion (%)	0.50	0.095	-7.92	0.05	-0.000005	386.5	2864.0
	D_{16}	0.42	0.115	-8.70	0.05	-0.000005	381.1	2685.6
Laspuña DS	D_{84}	0.00	0.971	0.10	0.00	0.000002	2723.0	7601.5
	Area proportion (%)	0.98	**0.009**	-9.37	0.07	-0.000021	0.0	0.0
	D_{50}	0.00	0.971	0.19	0.00	0.000003	2033.0	5527.6
	Number proportion (%)	0.97	**0.002**	-44.43	0.33	-0.000123	176.7	501.2
	D_{16}	0.92	**0.022**	-32.99	0.24	-0.000086	188.6	654.2
Ainsa	D_{84}	1.00	**0.043**	0.51	-0.01	0.000085	427.2	1113.4
	Area proportion (%)	1.00	**0.001**	-20.67	0.20	-0.000081	167.6	892.7
	D_{50}	0.99	**0.033**	-17.16	0.16	-0.000052	178.4	966.9
	Number proportion (%)	1.00	**0.000**	-49.85	0.49	-0.000306	134.4	377.1
	D_{16}	1.00	**0.000**	-47.44	0.46	-0.000288	135.6	393.5
Campo DS	D_{84}	0.13	0.373	1.40	-0.01	0.000032	782.5	1903.9
	Area proportion (%)	0.68	0.079	24.02	-0.25	0.000638	327.4	574.5
	D_{50}	0.48	0.116	32.62	-0.33	0.000777	335.3	555.1
	Number proportion (%)	0.83	**0.037**	41.22	-0.45	0.001225	277.9	456.8
	D_{16}	0.83	**0.016**	46.60	-0.49	0.001268	290.3	463.6
Pyramides	D_{84}	0.56	**0.031**	32.07	-0.36	0.000954	298.8	498.2
	Area proportion (%)	0.84	**0.015**	40.03	-0.51	0.001613	233.7	392.3
	D_{50}	0.77	**0.008**	59.15	-0.70	0.001992	251.0	389.1
	Number proportion (%)	0.85	0.389	10.84	-0.22	0.001228	171.8	356.5
	D_{16}	0.84	0.079	31.51	-0.45	0.001677	208.0	365.2

Table 6.2: Partial and full mobility critical discharge prediction from the 2 order polynomial models with their coefficient (α , β_1 , and β_2), coefficient of correlation (R^2) and p value, for the proportion of surface area of mobile grains, the number of mobile grains and the fractions to which the D_{16}, D_{50} and D_{84} percentiles belong and the associated **dimensional** threshold critical flows generating

Reaches	Bed mobility variable	Mobile proportion = $\alpha + \beta_1 Q + \beta_2 Q^2$					$Q_{cr\ partial}$ (10%) bed mobility (m^3s^{-1})	$Q_{cr\ full}$ (90%) bed mobility (m^3s^{-1})
		R^2	p value	α	β_1	β_2		
Laspuña US	D_{84}	0.53	0.404	-5.96	0.66	-0.0008	25.0	186.5
	Area proportion (%)	0.61	0.234	-5.87	0.82	-0.0015	20.1	171.4
	D_{50}	0.52	0.257	-6.83	0.91	-0.0019	19.4	161.6
	Number proportion (%)	0.50	0.095	-7.92	1.42	-0.0043	13.1	97.4
	D_{16}	0.42	0.115	-8.70	1.50	-0.0046	13.0	91.3
Laspuña DS	D_{84}	0.00	0.971	0.10	-0.01	0.0001	422.0	1178.2
	Area proportion (%)	0.98	**0.009**	-9.37	0.44	-0.0009	x	x
	D_{50}	0.00	0.971	0.19	-0.01	0.0001	315.2	856.8
	Number proportion (%)	0.97	**0.002**	-44.43	2.13	-0.0051	27.4	77.7
	D_{16}	0.92	**0.022**	-32.99	1.57	-0.0036	29.2	101.4
Ainsa	D_{84}	1.00	**0.043**	0.51	-0.08	0.0027	76.0	198.2
	Area proportion (%)	1.00	**0.001**	-20.67	1.10	-0.0026	29.8	158.9
	D_{50}	0.99	**0.033**	-17.16	0.91	-0.0017	31.8	172.1
	Number proportion (%)	1.00	**0.000**	-49.85	2.73	-0.0097	23.9	67.1
	D_{16}	1.00	**0.000**	-47.44	2.60	-0.0091	24.1	70.0
Campo DS	D_{84}	0.13	0.373	1.40	-0.12	0.0024	90.0	219.0
	Area proportion (%)	0.68	**0.079**	24.02	-2.19	0.0482	37.6	66.1
	D_{50}	0.48	0.116	32.62	-2.85	0.0588	38.6	63.8
	Number proportion (%)	0.83	**0.037**	41.22	-3.94	0.0926	32.0	52.5
	D_{16}	0.83	**0.016**	46.60	-4.30	0.0958	33.4	53.3
Pyramides	D_{84}	0.56	**0.031**	32.07	-2.60	0.0501	41.2	68.7
	Area proportion (%)	0.84	**0.015**	40.03	-3.66	0.0847	32.3	54.1
	D_{50}	0.77	**0.008**	59.15	-5.04	0.1046	34.6	53.7
	Number proportion (%)	0.85	0.389	10.84	-1.56	0.0645	23.7	49.2
	D_{16}	0.84	**0.079**	31.51	-3.28	0.0881	28.7	50.4

partial mobility ($Q_{cr\ )partial}$ and those generating full mobility ($Q_{cr\ full}$).

Observations of fractional mobility in the Ésera river show that simple analysis of flow competence (D_{max} mobile ~ magnitude) is not sufficient to characterize the impact of hydropeaks on substrate stability/destabilization. In Campo, the lowest intensity hydropeaks observed (<200% of Q_{50}) were able to mobilize grains from the 11.3 and 32 mm fractions (Figure 6.14 **B**). These fractions were considered to be relatively totally mobile (red squares) due to their over-representation in the mobilized grains compared with their proportion at the surface. However, only a marginal quantity of these fractions was mobilized (Figure 6.14 **A**, graph above, no points in the shaded area for flows below 200% of Q_{50}). Bed destabilization may be low despite the relatively coarse grains mobilized close to D_{50} due to their shape and arrangement on the bed (Buffington and Montgomery, 1997; Hodge et al., 2013).

6.3.7 Frequency and timing of bed destabilization linked to hydropeaks and floods

The multi-decennial flow series available at the Escalona$_{CHE}$ and Campo$_{CHE}$ stations, transformed into $Q_{max\ DAY}$ series, are shown in Figure 6.15 **A**. On the basis of these data series and those available from the Laspuña US and DS measurement probes on the Cinca and Pyramides and Santaliestra on the Ésera, GAM-type models have been established to reconstruct the flows in these reaches (Figure 6.15 **B**).

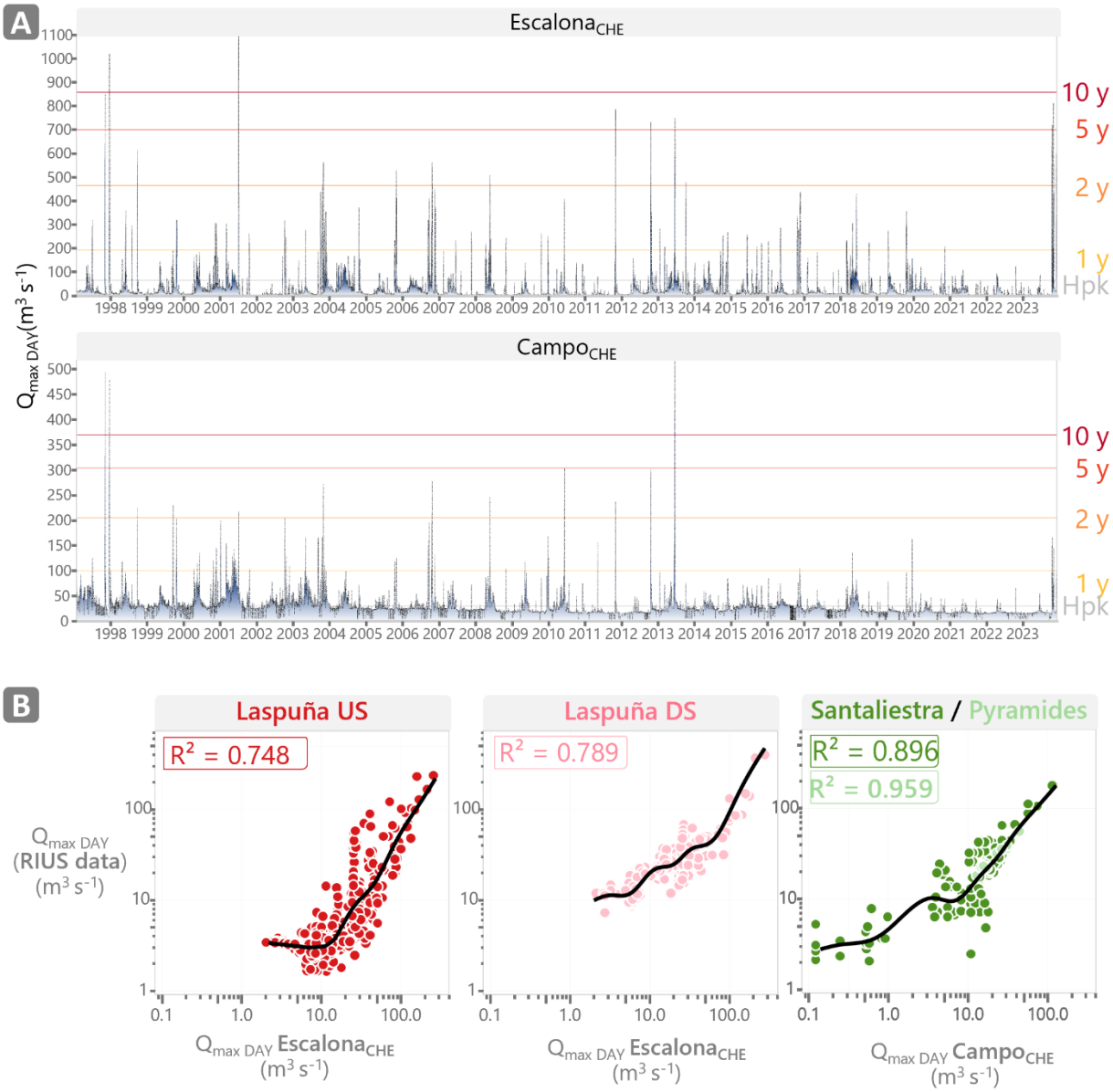

Figure 6.15: A Series of multi-decadal flows. **B** GAM models for reconstructing multi-decennial flows for the Laspuña US, Laspuña DS and Santaliestra/Pyramides stations.

Figure 6.16 shows, for each reach, an estimate of the influence of the flow on the degree of bed destabilization over time. Each graph represents the presumed intensity of daily mobility between 1st January 1997 and 9th December 2023, on the 5 reaches studied and for the grains corresponding to percentiles D_{16}, D_{50} and D_{84}, which can be presumed to be stable, partially mobilized by hydropeaks, partially mobilized by natural events and fully mobile.

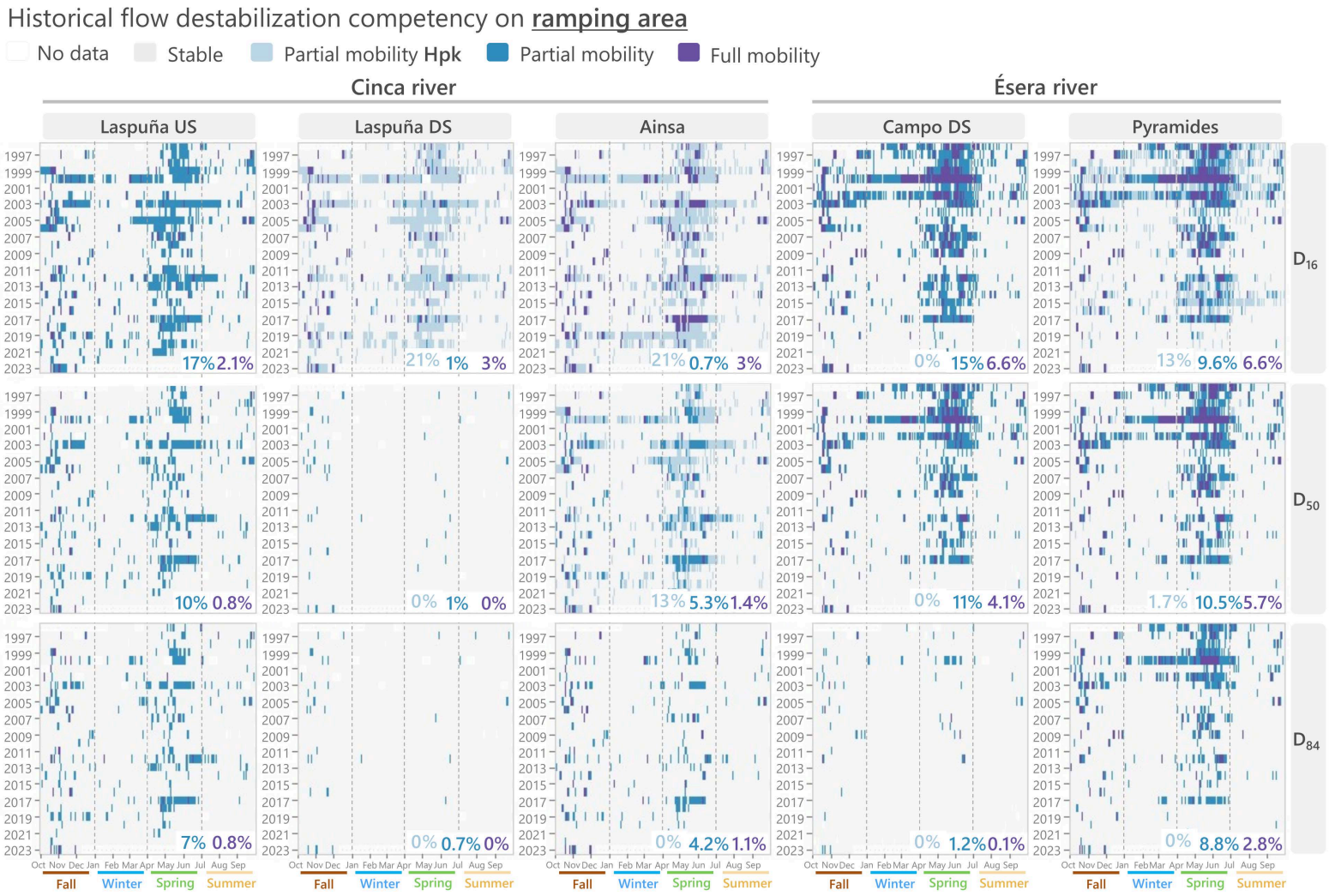

Figure 6.16: Intensity of mobility of grain fractions corresponding to percentiles D_{16} (top), D_{50} (middle) and D_{84} (bottom) over time for the 5 reaches studied on the two river segments (left Cinca and right Ésera). The reaches are ordered from upstream (left) to downstream (right). $Q_{max\ DAY}$ data are ordered by hydrological year on the *y*-axis and by month on the *x*-axis. The immobile bed is represented in grey, the partial mobility attributed to hydropeaks in light blue, the partial mobility attributed to natural events in dark blue and the full mobility in purple. Missing data are shown in white. The occurrence (%) of each type of mobility is shown at the bottom right of each graph.

These frequencies of occurrence of partial and full mobility are only estimates and are only valid for the units sampled, i.e. the ramping area. Additionally, the destabilization thresholds may vary over time depending on the evolution of the arrangement of the grains between them and the flow magnitude histories to which the bed is subjected (Masteller et al., 2019b; Masteller and Finnegan, 2017; Ockelford et al., 2019; Pender et al., 2007). Nevertheless, the data observed to build these models represent a certain proportion of this potential temporal variability of mobilization thresholds.

Partial and full mobility seems to occur mainly in spring and to a lesser extent in autumn. The bed mobility regime therefore seems to follow the seasonal hydrological regime. The frequency of bed destabilization varies greatly from year to year. The years 2000 and 2002 on the Ésera and 2000 and 2003 on the Cinca appear to have presented a high potential for bed destabilization. The historical rainfall estimates available on the Aragon Climatic Atlas website (Saz et al., 2020) show significant rainfall throughout these years in all the basins (see Supplementary material). These estimates do not appear to be errors due to anomalous data resulting from incorrectly estimated flows at the $Escalona_{CHE}$ and $Campo_{CHE}$ stations.

The presumed or estimated frequency of mobilization decreases with increasing grain size. The D_{16} percentile is mobilized more often than the D_{50} percentile, and the D_{50} percentile more often than the D_{84} percentile. One exception can be seen. At Laspuña DS, the D_{50} and D_{84} show similar mobilization frequencies. This section is relatively narrow (ratio of base flow width to active width=0.77) compared with the others on the same river (ratio of ≤ 0.3) for a similar slope and is located at the outlet of the HP. It is therefore subject to stronger hydropeaks (magnitude of Q_{max} and $MARR_{IC}$) than downstream, as demonstrated in Chapter 3, Section 3.2.1. It also has the coarsest particle size (D_{50} = 114 mm). López et al. (2020) showed that the flow had the greatest competence at this point. This reach therefore seems to represent a section dominated by transport with a very stable bed. Although the Laspuña dam can allow sediment to pass through (infrequently, during flood periods), this reach has a certain sediment deficit of medium and coarse grain due to competent transport (around two hydropeaks per day). Little sediment is available.

The frequency of movement of D_{16} appears to be similar for the two reaches of Laspuña DS and Ainsa impacted by the hydropeaks. Of the 24% of the time when D_{16} was at least partially mobilized, 87.5% (i.e. 21% of the time) was potentially linked to artificial events. At Ainsa, the D_{50} was potentially partially mobilized 18.3% of the time, 78% of which could be linked to artificial events.

On the river Ésera, of the two reaches studied, only the Pyramides reach appears to show mobility episodes linked to hydropeaks. Of the 3 percentiles studied, only the grains corresponding to D_{16} appear to be affected by hydropeaks. Of the 29.2% of the time when the grains in D_{16} are at least partially mobile, 44% (or 13% of the total time) are potentially linked to artificial events.

6.3.8 Summary of the longitudinal changes of particle mobility

The two complementary methods used, namely flow competence and the degree of mobility with respect to a reference threshold, based on photographic observations processed with the *PhotoMOB* tool, made it possible to characterize various aspects of grain mobility. Models were established to estimate, longitudinally, the degree of bed destabilization of different magnitudes event (i.e. hydropeak and flood) on bed grain mobility.

Figure 6.17 illustrates the application of the models established for modelling the 3 reference flows ($Med_{Hpk}\ Q_{max}$, $Max_{Hpk}\ Q_{max}$, $Q_{1-year\ flood}$) on the two river segments concerning the maximum movable size (Figure 6.17 **A**) and the degree of destabilization of grain fractions corresponding to D_{16}, D_{50} and D_{84} (Figure 6.17 **B**). The solid curves represent the Ésera river segment, while the dashed curves represent the Cinca river segment.

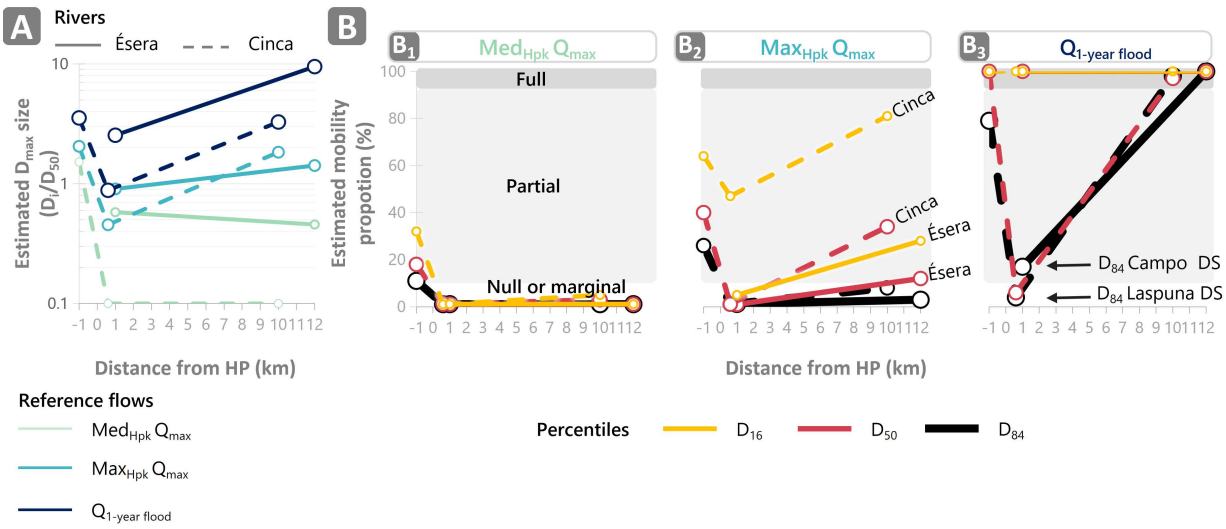

Figure 6.17: Models for longitudinal assessment of the effect of hydropeaks on bed mobility. **A** Models to predict the movable D_{max} per reach. The 3 reference flows are modelled. **B** Models predicting the mobile proportion for the 3 percentiles D_{16}, D_{50} and D_{84}. The 3 reference flows are modelled (**B1**, the median of the peak flows of the hydropeaks, **B2**, the maximum peak flow of the detected hydropeaks, **B3**, the annual flood).

Q_{max} magnitudes corresponding to those of the hydropeaks ≤ the $Med_{Hpk}\ Q_{max}$ (light green curves in Figure 6.17 **A** and panel **B1**) do not appear to lead to mobilization of the bed grains in the reach affected by the hydropeaks in the Cinca river (Figure 6.17 **A**, light green dashed curve). In the river Ésera (continuous light green curve), on both the upstream and downstream reaches, such magnitudes can result in maximum relative grain sizes (D_{max}/D_{50}) of between 0.5 and 0.6. However, this only represents marginal transport of a few grains close to D_{16} (Figure 6.17 panel **B1**).

The magnitudes corresponding to the strongest hydropeaks detected ($Max_{Hpk}\ Q_{max}$) (Figure 6.17 **A**, light blue curves and Panel **B2**) may be responsible for the mobilization of grain sizes ≤ D_{50} on the two sections close to the HP (0.6 km Laspuña DS and 1km Campo DS). There are marginal (<10%) in Campo DS. At Laspuña (Cinca), relatively fine grains (D_{16}, yellow curve) were partially destabilized (panel **B2**, 0.6 km). On the other hand, downstream for the two reaches located 10 and 12 km away (Ainsa on the Cinca and Pyramides on the Ésera respectively), the maximum movable grain sizes for such a magnitude are > D_{50} and the fine and median grain sizes can be considered as partially destabilized (extremity of the red and yellow curves in the intermediate grey zone on panels **B2**).

Finally, the annual floods (Figure 6.17 **A** dark blue curves and Panel **B3**) appear to be able to destabilize the bed of the Ésera segment to a greater extent than that of the Cinca, with coarser movable grains downstream (almost 10 times the D_{50} at Pyramides - 12 km - compared with barely 3 at Campo DS - 1 km). The fine (D_{16}) and medium (D_{50}) grains are completely destabilized both upstream and downstream (Figure 6.17 panel **B3**, continuous yellow and red curve), while the coarser grains (D_{84}, black curve) are only partially destabilized at Campo DS. In the Cinca, there seems to be a significant disparity between the Laspuña DS reach, near the HP 0.6 km, and the other two, which show similar mobility. The maximum movable sizes are the smallest and remain below the D_{50}. Grains of relatively medium to coarse size are not mobilized or only marginally (Figure 6.17 Panel **B3**, 0.6 km).

6.4 CONCLUSION

This study presents a longitudinal assessment of the effect of flood and hydropeaks on the bed material mobility in ramping areas, which are highly subject to hydropeaking flow variations. The *PhotoMOB* photographic method was used to monitor bed mobility over two approximately 10 km long segments of mountain rivers located in the Pyrenees. The two basins have similar climatic and geological characteristics, but different valley and channel morphologies and hydropeaking regimes.

The main conclusions of this study are as follows:

1. The results obtained using the "Area-by-Number" photographic approach to characterize grain size distribution were compared with those obtained using the "Grid-by-Number" approach with measurements of the *b*-axis by template if conversion related to the flatness of the particles are applied. The two approaches produced comparable results, with general differences of between 3 and 20%.

2. Comparative analyses of particle size distributions PRE- and POST-hydrological events showed that hydropeaks close to Med_{Hpk} Q_{max}, did not lead to significant changes in particle size composition (GSD) in the short term.

3. The hydrological characteristics of the hydropeaks that best explain the mobility of bed material are peak flow ($Q_{max\ norm}$) and the maximum ramping rate of, increase ($MARR_{norm\ IC}$). Nevertheless, the observations showed a wide dispersion, probably related to the spatial and temporal variability of the grain characteristics (size, weight, arrangement between them).

4. The degree of mobility of grains close to a size of D_{50} and D_{16} can be examined indirectly by assessing the proportion of the bed area mobilized and the proportion of the number of mobile grains, respectively.

5. It was observed, that only hydropeaks with peak flows greater than the median peak flow (> 180-200% of Q_{50}), could lead to significant bed grain destabilization, of partial type.

6. Partial mobility mainly concerned the downstream reaches located 10 and 12 km from the HPs, where the grain sizes were finer due to the contribution of tributaries, rather than those closer, located 0.6 and 1 km.

7. The particles of the coarsest fractions that were mobilized downstream with a significant partial degree of mobility ($\geq$ 10% mobility) and whose diameter was $\leq D_{50}$, as a result of these artificial peaks, belonged to the grain fractions 32 - 45.3 mm.

8. It was observed that hydropeaks of similar intensity on the two downstream sections could marginally set in motion coarse grains reaching up to 1.7 times the D_{50}, i.e. 123 mm (small cobble) at Pyramides and 67 mm (small cobble) at Ainsa.

9. The observed hydropeaks mobilized smaller grain sizes and quantities than floods. However, given that the frequency of occurrence of artificial peaks is greater than that of floods, it was estimated that hydropeaks could be associated with between 44% and 87% of the time when the bed was at least partially destabilized, respectively on the Ésera at Pyramides and at both Cinca reaches.

Supplementary material

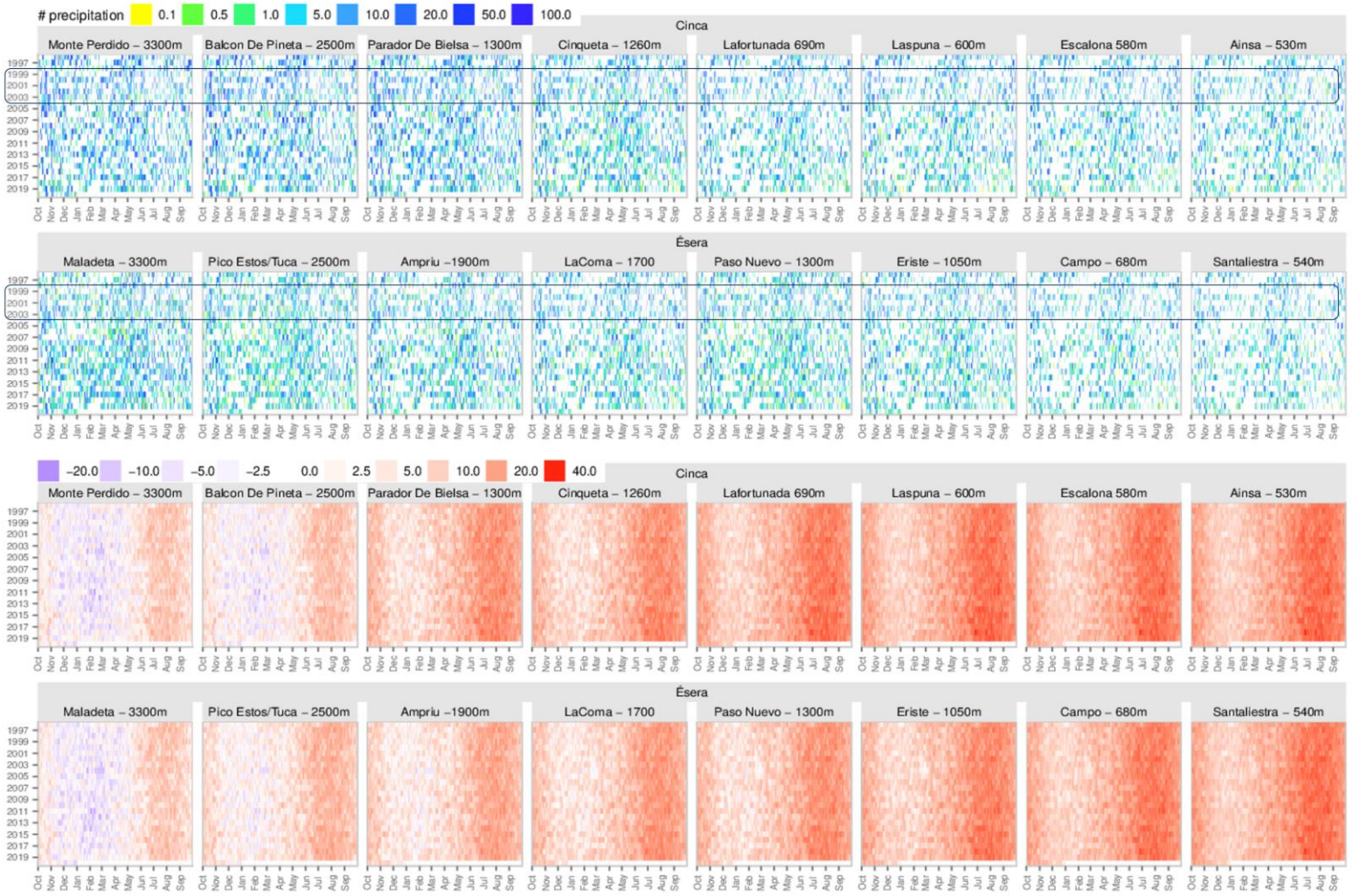

Historical estimates of daily rainfall in mm (top) and average daily temperatures (bottom) at several points in the two basins (Upper Cinca, 1st line and Upper Ésera 2nd line) over the period 1997-2023). Data are ordered by hydrological year on the y-axis and by month on the x-axis. Data source: Saz et al. (2020)

INDEX

REFERENCES

Alonso, C., **Román, A.**, **Bejarano, M.D.**, **Garcia de Jalon, D.** and **Carolli, M.** (2017) A graphical approach to characterize sub-daily flow regimes and evaluate its alterations due to hydropeaking. *Sci. Total Environ.*, **574**, 532–543. DOI:10.1016/j.scitotenv.2016.09.087

Attali, D. (2023) shinydisconnect: Show a nice message when a "Shiny" app disconnects or errors. ,https://CRAN.R-project.org/package=shinydisconnect

Attali, D. (2021) shinyjs: Easily improve the user experience of your shiny apps in seconds. ,https://CRAN.R-project.org/package=shinyjs

Bätz, N., **Judes, C.** and **Weber, C.** (2023) Nervous habitat patches: The effect of hydropeaking on habitat dynamics. *River Research and Applications*, **39**, 349–363. DOI:10.1002/rra.4021

Béjar, M., **Gibbins, C.N.**, **Vericat, D.** and **Batalla, R.J.** (2017) Effects of Suspended Sediment Transport on Invertebrate Drift. *River Res. Appl.*, **33**, 1655–1666. DOI:10.1002/rra.3146

Bejarano, M.D., **Sordo-Ward, Á.**, **Alonso, C.** and **Nilsson, C.** (2017) Characterizing effects of hydropower plants on sub-daily flow regimes. *J. Hydrol.*, **550**, 186–200. DOI:10.1016/j.jhydrol.2017.04.023

Boavida, I., **Harby, A.**, **Clarke, K.D.** and **Heggenes, J.** (2017) Move or stay: Habitat use and movements by Atlantic salmon parr (Salmo salar) during induced rapid flow variations. *Hydrobiologia*, **785**, 261–275. DOI:10.1007/s10750-016-2931-3

Buffington, J.M. and **Montgomery, D.R.** (1997) A systematic analysis of eight decades of incipient motion studies, with special reference to gravel-bedded rivers. *Water Resources Research*, **33**, 1993–2029. DOI:10.1029/96WR03190

Bunte, K. and **Abt, S.R.** (2001) Sampling surface and subsurface particle-size distributions in wadable gravel-and cobble-bed streams for analyses in sediment transport, hydraulics, and streambed monitoring. *U.S. Department of Agriculture, Forest Service, Rocky Mountain Research Station*, Ft. Collins, CO. DOI:10.2737/RMRS-GTR-74

Chang, W. and **Borges Ribeiro, B.** (2021) shinydashboard: Create dashboards with "Shiny." ,https://CRAN.R-project.org/package=shinydashboard

Chang, W., **Cheng, J.**, **Allaire, J.**, **Sievert, C.**, **Schloerke, B.**, **Xie, Y.**, **Allen, J.**, **McPherson, J.**, **Dipert, A.** and **Borges, B.** (2023) shiny: Web application framework for r. https://CRAN.R-project.org/package=shiny

Church (2006) BED MATERIAL TRANSPORT AND THE MORPHOLOGY OF ALLUVIAL RIVER CHANNELS. *Annual Review of Earth and Planetary Sciences*, **34**, 325–354. DOI:10.1146/annurev.earth.33.092203.122721

Courret, D., **Baran, P.** and **Larinier, M.** (2021) An indicator to characterize hydrological alteration due to hydropeaking. *Journal of Ecohydraulics*, **6**, 139–156. DOI:10.1080/24705357.2020.1871307

Dey, S. (2014) Fluvial Hydrodynamics: Hydrodynamic and Sediment Transport Phenomena. *Springer Berlin Heidelberg*, Berlin, Heidelberg. DOI:10.1007/978-3-642-19062-9

Dey, S. and **Ali, S.Z.** (2019) Bed sediment entrainment by streamflow: State of the science. *Sedimentology*, **66**, 1449–1485. DOI:10.1111/sed.12566

Edwards, S.M. (2023) lemon: Freshing up your "ggplot2" plots. https://CRAN.R-project.org/package=lemon

Firke, S. (2023) janitor: Simple tools for examining and cleaning dirty data. ,https://CRAN.R-project.org/package=janitor

Folk, R.L. and **Ward, W.C.** (1957) Brazos River bar [Texas]; a study in the significance of grain size parameters. *Journal of Sedimentary Research*, 3–26. DOI: https://doi.org/10.1306/74D70646-2B21-11D7-8648000102C1865D

Fryirs, K.A. and **Brierley, G.J.** (2013) Geomorphic analysis of river systems: an approach to reading the landscape, 1. publ. *Wiley-Blackwell*, Chichester.

García-Ruiz, J.M., **Puigdefábregas, J.** and **Novau, J.C.** (1986) La acumulación de nieve en el pirineo central y su influencia hidrológica. *Pirineos*, **127**, 27–72. DOI: http://hdl.handle.net/10261/95396

Gibbins, C., **Vericat, D.** and **Batalla, R.J.** (2007) When is stream invertebrate drift catastrophic? The role of hydraulics and sediment transport in initiating drift during flood events. *Freshwater Biol*, **52**, 2369–2384. DOI:10.1111/j.1365-2427.2007.01858.x

Gilbert, G.K. (1914) The Transportation of Debris by Running Water. *California Water Science Center, U.S. Geological Survey*. DOI:10.3133/pp86

Graham, D.J., **Rice, S.P.** and **Reid, I.** (2005) A transferable method for the automated grain sizing of river gravels. *Water Resour. Res.*, **41**, 1–12. DOI:10.1029/2004WR003868

Graham, D.J., **Rollet, A.-J.**, **Rice, S.P.** and **Piégay, H.** (2012) Conversions of Surface Grain-Size Samples Collected and Recorded Using Different Procedures. *J. Hydraul. Eng.*, **138**, 839–849. DOI:10.1061/(ASCE)HY.1943-7900.0000595

Greimel, F., **Grün, B.**, **Hayes, D.S.**, **Höller, N.**, **Haider, J.**, **Zeiringer, B.**, **Holzapfel, P.**, **Hauer, C.** and **Schmutz, S.** (2023) PeakTrace : Routing of hydropeaking waves using multiple hydrographsA novel approach. *River Research and Applications*, **39**, 326–339. DOI:10.1002/rra.3978

Haschenburger, J.K. and **Wilcock, P.R.** (2003) Partial transport in a natural gravel bed channel. *Water Resources Research*, **39**, 2002WR001532. DOI:10.1029/2002WR001532

Hassan, M.A. and **Ergenzinger, P.** (2003) Use of tracers in fluvial geomorphology. In: (Ed. G.M. Kondolf and H. Piégay), *John Wiley & Sons, Ltd*, Chichester, UK, 397–423. DOI:10.1002/0470868333.ch14

Hauer, C., **Schober, B.** and **Habersack, H.** (2013) Impact analysis of river morphology and roughness variability on hydropeaking based on numerical modelling: RIVER MORPHOLOGICAL IMPACTS ON HYDROPEAKING PROCESSES. *Hydrol. Process.*, **27**, 2209–2224. DOI:10.1002/hyp.9519

Hauer, F.R., **Locke, H.**, **Dreitz, V.J.**, **Hebblewhite, M.**, **Lowe, W.H.**, **Muhlfeld, C.C.**, **Nelson, C.R.**, **Proctor, M.F.** and **Rood, S.B.** (2016) Gravel-bed river floodplains are the ecological nexus of glaciated mountain landscapes. *Science Advances*, **2**, e1600026. DOI:10.1126/sciadv.1600026

Hayes, D.S., **Bruno, M.C.**, **Alp, M.**, **Boavida, I.**, **Batalla, R.J.**, **Bejarano, M.D.**, **Noack, M.**, **Vanzo, D.**, **Casas-Mulet, R.**, **Vericat, D.**, **Carolli, M.**, **Tonolla, D.**, **Halleraker, J.H.**, **Gosselin, M.-P.**, **Chiogna, G.**, **Zolezzi, G.** and **Venus, T.E.** (2023) 100 key questions to guide hydropeaking research and policy. *Renewable and Sustainable Energy Reviews*, **187**, 113729. DOI:10.1016/j.rser.2023.113729

Hodge, R.A., **Sear, D.A.** and **Leyland, J.** (2013) Spatial variations in surface sediment structure in rifflepool sequences: a preliminary test of the Differential Sediment Entrainment Hypothesis (DSEH). *Earth Surface Processes and Landforms*, **38**, 449–465. DOI:10.1002/esp.3290

Jowett, I.G., **Richardson, J.**, **Biggs, B.J.F.**, **Hickey, C.W.** and **Quinn, J.M.** (1991) Microhabitat preferences of benthic invertebrates and the development of generalised *Deleatidium* spp.

habitat suitability curves, applied to four New Zealand rivers. *New Zealand Journal of Marine and Freshwater Research*, **25**, 187–199. DOI:10.1080/00288330.1991.9516470

Kennedy, T.A., **Muehlbauer, J.D.**, **Yackulic, C.B.**, **Lytle, D.A.**, **Miller, S.W.**, **Dibble, K.L.**, **Kortenhoeven, E.W.**, **Metcalfe, A.N.** and **Baxter, C.V.** (2016) Flow Management for Hydropower Extirpates Aquatic Insects, Undermining River Food Webs. *BioScience*, **66**, 561–575. DOI:10.1093/biosci/biw059

Komar, P.D. (1987) Selective gravel entrainment and the empirical evaluation of flow competence. *Sedimentology*, **34**, 1165–1176. DOI:10.1111/j.1365-3091.1987.tb00599.x

Komsta, L. and **Novomestky, F.** (2022) moments: Moments, cumulants, skewness, kurtosis and related tests. ,https://CRAN.R-project.org/package=moments

Le Coarer, Y., **Lizée, M.-H.**, **Beche, L.** and **Logez, M.** (2023) Horizontal ramping rate framework to quantify hydropeaking stranding risk for fish. *River Research and Applications*, **39**, 478–489. DOI:10.1002/rra.4087

López, R., **Garcia, C.**, **Vericat, D.** and **Batalla, R.J.** (2020) Downstream changes of particle entrainment in a hydropeaked river. *Science of The Total Environment*, **745**, 140952. DOI:10.1016/j.scitotenv.2020.140952

López, R., **Ville, F.**, **Garcia, C.**, **Batalla, R.J.** and **Vericat, D.** (2023) Bed-material entrainment in a mountain river affected by hydropeaking. *Science of The Total Environment*, **856**, 159065. DOI:10.1016/j.scitotenv.2022.159065

MacKenzie, L.G., **Eaton, B.C.** and **Church, M.** (2018) Breaking from the average: Why large grains matter in gravel-bed streams: Breaking from the average. *Earth Surf. Process. Landforms*, **43**, 3190–3196. DOI:10.1002/esp.4465

Mair, D., **Witz, G.**, **Do Prado, A.H.**, **Garefalakis, P.** and **Schlunegger, F.** (2023) Automated detecting, segmenting and measuring of grains in images of fluvial sediments: The potential for large and precise data from specialist deep learning models and transfer learning. *Earth Surface Processes and Landforms*, esp.5755. DOI:10.1002/esp.5755

Mao, L. (2018) The effects of flood history on sediment transport in gravel-bed rivers. *Geomorphology*, **322**, 196–205. DOI:10.1016/j.geomorph.2018.08.046

Mao, L. and **Lenzi, M.A.** (2007) Sediment mobility and bedload transport conditions in an alpine stream. *Hydrol. Process.*, **21**, 1882–1891. DOI:10.1002/hyp.6372

Masteller, C.C. and **Finnegan, N.J.** (2017) Interplay between grain protrusion and sediment entrainment in an experimental flume. *J. Geophys. Res. Earth Surf.*, **122**, 274–289. DOI:10.1002/2016JF003943

Masteller, C.C., **Finnegan, N.J.**, **Turowski, J.M.**, **Yager, E.M.** and **Rickenmann, D.** (2019) History - Dependent Threshold for Motion Revealed by Continuous Bedload Transport Measurements in a Steep Mountain Stream. *Geophys. Res. Lett.*, **46**, 2583–2591. DOI:10.1029/2018GL081325

Meyer, F. and **Perrier, V.** (2023) shinybusy: Busy indicators and notifications for "Shiny" applications. ,https://CRAN.R-project.org/package=shinybusy

Ockelford, A.M. and **Haynes, H.** (2013) The impact of stress history on bed structure. *Earth Surf. Process. Landf.*, **38**, 717–727. DOI:10.1002/esp.3348

Ockelford, A., **Woodcock, S.** and **Haynes, H.** (2019) The impact of inter-flood duration on non-cohesive sediment bed stability. *Earth Surf. Process. Landf.*, **44**, 2861–2871. DOI:10.1002/esp.4713

Ooms, J. (2023) writexl: Export data frames to excel "xlsx" format. https://CRAN.R-project.org/package=writexl

Owen, J. (2021) rhandsontable: Interface to the "Handsontable.js" library. https://CRAN.R-project.org/package=rhandsontable

Pender, G., **Haynes, H.** and **Pender, G.** (2007) Stress History Effects on Graded Bed Stability. DOI:10.1061/(ASCE)0733-9429(2007)133:4(343)

Perrier, V., **Meyer, F.** and **Granjon, D.** (2024) shinyWidgets: Custom inputs widgets for shiny. https://CRAN.R-project.org/package=shinyWidgets

Power, M.E., **Parker, M.S.** and **Dietrich, W.E.** (2008) SEASONAL REASSEMBLY OF A RIVER FOOD WEB: FLOODS, DROUGHTS, AND IMPACTS OF FISH. *Ecological Monographs*, **78**, 263–282. DOI:10.1890/06-0902.1

Quinn, J.M. and **Hickey, C.W.** (1994) Hydraulic parameters and benthic invertebrate distributions in two gravel-bed New Zealand rivers. *Freshwater Biology*, **32**, 489–500. DOI:10.1111/j.1365-2427.1994.tb01142.x

R Core Team (2023) R: A language and environment for statistical computing. *R Foundation for Statistical Computing*, Vienna, Austria. https://www.R-project.org/

Ram, K. and **Wickham, H.** (2023) wesanderson: A wes anderson palette generator. https://CRAN.R-project.org/package=wesanderson

Rinker, T. (2023) qdapRegex: Regular expression removal, extraction, and replacement tools. https://CRAN.R-project.org/package=qdapRegex

Robinson, C.T., **Aebischer, S.** and **Uehlinger, U.** (2004) Immediate and habitat-specific responses of macroinvertebrates to sequential, experimental floods. *Journal of the North American Benthological Society*, **23**, 853–867. DOI:10.1899/0887-3593(2004)023<0853:IAHROM>2.0.CO;2

Saz, M., **de Luis, M.** and **Serrano-Notivoli, R.** (2020) ATLAS CLIMÁTICO DE ARAGÓN. Gobierno de Aragón. https://icearagon.aragon.es/atlas/Clima/info/atlas-climatico-aragon

Schmutz, S., **Bakken, T.H.**, **Friedrich, T.**, **Greimel, F.**, **Harby, A.**, **Jungwirth, M.**, **Melcher, A.**, **Unfer, G.** and **Zeiringer, B.** (2015) Response of fish communities to hydrological and morphological alterations in hydropeaking rivers of austria. River Research and Applications. DOI:10.1002/rra.2795

Tena, A., **Ville, F.**, **Reñe, A.**, **Yarnell, S.M.**, **Batalla, R.J.** and **Vericat, D.** (2022) Hydrological characterization of hydropeaks in mountain rivers (examples from Southern Pyrenees). *River Research & Apps*, rra.4058. DOI:10.1002/rra.4058

Vaidyanathan, R., **Xie, Y.**, **Allaire, J.**, **Cheng, J.**, **Sievert, C.** and **Russell, K.** (2023) htmlwidgets: HTML widgets for r. https://CRAN.R-project.org/package=htmlwidgets

van den Brand, T. (2024) ggh4x: Hacks for "ggplot2." ,https://CRAN.R-project.org/package=ggh4x

Vanzo, D., **Zolezzi, G.** and **Siviglia, A.** (2016) Eco-hydraulic modelling of the interactions between hydropeaking and river morphology. *Ecohydrology*, **9**, 421–437. DOI:10.1002/eco.1647

Vericat, D., **Ville, F.**, **Palau-Ibars, A.** and **Batalla, R.J.** (2020) Effects of hydropeaking on bed mobility: Evidence from a pyrenean river. *Water*, **12**, 178. DOI:10.3390/w12010178

Waring, E., **Quinn, M.**, **McNamara, A.**, **Arino de la Rubia, E.**, **Zhu, H.** and **Ellis, S.** (2022) skimr: Compact and flexible summaries of data. ,https://CRAN.R-project.org/package=skimr

Wickham, H., **Averick, M.**, **Bryan, J.**, **Chang, W.**, **McGowan, L.D.**, **François, R.**, **Grolemund, G.**, **Hayes, A.**, **Henry, L.**, **Hester, J.**, **Kuhn, M.**, **Pedersen, T.L.**, **Miller, E.**, **Bache, S.M.**, **Müller, K.**, **Ooms, J.**, **Robinson, D.**, **Seidel, D.P.**, **Spinu, V.**, **Takahashi, K.**, **Vaughan, D.**, **Wilke, C.**, **Woo, K.** and **Yutani, H.** (2019) Welcome to the tidyverse. *Journal of Open Source Software*, **4**, 1686. DOI:10.21105/joss.01686

Wilcock, P.R. and **McArdell, B.W.** (1993) Surface-based fractional transport rates: Mobilization thresholds and partial transport of a sand-gravel sediment. *Water Resour. Res.*, **29**, 1297–1312. DOI:10.1029/92WR02748

Wilcock, P.R. and **McArdell, B.W.** (1997) Partial transport of a sand/gravel sediment. *Water Resour. Res.*, **33**, 235–245. DOI:10.1029/96WR02672

Wilke, C.O. (2024) cowplot: Streamlined plot theme and plot annotations for "ggplot2." ,https://CRAN.R-project.org/package=cowplot

Wilke, C.O. and **Wiernik, B.M.** (2022) ggtext: Improved text rendering support for "ggplot2." ,https://CRAN.R-project.org/package=ggtext

Wolman, M.G. (1954) A method of sampling coarse river-bed material. *Trans. Am. Geophys. Union*, **35**, 951. DOI:10.1029/TR035i006p00951

Wood, S.N. (2011) Fast stable restricted maximum likelihood and marginal likelihood estimation of semiparametric generalized linear models. *Journal of the Royal Statistical Society (B)*, **73**, 3–36.

Xie, Y., **Cheng, J.** and **Tan, X.** (2023) DT: A wrapper of the JavaScript library "DataTables." ,https://CRAN.R-project.org/package=DT

Yager, E.M., **Schmeeckle, M.W.** and **Badoux, A.** (2018) Resistance Is Not Futile: Grain Resistance Controls on Observed Critical Shields Stress Variations. *J. Geophys. Res. Earth Surf.*, **123**, 3308–3322. DOI:10.1029/2018JF004817

Chapter 7

Discussion and conclusions

Overview of a section of gorge on the Upper Ésera River during a photogrammetric flight, 28/11/2018. Author: Damia Vericat

7.1 DISCUSSION

Hydro-morpho-sedimentary conditions constitute the fluvial environment (Maddock, 1999). The diversity of fluvial forms and the composition of riverbeds support habitats that interact with variations in hydraulic conditions such as flow velocity and water depth. Changes in hydraulic flows can affect the stability of riverbeds. Although organisms react directly to flows, they are also influenced by the way in which the changes in flow affect the sedimentary conditions (Hauer, 2015; Jowett et al., 1991; Jowett, 2003; Quinn and Hickey, 1994). Hydroelectric Power stations (HP), due to their functioning, disturb the hydrology by creating artificial water level fluctuations in the impacted downstream reaches, also regularly flooding and drying out the *ramping area* lateral margins of the channels (Hauer et al., 2013; Hauer et al., 2014b; Le Coarer et al., 2023; Vanzo et al., 2016b). The presence of dams and weirs can also have a negative impact on biological and sediment continuity. Taken together, this results in a deterioration of habitats and significant stress on aquatic ecology (Bunn and Arthington, 2002; Habersack and Piégay, 2007; Kondolf, 1997; Moog, 1993).

Nevertheless, there is a heterogeneity of hydropower schemes (e.g., operation, head, stored water volume; Couto and Olden, 2018; Egre and Milewski, 2002; McManamay et al., 2016; Smokorowski, 2022), distributed in a wide range of geomorphic contexts (e.g. valley shapes, position within basins, channel shapes, variability of water and sediment inputs). Each spatial and temporal context implies specific adjustments and response processes (Wohl, 2018).

The work in this thesis focused on the temporal and spatial (i.e. longitudinal) hydrological characterization of artificial fluctuations and their effects on bed mobility dynamics. The downstream effect of water releases from HPs positioned at the end of cascades, responding to peak electricity demand, was analysed through two distinct segments of mountain rivers. The basins had similar climatic and geological characteristics, but their morphologies and hydropeak regimes were different. On the Upper Cinca, the 12 km segment had a wandering fluvial form with an open valley, while the Upper Ésera, draining a 13% smaller basin, had mainly a single channel confined within a tortuous valley.

The two hydroelectric schemes formed a cascade of Run-Of-River (ROR) schemes that could be described as "modified" (Smokorowski, 2022). See Figure 2.1, p.34, for the location of the hydroelectric schemes upstream of the basins and Figure 2.2, p.35, for details of their configuration. The water did not come entirely from natural flows, but came largely from small upstream reservoirs formed by lakes and dams with a storage capacity limited to a few days. It was then conveyed to the power stations via headrace canals, the elevation of which was kept at the same level as the water intake in order to maintain a high head (see Figure 2.2, p.35). On the Cinca, the dams allowed sediment to pass through during flood periods, which was not the case on the Ésera. The cumulative height of fall for the whole hydroelectric scheme in the Cinca basin studied was 1 720 meters, whereas it was 40% lower on the Ésera (i.e. 1 017 meters). The overall storage capacity of the reservoirs was equivalent to around 2.5 days' average flow on the Cinca and almost the double on the Ésera, i.e. around 4 days (i.e. less head but more volume).

The Cinca segment studied had an upstream bypassed reach of the river of around 20 km between the Laspuña dam (storage capacity of a few hours) allowing water to be diverted to the power station of the same name. The volumes of water available for conveyance to the Laspuña HP depended mainly on the volumes used and released by the upstream HPs at LaFortunada-Cinca and LaFortunada-Cinqueta. During the hydrological analysis presented in **Chapter 3**, Section 3.2.1 (p.101), floods and artificial peaks were detected in the bypassed reach (see Figure 3.13, p.111; Figure 3.14, p.115, Figure 3.15, p.116). These peaks appeared when the Laspuña HP was not operating or when its maximum production capacity had been reached. The peaks generated by the upstream HPs were then returned to the river at the Laspuña dam and circulated in the normally bypassed reach.

The end part of this bypassed reach was monitored (Laspuña US, -1 km) in order to assess the water and sediment inputs provided to the 10 km long downstream impacted reach by the hydropeaks from the Laspuña HP, between the two stations of Laspuña DS (0.6 km) and Ainsa (10 km) receiving all the flows.

The Ésera segment did not have exactly the same configuration, as the Campo HP was located at the foot of the dam (bearing the same name) directly on the course of the river (height: 12 m, storage capacity: a few hours of runoff). This dam was a barrier to sediment continuity. The available volumes turbined did not come solely from a natural flow but were mainly modulated and dependent on the hydroelectric facilities on the upstream course. The 18.5 km segment studied between the Campo dam and the village of Santaliestra received all the artificial and natural flows.

7.1.1 Hydropeaking regime

Despite the regulation of runoff volumes, the hydrological regime of the Cinca maintained a degree of natural variability. Cluster analysis of the peaks identified, carried out in **Chapter 3**, Section 3.1.1 (p.74), highlighted differences in magnitude and duration between seasons, particularly in spring with relatively high base flows. The shapes of the peaks were predominantly *Rectangle* or *Spike* (i.e. *Rectangle* but of short duration) and to a lesser extent *Front Step*. On the Ésera, on the other hand, water volumes were much more modulated. Natural seasonal variations or even natural waves on the scale of precipitation events were attenuated (e.g. autumn thunderstorms; see Figure 6.12 (p.283) for a comparative example). More than 70% of the annual volume available was used for peak electricity production (compared with 30 to 50% on the Cinca, see Figure 3.15, p.116) and the occurrence of peak forms varied more over the seasons, suggesting that water resource management was adjusted to capture inflows for subsequent optimized production. However, the *Front Step* form was dominant in this management method on the Ésera, resulting in intense fluctuations between the base flow (Q_{base}) and the peak flow (Q_{max}). The median Q_{base} left in the river was only 11% of the Q_{50}, or 0.1-fold the Q_{50} (1.25 $m^3 s^{-1}$), compared with 55% of the Q_{50} (8.5 $m^3 s^{-1}$) on the Cinca. The amplitudes of the variations were around 125% of the median annual flow (Q_{50}) for the dominant *Front Step* form (i.e. Q_{base}/Q_{max} ratio of 1:12.5) compared with amplitudes on the Cinca of between 50 and 25% of the Q_{50} for the two dominant *Front Step* and *Spike* forms (ratio 1:4 to 1:2.5). At the outlet of the two HP, Laspuña on the Cinca and Campo on the Ésera, the *Front Step* form had similar median Q_{max} of 140 and 154% of Q_{50} respectively, as well as increase phase duration of 0.75 and 1 hour respectively. However, at Campo, reaching a Q_{max} similar to that of Laspuña, over an almost identical duration, starting from a very low Q_{base}, due to storage in the reservoirs, implied ramping rates almost twice as high (300 compared with 173% of Q_{50} h^{-1}). These phenomena were more marked in dry years associated with lower Q_{base}.

These results indicate that for a similar type of hydropower scheme (here modified ROR), large disparities in hydropeak regimes can be generated. As already pointed out by Ashraf et al. (2018), in a study carried out on 92 regulated rivers in the Nordic European countries, low-head ROR systems (e.g. Ésera cascade) generate higher ramping rates due to a higher flow requirement to produce the same amount of energy compared to a similar system with a higher head. These results also show that modified ROR systems, in certain configurations, can alter the seasonal hydrological regime, particularly during low-water periods (Q_{base}). Kuriqi et al. (2019) found on different rivers in the Iberian Peninsula that this was particularly noticeable for rivers with a pluvio-nival regime (similar to those of the Ésera and Cinca) rather than a pluvial one.

7.1.2 Longitudinal variation of hydropeaks

The results of the study of longitudinal changes in the characteristics of the hydropeaks showed that for the dominant shape *Front Step* (peak of high intensity and long duration), presented a different pattern of propagation between the two segments. On the Cinca, the median MAx Ramping Rate (MARR) of both increase/decrease (IC/DC) variations showed a reduction of 60% at 3 km and 70% at 10 km at Ainsa downstream of the HP (see Figure 3.21, p.129). Such observations of reduction over a similar distance have already been reported on Austrian rivers by Greimel et al. (2016a) and Hauer et al. (2017a). On the other hand, on the Ésera, the MARR of IC seemed to increase slightly at 12 km (Pyramides) and then decrease very slightly at 18.5 km, showing only very partial attenuation over the entire length of the segment. A form of peak generated by the Campo HP with a Q_{max} positioned at least 16% of the total duration of the peaks seemed to produce two waves, the first of low intensity and the second corresponding to the Q_{max}, with different propagation velocities which ended up being superimposed between Campo (0.3 km) and Pyramides (12 km), probably in a long section of gorge generating significant friction (Rennie et al., 2018), slowing more strongly the first low-intensity wave. The DC MARRs generated by the HP were weaker than those of the ICs (i.e. slower variations over a longer period of time) and their importance decreased by up to 70% downstream (similar to the Cinca).

These differences in IC variation between the two river segments are attributable to their morphology. Due to its wandering morphology, the Cinca segment had a relatively large wetted width at Q_{max}. This resulted in a high degree of roughness and an enhanced retention effect. As already pointed out by Hauer et al. (2013), the difference in total wetted width between Q_{base} and Q_{max} is positively correlated with a decrease in Q_{max} downstream. On the Ésera, the channel being relatively confined, the slight increase in the ramping rate could be caused by an increase in mean velocities (and specific discharge) due to a relatively smaller peak wetted width. Similar observations were made by Greimel et al. (2023) on the Predella-Martina Upper river in Austria. Over a total reach of 30 km with stations at approximately 10, 16 and 30 km, between points 10 and 16 km the MARR showed an increase then a decrease at 30 km. This feature intensified with the increase of the initial Q_{max} released at the HP. These facts are not commented further, but it seems nevertheless after visualization via Google Earth that this river presents very narrow sections (i.e. similar to the Ésera) and channelized.

7.1.3 Influence of hydropeaks on the degree of bed destabilization at short term

Both river segments showed episodes of partial mobility attributable to hydropeaks on the *ramping area* (i.e. lateral margin regularly flooded and dewatered). Only certain peaks of relatively high intensity, at least greater than the median Q_{max}, or even close to the maximum Q_{max} detected, often superimposed on natural waves, were sufficiently competent to cause partial destabilization of the bed ($> 10\%$). The degree of bed destabilization differed between river segments and upstream and downstream positions. The hydropeaks did not destabilize the bed of the Ésera at Campo DS, but could cause partial mobility of fine grains ($\approx D_{16}$) downstream at Pyramides (12 km) and on the studied reaches of the Cinca (Laspuña DS and Ainsa). On the two rivers Ésera and Cinca, over the period 1997-2023, approximately 44% and 87% respectively of partial mobility episodes were estimated to be attributable to hydropeaks. Generally speaking, all the hydropeaks observed (low and high magnitudes) did not lead to any significant short-term change in the grain size composition of the bed in these lateral areas.

It is difficult to compare these results regarding the degree of bed mobility (null, marginal, partial, full) associated exclusively to hydropeaks with other rivers. Few studies exist on the impact of hydropeaks on the degree of substrate destabilization and its frequency of occurrence, either in channels or in *ramping areas*. However, destabilization of *ramping areas* can affect the composition of benthic communities (Cobb et al., 1992; Kennedy et al., 2016), which are at the start of the food chain, or disrupt fish communities through erosion and the disruption of spawning areas (Casas-Mulet et al., 2015c). Most studies of downstream dams focus on their effect on the sediment deficit and the mobility of bed materials associated with floods (Vericat et al., 2008a ; Vericat and Batalla, 2005).

Also, the very marginal or partial mobility associated with hydropeaks is generally close to the detection limit of commonly used methods. In addition, these methods would require long and extensive measurement efforts in rivers where artificial flow fluctuations are frequent and allow little time for measurements. For example, during Helley-Smith type in situ sampling, the quantity of transported grains may be too small compared to the minimum quantity required for reliable quantification of mobile sizes and transport rates (Ferguson and Paola, 1997). Similar, the Bunte bedload sampler requires very long in situ sampling time (Bunte et al., 2004). Finally, transport of only relatively large particles may be traced by RFID, and painted tracing particles yield low quantity of observations and return rates (Hassan and Ergenzinger, 2005). The development of the PhotoMOB method (**Chapter 5**, p.129) is seen as a major contribution of this work, facilitating the observation and measurement of bed mobility particularly in contexts of partial mobility and in contexts where the possible duration of measurement is limited by frequent flow fluctuations.

7.1.4 Temporal and longitudinal dynamics of the mobility in impacted river segments

The two segments show a long-term effect of the impact of the hydraulic facilities and their functioning on the composition of the bed and the mobility dynamics. Near the outlet of the HP, the grain sizes were relatively coarse and the proportion of mobile bed low. On the Ésera at Campo, the dam on the course of the river caused a sediment deficit. The entrainment of the finest grains during hydropeaks, and of coarser grains during relatively frequent floods, with no upstream supply, has led to a coarsening of the surface, which can now only be partially mobilized by floods. On the Cinca at Laspuña DS, despite a significant flow competence, already pointed out by López et al. (2020) and obviously due to the very coarse grain size, only grains of a size similar to D_{16} were mobile during hydropeaks and for floods with return periods greater than 1-year. Despite a sediment supply maintained due to the opening of the dam during floods, the reach just downstream of the HP underwent substrate stabilization. The supply of materials in the bypassed reach and their conveyance through it to the Laspuña DS reach occurs on a slower temporal scale than that of materials transiting through the Laspuña DS reach due to the production of approximately two hydropeaks per day.

These bed armouring effects ($D_{50surface}/D_{50subsurface}$ ratio,i.e., D_{50}/D_{50s}, of 2.8 at Laspuña DS, and 2 to 1.5 between Campo US and DS) are compensated downstream by the contribution of tributaries which induce finer grain size distributions and therefore more frequent bed mobility (D_{50}/D_{50s} of 1.1 at Ainsa, 0.7 at Pyramides and 1.3 at Santaliestra). This dynamic is similar to that described in the neighbouring Pyrenean basin of the Noguera Pallaresa river by Vericat et al. (2020) (Section A.1 of this thesis).

In addition, most of the tributaries had badland surfaces that could deliver considerable quantities of fine material transported in suspension (Alatorre et al., 2010; Béjar et al., 2018; Llena et al., 2021). The present work developed in this thesis did not aim to study the effect of hydropeaks on the dynamics of suspended sediment. However, deposits of fine sediment were frequently observed in the downstream part of the Ésera segment following rainfall events, which then appeared to be rapidly remobilized by successive hydropeaks.

As the wetted widths were similar between low and high flows and the hydropeaks were powerful and almost daily, the fine materials supplied were mobilized and exported downstream very quickly. Such transport phenomena, following flood events (i.e. disturbance events), over more or less long periods (depending on the duration of the hydropeaks) and repeated daily over several days until total depletion of the deposits, could cause severe impacts on the biological communities (Hauer, 2015), in addition to the strong daily ramping rate, clearly identified in the literature as a factor that can cause organisms to drift and disrupt their life cycle such as resting, reproduction and foraging (Bipa et al., 2024; Schmutz et al., 2015; Smokorowski, 2022). Preliminary studies on the same study segments on the Cinca by Palau-Nadal et al. (2018) and the Ésera by Palau-Nadal et al. (2019) (Figure C.1 of this thesis) have shown changes in the trophic organization in the fluvial system with an increase in the benthic algal cover close to the HP due to substrate stability and a proportion of the number of scraper organisms significantly higher than in the more often destabilized downstream reaches.

7.1.5 Onset of motion

The two analyses carried out in **Chapters 4** (p.137) and **6** (p.261) concerning mobility, in the channels and on the *ramping areas* respectively, showed that the segments studied exhibited transport of particles of a partially selective type. The critical entrainment discharge of grains is not totally conditioned by their weight, but neither is it equal for all fractions. Observations have shown that coarse particles can sometimes begin to be destabilized at the same discharge as relatively finer particles. On the Ésera, at Campo DS and Pyramides, grain fractions of 32 and 64 mm respectively showed marginal mobility ($< 10\%$) during hydropeaks, with several smaller grain size classes showing a single mobile grain (see Figure 6.14, p.286).

In **Chapter 4** (p.137), entrainment observations on the Ésera in relation to dimensionless critical shear stress were compared to a large database of various rivers around the world. The points corresponding to the mobility observations made in 2018 on the Ésera were aligned along the lower envelope of the data point cloud. Compared with other rivers, particles appeared to be mobilized more easily. The equations of commonly used solid transport models tended to overestimate the critical discharge rate.

The most recent observations (2019-2020) of mobility acquired by photographic method in **Chapter 6** (p.261) have not yet been related to the shear stress associated to the hydrological events (averaged over the section or locally above the patches). Nevertheless, all the D_{max} observation data normalized by the D_{50}, in relation to the Q_{max} normalized (and not the shear stress), analysed and discussed in the course of this thesis work, have been assembled in Figure 7.1 (n= 73).

The observations collected on the river Ésera using the photographic method (purple dots, **Chapter 6**) and those using painted tracers (blue dots, **Chapter 4**) appear to be relatively well aligned despite the different measurement techniques and sampled areas ("channel" vs. "ramping" area). On the Cinca, the observations collected in **Chapter 6** (orange and grey squares with thin edges) show more dispersion than those from the study carried out by López et al. (2020) on the same reach of river (yellow squares and grey squares with thick edges). These new observations taken together show the same trend as described in **chapter 4**. To mobilize a given relative grain size, a lower relative discharge is required on the Ésera compared with other rivers.

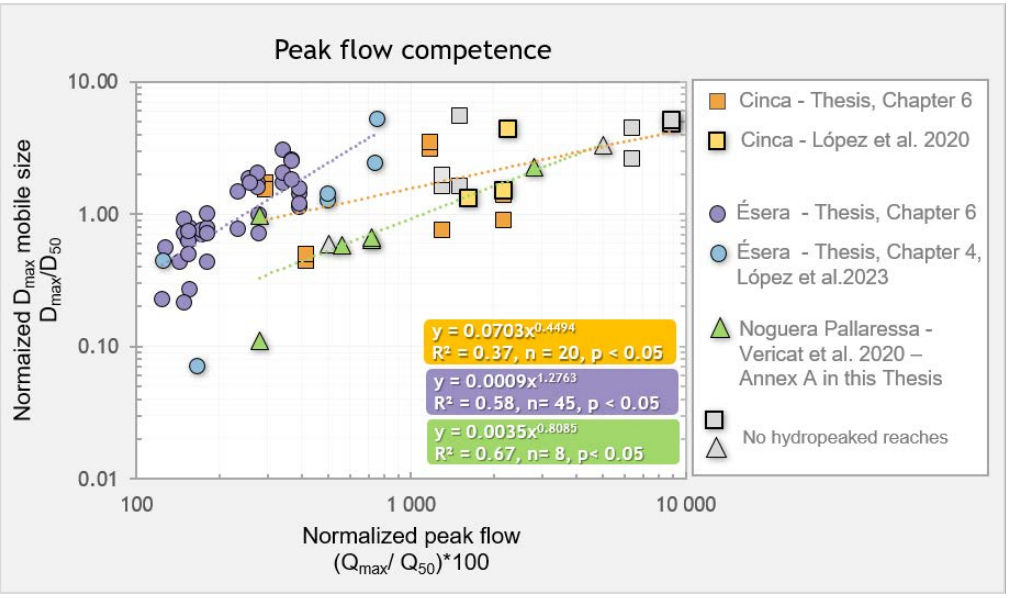

Figure 7.1: Regression relationship between normalized peak flow and the maximum diameter of mobile grains in relation to the D_{50} of bed surface materials. The grey dots indicate observations on reaches not impacted by hydropeaks. The round dots correspond to observations made on the Upper Ésera River (blue from **Chapter 4**, López et al., 2023); and purple from **Chapter 6**). The purple dotted line corresponds to the model based on all the observations made on Ésera (blue and purple dots). The square dots represent observations made on the segment of the Upper Cinca River by López et al. (2020) (yellow square and thick-edged grey squares) and from **Chapter 6** of this thesis (orange and thin-edged grey squares). The orange dotted line corresponds to the model based on all the observations made on the Cinca (blue and purple dots) The triangles correspond to the mobility observed on the Noguera Pallaresa river by Vericat et al. (2020) (Section A.1).

As already discussed in **Chapter 3**, Section 3.2.1 (p.101), and highlighted by numerous authors (Bürgler et al., 2023; Hauer et al., 2013; Hauer et al., 2017a; Vanzo et al., 2016b), flow fluctuations linked to hydropeaks are highly unsteady processes. The arrival of the hydropeak front causes a sudden change in flow conditions in the channel, and totally on the ramping areas which are initially dry. This wall of water could, according to theory of Alexander and Cooker (2016) for flash floods, generate significant transient forces in addition to the drag of the mean flow. Instantaneous fluctuations in velocity and pressure fields in the immediate vicinity of the protruding particles on the bed could exert impulsive forces. These additional forces could reduce the drag forces required to set the grains in motion on the scale of a few seconds or minutes.

As the ramping rates on the Ésera are very high, with a median Q_{base}/Q_{max} ratio of 1:12.5, these potential additional impulsive forces associated to the peak front could explain the mobilization of relatively coarse particles for relatively low flows in the Ésera data (Figure 7.1), and the overestimation of critical discharges by models based on dimensionless shear stress assuming a permanent flow. These episodes of intense impulse are only transient and cease once the front has passed, causing only a short distance of displacement, or simply an adjustment of the position of the grains towards a more stable position. Such processes over very short periods (seconds, minutes) but very frequently (daily) could have an impact on the texture of the bed by modifying the arrangement of the grains (e.g. compaction, imbrication, orientation).

The results presented in this work, concerning the effects of high-intensity hydropeaks on the mobility dynamics of the Ésera river, seem important, given that the configuration of this river is representative of a basin that is favourable to hydroelectric production, due to its steep gradients, narrow widths and alluvial pockets that allow dams to be implemented.

7.2 CONCLUSIONS

This thesis analysed the downstream effects of artificial flow fluctuations, linked to hydropower peak production, on hydrological regimes and bed mobility from a longitudinal point of view within two 10 and 18.5 km segments of Pyrenean mountain rivers with contrasting characteristics, the Upper Cinca and Upper Ésera respectively.

Main conclusions can be drawn as follows:

(1) For the two river segments located downstream of a hydroelectric cascade scheme operating mainly in modified Run-Of-River mode, with storage volumes of a few days, the segment of the Upper Ésera impacted by the network of power stations with the lowest cumulative head is the one with the most severely altered hydrological regime. 70% of the annual runoff is used for peak electricity production, compared with 30 to 40% on the Upper Cinca. The median Q_{base} left in the river is 11% of the Q_{50}, or 0.1 times the Q_{50} (1.25 $m^3 s^{-1}$) compared with 55% of the Q_{50} (8.5 $m^3 s^{-1}$) on the Upper Cinca. The median Q_{base}/Q_{max} ratios of the dominant *Front Step* peak shape are 1:12.6 compared with only 1:4 on the Upper Cinca, and the rates of fluctuation are very high, with median MARRs of 300% of Q_{50} h^{-1} (37 $m^3 s^{-1} h^{-1}$) compared with 173% of Q_{50} h^{-1} (i.e. 25 $m^3 s^{-1} h^{-1}$).

The propagation the variations of increase (IC) is the characteristic that varies most according to river morphology. On the Upper Cinca, the MARRs are attenuated by 60% from 3 km, as a result of the relatively large wetted width at Q_{max}, which causes a retention effect. On the Upper Ésera segment, the narrow channel, strongly confined by the tortuous valley, shows no significant attenuation until 18.5 km downstream.

(2) Grain mobility is partially selective in both segments. However, flow competence varies between the two river segments and between the upstream and downstream reaches of the same segment. For a given relative peak magnitude, relatively coarser grain can be mobilized on the Upper Ésera than on the Upper Cinca. The upstream reaches are limited in sediment supply by the presence of dams, either totally at Campo on the Upper Ésera, or partially at Laspuña on the Upper Cinca. The coarsest grains mobilized are observed downstream as a result of sedimentary supply from tributaries. The maximum size mobilized by a hydropeak was 123 mm (small cobbles) on the Ésera at Pyramides (12 km) and 67 mm (small cobbles) at Ainsa (10 km).

(3) The *PhotoMOB* photographic processing method enables mobility observations to be made rapidly on site for a large number of grains. The root mean square error in estimating the percentiles of the grain size distribution is 9.5% for Area-by-Number and 16.6% for Grid-by-Number. The mobility estimation errors are around 8% after 10 min of manual revision of the grain boundary. In the near future, the correction time will be reduced.

(4) The PhotoMOB method was applied to measure variations in the composition of surface grain sizes and the degree of bed destabilization on the lateral margins subject to large fluctuations in hydraulic conditions. Hydropeaks do not induce any significant change in grain size distribution in the short term. Only high-intensity hydropeaks with a Q_{max} at least greater than the median Q_{max}, often superimposed on natural waves, can destabilize the bed, and only partially (between 10 and 90%). The degree of destabilization caused by hydropeaks differs between the two segments and upstream and downstream of the same segment. On the Ésera at Campo (1 km), the hydropeaks are not responsible for any mobility episodes. Only floods have the power to completely mobilize grains up to a size similar to D_{50}, and only partially for the coarsest. Downstream of tributaries, high-intensity hydropeaks are competent to partially mobilize relatively fine fractions close to D_{16}. It has been estimated that hydropeaks could be potentially responsible for 44% of the time that the bed was destabilized over the period 1997-2023. On the Upper Cinca, both upstream and downstream, the fine fractions can be partially mobilized for high-intensity hydropeaks. It was estimated that hydropeaks could be responsible for 87.5% of the time that the D_{16} fraction was partially mobile between 1997 and 2023.

7.3 LIMITATIONS

The estimation of flows by rating curve and the hydraulic variables used based on steady 2D hydraulic modelling can be considered as one of the main limitations of the work carried out in this thesis.

Hydrology

On the Cinca river, few data were available to validate the rating curves. Nevertheless, by cross-checking the discharges obtained with data from the company Acciona (operator of the Laspuña HP), those from the official measuring station at $Escalona_{CHE}$, as well as those previously acquired by the RIUS research group, it appears that the estimated discharges on the Cinca are correct.

Uncertainties have been detected in the data from official sources ($Escalona_{CHE}$ and $Campo_{CHE}$). The annual water yield data series, upon which years were classified as dry, average or wet in **Chapter 3**, may be affected. Under-estimations at low water have been identified; however, these data do not appear to present problems for medium to high flows.

The classification of years may also vary slightly depending on the number of historical years taken into account and whether or not missing historical data is filled in. There is a disparity between the classifications of hydrological years between Section 3.1.1 (p.74) and Section 3.2.1 (p.101) of **Chapter 3** concerning the flow series for Escalona and Ainsa in 2014/15 and 2015/16. Nevertheless, the relative differences between the stations remain the same, and are similar to those for 2018/19 and 2019/20 at the Laspuña DS station (see Figure 3.11, p.108). This fact has no impact on the results obtained. The only consequence would be greater variability in the analysis of central tendencies due to the merging of peaks from two different contrasting years into a single group, which does not appear to be the case here.

During the manual segmentation in **Chapter 3,** Section 3.1.1, and the corrected automatic segmentation in **Chapter 3,** Section 3.2.1, misclassifications of peak shapes may have occurred. However, given the large number of peaks studied, over 2 350 in Section 3.1.1 and over 6 300 in Section 3.2.1, it is unlikely that a few erroneous shape classifications influenced the results. In Section 3.2.1, the method prevents possible extreme values by focusing only on central tendencies.

Determination of discharge by rating curve using the "water height/discharge" relationship can be limiting for the study of ramping rates (MARR and MERR). The "water height/discharge" relationship can be affected by a hysteresis phenomenon (Baldassarre and Montanari, 2009), which can intensify as the peak flow increases. In addition, the accuracy of MARR and MERR is highly dependent on the temporal resolution of the hydrograph (Greimel et al., 2023). The values may be underestimated if the temporal resolution is too low, which could be the case. Photographic traps installed on the Ésera have sometimes shown variations between base flow and peak flow which seem to occur over a period < 15 min. Measurements with a temporal resolution of 5 or 1 min could be carried out over a temporary period in order to verify this.

Hydraulics

The mobility observations were related to average variables for the reaches studied, i.e. dimensionless shear stress in **Chapter 4** and peak flows in **Chapter 6**. The high variability of the data could be reduced by unsteady flow 2D hydraulic simulation of the forces exerted by the fluid locally at the tracers. The availability of water level data series distributed along the segments would make it possible to calibrate and validate hydraulic models with the use of variable roughness based on the roughness map estimates established in **Chapter 2**.

REFERENCES

Alatorre, L.C., **Beguería, S.** and **García-Ruiz, J.M.** (2010) Regional scale modeling of hillslope sediment delivery: A case study in the Barasona Reservoir watershed (Spain) using WATEM/SEDEM. *J. Hydrol.*, **391**, 109–123. DOI:10.1016/j.jhydrol.2010.07.010

Alexander, J. and **Cooker, M.J.** (2016) Moving boulders in flash floods and estimating flow conditions using boulders in ancient deposits. *Sedimentology*, **63**, 1582–1595. DOI:10.1111/sed.12274

Ashraf, F.B., **Haghighi, A.T.**, **Riml, J.**, **Alfredsen, K.**, **Koskela, J.J.**, **Kløve, B.** and **Marttila, H.** (2018) Changes in short term river flow regulation and hydropeaking in Nordic rivers. *Scientific Reports*, **8**, 17232. DOI:10.1038/s41598-018-35406-3

Baldassarre, G.D. and **Montanari, A.** (2009) Uncertainty in river discharge observations: a quantitative analysis. *Hydrol. Earth Syst. Sci.*, **13**, 913–921. DOI:10.5194/hess-13-913-2009

Béjar, M., **Vericat, D.**, **Batalla, R.J.** and **Gibbins, C.N.** (2018) Variation in flow and suspended sediment transport in a montane river affected by hydropeaking and instream mining. *Geomorphology*, **310**, 69–83. DOI:10.1016/j.geomorph.2018.03.001

Bipa, N.J., **Stradiotti, G.**, **Righetti, M.** and **Pisaturo, G.R.** (2024) Impacts of hydropeaking: A systematic review. *Science of The Total Environment*, **912**, 169251. DOI:10.1016/j.scitotenv.2023.169251

Bunn, S.E. and **Arthington, A.H.** (2002) Basic Principles and Ecological Consequences of Altered Flow Regimes for Aquatic Biodiversity. *Environmental Management*, **30**, 492–507. DOI:10.1007/s00267-002-2737-0

Bunte, K., **Abt, S.R.**, **Potyondy, J.P.** and **Ryan, S.E.** (2004) Measurement of Coarse Gravel and Cobble Transport Using Portable Bedload Traps. *J. Hydraul. Eng.*, **130**, 879–893. DOI:10.1061/(ASCE)0733-9429(2004)130:9(879)

Bürgler, M., **Vetsch, D.F.**, **Boes, R.M.** and **Vanzo, D.** (2023) Systematic comparison of 1D and 2D hydrodynamic models for the assessment of hydropeaking alterations. *River Research and Applications*, **39**, 460–477. DOI:10.1002/rra.4051

Casas-Mulet, R., **Saltveit, S.J.** and **Alfredsen, K.** (2015) The Survival of Atlantic Salmon (*Salmo Salar*) Eggs During Dewatering in a River Subjected to Hydropeaking: SALMON EMBRYO SURVIVAL IN A HYDROPEAKING RIVER. *River Res. Appl.*, **31**, 433–446. DOI:10.1002/rra.2827

Cobb, D.G., **Galloway, T.D.** and **Flannagan, J.F.** (1992) Effects of Discharge and Substrate Stability on Density and Species Composition of Stream Insects. *Can. J. Fish. Aquat. Sci.*, **49**, 1788–1795. DOI:10.1139/f92-198

Couto, T.B. and **Olden, J.D.** (2018) Global proliferation of small hydropower plants science and policy. *Frontiers in Ecology and the Environment*, **16**, 91–100. DOI:10.1002/fee.1746

Egre, D. and **Milewski, J.C.** (2002) The diversity of hydropower projects. *Energy Policy*, **30**, 1225–1230. DOI:10.1016/S0301-4215(02)00083-6

Ferguson, R.I. and **Paola, C.** (1997) Bias and precision of percentiles of bulk grain size distributions. *Earth Surface Processes and Landforms*, **22**, 1061–1077. DOI:10.1002/(SICI)1096-9837(199711)22:11<1061::AID-ESP809>3.0.CO;2-L

Greimel, F., **Grün, B.**, **Hayes, D.S.**, **Höller, N.**, **Haider, J.**, **Zeiringer, B.**, **Holzapfel, P.**, **Hauer, C.** and **Schmutz, S.** (2023) PeakTrace : Routing of hydropeaking waves using multiple hydrographsA novel approach. *River Research and Applications*, **39**, 326–339. DOI:10.1002/rra.3978

Greimel, F., **Zeiringer, B.**, **Hauer, C.**, **Holzapfel, P.**, **Fuhrmann, M.** and **Schmutz, S.** (2016) LONGITUDINAL ASSESSMENT OF HYDROPEAKING IMPACTS AND EVALUATION OF MITIGATION MEASURES. *11th International Symposium on Ecohydraulics*, Melbourn, Autralia,

Habersack, H. and **Piégay, H.** (2007) 27 River restoration in the Alps and their surroundings: past experience and future challenges. *Elsevier*, 11, 703–735. DOI:10.1016/S0928-2025(07)11161-5

Hassan, M.A. and **Ergenzinger, P.** (2005) Use of Tracers in Fluvial Geomorphology. In: *Tools in Fluvial Geomorphology* (Ed. G.M. Kondolf and H. Piégay), *John Wiley & Sons, Ltd*, Chichester, UK, 397–423. DOI:10.1002/0470868333.ch14

Hauer, C. (2015) Review of hydro-morphological management criteria on a river basin scale for preservation and restoration of freshwater pearl mussel habitats. *Limnologica*, **50**, 40–53. DOI:10.1016/j.limno.2014.11.002

Hauer, C., **Holzapfel, P.**, **Leitner, P.** and **Graf, W.** (2017) Longitudinal assessment of hydropeaking impacts on various scales for an improved process understanding and the design of mitigation measures. *Sci. Total Environ.*, **575**, 1503–1514. DOI:10.1016/j.scitotenv.2016.10.031

Hauer, C., **Schober, B.** and **Habersack, H.** (2013) Impact analysis of river morphology and roughness variability on hydropeaking based on numerical modelling: RIVER MORPHOLOGICAL IMPACTS ON HYDROPEAKING PROCESSES. *Hydrol. Process.*, **27**, 2209–2224. DOI:10.1002/hyp.9519

Hauer, C., **Unfer, G.**, **Holzapfel, P.**, **Haimann, M.** and **Habersack, H.** (2014) Impact of channel bar form and grain size variability on estimated stranding risk of juvenile brown trout during hydropeaking. Earth Surface Processes and Landforms. DOI:10.1002/esp.3552

Jowett, I.G. (2003) Hydraulic constraints on habitat suitability for benthic invertebrates in gravel-bed rivers. *River Research and Applications*, **19**, 495–507. DOI:10.1002/rra.734

Jowett, I.G., **Richardson, J.**, **Biggs, B.J.F.**, **Hickey, C.W.** and **Quinn, J.M.** (1991) Microhabitat preferences of benthic invertebrates and the development of generalised *Deleatidium* spp. habitat suitability curves, applied to four New Zealand rivers. *New Zealand Journal of Marine and Freshwater Research*, **25**, 187–199. DOI:10.1080/00288330.1991.9516470

Kennedy, T.A., **Muehlbauer, J.D.**, **Yackulic, C.B.**, **Lytle, D.A.**, **Miller, S.W.**, **Dibble, K.L.**, **Kortenhoeven, E.W.**, **Metcalfe, A.N.** and **Baxter, C.V.** (2016) Flow Management for Hydropower Extirpates Aquatic Insects, Undermining River Food Webs. *BioScience*, **66**, 561–575. DOI:10.1093/biosci/biw059

Kondolf, G.M. (1997) Hungry Water: Effects of Dams and Gravel Mining on River Channels. *Environmental Management*, **21**, 533–551. DOI:10.1007/s002679900048

Kuriqi, A., **Pinheiro, A.N.**, **Sordo-Ward, A.** and **Garrote, L.** (2019) Flow regime aspects in determining environmental flows and maximising energy production at run-of-river hydropower plants. *Applied Energy*, **256**, 113980. DOI:10.1016/j.apenergy.2019.113980

Le Coarer, Y., **Lizée, M.-H.**, **Beche, L.** and **Logez, M.** (2023) Horizontal ramping rate framework to quantify hydropeaking stranding risk for fish. *River Research and Applications*, **39**, 478–489. DOI:10.1002/rra.4087

Llena, M., **Batalla, R.J.**, **Smith, Mw.** and **Vericat, D.** (2021) Do badlands (always) control sediment yield? Evidence from a small intermittent catchment. *CATENA*, **198**, 105015. DOI:10.1016/j.catena.2020.105015

López, R., **Garcia, C.**, **Vericat, D.** and **Batalla, R.J.** (2020) Downstream changes of particle entrainment in a hydropeaked river. *Science of The Total Environment*, **745**, 140952. DOI:10.1016/j.scitotenv.2020.140952

López, R., **Ville, F.**, **Garcia, C.**, **Batalla, R.J.** and **Vericat, D.** (2023) Bed-material entrainment in a mountain river affected by hydropeaking. *Science of The Total Environment*, **856**, 159065. DOI:10.1016/j.scitotenv.2022.159065

Maddock, I. (1999) The importance of physical habitat assessment for evaluating river health. *Freshwater Biology*, **41**, 373–391. DOI:10.1046/j.1365-2427.1999.00437.x

McManamay, R.A., **Oigbokie, C.O.**, **Kao, S.-C.** and **Bevelhimer, M.S.** (2016) Classification of US Hydropower Dams by their Modes of Operation: Hydropower Modes of Operation. *River Research and Applications*, **32**, 1450–1468. DOI:10.1002/rra.3004

Moog, O. (1993) Quantification of daily peak hydropower effects on aquatic fauna and management to minimize environmental impacts. *Regulated Rivers: Research & Management*, **8**, 5–14. DOI:10.1002/rrr.3450080105

Palau-Nadal, A., **Palau-Ibars, A.**, **Alcázar, J.** and **Béjar, M.** (2018) Preliminary analysis of effects of hydropeaking on water temperature and macroinvertebrates population in a mountain river in the pyrenees (ne, spain). Poster presentation, 12th International Symposium on Ecohydraulics, Tokyo, Japan.

Palau-Nadal, A., **Ville, F.**, **Vericat, D.** and **Palau-Ibars, A.** (2019) Longitudinal organitzation of macrobenthos community in a reach affected by hydropeaking. Poster presentation, *Limnos*, Brazil.

Quinn, J.M. and **Hickey, C.W.** (1994) Hydraulic parameters and benthic invertebrate distributions in two gravel-bed New Zealand rivers. *Freshwater Biology*, **32**, 489–500. DOI:10.1111/j.1365-2427.1994.tb01142.x

Rennie, C.D., **Church, M.** and **Venditti, J.G.** (2018) Rock Control of River Geometry: The Fraser Canyons. J Geophys Res Earth Surf. doi: 10.1029/2017JF004458 DOI:10.1029/2017JF004458

Schmutz, S., **Bakken, T.H.**, **Friedrich, T.**, **Greimel, F.**, **Harby, A.**, **Jungwirth, M.**, **Melcher, A.**, **Unfer, G.** and **Zeiringer, B.** (2015) Response of fish communities to hydrological and morphological alterations in hydropeaking rivers of austria. River Research and Applications. DOI:10.1002/rra.2795

Smokorowski, K.E. (2022) The ups and downs of hydropeaking: a Canadian perspective on the need for, and ecological costs of, peaking hydropower production. *Hydrobiologia*, **849**, 421–441. DOI:10.1007/s10750-020-04480-y

Vanzo, D., **Zolezzi, G.** and **Siviglia, A.** (2016) Eco-hydraulic modelling of the interactions between hydropeaking and river morphology. *Ecohydrology*, **9**, 421–437. DOI:10.1002/eco.1647

Vericat, D. and **Batalla, R.J.** (2005) Sediment transport in a highly regulated fluvial system during two consecutive floods (lower Ebro River, NE Iberian Peninsula). *Earth Surf. Process. Landf.*, **30**, 385–402. DOI:10.1002/esp.1145

Vericat, D., **Batalla, R.J.** and **Garcia, C.** (2008) Bed-material mobility in a large river below dams. *Geodinamica Acta*, **21**, 3–10. DOI:10.3166/ga.21.3-10

Vericat, D., **Ville, F.**, **Palau-Ibars, A.** and **Batalla, R.J.** (2020) Effects of hydropeaking on bed mobility: Evidence from a pyrenean river. *Water*, **12**, 178. DOI:10.3390/w12010178

Wohl, E. (2018) Geomorphic context in rivers. *Progress in Physical Geography: Earth and Environment*, **42**, 841–857. DOI:10.1177/0309133318776488

Chapter 8

Perspectives and insight of work initiated

Pyramides reach a day of high turbidity,26/03/2019. Author: Fanny Ville

Overview

This chapter presents an overview of 4 tasks initiated during the PhD with the objective to improve the understanding of the effects of hydropeaks on aquatic habitats and bed mobility and to examine the various points raised in the discussion of the thesis.

8.1 CALIBRATION OF UNSTEADY 2D HYDRAULIC MODELS

Unsteady 2D hydraulic models are currently being calibrated in order to continue studying the impact of hydropeaks and their propagation on flow hydraulics. These models will enable a better characterization of ramping rates, which are highly unstable phenomena, and the detection of possible hysteresis effects in depth-flow rating curves. Once calibrated, these analyses will be used to validate the increase in ramping rates in the middle of the Upper Esera segment, and the simulation results will be correlated with the grain mobility data observed in **Chapter 6**. This will help to improve the reliability of the two papers currently being prepared (**Chapter 3**, part 2 and **Chapter 6**).

Several tasks were carried out to calibrate the unsteady simulation performed with the IBER 2D hydraulic models (Bladé et al., 2014):

(1) Extraction of 2 hydropeaks from the time series of flow and water surface elevation data at each monitoring station along the river segments (one peak for calibration and the second for validation). Periods with the least possible water input from tributaries were selected.

(2) Definition of a mesh of variable size with finer resolution in the zones of interest (mobility monitoring zone) in order to obtain quality results with reasonable calculation times.

(3) Calibration of the hydraulic models by sensitivity analysis of hydraulic parameters such as roughness and turbulence. A hydrograph (water level) is generated from the hydrograph extracted at measurement stations near the power stations. The optimum calibration is the one that best reproduces the temporal variations in Water Surface Elevation at the downstream measurement stations distributed along the river.

Figure 8.1 shows an analysis of the sensitivity of roughness on the Esera segment for simulations with uniform roughness (blue curve) and for variable roughness using the D_{50} maps obtained in **Chapter 2**. For variable roughness, different simulations were carried out with different numbers of roughness classes (examples, 4 and 7 different classes in Figure 8.1). The results are similar for simulations with variable roughness (n_{var}).

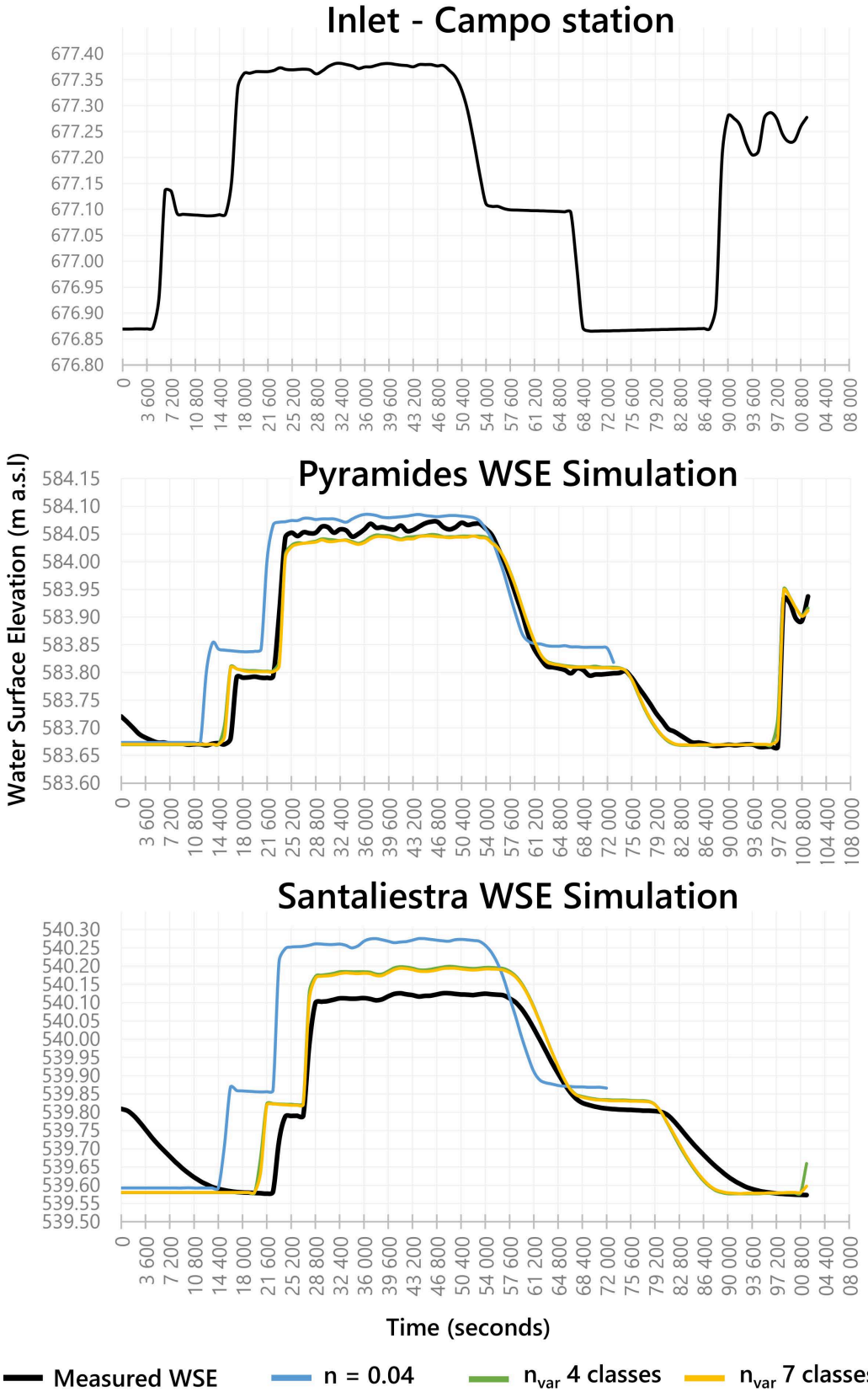

Figure 8.1: Calibration of unsteady hydraulic models by sensitivity analysis as a function of the roughness used. Top, hydrograph extracted from Campo station data and used as upstream boundary condition. Middle and bottom, simulation results for different roughness compared with data measured at the stations (black curve) at Pyramides (12 km from the power station) and Santaliestra (18.5 km from the power station) respectively.

8.2 MEASUREMENT OF BED VELOCITY

The apparent velocity of bed material could be useful to better understand mobility pattern (Rennie et al., 2002; Williams et al., 2015) during targeted flows (floods and hydropeaks), possibly identifying the timing of grain entrainment within a peak, and can be used as proxy to estimate bedload transport rates once calibrated (Rennie et al., 2002) and so their role in re-shaping channel morphology affecting physical habitats. The apparent velocity of bed movement (sediment being transported) was measured by means of an ADCP (Figure 8.2 **A**). The use of an ADCP (Sontek RiverSurveyor M9®) with a Real-Time Global Navigation Satellite System (RTK-GNNS; Leica GS15®) and bottom tracking (BT) enable a safe, contactless, accurate and fast hydraulic measurements (depth, water velocity, flow) under immobile bed conditions. The bottom tracking (BT) is used to measure the spatial average of water velocity component across the vertical water column relative to the ADCP datum. Because the device is mounted on a moving boat, the boat velocity has to be determined to calculate only the water velocity. The boat velocity can be identifying by the bottom tracking itself with a good accuracy. The RTK-GNNS allows georeferencing the positions of the boat and it displacements and therefore also velocity data collected below it. As the bed start to be mobile, the bottom tracking is biased by sediment motion. Bed movements are taken as boat movement. To record accurate data is necessary to couple the RTK-GNNS data to the ADCP, calculating the true velocity of the boat. However, this bias between real boat velocity obtains by RTK-GNNS and wrong boat velocity obtain by BT can be exploited to estimate the apparent bed velocity (bed material transport; how fast the bed moves).

In order to estimate the amount of sediment transported (g/s) from these apparent velocities measurements (m/s), a calibration is required (Rennie et al., 2017). Bedload samples have to be collected just downstream the ADCP device in the same flux of flow (Figure 8.2 **B**).

The sediment transport rate was measured from the Santaliestra bridge using a Helly-Smith (Helley and Smith, 1971) sampler. Measurements were conducted during 2 surveys in December 2019 and 2020. This sampler consists of a basket with a very fine mesh attached to a metal structure, in which moving sediments enter a 76-mm nozzle and are trapped in the basket. This instrument is designed to maintain ambient fluid pressures at the inlet. The sampler was deposited at the bottom of the bed, without agitating the bed, and for a predetermined period (5 or 10 min depending on the intensity of transport). The sampler was then removed from the water. The samples were labelled and taken back to the laboratory to be dried, weighed and sieved. This gives the weight of sediment transported over a given period for a specific point. These values were coupled with apparent velocity measurements from the ADCP to establish a calibration. A total of 29 bedload samples were collected to establish the calibration and 13 survey (similar to Figure 8.1 **D**) of bed velocity for different flow rate (hydropeak and flood) was carried out from the bridge of the Santaliestra for which bedload movements were observed.

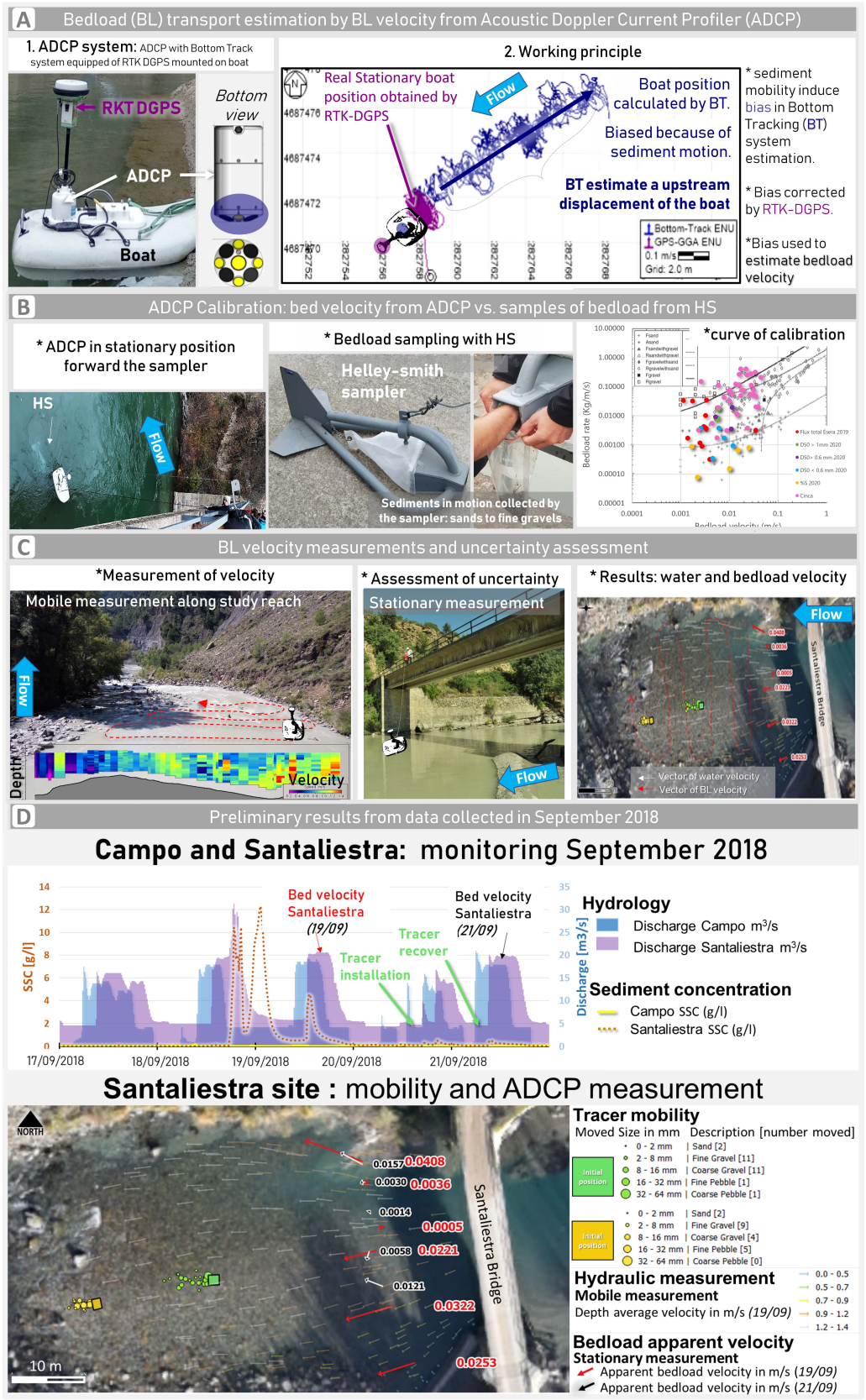

Figure 8.2: Bed velocity measurements and assessment of bedload transport rates. (**A**) Presentation of ADCP and working principle of the measurement. (**B**) 2019 calibration campaign of the ADCP for the Ésera River and comparison with other (pink point for Cinca river, and black and grey from Rees River, Fraser River, and Assiniboine River from@rennie2017). (**C**) Measurement of bed velocity and their estimation (**D**) Example of results during September 2018 campaign.

8.3 CHANGES ON BED TEXTURE

Changes in the arrangement of the bed particles during successive hydrological events (hydropeaks and floods) were measured by means of a high-resolution topographic survey using a Terrestrial Laser Scanning System (Leica BLK360®). Areas of the bed measuring 2m x 2m were successively sampled over time. Before and after each hydrological event, 4 scans (north, south, west, east) of the study area were carried out (Figure 8.3 **B**). These 4 scans produced a dense cloud of points with no shaded areas (i.e. covering all the upstream/downstream and/or lateral slopes). In order to combine the four scans and obtain a point cloud covering all viewpoints, four fixed targets were placed during each topographic survey. These targets are of a different colour on each of the scans Figure 8.3 **D**, making them easy to identify and to merge the scans. Finally, in order to georeference each daily merged point cloud locally in relation to the previous ones, a network of 4 permanent Ground Control Points (GSPs) was installed. During each survey, the total station was used to survey the 4 permanent GSPs and the targets. All the topographic surveys can be placed in the same local reference or coordinate system. In addition, during each survey, random points were taken at the total station in order to assess the altimetric quality of the point cloud generated (in terms of precision and accuracy). This micro-topographic data will make it possible to measure changes in the porosity, orientation and slope of the particles present as a function of the competence of the hydrological events that occurred. In addition, recent algorithms could help identify each particle present in the point cloud and determine whether or not they are still present or whether or not their position has changed between two surveys (i.e. like the *PhotoMOB* method but

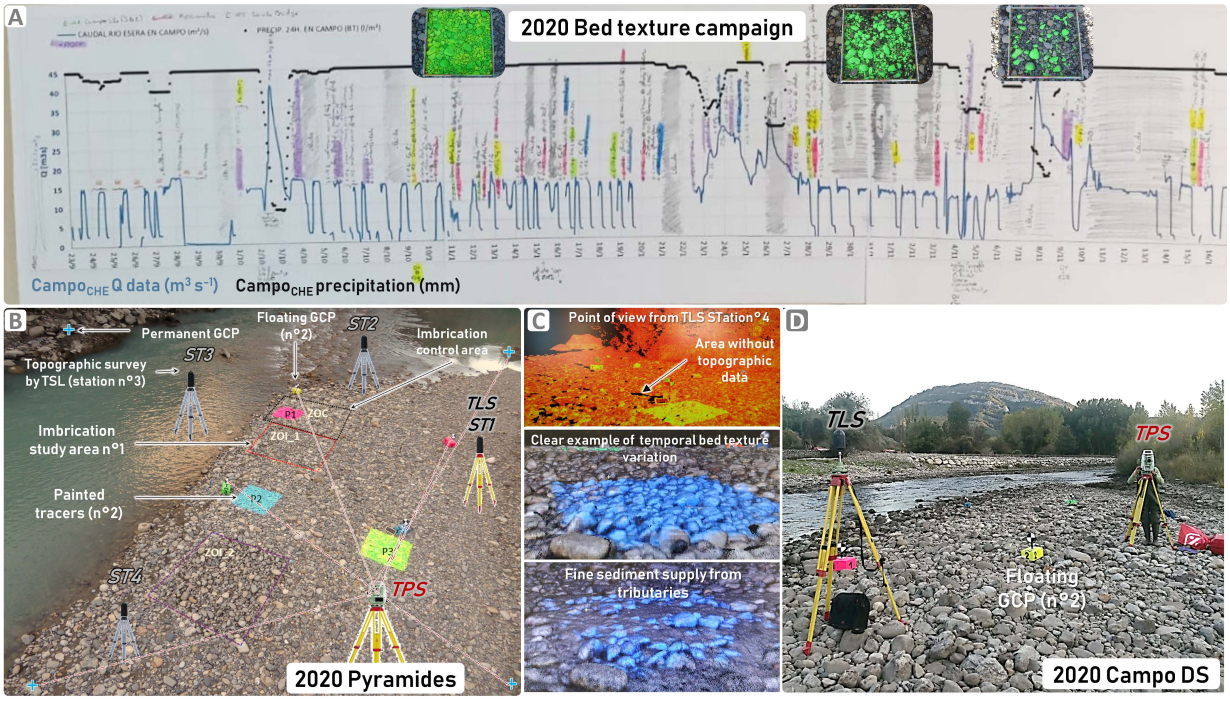

Figure 8.3: Bed texture measurement campaign in autumn 2020. **A** Daily field works. **B** Example of monitoring mobility using painted tracers and bed texture using a TLS survey in the Pyramides study reach. **C** Point cloud from the TLS campaign. **D** Survey of bed texture in the Campo DS study reach.

8.4 SUSPENDED SEDIMENT LOAD

Continuous temporal measurements of water turbidity (i.e. the suspended matter content that clouds the water due to scattering and absorption of light by the suspended matter) at 15-minute intervals were made using McVann ANALITE® NEP-9530 probes (0-3000 NTU range) recorded by a Campbell® CR200X data logger in LUSMS and Campbell® OBS300 probes (0-4000 NTU range) at the Ainsa, Campo and Santaliestra stations. To convert these turbidity values (NTU) into concentrations of suspended solids, punctual water samples were taken. Water samples in the vicinity of the turbidity sensors were collected automatically using an ISCO autosampler, which pumps water into bottles holding up to 24 samples. The sampler was set to take samples on a fixed date or when a certain water level was reached, in order to collect a succession of samples at fixed or variable time intervals. For each sample taken, the date and time were recorded. Before and after each sample was taken, an air purge was performed to clear the suction line to avoid any contamination between samples. During the next field visit, all 24 samples were taken, the bottles cleaned and put back in place for subsequent sampling. The samples were taken back to the laboratory to be filtered and dried to determine the concentration of suspended solids. A total of 750 samples were filtered during the study period. These concentration values were coupled with the turbidity values recorded by the probes to convert the turbidity data into suspended solids concentration (Figure 8.4 **A**, **B** and **C**). Manual samples were also taken for various purposes: (i) along the cross-section near the probes (often from a nearby bridge) in order to assess the intra-sectional variation in the concentration of suspended sediment, (ii) and at various points in the reach studied (upstream, downstream, in tributaries) in order to assess the dynamics of suspended sediment during rainfall or floods (Figure 8.4 **D**).

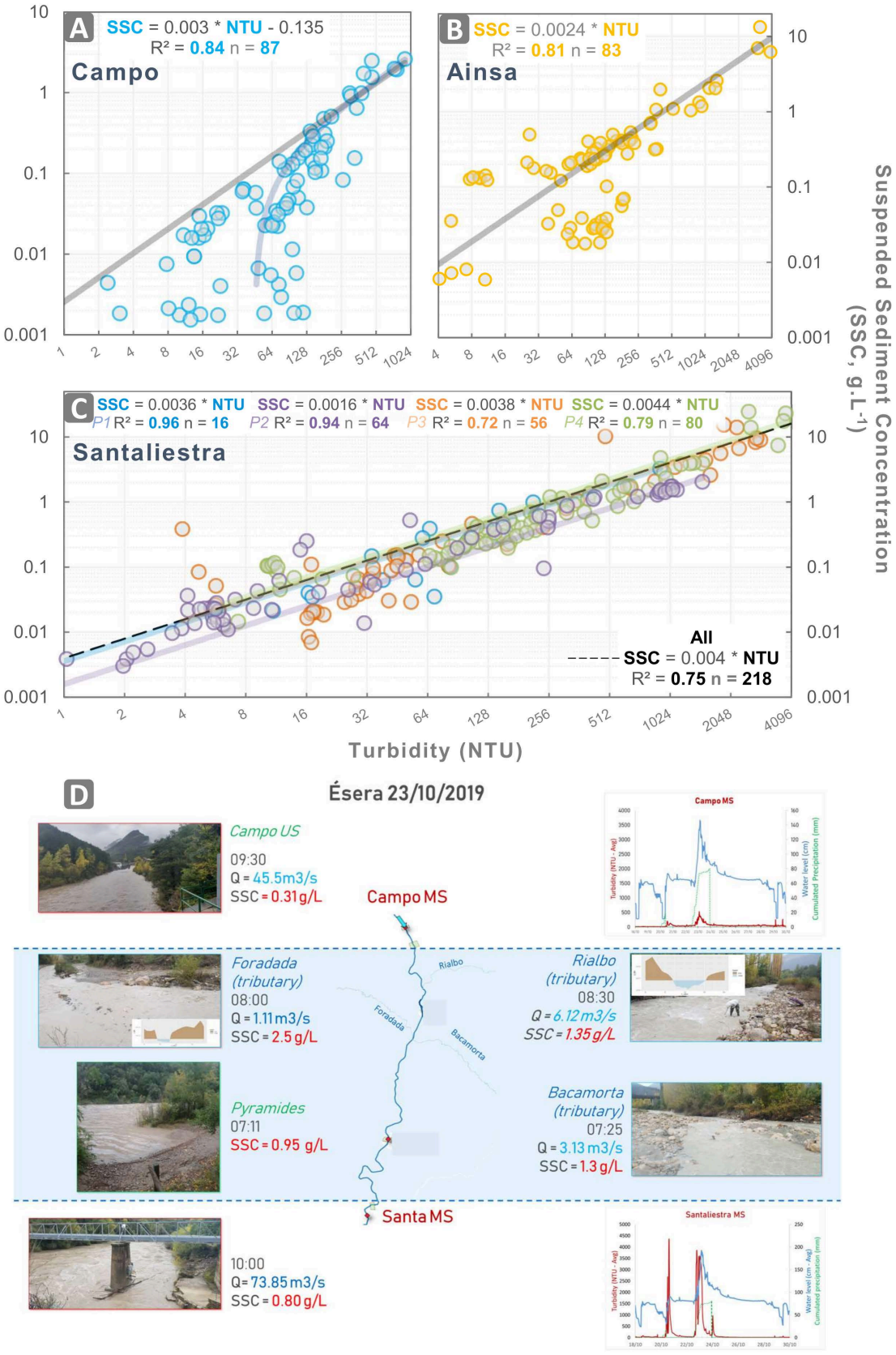

Figure 8.4: Turbidity calibration for the (**A**) Campo station, (**B**) Ainsa station and (**C**) Santaliestra station. Different calibration curves were required after turbidity probes were changed due to malfunctions (**D**) Example of punctual assessment of suspended dynamics by field observation through the entire segments (main channel and tributaries)

REFERENCES

Bladé, E., **Cea, L.**, **Corestein, G.**, **Escolano, E.**, **Puertas, J.**, **Vázquez-Cendón, E.**, **Dolz, J.** and **Coll, A.** (2014) Iber: herramienta de simulación numérica del flujo en ríos. *Revista Internacional de Métodos Numéricos para Cálculo y Diseño en Ingeniería*, **30**, 1–10. DOI:10.1016/j.rimni.2012.07.004

Helley, E.J. and **Smith, W.** (1971) Development and calibration of a pressure-difference bedload sampler. *Water Resour.Div, U. S. Geol. Surv.*, Menlo Park, Calif, https://api.semanticscholar.org/CorpusID:126520279

Rennie, C.D., **Millar, R.G.** and **Church, M.A.** (2002) Measurement of Bed Load Velocity using an Acoustic Doppler Current Profiler. *J. Hydraul. Eng.*, **128**, 473–483. DOI:10.1061/(ASCE)0733-9429(2002)128:5(473)

Rennie, C.D., **Vericat, D.**, **Williams, R.D.**, **Brasington, J.** and **Hicks, M.** (2017) Calibration of Acoustic Doppler Current Profiler Apparent Bedload Velocity to Bedload Transport Rate. In: *Gravel-Bed Rivers* (Ed. D. Tsutsumi and J.B. Laronne), *John Wiley & Sons, Ltd*, Chichester, UK, 209–233. DOI:10.1002/9781118971437.ch8

Williams, R.D., **Rennie, C.D.**, **Brasington, J.**, **Hicks, D.M.** and **Vericat, D.** (2015) Linking the spatial distribution of bed load transport to morphological change during high - flow events in a shallow braided river. *J. Geophys. Res. Earth Surf.*, **120**, 604–622. DOI:10.1002/2014JF003346.Received

ANNEX

PUBLICATION RELATED TO THE THESIS TOPIC

Upstream view of the Cinca and snow-covered Monte Perdido in the background, 20/02/2020. Author: Fanny Ville

Annex A

Effects of Hydropeaking on Bed Mobility: Evidence from a Pyrenean River

River Noguera Pallaresa during hydropeaking just downstream the Unarre tributary, 27/07/2022. Author: Fanny Ville

This annex contains the following accepted and already online published paper in the journal Water. JCR-SCI Impact Factor: 3.4. 1st Quartile. Vericat, D., Ville, F., Palau-Ibars, A., Batalla, R.J., 2020. Effects of Hydropeaking on Bed Mobility: Evidence from a Pyrenean River. Water 12, 178. https://doi.org/10.3390/w12010178

Abstract: Hydropower production involves significant impacts on the dynamics and continuity of river systems. In this paper we analyse the effects of hydropeaks on river-bed particle mobility along a 2-km river channel. For this, a total of four study reaches were stablished: one considered a control reach (no impact by hydropeaking) and three impacted (upstream and downstream from the confluence of tributaries). Mobility related to three hydrological scenarios considered representative of the entire flow conditions in the control and impacted reaches was investigated. Results indicate that sediment availability and dynamics proved different in the control reach to those observed downstream in reaches daily affected by hydropeaks. In the absence of large floods capable of resetting the system from a sedimentary point-of-view, only the role of tributaries during small flow events reduces the effects of hydropeaks on river-bed particles availability and mobility. The effects of a hydropeaked regime are not observed for the whole spectrum of grain-sizes present in the river-bed. While the structural large elements (i.e., boulders) in the channel do not move, sand and fine gravel stored in patches of the bed are constantly entrained, transported and depleted whereas, in between, medium and large gravel are progressively winnowed. Our results point out that hydropeaked flows, which are generally not considered as disturbances in geomorphic terms, initiate frequent episodes of (selected) bed mobility and, consequently, the river-bed becomes depleted of fine sediments from patches and progressively lacks other fractions such as medium gravels, all of which are highly relevant from the ecological point of view.

Key words: hydropeaking; bed-mobility; patches; sediment availability; floods; flow competence; sediment depletion

A.1 INTRODUCTION

The use of clean sources to meet current and future energy demands, together with the international consensus to reduce emissions of greenhouse gases, place hydropower energy as a major sustainable energy alternative. However, hydropower production involves significant impacts on the dynamics and continuity of river systems. The rapid oscillations of flow generated by hydropower facilities (i.e., water pulses called hydropeaks) meaningfully interfere with the flow and sedimentary regimes of rivers, as well as on their ecological functioning. The high instability of channel habitats is the main limiting factor for the normal functioning of such ecosystems, i.e., hydropeaking modifies flow hydraulics, sedimentary structure of the river-bed, sediment transport and habitat availability. It is important, therefore, to analyse such biophysical processes and the associated impacts to achieve a balance between energy production and conservation of fluvial ecosystems, in which hydropower generation takes place. Occasionally, the morphological and sedimentary dynamics of river systems are affected by the joint effect of reservoir sedimentation in addition to hydropeaking. Dams alter the transfer of water and sediment to downstream reaches (e.g., Yang et al., 2007; De Vincenzo et al., 2017), causing sediment deficit that locally generates river-bed incision and eventually armouring (hungry water as per Kondolf, 1997), and the lack of fine sediment to associated ecosystems such as estuaries, deltas and coastal areas (e.g., Vericat and Batalla, 2006).

Sediments in rivers experience cycles of entrainment, transport and deposition (Church, 2006). Floods are major natural disturbances that together with anthropic impacts control or modify such cycles. Examples of impacts are dams (e.g., Batalla and Vericat, 2009), gravel mining (e.g., Rempel and Church, 2009), channelization and channel constriction by embankments and rip-rapping (e.g., Llena et al., 2020), and hydropeaking, to which this paper is devoted, affecting a suite of bio-physical processes, notably flow hydraulics and the sedimentary structure or river-channels (e.g., Gostner et al., 2011).

Fluvial sediments are usually highly variable both in the cross-sectional and the vertical dimensions of the channel, and their distribution controls the mobility of river-bed particles of various sizes. The presence of a coarse surface layer with varying degree of armouring primarily exerts the control on particle mobility (e.g. Parker and Klingeman, 1982; Wilcock and DeTemple, 2005; Vericat et al., 2006). Additionally, mobility is also conditioned by bed structuring, which have a direct effect on particle hiding and protrusion (e.g. White, 1982; Vericat et al., 2008c; Batalla et al., 2010). This means that fine particles may require a higher threshold than larger particles. Bed structure and mobility is also influenced by the supply of sediment. Therefore, understanding the frequency in which the flow exceeds the mobility threshold and the magnitude of the excess energy of the flow is fundamental to achieve a correct characterization of the sediment mobility of a given river reach.

Of special relevancy for river functioning and ecosystem dynamics is the presence of patches of fine sediments in the bed. Surface patches are generally defined by accumulations of sand and gravels around sediments of larger calibre that generate a protective effect and favour sedimentation (e.g., Garcia et al., 1999). The entrainment and transport of sediments from such structures hardly modifies channel morphology, but may have a direct impact on fluvial habitats and benthic communities. For instance, Vericat et al. (2008c), Batalla et al. (2010), and Gibbins et al. (2007a) reported how incipient bedload rates from patches trigger involuntary macroinvertebrate drift in gravel bed rivers. Their results also pointed out that such patches are depleted if replacement from upstream does not occur, or if flow conditions do not reach the threshold to destabilise the armour layer. Processes of partial bed mobility driven by the entrainment of sediments from patches are frequent in reaches affected by hydropeaking, in which flow is artificially increased without an upstream supply of sediments; this situation generates a sedimentary deficit that may affect a variety of processes (e.g., fish spawning, invertebrate refugee). The deficit may be mitigated by natural floods that regularly provide sediments from upstream and propitiate an increase in the availability of such small sizes and the reappearance of the associated sedimentary structures (e.g., patches). Although there is a number of works describing the environmental effects of hydropeaking on rivers (e.g., Bruno et al., 2009; Casas-Mulet et al., 2015b; Céréghino et al., 2002; Cushman, 1985; Frutiger, 2004; Heggenes et al., 2007; Lagarrigue, 2002; Lauters et al., 1996; Liebig et al., 1999; Schmutz et al., 2015), there is still a lack of studies examining their specific effects on sediment entrainment and mobility of bed-material particles. Within this context, the objective of this work is to analyse river bed mobility in relation to the frequency and the magnitude of hydropeaks and natural flood events. This paper also examines the role of tributaries in the downstream recovery of sediment availability. For this, a historically hydropeaked 2-km river reach was selected in the Upper Noguera Pallaresa (Southern Pyrenees), a major tributary of the River Ebro (Figure A.1).

A.2 STUDY AREA

A.2.1 The Basin

The Noguera Pallaresa river basin drains an area of 2 820 km^2 and is the main tributary of the River Segre (main tributary of the Ebro, NE Iberian Peninsula). Catchment altitude ranges from >3 000 m a.s.l. to 255 m a.s.l. in the confluence with the Segre (Figure A.1). The Noguera Pallaresa belongs to the Mediterranean climatic domain (Cfb according to Köppen climate classification) but shows trends specific of mountainous regions (i.e., dry sunny winters that contrast with summer thunderstorms). The wettest season are spring and autumn, with snow occurring at the headwaters mostly during winter. Mean precipitation in the catchment (from the period 1920-2002) ranges from 1250 mm/year in the headwaters to 400 mm/year at the catchment outlet (Frutiger, 2004). Mean annual temperature ranges from 4 °C at the headwaters to 14 °C in the lowlands. Most of the catchment area (83%) is covered by forests and grassland, 9% is occupied by agriculture (located in lowlands and valley bottoms), while the remaining 8% belong to small villages and rocky outcrops (Buendia et al., 2015; Herrero et al., 2017).

As already reported by Buendia et al. (2015) the annual water yield of the whole catchment averages 1 330 hm^3/year (1 hm^3 = 1 x 10^6 m^3) with May and June concentrated most of it (180 hm^3 and 260 hm^3, respectively), typically due to snowmelt. The flow regime of the river has been altered by dams that were built up along the 20th century for hydropower production. The largest are located in the Noguera Pallaresa mainstem (i.e., form upstream to downstream: Sant Antoni 207 hm^3 in operation since 1916; Terradets 33 hm^3, 1935; and Camarasa 163 hm^3, 1920), whereas several others patch the main tributaries (Flamisell and Ribera de Cardós). The total hydropower capacity including power pumping of reversible power stations attains >1 000 MW with a total of 29 stations installed in the overall catchment (see also Herrero et al., 2017) for details on how climate and land use changes can affect the basin's hydrological regime).

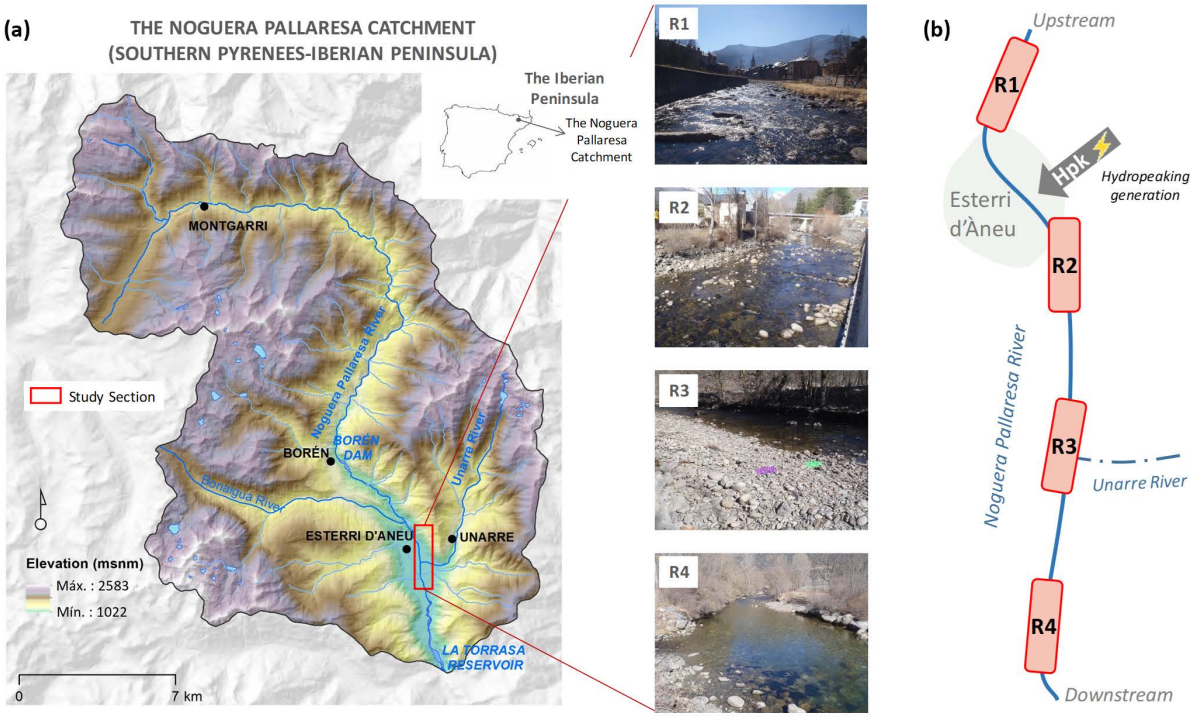

Figure A.1: (**a**) Location of the Upper Noguera Pallaresa River (NE Iberian Peninsula) and the study section. (**b**) Schematic view of the study section and the specific four study reaches, together with general pictures showing the various river-channel configurations observed in the study reach.

A.2.2 The Study Site

The catchment at the study segment (upstream La Torrasa Reservoir, Figure A.1) has an area of approximately 330 km^2. Upstream the study segment there is the Borén Reservoir (1 hm^3 built in 1958), receiving a mean annual runoff of ca. 125 hm^3. The Borén Reservoir stores and derives water to the Esterri-Unarre hydropower complex through a series of pipes and underground storage facilities (i.e., maximum generation capacity equates to 43 MW, whereas maximum discharge through turbines is around 23 m^3/s) (see Figure A.1 **b** for location of the hydropeaking generation within the study reach). A discharge (Q) of 0.3 m^3/s is released from the Borén Dam as environmental flow (i.e., Q_{95} of the flow duration curve). The hydrological regime is highly altered by the hydropower production; a typical hydropeak (Figure A.2) may attain ca. 20 m^3/s and can occur twice a day. Flow duration curves display a median discharge (Q_{50}) of 1.05 m^3/s in the control reach upstream from the Hydropower Station (HP) where hydropeaks are generated, a discharge that increases to 4.06 m^3/s in the downstream reach. Q_{90} and Q_{10} discharges are 0.49 m^3/s and 2.66 m^3/s in the control reach, and 1.73 m^3/s and 16.52 m^3/s n the impacted reach, respectively. Figure A.2 **b** illustrates the fluctuations of the daily Q observed downstream from the HP station.

The station produces energy from a minimum of 4.1 h/day in August to a maximum of 23.8 h/day in May (information provided by the company in charge of the dams and the HP facilities, i.e., Empresa Nacional de Electricidad Sociedad Anónima (ENDESA).

The river displays a transitional morphology (i.e., step-pool to riffle-pool) in the reach upstream from the HP station (i.e., control reach), and a riffle pool configuration downstream from the station (i.e., impacted reach). Alternated bars are present during low flow conditions. Mean channel slope is 0.013 m/m and 0.007 m/m in the upstream and downstream reaches, respectively. River-bed-materials are composed by three well-differentiated sediment fractions (see Section A.3.1 for more details): (i) The so-called structural materials mainly composed by large cobbles and boulders (D_{50} ranging from 880 mm in the control reach to 370 mm in the impacted reach); (ii) coarse movable particles mainly formed by gravels and cobbles with D_{50} ranging from 52 mm to 65 mm in both reaches, and (iii) patches of fine materials, mostly fine gravels and sand with a D_{50} of 1.9 mm in the control section and 0.8 mm in the impacted reach. The median size of subsurface materials ranges from 9 mm to 18 mm

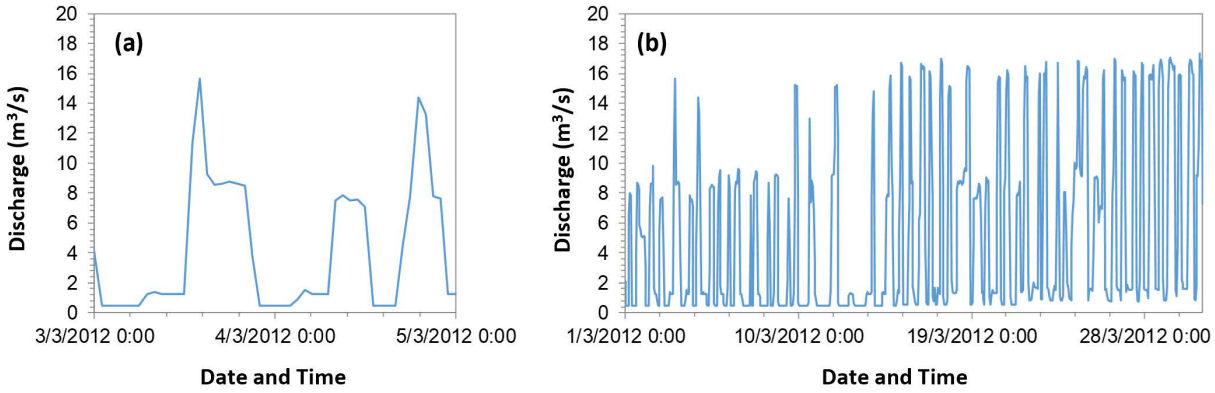

Figure A.2: Detail of typical hydropeaks (**a**) in the Noguera Pallaresa study reach and (**b**) the related general hydropeaked regime.

A.3 METHODS

Four river reaches were monitored. One river is considered the control reach, located upstream from the HP station (i.e., R1, Figure A.1), while the other three are located downstream (i.e., R2, R3, and R4, Figure A.1 **b**), being considered the impacted reaches. In the following sections we provide the details of methods used to survey channel topography and river-bed sediments, and characterise flow hydraulics and bed mobility.

A.3.1 Channel Topography

Topography was obtained to derive channel geometry and allow hydraulic modelling tasks (Figure A.1). Topographic surveys started in December 2011 and were completed in February 2012. For this, a Leica VIVA® GS15 RTK-GPS (Heerbrugg, Sankt Gallen, Switzerland) has been used. A reference station was set up. The coordinates of this station were post-processed using the Receiver Independent Exchange Format (RINEX) data of the three closest permanent reference stations operated by the Institut Cartografic i Geologic de Catalunya (ICGC). Data post-processing was carried out using the Leica Geo Office® 7.0.1 software (Heerbrugg, Sankt Gallen, Switzerland). The 3d quality (positioning and height) of the final coordinates was 0.0086 m. The quality of the information surveyed with the mobile GPS unit was ca. 1 cm. In total, eight-hundred topographic observations were taken distributed through cross sections 10 m to 20 m spaced.

A total of 24 cross-sections were surveyed together with a longitudinal profile for each of the reaches. The longitudinal profiles were used to calculate the averaged bed slope in each reach. The number of observations in each section varied depending on their topographic complexity. Water stage during surveys was obtained to support calibration and validation of the hydraulic model. The mobile GPS unit was also used to position photographs of bed sediments and to locate tracers during bed mobility experiments.

A.3.2 Flow Hydraulics and Hydrological Scenarios

Flow hydraulics were characterized by means of 1d modelling using HEC-RAS® (developed by the US Army Corps of Engineers, Davis, CA, USA). Modelled hydraulics were subsequently evaluated by means of direct field velocity measurements and continuous water depth data provided by a capacitive sensor (TruTrack WT-HR® (Christchurch, New Zealand) 1.5 m length) located in R1. Water depth was recorded every 15 min. A specific statistical relationship to transform water depth to discharge (h/Q) was derived. For each cross-section, the hydraulic conditions associated to peak flows of three different hydrological scenarios were modelled. These scenarios are fully characterised in the results section and further discussed, and are considered representative of the entire flow conditions in the control and impacted reaches. Specifically, Scenario 1 represents the combination of: (i) base flow conditions and low magnitude floods in the control reach (R1); and (ii) a series of highly frequent hydropeaks of similar magnitude in the impacted reaches (R2 to R4). Scenario 2 represents a high magnitude flood in both control and impacted reaches, together with the effects of hydropeaking and tributaries inflows in the impacted reaches. Finally, Scenario 3 represents an isolated hydropeak occurring in R2, R3, and R4. Flow data for each scenario were obtained by means of: (i) the water stage sensor located in R1; (ii) the flow data provided by the hydropower plant (data supplied by ENDESA); and (iii) the flow records available at the La Torrassa Reservoir (data supplied by ENDESA), which is located further downstream (see Figure A.1 for location details).

A.3.3 Bed Materials Characterization

A.3.3.1 Surface Materials

River-bed materials are composed of three well-differentiated sediment fractions, which have a direct effect on the mobility patterns observed in the channel: (i) structural materials (Figure A.3 **a**), (ii) coarse movable particles (Figure A.3 **b**), and (iii) patches of fine materials (Figure A.3 **c**). The methodological design for the characterization of the bed materials was based on these observed components. The grain-size characterization of the surface materials was carried out in two phases. Phase I assessed the proportion of the three sediment fractions in each of the study reaches, while Phase II undertook the characterization of the grain-sizes properly.

For Phase I, a variant of the pebble count method (Wolman, 1954) was used, with the objective of quantifying the proportion of each of the three fractions over a total of 100 measuring points distributed along linear transects in each reach. The type of material (i.e., structural, coarse or patch) sitting in each observational point was annotated, so the percentage of each component was assessed. Particle sizes were then characterized (Phase II). The two coarser grain-size fractions (structural materials and coarse surface layer, see Figure A.3 **a**, **b**) were measured following the pebble count method (Rice and Church, 1996; Wolman, 1954). Particles were classified (b-axis) by passing them through a template divided into ½Φ size intervals (e.g., Lisle and Madej, 1992). The b-axis of the structural sediments was obtained by means of a ruler. The classification of the sediments was based on the Wentworth scale (where $\Phi_i = -log_2 D$, being D the size of the particles in meters). In total, 450 particles were measured.

For the characterization of the fine surface sediments that form the patches, a photographic method was used. The photographic method represents an indirect method to obtain Grain-Size Distributions (GSD), allowing for the characterization of sedimentary units without modifying their

structure. The photographs were analysed using the Digital Gravelometer® (University of Loughborough, Leicestershire, UK). This software allows the rectification of the photographs through knowing the distance between control points (i.e., the real length between points identified in the photos), the identification of particles and the automatic calculation of the length of the axes of these. GSD resulted from the two methods, in which the particle's *b*-axis and their accumulated frequency are displayed, allowing the extraction of characteristic grain-size percentiles such as the median particle size (D_{50}), the D_{84} and the D_{16}.

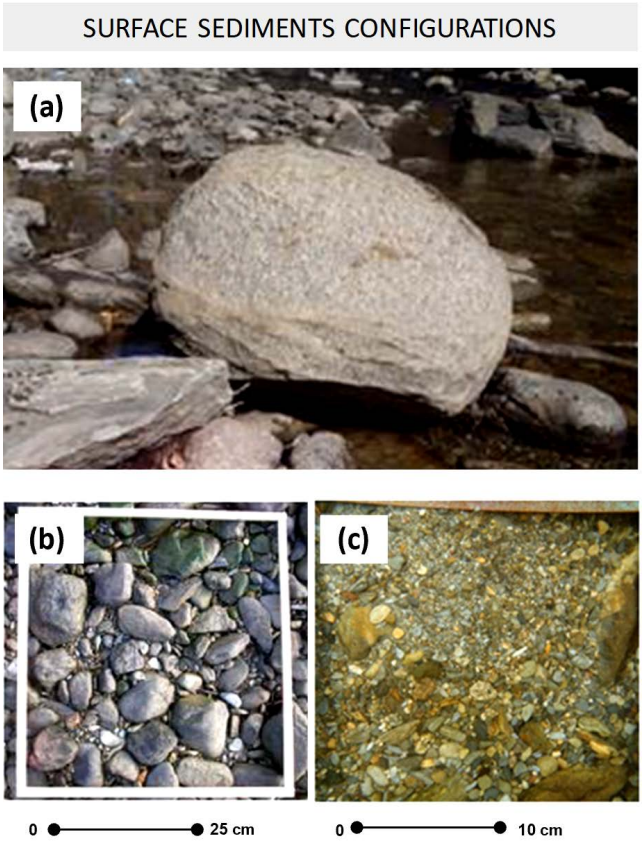

Figure A.3:
Surface sediments configurations: (**a**) Structural bed-material, (**b**) Coarse surface layer formed formed by movable cobbles and gravels and (**c**) Patches of fine sediments (fine gravels and sand)

A.3.3.2 Subsurface Materials

Subsurface materials were sampled in two of the four reaches (i.e., R2 and R4; see Figure A.1 for location). The spatial variability of subsurface materials can be considered small among relatively localized reaches. Sediments were characterized by means of the volumetric method after extraction of the surface layer in exposed bars during low flows. An area of 1 m^2 was delimited and painted with quick-drying spray paint; painted particles were removed, exposing the underneath subsurface materials. For the determination of the total volume of the sample, it was considered that the largest subsurface particle (D_{max}) did not exceed 3% of the total weight of the sample (Church et al., 1987), a criterion that is considered adequate when the median of the material to be characterized is located in the fractions of coarse gravels and pebbles. The *b*-axis of the D_{max} ranged between 75 mm and 100 mm. The largest fractions were sieved in the field while the finer were processed in the laboratory. As in the case of surface material, the sieves followed ½ Φ intervals. A total of 60 kg of material were processed. Once sieved, a grain-size curve for each sample was plotted. The comparison of the medians (i.e., D_{50}) of the surface and subsurface GSD permits quantification of the degree of armouring (Bunte and Abt, 2001). When the ratio is >1.5, it is considered that there is a marked difference between the surface and the subsurface materials, while when the ratio approaches to 2 indicates incipient armouring. Higher ratios correspond to well armoured structures, often induced and controlled by sedimentary imbalances such as those occurring downstream from dam (e.g. Vericat and Batalla, 2006).

A.3.4 Bed-Material Mobility

A.3.4.1 Mobility

Bed-material mobility was studied by means of tracer stones (e.g. Liébault et al., 2012). The objective was to determine the size, the distance and the trajectory of displacement of traced sediments after each of the monitored flow scenarios. Although there are different methods, we traced sediments by means of painting (e.g., the origin of the tracer is available based on the colour of the paint) and by means of passive sensors (or tags), in our case Radio Frequency Identification (RFID).

Painted particles (Figure A.4) allow tracking their movement by re-surveying their position once competent flows entrain and displace them. Their position is obtained by means of the RTK-GPS (see Section A.3.1 for details). The size of the particles was also measured. This method is simple but it allows for the tracing of many particles at a time, which is important to have a representative sample of the bed material. Although particles can be traced independently (one by one), a complementary alternative to the method is to paint small areas of the bed (e.g., around 1 m2). This method does not allow sediment tracing in the active (wet) channel but, conversely, allows sediment to be traced without modification of the sedimentary structure of the bed (exposed bars). This is important in rivers with high grain-size complexity where imbrication and surface compaction, together with the presence of sedimentary structures, can control the conditions of the onset of movement, as is the case of the Noguera Pallaresa. In this case, the initial location of the painted particles is considered at the centroid of the painted square. While this yields an uncertainty in the real initial position of each of the painted pebble recovered after a competent flow event; yet, when mobility is relatively high (meters), the uncertainty is compensated for by the large number of pebbles traced and recovered.

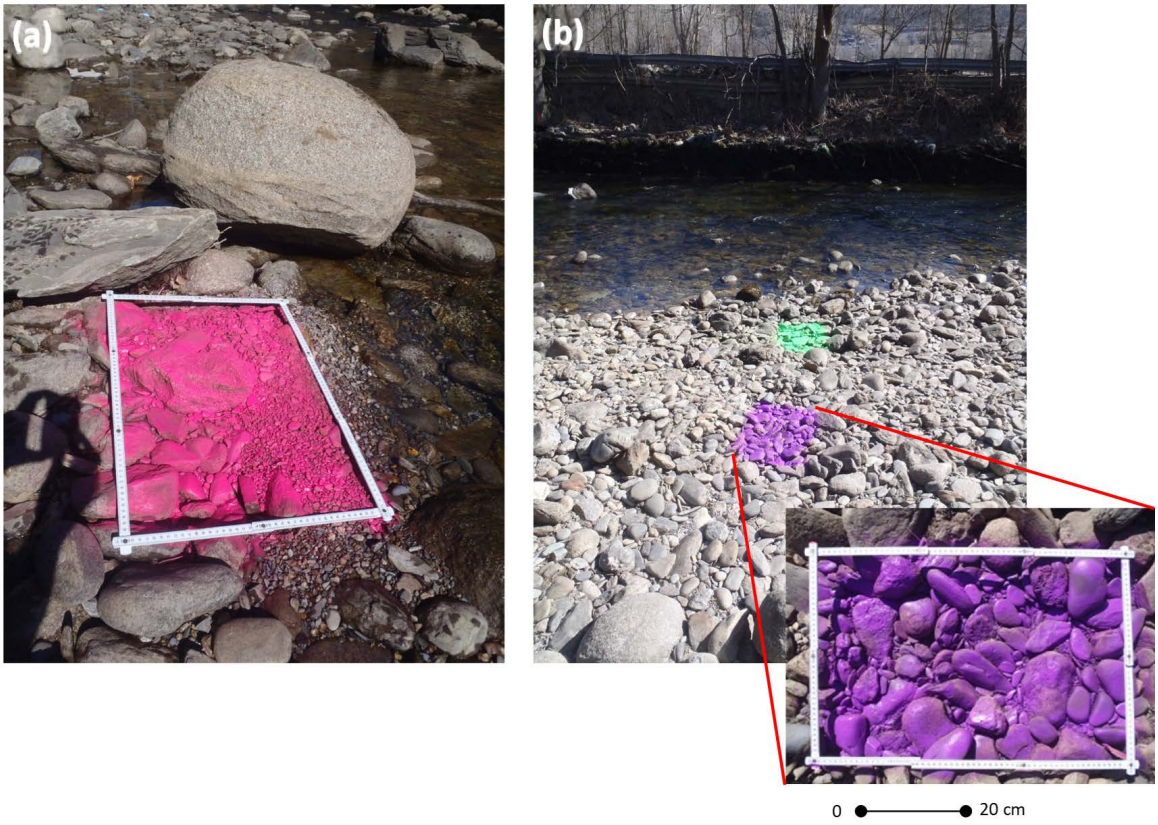

Figure A.4: Painted tracers to monitor bed-material mobility. Examples are for river reaches (**a**) R2 and (**b**) R3

The recovery rate associated with painted pebbles is relatively low (<50%), but the high number of traced particles allows obtaining representative data. In our case, this method has been applied to the coarse movable particles and to the patches of fine materials exposed in dry areas during low flow conditions. The method has proven useful to observe the mobilization of relatively fine sediments, materials of great importance for the habitat (fine gravels and sand) that, due to their size, cannot be traced by means of RFID. The average grain-size (*b*-axis) of the painted tracers found after mobility ranged between 9.4 mm and 18.2 mm.

Larger particles were marked by means of 'passive' (i.e., do not need battery and are activated only when they are detected from a mobile receiver or antenna) RFID tags (Figure A.5). These types of sensors contain antennas to respond to radiofrequency requests, allowing to register the RFID code once it is detected, which is unique per each particle. The size of the RFID tags is a limiting factor since they have to be introduced and sealed inside the particles. In this study, 22-mm and 32-mm sensors were used, which limited their applicability to sediments with *b*-axis smaller than 50 mm (i.e., coarse gravels). These tracers can be used in the active channel and the recovery rate may attain >80%. In our case, a total of 65 tracers between 48 mm and 174 mm of the *b*-axis were in two of the study reaches. The mean particle diameter was 94.5 mm in R1 (n = 33) and 90.5 mm in R2 (n=32).

Figure A.5: Examples of RFID tracers deployed in the study reaches. This technique was used in reaches R1 (reference) and R2 (immediately downstream the hydropower station). (**a**,**b**) Tracers and equipment used. (**c**) Recovering tracers after mobility. (**d**,**e**) Tracers seeded in the river-bed of sections R2 and R1 respectively.

A.3.4.2 Entrainment Conditions

Theoretical or predicted critical shear stress for selected particle sizes was calculated using the Shield's Equation:

$$\tau_c = \tau_c * Q\rho' g$$

where τ_c is the theoretical critical shear stress (N/m^2) for a particle size D, ρ is the submerged sediment density (kg/m^3), g is the acceleration to gravity (9.8 m/s^2) and τ_c^* is the dimensionless shear stress (or Shield's number) modified for gravel mixtures (0.045, as suggested by Church, 2006).

We have considered the observed critical shear stress for a given particle as the value obtained in each reach based on: (i) the largest mobilized particle size; and (ii) the average water depth associated to the peak flow for the given mobility period (i.e., time between surveys). Water depth and shear stress values were obtained from the 1d modelling, based on the DuBoys equation.

Additionally, the specific stream power associated to the peak discharge of each scenario was calculated using the following Equation:

$$\omega = (\rho g S Q)/w$$

where ω is the specific stream power (W/m^2), ρ is the water density (kg/m^3), Q is the peak discharge (m^3/s) and w is the channel width (m).

A.4 RESULTS

A.4.1 River-Bed Topography and Grain-Size

Channel geometry was similar in all of the study reaches (Figure A.6). Mean wet channel width associated with the median discharge (Q_{50}) was around 10 m, with mean water depth ranging between 0.11 m and 0.20 m. Channel geometry in R1 and R2 is constrained by a series of embankments of around 2 m high (above the thalweg), determining that, during flood events, an increase in Q is mainly controlled by an increase in depth and velocity. However, these embankments do not affect any of the hydraulic and sediment transport analyses presented in this manuscript due to the length of the active channel width in relation to the studied flows. Mean slope in R1 is 0.013 m/m, while downstream it reduced to 0.008 (R2), 0.007 (R3) and 0.006 m/m (R4). These differences have a direct influence on flow competence. For the same Q, and taking into account the similar channel geometry observed in all reaches, the higher slope in R1 provided larger shear stress. However, and as discussed below, higher shear stresses do not necessarily mean greater mobility, since this is ultimately controlled by the size of the particles and the local river-bed structure.

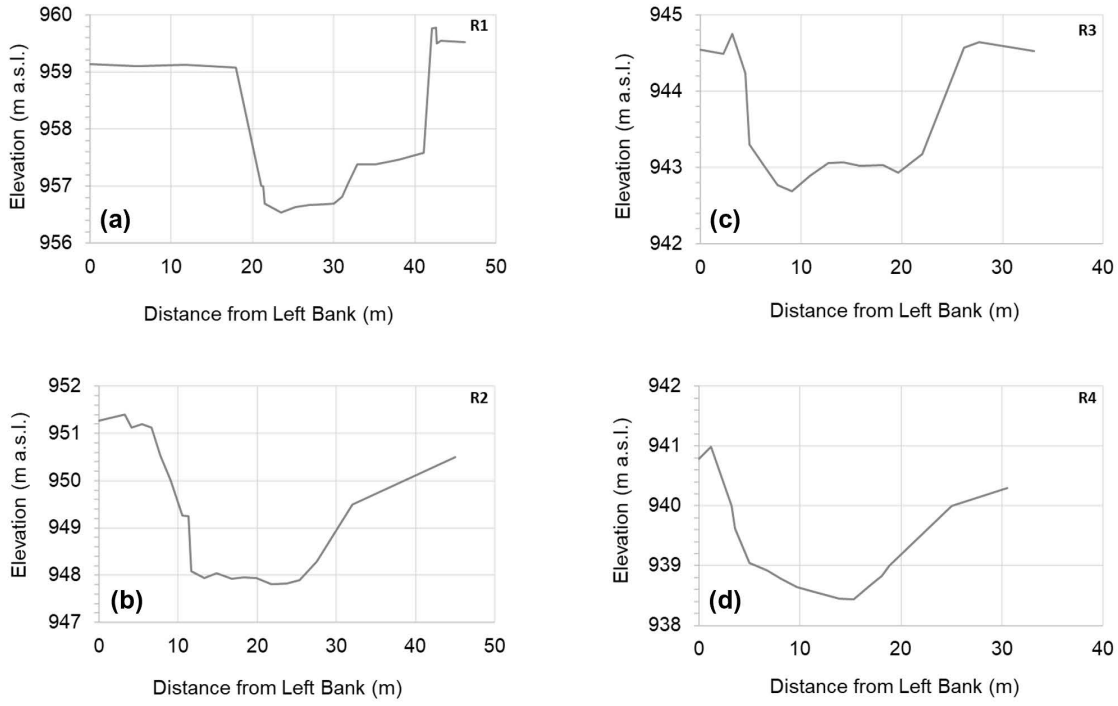

Figure A.6: Representative cross-sections for the four study reach: (**a**) Reach 1 (R1), (**b**) Reach 2 (R2), (**c**) Reach 3 (R3) and (**d**) Reach 4 (R4).

Table A.1 shows a summary of the river-bed grain-size values obtained in each study reach, while Figure A.7 shows their respective GSD. The proportion of Structural surface materials, Coarse movable surface materials and Patches of surface fine materials varied between reaches. The reach presenting more structural materials was R1 (15%), while the presence of these elements in R3 and R4 was marginal (ca. 5%). The size of the structural elements ranged between 881 mm in R1 and 373 mm in R4. These particles have limited mobility but play an important role on channel hydraulics and mobility of finer materials, mainly through hiding and protrusion (e.g. White, 1982). The percentage of fine materials in patches oscillated between 12% (in R2) and 22% (in R4), although the proportion was variable through time associated to hydropeaking and sediment supply from upstream and from tributaries, as discussed below. The size of these materials was similar, all in the range of coarse sands and fine gravels (around 1-2 mm). The majority of the bed was covered by coarse-mobile surface materials (between the 67% and 78% of the bed). Median sizes were in the range of coarse gravels, with moderate to poorly sorted distributions as indicated by the sorting (Folk and Ward, 1957) values (Table A.1).

Table A.1: Characteristic grain-size values of the various sedimentary fractions of the river-bed (see Section A.3.3 for methodological details).

Characteristic Grain-Size Values	Surface Sediments Configurations												Subsurface Sediments			
	Structural Bed-Material				Coarse Surface Layer (Movable)				Patches of Fine Sediments							
	R1	R2	R3	R4	R1	R2	R3	R4	R1	R2	R3	R4	R1	R2	R3	R4
Proportion (%)	15	10	5	4	67	78	77	74	18	12	18	22	-	-	-	-
Percentile 16 (D_{16})	-	-	-	-	29	32	35	34	0.66	0.6	0.58	0.56	1.4	-	2.3	-
Percentile 50 (D_{50})	881	717	442	373	52	64	63	65	1.12	0.88	0.82	0.73	9.7	-	18	-
Percentile 84 (D_{84})	-	-	-	-	126	136	120	117	2.37	1.53	1.4	1.21	58	-	62	-
Sorting ($\sigma_{F\&W}$)	-	-	-	-	1.18	1.05	0.98	0.98	0.89	0.68	0.65	0.55	2.5	-	2.3	-
Armouring (A_r)	-	-	-	-	5.4	3.5	3.5	3.6	-	-	-	-	-	-	-	-

Two subsurface samples of the bed material were obtained, one in R1, representing the control reach, and another one in R3, a reach impacted by hydropeaking. Median subsurface particles were in the range of median to coarse gravels. Although both GSDs are very poorly sorted, there is slight difference in terms of the median particle size (Table A.1). In general, the river-bed is armoured, although armouring in R1 is clearly higher than the one obtained for the hydropeaked reaches.

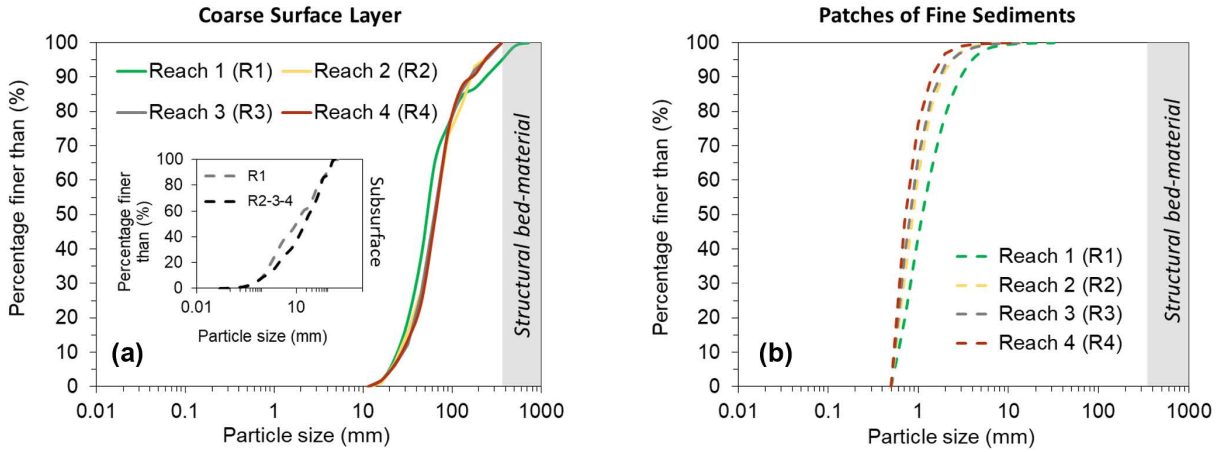

Figure A.7: Grain-size distribution of the study reaches in the Noguera Pallaresa: (**a**) Coarse Surface Layer and Subsurface materials, and (**b**) Patches of Fine Sediments. Note that the range of sizes for the structural bed-material configuration is also identified in both distributions as reference.

A.4.2 Flow Scenarios

Flow hydraulics and associated bed mobility were analysed based on the three different flow scenarios, taken as representative of the entire flow conditions in the control and impacted reaches (Figure A.8) during the study period.

A.4.2.1 Scenario 1

The specific period under this scenario was 1 March to 18 April 2012 (Figure A.8 **a**). The mean Q in R1 was around 0.7 m^3/s, while the peak flow of the unique flood registered in this section was ca. 5 m^3/s. The mean daily Q during the flood was 1.2 m^3/s. This value corresponds to a flow equalled or exceeded the 41% of the time (Figure A.9). Shear stress associated with the peak flow was 48 N/m^2 while the specific stream power was 46 W/m^2 (see flows in Table A.2 and specific stream power values in Table A.3). Downstream, in R2, R3 and R4, flows were significantly different in comparison to R1 due to the effect of the hydropeaks (Figure A.8 **a**). Hourly Q ranged between 0.5 m^3/s and 17 m^3/s (average flow of 7 m^3/s). Maximum daily flow was 13.9 m^3/s and it was equalled or exceeded the 15% of the time (Figure A.9). Shear stress associated with the maximum Q ranged between 33 N/m^2 (R4) and 42 N/m^2 (R2); specific stream power oscillated between 67 W/m^2 and 88 W/m^2 (Table A.2 and Table A.3). Flow differences between the control and impacted reaches were evident. These differences are not directly translated to shear stress. This fact is mainly due to the role of the channel gradient on the shear stress computation. Differences are, however, evident in terms of stream power. The persistence of characteristic Q values in each reach was highly distinct, i.e., whereas in R1, the peak Q (5 m^3/s) constituted a single observation during the whole period, peak values around 17 m^3/s were observed daily in the downstream reaches (Figure A.8 **a**). Differences in the magnitude and frequency of the hydraulic conditions had a direct impact on bed mobility and, subsequently, on physical habitat availability.

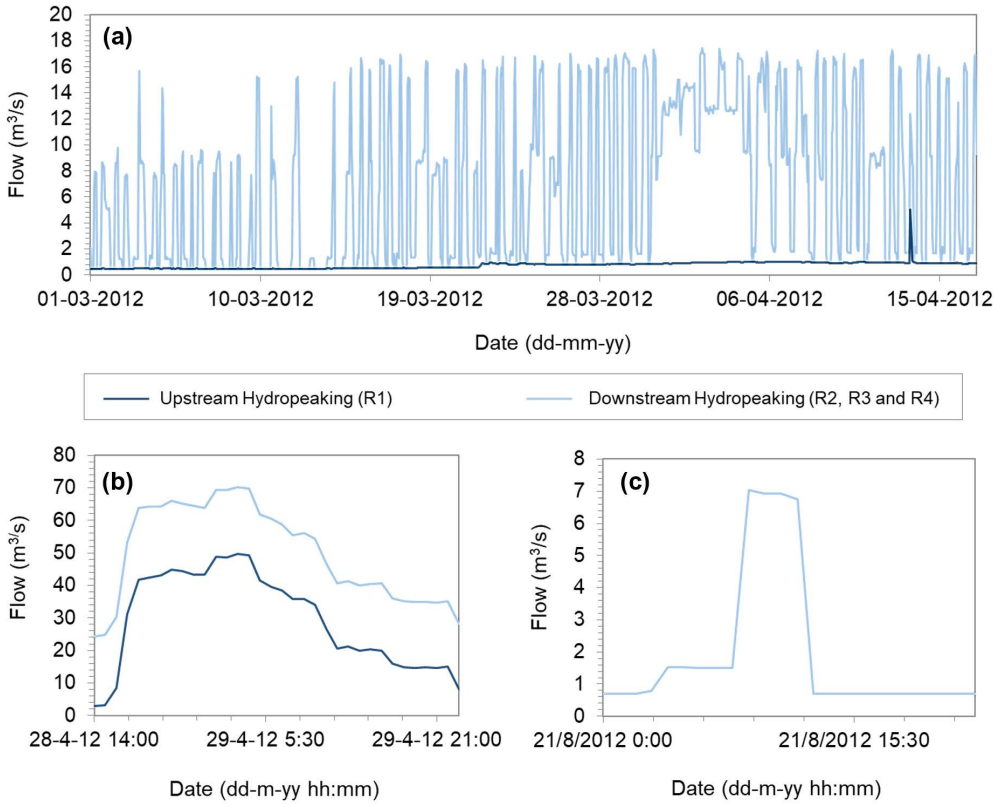

Figure A.8: Flow scenarios taken to characterise river's regime in the Noguera Pallaresa: (**a**) Small magnitude flood and hydropeaking (Scenario 1); (**b**) High magnitude flood and hydropeaking (Scenario 2); and (**c**) A single Hydropeak (Scenario 3).

A.4.2.2 Scenario 2

The period analysed in this scenario encompassed 28 to 29 April 2012 (Figure A.8 **b**). The maximum Q registered in R1 was around 50 m^3/s, yielding an average daily Q of 30 m^3/s. This value was equalled or exceeded the 0.1% of the time (according to the flow duration curve of the river; Figure A.9). Therefore, it can be considered a high magnitude flood. Shear stress associated to the peak flow in R1 was 124 N/m^2, while the specific stream power was 303 W/m^2 (Table A.2 and Table A.3). R2, R3, and R4 experienced the additive effect of hydropeaking and tributaries, increasing the peak Q to 70 m^3/s, yielding a mean daily Q of ca. 50 m^3/s, again equalled or exceeded the 0.1% of the time (Figure A.9). Shear stress in the impacted reach R2 attained 99 N/m^2. Differences in the specific stream power between R1 and R2 were insignificant (Table A.3).

Table A.2: Field observations for the different hydrological scenarios: flow, particles mobilized and step lengths. Note that (i) mobility was measured just in R1 and R2 during scenario 2 (representative of the non-impacted and impacted reaches respectively), and that (ii) no mobility was observed in R4 during scenario 3.

	Scenario 1 Small Magnitude Flood and Hydropeaking					Scenario 2 High Magnitude Flood and Hydropeaking					Scenario 3 A Single Hydropeak				
	Flow	Particle Size Mobilised Coarse Surface Layer		Step Length		Flow	Particle Size Mobilised Coarse Surface Layer		Step Length		Flow	Particle Size Mobilised Coarse Surface Layer		Step Length	
		Largest	Mean	Longest	Mean		Largest	Mean	Longest	Mean		Largest	Mean	Longest	Mean
Reach	(m^3/s)	(mm)	(mm)	(m)	(m)	(m^3/s)	(mm)	(mm)	(m)	(m)	(m^3/s)	(mm)	(mm)	(m)	(m)
R1	5	31	1	-	-	50	171	98	96	29	-	-	-	-	-
R2	18	41	13	6	3	70	146	101	146	42	7	7	5	1.5	1.4
R3	18	42	21	1.8	0.9	70	-	-	-	-	7	62	17	7.1	2.6
R4	18	38	13	2.3	0.9	70	-	-	-	-	7	-	-	-	-

Table A.3: Hydraulic estimations associated to largest particle mobilized for the different hydrological scenarios. Note that (i) mobility was measured just in R1 and R2 during scenario 2 (representative of the non-impacted and impacted reaches respectively), and that (ii) no mobility was observed in R4 during scenario 3.

	Entrainment Thresholds Observed Values								
	Scenario 1			Scenario 2			Scenario 3		
	Largest particle	Shear Stress	Specific Stream power	Largest particle	Shear Stress	Specific Stream power	Largest particle	Shear Stress	Specific Stream power
Reach	(mm)	(N/m^2)	(W/m^2)	(mm)	(N/m^2)	(W/m^2)	(mm)	(N/m^2)	(W/m^2)
R1	31	48	46	171	124	303	-	-	-
R2	41	36	88	174	99	305	7	29	37
R3	42	42	73	-	-	-	62	32	37
R4	38	33	67	-	-	-	-	-	-

A.4.2.3 Scenario 3

In this case only the conditions associated with hydropeaking were analysed and, consequently, only R2, R3 and R4 reaches are considered (Figure A.8 **c**). Note that no mobility was observed in R4 during this scenario. The studied hydropeak was registered on 21st August 2012. Maximum Q was ca. 7 m^3/s, significantly smaller than the maximum Q that the HP station can generate (i.e., 23 m^3/s). Differences in terms of shear stress and specific stream power between reaches were minimum (Table A.2 and Table A.3). The mean Q of the hydropeak was 1.9 m^3/s (Figure A.8 **c**), equalled or exceeded the 63% of the time (Figure A.9). This mean value is equalled or exceeded the 85% of time in the impacted flow duration curve (Figure A.9). The high frequency of these flows (more than the magnitude) plays an important role on particle mobility and in-channel sediment depletion.

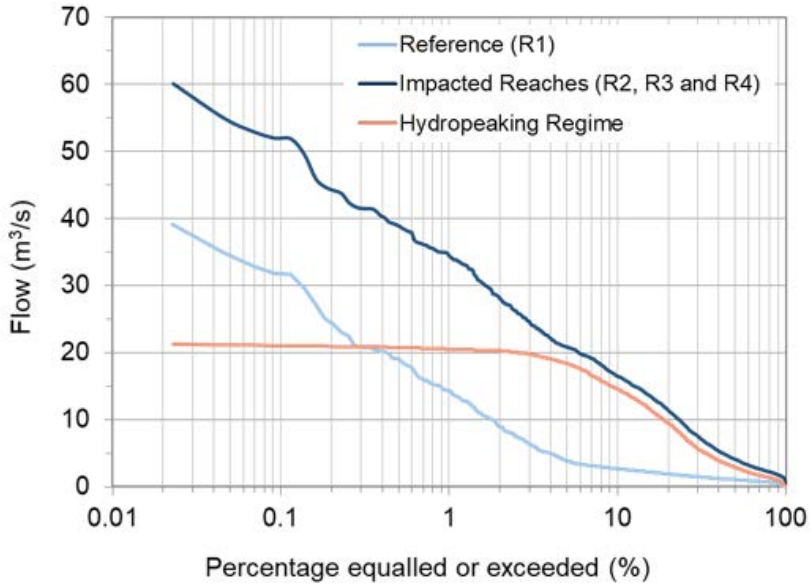

Figure A.9: Flow duration curves for the different hydrological conditions observed in the study reaches.

A.4.3 Bed-Material Mobility

Bed mobility in the control and impacted reaches was assessed through the analyses of (i) particles entrained and (ii) the entrainment thresholds under each of the flow scenarios.

A.4.3.1 Field Observations

The size and step-length of the entrained particles was remarkably different between scenarios and reaches. A summary of the bed mobility observations is presented in Table A.2. Table A.3 presents the largest particle size mobilized in each scenario and the shear stress and specific stream power associated to each analysed peak flow.

A.4.3.1.1 Scenario 1

Only the small fractions of the coarse-mobile GSD were entrained in R1. The mean size of the entrained particles was 1 mm, while the largest entrained particle was 31 mm (Table A.2), smaller than the surface D_{16} (movable component). The results indicate that the relatively small peak flood in the control section (5 m^3/s) were sufficient to entrain coarse sands and fine gravels from the patches. Although the flow was competent, step length was marginal (lower than 0.5 m). Further downstream, in the impacted reaches (R2 to R4), mobility patterns were substantially different to those observed in the control section. Maximum Q was more than threefold larger, with daily oscillations.

The size of the entrained particles increased; the largest entrained particles ranged between 38 mm and 42 mm (i.e., larger than the D_{20}), while the mean of the mobilised sizes varied between 13 mm and 21 mm (Table A.2). The step-length was very variable, probably attributed to the complexity of the surface materials and the hiding and protrusion effects of the immobile particles. Figure A.10 shows the GSD of the recovered tracers together with their step-length. The largest step length was ca. 6 m (observed in R2). Overall, the data show that the hydropeaks were capable of entraining the full range of the fine particles of the patches and the finer ~30% of the GSD for the coarse movable fraction of the bed material. Structural elements did not move in any of the study reaches. Overall, mobility analysis in this scenario indicates a size-selective pattern associated with the distinct hydraulic conditions (both in terms of frequency and magnitude) observed in the control and impacted reaches.

A.4.3.1.2 Scenario 2

Only data in R1 and R2 were obtained under this scenario, which are representative of the both control and impacted reaches. Large floods were able to entrain the full range of coarse-mobile particles in both reaches. The largest entrained particle in R1 was 171 mm, larger than the D_{84} of the movable component. Similar competence (i.e., particle calibre) was observed in the impacted reach, but particles were transported further downstream (1.5 times more) in comparison to the control reach (Figure A.10). This fact may be attributed to the additive hydraulic impact of the hydropeaks, as can be seen in Figure A.8 **b** (Table A.2). The step-length was not, however, clearly controlled by the size of the particles, as was evident in the scenario 1. In general, the results indicated that high magnitude flood events were able to entrain the totality of the mobile components of the river-bed materials (i.e., full mobility conditions) in both the control and the impacted reaches.

A.4.3.1.3 Scenario 3

The effects of an isolated low magnitude hydropeak were also analysed. Entrainment was only observed in R2 and R3, no mobility was seen in R4. Results for this scenario are similar to the ones observed under scenario 1, although differences between reaches are more significant. In general, mobility was higher in R3 than in R2. The largest entrained particles in R3 was one order of magnitude higher than in R2 (7 vs. 62 mm, Table A.2). These values encompass all the size range found in the patches and up to the D_{50} of the coarse movable component in the case of R3. Differences are smaller when the average entrained particle sizes are compared. The mean and largest step length in R2 were similar, i.e., around 1.5 m (Figure A.10). As in scenario 1, patterns observed in R3 indicated that the range of particle sizes having short displacements was large when compared to the one associated to the largest step-lengths. Particles were displaced further in R3; 2.6 m on average with a maximum step-length of around 7 m. These observations highlight the importance of sediment availability during hydropeaking.

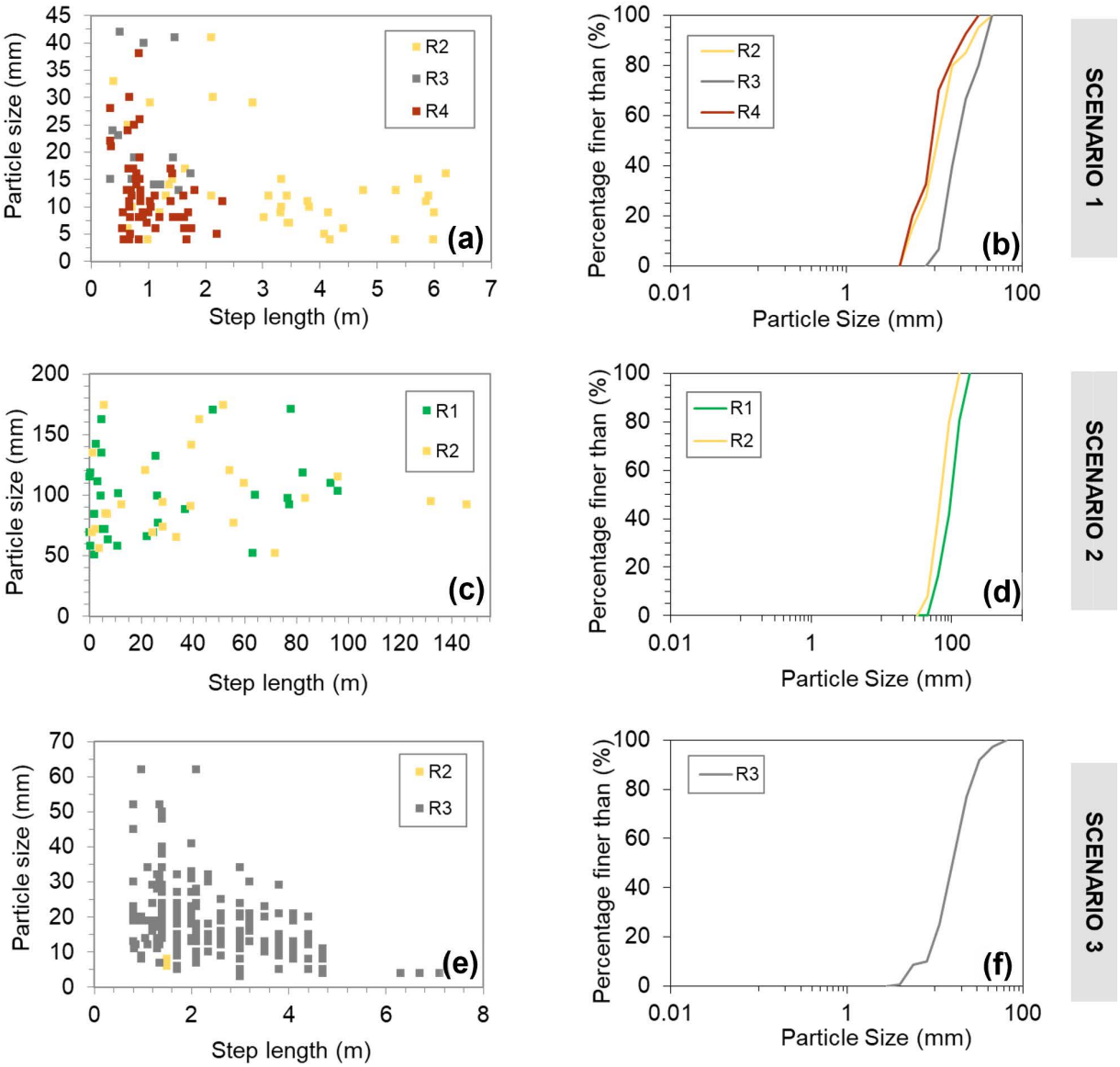

Figure A.10: Mobility of tracer stones in the study reaches: step-length and GSD of mobilised particles: (**a**,**b**) Scenario 1 (Small magnitude flood plus hydropeaking); (**c**,**d**) Scenario 2 (High magnitude flood and hydropeaking); and (**e**,**f**) Scenario 3 (Single hydropeak, see Section A.3.2 for details).

A.4.3.2 Entrainment Thresholds

Figure A.11 shows a relation linking critical shear stress and specific stream power to the mean particle size mobilized (i.e., the mean *b*-axis of the recovered particles). Although the small number of observations, results indicate that exists a general positive relationship between the stress generated by the flow and the mean particle size mobilized under the different hydrological scenarios. In terms of minimum shear stress, mobility was observed around 32 N/m^2, while in terms of stream power, a minimum of 37 W/m^2 are required to entrain the mobile components of the substrate along the entire study segment. These values were observed in R3 during the 'A single hydropeak' scenario (i.e., S3). The largest values of stress and specific stream power were observed during the high magnitude flood event (i.e., S2). Although both lineal models fitted to the data present a high coefficient of determination, it is clear that the one for the specific stream power is higher.

These differences may be attributed to the way both variables are calculated. In the case of the shear stress, the values are calculated by means of the DuBoys approach, while the characteristics of the flows and the channel may not be the appropriate as will be extended below. Data observed in Figure A.11 **b** fits above the majority of the published relations linking critical unit stream power to the size of material in gravel-bed rivers (e.g., Petit et al. (2005)). These differences may be attributed to the hiding effects caused by the structural large elements in the bed, as suggested by the high variability of the magnitude of the step-lengths observed, which is probably due to the complexity of the surface materials which may, in turn, delay the entrainment of the particles in the study segment.

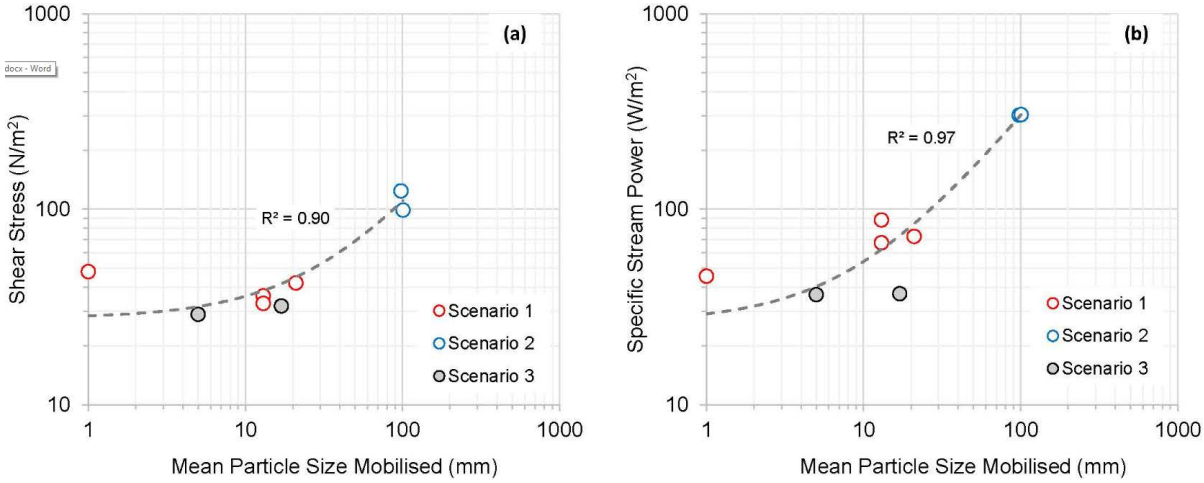

Figure A.11: Relation linking (**a**) critical shear stress and (**b**) specific stream power to the mean particle size mobilized. Note that the critical shear stress and the specific stream power values are attributed to the peak flows of each hydrological scenario (see Section A.4.2 for details). Note that a lineal model is fitted to all data together with the R^2 of the relationship. Even so, these models aim at indicating the general trend but in any case the objective is to predict bed mobility.

Theoretical critical shear stress for the largest particles mobilized in each scenario was assessed following the Shields's approach. Results were compared to the shear stress associated to the peak Q of each scenario estimated by means of the DuBoys approach (based on the 1d modelling results, mean values). Table A.4 summarizes both entrainment thresholds. Additionally, it also shows the predicted values of critical shear stress for representative percentiles of the coarse component of the GSD.

Table A.4: Entrainment thresholds in the study reaches of the Noguera Pallaresa: Predicted shear stress values for representative percentiles of the coarse surface layer and for the largest particles mobilized.

	Entrainment Thresholds Predicted Values of Critical Shear Stress									
	Percentile 16 (D_{16})		Percentile 50 (D_{50})		Percentile 84 (D_{84})		Largest Particle Mobilised (Predicted vs. Observed)			
	Size	Shear Stress	Size	Shear Stress	Size	Shear Stress	Size	Predicted Shear Stress	Observed Shear Stress	Residual (Observed - Predicted)
Reach	(mm)	(N/m²)	(mm)	(N/m²)	(mm)	(N/m²)	(mm)	(N/m²)	(N/m²)	
R1	29	21	52	38	126	91	171	124	124	0
R2	32	23	64	47	136	99	174	127	99	-28
R3	35	25	63	46	120	87	62	45	32	-13
R4	34	25	65	47	117	86	38	28	33	5

Results indicate that theoretical thresholds are underestimated when compared to the observed critical shear stress needed to entrain the largest particle sizes mobilised in R2 and R3 (see residuals in Table A.4). Results in R1 and R4, however, indicated an agreement between both observed and predicted thresholds. Even so, when the full spectrum for mobilised particles are analysed, the results indicate that theoretical thresholds tend to be underestimated. For instance, theoretical critical shear stress for particles between 29 mm and 35 mm ranges from 21 N/m² to 25 N/m², while field observations associated to scenario 1 indicate that the critical shear stress to entrain particles between 31 mm and 42 mm ranged from 33 N/m² to 48 N/m².

A.5 DISCUSSION

A.5.1 Spatial and Temporal Effects of Hydropeaking on River-Bed Mobility

Our results indicated as the effects of hydropeaking on mobility are not observed for the whole spectrum of grain-sizes present in the river-bed. These are also controlled by sediment availability, mainly those sizes present in the coarse mobile component of the substrate and in the patches of fine materials. In the absence of relatively large floods only the sediment supplied from tributaries during small flood events may reduce the effects of hydropeaks on river-bed particles' availability. Figure A.12 shows a close-range picture of R3 in two different periods illustrating the differences in sediment availability which in this reach is controlled by the sediment supply from the River Unarre (see Figure A.1 for location details). The figure also shows that the bed armour was not strong. These facts are key to understand the differences in mobility between reaches. Further downstream, field observations pointed out that the presence of fine sediments (fine gravels) in R4 was much lower than in R3. This fact may suggest a delay in the transfer of this type of materials from the Unarre by the time the mobility episode was analysed. In summary, our results pointed out that single hydropeaks, even of reduced magnitude, have enough competence to entrain an important part of the river-bed materials i.e., all sediments range from patches and a significant proportion of the coarse movable surface materials. Mobility is spatially variable in relation to local sediment availability and flow hydraulics. Sediment availability changes through time in relation to sediment supply from upstream and tributaries, mainly during flood events.

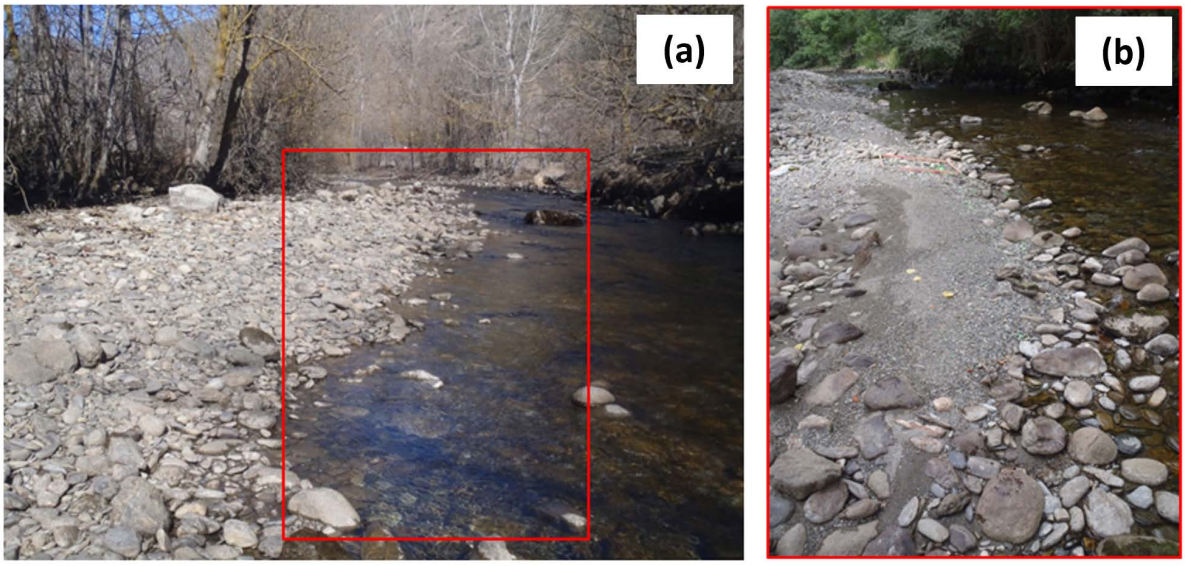

Figure A.12: Fine sediment availability in reach R3, downstream from the confluence of the River Unarre (see Figure A.1 for locations details). (**a**) General view of the coarse surface layer with a marginal presence of fine after a series of hydropeaks (depletion). The red square illustrates the location of the photo presented in (**b**) where fine sediments transferred and deposited after a flood event can be clearly observed.

Results from this study indicate that hydropeaked rivers may be subjected to two general bed mobility models (Figure A.13):

(a) Size-dependent model in which the displacement of sediments is inverse to their size. This model can be attributed to low magnitude floods and to the entire hydropeaking regime, mainly affecting fine surface sediments (typically from patches) and the finer part of the coarse movable GSD. Flow hydraulics during these conditions are of low magnitude and high frequency and are not competent to entrain and transport the entire spectrum of the surface bed materials (mobile fractions). This model is also conditioned by sediment availability, a fact of great importance in the hydropeaked reaches where the frequency of these flows is daily and the entrainment of bed materials is not balanced by the supply of sediment from upstream. Under these conditions the river-bed becomes depleted of fine sediments from patches (e.g. Vericat et al., 2008c) and progressively lacks other fractions such as medium gravels, all of which are highly relevant from an ecological point of view. These reaches can be classed as supply-limited, as their incipient sedimentary recovery can be observed downstream from tributaries (as the Unarre in our study case) that periodically supplies fresh new sediments to the mainstem Noguera Pallaresa, and also due to the loss of competence of hydropeaks as they are routed downstream.

(b) 'Hydraulic-dependent mobility model' in which the displacement of particles is not conditioned by their size, but depends on the magnitude and duration of a given competent flow. This model is generally linked to high magnitude floods that exhibit the capacity to mobilize most of the mobile sediments in the channel, i.e., all except the structural elements. The frequency of these flows is relatively low but they determine the supply of sediment to both the control and impacted reaches. High competence may cause the break-up of the armour layer (see for instance examples in dammed rivers e.g. Vericat et al., 2006), supplying fine subsurface sediments and, together with the overall sediment supply from upstream, increasing their availability along the river channel. The frequency of these flows also influences the mobility observed during hydropeaking, a fact that is again related to the availability of sediment in the river bed (Figure A.13).

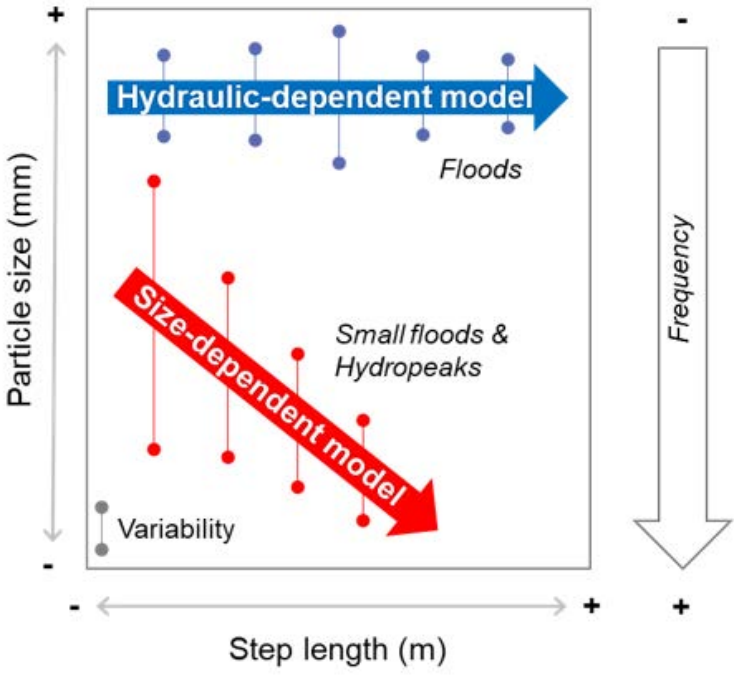

Figure A.13: Conceptual diagram showing the two general bed mobility models in hydropeaked rivers according to their frequency of occurrence.

The combination of these two mobility models generates counter-clockwise hysteresis cycles in the availability of fine sediments (sand and gravels) in relation to the time elapsed since the last high magnitude event occurred (Figure A.14). These cycles occur mainly in reaches subjected to hydropeaking. Sediment availability in non-hydropeaked reaches is determined by the balance between the supply of sediment from upstream and the export during competent events. There is therefore an upstream transfer and continuity in sediment transport and in-channel sediment availability does not change significantly if a flood event does not occur (Figure A.14). In contrast, conditions are different in the hydropeaked reaches where flows are altered daily, often reaching critical conditions to entrain fine sediments from the bed. As explained above, those flows yield a size-dependent model, in which fine sediments are entrained without replacement from upstream (and eventually depleted), while larger materials (e.g., coarse gravels) remain relatively immobile. The size of the loop of the hysteresis is inverse to the distance from the point where the hydropeaks are generated. Close to the hydropower station in R2, sediment availability reduces significantly and relatively rapidly (related to the frequency of competent hydropeaks). Further downstream, these processes are mostly modulated by tributaries which periodically supply sediments and flow to the mainstem river (e.g., Figure A.12). In the particular case of our study, flow hydraulics and hence flow competence, does not change substantially downstream, therefore the role of the tributary is highly relevant. Once a high magnitude flood occurs hydraulically-dependent bed-mobility dynamics takes place and a new situation of sediment availability was generated to all reaches (i.e., dashed lines in Figure A.14). The direction of change is variable and it will be determined by the amount of sediment supplied from upstream and the flow competence and capacity, which varies in time and space.

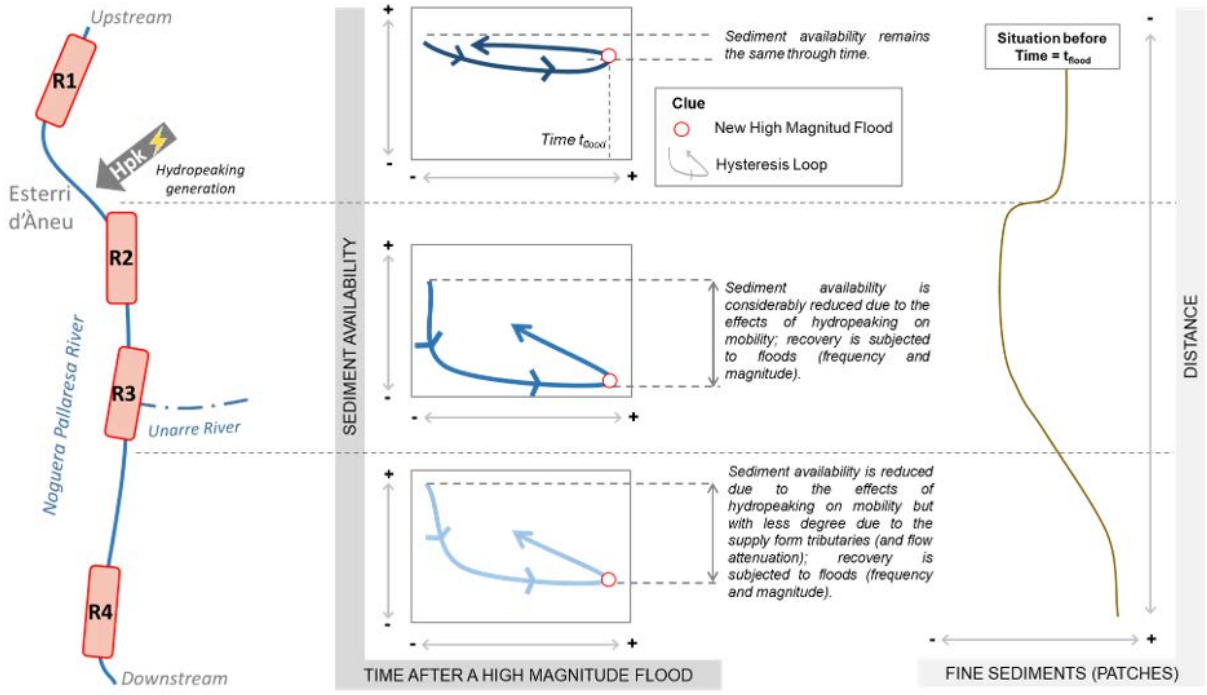

Figure A.14: Conceptual model of spatial and temporal river-bed dynamics in hydropeaked reaches based on the observed bed mobility patterns (Figure A.12).

A.5.2 Bed Mobility and Habitat

Results from this work indicate that hydropeaks enhance the mobility of the relatively fine fraction of the river-bed sediment that becomes depleted until a natural flood re-supplies the reach and sediment becomes newly available. Sediment entrainment and depletion form patches of fine materials have been reported before, often attributed to the early stages of floods or during low magnitude events in which flow competence is limited (e.g. Garcia et al., 2007). Vericat et al. (2008c) reported that depletion of fine sediments from patches in gravel beds occurs rapidly, with bed load rates and particle sizes decreasing only five minutes after the shear stress reached the critical condition for entrainment. Further, Vericat et al. (2008c) reported that, although the critical shear stress to entrain materials from patches is not that high as the values obtained during flood events, they are still higher than the theoretical values estimated using the Shields approach. Similar results has also been reported in this study, and can be mainly attributed to the hiding effect (e.g. Egiazaroff, 1965). Even so, differences between predicted and observed values may be also conditioned to other multiple aspects, both related to the assessment of the theoretical critical shear stress and/or to the computed threshold values based on field observations. First, the DuBoys approach should be applicable to regular channel geometries, wide channels with homogenous materials and subjected to uniform flows (e.g. Gordon et al., 2004; Gore, 1996; Schwendel et al., 2010). Additionally, this approach does not include the effects of bedforms (Carson and Griffiths, 1987). These limitations have a direct impact (uncertainty) on the computation of the critical shear stress associated to the peak Q of each scenario based on field observations. Second, in relation to the Shields approach, it was developed for uniform sediments and does not take into account bedforms either. All study reaches present a notable river-bed complexity (as stated by the three sedimentary components described above), a fact that implies protrusion and hiding effects. These effects enhance flow turbulence and cause disruption and high variability in water depth and velocity fields. Larger particles have a greater exposure to the flow (i.e., protrusion), and the critical entrainment conditions can be lower than those estimated theoretically. In contrast, relatively small particles are protected by the surrounding larger particles (i.e., hiding). This protection means that the strength required to initiate the movement of these sediments has to be greater than that assessed theoretically. One way to analyse the effect of sedimentary structures on reducing or increasing the critical stress is by the assessment of the hiding function for a given GSD (e.g. Egiazaroff, 1965). This coefficient can be used as a multiplier of the critical shear stress to provide what is called the effective critical shear stress (e.g. Sutherland, 1992). Uncertainties related to GSD, river-bed structure, channel geometry, and flow hydraulics need to be considered when assessing entrainment conditions, but the analysis of their relative impact on bed-mobility in the particular case of the Noguera Pallaresa is out of the scope of this paper.

Sediment entrainment and depletion cycles vary not just at-a-section as a function of the frequency and magnitude of the hydropeaks, but also longitudinally in relation to channel geometry, river-bed characteristics (amplitude of grain-size) and the presence of tributaries. Tributaries cause a change in sediment supply that ultimately has a direct effect on sediment availability (e.g. Marteau et al., 2018). The range of particles mobilised during hydropeaking ranged between fine gravels to, eventually, medium to large gravels. According to an early study by Kondolf and Wolman (1993), median diameters of salmonid spawning gravels ranged from 5.4 mm to 78 mm, which is exactly the same range as the sizes reported here. In our case, hydropeaks cause the daily mobility of such relevant grain-sizes for spawning and deplete the river from them, eventually causing an impact on fish communities (for instance common trout i.e., Salmo trutta fario). In addition, the mobility of fine materials from patches in gravel-bed rivers has marked effects on macroinvertebrate drift (as a suite of previous works has indicated e.g., Ceola et al., 2013; Jowett, 2003), with the incipient motion of such particles, causing massive involuntary drift (even only agitation of individual grains takes place, White, 1982). Although patches of fine material may occupy just a small proportion of the river-bed, the involuntary movement of those animals is highly frequent under hydropeaking conditions.

Consequently, hydropeaked flows, which are generally not considered as disturbances in geomorphic terms, initiate frequent episodes of involuntary mass drift (also called catastrophic drift) from patches of fine materials in gravel-bed rivers, a fact that may have consequences over the entire food-chain in river systems.

A.6 CONCLUSION

The investigation in the Noguera Pallaresa provides evidence on the effects of hydropeaks on river-bed particle mobility, whereas outlines the role of such sudden changes in river flow on the short-term sedimentary cycles in gravel-bed rivers. Sediment availability and dynamics proved different in control reaches upstream from the hydropower facilities than those observed downstream in reaches daily affected by hydropeaks. In the absence of large floods capable of resetting the fluvial system from a sedimentary point-of-view, only the sediment supplied from tributaries during small flood events reduces the effects of hydropeaks on river-bed particles' availability and mobility. The effects of a hydropeaked regime are not observed for the whole spectrum of grain-sizes present in the river-bed. While the structural large elements in the channel do not move, sand and fine gravel stored in patches of the bed are constantly entrained and, in between them, medium and large gravels are progressively washed away. The analysis of the direct effects of these complex phenomena on river habitat (fish, invertebrates) was out of the scope of this study. However, we have outlined and discussed some of the ecological consequences of hydropeaks, justifying the need of comprehensive evaluations and diagnostics prior to rehabilitation and mitigation measures being implemented in such fragile mountain fluvial ecosystems.

Author Contributions:

Conceptualization, D.V., A.P.-I. and R.J.B. Methodology, D.V. and R.J.B. Formal analysis, D.V., F.V., A.P.-I. and R.J.B. Writing- original draft preparation, D.V. Writing-review and editing, D.V., F.V., A.P.-I. and R.J.B. Validation, F.V., A.P.-I. and R.J.B. Data curation, D.V. and F.V. Visualization, D.V., F.V. Supervision, R.J.B. Funding acquisition, D.V., A.P.-I. and R.J.B. All authors have read and agreed to the published version of the manuscript.

Funding:

This research was undertaken under the MorphPeak (CGL2016-78874-R) project funded by the Spanish Ministry of Economy and Competiveness and the European Regional Development Fund Scheme (FEDER). Authors acknowledge the support from ENDESA S.A. at the first stage of the research. D.V. (first author) is funded through the Serra Hunter Programme (Catalan Government). F.V. (second author) has a grant funded by the Ministry of Science, Innovation and Universities, Spain (BES-2017-081850). Authors acknowledge the support from the Economy and Knowledge Department of the Catalan Government through the Consolidated Research Group 'Fluvial Dynamics Research Group' -RIUS (2017 SGR 459).

Acknowledgments:

ENDESA S.A. provided hydrological data and access to facilities during fieldwork for which authors are indebted. We thank Mark Smith for the revision of the first version of the manuscript and the members of the Fluvial Dynamics Research Group for the field assistance provided. This manuscript has benefited of all comments and suggestions received by three anonymous referees.

Conflicts of Interest:
The authors declare no conflict of interest.

REFERENCES

Batalla, R.J. and **Vericat, D.** (2009) Hydrological and sediment transport dynamics of flushing flows: Implications for management in large Mediterranean Rivers. *River Res. Appl.*, **25**, 297–314. DOI:10.1002/rra.1160

Batalla, R.J., **Vericat, D.**, **Gibbins, C.N.** and **Garcia, C.** (2010) Incipient bed-material motion in a gravel-bed river: field observations and measurements. *US Geol. Surv. Sci. Investig. Rep*, **5091**, 15. https://pubs.usgs.gov/sir/2010/5091/papers/Batalla.pdf

Bruno, M.C., **Maiolini, B.**, **Carolli, M.** and **Silveri, L.** (2009) Impact of hydropeaking on hyporheic invertebrates in an Alpine stream (Trentino, Italy). *Annales de Limnologie - International Journal of Limnology*, **45**, 157–170. DOI:10.1051/limn/2009018

Buendia, C., **Sabater, S.**, **Palau, A.**, **Batalla, R.J.** and **Marcé, R.** (2015) Using equilibrium temperature to assess thermal disturbances in rivers: Detecting Thermal Effects of Hydraulic Infrastructures. *Hydrological Processes*, **29**, 4350–4360. DOI:10.1002/hyp.10489

Bunte, K. and **Abt, S.R.** (2001) Sampling surface and subsurface particle-size distributions in wadable gravel-and cobble-bed streams for analyses in sediment transport, hydraulics, and streambed monitoring. *U.S. Department of Agriculture, Forest Service, Rocky Mountain Research Station*, Ft. Collins, CO. DOI:10.2737/RMRS-GTR-74

Carson, M.A. and **Griffiths, G.A.** (1987) BEDLOAD TRANSPORT IN GRAVEL CHANNELS. *Journal of Hydrology (New Zealand)*, **26**, 1–151. http://www.jstor.org/stable/43944586

Casas-Mulet, R., **Alfredsen, K.**, **Hamududu, B.** and **Timalsina, N.P.** (2015) The effects of hydropeaking on hyporheic interactions based on field experiments. *Hydrol Process.* DOI:10.1002/hyp.10264

Ceola, S., **Hödl, I.**, **Adlboller, M.**, **Singer, G.**, **Bertuzzo, E.**, **Mari, L.**, **Botter, G.**, **Waringer, J.**, **Battin, T.J.** and **Rinaldo, A.** (2013) Hydrologic Variability Affects Invertebrate Grazing on Phototrophic Biofilms in Stream Microcosms. *PLoS ONE*, **8**, e60629. DOI:10.1371/journal.pone.0060629

Céréghino, R., **Cugny, P.** and **Lavandier, P.** (2002) Influence of Intermittent Hydropeaking on the Longitudinal Zonation Patterns of Benthic Invertebrates in a Mountain Stream. *Int. Rev. Hydrobiol.*, **87**, 47. DOI:10.1002/1522-2632(200201)87:1<47::AID-IROH47>3.0.CO;2-9

Church (2006) BED MATERIAL TRANSPORT AND THE MORPHOLOGY OF ALLUVIAL RIVER CHANNELS. *Annual Review of Earth and Planetary Sciences*, **34**, 325–354. DOI:10.1146/annurev.earth.33.092203.122721

Church, M.A., **McLean, D.G.** and **Wolcott, J.F.** (1987) River bed gravels: Sampling and analysis. In: John willey & son (Ed. C. Thorne, J.C. Bathurst, and R.D. Hey), *J. Wiley*, New York, NY, USA, 43–88. ,https://doi.org/10.1002/esp.3290140809

Church, M. and **Hassan, M.A.** (2002) Mobility of bed material in Harris Creek: MOBILITY OF BED MATERIAL IN HARRIS CREEK. *Water Resour. Res.*, **38**, 19-1-19-12. DOI:10.1029/2001WR000753

Cushman, R.M. (1985) Review of Ecological Effects of Rapidly Varying Flows Downstream from Hydroelectric Facilities. *North American Journal of Fisheries Management*, **5**, 330–339. DOI:10.1577/1548-8659(1985)5<330:ROEEOR>2.0.CO;2

De Vincenzo, A., **Jacopo Molino, A.**, **Molino, B.** and **Scorpio, V.** (2017) Reservoir rehabilitation: The new methodological approach of Economic Environmental Defence. *International Journal of Sediment Research*, **32**, 288–294. DOI:10.1016/j.ijsrc.2016.05.007

Egiazaroff, I.V. (1965) Calculation of nonuniform sediment concentrations. *J. Hydraul. Div. Am. Soc. Civ. Eng*, **91**, 225–247. DOI:10.1061/jyceaj.0001277

Folk, R.L. and **Ward, W.C.** (1957) Brazos River bar [Texas]; a study in the significance of grain size parameters. *Journal of Sedimentary Research*, 3–26. DOI: https://doi.org/10.1306/74D70646-2B21-11D7-8648000102C1865D

Frutiger, A. (2004) Ecological impacts of hydroelectric power production on the River Ticino. Part 1: Thermal effects. *Archiv für Hydrobiologie*, **159**, 43–56. DOI:10.1127/0003-9136/2004/0159-0043

Garcia, C., **Cohen, H.**, **Reid, I.**, **Rovira, A.**, **Úbeda, X.** and **Laronne, J.B.** (2007) Processes of initiation of motion leading to bedload transport in gravel-bed rivers. *Geophysical Research Letters*, **34**, 2006GL028865. DOI:10.1029/2006GL028865

Garcia, C., **Laronne, J.B.** and **Sala, M.** (1999) Variable source areas of bedload in a gravel-bed stream. *Journal of Sedimentary Research*, **69**, 27–31. DOI:10.2110/jsr.69.27

Gibbins, C., **Vericat, D.** and **Batalla, R.J.** (2007) When is stream invertebrate drift catastrophic? The role of hydraulics and sediment transport in initiating drift during flood events. *Freshwater Biol*, **52**, 2369–2384. DOI:10.1111/j.1365-2427.2007.01858.x

Gordon, N., **McMahon, T.**, **Finlayson, B.**, **Gippel, C.** and **Nathan, R.** (2004) Stream Hydrology. An Introduction for Ecologists. 446 pp.

Gore, J.A. (1996) Discharge Measurements and Streamflow Analysis. In: 2nd edn. (Ed. F.R. Hauer and G.A. Lamberti), *Accademic Press*, Cambridge, MA, USA, 53–74.

Gostner, W., **Lucarelli, C.**, **Theiner, D.**, **Kager, A.**, **Premstaller, G.** and **Schleiss, A.J.** (2011) A holistic approach to reduce negative impacts of hydropeaking. *Dams Reserv. Chang. Chall.*, 857–865.

Heggenes, J., **Omholt, P.K.**, **Kristiansen, J.R.**, **Sageie, J.**, **Økland, F.**, **Dokk, J.G.** and **Beere, M.C.** (2007) Movements by wild brown trout in a boreal river: response to habitat and flow contrasts. *Fisheries Management and Ecology*, **14**, 333–342. DOI:10.1111/j.1365-2400.2007.00559.x

Herrero, A., **Buendía, C.**, **Bussi, G.**, **Sabater, S.**, **Vericat, D.**, **Palau, A.** and **Batalla, R.J.** (2017) Modeling the sedimentary response of a large Pyrenean basin to global change. *Journal of Soils and Sediments*, **17**, 2677–2690. DOI:10.1007/s11368-017-1684-6

Jowett, I.G. (2003) Hydraulic constraints on habitat suitability for benthic invertebrates in gravel-bed rivers. *River Research and Applications*, **19**, 495–507. DOI:10.1002/rra.734

Kondolf, G.M. (1997) Hungry Water: Effects of Dams and Gravel Mining on River Channels. *Environmental Management*, **21**, 533–551. DOI:10.1007/s002679900048

Kondolf, G.M. and **Wolman, M.G.** (1993) The sizes of salmonid spawning gravels. *Water Resources Research*, **29**, 2275–2285. DOI:10.1029/93WR00402

Lagarrigue, T. (2002) Diel and seasonal variations in brown trout (Salmo trutta) feeding patterns and relationship with invertebrate drift under natural and hydropeaking conditions in a mountain stream. *Aquatic Living Resources*, **15**, 129–137. DOI:10.1016/S0990-7440(02)01152-X

Lauters, F., **Lavandier, P.**, **Lim, P.**, **Sabaton, C.** and **Belaud, A.** (1996) INFLUENCE OF HYDROPEAKING ON INVERTEBRATES AND THEIR RELATIONSHIP WITH FISH FEEDING HABITS IN A PYRENEAN RIVER. *Regulated Rivers: Research & Management*, **12**, 563–573. DOI:10.1002/(SICI)1099-1646(199611)12:6<563::AID-RRR380>3.0.CO;2-M

Liébault, F., **Bellot, H.**, **Chapuis, M.**, **Klotz, S.** and **Deschâtres, M.** (2012) Bedload tracing in a high-sediment-load mountain stream. *Earth Surface Processes and Landforms*, **37**, 385–399. DOI:10.1002/esp.2245

Liebig, H., **Céréghino, R.**, **Lim, P.**, **Belaud, A.** and **Lek, S.** (1999) Impact of hydropeaking on the abundance of juvenile brown trout in a Pyrenean stream. *Fundamental and Applied Limnology*, **144**, 439–454. DOI:10.1127/archiv-hydrobiol/144/1999/439

Lisle, T.E. and **Madej, M.A.** (1992) Spatial variation in a channel with high sediment supply. In: (Ed. P. Billi, R.D. Hey, C.R. Thorne, and P. Tacconi), *John Willey*, Hoboken, NJ, USA, 277–291.

Llena, M., **Vericat, D.**, **Martínez-Casasnovas, J.A.** and **Smith, M.W.** (2020) Geomorphic adjustments to multi-scale disturbances in a mountain river: A century of observations. *CATENA*, **192**, 104584. DOI:10.1016/j.catena.2020.104584

Marteau, B., **Batalla, R.J.**, **Vericat, D.** and **Gibbins, C.** (2018) Asynchronicity of fine sediment supply and its effects on transport and storage in a regulated river. *J. Soils Sediments*, **18**, 2614–2633. DOI:10.1007/s11368-017-1911-1

Parker, G. and **Klingeman, P.C.** (1982) On why gravel bed streams are paved. *Water Resources Research*, **18**, 1409–1423. DOI:10.1029/WR018i005p01409

Petit, F., **Gob, F.**, **Houbrechts, G.** and **Assani, A.A.** (2005) Critical specific stream power in gravel-bed rivers. *Geomorphology*, **69**, 92–101. DOI:10.1016/j.geomorph.2004.12.004

Rempel, L.L. and **Church, M.** (2009) Physical and ecological response to disturbance by gravel mining in a large alluvial river. *Canadian Journal of Fisheries and Aquatic Sciences*, **66**, 52–71. DOI:10.1139/F08-184

Rice, S. and **Church, M.** (1996) Sampling surficial fluvial gravels; the precision of size distribution percentile sediments. *Journal of Sedimentary Research*, **66**, 654–665. DOI:10.2110/jsr.66.654

Schmutz, S., **Bakken, T.H.**, **Friedrich, T.**, **Greimel, F.**, **Harby, A.**, **Jungwirth, M.**, **Melcher, A.**, **Unfer, G.** and **Zeiringer, B.** (2015) Response of fish communities to hydrological and morphological alterations in hydropeaking rivers of austria. River Research and Applications. DOI:10.1002/rra.2795

Schwendel, A.C., **Death, R.G.** and **Fuller, I.C.** (2010) The assessment of shear stress and bed stability in stream ecology. *Freshwater Biology*, **55**, 261–281. DOI: 10.1111/j.1365-2427.2009.02293.x

Spieker, R. and **Ergenzinger, P.** (1990) New developments in measuring bed load by the magnetic tracer technique. In: (Ed. D.E. Walling, A. Yair, and S. Berkowicz), *IAHS*, Wallingford, UK, 169–178.

Sutherland, A. (1992) Grain sorting seminar. *Proc., Int. Association of Hydraulic, Research Int.*, ETH,Zurich. Switzerland, 117,

Vericat, D. and **Batalla, R.J.** (2006) Sediment transport in a large impounded river: The lower Ebro, NE Iberian Peninsula. *Geomorphology*, **79**, 72–92. DOI:10.1016/j.geomorph.2005.09.017

Vericat, D., **Batalla, R.J.** and **Garcia, C.** (2006) Breakup and reestablishment of the armour layer in a large gravel-bed river below dams: The lower Ebro. *Geomorphology*, **76**, 122–136. DOI:10.1016/j.geomorph.2005.10.005

Vericat, D., **Batalla, R.J.** and **Garcia, C.** (2008a) Bed-material mobility in a large river below dams. *Geodin. Acta*, **21**, 3–10. DOI:10.3166/ga.21.3-10

Vericat, D., **Batalla, R.J.** and **Gibbins, C.N.** (2008b) Sediment entrainment and depletion from patches of fine material in a gravel-bed river. *Water Resour. Res.*, **44**, 1–15. DOI:10.1029/2008WR007028

White, R.W. (1982) Transport of graded gravel bed-material. In: (Ed. J.C. Hey, J.C. Bathurst, and C.R. Thorne), *John Wiley*, New York, 181–223.

Wilcock, P.R. and **DeTemple, B.T.** (2005) Persistence of armor layers in gravel-bed streams. *Geophysical Research Letters*, **32**, 2004GL021772. DOI:10.1029/2004GL021772

Wolman, M.G. (1954) A method of sampling coarse river-bed material. *Trans. Am. Geophys. Union*, **35**, 951. DOI:10.1029/TR035i006p00951

Yang, S.L., **Zhang, J.** and **Xu, X.J.** (2007) Influence of the Three Gorges Dam on downstream delivery of sediment and its environmental implications, Yangtze River. *Geophysical Research Letters*, **34**, 2007GL029472. DOI:10.1029/2007GL029472

Annex B

PhotoMOB. An automated tool for fractional bed mobility analysis in gravel bed rivers

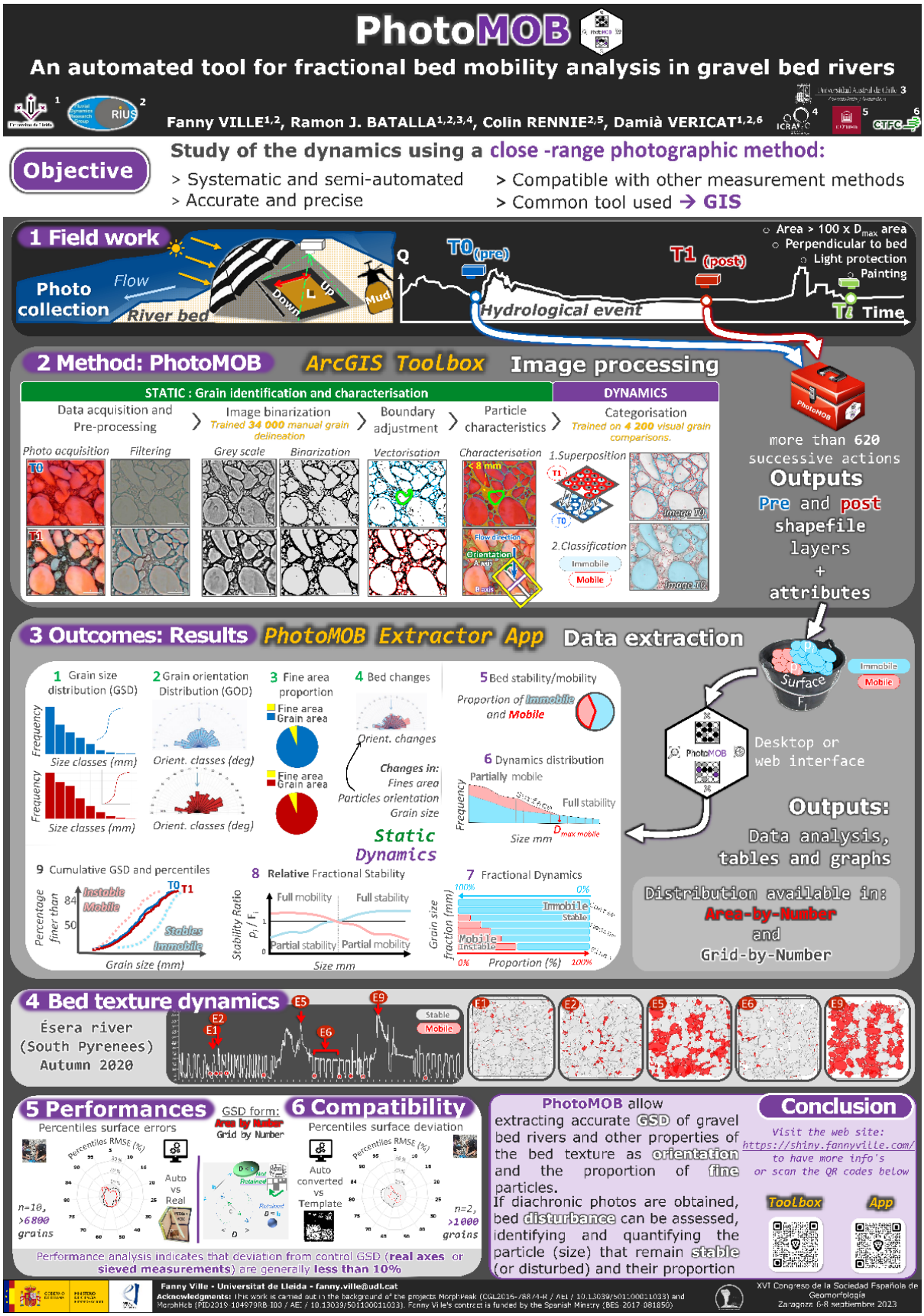

Figure B.1: Poster presented at the XVI Congreso de la Sociedad Española de Geomorfología (6 - 8 September 2023, Zaragoza, Spain)

Annex C

Longitudinal organization of macrobenthos community in a reach affected by hydropeaking

LONGITUDINAL ORGANITZATION OF MACROBENTHOS COMMUNITY IN A REACH AFFECTED BY HYDROPEAKING

Palau-Nadal, A., Ville, F. , Vericat, D. , Palau-Ibars, A.

[1] Fluvial Dynamics Research Group (RIUS), Department of Environment and Soil Sciences, University of Lleida.

1. STUDY HYPOTHESIS

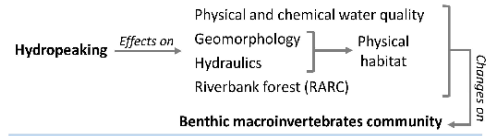

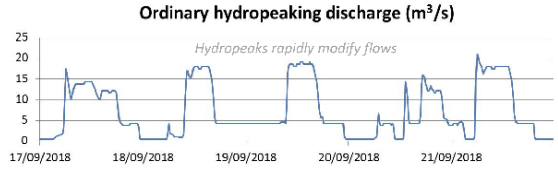

Hydropeaking generate negative impacts in benthic macroinvertebrate community in terms of composition, density, biomass and ecological quality. Major impacts are expected in rivers sections immediately downstream hydropower plants.

2. METHODS

- **Study area/section**: The Ésera River (Ebro Basin, NE Spain) has a nivopluvial hydrological regime. A river reach of 17.5 km long has been selected downstream the Campo Hydropower Plant (680 m a.s.l.).
- **Sampling design**: Fieldwork was carried out in September 2018 under an average discharge of 7.2 m^3/s (= Q_{280}). A total of 5 type of variables were measured in 6 sections (P1-P6) along the study reach: (1) Physical and chemical water quality; (2) Hydraulics; (3) Geomorphology; (4) Riparian conditions & (5) Composition and structure of benthic macroinvertebrates community: density, biomass, ecological quality (IBMWP Index), diversity (*K*-Margalef Index) and trophic functions (Shredders, Collectors, Scrapers and Predators).

3. PRELIMINARY RESULTS

- **Physical and chemical water quality** variables indicate that hydropeaking and tributary effects are not limiting to the benthic community. There is not a remarkable thermic impact (thermopeaking).
- Hydropeaking impacts on fluvial **geomorphology.** Surface median particle size (D_{50}) tends to decrease downstream the studied reach, from 113 to 74. This implies that flow competence increases downstream, i.e. the peak of the hydropeaks is able to entrain particles in the lowermost sections. Sediment contribution supply from tributaries determines a significant decrease of the D_{50} in P5.
- **Hydraulic** conditions change along the studied river reach; **riverbank forests structure** (measured through the RARC; Rapid Appraisal of Riparian Conditions) and **ecological quality** decreases downstream, with a minimum value in P2 and P3, respectively.

Low flow (2-3m³/s)					
Sections	Velocity (m/s)	Depth (m)	Sections	Velocity (m/s)	Depth (m)
P1	0.11	0.28	P5	0.24	0.50
P2	0.45	0.20	P6	0.30	0.33

RARC values			
Sections		Sections	
P1	36	P4	26
P2	25	P5	27
P3	29	P6	26

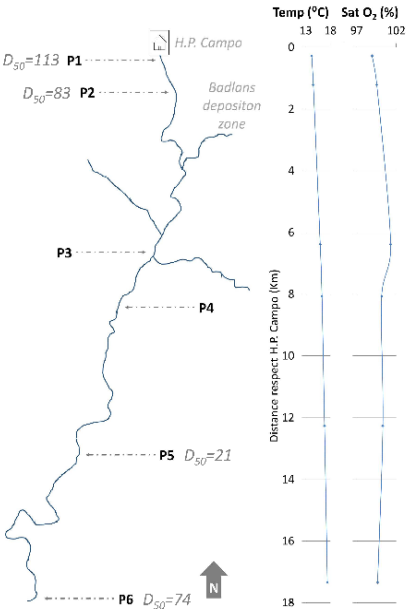

Study area, temperature and oxygen saturation in the 6 study sections.

- Changes in **benthic macroinvertebrate community** can be summarized as follows. Hydropeaking impacts negatively on some characteristics as density and biomass, which tend to increase downstream. Other aspects as the ecological quality (IBMWP) remains high and relatively stable (90-120), and *K*-Margalef diversity Index decreases because the density increase, while the number of taxa almost does not change from P1 to P6. The Shredders/Scrapers ratio not varies between P1 (under more adverse conditions) and P6 (the furthest section), although it shows appreciable spatial changes along the reach.
- The **Pearson correlation coefficient (r)** shows significant positive correlations ($p < 0.05$) between density *vs* biomass and *K*-diversity Index *vs* Shredders/Scrapers ratio; and negative correlations between *K*-diversity *vs* density. In terms of the impact of hydropeaking, data indicates that the macrobenthos loses diversity by the decrease of the Shredders/Scrapers ratio.

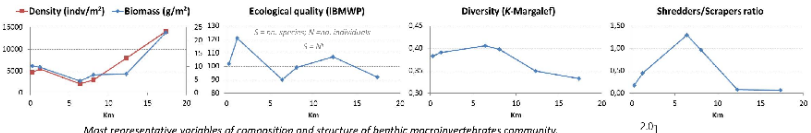

Most representative variables of composition and structure of benthic macroinvertebrates community.

- The first axis of the **PCA** (62.1% variance) indicates that density and biomass increase with the distance from the Hydropower Plant, while the Shredders/Scrapers ratio decreases in the same direction. The RARC, which should increase with Shredders/Scrapers ratio, does not seem a good indicator. The second axis (26.4% variance), indicates an inverse relationship between D_{50} and distance, which means that the river bed is more armored and thus stable in the area near than Hydropower Plant. The relationship between D_{50} and Shredders/Scrapers ratio also shown an inverse correlation, which indicate that the larger is D_{50} the better the conditions of colonization for the scrapers.

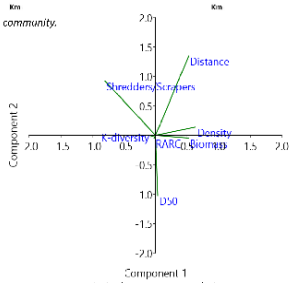

Principal Component Analysis.

4. CONCLUSIONS

- The impact of hydropeaking on the benthic macroinvertebrates community is not easy to measure. Demographic variables seem to respond negatively (density and biomass) and other more structural characteristic (diversity and ecological quality) do not reflect negative effects. Taking into account the conjectural character of the demographic variables (high spatial-temporal variability), the correct determination of impact oh hydropeaking probably should be by the study of the structural characteristics of the community and particularly in relation to the Shredders/Scrapers ratio that integrates the role of the substrate, channel-riverbank conditions, the availability of CPOM (Coarse Particulate Organic Matter) and, definitively, the autotrophic or heterotrophic character of the river. Some indices designed to measure the quality of the riverbank forest do not seem adequate to establish the important role which play in benthic macroinvertebrate communities.

CONTACT: palaunadal@macs.udl.cat

Acknowledgments: This research was developed in the frame of the project MorphPeak (CGL2016-78874-R) funded by the Spanish Ministry of Economy and Competitiveness and the European Regional Development Fund Scheme. Authors acknowledge the support from the Economy and Knowledge Department of the Catalan Government through Consolidated Research Group (RIUS 2017 SGR 459). The first author has a PhD grant funded by the University of Lleida and the second by the Ministry of Economy and Competitiveness (BES-2017-081850).

Figure C.1: Poster presented at the Limnos congress (2019, Brazil)

End cover photo: Ésera river downstream Campo Dam during hydropeak,

August 2019.

Author: Fanny Ville

Many mountain rivers are subjected to hydropeaks, rapid water releases from hydroelectric power stations for electric production. This thesis focuses on the temporal and spatial (i.e. longitudinal) hydrological characterization of artificial fluctuations and their effects on bed mobility dynamics in two contrasting river systems. Two Pyrenean Mountain river segments were studied: a 12 km segment in the Upper Cinca and a 18.5 km segment in the Upper Ésera. The development of the PhotoMOB tool, which makes it possible to obtain the size and dynamics of particles from consecutive photos of the bed, has enabled detailed observations and analysis of the competence of hydropeaks and floods. The analyzed hydropeaks did not lead to significant changes in the bed grain size distribution at the event scale but they could cause marginal mobility in the ramping area up to entrain relatively coarse grain sizes.